Massive forest study offers hope for a burning West p. 1300

Rewarding academics for innovation and entrepreneurship p. 1312

Newfound CRISPR enzyme targets RNA p. 1349

Science

$15
17 SEPTEMBER 2021
science.org

AAAS



CRYOFORGED TITANIUM

Nanotwins enhance strength and ductility p. 1363



EMPOWER WITH EVIDENCE

AAAS | ANNUAL MEETING

The hybrid 2022 AAAS Annual Meeting will convene in Philadelphia February 17-20 and Online. Registration and meeting program available this Fall.



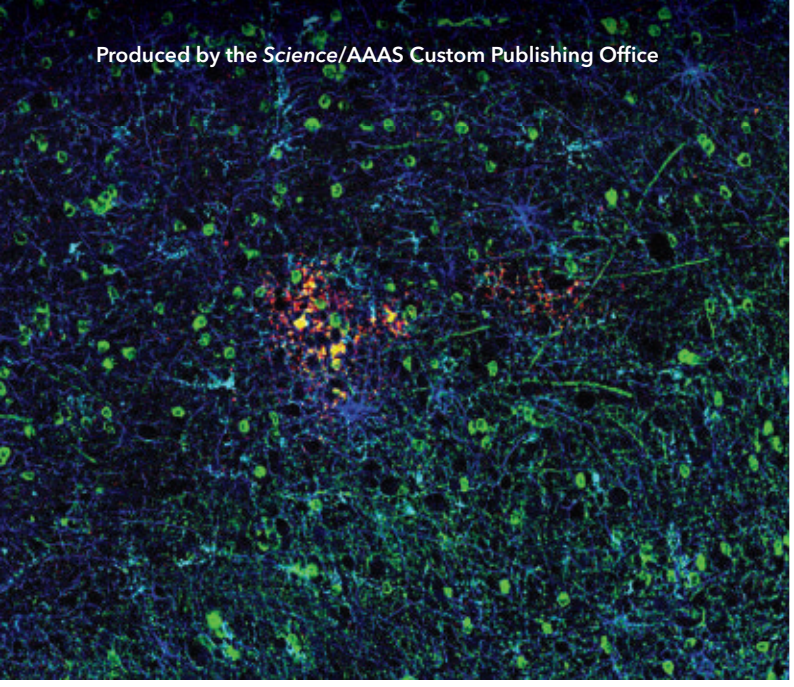
Susan G. Amara, Ph.D.
President, AAAS
Chair, 2022 Annual Meeting

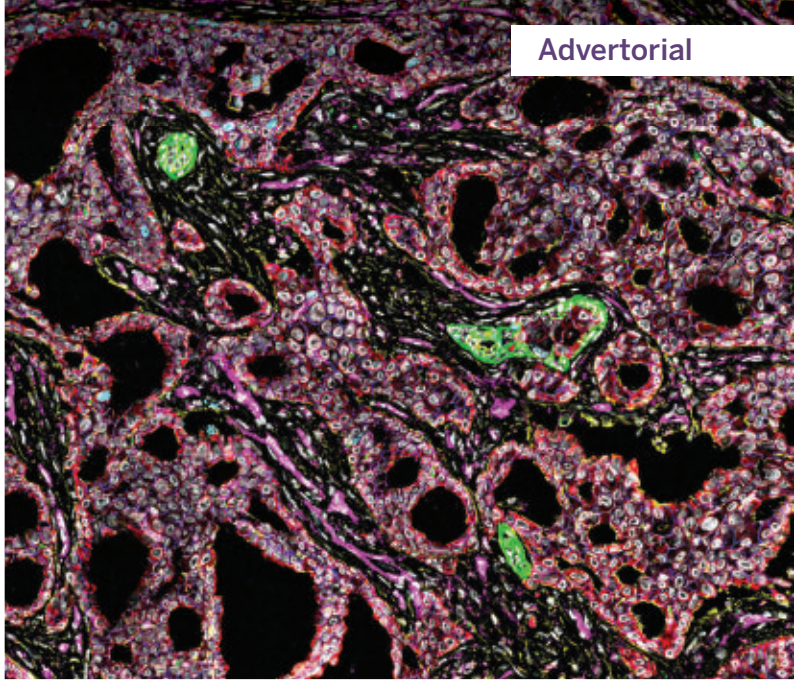
Philly, here we come!

We invite those who are comfortable doing so to join us February 17-20 in Philadelphia. To ensure that as many people as possible are able to participate in the Scientific Sessions, they will be entirely virtual. Speakers can participate from wherever they feel comfortable, including Philly. For those who join us in Philly, we'll have Community Viewing Pods where attendees can view the Scientific Sessions with friends and colleagues, enabling those spontaneous hallway connections and conversations that we've all missed.

After a year of attending virtual convenings, we've come to appreciate many benefits, but we still long for the things that can only happen in person. Impact those who empower with evidence—by sponsoring the world's largest interdisciplinary science meeting.

aaas.org/meetings | #AAASmtg





Akoya's CODEX system created images of the brain tissue of a patient with Alzheimer's disease (**left**) and breast tissue of a patient with ductal adenocarcinoma (**right**).

A new era of anatomy: Adding context one cell at a time

Multitasking marvel: Akoya Biosciences' CODEX technology lets scientists analyze dozens of proteins in many cells–all at once.

Going beyond merely providing a description of tissues and their locations, today's spatial biology analyzes structures down to the single-cell level. Molecular markers further distinguish cells based on the surface proteins they carry.

"Biologically speaking, it's very important to understand different cell types at the single-cell level," says Kai Tan, professor of pediatrics at the Children's Hospital of Philadelphia and the Perelman School of Medicine at the University of Pennsylvania. This understanding can include determining the kinds of proteins on or in specific cells, as well as the genes that produce them. "Not long ago, we didn't have resources to look at those kinds of things," Tan says.

Today, systems like CODEX (CO-Detection by indEXing) from Akoya Biosciences can track more than 40 protein markers in single cells. Plus, the samples can be fresh frozen or formalin-fixed, paraffin-embedded (FFPE). This technology has significantly impacted the study of spatial biology.

Cartography of cancer

In 2016, the U.S. Congress funded the Cancer Moonshot initiative to speed up research in oncology. Part of the funding supports the Human Tumor Atlas Network (HTAN), which is building 3D maps of human cancers. Tan and his colleagues are working on high-risk pediatric cancers, including gliomas and neuroblastomas.

"Using single-cell techniques, including spatial-resolving technology like Akoya's, we are generating a reference map for these cancers," Tan explains. This work includes determining the states of specific cells in and around tumors. For example, a T cell's proteins might change when it's near a tumor. Knowing the states of these cells, Tan says, "gives scientists a lot more variety to keep track of in tumors."

Building these cancer atlases requires human samples. "So, biobanking is crucial," Tan explains. "It's really teamwork among physicians, surgeons, and pathologists." He adds, "You want to make sure you're getting the best samples that you can."

More muscle power

At Stanford University School of Medicine, postdoctoral fellow Will Wang and his colleagues study the spatial biology of skeletal muscles. This work involves various technologies, including CODEX. He says that this platform "really facilitates our understanding of how cells are organized within a tissue." This organization arises from "multiple cell types and functional subsets of those cell types that make up a tissue," Wang explains.

Before technologies like CODEX, scientists could only study a couple of cell types at a time. "Now, we're moving into more molecular understandings of different cell types, driven by single-cell technology," Wang notes. Today, scientists can compare healthy and diseased tissue to "understand the changes at the single-cell level [that tell us] how a disease progresses or how a treatment works," he explains. This level of spatial knowledge provides new opportunities in treatments. "You can really drill down to discovering new targets, overcoming side effects, or designing modifications to therapies that make them more targeted," Wang states.

With CODEX, Wang and his colleagues can analyze an entire mouse muscle. In one project, he simultaneously tracked 30 different cell types. "So in a single piece of tissue, you can see how these cell types either colocalize or are dispersed," he says. "You can look for common associations between cell types to predict how these cells work together to perform a biological process."

Making a difference in differential diagnoses

One day, Tan envisions single-cell platforms being employed in point-of-care medicine. "There are commercial technologies being used in clinics, like histochemistry, to look at two or three markers for diagnostics," Tan says, "but an easy-to-use and robust spatial-imaging platform could increase that to 10 or 20 markers, which would significantly change how pathologists gather information to make a diagnosis." With breakthroughs such as this on the horizon, it's clear that single-cell analyses will advance basic biology and medicine even more in the future.

Sponsored by

AKOYA BIOSCIENCES®
THE SPATIAL BIOLOGY COMPANY®

IMAGES PROVIDED BY AKOYA BIOSCIENCES



A pipette masterpiece celebrates its 60th birthday

60 years ago, Eppendorf launched the world's first industrially manufactured piston-stroke pipette, changing laboratory work forever.

In 1961, Eppendorf introduced the »Marburg Pipette« - a completely new instrument for handling liquids in the laboratory at that time. The Marburg pipette already had the same basic elements that characterize modern piston-stroke pipettes: a spring-loaded piston that stops precisely at a set volume level, and a removable pipette tip made of plastic. This innovation made it possible to pipette liquids in the microliter range easily, reliably and safely for the very first time. Together with the first Eppendorf Tube® (»Eppi®«), a microliter centrifuge, and a thermomixer, the Marburg pipette formed the Eppendorf microliter system - a revolutionary toolset that paved the way for modern clinical analysis and molecular biology research.

But the story does not end here. Over the past six decades, Eppendorf's commitment to providing the best liquid handling solutions has repeatedly led to innovative designs that have made laboratory work ever more efficient, safe, and generally better.

Today, Eppendorf customers can choose from a wide range of instruments, consumables and services to meet their liquid handling needs and further drive the efficiency of their research.












Pipettes no longer suck
Until the 1950s, scientists pipetted liquids by aspirating them into thin glass tubes by mouth - an unreliable and sometimes even dangerous technique. Frustrated by the inadequacies of mouth-pipetting, German physician Heinrich Schnitger constructed a "device for the rapid and accurate pipetting of small quantities of liquid" using a converted tuberculin syringe and applied for a patent in 1958. Eppendorf was the first to recognize its importance and further developed it into the »Marburg Pipette« by 1961.

Ready, set, pipette!
The global dissemination of pipettes picked up speed between 1961 and the 1980s, bringing with it new challenges and new developments. For example, the microplate gradually gained acceptance for various assays and analyses, and the single-channel pipette proved to be a bottleneck for efficient dispensing. The solution: multi-channel pipettes, such as the Titerman pipette launched by Eppendorf in 1993. With the ability to dispense up to 12 reagents simultaneously, the Titerman was the optimal complement to the microplate.

Think of your thumbs: the ergonomics of pipettes
Eppendorf considered clever ergonomic design as early as the 1970s, and always had the user in mind when developing new products. With the introduction of the Eppendorf PhysioCare Concept® in 2003, the company anchored a holistic ergonomics concept in product development. A result of this time are also the first electronic pipettes, which contribute to safer work with revolutionary speed, accuracy and precision to this day.

The future of pipettes is now
Demand for innovative laboratory designs is increasing as the fast and reliable processing of high workloads becomes more and more important. One example is high-throughput analysis, where automated pipetting systems such as the epMotion® systems from Eppendorf are used. Another component is the increasing digitalization of laboratories, where networked pipettes will play an important role in saving more time, reducing repetitive tasks and providing more accurate results.



Celebrate with us!

We have compiled all the experience we have gained over the last 60 years and created a comprehensive guidebook with many tips & tricks on choosing the right pipette and correct pipetting techniques.

Learn more about the Pipette Anniversary and download your free eBook copy here:
www.eppendorf.com/60-Years

CONTENTS

17 SEPTEMBER 2021 • VOLUME 373 • ISSUE 6561



1300

Researchers are working to lower the odds of intense fires, such as this 2015 blaze in Oregon.

PHOTO: LES ZAITZ/THE OREGONIAN/OREGONLIVE VIA AP

NEWS

IN BRIEF

1290 News at a glance

IN DEPTH

1293 Schools begin mass testing with vexing questions
Scientific uncertainties, access, and logistics are hurdles to routine screening
By J. Couzin-Frankel

1294 'Zero COVID' countries seek exit strategies
They successfully kept the the virus at bay. Now, some are gingerly opening up
By D. Normile

1296 Forget oil or water. Icelandic drillers seek magma
Probe of volcano could reveal magma composition and guide early warning systems
By P. Voosen

1297 Vaccine equity hopes dashed
Latest forecast slashes this year's global supply by 25% *By J. Cohen*

1298 Climate policies loom large in German election
Chancellor Angela Merkel, a former scientist, will cede power *By G. Vogel*

1299 U.S. judge acquits researcher charged with hiding China ties
Decision to free former engineering professor Anming Hu could have implications for other China Initiative cases *By J. Mervis*

FEATURES

1300 Clearing the tinderbox
As the climate warms, a huge forest experiment aims to reduce wildfire risk and find common ground between loggers and environmentalists *By W. Cornwall*

INSIGHTS

PERSPECTIVES

1304 Human microphysiological systems for drug development
Organs-on-chips could be used to assess drug efficacy and support personalized medicine
By A. Roth and MPS-WS Berlin 2019

1306 Opposing roles of the immune system in tumors
Inflammation promotes early tumorigenesis but must be evaded as tumors progress
By W. J. Ho and L. D. Wood
RESEARCH ARTICLES pp. 1326 & 1327

1308 A silver assist for microbial fuel cell power
Silver nanoparticles in *Shewanella* membranes boost electron transfer to graphene electrodes
By E. M. Gaffney and S. D. Minteer
RESEARCH ARTICLE p. 1336

1309 An electron walks into a quantum bar...
Quantum electron-light interaction may find use in microscopy applications
By F. Carbone
RESEARCH ARTICLE p. 1324

1310 Homogeneous neuromorphic hardware
Bifunctional ferroelectric transistors enable collocation of memory and processing *By F. Rao and X. Tao*
RESEARCH ARTICLE p. 1353

POLICY FORUM

1312 Innovation, entrepreneurship, promotion, and tenure
Academic incentives must reward broader societal impacts
By R. G. Carter et al.

BOOKS *ET AL.*

1315 Rethinking resilience
A flexible mindset can help us bounce back after adversity *By J. Gruber*

1316 Common ground and the climate crisis
Invoking shared values can help convince skeptics of the need to mitigate climate change
By M. Aczel

LETTERS

1317 Save the white-bellied heron from extinction
By G. Maheswaran et al.

1317 A flood of disaster response challenges
By M. Dietze and U. Ozturk

1318 Institutions' role in postpandemic support
By A. de Morree and A. Alvarez

1318 Technical Comment abstracts

RESEARCH

IN BRIEF

1319 From *Science* and other journals

REVIEW

1322 Social evolution
Social evolution in mammals
T. Clutton-Brock
REVIEW SUMMARY; FOR FULL TEXT: DOI.ORG/10.1126/SCIENCE.ABC9699



RESEARCH ARTICLES

1323 Immunology
Serum amyloid A delivers retinol to intestinal myeloid cells to promote adaptive immunity
Y.-J. Bang et al.
RESEARCH ARTICLE SUMMARY; FOR FULL TEXT: DOI.ORG/10.1126/SCIENCE.ABF9232

1324 Quantum optics
Imprinting the quantum statistics of photons on free electrons *R. Dahan* et al.
RESEARCH ARTICLE SUMMARY; FOR FULL TEXT: DOI.ORG/10.1126/SCIENCE.ABJ7128
PERSPECTIVE p. 1309

1325 Coronavirus
Immune correlates of protection by mRNA-1273 vaccine against SARS-CoV-2 in honhuman primates *K. S. Corbett* et al.
RESEARCH ARTICLE SUMMARY; FOR FULL TEXT: DOI.ORG/10.1126/SCIENCE.ABJ0299
REPORT p. 1372

CANCER

1326 Epithelial memory of inflammation limits tissue damage while promoting pancreatic tumorigenesis
E. Del Poggetto et al.
RESEARCH ARTICLE SUMMARY; FOR FULL TEXT: DOI.ORG/10.1126/SCIENCE.ABJ0486

1327 The adaptive immune system is a major driver of selection for tumor suppressor gene inactivation
T. D. Martin et al.
PERSPECTIVE p. 1306

1336 Microbial fuel cells
Silver nanoparticles boost charge-extraction efficiency in *Shewanella* mircrobial fuel cells
B. Cao et al.
PERSPECTIVE p. 1308

REPORTS

1340 Quantum gases
Observation of fragmentation of a spinor Bose-Einstein condensate *B. Evrard* et al.

1344 Fluid mechanics
Three-dimensional capillary ratchet-induced liquid directional steering *S. Feng* et al.

1349 CRISPR
The gRAMP-CRISPR-Cas effector is an RNA endonuclease complexed with a capase-like peptidase *S. P. B. van Beljouw* et al.

1353 Neuromorphic chips
2D materials–based homogeneous transistor-memory architecture for neuromorphic hardware *L. Tong* et al.
PERSPECTIVE p. 1310

1359 Quantum gases
Observation of a superradiant quantum phase transition in an intracavity degenerate Fermi gas
X. Zhang et al.

1363 Metallurgy
Cryoforged nanotwinned titanium with ultrahigh strength and ductility
S. Zhao et al.

1368 Paleobotany
Reproductive innovations and pulsed rise in plant complexity
A. B. Leslie et al.

1372 Coronavirus
Durability of mRNA-1273 vaccine–induced antibodies against SARS-CoV-2 variants
A. Pegu et al.
RESEARCH ARTICLE p. 1325

1377 Protein biogenesis
Structural insight into the SAM-mediated assembly of the mitochondrial TOM core complex
Q. Wang et al.

DEPARTMENTS

1285 Editorial
Climate science speaks: "Act now"
By Jane Lubchenco and John F. Kerry

1406 Working Life
On my own but not alone
By Nasreen Choudhury

ON THE COVER

False-color micrograph of pure titanium with a nanotwinned structure, where each color represents a region with an identical crystallographic orientation. The nanotwinned structure was produced via a multistep cryoforging process carried out in liquid nitrogen, followed by annealing at 400°C. As a result, the processed material exhibits ultrahigh strength and ductility, especially at cryogenic temperatures. See page 1363.
Image: Shiteng Zhao



Science Staff 1284
GRC Supplement 1382
Science Careers 1392

IMAGE: ANDREW LESLIE

SCIENCE (ISSN 0036-8075) is published weekly on Friday, except last week in December, by the American Association for the Advancement of Science, 1200 New York Avenue, NW, Washington, DC 20005. Periodicals mail postage (publication No. 484460) paid at Washington, DC, and additional mailing offices. Copyright © 2021 by the American Association for the Advancement of Science. The title SCIENCE is a registered trademark of the AAAS. Domestic individual membership, including subscription (12 months): $165 ($74 allocated to subscription). Domestic institutional subscription (51 issues): $2148; Foreign postage extra: Air assist delivery: $98. First class, airmail, student, and emeritus rates on request. Canadian rates with GST available upon request, GST #125488122. Publications Mail Agreement Number 1069624. **Printed in the U.S.A.**
Change of address: Allow 4 weeks, giving old and new addresses and 8-digit account number. **Postmaster:** Send change of address to AAAS, P.O. Box 96178, Washington, DC 20090–6178. **Single-copy sales:** $15 each plus shipping and handling available from backissues.sciencemag.org; bulk rate on request. **Authorization to reproduce** material for internal or personal use under circumstances not falling within the fair use provisions of the Copyright Act can be obtained through the Copyright Clearance Center (CCC), www.copyright.com. The identification code for *Science* is 0036-8075. *Science* is indexed in the *Reader's Guide to Periodical Literature* and in several specialized indexes.

Science AAAS

Editor-in-Chief Holden Thorp, hthorp@aaas.org

Executive Editor Monica M. Bradford

Editors, Research Valda Vinson, Jake S. Yeston **Editor, Insights** Lisa D. Chong

DEPUTY EDITORS Julia Fahrenkamp-Uppenbrink (UK), Stella M. Hurtley (UK), Phillip D. Szuromi, Sacha Vignieri **SR. EDITORIAL FELLOW** Andrew M. Sugden (UK) **SR. EDITORS** Gemma Alderton (UK), Caroline Ash (UK), Brent Grocholski, Pamela J. Hines, Di Jiang, Marc S. Lavine (Canada), Yevgeniya Nusinovich, Ian S. Osborne (UK), Beverly A. Purnell, L. Bryan Ray, H. Jesse Smith, Keith T. Smith (UK), Jelena Stajic, Peter Stern (UK), Valerie B. Thompson, Brad Wible, Yuen Yiu, Laura M. Zahn **ASSOCIATE EDITORS** Michael A. Funk, Priscilla N. Kelly, Tage S. Rai, Seth Thomas Scanlon (UK), Yury V. Suleymanov **LETTERS EDITOR** Jennifer Sills **LEAD CONTENT PRODUCTION EDITORS** Harry Jach, Lauren Kmec **CONTENT PRODUCTION EDITORS** Amelia Beyna, Jeffrey E. Cook, Chris Filiatreau, Julia Haber-Katris, Nida Masiulis, Abigail Shashikanth, Suzanne M. White **SR. EDITORIAL COORDINATORS** Carolyn Kyle, Beverly Shields **EDITORIAL COORDINATORS** Aneera Dobbins, Joi S. Granger, Jeffrey Hearn, Lisa Johnson, Maryrose Madrid, Ope Martins, Shannon McMahon, Jerry Richardson, Hilary Stewart (UK), Alana Warnke, Alice Whaley (UK), Anita Wynn **PUBLICATIONS ASSISTANTS** Jeremy Dow, Alexander Kief, Ronmel Navas, Brian White **EXECUTIVE ASSISTANT** Jessica Slater **ASI DIRECTOR, OPERATIONS** Janet Clements (UK) **ASI SR. OFFICE ADMINISTRATOR** Jessica Waldock (UK)

News Editor Tim Appenzeller

NEWS MANAGING EDITOR John Travis **INTERNATIONAL EDITOR** Martin Enserink **DEPUTY NEWS EDITORS** Elizabeth Culotta, Lila Guterman, David Grimm, Eric Hand (Europe), David Malakoff **SR. CORRESPONDENTS** Daniel Clery (UK), Jon Cohen, Jeffrey Mervis, Elizabeth Pennisi **ASSOCIATE EDITORS** Jeffrey Brainard, Kelly Servick, Catherine Matacic **NEWS REPORTERS** Adrian Cho, Jennifer Couzin-Frankel, Jocelyn Kaiser, Rodrigo Pérez Ortega (Mexico City), Robert F. Service, Erik Stokstad, Paul Voosen, Meredith Wadman **INTERNS** Menna Ibrahim, Sofia Moutinho, Anil Oza, Alex Viveros **CONTRIBUTING CORRESPONDENTS** Warren Cornwall, Andrew Curry (Berlin), Ann Gibbons, Sam Kean, Eli Kintisch, Kai Kupferschmidt (Berlin), Andrew Lawler, Mitch Leslie, Eliot Marshall, Virginia Morell, Dennis Normile (Tokyo), Elisabeth Pain (Careers), Charles Piller, Michael Price, Tania Rabesandratana (Barcelona), Joshua Sokol, Emily Underwood, Gretchen Vogel (Berlin), Lizzie Wade (Mexico City) **CAREERS** Rachel Bernstein (Editor), Katie Langin (Associate Editor) **COPY EDITORS** Julia Cole (Senior Copy Editor), Morgan Everett, Cyra Master (Copy Chief) **ADMINISTRATIVE SUPPORT** Meagan Weiland

Creative Director Beth Rakouskas

DESIGN MANAGING EDITOR Marcy Atarod **GRAPHICS MANAGING EDITOR** Alberto Cuadra **PHOTOGRAPHY MANAGING EDITOR** William Douthitt **WEB STRATEGY MANAGER** Kara Estelle-Powers **MULTIMEDIA MANAGING PRODUCER** Joel Goldberg **DESIGN EDITOR** Chrystal Smith **DESIGNER** Christina Aycock **GRAPHICS EDITOR** Nirja Desai **INTERACTIVE GRAPHICS EDITOR** Kelly Franklin **SENIOR GRAPHICS SPECIALISTS** Holly Bishop, Nathalie Cary **SENIOR SCIENTIFIC ILLUSTRATORS** Valerie Altounian, Chris Bickel **SCIENTIFIC ILLUSTRATOR** Ashley Mastin **SENIOR PHOTO EDITOR** Emily Petersen **PHOTO EDITOR** Kaitlyn Dolan **SOCIAL MEDIA STRATEGIST** Jessica Hubbard **SOCIAL MEDIA PRODUCER** Sabrina Jenkins **WEB DESIGNER** Jennie Pajerowski **SENIOR PODCAST PRODUCER** Sarah Crespi **VIDEO PRODUCER** Meagan Cantwell **INTERN** Claire Hogan

Chief Executive Officer and Executive Publisher Sudip Parikh

Publisher, Science Family of Journals Bill Moran

DIRECTOR, BUSINESS SYSTEMS AND FINANCIAL ANALYSIS Randy Yi **DIRECTOR, BUSINESS OPERATIONS & ANALYSIS** Eric Knott **DIRECTOR OF ANALYTICS** Enrique Gonzales **MANAGER, BUSINESS OPERATIONS** Jessica Tierney **SENIOR BUSINESS ANALYST** Cory Lipman **FINANCIAL ANALYST** Isacco Fusi **ADVERTISING SYSTEM ADMINISTRATOR** Tina Burks **DIGITAL/PRINT STRATEGY MANAGER** Jason Hillman **SENIOR MANAGER, PUBLISHING AND CONTENT SYSTEMS** Marcus Spiegler **ASSISTANT MANAGER DIGITAL/PRINT** Rebecca Doshi **SENIOR CONTENT AND PUBLISHING SYSTEMS SPECIALIST** Jacob Hedrick **SENIOR CONTENT SPECIALISTS** Steve Forrester, Antoinette Hodal, Lori Murphy **PRODUCTION SPECIALIST** Kristin Wowk **DIGITAL PRODUCTION MANAGER** Lisa Stanford **CONTENT SPECIALIST** Kimberley Oster **ADVERTISING PRODUCTION OPERATIONS MANAGER** Deborah Tompkins **DESIGNER, CUSTOM PUBLISHING** Jeremy Huntsinger **SR. TRAFFIC ASSOCIATE** Christine Hall **SPECIAL PROJECTS ASSOCIATE** Sarah Dhere

ASSOCIATE DIRECTOR, BUSINESS DEVELOPMENT Justin Sawyers **GLOBAL MARKETING MANAGER** Allison Pritchard **DIGITAL MARKETING MANAGER** Aimee Aponte **JOURNALS MARKETING MANAGER** Shawana Arnold **MARKETING ASSOCIATES** Ashley Hylton, Mike Romano, Tori Velasquez, Jenna Voris, Justin Wood **SENIOR DESIGNER** Kim Huynh

DIRECTOR AND SENIOR EDITOR, CUSTOM PUBLISHING Sean Sanders **ASSISTANT EDITOR, CUSTOM PUBLISHING** Jackie Oberst

DIRECTOR, PRODUCT & PUBLISHING DEVELOPMENT Chris Reid **DIRECTOR, BUSINESS STRATEGY AND PORTFOLIO MANAGEMENT** Sarah Whalen **ASSOCIATE DIRECTOR, PRODUCT MANAGMENT** Kris Bishop **PRODUCT DEVELOPMENT MANAGER** Scott Chernoff **PUBLISHING TECHNOLOGY MANAGER** Michael Di Natale **SR. PRODUCT ASSOCIATE** Robert Koepke **PRODUCT ASSOCIATE** Anne Mason **SPJ ASSOCIATE MANAGER** Samantha Bruno Fuller **SPJ ASSOCIATE** Casey Buchta

DIRECTOR, INSTITUTIONAL LICENSING Iquo Edim **MARKETING MANAGER** Kess Knight **BUSINESS DEVELOPMENT MANAGER** Rasmus Andersen **SENIOR INSTITUTIONAL LICENSING MANAGER** Ryan Rexroth **INSTITUTIONAL LICENSING MANAGER** Marco Castellan, Claudia Paulsen-Young **CUSTOMER SUCCESS MANAGER** Judy Lillibridge **SENIOR OPERATIONS ANALYST** Lana Guz **FULFILLMENT COORDINATOR** Melody Stringer

DIRECTOR, GLOBAL SALES Tracy Holmes **US EAST COAST AND MID WEST SALES** Stephanie O'Connor **US MID WEST, MID ATLANTIC AND SOUTH EAST SALES** Chris Hoag **US WEST COAST SALES** Lynne Stickrod **ASSOCIATE DIRECTOR, ROW** Roger Goncalves **SALES REP, ROW** Sarah Lelarge **SALES ADMIN ASSISTANT, ROW** Victoria Glasbey **DIRECTOR OF GLOBAL COLLABORATION AND ACADEMIC PUBLISHING RELATIONS, ASIA** Xiaoying Chu **ASSOCIATE DIRECTOR, INTERNATIONAL COLLABORATION** Grace Yao **SALES MANAGER** Danny Zhao **MARKETING MANAGER** Kilo Lan **ASCA CORPORATION, JAPAN** Yoshimi Toda (Tokyo), Miyuki Tani (Osaka)

DIRECTOR, COPYRIGHT, LICENSING AND SPECIAL PROJECTS Emilie David **RIGHTS AND LICENSING COORDINATOR** Jessica Adams **RIGHTS AND PERMISSIONS ASSOCIATE** Elizabeth Sandler **LICENSING ASSOCIATE** Virginia Warren

MAIN HEADQUARTERS
Science/AAAS
1200 New York Ave. NW
Washington, DC 20005

SCIENCE INTERNATIONAL
Clarendon House
Clarendon Road
Cambridge, CB2 8FH, UK

SCIENCE CHINA
Room 1004, Culture Square
No. 59 Zhongguancun St.
Haidian District, Beijing, 100872

SCIENCE JAPAN
ASCA Corporation
Sibaura TY Bldg. 4F, 1-14-5
Shibaura Minato-ku
Tokyo, 108-0073 Japan

EDITORIAL
science_editors@aaas.org

NEWS
science_news@aaas.org

INFORMATION FOR AUTHORS
sciencemag.org/authors/science-information-authors

REPRINTS AND PERMISSIONS
sciencemag.org/help/reprints-and-permissions

MEDIA CONTACTS
scipak@aaas.org

MULTIMEDIA CONTACTS
SciencePodcast@aaas.org
ScienceVideo@aaas.org

INSTITUTIONAL SALES AND SITE LICENSES
sciencemag.org/librarian

PRODUCT ADVERTISING & CUSTOM PUBLISHING
advertising.sciencemag.org/products-services
science_advertising@aaas.org

CLASSIFIED ADVERTISING
advertising.sciencemag.org/science-careers
advertise@sciencecareers.org

JOB POSTING CUSTOMER SERVICE
employers.sciencecareers.org
support@sciencecareers.org

MEMBERSHIP AND INDIVIDUAL SUBSCRIPTIONS
sciencemag.org/subscriptions

MEMBER BENEFITS
aaas.org/membership/benefits

AAAS BOARD OF DIRECTORS
CHAIR Claire M. Fraser
PRESIDENT Susan G. Amara
PRESIDENT-ELECT Gilda A. Barabino
TREASURER Carolyn N. Ainslie
CHIEF EXECUTIVE OFFICER Sudip Parikh
BOARD Cynthia M. Beall, Rosina M. Bierbaum, Ann Bostrom, Janine Austin Clayton, Laura H. Greene, Kaye Husbands Fealing, Maria M. Klawe, Robert B. Millard, William D. Provine

Science serves as a forum for discussion of important issues related to the advancement of science by publishing material on which a consensus has been reached as well as including the presentation of minority or conflicting points of view. Accordingly, all articles published in *Science*—including editorials, news and comment, and book reviews—are signed and reflect the individual views of the authors and not official points of view adopted by AAAS or the institutions with which the authors are affiliated.

BOARD OF REVIEWING EDITORS (Statistics board members indicated with **(S)**)

Erin Adams, *U. of Chicago*
Takuzo Aida, *U. of Tokyo*
Leslie Aiello, *Wenner-Gren Fdn.*
Deji Akinwande, *UT Austin*
Judith Allen, *U. of Manchester*
Marcella Alsan, *Harvard U.*
Sebastian Amigorena, *Inst. Curie*
James Analytis, *UC Berkeley*
Trevor Archer, *NIEHS, NIH*
Paola Arlotta, *Harvard U.*
David Awschalom, *U. of Chicago*
Clare Baker, *U. of Cambridge*
Delia Baldassarri, *NYU*
Nenad Ban, *ETH Zürich*
Nandita Basu, *U. of Waterloo*
Franz Bauer, *Pontificia U. Católica de Chile*
Ray H. Baughman, *UT Dallas*
Carlo Beenakker, *Leiden U.*
Yasmine Belkaid, *NIAID, NIH*
Philip Benfey, *Duke U.*
Kiros T. Berhane, *Columbia U.*
Joseph J. Berry, *NREL*
Alessandra Biffi, *Harvard Med.*
Chris Bowler, *École Normale Supérieure*
Ian Boyd, *U. of St. Andrews*
Emily Brodsky, *UC Santa Cruz*
Ron Brookmeyer, *UCLA* **(S)**
Christian Büchel, *UKE Hamburg*
Dennis Burton, *Scripps Res.*
Carter Tribley Butts, *UC Irvine*
György Buzsáki, *NYU School of Med.*
Mariana Byndloss, *Vanderbilt U. Med. Ctr.*
Annmarie Carlton, *UC Irvine*
Simon Cauchemez, *Inst. Pasteur*
Ling-Ling Chen, *SIBCB, CAS*
M. Keith Chen, *UCLA*
Zhijian Chen, *UT Southwestern Med. Ctr.*
Ib Chorkendorff, *Denmark TU*
Amander Clark, *UCLA*
James J. Collins, *MIT*
Robert Cook-Deegan, *Arizona State U.*
Virginia Cornish *Columbia U.*
Carolyn Coyne, *Duke U.*
Roberta Croce, *VU Amsterdam*
Ismaila Dabo, *Penn State U.*
Jeff L. Dangl, *UNC*
Chiara Daraio, *Caltech*
Nicolas Dauphas, *U. of Chicago*
Christian Davenport, *U. of Michigan*
Frans de Waal, *Emory U.*
Claude Desplan, *NYU*
Sandra Díaz, *U. Nacional de Córdoba*
Ulrike Diebold, *TU Wien*
Stefanie Dimmeler, *Goethe-U. Frankfurt*
Hong Ding, *Inst. of Physics, CAS*
Dennis Discher, *UPenn*
Jennifer A. Doudna, *UC Berkeley*
Ruth Drdla-Schutting, *Med. U. Vienna*
Raissa M. D'Souza, *UC Davis*
Bruce Dunn, *UCLA*
William Dunphy, *Caltech*
Scott Edwards, *Harvard U.*
Todd Ehlers, *U. of Tübingen*
Andrea Encalada, *U. San Francisco de Quito*
Nader Engheta, *UPenn*
Karen Ersche, *U. of Cambridge*
Beate Escher, *UFZ & U. of Tübingen*
Barry Everitt, *U. of Cambridge*
Vanessa Ezenwa, *U. of Georgia*
Michael Feuer, *GWU*
Toren Finkel, *U. of Pitt. Med. Ctr.*
Gwenn Flowers, *Simon Fraser U.*
Peter Fratzl, *Max Planck Inst. Potsdam*
Elaine Fuchs, *Rockefeller U.*
Jay Gallagher, *U. of Wisconsin*
Daniel Geschwind, *UCLA*
Ramon Gonzalez, *U. of South Florida*
Sandra González-Bailón, *UPenn*
Nicolas Gruber, *ETH Zürich*
Hua Guo, *U. of New Mexico*
Taekjip Ha, *Johns Hopkins U.*
Sharon Hammes-Schiffer, *Yale U.*
Wolf-Dietrich Hardt, *ETH Zürich*
Louise Harra, *U. Coll. London*
Jian He, *Clemson U.*
Carl-Philipp Heisenberg, *IST Austria*
Ykä Helariutta, *U. of Cambridge*
Janet G. Hering, *Eawag*
Heather Hickman, *NIAID, NIH*
Hans Hilgenkamp, *U. of Twente*
Kai-Uwe Hinrichs, *U. of Bremen*
Deirdre Hollingsworth, *U. of Oxford*
Randall Hulet, *Rice U.*
Auke Ijspeert, *EPFL*
Akiko Iwasaki, *Yale U.*
Stephen Jackson, *USGS & U. of Arizona*
Erich Jarvis, *Rockefeller U.*
Peter Jonas, *IST Austria*
Matt Kaeberlein, *U. of Wash.*
William Kaelin Jr., *Dana-Farber Cancer Inst.*
Daniel Kammen, *UC Berkeley*
Kisuk Kang, *Seoul Nat. U.*
Sabine Kastner, *Princeton U.*
V. Narry Kim, *Seoul Nat. U.*
Robert Kingston, *Harvard Med.*
Nancy Knowlton, *Smithsonian Institution*
Etienne Koechlin, *École Normale Supérieure*
Alex L. Kolodkin, *Johns Hopkins U.*
Julija Krupic, *U. of Cambridge*
Paul Kubes, *U. of Calgary*
Gabriel Lander, *Scripps Res.* **(S)**
Mitchell A. Lazar, *UPenn*
Wendell Lim, *UCSF*
Luis Liz-Marzán, *CIC biomaGUNE*
Omar Lizardo, *UCLA*
Jonathan Losos, *Wash. U. in St. Louis*
Ke Lu, *Inst. of Metal Res., CAS*
Christian Lüscher, *U. of Geneva*
Jean Lynch-Stieglitz, *Georgia Inst. of Tech.*
David Lyons, *U. of Edinburgh*
Fabienne Mackay, *QIMR Berghofer*
Anne Magurran, *U. of St. Andrews*
Asifa Majid, *U. of York*
Oscar Marín, *King's Coll. London*
Charles Marshall, *UC Berkeley*
Christopher Marx, *U. of Idaho*
David Masopust, *U. of Minnesota*
Geraldine Masson, *CNRS*
Jason Matheny, *Georgetown U.*
Heidi McBride, *McGill U.*
C. Robertson McClung, *Dartmouth*
Rodrigo Medellín, *U. Nacional Autónoma de México*
Jane Memmott, *U. of Bristol*
C. Jessica Metcalf, *Princeton U.*
Baoxia Mi, *UC Berkeley*
Tom Misteli, *NCI, NIH*
Alison Motsinger-Reif, *NIEHS, NIH* **(S)**
Suresh Naidu, *Columbia U.*
Danielle Navarro, *U. of New South Wales*
Daniel Nettle, *Newcastle U.*
Daniel Neumark, *UC Berkeley*
Beatriz Noheda, *U. of Groningen*
Helga Nowotny, *Vienna Sci. & Tech. Fund*
Rachel O'Reilly, *U. of Birmingham*
Pilar Ossorio, *U. of Wisconsin*
Andrew Oswald, *U. of Warwick*
Isabella Pagano, *Istituto Nazionale di Astrofisica*
Elizabeth Levy Paluck, *Princeton U.*
Jane Parker, *Max Planck Inst. Cologne*
Giovanni Parmigiani, *Dana-Farber Cancer Inst.* **(S)**
Daniel Pauly, *U. of British Columbia*
Ana Pêgo, *U. do Porto*
Samuel Pfaff, *Salk Inst.*
Julie Pfeiffer, *UT Southwestern Med. Ctr.*
Philip Phillips, *UIUC*
Matthieu Piel, *Inst. Curie*
Kathrin Plath, *UCLA*
Martin Plenio, *Ulm U.*
Katherine Pollard, *UCSF*
Elvira Poloczanska, *Alfred-Wegener-Inst.*
Julia Pongratz, *Ludwig Maximilians U.*
Philippe Poulin, *CNRS*
Jonathan Pritchard, *Stanford U.*
Lei Stanley Qi, *Stanford U.*
Trevor Robbins, *U. of Cambridge*
Joeri Rogelj, *Imperial Coll. London*
Amy Rosenzweig, *Northwestern U.*
Mike Ryan, *UT Austin*
Miquel Salmeron, *Lawrence Berkeley Nat. Lab*
Nitin Samarth, *Penn State U.*
Erica Ollmann Saphire, *La Jolla Inst.*
Joachim Saur, *U. zu Köln*
Alexander Schier, *Harvard U.*
Wolfram Schlenker, *Columbia U.*
Susannah Scott, *UC Santa Barbara*
Anuj Shah, *U. of Chicago*
Vladimir Shalaev, *Purdue U.*
Jie Shan, *Cornell U.*
Beth Shapiro, *UC Santa Cruz*
Jay Shendure, *U. of Wash.*
Steve Sherwood, *U. of New South Wales*
Brian Shoichet, *UCSF*
Robert Siliciano, *JHU School of Med.*
Lucia Sivilotti, *U. Coll. London*
Alison Smith, *John Innes Ctr.*
Richard Smith, *UNC* **(S)**
Mark Smyth, *QIMR Berghofer*
John Speakman, *U. of Aberdeen*
Tara Spires-Jones, *U. of Edinburgh*
Allan C. Spradling, *Carnegie Institution for Sci.*
V. S. Subrahmanian, *Dartmouth*
Ira Tabas, *Columbia U.*
Eriko Takano, *U. of Manchester*
Patrick Tan, *Duke-NUS Med. School*
Sarah Teichmann, *Wellcome Sanger Inst.*
Rocio Titiunik, *Princeton U.*
Shubha Tole, *Tata Inst. of Fundamental Res.*
Maria-Elena Torres Padilla, *Helmholtz Zentrum München*
Kimani Toussaint, *Brown U.*
Barbara Treutlein, *ETH Zürich*
Wim van der Putten, *Netherlands Inst. of Ecology*
Henrique Veiga-Fernandes, *Champalimaud Fdn.*
Reinhilde Veugelers, *KU Leuven*
Bert Vogelstein, *Johns Hopkins U.*
David Wallach, *Weizmann Inst.*
Jane-Ling Wang, *UC Davis* **(S)**
Jessica Ware, *Amer. Mus. of Natural Hist.*
David Waxman, *Fudan U.*
Chris Wikle, *U. of Missouri* **(S)**
Terrie Williams, *UC Santa Cruz*
Ian A. Wilson, *Scripps Res.* **(S)**
Hao Wu, *Harvard U.*
Wei Xie, *Tsinghua U.*
Yu Xie, *Princeton U.*
Jan Zaanen, *Leiden U.*
Kenneth Zaret, *UPenn School of Med.*
Bing Zhu, *Inst. of Biophysics, CAS*
Xiaowei Zhuang, *Harvard U.*
Maria Zuber, *MIT*

EDITORIAL

Climate science speaks: "Act now"

Jane Lubchenco
is the deputy director for climate and environment at the White House Office of Science and Technology Policy. jane.a.lubchenco@ostp.eop.gov

John F. Kerry
is the US special presidential envoy for climate. climatecomms@state.gov

Last month, one of the most remarkable scientific endeavors on the planet delivered a report to the world. Hundreds of international scientists volunteered thousands of hours to evaluate more than 14,000 scientific publications, respond to over 78,000 comments, and produce a comprehensive scientific assessment to inform government policy-makers. What topic could justify such an intense global effort? The crisis posed by climate change.

For over 30 years, the Intergovernmental Panel on Climate Change (IPCC) has been assessing the science of climate change. Each successive report has provided stronger evidence and deeper understanding, giving governments much of the information they need to develop a response. The fifth IPCC report, released in 2014, catalyzed the Paris Agreement, which aspires to limit the increase in average global temperature to well below 2°C above preindustrial levels, and preferably to 1.5°C.

The Working Group I contribution to the IPCC's 2021 Sixth Assessment reflects our ever-growing understanding of the physical science basis of climate change, including advances that allow scientists to decipher the fingerprint of climate change in heat waves, heavy rainfall and floods, droughts, and wildfires. These increasingly frequent and severe events are dominating global headlines and stoking public awareness of the economic and humanitarian consequences facing the world because of climate change. The report is full of other noteworthy advancements—more observations of ocean heat waves, improvements in modeling ice sheet dynamics, greater appreciation of the role of short-lived greenhouse gases such as methane, more realistic scenarios of sea level rise, and an understanding of what remains unknown.

Two stark findings command attention. Some changes underway in the ocean and the Arctic are potentially irreversible on human time scales. And the pathway for limiting warming to 1.5°C is narrowing rapidly. These results underscore the urgency of vastly enhancing global ambitions to tackle this threat. Every bit of avoided warming matters.

The United States is confronting this challenge with a bold pledge to reduce emissions by 50 to 52% in 2030. To reach this goal, the Biden-Harris administration is implementing executive actions to cut emissions and bolster resilience to the effects of climate change that are already being felt. This includes mobilizing the leadership from 21 federal agencies and departments to decarbonize the power sector, spur electric vehicle adoption, conserve lands and waters, and protect public health. The White House is also working with Congress to pass the US bipartisan Infrastructure Investment and Jobs Act to develop a new clean-energy economy. At the same time, the nation is investing in research that will guide a rapid transition to a low-carbon future while providing technical and financial assistance to communities most vulnerable to impacts such as heat waves, flooding, and sea level rise. The administration is committed to achieving this unprecedented package of actions by creating jobs and supporting communities that have been historically marginalized and overburdened by pollution and underinvestment.

> "It is now up to leaders in every country... to act boldly."

Because no single nation can solve the crisis alone, the United States is working with other countries to lower their own emissions and improve their resilience while assisting those places already suffering from climate change. The next decade will be critical. To keep the 1.5°C target within reach, all major economies must do more, with immediate, robust, and sustained action to reach net-zero emissions by 2050. This means deploying technological and natural climate solutions, such as conserving and restoring terrestrial and mangrove forests, saltmarshes, and seagrass beds. It means focusing not only on terrestrial activities but also on ocean-based ones such as generating renewable wind, current, and tidal energy; decarbonizing shipping; and protecting existing stores of carbon on the seabed. It means becoming better at helping communities, economies, and ecosystems adapt to climate disruptions.

The world owes a huge debt of gratitude to the hundreds of contributors who labored during a global pandemic to bring the IPCC's timely findings to policymakers. Science has delivered the clarity of knowledge. It is now up to leaders in every country—but especially the major economies—to act boldly. This year's United Nations Climate Change Conference (COP26) in November must be a turning point—the moment when the world heeds scientific findings and collectively rises to meet the greatest challenge of our time.

–Jane Lubchenco and John F. Kerry

10.1126/science.abm3757

Shandong University turns 120: Celebrating a legacy of innovation

Shandong, the hometown of China's ancient sage Confucius, which is located on the northeast coast of the country, has a rich background in education. With its history of over a century, Shandong University is one of the best representatives of such a culture in China.

On October 15, Shandong University celebrates its 120th birthday. *Science* talks with its President, Liming Fan, about the school's legacy and its focus on innovation.



Photographer: Wanli Jia

Science: *Shandong University is celebrating its 120th anniversary this year. Could you describe the historical legacy of the school, its spirit, and what kind of university it is today?*

Fan: Shandong University was established in 1901. It is one of the original schools in China's modern higher education system and the first university in China to run in accordance with a chartered constitution. Furthermore, its medical department can be traced back to one of the first modern private schools established in China (in 1864).

The school has gone through many mergers and splits, especially during wartime. Despite its numerous transitions, it has inherited the communal context of Shandong Province, and has always included a mixture of domestic and foreign scholars. In 2000, three universities–the former Shandong University, Shandong Medical University, and Shandong University of Technology–merged to form the school we see today, with campuses in Jinan, Weihai, and Qingdao.

Our school has a reputation for its literature and history studies as well as its fundamental research. We have nurtured pioneers in many fields, such as Dizhou Tong, the "father of Chinese cloning studies," Xingbei Shu, "father of Chinese radar studies," and Chengkui Zeng, "father of Chinese algae research."

Shandong University has graduated over 600,000 students throughout the years. It now has 67,000 full-time students, with 4,500 teachers overseeing their growth. Many of our students have become distinguished scientists in important fields, such as Qikun Xue in condensed matter physics, Dawei Ma in organic chemistry, and Shige Peng in financial mathematics, all of whom are awardees of the Future Science Prize, one of China's biggest awards in science, initiated by entrepreneurs and scientists in 2016. In addition to the aforementioned subjects, Shandong University is also well known for its research in crystal materials, microbiology, reproductive medicine, cardiovascular and cerebrovascular function repair, new drug manufacturing, machinery, underground engineering, and Chinese classical studies.

Today, the school is moving forward with an emphasis on cultural studies and is becoming one of the most prominent universities in the field of Chinese traditional culture. With a school motto of "Noble in Spirit; Endless in Knowledge," Shandong echoes the demands of the nation and of society–instilling the spirit of patriotism, responsibility, truth-seeking, and innovation already present in its genes.

Science: *What are some of the leading subjects at Shandong University? What achievements have been made in these areas?*

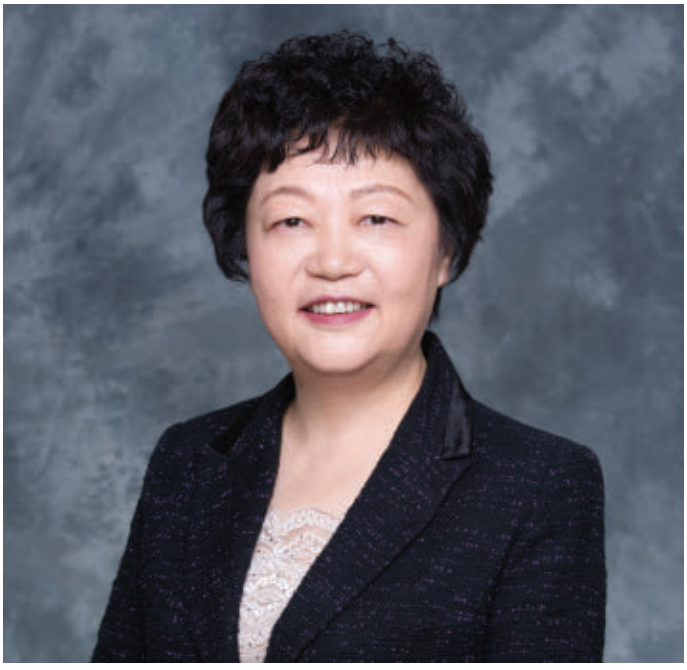
Fan: In recent years, Shandong University has seen a leap forward in its many subjects. In 2021, five of the university's subjects–chemistry, engineering, material sciences, pharmacology and toxicology, and clinical medicine–were listed in the top 1‰ of subjects in the Essential Science Indicators (ESI), an index showing the competitiveness of a subject and published bimonthly by the Institute for Scientific Information.

In mathematics and data science, our financial mathematicians created a new theory of "backward stochastic differential equations;" our cryptologists have taken the lead in formulating the international cryptographic algorithm standard; and our systems engineers have achieved breakthroughs in technologies such as component preparation and optimized control, enabling the development of high-performance photovoltaic power-generation systems.

In chemistry and materials science, our researchers made a breakthrough in high-temperature alumina fiber material technology, and our organic silicon chemists developed key technologies that are widely used in aerospace and other fields.

In materials science and in processing and manufacturing, our scientists have developed high-quality large crystals, light aluminum alloys, and carbon fiber

PHOTO PROVIDED BY SHANDONG UNIVERSITY



President Liming Fan

materials. The latter two are widely used in large engineering projects such as high-speed trains.

In Chinese traditional studies, the University leads a national key cultural project to collect and analyze ancient Chinese books from around the world. We have also successfully hosted a number of important conferences, such as the 22nd International Congress of Historical Science in 2015; this congress is often known as the "Olympics of History Studies."

In clinical medicine and major diseases, our researchers have made significant breakthroughs in understanding early human embryo development and the heritability of infertility, while cardiologists have uncovered the molecular mechanism underlying cardiovascular remodeling, providing new solutions for the treatment of cardiovascular diseases.

To foster more interdisciplinary studies, the University has created several emerging interdisciplinary research institutions, such as the Frontier Interdisciplinary Research Institute, the Institute of Data Science, and the Institute for Advanced Medical Research, in order to boost subjects such as artificial intelligence, scientific and technological archaeology, integrated circuit design, and intelligent medical engineering.

Science: *What is Shandong University's philosophy of education?*

Fan: It inherits the wisdom of Confucius, who was born in Shandong and believed in "teaching students in accordance with their aptitude." It supports "equal education for everyone" and espouses that "teaching and studying promote one another."

In practice, we have improved the diversity of talent selection and are recruiting those with potential as well as those who have already shown outstanding performance. Additionally, we customize curricula according to students' specialties and interests, introducing the "3Ms": major, minor, and micro subjects. We also look for comprehensive development in students, nurturing them through general education, professional education, innovation, and entrepreneurship education.

Science: *What are some of Shandong University's primary achievements since you took office in 2017?*

Fan: In recent years, Shandong University has moved to a fast track, a new phase of development. We fully exceeded the goals and tasks of the first round of the national "double top-tier" university construction, and significantly improved our core competitiveness and international influence.

We are developing top-tier academics, promoting construction of "big platforms and big teams," and striving to produce original, iconic, and leading academic achievements. The school is carrying out a plan for disciplinary integration and innovation by introducing five mechanisms in subject planning, innovation, management, cooperation, and policies and an environment which supports interdisciplinary development.

We are dedicated to cultivating top-tier talents for the nation. We see the teaching of virtue as the core of education and center our endeavor around the growth of students. From 2016 to 2020, students from Shandong University won 151 awards in innovation and entrepreneurship competitions.

We are also dedicated to serving regional economic and social development. With the advantage of our campuses, we have built 106 campus–school–enterprise cooperation platforms, exemplified by the Shandong Institute of Industrial Technology in Jinan, constructed in cooperation with local governments. We are also planning to build a new Longshan Campus, an innovation harbor that will be an engine for promoting high-quality economic and social development.

Science: *How is Shandong University pursuing its internationalization strategy?*

Fan: Shandong University has established cooperation with nearly 200 universities and academic institutions in over 30 countries or regions. Aiming to nurture talent with international vision and competency, it has also attracted over 3,000 international students from more than 130 countries through its many programs, such as English-taught programs including a Master's in China Studies and a combined Bachelor of Medicine and Bachelor of Surgery (MBBS).

Researchers at the school actively participate in major international projects, such as AMS, ATLAS, STAR, BESIII, and LHAASO. Scientists at the University are playing important roles in these projects, striving to explore the myths of the universe; they are also trying to understand major scientific issues facing the human race, including human health and climate change, by establishing cross-border research platforms such as the SDU-KI Translational Medicine Collaborative Research Platform and the SDU-Nottingham Green Energy and Materials Research Center.

Science: *Where do you think the University's greatest strengths lie?*

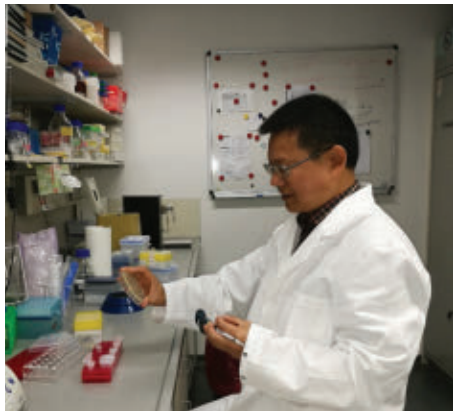
Fan: By 2051, when the school is 150 years old, we hope it will have become one of the top-tier universities in the world. With its seven core strategies in talent, academics, culture, local social service internationalization, integrated and interdisciplinary development, it is on track to be an influential science and innovation center where talent flows like spring water.

Countless academic stars have graced Shandong University. They have made important contributions over the years, laying solid foundations in a range of fields, including the 12 general disciplines of the school. These are just a few of the outstanding groups we have at Shandong University:

PHOTO PROVIDED BY SHANDONG UNIVERSITY



Shige Peng



Youming Zhang



Zi-Jiang Chen

1. Financial mathematics

With over 90 years of history behind it, mathematics studies at Shandong University is one of the most important education and research bases for higher mathematics in China. It has contributed to world-class research findings in both fundamental and applied mathematics, and has been instrumental in the education of a number of students who later became academicians.

The department has made impressive progress in interdisciplinary research combining mathematics and finance, a paradigm that has expanded to biology, data science, and marine science. Led by Shige Peng, the Research Center for Mathematics and Interdisciplinary Sciences was established in 2018 in Qingdao. The center carries out forward-looking research, creating a bastion as a leader and innovator for exceptional student training.

Current and former mathematicians from the department have impressed the world with their findings. Peng, one of the leading figures in financial mathematics, derived the general theory of backward stochastic differential equations (BSDEs) in 1990, a theory that is critical for determining the scale of risk and has fundamentally revolutionized its application in finance.

2. Microbial technology

Begun in the 1950s, Shandong University's microbiology program has a long and brilliant history; it is where China's earliest Doctoral and Master's degrees in microbiology were awarded. In 1995, the Institute of Microbial Technology was officially approved by the Ministry of Science and Technology as one of the national key laboratories in China. Today, the institute is a leading scientific research platform and an internationally renowned laboratory in the field of microbial technology.

Rooted in the university's tradition of multidisciplinary and comprehensive learning, the institute focuses on three cutting-edge topics in life science: microbial genome editing and molecular modification; microbial biocatalysis and biosynthesis; and microbial ecology and resource utilization. Over the past 30 years, the institute has achieved a number of outstanding scientific breakthroughs, including improvement of the Red/ET DNA recombineering and DNA direct cloning techniques; industrial application of the cellulase overproducing *Penicillium* strains; discovery of the mechanisms underlining biogeochemical cycling driven by marine microorganisms; exploration of myxobacterial genetics and chemoecology; and development of biomass-based bioproduction of high-value-added chemicals, to name a few.

As director of the institute, Youming Zhang is a pioneer in recombinogenic engineering and an academician of the European Academy of Sciences as well as the German National Academy of Science and Engineering. Under his leadership, a group of the institute's internationally recognized microbiologists have dedicated themselves to the development of innovative microbial technologies to fuel, feed, heal, and clean the world.

3. Reproductive medicine

Led by Zi-Jiang Chen, an academician of the Chinese Academy of Sciences, Shandong University's Center for Reproductive Medicine is among the earliest to conduct assisted reproductive technology (ART) in China. It has a team of over 100 professors, researchers, physician scientists, and attendees. China's unique National Research Center for ART and Reproductive Genetics implements ART treatment for more than 20,000 cycles annually.

Chen's team has endeavored to understand the etiology of infertility, prevent birth defects, and provide safe therapeutic strategies for patients seeking ART treatment. She identified novel pathogenic or susceptible genes/loci for premature ovarian insufficiency (POI) and polycystic ovarian syndrome (PCOS), facilitating a systematic explanation for the pathogenesis of these reproductive disorders. She also revealed the dynamics atlas of 3D chromatin structure in early human embryos, providing pivotal chromatin accessibility information for human embryogenesis.

Moreover, Chen has led a series of multicenter randomized controlled trials (RCTs) to provide first-level evidences and guidance for the safety of frozen embryo transfer strategy in ART for infertile ovulatory and PCOS patients. Her series of RCTs not only advance clinical infertility treatment internationally but also fuel the development of China's clinical trials, as noted by Robert Barbieri, head of the Department of Obstetrics, Gynecology and Reproductive Biology at Brigham and Women's Hospital, Harvard Medical School: "China has become the world leader of clinical trials in infertility treatments." Some of Chen's prominent work has been published in prestigious journals, such as *The New England Journal of Medicine*, *Lancet*, *Nature*, and *Cell*.

In addition to their academic achievements, Chen and her team have invented multiple reproductive medical technologies, such as gamete intrauterine transfer (GIUT) and mitochondrial replacement techniques, effectively solving fertility problems and preventing birth defects. The birth of the first baby through her GIUT process attracted extensive social attention in China and ranked in the top 10 medical science and technology news events of 1992.

Chen has also directed the enactment of a variety of Chinese guidelines and consensuses in the ART field, such as the Diagnostic Guidelines for PCOS, the Chinese Experts' Consensus on the Diagnosis and Treatment of POI, and the

PHOTOS PROVIDED BY SHANDONG UNIVERSITY



Yun Zhang



Shucai Li



Hui Fang

Diagnosis and Treatment Guidelines for Abnormal Uterine Bleeding of Ovulatory Disorders, which have largely filled the gap between medical frontiers and clinical practice.

4. Cardiovascular remodeling and function research

Founded in 2002, the Key Laboratory of Cardiovascular Remodeling and Function Research is one of the national key laboratories at Shandong University.

The laboratory contains more than 500 pieces of equipment exceeding RMB 70 million (USD 11 million) in value. It comprises 12 laboratories, encompassing animal husbandry, cytology, genetics, protein chemistry, pathology, and patch-clamp technologies.

Its current director, Yun Zhang, is an academician of the Chinese Academy of Engineering and a Fellow of the American College of Cardiology. Zhang is a pioneer in several fields, including echocardiography, animal models of atherosclerosis, and the diagnosis of heart failure.

The hospital's academic group was the first cardiology team to be awarded the Innovative Research Groups Fund by the National Natural Science Foundation of China in 2010.

5. Civil engineering

Founded in 1947, the School of Civil Engineering currently has four undergraduate teaching departments, one provincial and ministerial key laboratory, four provincial and ministerial engineering research centers, and one experimental center.

One of the centers, the Geotechnical Engineering Center, is led by Shucai Li, an academician of the Chinese Academy of Engineering. Li focuses on geohazards prevention and control in tunnels and underground engineering. In response to the challenges of underground construction in China, complex geological conditions, frequent water and mud inrush, and other disasters, he has made great progress in geological forecasting of tunnel disasters and the treatment of major water inrush disasters.

Under his leadership, the center has undertaken and completed more than 100 national, provincial, and ministerial-level scientific research projects and large-scale commissioned engineering projects.

Li's team was selected as one of a group of innovation teams working in key research areas by the Ministry of Science and Technology.

6. Archaeology

Around 1928, Jinding Wu, assistant professor at Qilu University, a precursor to Shandong University, discovered the site of Chengziya in Longshan Town, which began the study of Longshan culture. His discovery also marked the start of the archaeological discipline in the School of History and Culture at Shandong University.

The school is an early leader in archaeology studies. It invited Canadian oracle bone expert James Menzies to teach there in 1932, opening one of the first archaeology courses in the nation. It established an archaeology major in 1972, becoming one of the first schools in China to do so.

In the 25 years since its establishment in 1996, the school has built more than 10 laboratories, becoming an important base for Chinese archaeological research and training. According to the school's dean Hui Fang, it bases its education on a "class–field–laboratory" system, in order to train students with a solid theoretical foundation, strong field practice abilities, and international academic vision.

It also makes a concerted effort to integrate knowledge and technologies from other fields in order to comprehensively find, identify, analyze, and conserve the remains unearthed at archaeological sites.

Excavations directed by Shandong University have been named among China's Top 10 Archaeological Discoveries eight times by China's National Cultural Heritage Administration. Furthermore, Joint International Research Laboratory of Environmental and Social Archaeology, which is affiliated with Yale University and approved by the Ministry of Education, is a great platform for international collaboration and leads China's research in environmental and social archaeology.

Sponsored by

山东大学
120周年校庆
120th Anniversary of Shandong University
1901–2021

PHOTOS PROVIDED BY SHANDONG UNIVERSITY

NEWS

> “Amazon is directly profiting from the sensationalism of anti-vaccine misinformation.”
>
> **Representative Adam Schiff (D–CA),** in a letter to the e-commerce giant complaining that its algorithms promote books containing conspiracy theories and debunked claims about COVID-19.

IN BRIEF

Edited by **Jeffrey Brainard**



CONSERVATION

Ban on deep-sea mining sought

Workers disembark from a research vessel that collected data in the Pacific Ocean for studies about the potential environmental effects of deep-sea mining.

A conservation congress last week called for a global moratorium on deep-sea mining until strict reviews are put in place. The controversial activity, which targets valuable elements such as manganese and nickel, is regulated on the high seas by the International Seabed Authority, a U.N.-chartered organization. The group has issued 30 exploration licenses, but no commercial mining permits, because the authority has not finalized regulations. Conservationists worry deep-sea mining will destroy biologically rich seamounts, hydrothermal vents, and other habitats. In addition to calling for the mining moratorium, the International Union for Conservation of Nature, which maintains a Red List of threatened species, also approved a separate resolution calling for the protection of 80% of the Amazon by 2025. The measure was proposed by Indigenous organizations, which were able to fully vote for the first time at the meeting, the union’s quadrennial World Conservation Congress.

Biden mandates U.S. shots

COVID-19 | President Joe Biden’s administration may face lawsuits challenging the mandates he announced last week to compel more Americans to receive COVID-19 vaccines, but many legal experts suggest the policy is on solid ground. Companies with 100 or more employees could be fined if their workers are not either vaccinated against the pandemic coronavirus or regularly tested for it. In addition, all federal employees and contractors, and health care workers who participate in Medicare or Medicaid programs, must be vaccinated, with no testing opt-out. Some public health experts said the federal mandates should have gone further, to require proof of vaccination for airline passengers, for example. In his announcement, Biden voiced frustration that 25% of the Americans who are eligible for the vaccine—nearly 80 million people—have not received one shot. States that have the lowest uptake have had the highest rates of severe cases and deaths. As for threats of legal challenges, “have at it,” Biden said; the U.S. military requires several vaccines, as do states for children to attend schools, and these rules have withstood challenges all the way to the U.S. Supreme Court.

Facebook acknowledges bad data

SOCIAL MEDIA | Facebook apologized last week for providing 110 social scientists from the research consortium Social Science One with incomplete data on its users from the United States. The researchers, who were studying the impacts of social media on democracy and elections, thought they were receiving information on all U.S. Facebook users. But the data only covered about half of them—those who had indicated clear political leanings on the social media giant’s platform. The revelation came after researcher Fabio Giglietto of the University of Urbino noticed discrepancies between recent, publicly released Facebook data and the information academics received from the company starting in February 2020. Facebook had provided the data in an aggregated form that kept academics from spotting the error sooner, according to Gary King of Social

PHOTO: CAROLYN COLE/*LOS ANGELES TIMES*/GETTY IMAGES

Science One. He says Facebook's "remarkably sloppy" mistake could make the users appear more politically polarized than they actually are. But researchers won't know the full extent of the damage until they reanalyze corrected data provided by Facebook in the coming months.

Journals pull papers on Uyghurs

RESEARCH INTEGRITY | Two journals have retracted four papers by authors in China that used genetic data from Uyghurs and other Chinese minorities without evidence of proper informed consent. Human rights activists worry the data could be used for security purposes, adding to the intensive surveillance and detentions already imposed on the Uyghurs. The authors did not agree to the retractions, according to the notices covering three of the papers posted on 7 September by the *International Journal of Legal Medicine* and for the fourth by *Human Genetics* on 30 August. A spokesperson for Springer Nature, publisher of both journals, says about 40 papers published in its titles remain under investigation.

Meows take Ig Nobel Prize

HUMOR | Research on the "meowsic" of cat calls snagged one of this year's Ig Nobel Prizes, a tongue-in-cheek annual tribute to off-beat studies, at an online ceremony last week. Researcher Susanne Schötz at Lund University won the biology prize for her analyses of a range of cat sounds—from purrs, trills, and tweedles to meows, yowls, and hisses. In one study, she found humans could predict, based on a meow's intonation alone, whether the cat was anxious about being taken to the vet or was asking for food. (Food meows rise at the end, whereas vet meows fall.) In her acceptance speech, Schötz demonstrated 12 distinct cat sounds. Other Ig Nobels went to an analysis of bacteria that hitch a ride on used chewing gum and a method to rid submarines of cockroaches.

Retraction draws complaints

PUBLISHING | The journal *Scientometrics* drew fire last week for retracting an article about "predatory" journals after a publishing executive criticized the paper for relying on a controversial list of such journals that includes his company's titles. Frederick Fenter, chief executive editor at publisher Frontiers, faulted Beall's List of predatory journals as biased and unreliable in a 6 May letter to *Scientometrics*, first reported by Retraction Watch. Librarian Jeffrey Beall had maintained the list until 2017 when he shut it down following criticism from Frontiers. In a retraction notice, *Scientometrics*, which carries research about scholarly publishing, did not mention Beall's List, but said the paper contained methodological flaws. Some members of the journal's board of reviewers have strongly disagreed with the decision, criticizing what they see as undue pressure by Frontiers. (The majority shareholder of Springer Nature, which publishes *Scientometrics,* is Holtzbrinck Publishing Group, which has also invested in Frontiers.) The authors also criticized the retraction, pointing out that their article discussed shortcomings of Beall's List. How to accurately define a predatory publisher or journal has been a topic of continuing scholarly debate.

Research seminars gain new life

TOOLS | Universities collectively hold hundreds of thousands of research seminars a

BY THE NUMBERS

4000

Tons of carbon dioxide that will be removed annually from the atmosphere by the world's largest carbon-capture plant, which began operations last week in Iceland.

216 million

People who may be forced to migrate within their own countries to escape the effects of climate change, such as drought, by 2050. (World Bank)



IMAGES: DEPARTMENT OF SCIENTIFIC RESEARCH AND DEPARTMENT OF PAINTINGS CONSERVATION/METROPOLITAN MUSEUM OF ART. ORIGINALLY PUBLISHED BY S.A. CENTENO, D. MAHON, F. CARÒ, AND D. PULLINS, *HERITAGE SCIENCE* (SPRINGER OPEN), 2021

HISTORY OF SCIENCE

Changes that hid chemistry giants' wealth unmasked

Completed around 1788, the iconic portrait by Jacques-Louis David of Antoine Lavoisier and his wife, Marie Anne Paulze Lavoisier, celebrates a pioneer of modern chemistry and the woman historians credited as his close collaborator. Now, researchers have found evidence that David altered the image to obscure signs of their wealth—including her large, ornate hat and his desk, originally shown as decorated with gilt bronze. Conservators at the Metropolitan Museum of Art glimpsed the changes during work in 2019 to restore the painting; they used infrared and x-ray spectroscopy to peer through its layers and identify the chemical composition of its pigments. The techniques revealed areas of paint containing mercury (red, above right) that were later covered over. On 30 August in *Heritage Science*, the team suggested the changes may have been a deliberate attempt to placate leaders of the brewing French Revolution. Even so, in 1794 they guillotined Antonie Lavoisier, who had also been a tax collector. But Marie Anne Paulze Lavoisier survived, and helped establish her husband's scientific legacy by publishing his papers.

year, but scientists have lacked an easy way to make, find, and view recordings of them. Spurred by the surge of remote meetings during the pandemic, a new website aims to fix that. Cassyni.com was launched on 1 September with more than 5000 seminars from 650 research institutions in 34 countries. Many are indexed with speakers' names, transcripts, slides, and remote attendees' comments, and each seminar can be assigned a digital object identifier (DOI) number so it can be systematically cited. The platform also allows users to schedule and hold seminars integrated with Zoom. Named for the 17th century astronomer Giovanni Domenico Cassini, the service charges varying fees depending on clients' size.

Probe faults researcher of aging

#METOO | The antiaging SENS Research Foundation last week published the findings of an independent probe that led to the ouster of the organization's co-founder and chief science officer, gerontologist Aubrey de Grey. An investigation by a law firm concluded de Grey sexually harassed two women who are now biotech entrepreneurs; he pursued one when she was 17 and 18 years old and told another woman, then a student, that she should entice foundation donors with her "womanhood." It also found that de Grey interfered with the probe, leading SENS to dismiss him on 21 August. In a Facebook comment, de Grey challenged the probe's evidentiary standards.

EPA opposes Alaska mine

CONSERVATION | The U.S. Environmental Protection Agency (EPA) last week reversed itself—again—and said it wants to block a controversial gold and copper mine in the headwaters of Alaska's Bristol Bay, near the Aleutian Islands, home to the world's largest sockeye salmon run. In 2014, EPA under then-President Barack Obama proposed barring federal permits for the Pebble Mine because it would endanger surrounding ecosystems and a $300-million-a-year commercial salmon fishery. In 2019, under then-President Donald Trump, the agency reversed that decision. Now, with President Joe Biden in the White House, EPA says it will ask a federal court to cancel the Trump-era decree, clearing the way for the agency to again consider blocking the mine. Its backers already suffered a serious blow in 2020, when the U.S. Army Corps of Engineers refused to issue a permit over environmental concerns.



ENERGY

Innovative magnet raises hopes for fusion power

The elusive goal of fusion energy may be closer after Commonwealth Fusion Systems (CFS) announced last week that a powerful new magnet produced a field of 20 Tesla, twice as strong as that of conventional superconducting magnets. The 2-meter-long, D-shaped electromagnet (above, center), developed at the Massachusetts Institute of Technology, is the largest ever fashioned from exotic materials that can function as superconductors at high temperatures. CFS researchers will use the magnets in a planned fusion reactor, or tokamak, to confine a hot plasma so that some of the nuclei in it fuse and release more energy than needed to sustain the reaction—a long-sought goal for the field. The CFS design will be smaller than that of other tokamaks, such as ITER, a big reactor funded by multiple countries.

THREE QS

Landsat's 'mother' looks back

Next week, NASA and the U.S. Geological Survey will launch the Landsat 9 Earth observing satellite, kicking off the program's 50th anniversary. Attending will be engineer Virginia Norwood, known as the mother of the groundbreaking satellite series. Now 94 and retired, she designed the first multispectral sensor, which was shot into space aboard Landsat 1 in 1972. That paved the way for future novel remote sensing instruments, which made it possible to track forest loss and see hidden geological features. Newer types of satellites can record images with higher resolution, but researchers continue to value the Landsat data set for documenting Earth's changes. Despite resistance to women in science when Norwood began her career, she attributes her NASA successes to never taking "no" for an answer. (A longer version of this interview is at scim.ag/LandSat50.)

Q: What innovations did you develop that enabled the multispectral scanner?
A: Being multispectral and desiring the widest spread possible meant that you are necessarily having a completely different device. Each band takes different detectors and different techniques, and each has its own little problems. Then you had to fit them all together. So, you had to do a lot of adaptation to make those bands [into one image] so they can be compared with each other. And it was the first time that data from space had been digitized.

Q: How did you persuade NASA to trust this method?
A: Because of the diversity of the spectral bands, [NASA] realized that it was important to try [it]. … The delightful thing to me was that after [Landsat] launched, various users would say, "I just was able to do this or that" that they had never thought they could before.

Q: Do you feel part of Landsat 9?
A: I do. For example, it has thousands of detectors that are in a "push broom array." I originally would have liked to have done [the first scanner] that way, but I was without a prayer of being able to do it because the detector technology was not available.

SCIENCE.ORG/NEWS
Read more news from *Science* online.

PHOTO: GRETCHEN ERTL, CFS/MIT-PSFC, 2021



A child receives a COVID-19 test as part of the universal testing program in Los Angeles schools.

PHOTO: XINHUA/XINHUA NEWS AGENCY/NEWSCOM

COVID-19

Schools begin mass testing with vexing questions

Scientific uncertainties, access, and logistics are hurdles to routine screening

By **Jennifer Couzin-Frankel**

Yellow school buses are plying the streets again, and cafeterias are abuzz. In the United States and abroad, children are back in school, many for the first time in 18 months. Those who are 12 and older can be vaccinated, and wearing masks and distancing are common in schools. But as the highly contagious Delta variant proliferates, administrators and public health officials are grappling with whether and how to incorporate another layer of protection: routine mass testing of students and staff. "Delta has changed the risk calculus in a lot of ways," says Amy Greer, an infectious disease epidemiologist at the University of Guelph. What's more, "We have suboptimal vaccine rates, and we have entire cohorts of young kids who are fully unvaccinated."

The risks are already coming into focus: Nearly 1700 U.S. schools that began the school year in person have had to shut because of COVID-19 cases, according to burbio, an organization aggregating school data. Many scientists believe intensive, regular testing should help prevent in-school spread. Some schools, cities, and even entire countries are already testing asymptomatic children as well as adults, swabbing millions of noses or collecting saliva on a grand scale. Last week, the Biden administration urged U.S. schools to routinely screen unvaccinated staff and students. But access to mass testing and quick results is spotty, and data on how well different methods control spread in schools are sparse.

Last year, measures such as mask wearing, distancing, and ventilation generally kept the virus at bay in schools that held in-person classes, says infectious disease modeler Meagan Fitzpatrick of the University of Maryland School of Medicine. Large school outbreaks were infrequent. "That," she says, "was a huge relief." But then came the Delta variant, which is at least twice as transmissible as the original pandemic coronavirus.

With no protections, a Delta case in an unvaccinated person is estimated to infect about six unvaccinated people. Computer models such as Fitzpatrick's suggest the number plummets in a school with excellent safeguards, but it's still about double the pre-Delta risk. "That is just a huge shift in the outbreak potential of your school," Fitzpatrick says.

Last month, Julie Swann, a systems engineer at North Carolina State University, and her colleagues made headlines with a preprint suggesting school-age children would be highly vulnerable to contracting Delta this fall—but regular, widespread testing could slash that risk. In a computer model, her team found that when there's universal masking and one-half of a school's population has immunity from either prior infection or vaccination, about 24% of unvaccinated students would be infected by mid-December. Testing one-half of all students weekly sliced that number to 13%. A model by Fitzpatrick and others found, similarly, that weekly universal testing prevents about 50% of in-school transmission.

Around the world, schools are trying a range of strategies. In Germany, schools test unvaccinated students and teachers two or three times a week, relying on rapid tests that give results in about 15 minutes. The United Kingdom urges twice-weekly testing for those 12 and older for at least the first month of school, also using rapid tests. The Los Angeles Unified School District is spending $350 million to administer about 500,000 slower, more sensitive polymerase chain reaction tests once a week to all staff and students. And Pennsylvania is offering schools "pooled testing" that combines samples from a group, such as children in one classroom; if the pool flashes positive, students can then be tested individually.

How these efforts will play out is unclear. "There is definitely uncertainty" about the ability of mass testing to stem school outbreaks, says Kanecia Zimmerman, a pediatrician at Duke University who has been studying schools across North Carolina for more than a year to help them reopen and stay open safely. "Let's generate the evidence."

Zimmerman's team is probing the value of one testing strategy called surveillance, which regularly samples a random subset of the population. Among participating schools, between one-third and one-half of staff and students who opt in are tested each week, and the results are compared with other schools that aren't in the testing program. So far, this approach "doesn't seem to help," she says, though her group is still analyzing data and hopes to publish later this fall.

Zimmerman suspects more frequent testing on more people would work better. "I'm a little skittish about once a week," even on everyone, "really being enough." Delta replicates so rapidly in the nose that twice-weekly testing may net more infected people early on, when they are contagious but don't yet have symptoms.

> **"I'm a little skittish about once a week [testing] really being enough."**
>
> **Kanecia Zimmerman**, Duke University

One major hurdle Zimmerman has seen is that "parents aren't superthrilled" about testing when their child has no symptoms, because a positive result could lead to a disruptive quarantine, including for parents who can't afford take time off work. As many as 70% of parents with children in the schools Zimmerman is working with decline the screening. Although some districts, including Los Angeles and Baltimore, mandate testing students and staff, in many places, it's now voluntary.

In addition to getting buy-in from parents, "The school has to be willing to act on the information it receives," Fitzpatrick says. In her computer model, weekly surveillance testing of 10% of a school's population can stem outbreaks only if the school responds to each new case by testing 90% of its population the next day, including vaccinated individuals. This is because finding one case in 10% of a population suggests there are more.

Parents and administrators may be more welcoming of a different kind of strategy called test to stay, which can minimize quarantining after an exposure. Instead of being sent home, exposed individuals get tested daily or every other day for about a week and attend class normally. This summer, a group at the University of Oxford posted a preprint analyzing results from a spring experiment in about 200 schools. Of students and staff exposed to a positive case, half were randomized to test to stay and the rest to a 10-day quarantine. They found that allowing contacts to stay in school didn't fuel spread; less than 2% of contacts in either group contracted the virus, and daily testing quickly caught any cases.

"We've been really pushing schools to do test to stay," says Rebecca Lee Smith, an epidemiologist at the University of Illinois, Urbana-Champaign, who is helping the state bring weekly mass saliva testing to its schools. Schools in Israel are also planning to try test to stay. "I think that this program should be given a chance, in order to minimize the damage that happened last year" when many classes were quarantined, says Zachi Grossman, president of the Israel Pediatric Association.

In the United States, finding and paying for a steady supply of tests that return results quickly can be the biggest hurdle for school testing, as Fitzpatrick learned from the struggles of her son's preschool. "If the government had said, 'We're going to prioritize tests that cost $1 or less,'" ultracheap tests that deliver fast results would likely be widespread, Swann says in frustration. In Germany, about 60 different rapid tests are approved for use and cost less than $1. The U.S. Food and Drug Administration (FDA) has given just a handful of at-home rapid tests the green light; one runs $24 for a pack of two tests and another about $35 for one. It wasn't until March that FDA streamlined the process for authorizing such tests. Last week, the Biden administration's plan noted that some major retailers will sell rapid tests "at cost" for the next 3 months, a price reduction estimated at "up to 35%"—still well above what many say is needed.

How aggressively to test may vary from place to place, depending in part on community and school vaccination rates and the degree to which local hospitals are over-burdened, Swann says. In San Francisco, about 90% of 12- to 17-year-olds are fully vaccinated, and no in-school transmission has been reported yet. That said, it's important not to become complacent, says Michael Wagner, a microbial ecologist at the University of Vienna, who has been studying testing strategies in schools. Scientists are still trying to understand how readily vaccinated people can contract and spread the virus. For now, Wagner says, "We should assume everyone can transmit." ■

With reporting by Gretchen Vogel.

COVID-19

'Zero COVID' countries seek exit strategies

They successfully kept the the virus at bay. Now, some are gingerly opening up

By **Dennis Normile**

Some of the countries that have been most successful at keeping COVID-19 at bay are now seeking ways to gingerly lower the barriers that protect them while minimizing the risk that the disease will become endemic.

China, Australia, New Zealand, Singapore, and Taiwan all closed their borders last year and forced the few people allowed to enter into strict hotel quarantines. Internally, they quashed outbreaks early, using lockdowns and other restrictions. As a result, residents could live near-normal lifestyles most of the time.

Countries with this "zero COVID" strategy, as it has been dubbed—scientists prefer the term "elimination"—"have generally fared better than countries that opt for mitigation," Miquel Oliu-Barton, of Paris Dauphine University, and co-authors wrote in a June paper in *The Lancet*. They found the elimination cohort had lower per capita death rates, shorter and less strict lockdowns, and faster economic recoveries than the mitigation camp, including the United States and Europe, which have used vaccines and other measures to try to blunt massive waves of infection.

But the spread of the highly infectious Delta variant, the economic burden of closed borders, lockdown fatigue, and increasing vaccine availability are changing the equation. "In the long term [zero COVID] is not really economically sustainable," says Ben Cowling, an epidemiologist at the University of Hong Kong (HKU). "Countries are going to need to test out different approaches to find the right balance between infection prevention and control and normalizing societal activities," adds epidemiologist Keiji Fukuda, also at HKU.

Australia and New Zealand, which once had similar strategies, are now sharply diverging as they seek that balance.

Australia is in the midst of a severe Delta-driven outbreak, with close to 2000 new



Police clashed with thousands of people protesting a COVID-19 lockdown in Melbourne, Australia, on 24 July.

PHOTO: CON CHRONIS/AFP/GETTY IMAGES

cases daily that started with a single infection in Sydney, in the state of New South Wales, in mid-June. Nationwide elimination is no longer an option, says Ivo Mueller, an infectious disease epidemiologist at the Walter and Eliza Hall Institute of Medical Research in Parkville, Australia. "The Delta variant is sufficiently entrenched in New South Wales and Victoria that you won't get that to zero," he says. Meanwhile, lockdowns and other restrictions that affect roughly half of the country's population of 25 million have led to large and sometimes violent demonstrations.

On 6 August, the Australian government approved a national COVID-19 transition plan that abandons the elimination strategy. It is backed by a modeling study from the Peter Doherty Institute for Infection and Immunity at the University of Melbourne showing that restrictions can be gradually relaxed without overburdening the health care system once 70% of the population is fully vaccinated. (The current rate is 60%.) More freedoms are possible when the 80% benchmark is reached.

Australia's eight states and territories will control how the plan is implemented. On 9 September, New South Wales, particularly keen to open up, released a "roadmap to freedom" presenting some details. When the state reaches the 70% vaccination rate, stay-at-home orders will be lifted for all those who've received two doses, but mandatory face masks in indoor public spaces and restrictions on large gatherings will remain for now. In an example of what Emma Miller, an epidemiologist at Flinders University, calls Australia's "fractious approach," some other states will keep in place such elimination measures as barring visitors from other regions.

Miller also sees a deeper issue: Australians will have to accept an increase in severe cases and deaths. "Some consensus on what sort of numbers the community will accept is really required here," she says.

New Zealand, in contrast, is sticking with its elimination strategy, which has been more successful than Australia's. The country has taken a "rapid, decisive approach" in "applying maximum lockdown measures as soon as it detects unexplained cases of COVID-19," says Michael Baker, a public health scientist at the University of Otago, Wellington. It appears to be on the cusp of containing its latest COVID-19 outbreak, which began on 17 August and triggered a nationwide lockdown. Daily infections reached 84 on 28 August and again on 2 September, but have trended downward since. "The country's elimination status will be regained in coming weeks," predicts Nick Wilson, a public health scientist at Otago. Despite the painful lockdowns, the zero COVID strategy remains popular, he says.

Last month, an advisory panel said staying the course is "the best option at this stage of the pandemic." Increasing vaccination coverage and improved contact tracing could allow some of the strictest controls to be relaxed, however. Currently, about 35% of New Zealanders over age 12 are fully vaccinated, but Wilson expects 80% to 90% coverage by the end of the year.

That level could set the stage for allowing vaccinated individuals entering the country to skip the now-mandated quarantine sometime in 2022, the panel suggests, if they agree to such conditions as repeated testing and tracking. Because vaccinated people can still be infected with SARS-CoV-2, it is "inevitable that people carrying the virus will enter New Zealand on a regular basis," causing "some community transmission," the panel said. But stamping out resulting outbreaks should be feasible.

Other elimination countries fall between these two poles. China has not announced plans to change its strategy and "may well decide to continue with COVID elimination," Cowling says. The country followed its strict elimination playbook to gain control of a Delta variant outbreak that started in late July in Nanjing and popped up in a number of other cities; daily cases had dropped from nearly 150 to zero by early September. But Delta infections reappeared: Southeast Fujian province reported 59 locally acquired cases on 13 September.

Taiwan's zero COVID strategy was tested in May, when the island saw cases spike to more than 700 daily, but has proved to be robust; this week, there were fewer than 10 daily cases on average. Still, some are calling for Taiwan to relax its stringent entry restrictions and prepare the island for "limited endemicity," says Lin Hsien-Ho, an epidemiologist at National Taiwan University. Daily case numbers would likely have to remain in the double digits for the public to accept those changes, he says: Having had so little COVID-19 for so long, Taiwan "has high expectations that there will be very few cases."

Singapore, meanwhile, is cautiously relaxing border controls. Starting 8 September, it began to allow immunized travelers from Brunei and Germany to enter without quarantining, on a reciprocal basis, as a trial step. But expansion of this scheme may be put on hold because the city-state is in the midst of its worst outbreak in more than a year, with 450-plus cases reported on 9 September, despite nearly 80% of residents being fully vaccinated.

For all these countries, edging out of their COVID-19 bubble is a momentous decision. Elimination has helped minimize the public health and economic impacts of the pandemic and bought countries time to await the development and testing of vaccines and drugs. Abandoning zero COVID, on the other hand, is almost certainly a one-way street. In New Zealand, Baker says, "One of the main benefits of the elimination strategy is that it keeps … options open." ■



In 2009, well diggers seeking geothermal energy accidentally tapped a magma chamber that vented a plume of steam and glass shards.

VOLCANOLOGY

Forget oil or water. Icelandic drillers seek magma

Probe of volcano could reveal magma composition and guide early warning systems

By **Paul Voosen**, *at the Krafla volcano in Iceland*

After years of effort, volcanologists are ready to open a gateway to hell.

From the rim of the Víti ("hell" in Icelandic) crater—a smaller crater within Krafla's 10-kilometer caldera—Ottó Elíasson looks down on at a tranquil grassy field disturbed only by a spindly weather station. That will change soon, says Elíasson, science chief at Eimur, a geothermal research center. "Ten years from now, this could be the center of volcanology."

The main attraction lies 2 kilometers below this spot on this volcanically hyperactive island, which is being split in two by the spreading Mid-Atlantic Ridge. In 2009, drillers trying to tap hot water for geothermal energy here accidentally pierced a hidden magma chamber. After an outpouring of steam and glass shards from quenched magma, the borehole created the hottest geothermal well ever measured—until the casing failed.

Now, researchers are returning to penetrate the molten rock on purpose, using hardier equipment, to create the world's only long-term magma observatory. "We've been to Mars. We've been to Venus," says Paolo Papale, research director at Italy's National Institute of Geophysics and Volcanology. "But we have never observed magma below the Earth's surface." Results could help explain how magma moves through the crust, while improving eruption forecasts. They could also shed light on how the continents formed and grew.

In May, the Krafla Magma Testbed (KMT) received financing from the International Continental Scientific Drilling Program, which said the project was one of its top priorities for the decade. With that support, along with several million dollars in funding from Iceland and other European science agencies, the project this month entered its preparation phase. It will prove out the technologies needed to hold the well open despite the corrosion that comes with superheated water, take geophysical soundings of the magma chamber, and model how the chamber will behave once penetrated. The first borehole, costing as much as $25 million, could begin as soon as 2023.

Unable to study magma directly, volcanologists rely on surface measurements from seismometers, GPS sensors, and radar satellites to guess its movements. They can examine solidified magma chambers exhumed by Earth's upheavals—but those remnants are incomplete, selectively depleted by ancient lava flows. They can study lava at the surface, but the samples have by then lost most of the trapped gases that drive eruptions and influence the magma's original temperature, pressure, and composition. Crystals, inclusions, and bubbles in the hardened lava hold clues to its original state. But a sample from the Krafla chamber will tell researchers whether those estimates "are fictional or reliable," says John Eichelberger, a volcanologist at Southern Methodist University and KMT leader.

Getting a sample will also reveal the true nature of the magma chamber. Most scientists reject the cartoonish view of magma chambers as hellish underground lakes. "We think of these systems as a mush"—small amounts of liquid between crystallized grains—"rather than a liquid balloon," says Marie Edmonds, a petrologist at the University of Cambridge.

But Krafla, which last erupted in 1984, may be an exception. The glassy bits from the 2009 drilling campaign hinted that the magma was not only liquid, but also circulating, interacting with melt lower down. "That's the most shocking thing from what little we've gleaned so far," Eichelberger says. But little is known about the magma chamber's size or how long it has persisted—questions KMT can help answer. "It's seeing through a glass darkly, as it were," Eichelberger says.

Island of fire and ice

Riven by tectonic plates, Iceland hosts many active volcanoes. At Krafla, magma is close to the surface.



CREDITS: (PHOTO) G.O. FRIDLEIFSSON/IDDP; (GRAPHIC) N. DESAI/*SCIENCE*; (DATA) P. BIRD, *GEOCHEMISTRY, GEOPHYSICS, GEOSYSTEMS*, 4(3), 2003, DOI:10.1029/2001GC000252

KMT will also help answer basic questions about the raw material of continental crust. The world's sea floors, and much of Iceland, take shape from basaltic magma—much the same stuff that exists in the mantle. But the granite rocks of the continents form from a stickier, silica-rich "rhyolitic" magma that is thought to lie below the KMT site. No one is sure how the continent-forming magma originates; one idea is that basaltic magma gets altered by seawater, remelts, and eventually erupts from volcanoes as rhyolite. Samples of rhyolite from basalt-dominated Iceland could provide a window on how this process works worldwide, Eichelberger says.

KMT intends to collect multiple samples over time and embed sensors in and near the magma to measure heat, pressure, and even chemistry despite temperatures of more than 1000°C. "The technical challenges are formidable," says Wendy Bohrson, a volcanologist at the Colorado School of Mines. KMT's drilling partners are testing flexible couplings that can allow the steel liner of the well to expand and contract with extreme heat. And others are developing innovative electronics to withstand the heat and pressure, which could someday be used on Venus.

The technologies could also benefit Iceland's many geothermal energy companies, which have shied away from the hottest rock. Getting closer to magma could dramatically increase the power potential of individual wells—as was clearly seen with the accidental 2009 well, which on its own could have powered a small city. "The geothermal industry is really looking to understand the real source of its energy," says Hjalti Páll Ingólfsson, managing director of Iceland's Geothermal Research Cluster.

The large amounts of water injected to cool and lubricate the drill will likely perturb the volcanic system a bit, and geophysicists will be watching closely. (There is little worry of triggering an eruption, given the mild behavior of the 2009 borehole, but the site's remote, uninhabited location is another selling point.) Changes in the speed of seismic waves after drilling could reveal the magma's extent, Papale says. Watching these subtle changes could also help with predicting future rhyolite eruptions. Although scientists have gotten quite good at detecting a volcano's warning signs, false alarms abound.

And if KMT remains in place, scientists will eventually get to watch an eruption in action—from the perspective of the underground source of magma. "That will be gold," says Yan Lavallee, a volcanologist at the University of Liverpool. "It is bound to happen." ■

COVID-19

Vaccine equity hopes dashed

Latest forecast slashes this year's global supply by 25%

By **Jon Cohen**

At a time when plans by multiple rich nations to roll out booster shots are again highlighting global inequities in access to COVID-19 vaccines, the wait has grown longer for the world's poorer countries.

The COVID-19 Vaccines Global Access (COVAX) Facility, the main supplier of COVID-19 vaccines to low-income countries, last week scaled back its forecast of available doses for this year by about 25%—from 1.8 billion to 1.4 billion doses. "I'm disappointed, but we aim for transparency," says Seth Berkley, who heads GAVI, the Vaccine Alliance, which helps coordinate COVAX. A complex set of factors—including regulatory delays, manufacturing problems, and the refusal of India, a major producer of COVID-19 vaccines, to allow exports—has slowed the promised ramp up of vaccine supplies.

COVAX, established by the World Health Organization (WHO) and its partners to provide "equitable access" to the shots to the world's 92 middle- and lower income countries, had only shipped 255 million vaccine doses as of 13 September. It had banked on another 230 million coming this year from the Serum Institute of India, which is contracted to supply the vaccine developed by the AstraZeneca and University of Oxford collaboration and one made by Novavax.

> **"It's a matter of countries not being willing to say, 'I'll take my supply later.'"**
> **Nicole Lurie**, Coalition for Epidemic Preparedness Innovations

But because of the country's surge in cases this spring, the Indian government compelled the company to stop exporting product; it is not clear when the export restrictions will be lifted.

Novavax had also promised another 100 million doses of its protein subunit vaccine from manufacturing plants outside India. But its shot still has not received authorization from WHO or any country. The rest of the shortfall is attributed to missing doses from Johnson & Johnson, whose main U.S. plant ran into manufacturing problems; the Chinese company Clover Biopharmaceuticals, which doesn't yet have efficacy data for its vaccine; and another supplier of the AstraZeneca-Oxford vaccine.

The delays cast further doubt on WHO's vaccination targets. It urged all countries to fully vaccinate 10% of their populations by the end of September and 40% by the year's end. Although 90% of high-income countries have met the first target and 70% have hit the second, only 1.9% of people in low-income countries have received a single dose. COVAX has commitments for 4.5 billion doses, enough to meet the global targets, but vaccine manufacturers have cut deals with wealthy countries that put them at the front of the line.

"It's a matter of countries not being willing to say, 'I'll take my supply later,'" says Nicole Lurie, U.S. director of the Coalition for Epidemic Preparedness Innovations, a COVAX partner.

India is taking the same stance. The country's surge has abated and it has administered more than 700 million doses, but only 12% of its population is fully vaccinated. "It's hard to be judgmental here," says Soumya Swaminathan, chief scientist at WHO and a former Indian government health official. "Every country has looked after its own citizens."

Increased donations to COVAX could fill some of the gap. The United States has donated 140 million doses; it has promised to provide an additional 200 million doses by the end of the year and another 300 million by the middle of 2022. U.S. officials insist they will fulfill those pledges even if boosters are approved and offered at home, but global health officials fear other rich countries that are not big donors will opt for boosters at the expense of donations, decreasing supplies available to COVAX.

WHO Director-General Tedros Adhanom Ghebreyesus has urged manufacturers and wealthy countries alike to, at the least, help every country immunize its most vulnerable groups and health care workers. He has called for a "global moratorium" on extra booster doses until the end of the year.

"I will not stay silent when the companies and countries that control the global supply of vaccines think the world's poor should be satisfied with leftovers," he said at a press conference 8 September. ■

EUROPE

Climate policies loom large in German election

Chancellor Angela Merkel, a former scientist, will cede power

By **Gretchen Vogel**

After 16 years, Europe's largest economy will no longer be led by someone with a Ph.D. in physical chemistry. German Chancellor Angela Merkel, a former scientist, will step down following parliamentary elections on 26 September, and all three politicians vying to replace her studied law. "We have been very lucky with Angela Merkel to have a chancellor who knows how science works," says Martin Stratmann, president of the Max Planck Society, which funds research at its 86 member institutes.

Yet scientists have little to worry about, at least in terms of research funding. Annual rises of 3% are locked in through 2030, and all the major parties vouch for the importance of science. "There has always been a broad consensus on this, and I am confident that whatever the new government will look like, this basic attitude will not change," says Otmar Wiestler, president of the Helmholtz Association, which includes 18 research centers.

The competing parties differ on other issues, however, including how to promote innovation and biomedical research, and how to address climate change, one part of Merkel's legacy that many scientists are disappointed with. Although she publicly emphasized the importance of the issue, Germany has repeatedly failed to meet its emissions targets. Under her leadership, the country phased out nuclear power and solidified plans to keep its coal power plants running through 2038, while building a new natural gas pipeline from Russia. "I am not as happy about those policies as I am about the budgets," says Johannes Orphal, a climate researcher at the Karlsruhe Institute of Technology.

It is far from clear who might replace Merkel. Her own party, the center-right Christian Democratic Union (CDU), and its Bavarian sister party—together called "the Union"—are lagging in the polls. Their candidate, Armin Laschet, governor of North Rhine-Westphalia, Germany's most populous state, has been criticized for his response to massive floods in June and his laissez-faire approach to the coronavirus pandemic. Leading the race is the center-left Social Democratic Party (SPD), the junior partner in the "grand coalition" with the CDU that has been in power since 2013. Its candidate, Olaf Scholz, is the current finance minister and has campaigned as a source of stability and an heir to Merkel. Polling in third place is the environmentalist Green Party, led by Annalena Baerbock. In the weeks following her announcement as candidate, the Greens shot to the lead in the polls, reaching a record 26%, but accusations of plagiarism in her recent book about her vision for Germany and other stumbles have since dampened some voters' enthusiasm.



Who's next?

The wide-open race to succeed Angela Merkel as chancellor means a three-way governing coalition is likely, a first for Germany. The parties' climate policies, including their target date for zero net emissions, vary significantly.

PARTY	CANDIDATE	POLLING	POLITICS	CLIMATE NEUTRAL DATE
Social Democratic Party	Olaf Scholz	26%	Center left	2045
Christian Democratic Union	Armin Laschet	21%	Center right	2045
Green Party	Annalena Baerbock	16%	Center left, environmentalist	2041
Free Democratic Party	None	13%	Center right, libertarian	2050
Alternative for Germany Party	None	12%	Far right	None
Left Party	None	6%	Left	2035

No one is set to win a majority—typical in Germany's political system, where six parties are likely to win seats in the parliament. If current polling holds, three of the six will need to cobble together a coalition to form a government—which could blunt strong policy shifts as the parties hammer out inevitable compromises.

Although Afghanistan, digital infrastructure, and tax cuts have all made headlines, climate change is the problem the largest number of voters—43%—say is most important, overtaking the coronavirus pandemic in polls in late August. In April, the country's highest court found the government's 2019 Climate Change Act unconstitutional, agreeing with young activists who claimed that by postponing most emissions cuts until after 2030, the law restricted their future freedom. In response, the parliament passed a revised law in June mandating that Germany by 2030 reduce its greenhouse emissions 65% compared with 1990 levels and be climate neutral by 2045.

The parties differ, however, on how to meet the 2045 deadline. The Greens say their plan, which includes a new climate ministry, would achieve climate neutrality by 2041. The Union plan would boost investment in renewable power to reach zero net emissions by 2045. The SPD also sticks to the 2045 goal, focusing on emissions trading as well as subsidies for electric vehicles and clean heating systems. (Other approaches range from that of the socialist Left Party, which aims to be climate neutral by 2035, to the far-right Alternative for Germany Party, which denies that human activity is affecting the climate.)

The Green and Left parties also pledge to help state governments rebuild crumbling university buildings sustainably. "If the public sector would invest on the side of climate innovation … that would be a big move forward," says Antje Boetius, director of the Alfred Wegener Institute. Procurement laws and limited budgets often thwart climate-friendly decisions, she says. In everything from planning a new research vessel to choosing electricity providers, rules generally require

CREDITS: (PHOTO) MICHAEL KAPPELER/PICTURE ALLIANCE/GETTY IMAGES; (DATA) WAHLRECHT.DE

giving contracts to the lowest bidder, with few standards for climate impacts.

All of the main parties mention "innovation" in their election platforms. The libertarian Free Democratic Party and the Greens call for a new funding agency focused on technology transfer. The SPD wants to amp up the state-owned investment and development bank to "become a modern investment and innovation agency," whereas the Union wants to increase tax breaks for companies that do R&D and strengthen existing programs that fund tech transfer. For any of these plans to work, leaders will need to step back, says Wilhelm Krull, director of the New Institute, which funds research on ecology, economics, and democracy. "It's very difficult in Germany to take risks and to accept that of course you will have quite a number of failures," he says. Any new innovation scheme will need "a different governance structure that is at least at arm's length—if not further away—from the government."

The CDU also calls for a new national agency focused on biomedical research and development that, like the U.S. National Institutes of Health, would combine basic and clinical research. Although the German company BioNTech developed one of the most successful coronavirus vaccines—the messenger RNA shot produced by Pfizer—the pandemic has also highlighted weaknesses in the country's clinical research capacities, says Georg Schütte, secretary general of the Volkswagen Foundation, a large private research funder. For example, he says, "Germany is a powerhouse for life science research, but there is no national platform for clinical trials."

Enacting these policies and creating these agencies will depend heavily on who ends up in charge of the research and education ministry. The current minister, CDU member Anja Karliczek, who helped shepherd through the 2019 budget agreement guaranteeing research funding rises, has said she would be happy to continue, but many say that is unlikely even if the Union ends up in the governing coalition because she is not part of Laschet's inner circle. "We are all a bit nervous" about who might fill the post, Orphal says. The eventual choice will depend on coalition negotiations, certain to involve horse trading for control of different ministries.

Still, a three-way coalition could have advantages, says Matthias Kleiner, president of the Leibniz Association, which includes nearly 100 research institutes. A coalition "can be a fruitful source of different perspectives to solve the big problems that we face," he says, forcing disparate parties to find common ground. "In the end, it can be good when multiple parties come together." ■

FOREIGN INFLUENCE

U.S. judge acquits researcher charged with hiding China ties

Decision to free former engineering professor Anming Hu could have implications for other China Initiative cases

By **Jeffrey Mervis**

For the first time, a federal judge has handed down a verdict in one of the cases brought by the U.S. Department of Justice (DOJ) against dozens of academic researchers with ties to China—and the government lost. On 9 September, U.S. District Judge Thomas Varlan acquitted Anming Hu, a former University of Tennessee, Knoxville (UTK), engineering professor, of lying to NASA about his funding ties to institutions in China. In addition to freeing Hu from 18 months of house arrest, Varlan made clear in his 52-page ruling that he was not impressed by prosecutors' claims that Hu's reporting issues amounted to fraud. Although each case is unique, the judge's opinion could have implications for other cases under what the government calls its China Initiative.

> **"There is no evidence that the defendant intended to deceive NASA."**
>
> **Thomas Varlan**, U.S. district judge

In many of the prosecutions, the government has alleged that a scientist hoodwinked the federal agency that funded the work by failing to disclose financial support from China. The agency wouldn't have given the researcher the grant if it had known about those links, prosecutors say. As a result, DOJ claims the tainted award represents a misuse of government money.

Such charges can carry the threat of hefty penalties. In a case that did not go to trial, Song Guo Zheng, a former Ohio State University, Columbus, rheumatologist, pleaded guilty in May to lying about his Chinese affiliations on a National Institutes of Health (NIH) grant application. A federal judge sentenced him to 37 months in prison and ordered him to repay NIH some $3.4 million. Before Zheng was sentenced, a senior NIH official told the court that his "lack of candor in his application calls into questions the validity of his entire research. As a result, the NIH is not able to rely on any of the research [he] produced."

Hu's case is one of several brought under a 2011 law barring NASA from funding bilateral research involving the Chinese government. Prosecutors claimed Hu knew he was violating that law, which has never been tested in court, and deliberately lied to university officials and federal agents. But Varlan ruled the government had overreached. "There is no evidence that NASA did not receive exactly the type of research that it bargained for," Varlan wrote about work that started in 2016. Moreover, he says, "There is no evidence that the defendant intended to deceive NASA … [or] had a scheme to defraud NASA."

The judge noted that Hu had repeatedly disclosed his relationship to the Beijing University of Technology (BJUT) to UTK, but that university officials told him the restriction didn't apply to his NASA research. Varlan also faulted the university for doing a poor job of explaining the ban on work with China. "Rather than providing clarification that the defendant's affiliation with BJUT may violate the restriction," Varlan wrote, "UTK's language could reasonably be construed as exempting defendant from the restriction altogether."

Varlan's ruling could strengthen a defense used by other accused researchers. Lawyers representing Mingqing Xiao, a Southern Illinois University math professor accused of hiding his Chinese affiliations in a grant application to the National Science Foundation, this month asked the court to throw out the case because of "fundamental ambiguities" in NSF's disclosure rules for grant applicants. Their brief even cites Eric Lander, science adviser to President Joe Biden, who told *Science* earlier this year that "it's very hard to figure out what you're supposed to be disclosing. … Agencies have different rules, and their definitions vary."

DOJ has not said whether it will appeal Varlan's ruling, and Hu issued a statement through his lawyer that said "the painful memories are still there, so I prefer to remain silent." Civil rights groups praised the decision as a rejection of what they see as the government's persistent racial profiling of Chinese American scientists. ■



A firefighter in Oregon sets a prescribed burn designed to clear grass, brush, and young trees that can make forests vulnerable to intense wildfires.

CLEARING THE TINDERBOX

As the climate warms, a huge forest experiment aims to reduce wildfire risk and find common ground between loggers and environmentalists

By **Warren Cornwall**, *in the Malheur National Forest in Oregon*

In a Sun-dappled glade here, James Johnston could see two possible futures for the forests that blanket the Blue Mountains. During a recent visit, the ecologist stood among orange-hued ponderosa pine trees with trunks so broad it would take two people to encircle one with their arms. Grasses carpeted the wide gaps between the pines, creating the feel of an alpine park.

Just 200 meters away, however, swaths of dead trees, their trunks weathered to a polished silver, rose from powdery dirt. "That's old-growth ponderosa pine killed by the southern edge of the Canyon Creek Fire," which struck in 2015, explained Johnston, who works at Oregon State University (OSU), Corvallis.

A key difference? The living trees sat within a forest tract that had been carefully logged—"treated" in the parlance of researchers—as part of an ambitious experiment, launched in 2006, that aims to prevent the kinds of intense wildfires now destroying forests across western North America. The effort seeks to demonstrate ways of reversing more than 100 years of mismanagement that have transformed many forests into tinderboxes. It is also a study in how to overcome decades of disagreements among scientists, environmentalists, and forest workers on how to best protect both ecosystems and local economies. Here, environmentalists are welcoming chainsaws, and loggers are collaborating with scientists once reviled by the timber industry.

The massive experiment involves intensively monitoring some 550 plots, each 1000 square meters, scattered across nearly 700,000 hectares, to learn how best to deploy two standard techniques for making a forest more fire resistant: prescribed burning and limited logging. It has made the Malheur National Forest "one of the best studied national forests" in the United States, Johnston says. Funded chiefly by state and federal land management agencies, the research has become increasingly relevant as a warming climate increases the risks of wildfires so intense that they sterilize soils and kill massive old trees. Helping forests become more resilient is critical, Johnston says, because "we're going to have a hard time growing trees under hotter, drier conditions."

The lessons being learned here are as much about social science as about forestry. They point to the potential for grassroots collaborations to make a noticeable dent in an ecological problem that spans vast stretches

PHOTO: BLM OREGON AND WASHINGTON/CC BY 2.0

of a continent, and make progress on solutions often stymied by fierce social conflicts.

As if to drive home the stakes, the air was tinged with the scent of fire during Johnston's visit to the Blue Mountains in late July—smoke from the Bootleg Fire burning 230 kilometers to the southwest. That blaze would eventually grow to more than 160,000 hectares. It was just one of more than 80 large wildfires that have broken out this summer in the United States and Canada, destroying communities and enveloping the continent in a persistent brown haze.

THE START of the Malheur forest project was not auspicious. An environmental lawyer brought a bodyguard to the first meeting.

In 2003, Susan Jane Brown, an attorney for the Western Environmental Law Center, had just won the latest in a string of lawsuits challenging logging projects in the national forest, home to old-growth woodlands and such notable features as the world's largest living organism—a fungus dubbed the "humongous fungus." It is also a source of jobs. Boyd Britton, a county commissioner in Grant county, which spans much of the forest, had approached Brown and asked whether they could take a trip into the woods together, hoping it might help break the impasse over logging.

Brown and Britton lived just 320 kilometers apart, but in very different worlds. Brown was an environmental activist from Portland, a city synonymous with a liberal ethos. Britton was a welder from a county that's home to fewer than 8000 people and is shaped by a tradition of logging, mining, and ranching. Politically, it has a conservative streak so deep that former President Donald Trump won 77% of the vote in 2020. "Grant county is not always a safe place for people like me," Brown says. She agreed to the meeting but brought along a large male colleague.

Yet Britton and Brown found a sliver of common ground over 3 days touring the woods, looking at both logged and untouched patches. They each had a deep affection for the forests. And both had something to lose from the never-ending conflicts over how they were managed. Lumber mills in Grant county were dwindling as lawsuits and a changing political climate slowed logging. But some environmentalists, including Brown, had concluded that stopping logging wasn't enough. "The science was really starting to come out and point to the fact that active management was necessary to restore many forests," Brown says.

Before Europeans arrived en masse, forests in this region were a patchwork of meadows and unevenly aged stands with a preponderance of big trees. Fires were frequent, but smaller and less intense than today. Before 1890, Johnston's research has shown, chunks of forest typically burned every 11 to 21 years, the scorch marks visible in a tree's annual growth rings.

By the time of Brown's and Britton's visit, more than 100 years of logging and cattle grazing, as well as a national policy of snuffing out all wildfires, had left the landscape overcrowded with trees. Most sites haven't burned in recent decades. "It's like a faucet got shut off," Johnston says.

Drought- and fire-tolerant species—particularly ponderosa pines with their spare tufts of long needles and thick, heat-resistant bark—now compete with other species, including grand firs. The firs' thin bark, prolific needles, and close-to-the-ground branches provide less protection against fire, but the species thrives in the shade of other trees and grows quickly. Using pencil-thin cores taken from trees to reconstruct how the forest looked at different times, Johnston found that, over the past 150 years, many forests had come to hold 1.5 to eight times more wood than before, creating a huge reservoir of fuel.

This process, repeated across much of the West, has increased the risk of bigger, hotter, and more frequent fires. In California's Sierra Nevada mountains, for example, researchers found evidence that the proportion of fires that burned with "high severity" has more than quadrupled since the early 20th century.

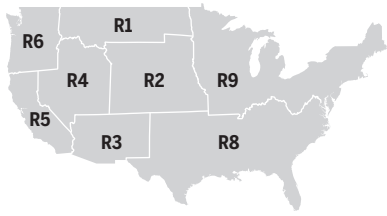
Researchers and forest managers long ago identified ways to reduce fire risks, a combination of "thinning" forests with selective logging to make them more open and intentionally setting "prescribed" burns that mimic gentler wildfires. But in many places, these practices have made slow progress, for a constellation of reasons. Fears of air pollution from smoke, as well as a shortage of trained workers and funding, have hampered the use of prescribed fires. As a result, the area intentionally burned each year in the western United States remained virtually unchanged between 1998 and 2018.

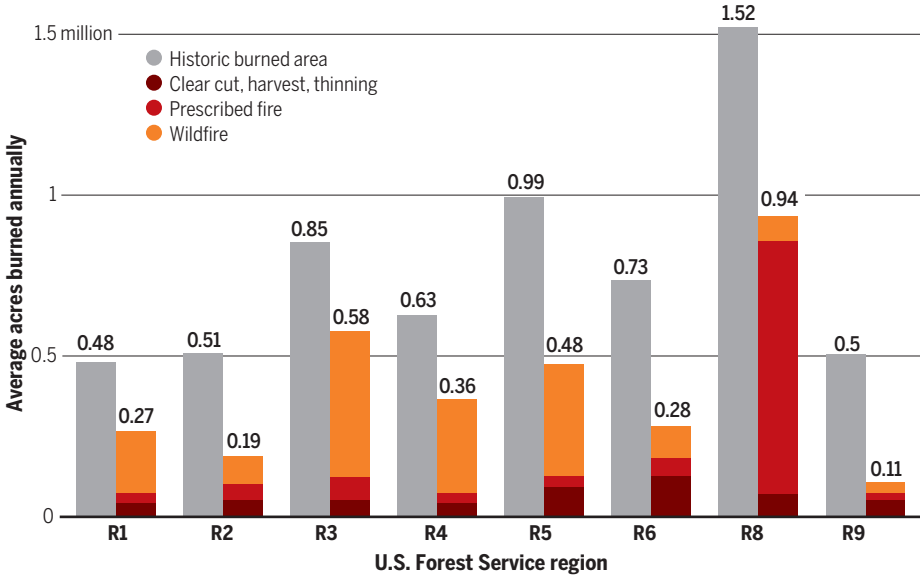
Environmentalists, meanwhile, sometimes oppose thinning projects, seeing them as a backdoor effort to increase logging. The decline of local timber industries has, paradoxically, made it difficult to thin some forests. In northern Arizona, an ambitious U.S. Forest Service (USFS) program to log nearly 1 million hectares was slowed as private contractors struggled to find a market for the wood.

In many regions, forest managers would need to double burns or thinning projects to equal the area of forest historically

A fiery deficit

The U.S. Forest Service is falling short in efforts to match the area of forest that burned before the 20th century on the 78 million hectares of land it manages in nine regions (right). Thinning, prescribed burns, and wildfires combined amounted to just 45% of historic, natural fire levels between 2008 and 2012, according to agency scientists.





CREDITS: (GRAPHIC) K. FRANKLIN/*SCIENCE*; (DATA) N. VAILLANT AND E. REINHARDT, *J. FOR.* 115(4):300 DOI: 10.5849/JOF.16-067

"cleaned up" by natural wildfires, according to a 2017 study by researchers with USFS. Restoration efforts "need to be done on a very large scale and very quickly, or [forests] are going to get caught in one of these firestorms," says forest ecologist Jerry Franklin of the University of Washington, Seattle.

IN THE BLUE MOUNTAINS, people cite two reasons why traditional adversaries have been able to break the gridlock: science and beer.

After their initial meeting, Brown, Britton, and others embarked on an uneasy courtship. They recruited a handful of people from different sides whom they thought could work together, and a facilitator to help avoid breakdowns. In 2006, they launched the Blue Mountains Forest Partners, a nonprofit whose members included environmentalists, timber interests, and others with a stake in how the Malheur forest is managed. Their goal was to find common ground on restoration projects and press USFS to implement them. Early on, they agreed to lean on science to give a factual foundation to their deliberations.

Brown suggested consulting two of the Pacific Northwest's most prominent forest scientists, Franklin and Norm Johnson of OSU. The pair is known for pioneering work on wetter old-growth forests closer to the Pacific coast, research that in the 1990s led to the end of most logging on federally owned old-growth forests in the northwestern United States. To Brown's surprise, Britton and others in Grant county agreed.

The two scientists offered diagnoses that included something attractive for each side. The forest needed more logging and fire, Franklin and Johnson said. But don't touch the old-growth ponderosas, they added. "In the beginning, both sides were somewhat ruled by their emotions, and science helped bring everybody to the middle," says Dave Hannibal, a manager for the forest restoration company Grayback Forestry, who joined the partnership in 2006.

The collaboration started small, endorsing a 2009 project to remove young, skinny trees from 200 hectares. Within 4 years, its ambitions had grown. The partnership helped craft a plan to treat 100,000 hectares and a 10-year contract between USFS and a local company, Iron Triangle, to do much of the work. Although the partnership doesn't have regulatory authority or money to fund work in the forest, USFS officials look to it to help navigate the rocky politics of forest management so that the service can expand its efforts.

"We were trying to do restoration, but it was at a very small scale. We just didn't want to offend anybody," says Roy Walker, a longtime officer at the Malheur forest who is a liaison to the partnership. "What the collaboration allowed us to do was think bigger."

Today, Johnston, a former Ph.D. student of Johnson's, oversees teams monitoring the plots set up to study the forest's response to different treatments, including thinning of varying intensities, logging of burned forest, and prescribed fires. Each summer, technicians laboriously walk many of the sites, noting every plant and measuring every tree, even fallen branches.

The work has illuminated the forest's history and evolution, and has helped answer some thorny questions, such as whether some big trees that are protected should be removed. Since the mid-1990s, federal guidelines meant to protect old-growth forests in eastern Oregon and Washington have barred cutting any tree bigger than 53 centimeters in diameter. In the Blue Mountains, loggers chafed against this one-size-fits-all restriction. But environmentalists feared loosening the limit would lead to the loss of vital trees. The partnership turned to Johnston for answers.

Using the research plots, Johnston found that the size limit made it difficult to cut down enough trees in some areas to recreate the more spacious landscape of the past. For example, if loggers left big grand firs untouched, they would constitute nearly 30% of the forest after a thinning project—double their historical share, researchers reported this year in *Ecosphere*.

Such findings helped persuade Brown that bigger grand firs needed to come down, and helped lead to an easing of the federal restrictions. "You've got to get over your worship of large trees," she says. "That's still hard for me, because I like big trees. But I want the right big trees."

Six years ago, after the Canyon Creek Fire burned more than 45,000 hectares of forest, the partnership again turned to scientists to help resolve their differences. Timber workers wanted to cut many of the standing burned trees before they rotted. Environmentalists feared such "salvage" logging could harm forest dwellers such as woodpeckers, which rely on dead trees for nests and insects to eat.

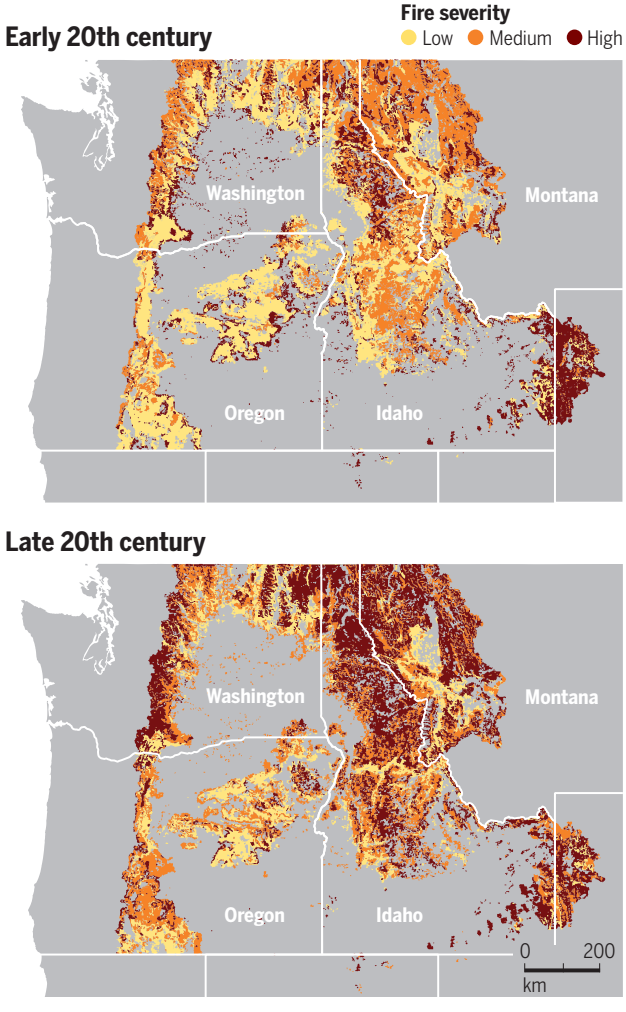
The two sides agreed to ask USFS to use the postfire logging as an experiment, to see how different kinds of logging affected three species of woodpeckers. They also wanted to evaluate a USFS computer model designed to pinpoint areas that could be logged with minimal harm, based on the habitat needed by different woodpeckers.

Preliminary results suggest the modeling and certain kinds of salvage logging are useful, says Vicki Saab, a USFS wildlife biologist who led the study. "The salvage did provide economic benefits locally," Saab says. "At the same time we were maintaining habitat."

Researchers, meanwhile, were also seeing signs that the treated forest plots were better at with-

Wildfires turn up the heat

In the northwestern United States, mismanagement and climate change have increased the risk of more severe wildfires. Blazes that kill 70% of trees became more likely, modeling studies show.



CREDITS: (GRAPHICS) K. FRANKLIN/*SCIENCE*; (DATA) INTERMOUNTAIN FIRE SCIENCE LAB



Researchers fear intense blazes, such as the Bootleg Fire in Oregon this year, will kill old-growth trees and damage soil, making it more difficult for forests to regenerate.

standing fire. Trees in one area thinned in 2014 grew at more than twice the rate of nearby forests that weren't logged, according to monitoring by Johnston's team, probably because fewer trees were competing for scarce water. That was good news, because bigger trees usually withstand fire better. And the intensity and speed of fires had decreased several years after the thinning, computer simulations suggested.

Last month, some of the treated areas were put to a real test. A lightning strike ignited a blaze that eventually grew to more than 8000 hectares. When it reached areas that had been treated starting in 2016, wildfire fighters reported that flames that were burning through the treetops eased and moved to the ground, enabling firefighters to control the blaze, says Sarah Bush, a wildfire analyst and fire manager in the national forest. "Their words were: 'Those fuel treatments saved the Prairie City Ranger District,'" Bush says.

IT TOOK MORE THAN DATA to span the economic, political, and cultural chasms that separated members of the partnership. Several participants point to another factor: a backroom bar at The Outpost, a restaurant on the main street of John Day, a small town that's the business center of Grant county. After long meetings in the woods, the diverse crew would gather there. Conversations turned to more personal matters: whose kid played soccer, who had brought an elk home from a hunting trip. "You start to humanize the others," Brown recalls. "Then it turns out that enemies become friends. I think that honestly that is our secret sauce."

Britton, who moved to Arizona in 2018 but continues to follow the work, concurs. "It's hard to hate the other guy at the table when you're drinking with him," he says.

Personal chemistry, however, isn't all it takes for such initiatives to succeed, says Emily Jane Davis, an OSU social scientist who studies collaborative land management. Officials overseeing the forest were open to outside input, she notes. And a federal program to encourage collaborative forest management, created by Congress in 2009, provided an infusion of dollars. The 10-year contract, unusual in its scale and duration, helped provide stability and a long-term vision. "It's more socially complex than, 'Industry and environmentalists are friends now,'" Davis says.

Indeed, those involved in the project have faced criticism even from their own allies. In 2015, some environmental groups issued a letter blasting collaborative initiatives as "rubber stamping" federal agency proposals. In August, one of those groups sued to block a planned 16,000-hectare logging project in the Malheur forest that was endorsed by the partnership. On the other side, the Canyon Creek Fire intensified complaints about a lack of logging. "There's still local people that think if we're not cutting those big old pines before they get burned up, we're failing," says Zach Williams, a fifth-generation Grant county resident who helps run Iron Triangle and serves on the partnership board.

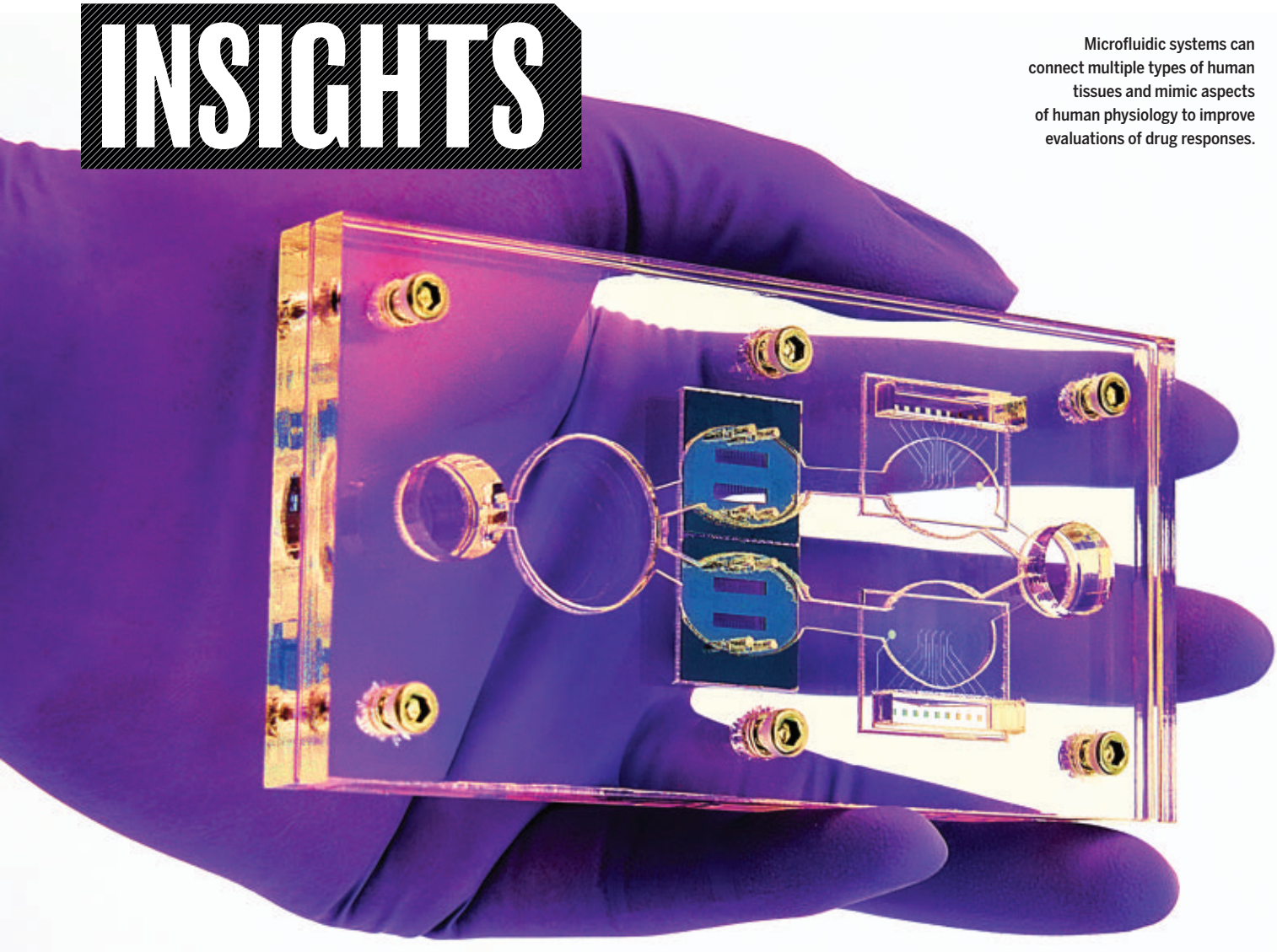


The stump of a ponderosa pine, a fire-resistant species, shows scars from past wildfires.

In the wake of wildfires elsewhere, recent studies have found that pairing prescribed burns with thinning reduces fire damage to trees better than just thinning. In the Malheur forest, however, Johnston estimates that, for a variety of reasons, workers have been able to set prescribed burns in just 20% of tracts thinned in recent years. Officials are now hoping to make up some ground by winning federal funds to continue the partnership's work for 10 more years and treat an additional 85,000 hectares.

For the moment, however, "we're behind," said Hannibal as he and Johnston toured one of the thinned tracts earlier this year. Hannibal gestured to a grand fir sapling that had begun to reach for the sky. "Prescribed fire's going to be necessary to kill this guy," he said. But then he reached down and yanked the little tree from the ground. One less piece of fuel to stoke a future blaze. ■

PHOTOS: (TOP TO BOTTOM) MARANIE STAAB/BLOOMBERG VIA GETTY IMAGES; W. CORNWALL/*SCIENCE*



Microfluidic systems can connect multiple types of human tissues and mimic aspects of human physiology to improve evaluations of drug responses.

PHOTO: HESPEROS INC.

PERSPECTIVES

MEDICINE

Human microphysiological systems for drug development

Organs-on-chips could be used to assess drug efficacy and support personalized medicine

By **Adrian Roth**[1] *and* **MPS-WS Berlin 2019**[2]

Microphysiological systems (MPS), such as microfluidic organs-on-chips, have rapidly evolved as promising in vitro tools to recapitulate human physiology by recreating key biological processes and disease states. However, their value for drug development is only now becoming clear. MPS combine microsystems engineering with cell biology, yielding cell-culture models that can display three-dimensional architecture, multicellular interactions, tissue-tissue interfaces, fluid flow, and organ-level mechanical cues. For example, they can incorporate breathing mechanics of human lungs (*1*), circulating immune cells trafficking through perfused microvasculature (*2*), living microbiotas (*3*), and interconnections with other organs (*4*, *5*). They add to the toolbox of assays to identify potential therapeutics for diseases, including COVID-19 (*6*). These features enable human multi–cell-type systems that can better replicate complex tissue and organ functions than conventional cell culture. Consequently, MPS have gained broader attention as a tool to improve the prediction of human efficacy and potential undesired effects of drugs before patients are exposed to them (*7*).

MPS technologies may provide a way to better understand and address the main failures of clinical programs: lack of efficacy or unacceptable side effects that are not predicted in animals or simpler cell systems during early preclinical stages. The key advantage that MPS offer is the creation of more physiologically relevant human organ–like models that can potentially yield data on drug action that will better trans-

late to humans than that from in vivo animal models or conventional cell systems. Whereas research data from animals do not always translate to humans because of differences in the physiology of the different species, traditional human in vitro models lack three-dimensionality, tissue-tissue interfaces, and mechanical cues, which leads to dedifferentiation of cultured cells and, consequently, reduced human relevance. Despite the mostly exploratory nature of current MPS, there is an appetite for the uptake of the technology by pharmaceutical and biotechnology industries to improve on human predictivity, with the long-term goal of eventually replacing animal models wherever possible. Simultaneously, both academic groups and multiple biotech companies are developing increasingly refined MPS models to meet the needs and quality standards required for drug development such as scalability and robustness.

Up to now, adoption of MPS was primarily for preclinical safety (drug toxicology and metabolism), and some test systems have already reached the requirements in the pharmaceutical industry for internal decision-making, often for application in a defined context of use that requires only limited validation efforts (*7*). MPS have also been used to address disparities between different preclinical animal models, as well as between animals and humans. For example, rat, dog, and human liver organs-on-chips were shown to reproduce species-specific toxicities previously observed in testing by pharmaceutical companies while also providing new insights into potential toxicity mechanisms (*8*). Because effects observed in preclinical animal species sometimes have an unclear potential to translate to humans, toxicity signals may lead to selection of suboptimal drug-candidate molecules for further development. Thus, systems to test for toxicities relevant to humans could greatly help advance the most promising candidates into the clinic.

MPS have also been used to model many other toxicities, including cases where no suitable animal models are available or where animal models are unable to predict human responses. For instance, a human blood vessel-on-a-chip recreated thrombotic toxicities that led to failure of a therapeutic monoclonal antibody in human clinical trials, toxicities that were never detected during preclinical testing of this drug in animals (*9*). A vascularized human bone marrow–on-a-chip that supports differentiation and maturation of multiple blood cell lineages also recapitulates myelo-erythroid toxicities after clinically relevant exposures to chemotherapeutic drugs and ionizing radiation, as well as bone marrow recovery after drug-induced myelosuppression (*10*). Moreover, an MPS model composed of bone tissue was exposed to hip implant–associated dissolved cobalt and chromium at clinically relevant concentrations, which led to the identification of direct cytotoxic effects and successfully verified the integration of chromium into cancellous bone and binding to intertrabecular matrix previously found in patients (*11*).

Often, determination of the schedule and dosing of combination therapy in oncology is done by trial and error in clinical trials. Cytotoxic therapies, which target the bone marrow, remain a mainstay of therapy, and for these drugs in combination with targeted therapy, bone marrow MPS could eventually improve clinical scheduling and dosing regimens as well as possibly provide inroads for personalized medicine by defining individual treatment regimens based on patient-specific MPS testing before dosing the patient.

Although addressing well-known shortcomings of preclinical safety testing was an early focus of MPS research, newer models now aim at efficacy testing. For example, a human lung airway–on-a-chip with an interfaced endothelium was used to measure responses to anti-inflammatory compounds that inhibit cytokine-induced recruitment of circulating neutrophils under flow and, more recently, to evaluate the effects of existing and potential antiviral therapeutics on severe acute respiratory syndrome coronavirus 2 (SARS-CoV-2) infection and host inflammatory responses (*6*). A bone marrow–on-a-chip was also used to model a rare genetic disorder (Shwachman-Diamond syndrome) using cells isolated from patients, which reproduced key hematopoietic defects of this disease (*10*). These studies demonstrate the potential value of using MPS for developing personalized approaches that make use of patient cells for therapy optimization and potentially assist in clinical trial design, which will be particularly useful for patients with disorders that are so rare that it would otherwise be difficult to carry out preclinical drug testing in a systematic manner.

Complex physiological processes in the human body typically involve more than one organ, and thus MPS researchers have started to model multiorgan interactions to better investigate disease biology or drug action. For example, multiorgan MPS have been established to study how neuroactive drugs, such as methamphetamine, cross the blood-brain barrier and exert effects on neurons of the brain (*12*). First-pass pharmacokinetic models composed of linked human liver, kidney, and intestine organs-on-chips have also been used in combination with computational modeling to quantitatively predict human drug pharmacokinetics and pharmacodynamics (*4*). Linked intestine, liver, brain, and kidney MPS models have been differentiated using induced pluripotent stem cells from a single donor (*13*), which might enable personalized donor-specific, multiorgan research and drug testing in the future. If combined with patient-derived stem cell or organoid approaches (*14*), such models could provide tailored precision medicine tools at the individual patient level, supporting ambitions for personalized treatments. However, introducing patient-derived cells can only be realized with broad acceptance through informed consent and ethics approvals that these cells can be obtained and used for research and precision medicine.

Unlike commonly used immune-deficient or semihumanized animal models, human MPS lend themselves to grafting with tumors (*15*) and to infection with microbial pathogens (*6*), with particular advantages for human-specific viruses. However, none of the MPS assays have so far been used as part of the regulatory documentation in the drug approval process (*7*) owing to lack of adequate validation and experience with this newly emerging technology. Thus, an important challenge is to make the leap from research-grade MPS assays into validated drug development tools that will produce results that meet the requirements of regulatory review. As drug development increasingly focuses on developing highly engineered therapeutic molecules that do not cross-react with targets in any animal model, there is often simply no other choice than to use human in vitro models. The use of nonhuman primates for drug and vaccine testing is also becoming more difficult because of shortages in supply (e.g., owing to COVID-19 vaccine testing), in addition to the attendant ethical concerns. Thus, there is now a greater need than ever before for in vitro alternatives to preclinical models with human cells.

MPS can also enable rapid development of new therapies to confront urgent medical needs [e.g., messenger RNA (mRNA) vaccines for pandemic viruses or chimeric antigen receptor (CAR) T cell cancer immunotherapies]. Although these therapies have been approved using traditional methods, postapproval follow-up studies will often be required for such innovative drug modalities to enlarge the safety and

[1]F. Hoffmann–La Roche Ltd., Personalized Healthcare Safety, Product Development Safety, Roche Innovation Center, Basel, Switzerland. [2]Microphysiological Systems-Workshop (MPS-WS) Berlin 2019. MPS-WS Berlin 2019 authors and affiliations are listed in the supplementary materials. Email: adrian_b.roth@roche.com

efficacy databases. MPS models could be of great value, for example, for bridging personalized "patient-on-chip" data with matched data from postapproval studies in a head-to-head manner, thus enabling a "prediction–reverse translation" loop where real world data help establish a model that can then be used for prediction. This approach could be greatly enhanced if either sponsors (including, for example, patient organizations for rare diseases) or clinical research organizations involved in pursuing such therapies would liaise with developers of MPS assays to ensure that disease features are emulated in a patient-specific manner. The success of this approach would be further strengthened by incorporating advice from the relevant regulatory authority into the on-chip trial design. For example, the US Food and Drug Administration Drug Development Tool qualification process could be used, much like it is used for the validation of biomarkers as part of the Innovative Science and Technology Approaches for New Drugs (ISTAND) Pilot Program that supports the development of new approaches to drug development that may be acceptable for regulatory use in the future. Together with advanced data analytics, in silico modeling, and simulation, exploring this approach in an iterative manner for one particular context of use (e.g., a particular disease and treatment modality) at a time could eventually result in acceptable datasets for regulators that are of higher predictive power than those previously generated with animal models. Once proof of concept is demonstrated successfully for one indication, others would follow. ■

REFERENCES AND NOTES

1. D. Huh *et al.*, *Science* **328**, 1662 (2010).
2. M. B. Chen *et al.*, *Proc. Natl. Acad. Sci. U.S.A.* **115**, 7022 (2018).
3. S. Jalili-Firoozinezhad *et al.*, *Nat. Biomed. Eng.* **3**, 520 (2019).
4. A. Herland *et al.*, *Nat. Biomed. Eng.* **4**, 421 (2020).
5. C. W. McAleer *et al.*, *Sci. Transl. Med.* **11**, eaav1386 (2019).
6. L. Si *et al.*, *Nat. Biomed. Eng.* **5**, 815 (2021).
7. U. Marx *et al.*, *ALTEX* **37**, 365 (2020).
8. K. J. Jang *et al.*, *Sci. Transl. Med.* **11**, eaax5516 (2019).
9. R. Barrile *et al.*, *Clin. Pharmacol. Ther.* **104**, 1240 (2018).
10. D. B. Chou *et al.*, *Nat. Biomed. Eng.* **4**, 394 (2020).
11. J. Schoon *et al.*, *Adv. Sci.* **7**, 2000412 (2020).
12. B. M. Maoz *et al.*, *Nat. Biotechnol.* **36**, 865 (2018).
13. A. P. Ramme *et al.*, *Future Sci. OA* **5**, FSO413 (2019).
14. S. E. Park, A. Georgescu, D. Huh, *Science* **364**, 960 (2019).
15. J. Hübner *et al.*, *Sci. Rep.* **8**, 15010 (2018).

ACKNOWLEDGMENTS

A.R. is an employee of F. Hoffmann-La Roche Ltd. and holds equity in F. Hoffmann-La Roche Ltd. See supplementary materials for the conflicts of interest of MPS-WS Berlin 2019 authors.

SUPPLEMENTARY MATERIALS

https://science.org/doi/10.1126/science.abc3734

10.1126/science.abc3734

CANCER

Opposing roles of the immune system in tumors

Inflammation promotes early tumorigenesis but must be evaded as tumors progress

By **Won Jin Ho**[1] *and* **Laura D. Wood**[1,2]

The immune system can both promote and constrain cancer development. Chronic inflammatory conditions predispose to cancer formation in multiple organs, highlighting the role of the immune system in promoting tumorigenesis (*1*). Conversely, the immune system can target and kill neoplastic cells, owing to their molecular differences from normal cells (*2*). Therefore, tumor development is aided by processes intrinsic to cancer cells that either exploit protumorigenic inflammation or evade antitumor immune responses. On pages 1326 and 1327 of this issue, Del Poggetto *et al.* (*3*) and Martin *et al.* (*4*), respectively, demonstrate how cancer cells may co-opt these opposing effects of the immune system during tumor development. Together, these studies highlight how the immune system influences the genetic and epigenetic alterations in cancer cells, which may lead to improved strategies for cancer prevention and therapy.

Del Poggetto *et al.* interrogate the role of inflammation in promoting early pancreatic tumorigenesis, describing the molecular and phenotypic impacts of transient inflammation on non-neoplastic pancreatic epithelial cells. Using a mouse model combining caerulein-mediated chemical induction of pancreatic inflammation with inducible expression of the oncogenic *Kras* G12D (Gly^{12}→Asp) mutation, the authors show increased tumor formation even after remote and transient pancreatitis (inflammation of the pancreas). This increase is driven by postinflammation cell-autonomous alterations in the pancreatic epithelial cells, which show epigenetic reprogramming—i.e., particularly increased chromatin accessibility at thousands of genomic regulatory elements—persisting long after resolution of the inflammatory insult. These sustained alterations in chromatin accessibility led to alterations in transcription factor activity and resultant changes in gene expression, which remained even after histological resolution of the inflammatory changes.

The authors identify and functionally validate a key transcription factor, early growth response protein 1 (EGR1), in this response, the expression of which is dependent on the secretion of interleukin-6 (IL-6) from macrophages involved in the inflammatory response. However, more work remains to elucidate the mechanistic details of these far-reaching alterations. Del Poggetto *et al.* also show that the pancreatic damage after a second inflammatory insult is attenuated compared to the first, suggesting that epigenomic reprogramming facilitates rapid transdifferentiation of acinar cells during subsequent bouts of pancreatic inflammation. These changes in acinar cell differentiation include decreased production of pancreatic enzymes (zymogens), which limits injury-induced zymogen release and thus prevents further tissue damage. Similarly, induction of oncogenic *Kras* G12D also triggered acinar cell changes to abrogate surrounding tissue injury during a subsequent inflammatory insult, raising an intriguing mechanism by which a tumor-initiating oncogenic mutation may be selected in the setting of pancreatitis.

Although the link between inflammation and cancer has long been appreciated more broadly, the study of Del Poggetto *et al.* illustrates an epigenetic mechanism by which inflammation leads to lasting molecular consequences in pancreatic epithelial cells, shaping early pancreatic tumorigenesis. This complements the findings from another recent study that demonstrated epigenetic reprogramming of mouse pancreatic cells with a combination of inflammation and *Kras* G12D mutation (*5*). An important caveat to these findings is that they rely on elegant genetic manipulations and time course experiments that are only possible in mouse models, and thus the relevance of these findings to human pancreatic tumorigenesis remains unclear. Although chronic pancreatitis is an

[1]Department of Oncology, Johns Hopkins University School of Medicine, Baltimore, MD, USA. [2]Department of Pathology, Johns Hopkins University School of Medicine, Baltimore, MD, USA. Email: ldwood@jhmi.edu

important risk factor for the development of pancreatic cancer in humans (*6*), pancreatic cancer is frequently diagnosed in the absence of such preceding inflammatory diseases. It is possible that subclinical local inflammation is a universal initiating event in human pancreatic tumorigenesis, but studies in humans are required to confirm or refute this hypothesis.

Conversely, Martin *et al.* explore the opposing role of the immune system in constraining tumor development through targeting neoplastic cells. The authors focus on the identification of molecular alterations that allow escape from immune-mediated destruction by performing in vivo genetic screens with the CRISPR-Cas9 system. CRISPR screens have been employed extensively both in vitro and in vivo to identify therapeutically targetable dependencies in cancer (*7*). The screens used by Martin *et al.*, performed in mouse cell lines from multiple tumor types and in two different mouse backgrounds, compared the selected alterations between wild-type mice and those lacking a mature immune system, allowing functional identification of genes that promote tumor cell growth in the setting of an intact immune microenvironment.

They found a substantial enrichment of previously identified tumor suppressor genes in the screens in wild-type mice, suggesting an unanticipated role for inactivation of tumor suppressor genes in immune evasion. This enrichment of tumor suppressor gene alterations was consistent across multiple distinct tumor types, but the genes that were specifically altered were quite variable, with <10% overlap between different cancer cell lines. This suggests tissue specificity for the molecular mechanisms of immune evasion, at least in the context of tumor suppressor genes. The mechanisms by which tumor suppressor gene loss enables immune evasion are not yet clear. The study of Martin *et al.* suggests that reduced antigen presentation and resistance to T cell killing are not prominent mechanisms. Detailed studies of one enriched tumor suppressor gene, guanine nucleotide binding protein α13 (*Gna13*), highlight the recruitment of M2-like CD206$^+$ immune-suppressive macrophages through C-C motif chemokine 2 (CCL2) secretion, a well-described phenomenon (*8*). Interrogation of the mechanisms of different tumor suppressor genes in immune evasion will require extensive additional functional studies.

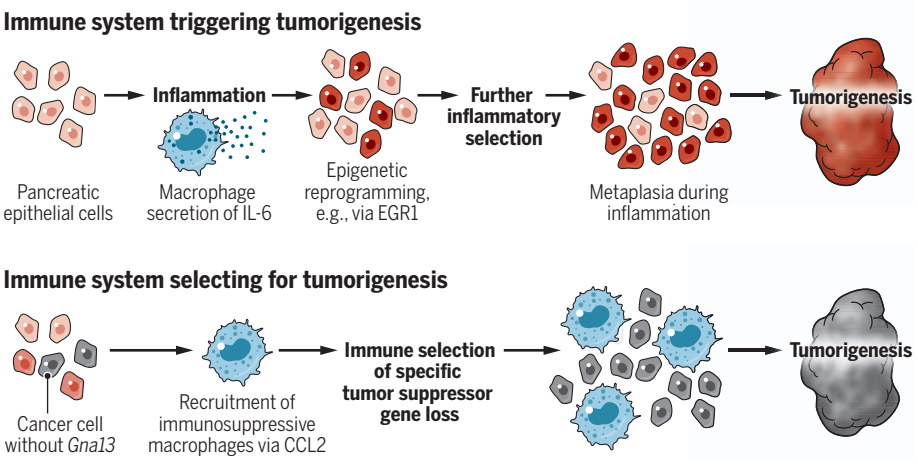
Previous studies of tumor suppressor genes have largely focused on their phenotypic impact within tumor cells, such as stimulation of proliferation and evasion of apoptosis. These cell-intrinsic phenotypes are likely selected after loss of some tumor suppressor genes, such as those identified in all screens regardless of the presence of immune cells. However, the promotion of immune evasion is a newly identified functional consequence of tumor suppressor gene loss and may help to explain a lack of phenotype in cells cultured in vitro for some tumor suppressor genes. Martin *et al.* highlight an interesting example in which cullin 3 (*Cul3*) loss is selected against in vitro owing to decreased proliferation but is selected for in wild-type animals because of its impact on evading the immune system. These findings support the possibility of multiple mutation-specific phenotypes for the same gene that may have opposing effects on overall tumor cell survival, highlighting the complexity of selection in a multicellular microenvironment.

Overall, these results demonstrate the importance of functional assessment of driver gene mechanisms in models with intact immune systems to avoid the flawed assumption that such genes have only cell-intrinsic phenotypic effects. Moreover, elucidation of the immune-evasion mechanisms of specific tumor suppressor genes may highlight therapeutic opportunities for restoration of immune targeting of tumor cells. However, an important caveat of this study is that some of the highest-scoring tumor suppressor genes in the CRISPR screen lack frequent mutations in human cancers. Although these results can be explained by the screening platform, validation of the findings in human cancer samples represents an important next step to ensure translatability.

Taken together, the studies of Del Poggetto *et al.* and Martin *et al.* provide far-reaching conceptual innovations in our understanding of how the immune system drives molecular alterations in tumor cells (see the figure). Even transient inflammation can result in sustained epithelial reprogramming that enables subsequent steps in tumorigenesis, underscoring the role of the immune system in promoting tumor formation. However, the immune-mediated targeting of established tumor cells also constrains tumor development, providing a potent selective pressure for genetic alterations that enable immune evasion. Although additional research is required to confirm the applicability of these findings to human tumorigenesis, these studies provide a foundation on which to build new strategies for immune interception and treatment of cancer. ■

The duality of the immune system in tumorigenesis

The immune system promotes tumorigenesis by inducing epigenetic reprogramming that facilitates metaplasia of pancreatic acinar cells during inflammatory insults. In responding to tumor cells, the immune system also selects for the loss of tumor suppressor genes that permit immune evasion and successful tumorigenesis.



CCL2, C-C motif chemokine 2; EGR1, early growth response protein 1; *Gna13*, guanine nucleotide binding protein α13; IL-6, interleukin-6.

GRAPHIC: KELLIE HOLOSKI/*SCIENCE*

REFERENCES AND NOTES

1. L. M. Coussens, Z. Werb, *Nature* **420**, 860 (2002).
2. G. P. Dunn, A. T. Bruce, H. Ikeda, L. J. Old, R. D. Schreiber, *Nat. Immunol.* **3**, 991 (2002).
3. E. Del Poggetto *et al.*, *Science* **373**, eabj0486 (2021).
4. T. D. Martin *et al.*, *Science* **373**, 1327 (2021).
5. D. Alonso-Curbelo *et al.*, *Nature* **590**, 642 (2021).
6. D. Yadav, A. B. Lowenfels, *Gastroenterology* **144**, 1252 (2013).
7. H. Yin, W. Xue, D. G. Anderson, *Nat. Rev. Clin. Oncol.* **16**, 281 (2019).
8. J. L. Gregory *et al.*, *J. Immunol.* **177**, 8072 (2006).

10.1126/science.abl5376

MICROBIAL FUEL CELLS

A silver assist for microbial fuel cell power

Silver nanoparticles in *Shewanella* membranes boost electron transfer to graphene electrodes

By **Erin M. Gaffney** and **Shelley D. Minteer**

Undegraded carbon sources provide an excellent fuel for bacteria, and the electrons generated by their oxidative respiration can be harvested with electrodes in microbial fuel cells (*1*). Many bacterial and material modification strategies have improved overall fuel cell power output (*2, 3*), but a more important measure is Coulombic efficiency (CE), the percentage of electrons harvested from the fuel (*4*). On page 1336 of this issue, Cao *et al*. (*5*) achieve a record-setting microbial fuel cell power density of 6.6 W/m^2 with an 81% CE (*5*) with a common electroactive bacterial species, *Shewanella*, by exploiting its intrinsic heavy-metal resistance to enhance electron transfer. A modified electrode material of reduced graphene oxide (rGO) and silver (Ag) creates silver ions (Ag^+) that migrate into the cellular membrane. Reduction of Ag^+ by proteins linked to lactate oxidative metabolism formed Ag nanoparticles (NPs), which created electron pathways that increase current and power density.

Department of Chemistry, University of Utah, Salt Lake City, UT 84112, USA. Email: minteer@chem.utah.edu

The benefits of bacteria for our bodies and for soil are well appreciated, but much less discussed is their potential in renewable energy generation. Although bacteria are a critical component for organic degradation in wastewater treatment, further pairing of the decontamination process with energy-harvesting technologies could allow wastewater to be a fuel source for electrical current generation. The amount of energy generated would not serve as a large-scale source to connect to the grid, but it could provide a renewable source for technologies with low-energy demands and could also drive important chemical synthesis processes.

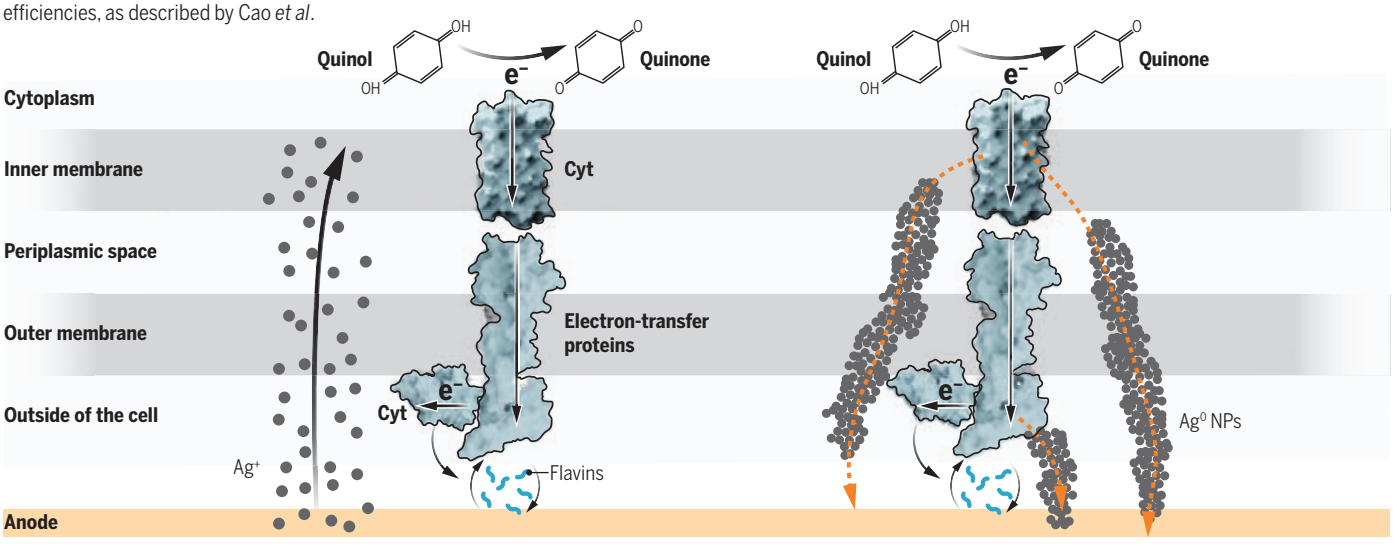
The study of microbial electrochemistry dates back to 1911, when it was discovered that microbes in plant soil could generate an electrical potential (*6*). Of the many electroactive species identified in soil and water, *Geobacter* and *Shewanella* have been the most extensively studied. Both can transfer extracellular electrons through outer-membrane cytochromes in direct contact with an electrode surface (*7*). Additionally, small-molecule shuttles such as flavins can mediate electron transfer from bacterial cells to electrode surfaces (*7*).

High CE is critical for high electron utilization and high yields when microbially generated electricity is used to synthesize chemicals. Rational engineering of enhanced CEs through synthetic biology strategies can only be done by a thorough understanding of the molecular mechanisms of electron transfer from the bacterial fuel source, such as glucose and lactate. Non-electroactive bacteria can be made electroactive by insertion of electroactive pathways into their genomes (*3*). Biosynthetic pathways can be introduced into electroactive bacterial genomes to power chemical production with bacterial microenergy, as demonstrated with a nitrogen-fixing cyanobacterium for renewable ammonia generation from air (*8*).

Extremophilic bacteria such as *Shewanella*, which are native to marine environments, have enhanced stability in changing environmental conditions, such as saline solutions needed for field-deployable microbial electrochemical technologies (*9, 10*). Cao *et al*. took advantage of the

Wiring the bacterial membrane

Electrons transfer from *Shewanella* cells to an electrode (the anode) of a microbial fuel cell. Silver nanoparticles improve electron extraction efficiencies, as described by Cao *et al*.



From fuel to electricity
Oxidizing fuel (such as lactate) in the cell also reduces quinone to quinol, which can be reoxidized by an inner-membrane cytochrome (Cyt). Electron transfer continues through a chain to an outer-membrane cytochrome, from which electrons can pass directly to the electrode surface or shuttle through small molecules such as flavins.

Silver nanoparticle pathways
A reduced graphene oxide/silver layer (rGO/Ag) on the electrode surface used by Cao *et al.*, generates Ag^+ ions that migrate into the membrane. Reduction from electrons escaping the transfer proteins creates Ag nanoparticles (NPs) that form chains that help conduct electrons to the electrode.

GRAPHIC: N. DESAI/*SCIENCE*

resistance of *Shewanella* to heavy-metal poisoning to create biofilms of this electroactive species in conjunction with rGO/Ag-modified electrodes, and in turn the most efficient microbial fuel cell reported (up to 81%). In doing so, they considered the mechanisms of heavy-metal resistivity of *Shewanella*. Before Ag^+ ions could negatively interfere with delicate cellular processes, the ions were reduced in the cellular membrane, which prevented them from entering into the cytoplasm (see the figure). The reduction process formed silver NPs in the cellular membrane that increased the CE substantially by decreasing electrical resistance across the membrane and enhancing the electron extraction from bacterial cell metabolism to the electrode. Cao *et al*. differentiate between increased electron extraction efficiency from a bacterial cell and other factors that could cause an increase in current and power by using scanning transmission electron microscopy with elemental mapping and electrochemical impedance spectroscopy.

The optimized electron extraction and high CE reported by Cao *et al*. showcase that knowledge of molecular mechanisms of bacterial electron transfer can aid in designing microbial electrochemical technologies. These electron-extraction efficiency strategies can greatly aid in other research aimed at boosting CEs for microbial electrosynthesis and renewable energy generation. The discovery of Ag NP production by mechanisms of heavy-metal resistance and resulting increase in electron-extraction efficiency from this study provide many avenues for exploration. For applications in biosensing, NPs can boost electrical signal and thereby reduce limits of detection. Additionally, increased the rate of electron transfer between electrodes and bacteria can greatly improve microbial electrosynthesis by boosting energy efficiency of chemical production. ■

REFERENCES AND NOTES

1. C. A. Hernandez, J. F. Osma, *Front. Environ. Sci.* **8**, 44 (2020).
2. A. A. Yaqoob, M. N. M. Ibrahim, S. Rodríguez-Couto, *Biochem. Eng. J.* **164**, 107779 (2020).
3. S. M. Glaven, *Microb. Biotechnol.* **12**, 819 (2019).
4. R. Wang *et al*., *Adv. Mater.* **33**, 2004051 (2021).
5. B. Cao *et al*., *Science* **373**, 1336 (2021).
6. M. C. Potter, *Proc. R. Soc. London Ser. B* **84**, 260 (1911).
7. P. Chiranjeevi, S. A. Patil, *Biotechnol. Adv.* **39**, 107468 (2020).
8. F. Dong *et al*., *Cell Rep. Phys. Sci.* **2**, 100444 (2021).
9. N. Shrestha *et al*., *Bioresour. Technol.* **255**, 318 (2018).
10. M. Grattieri, M. Suvira, K. Hasan, S. D. Minteer, *J. Power Sources* **356**, 310 (2017).

ACKNOWLEDGMENTS

We thank the Army Research Office MURI (grant W911NF1410263) for funding.

10.1126/science.abl3612

QUANTUM OPTICS

An electron walks into a quantum bar...

Quantum electron-light interaction may find use in microscopy applications

By **Fabrizio Carbone**

Since its conception more than a century ago, the duality between the wave and particle nature of light is perhaps the most well-known concept that connects classical and quantum physics. As such, one may expect it to play an indispensable role in explaining light phenomena. However, even the photoelectric effect, considered the first showcase for the quantum nature of light, can be described by treating light classically—as long as the energy distribution of the electrons in the material is quantized (*1*). On page 1324 of this issue, Dahan *et al*. (*2*) describe an experiment in which the quantum properties of a quantum light source can be transferred through entanglement to electrons. This realization adds to the short list of situations where quantum light is strictly necessary to describe photon-matter interaction and offers intriguing possibilities for both fundamental studies and applications, such as in ultrafast transmission electron microscopy (TEM).

"Exploiting the quantum nature of light-electron interaction may be the next frontier in electron microscopy."

By monitoring the energy distribution of an electron beam interacting with either a coherent or a thermal light source, Dahan *et al*. devised an experiment in which the transition from classical to quantum statistics is observed. Their method demonstrates a way to control the quantum properties of the light-electron interactions through the quantum coherence of the photons, which may lead to new exploits in electron microscopy applications.

To explain the peculiarity of the experiment, one can borrow from a common analogy for explaining random walks—the drunken bar patron (see the figure).

In the first scenario, an electron (the patron) goes to the pub and drinks classical beer, which represents coherent light. Because she does not get too drunk, some coherence is left in her and therefore her walk out of the pub will not be completely chaotic, but rather a mixture of random alcoholic stumbles and conscious choices to go either way. Being a quantum object, the coherent electron will interfere with herself during her walk, enhancing the probability of finding her at specific distances from the pub; this can be called a "quantum walk."

In the second scenario, an electron orders quantum beer from the pub, which represents thermal light that undergoes a quantum interaction with the electron. Immediately, she becomes drunk and entangled with the drink, so her coherence is washed out. Her walk out of the pub is now completely random and the probability of finding her somewhere is a gradually widening normal distribution; this can be called a "random walk."

Most notably, when interacting with the classical beer in the "quantum walk" case, the electron wave function only collapsed once it was detected. By contrast, upon interacting with the quantum beer in the "random walk" case, the collapse of the electron wave function happened immediately as the electron entangled itself with the beer.

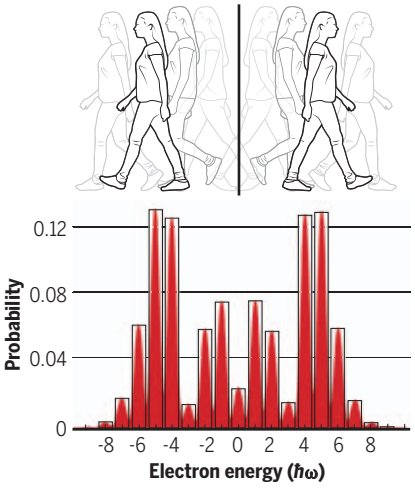
Dahan *et al*. observed the evolution between these two scenarios in their light-electron interaction experiment. By using a custom-made silicon-photonic nanostructure inside a TEM, the authors created a system in which individual free electrons can interact with light having statistics evolving from a thermal source all the way to a coherent one.

By requiring both the electron and the photon to have a quantum nature to describe their observation, Dahan *et al*. present a purely quantum picture for the photon-induced nearfield electron microscopy (PINEM) (*3*) effect. For context, the PINEM effect has previously been modeled with treating electrons as quantum and light as

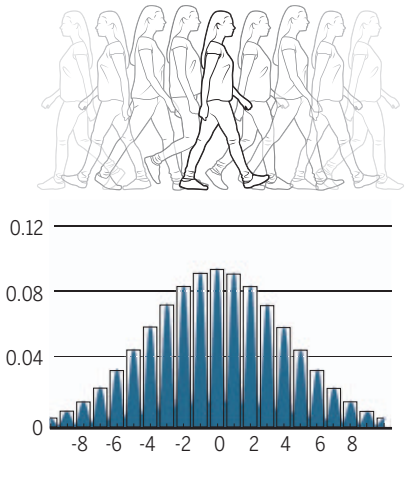
Institute of Physics, École Polytechnique Fédérale de Lausanne, Switzerland. Email: fabrizio.carbone@epfl.ch

"Quantum walk" versus "random walk"

In the drunk patron analogy, an electron (the patron) can interact either with "classical" beer or "quantum" beer. The subsequent probability distributions for the electron's energy state reflect the degree of electron decoherence as a result of the type of electron-photon interaction.



If the electron drinks **"classical"** beer, representing coherent light, the electron retains its coherence and shows an energy spectrum corresponding to a quantum walk, with well-defined peaks away from the origin.



If the electron drinks **"quantum"** beer, representing thermal light, the electron becomes entangled with the photon and shows an energy spectrum corresponding to a random walk, with a single peak centered at the origin.

classical, as in the alternative description of the photoelectric effect (*4*, *5*).

Provocatively, one can argue that in many situations in physics, the choice of whether to treat a system as quantum or classical has often been dictated by convenience rather than fundamental reasoning. These situations are generally thought of as "semiclassical." Although semiclassical theories may provide an adequate description for many experiments, they cannot always capture subtle quantum effects.

Dahan *et al*. have demonstrated such a case, namely the possibility of entangling light with an electron beam in a TEM, and obtaining de facto a quantum radiation source, in which the beam's particles are in a superposition of states that can be manipulated externally by light. The possibility of imprinting the quantum properties of photons into an electron beam may lead to new exploits for photonic quantum computers, which historically suffered from the fragility against decoherence of quantum light. Their observation that, after interacting with quantum light, an individual electron ceases to exist only to survive as a superposition of massive (electrons) and massless (photons) particles has intriguing consequences for interaction-free measurements, sometimes referred to as "ghost imaging" (*6*). This, and similar concepts, may help conceive the so-called quantum electron microscope, having among its main objectives the observation of radiation-sensitive biological specimens.

A full quantum mechanical treatment of PINEM has been developed only recently (*7*, *8*), and it is time to explore its consequences and opportunities. The findings of Dahan *et al*. open the door to reconstructing the quantum state of light in the proximity of nanostructures in TEMs with attosecond, millielectronvolt, and nanometer resolution. The ability to alter the wave function of electrons may help generate and control light beams for applications in sensing, biophysics, optoelectronics, accelerator physics, and even nuclear physics (*9*). Exploiting the quantum nature of light-electron interaction may be the next frontier in electron microscopy.

If the revolutionary operation of the transistor could have been summarized in its definition as a voltage-controlled current source, one may argue that we now have the ingredients for designing a light-controlled quantum radiation source. ■

REFERENCES AND NOTES

1. W. E. Lamb, M. O. Scully, CTS-QED-68-1 (1968).
2. R. Dahan *et al*., *Science* **373**, eabj7128 (2021).
3. B. Barwick *et al*., *Nature* **462**, 902 (2009).
4. S. T. Park, A. H. Zewail, *Phys. Rev. A* **89**, 013851 (2014).
5. F. J. García de Abajo *et al*., *Nano Lett*. **10**, 1859 (2010).
6. E. Rotunno, S. Gargiulo, G. M. Vanacore, arXiv:2106.08955 [quant-ph] (2021).
7. V. Di Giulio *et al*., *Optica* **6**, 1524 (2019).
8. O. Kfir, *Phys. Rev. Lett*. **123**, 103602 (2019).
9. I. Madan *et al*., *Appl. Phys. Lett*. **116**, 230502 (2020).

ACKNOWLEDGMENTS

We acknowledge funding from the ERC Consolidator grant ISCQuM.

10.1126/science.abl6366

COMPUTER ARCHITECTURE

Homogeneous neuromorphic hardware

Bifunctional ferroelectric transistors enable collocation of memory and processing

By **Feng Rao**[1] *and* **Xutang Tao**[1,2]

The exponential growth in data volume has imposed big requirements on efficient and fast data-centric computations. Digital hardware of von Neumann architecture, based on complementary metal-oxide semiconductor (CMOS) systems, substantially limits operation speed and energy efficiency as it shuttles data constantly between information processing and memory units (*1*, *2*). Neuromorphic computing architecture is built on dense nonvolatile memory (NVM) crossbar arrays and aims to perform calculation in situ at the exact sites where data are stored to tackle the bottleneck (*3*, *4*). However, the integration of these arrays into other devices and circuits has become a practical challenge for implementation. On page 1353 of this issue, Tong *et al*. (*5*) address this problem with two-dimensional (2D) WSe_2 film laid on a multidomain ferroelectric $LiNbO_3$ single crystal to construct a "homogeneously integrated" transistor-memory architecture with reconfigurable bifunction of analog signal processing and memory operating.

Neuromorphic computing strategies are analogous to the working mode of the human brain, in which information is processed in a massively connected network of neurons and synapses. The human brain, however, vastly outperforms all neuromorphic hardware in computing parallelism and power consumption (*4*). This is in part because neuromorphic hardware needs heterogeneous integration of crossbar selection devices and peripheral circuits to support large-scale parallel access to NVM arrays. As device dimension is scaled down, module integration incompatibility and interconnecting resistance mismatch become more prominent among the physically separated heterogeneous components (*3*, *6*).

[1]College of Materials Science and Engineering, Shenzhen University, Shenzhen 518060, China. [2]State Key Laboratory of Crystal Materials, Shandong University, Jinan 250100, China. Email: fengrao@szu.edu.cn; txt@sdu.edu.cn

GRAPHIC: V. ALTOUNIAN/*SCIENCE*

Ferroelectrics possess nonvolatile polarization states that can be orientated in opposite directions by applying an external electric field (*7*). A conventional ferroelectric random-access memory adopts a metal/ferroelectric/metal sandwich structure as a capacitor to integrate with a transistor to form the one-transistor one-capacitor (1T1C) cell (*7*). By contrast, a ferroelectric field-effect transistor (FeFET) employs a ferroelectric as a gate to either accumulate or deplete charge carriers in a conducting channel, resulting in nonvolatile changes in the channel resistance that can be used for signal processing and information storage (*8*). The FeFET exhibits a nondestructive reading characteristic with less-substantial scaling issues. Recently, intensive studies have been focused on renovating FeFET devices with emerging 2D channel materials other than graphene, such as strongly correlated oxides, transition metal dichalcogenides (TMDs), and van der Waals heterostructures (*8*, *9*). The new combinations are motivated by a potentially promising alternative to classic logic and memory technologies (*9*).

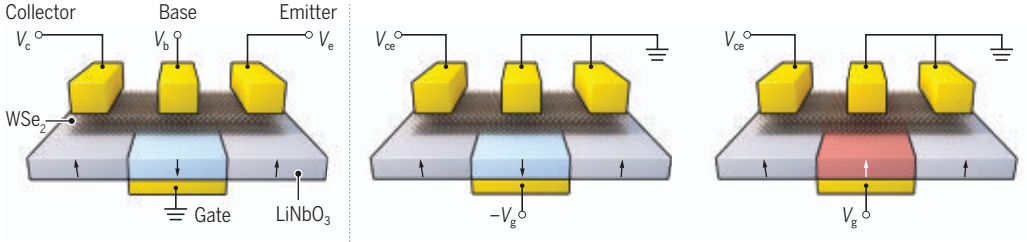
Tong *et al.* chose a few-layer TMD, WSe_2, as the semiconducting channel for the FeFET device, in which the commercialized $LiNbO_3$ single crystal serves as the underlying ferroelectric insulator. With a monodomain $LiNbO_3$, the FeFET device exhibits typical ferroelectric hysteretic curves for a qualified memory function (*8*), with a high-to-low resistance ratio of about 200. A distinct memory working mode is executed in the case of using tridomain $LiNbO_3$ insulator (see the figure), where the ferroelectric polarization state is fixed to be upward (P_u) for bilateral domains below the collector and emitter terminals, whereas the polarization direction of the central domain can be altered according to the gate voltage polarity—i.e., downward polarization (P_d) at negative bias $-V_g$ and P_u at positive V_g (zero gate voltage). Aligning three P_u leads to the low-resistance state of the FeFET memory device, whereas the P_u-P_d-P_u coupling results in the high-resistance state. The high-to-low data resolution is markedly increased to ~10^6, providing a broad space for the adjustment of numerous synaptic weights (*4*, *9*). Tong *et al.* also succeeded in tailoring the same tridomain FeFET device into a n-p-n bipolar junction transistor (BJT) on the P_u-P_d-P_u domains when the gate was grounded.

Unlike the heterogeneous integration scheme—1T1C or one-transistor one-resistor (1T1R)—of many memory technologies, the architecture by Tong *et al.* is more homogeneous, structurally and functionally, because an additional logic function is perfectly woven into a memory cell, and the symbiotic bifunction in a single FeFET device can be easily reconfigured upon different stimulus modes. Cascading multiple FeFETs together in a dense array makes it possible to provide rich module functions. It essentially reduces the integration difficulties as confronted in the heterogeneous case (*1*, *3*), circumventing the issues of module integration incompatibility and resistance mismatching. The long-distance data movement among memory and computing elements can be eliminated in the new architecture, offering a platform to realize high-bandwidth and low-latency computations (*1*), which should substantially lower the bar for the manufacturing of neuromorphic chips. Tong *et al.* used small arrays to demonstrate three basic functions of neuromorphic computing. The authors realized operational amplifier function for analog signal processing on a 12-BJT–connected circuit, with an order of magnitude lower power consumption against the complex CMOS-based system. The low-energy FeFET-based comparator was used for activation function, in series with the transimpedance amplifier in the circuit. They were integrated on the rear end of an array containing nine FeFET memory cells, performing binary classification tasks. After training, the authors achieved the recognition of pattern labels and predicted classes from both simulations and experiments. A ternary content-addressable memory with a 2T2R (3-FeFET) architecture allowed parallel search of massive datasets. These homogeneous architectures are superior to the CMOS counterparts in areal and energy efficiency.

It is possible that the homogeneous architecture could be used to develop analog-to-digital converters, digital-to-analog converters, and analog filters to construct a more powerful neuromorphic system. A high-density chip is a prerequisite in this regard, although it poses a great challenge to the 3D integration process of stacking layered FeFET arrays in sequence. Low-temperature synthesis of $LiNbO_3$ crystal and wafer-scale deposition of high-quality 2D channel materials seem to be insurmountable barriers. Efforts need to be made to implement other CMOS-compatible 2D ferroelectrics, like hafnium dioxide (*10*) or tin telluride (*11*), as well as opto- or thermosensitive channel materials, such as phase-change metamaterials or heterostructures (*12*), to shape a more feasible route for the mass production of sensory-computation-memory integrated chips, promoting the artificial intelligence applications (*3*) of object recognition, decision making, autonomous driving, and other technologies. ■

Ferroelectric field-effect transistor (FeFET) array

FeFET cells are composed of $LiNbO_3$ crystals as the ferroelectric insulator with a two-dimensional WSe_2 film as the conducting channel. Applying different voltages (*V*) or grounding changes the functionality of each cell, and multiple cells can be combined into larger functional arrays.



Bipolar junction transistor
A FeFET cell can serve as a n-p-n bipolar junction transistor (BJT) on P_u–P_d–P_u (↑–↓–↑) ferroelectric domains when the gate is grounded.

Memory
Reversing the polarity of gate bias, the FeFET cell can be switched between high- and low-resistance memory states, corresponding to P_u–P_d–P_u and P_u–P_u–P_u (↑–↑–↑) ferroelectric polarization coupling.

GRAPHIC: C. BICKEL/*SCIENCE*

REFERENCES AND NOTES

1. H.-S. P. Wong, S. Salahuddin, *Nat. Nanotechnol.* **10**, 191 (2015).
2. F. Rao *et al.*, *Science* **358**, 1423 (2017).
3. Q. Xia, J. J. Yang, *Nat. Mater.* **18**, 309 (2019).
4. G. W. Burr *et al.*, *Adv. Phys. X* **2**, 89 (2017).
5. L. Tong *et al.*, *Science* **373**, 1353 (2021).
6. P. Kapur, J. P. McVittie, K. C. Saraswat, *IEEE Trans. Electron Dev.* **49**, 590 (2002).
7. J. F. Scott, *Science* **315**, 954 (2007).
8. X. Hong, *J. Phys. Condens. Matter* **28**, 103003 (2016).
9. C. Liu *et al.*, *Nat. Nanotechnol.* **15**, 545 (2020).
10. H.-J. Lee *et al.*, *Science* **369**, 1343 (2020).
11. K. Chang *et al.*, *Science* **353**, 274 (2016).
12. K. Ding *et al.*, *Science* **366**, 210 (2019).

ACKNOWLEDGMENTS

F.R. thanks the National Natural Science Foundation of China (52032006), the Basic and Applied Basic Research Foundation of Guangdong (2020B1515120008), and the Science and Technology Foundation of Shenzhen (JCYJ20180507182248605). X.T. thanks the National Natural Science Foundation of China (51932004,61975098).

10.1126/science.abl4110

POLICY FORUM

ACADEMIC WORKFORCE

Innovation, entrepreneurship, promotion, and tenure

Academic incentives must reward broader societal impacts

By **Rich G. Carter[1], Karl Mundorff[2], Julie Risien[3], Jana Bouwma-Gearhart[4], Dawn Bratsch-Prince[5], Sandra A. Brown[6,7], Almesha L. Campbell[8], Joseph C. Hartman[9], Charles A. Hasemann[10], Peter J. Hollenbeck[11], Blanca Lupiani[12], Owen J. T. McCarty[13], Ian D. McClure[14], Katrina Mealey[15], Carol Mimura[16], Andrea J. Romero[17], Paola Sztajn[18], Laurie Van Egeren[19]**

Academic promotion and tenure (P&T) processes that typically prioritize faculty grants and publications can fail to fully assess and value entrepreneurial, innovative endeavors (*1*) that can produce the kind of societal impacts that universities are increasingly being called on to provide and that many faculty and students increasingly prioritize (*2*, *3*). A more inclusive assessment of scholarship and creative activity to better recognize and reward innovation and entrepreneurship (I&E) will require "broadening the bar" (*4*) to reflect evolving forms of faculty impact without diluting or increasing the requirements for advancement. Expanding what we value as scholarship can also help augment who we value as scholars and thus support a more innovative and diverse professoriate. We highlight work by the Promotion and Tenure–Innovation and Entrepreneurship (PTIE) coalition to promote policies and practices to recognize the impact of faculty I&E. We posit that this strategy can be broadly applicable (beyond I&E) to recognize the many and evolving dimensions along which faculty create societal impacts.

Benefits of I&E efforts by faculty can include "increased opportunities for research funding, access to unrestricted funds for further institutional investment, sustaining high scholarship level, student success, increased prestige, public benefit, and economic development" (*5*). In academe, basic research is still privileged (*6*, *7*), and processes and policies that reward faculty members' I&E work are not equally valued, including at research (R1 and R2) universities (*5*). In addition, I&E should be viewed as broadly inclusive of the science, technology, engineering, mathematics, and medicine (STEMM) disciplines as well as liberal arts and other areas of focus across campuses.

Reform of higher education's deeply embedded reward structure requires an approach that addresses long-standing norms and organizational cultures (*8*) as well as the multi-institutional nature of the faculty review process (P&T review typically includes input from external reviewers). Consequently, coordination across multiple institutions is needed to provide a fair and robust review of a given faculty candidate's contributions and to mitigate potentially limited or biased views of their accomplishments (*9*). For this transformation to occur, there must be intentionality, leadership, and commitment to both improving the inclusivity and equity in the process as well as incorporating recognition criteria for faculty who engage in evolving forms of scholarship.

The convergence of increased investment in I&E from funding agencies and universities, coupled with an amplified awareness of bias and the need for a more inclusive academy, have opened doors and minds to addressing the long-standing, often challenging topic of P&T reform. This breadth of engagement across the academy will, we believe, enable the majority of faculty to see benefits to the recommended changes without undermining basic and/or curiosity-driven research and while supporting academic freedom.

SCALABLE SOLUTIONS

An exploratory survey of university administrators and faculty (*10*) suggested that structures for evaluation of faculty's I&E impact in considerations of P&T are warranted but are largely absent at the department, college, and central administration levels. For example, faculty across multiple institution types with varying expectations for P&T noted that they struggled to meaningfully evaluate I&E in P&T considerations and typically did not receive any training for conducting these evaluations.

Recognizing the integrated, multi-institutional nature of peer review in the P&T process, the PTIE coalition, with membership from more than 65 universities and numerous stakeholder organizations, is collaborating to develop scalable solutions around a shared goal of improving assessment of I&E in P&T. Input has been gathered through conversations and structured group discussions from a broad cross section of groups and individuals with a range of roles on university campuses. The aim was to inform best practices and coalesce around consensus recommendations without the requirement to preemptively commit to adopting the findings. This enabled successes to be captured and adjustments to be made on the basis of lessons learned from individual member campuses. These conversations surfaced a consistent theme: Participants see a critical need for a coordinated effort for inclusively recognizing I&E to enable institutions to share the challenges they encountered attempting to effect change and support shared solutions. Recognizing that some institutions have had success in this area in part because of deeply embedded innovation cultures and resources that may not exist at most institutions, coalition members focused on more general, scalable approaches. True change will take time to realize (5 to 10 years minimum), and guideline changes alone will not be successful. Consequently, the coalition focused on holistic, multidimensional solutions that target expanding the culture on campus to be more inclusive of I&E. Coalition members agreed to take recommendations back to their home institutions to consider and, possibly, implement.

The resulting PTIE coalition recommendations contain four core elements needed to initiate changes that could meaningfully and

[1]Department of Chemistry, Oregon State University, Corvallis, OR, USA. [2]Office of Research, Oregon State University, Corvallis, OR, USA. [3]STEM Research Center, Oregon State University, Corvallis, OR, USA. [4]College of Education, Oregon State University, Corvallis, OR, USA. [5]Department of World Languages and Cultures, Iowa State University, Ames, IA, USA. [6]Department of Psychology, University of California at San Diego, La Jolla, CA, USA. [7]Department of Psychiatry, University of California at San Diego, La Jolla, CA, USA. [8]Division of Research and Economic Development, Jackson State University, Jackson, MS, USA. [9]Department of Mechanical Engineering, University of Massachusetts Lowell, Lowell, MA, USA. [10]MSU Innovation Center, Michigan State University, East Lansing, MI, USA. [11]Department of Biological Sciences, Purdue University, West Lafayette, IN, USA. [12]Department of Veterinary Pathobiology, Texas A&M University, College Station, TX, USA. [13]School of Biomedical Engineering, Oregon Health & Science University, Portland, OR, USA. [14]Office of the Vice President for Research, University of Kentucky, Lexington, KY, USA. [15]Department of Veterinary Clinical Sciences, Washington State University, Pullman, WA, USA. [16]Office of Intellectual Property and Industry Research Alliances, University of California at Berkeley, Berkeley, CA, USA. [17]Department of Family Studies and Human Development, The University of Arizona, Tucson, AZ, USA. [18]College of Education, North Carolina State University, Raleigh, NC, USA. [19]University Outreach and Engagement, Michigan State University, East Lansing, MI, USA. Email: rich.carter@oregonstate.edu

inclusively account for I&E (see the box). The coalition concluded that the comprehensive approach outlined in the recommendations needed to include each of these four key elements because solely changing the written P&T guidelines had limited effectiveness on PTIE member campuses. Without concurrent process changes to minimize bias during the review, no incentive is present for those who have been successful under the existing paradigm to support change. Those individuals who are not fully valued under the current paradigm will either leave the academy or continue to have their accomplishments discounted as compared with their peers.

Key aspects of these findings came from existing successes on PTIE coalition member campuses. For example, the suggested university-wide language and sample college-level language builds on wording used at Texas A&M University and Arizona State University, respectively, that many coalition members believe to have been successful. This recommended university language is critical for linking the evaluation of a faculty candidate's accomplishments with the mission and priorities of the university. PTIE coalition members consistently emphasized the importance of having this connection and its absence in most P&T review processes currently. The National Science Foundation has helped promote the expectation that applicants for and recipients of federal funding demonstrate impact to the public through its broader impact review criterion. Consequently, faculty should be able to connect their research, agnostic of whether it is basic or applied, to broader impacts that align with the institutional mission. In addition, this linkage provides a key pathway for recognition of other areas of scholarship not currently valued fully under the existing evaluation structure but aligned within the university's priorities.

The PTIE coalition suggested six sub-categories of suggested metrics, with specific examples provided within each category—including wording to provide inclusive recognition of I&E impacts beyond the STEMM disciplines [such as "installation of creative works, commissioned works" as examples of intellectual property and "startup/spinout organizations (including for-profit, nonprofits, and foundations to allow for broad recognition of societal impact)" within the entity creation subcategory]. Sample text within the evaluation criterion for scholarship and creative activity ensures that continued importance must be placed on peer review while including the opportunity to demonstrate impact to the public: Scholarship and creative activity are "based on a high level of professional expertise; must give evidence of originality; must be documented and validated as through peer review, critique, or validation by evidence of societal or disciplinary usage/benefit; and must be communicated in appropriate ways so as to demonstrate significant impact for the public and/or for the discipline itself (including future impact as appropriate)."

Four core elements of PTIE recommendations

These promotion and tenure innovation and entrepreneurship (PTIE) elements can provide a framework to reimagine other areas of scholarship in promotion and advancement.

1. University-wide language directly linking the evaluation of faculty to institutional mission, values, and goals across the multiple levels at an institution (unit, department, school, college, university, and system). Sample text: "Evaluation of faculty for promotion and/or tenure includes their contributions to the institution's mission and stated priorities. Evidence for broader (societal) importance of the work, either now or in the near future, should be included within their personal statement and/or other appropriate portions of their dossier."
2. Innovation and entrepreneurship (I&E) metrics to serve as indicator data to be used in a narrative thesis of impact. Metrics are grouped into six subcategories: intellectual property, sponsored research, use and licensing, entity creation, I&E career preparation, and I&E engagement.
3. I&E text for evaluation criterion to be incorporated into the (i) research (scholarship and creative activity), (ii) teaching and advising, and (iii) service categories typically evaluated for promotion and tenure (P&T).
4. Process changes for supporting systemic culture change, improving transparency, and addressing bias (for example, directions for personal statement, external reviewer resource and guidance, involvement of P&T process consultants, expanded training, and reframing and importance of diversity, equity, and inclusion).

Recommended process changes also benefited from the shared experiences of coalition members. For example, Oregon State University's experience with the Search Advocate program, which is used on dozens of campuses nationally to address implicit and explicit bias in the hiring process, informed the recommendation of process consultants. Considerable emphasis was placed on addressing bias in the review process to ensure that all faculty will benefit from the recommended changes through a more transparent process that addresses bias and reduces the potential for individuals in the P&T review process to improperly influence the outcome without accountability or for reasons outside of the established parameters. In addition, the recommended process changes amplify this dialogue about bias and holistic assessment through recommendations to provide a detailed letter of instruction for external reviewers and improve the clarity and structure of the personal statement provided by the candidate, and implementation of training on evaluating I&E outputs for faculty.

The coalition's recommendations are not intended to supplant or dilute the research, teaching, and service categories traditionally evaluated on university campuses. Instead, they suggest how to systematically measure and value faculty I&E impact as integrated within the teaching, research, and service categories. Faculty fully valued under the existing promotion and advancement structure must not be negatively affected by this more inclusive approach to valuing faculty's diverse forms of scholarship. Instead, the focus of PTIE is on broadening the opportunities for recognizing impact within a common structure that does not dilute or augment the overall requirements for promotion.

SUPERSTRUCTURE FOR EVOLVING FORMS OF IMPACT

I&E—along with diversity, equity, and inclusion (DEI); interdisciplinary team science; open science; community engagement; and others—represent examples of the many evolving forms of scholarship for the 21st-century faculty member. That said, these types of scholarship can be overlooked or undervalued in the process by which universities review, reward, and advance the academic workforce (*8*, *11*, *12*). As these evolutions are incorporated into the fabric of higher education, the faculty evaluation process thus needs to be updated to reflect this changing landscape.

Building on a view that expands the traditional definition of scholarship and research into discovery, integration, application, and teaching (*13*), we suggest that the evaluation framework proposed by the PTIE coalition

can extend beyond I&E to support evaluation of a variety of faculty impacts. In particular, the current omission of university-wide language and much needed process changes in existing P&T practices (see the box) hinders reforms to reward and advancement across many domains of scholarship and creative activity. Incorporation of these two elements (university-wide language and process changes) into the fabric of a university will support a more dynamic and inclusive ecosystem in which faculty can contribute and meet the mission and priorities of the university without damaging the core principle of any university to support the pursuit of knowledge.

The diverse and evolving forms of scholarship can often be viewed as an impediment to establishing a uniform structure for evaluation of a dossier for P&T. Instead of viewing these differences as barriers, we suggest that a common set of priorities already exists for building the appropriate criterion of a given type of scholarship. Any area of scholarship must (i) support the university mission; (ii) address an identified need by stakeholders (such as funding agencies; foundations; professional societies; employers; students; alumni; local, state, and/or federal organizations; and/or others); and (iii) embody a priority of the institution. In order for any area of scholarship to be effectively evaluated, the institution must (iv) utilize necessary processes, procedures, and cultural elements that support an unbiased evaluation; and (v) provide language that links the priorities, need, and mission to the evaluation process. With this architecture identified, faculty engaged in diverse and new forms of scholarship can benefit from a shared road map for facilitating systems-level change. Additionally, this superstructure provides a mechanism for collaboration among otherwise disconnected areas of focus on campus that will collectively affect the majority of university faculty and increase the likelihood for adoption within the university.

Recognizing the persistence of bias—whether it be the candidate's research topic or their ethnicity, gender, sexual orientation, and/or other diverse backgrounds—in the current process is essential to improving fairness and validity in the future of review and advancement. Consequently, the PTIE coalition recognized the overarching importance and intersection of DEI with I&E and embedded that thinking throughout development of the recommendations (including the explicit inclusion of minority-serving institution perspectives in the coalition conversations). Full acknowledgement that faculty members from diverse backgrounds engage in diverse forms of scholarly activity is essential to any productive discussion about change. This reality—that underrepresented faculty often face compounded bias on the basis of both their social identity group and their approach to scholarship—points to the need to update P&T processes to ensure the equitable evaluation of faculty impact. Many current P&T policies, practices, and cultures are rooted in eras when the academy was more homogeneous and less focused on creation of an inclusive environment that can evolve to meet the needs of a changing academy and student population.

Adjustment of the P&T guidelines alone is unlikely to facilitate the culture shift needed to see transformative change in how nontraditional forms of scholarship are valued (including I&E) and inequities are addressed. For example, reviewers bring with them both explicit and implicit biases to their evaluation of a candidate (*14*). Consequently, the PTIE coalition recommends a broad collection of process changes to start to address implicit and explicit bias within the review process, including expanded training and external reviewer resources. These improvements would benefit the entire academy—not just I&E-focused faculty—by supporting a more diverse academic workforce to engage in new forms of scholarship.

"Any area of scholarship must…support the university mission…"

The recommendations of the PTIE coalition enable inclusion and recognition of a diverse cross section of university faculty that extends well beyond the patent-licensing-startup paradigm to include entrepreneurial efforts such as social innovation; the creation and/or engagement of nonprofits, foundations, and other organizations; as well as I&E-related curricular developments and student mentorship. In addition, explicit discussion of aligning priorities between the faculty member and the university around their I&E efforts (traditionally referred to as conflict-of-interest management) is essential to address the financial aspects of some forms of I&E impact and ensure that the pursuit of knowledge is not motivated by financial gain. Universities should also be wary of pursuing I&E solely as a potential new revenue stream from technology transfers agreements, because often this is not the case (*15*). Rather, I&E should be viewed as an essential component of realizing the institution's mission to society.

The higher-education workforce and academia landscape are changing on a global scale. There is growing concern that the traditional systems that anchor institutions, including P&T practices, may no longer sufficiently support those very institutions to live up to their social contract with civic society. Groups including funders and academic associations are broadly addressing the need to modernize how we recruit, retain, and reward the academic workforce. Especially apparent in this time of awakening about systemic inequities and exclusion, universities should be leading the way by improving their own practices and making room for faculty to realize institutional ambitions to serve society. This necessitates both a bottom-up interest from faculty and a top-down commitment from university leadership. ■

REFERENCES AND NOTES

1. J. Bouwma-Gearhart, R. Carter, K. Mundorff, *Change* **53**, 18 (2021).
2. J. H. C. Clark *et al*., "The innovation impact of US universities: Rankings and policy conclusions" (June 2020); https://gwbcenter.imgix.net/Publications/Resources/gwbi-university-impact-report-ranks-exec-summary-full-report.pdf.
3. S. Mintz, *Inside, High. Educ*. **3** (2019).
4. The National Academies of Science, Engineering, and Medicine. 2020. *Re-envisioning Promotion and Advancement for STEM Faculty* (National Academies Press, 2020); https://doi.org/10.17226/25742
5. P. R. Sanberg *et al*., *Proc. Natl. Acad. Sci. U.S.A*. **111**, 6542 (2014).
6. M. S. Anderson, E. A. Ronning, R. Devries, B. C. Martinson, *J. Higher Educ*. **81**, 366 (2010).
7. P. Mendoza, S. D. Ocal, Z. Wang, E. Zhou, *Stud. High. Educ*. **45**, 1474 (2020).
8. K. O'Meara, in *Handbook of Engaged Scholarship: Contemporary Landscapes, Future Directions*, H. Fitzgerald, C. Burack, S. Seifer, Eds. (Michigan State Univ. Press, 2010), vol. 1, pp. 271–294.
9. J. Genshaft *et al*., *Technol. Innov*. **17**, 197 (2016).
10. J. Bouwma-Gearhart *et al*., *J. Open Innov*. **7**, 182 (2021).
11. K. A. O'Meara, L. Sandmann, J. Saltmarsh, D. Giles Jr., *Innovative High. Educ*. **36**, 83 (2011).
12. J. T. Klein, H. J. Falk-Krzesinski, *Res. Policy* **46**, 1055 (2017).
13. E. L. Boyer, D. Moser, T. C. Ream, J. M. Braxton, *Scholarship Reconsidered: Priorities of the Professoriate* (Jossey-Bass, 2015).
14. J. L. Cundiff, C. L. Danube, M. J. Zawadzki, S. A. Shields, *J. Higher Educ*. **89**, 611 (2018).
15. J. Marcus, "Think universities are making lots of money from inventions? Think again," *The Hechinger Report*, 17 January 2020; https://hechingerreport.org/think-universities-are-making-lots-of-money-from-inventions-think-again.

ACKNOWLEDGMENTS

B. Wall, I. Tumer, and T. Ozkan-Haller are acknowledged for their work on the organizing committee. C. Lenhart and H. Cho are acknowledged for their efforts in survey data management and analysis. The participants in the PTIE effort from across our country are graciously acknowledged for their engagement, input, and support. The National Science Foundation (CNS-1936073) is graciously acknowledged for support of this work. Additional support for aspects of this work was provided by the Lemelson Foundation and VentureWell.

SUPPLEMENTARY MATERIALS

https://science.org/doi/10.1126/science.abj2098

10.1126/science.abj2098



PSYCHOLOGY

Rethinking resilience

A flexible mindset can help us bounce back after adversity

By **June Gruber**

After a long shift at a Greenwich Village restaurant, Jed McGiffin was crossing a pedestrian intersection on his way home when he was violently crushed under the weight of a garbage truck. Jed awoke from a medically induced coma to find that the doctors had amputated his left leg. Yet as he gradually began to comprehend the details of the horrific accident he had just survived, he found himself feeling surprisingly okay. McGiffin's story is one of a number of gripping firsthand accounts that appear in George Bonanno's *The End of Trauma* from people who have bounced back from disabling accidents, tragic bereavement, violent assault, and even terrorist attacks.

The stories presented in this book do not necessarily align with long-standing scientific views of trauma, which tend to emphasize the enduring negative impacts that can be associated with such events. As Bonanno notes, much of the scientific literature had been dominated for decades by a focus on those who suffer from the most severe form of trauma response. Clinicians refer to this response as posttraumatic stress disorder (PTSD), a condition marked by a chronic and persistent cluster of symptoms including flashbacks, nightmares, intrusive thoughts, and other symptoms that substantially impair a person's functioning in daily life. Yet PTSD only manifests in a small percentage (<10%) of people who experience trauma.

By focusing on PTSD, scientists have made considerable advances in mapping the nature and etiology of extreme trauma responses. But, until recently, we have been missing the full picture of how humans experience and recover from life-altering incidents. Bonanno and others have focused their research efforts on this gap and have found that most people are highly resilient in the face of adversity. Accordingly, this book brings forward a fresh and updated perspective on trauma that includes a history of PTSD research, guidance for maximizing resilience, and lessons to help readers grapple with the COVID-19 pandemic.

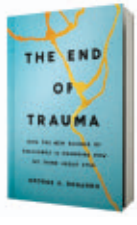
In the opening pages of the book, Bonanno describes what he calls the "resilience paradox," writing: "We can identify statistical correlates of resilience—the so-called traits of resilient people—but paradoxically, when something aversive happens, these correlates don't actually tell us much about who will be resilient and who will not." Characteristics that correlate with resilience include self-awareness, optimism, the ability to find meaning in life's challenges, grit, and even a healthy dose of humor. For example, Bonanno and colleagues have shown that bereaved spouses who were able to laugh—a behavioral signal of positive emotions and resilience—when interviewed about their partners showed fewer symptoms of grief over time. Yet the utility of specific behaviors and feelings depends greatly on context. What may work well in one situation will not necessarily work well in another.

This paradox brings to light perhaps the most important facet of resilience, which is the capacity to adapt in the face of trauma. Psychological flexibility provides us with the opportunity to fine-tune our feelings and gain better control of them when the world around us changes. Recall, for example, Jed McGiffin's optimism and confidence after his accident, both components of a flexible mindset.

COVID-19 "threw [us] for a loop," writes Bonanno. Social support, intermittent distractions from chronic stress, and a focus on moments of joy and connection with others have proven crucial to navigating the uncertainty that has accompanied the pandemic and will be critical for weathering the rest of it. The key, once again, is the ability to be flexible in when and how we deploy various coping strategies.

In the end, Bonanno adeptly succeeds in capturing the profound lived experience of trauma and in balancing these accounts with cutting-edge findings from psychology and neuroscience. This book will appeal to a wide readership, including those who want to learn more about trauma and resilience and the human capacity to survive and thrive in the face of adversity. ■

10.1126/science.abj9834



The End of Trauma: How the New Science of Resilience Is Changing How We Think About PTSD
George A. Bonanno
Basic Books, 2021. 336 pp.

Life-altering incidents do not always lead to extreme trauma responses. Cultivating resilience can help.

The reviewer is at the Department of Psychology and Neuroscience, University of Colorado Boulder, Boulder, CO 80309, USA. Email: june.gruber@colorado.edu

PHOTO: SRDJANPAV/ISTOCK.COM

SCIENCE COMMUNICATION

Common ground and the climate crisis

Invoking shared values can help convince skeptics of the need to mitigate climate change

By **Miriam Aczel**

Katharine Hayhoe's timely book *Saving Us* offers an optimistic and practical discussion of how we can reach across the divisions in our communities to start productive conversations on the climate crisis. Hayhoe stresses the need to find common values that we can use to begin conversations with our families and our communities, highlighting that the climate crisis is inherently linked to the issues we all care about—human health, economic strength, and the "stability of our world." Together, she says, we can find solutions.

Hayhoe begins by describing the hate-filled emails and confrontations she routinely faces as a climate scientist in Texas. She is used to defending her ideas to colleagues: "If a colleague disagrees with my ideas, it motivates me to collect more and better data…That's how science works. But what am I supposed to do when I'm called a 'climate ho'—somehow prove I'm not?"

Climate "Dismissives," she says, will discount anything that shows that the climate crisis is real, including scientific reports, the conclusions of experts, and more than two centuries of accumulated scientific data. While you are unlikely to convince someone in this camp, "93% of us aren't Dismissive," and these are the ones we can engage with.

As an example of how she begins conversations by finding common ground, Hayhoe recounts speaking before her local Rotary Club. She references a banner with the club's statement of guiding principles (Is it true? Is it fair? Will it build goodwill? Is it beneficial?) to encourage dialogue. The truth of climate change is based on scientific evidence, she explains. And climate change is unfair because it affects those, including farmers, who have done little to cause it. She ends by discussing positive steps taken at the local level to solve climate change, with resultant benefits to those communities. To open a dialogue, first take inventory of who you are—your home, what you love doing—and what you might have in common with others, she writes.

Hayhoe begins these sorts of discussions with her own inventory, referencing her identity as a Canadian living in Texas and then describing her passions, whom she loves, and finally what she believes. She then explains, adopting a conversational tone, that, like many, she loves her country but also sees the critical threats posed by climate change: from increasingly encroaching invasive species to growing wildfires, flood risk, melting permafrost, and sinking coastlines that have "already taken a toll on our True North."

Finding common ground with others through shared values and experiences creates an environment in which we can discuss the implications of climate change on those we love—our families and communities—and how we can work together on solutions. "Being a mom is fundamental to my identity," Hayhoe notes.

Her worries about climate change also connect to her religious convictions: "I believe that if you are someone who takes the Bible seriously, then you already care about climate change." Although white evangelicals in the US are less likely than other groups to be concerned with climate change, she says "it's the political polarization and tribalism… not the Bible, that cause them to reject what science says about a changing climate." Climate change, she notes, poses disproportionate risk to those who are poor, hungry, or ill—those individuals that the Bible instructs followers to take care of.

Hayhoe's advice and approach to reaching those who are "uncertain" is deeply personal, and she says that to start a conversation you do not necessarily need to be religious or a Rotarian. Begin by making a connection through a shared interest.

Fellow scientists may be satisfied by data, but how does one start a conversation with nonscientists about the potential impacts of climate change? Hayhoe suggests starting with a shared activity or interest—beer or wine, food, sports, etc.—and using that as a starting point for a conversation. Here, she describes how a high school ski racer from Quebec uses her network of skiers to "spread the message." The same outreach could be done by birders, hunters, enthusiasts of fly-fishing, snowmobilers, and gardeners.

Hayhoe concludes with a message of hope, writing that, while scientists tell us that we cannot avoid all the impacts of climate change, "it is *not* too late to avoid the most serious and dangerous impacts." "The future is in our hands," she notes, before issuing a call to act "with power, love, and a sound mind, so we can fix the climate before it fixes us." ■

The reviewer is at the California Institute for Energy and Environment, University of California, Berkeley, Berkeley, CA 94720, USA, and the Centre for Environmental Policy, Imperial College London, London SW7 1NE, UK. Email: aczel@berkeley.edu

Saving Us: A Climate Scientist's Case for Hope and Healing in a Divided World
Katharine Hayhoe
Atria, 2021. 320 pp.





Recreational divers assist in marine conservation efforts in Lauderdale-by-the-Sea, Florida.

PHOTO: JASON KOERNER/GETTY IMAGES FOR PEPSI STRONGER TOGETHER

10.1126/science.abj9760



LETTERS

The endangered white-bellied heron (*Ardea insignis*) has abandoned some of its prime breeding sites.

PHOTO: JASON EDWARDS/GETTY IMAGES

Edited by **Jennifer Sills**

Save the white-bellied heron from extinction

The white-bellied heron (*Ardea insignis*) is one of the most threatened bird species in Asia (*1*). Since 2007, the species has been categorized as Critically Endangered (*2*). The global population, which spans India, Bhutan, Myanmar, and China, is estimated to be about 60 individuals (*3*). The white-bellied heron's fast-flowing freshwater riverine habitats span three biodiversity hotspots—the Eastern Himalayas, Indo-Burma, and the Mountains of Southwest China (*4*)—as well as two Global 200 Ecoregions: the Terai-Duar savannah and grasslands and the Eastern Himalaya broadleaf and conifer forest (*5*). These habitats are threatened by overfishing, illegal hunting, sand mining, and boulder extraction (*6*), putting the white-bellied heron—already extinct in Bangladesh and Nepal (*7*)—at risk of global extinction.

In the past century, the white-bellied heron lost 59% of its prime habitats across 12,139 km^2 (*8*), especially in India and Myanmar. The species now breeds only in Bhutan and India, but evidence suggests that they are struggling to thrive in these regions as well. Only two active nests have recently been found in India (*9*). Five active breeding pairs were found in Bhutan, but the white-bellied herons have abandoned almost all nesting sites used before 2015 (*10*). The species has been trending northward, but it is unclear where breeding pairs might go next if they abandon their prime breeding sites.

Governments across the white-bellied heron's range countries should urgently initiate conservation actions by funding projects to generate awareness and identify possible reasons that successful nesting sites continue to be abandoned. Simultaneously, surveys should be conducted across all range countries to quantify the current population and provide baseline data for any future long-term ecological studies. To protect this vulnerable species, it is vital to understand their current distribution and nesting habits.

Gopinathan Maheswaran[1]*, Indra Prasad Acharja[2], Lalit Kumar Sharma[1], Himadri Sekhar Mondal[3], Tanoy Mukherjee[1], Imran Alam[1] and Amitava Majumder[1]

[1]Zoological Survey of India, New Alipore, Kolkata 700053, India. [2]Royal Society for Protection of Nature, Lhado Lam Kawajangsa, Thimpu, Bhutan. [3]Bombay Natural History Society, Hornbill House, Mumbai 400001, India.
*Corresponding author.
Email: maheswaran@zsi.gov.in

REFERENCES AND NOTES

1. EDGE of Existence, "97. White-bellied heron" (2020); www.edgeofexistence.org/species/white-bellied-heron/#overview.
2. BirdLife International, "*Ardea insignis*" (The IUCN Red List of Threatened Species, 2018); www.iucnredlist.org/species/22697021/134201407.
3. M. R. S. Price, G. L. Goodman, "White-bellied heron (*Ardea insignis*): Conservation strategy" (IUCN Species Survival Commission White-Bellied Heron Working Group, 2015).
4. N. Myers, R. A. Mittermeier, C. G. Mittermeier, G.A.B. da Fonseca, L. Kent, *Nature* **403**, 853 (2000).
5. D. M. Olson, E. Dinerstein, *Ann. Missouri Botan. Gard.* **89**, 199 (2002).
6. R. Menzies, M. Rao, R. Naniwadekar, *Bird Conserv. Int.* **31**, 255 (2021).
7. BirdLife International, "Species factsheet: *Ardea insignis*" (2021).
8. G. Maheswaran, L. K. Sharma, H. S. Mondal, T. Mukherjee, *Ecol. Informat.* 10.1016/j.ecoinf.2021.101383 (2021).
9. S. K. Reddy *et al.*, *Indian Birds* **17**, 115 (2021).
10. I. P. Acharja, *Bird Conserv. Int.* **30**, 599 (2020).

10.1126/science.abl9682

A flood of disaster response challenges

On 14 July, 60 to 180 mm of rain fell in just 22 hours in western Germany (*1*), causing heavy flooding. The storm was unexpectedly destructive because fast runoff and quickly rising streams interacted with mobilized sediment and debris, giving rise to a combination of effects not commonly observed in this central European landscape. As climate change produces more severe and frequent weather, such interactions will likely continue to cause unexpected results. Rather than just planning more of the same preparations, scientists must work to anticipate these challenges.

Hydrological models usually predict flood damage factors such as discharge and inundation (*2*) but ignore the role of organic and inorganic debris (*3*). The 14 July events were characterized by effects that are not commonly taken into account: Through saturation runoff and linear erosion, hill slopes routed water 10 to 100 times faster than expected (*4*). The rushing waters mobilized and carried large volumes of coarse woody debris, clogging bridges and extending the flooded area. Floodwaters running over sedimentary slopes cut back terraces outside the riverbed by hundreds of meters, undermining areas that were previously thought to be safe. Water overtopping a reservoir crown during the same event severely damaged a dam holding a volume of 1.2 million m^3. If the dam had collapsed, the ensuing flood would have added a further unforeseen complication to this hydrological disaster.

Progressive climate and environmental change in this region will destabilize forests, reduce the landscape's capacity to hold back water, and make extreme precipitation more frequent (*5*). As a result, rainfall similar to the 14 July event will

lead to more intense floods, and the floodwaters will move more quickly, mobilize more debris, and cause more erosion than those caused by equivalent rainfall in years past. The unexpected features visible in the 14 July event may become the norm.

To better anticipate the effects of future hydrometeorological extremes, robust approaches must include the ability to account for dynamically changing surface conditions during events. Models will have to explicitly describe the interactions between floodwater discharge and mobilized sediment as well as the transport and deposition of large woody debris. Detailed observations from newly affected flood areas will help to incorporate these factors into predictive models. These forensic observations must include high-resolution surface information (by airborne laser scanning) and detailed mapping of upper catchment and channel heads beyond the severely affected regions.

Michael Dietze[1,2]* and Ugur Ozturk[1,3]
[1]Helmholtz-Centre Potsdam–GFZ German Research Centre for Geosciences, Potsdam, Germany. [2]Geographical Institute, University of Bonn, Bonn, Germany. [3]Institute of Environmental Science and Geography, University of Potsdam, Potsdam, Germany.
*Corresponding author.
Email: mdietze@gfz-potsdam.de

REFERENCES AND NOTES

1. T. Junghänel *et al*., "Hydro-klimatologische Einordnung der Stark- und Dauerniederschläge in Teilen Deutschlands im Zusammenhang mit dem Tiefdruckgebiet 'Bernd' vom 12. bis 19. Juli 2021" (2021).
2. H. Kreibich *et al*., *Nat. Hazards Earth Syst. Sci.* **9**, 1679 (2009).
3. A. Lucía, M. Schwientek, J. Eberle, C. Zarfl, *Sci. Tot. Environ*. **640–641**, 315 (2018).
4. G. Govers, I. Takken, K. Helming, *Agronomie* **20**, 131 (2014).
5. V. Masson-Delmotte *et al*., Eds., "Global warming of 1.5°C: An IPCC Special Report on the impacts of global warming of 1.5°C above pre-industrial levels and related global greenhouse gas emission pathways, in the context of strengthening the global response to the threat of climate change, sustainable development, and efforts to eradicate poverty" (2018); www.ipcc.ch/sr15/.

10.1126/science.abm0617

Institutions' role in postpandemic support

In academia, we often feel as if we are only as good as our next publication, grant, or promotion. Mental health issues are prevalent among trainees in science and medicine, and the stigma of seeking mental health support creates a barrier to receiving help (*1*, *2*). The pandemic further exposed inequities that impede professional fulfillment (*3*), yet the push for advancement continues. As we return to classes and labs, institutions must proactively create a flexible and supportive environment for their employees.

Successful organizations are resilient (*4*); they can return to their original or an improved state of balance after enduring a turbulent environment such as the pandemic. Resilient organizations depend on resilient employees. To foster resilience among employees, institutions should provide a safe space for employees to share experiences, process events, and align work with purpose (*5*, *6*), enabling the necessary processing of past trauma. Institutions should also adopt incentive programs for mental health and recovery that do not require supervisor approval or time off. Principal investigators should be required to make plans to support the mental health of their trainees. All employees should be enrolled in support groups by default unless they opt out, lowering the barrier to seeking mental health support. To address the fears of transitioning back into the lab, institutions should ask for insights from employees on how to redesign workspaces and schedules based on lessons learned during the pandemic. Finally, recruiting processes must be assessed to ensure that candidates are not penalized for mental health challenges or decisions that may have been made to protect mental health.

Taking time to process will inevitably lead to lost opportunities for individual employees in the short run, leading to discomfort in an academic culture. However, in the long run, this intentional pause will allow individual scientists to be more engaged and adaptable (*7*, *8*). Because institutions benefit from healthy employees, it is in their best interest to provide incentives for employees to take the time they need and remove the barriers they may face.

Antoine de Morree[1,2]* and Al'ai Alvarez[3]
[1]Department of Biomedicine, Aarhus University, 8000 Aarhus, Denmark. [2]Department of Neurology and Neurological Sciences, Stanford University School of Medicine, Palo Alto, CA 94304, USA. [3]Department of Emergency Medicine, Stanford University School of Medicine, Palo Alto, CA 94304, USA.
*Corresponding author.
Email: demorree@stanford.edu

REFERENCES AND NOTES

1. T. M. Evans, L. Bira, J. B. Gastelum, L. T. Weiss, N. L. Vanderford, *Nat. Biotechnol.* **36**, 282 (2018).
2. A. L. Aaronson, K. Backes, G. Agarwal, J. L. Goldstein, J. Anzia, *Acad. Psychiat.* **42**, 469 (2018).
3. Smarten, "Covid-19: Impact on researchers" (2021); www.smarten.org.uk/covid-19-study.html.
4. S. S. Rai, S. Rai, S. K. Singh, *Environ. Dev. Sustain.* **23**, 12006 (2021)
5. M. C. Worline, J. E. Dutton, *Awakening Compassion at Work: The Quiet Power That Elevates People and Organizations* (Berrett-Koehler Publishers, ed. 1, 2017).
6. D. L. Coutu, *Harvard Bus. Rev.* **80**, 46 (2002).
7. C. Vercio *et al*., *Teach Learn Med.* 10.1080/10401334.2021.1879651 (2021).
8. M. A. Cohn, B. L. Fredrickson, S. L. Brown, J. A. Mikels, A. M. Conway, *Emotion* **9**, 3 (2009).

10.1126/science.abm2585

TECHNICAL COMMENT ABSTRACTS

Comment on "Aberrant type 1 immunity drives susceptibility to mucosal fungal infections"

Anne Puel and Jean-Laurent Casanova

Break *et al*. (Research Articles, 15 January 2021, eaay5731) suggest that chronic mucocutaneous candidiasis in humans with inborn errors of *AIRE* and autoimmune polyendocrine syndrome type 1 is due to excessive interferon-γ production and not to autoantibodies neutralizing interleukin-17 cytokines. We argue that both claims are not conclusively supported by their data and are at odds with 35 years of study.

Full text: dx.doi.org/10.1126/science.abi5459

Comment on "Aberrant type 1 immunity drives susceptibility to mucosal fungal infections"

Kai Kisand, Anthony Meager, Adrian Hayday, Nick Willcox

Break *et al*. (Research Articles, 15 January 2021, eaay5731) conclude that T cell overproduction of interferon-γ causes chronic mucocutaneous candidiasis (CMC), a typical early feature of autoimmune polyendocrinopathy–candidiasis–ectodermal dystrophy. This contradicts studies implicating interleukin IL-17 and IL-22 deficiencies as a cause of CMC. We propose that Break *et al*. have focused on late-arising events rather than more common primary causes of CMC.

Full text: dx.doi.org/10.1126/science.abi6235

Response to Comments on "Aberrant type 1 immunity drives susceptibility to mucosal fungal infections"

Timothy J. Break, Vasileios Oikonomou, Nicolas Dutzan, Jigar V. Desai, Marc Swidergall, Tilo Freiwald, Daniel Chauss, Oliver J. Harrison, Julie Alejo, Drake W. Williams, Stefania Pittaluga, Chyi-Chia R. Lee, Nicolas Bouladoux, Muthulekha Swamydas, Kevin W. Hoffman, Teresa Greenwell-Wild, Vincent M. Bruno, Lindsey B. Rosen, Wint Lwin, Andy Renteria, Sergio M. Pontejo, John P. Shannon, Ian A. Myles, Peter Olbrich, Elise M. N. Ferré, Monica Schmitt, Daniel Martin, Genomics and Computational Biology Core, Daniel L. Barber, Norma V. Solis, Luigi D. Notarangelo, David V. Serreze, Mitsuru Matsumoto, Heather D. Hickman, Philip M. Murphy, Mark S. Anderson, Jean K. Lim, Steven M. Holland, Scott G. Filler, Behdad Afzali, Yasmine Belkaid, Niki M. Moutsopoulos, Michail S. Lionakis

Puel and Casanova and Kisand *et al*. challenge our conclusions that interferonopathy, and not IL-17/IL-22 autoantibodies, promotes candidiasis in autoimmune polyendocrinopathy–candidiasis–ectodermal dystrophy. We acknowledge that conclusive evidence for causation is difficult to obtain in complex human diseases. However, our studies clearly document interferonopathy driving mucosal candidiasis with intact IL-17/IL-22 responses in *Aire*-deficient mice, with strong corroborative evidence in patients.

Full text: dx.doi.org/10.1126/science.abi8835

RESEARCH

IN *SCIENCE* JOURNALS

Edited by **Michael Funk**



A survey of fossilized ancient plants and extant specimens reveals increasing morphological complexity in reproductive structures through evolution.

PHOTO: ANDREW LESLIE

PALEOBOTANY

Evolutionary pulses of complexity

The evolution of land plants has been marked by an increase in the complexity of reproductive structures. Leslie *et al*. analyzed the temporal pattern of this increase in a study of fossil and extant land plants across the entire paleontological record. Reproductive complexity increased in two widely separated pulses corresponding to key innovations in reproductive biology: the origin of seeds in the very late Devonian and the origin of flowering plants in the mid-Cretaceous almost 250 million years later. After the origin of flowers, there was a rapid expansion in the morphological complexity of flowering plants. In contrast to many aspects of animal morphological diversity, which expanded early in evolutionary history, most complexity in plants was achieved relatively late. —AMS *Science*, abi6984, this issue p. 1368

QUANTUM GASES

Fragmenting the condensate

In a Bose-Einstein condensate, a sizable fraction of particles occupies a single quantum state. In some systems, it is in principle possible to have more than one such macroscopically occupied state. Evrard *et al*. observed this so-called fragmented condensate in an ultracold gas of bosonic sodium atoms with three spin states. Starting from a single condensate in a static magnetic field, the researchers decreased the field to zero, resulting in a three-fragment condensate. —JS

Science, abd8206, this issue p. 1340

METALLURGY

Titanium gets some twins

Introducing a network of nanotwins is known to improve the properties of face-centered cubic metal alloys. Zhao *et al*. used gentle compression in liquid nitrogen to introduce a similar network of nanotwins in hexagonal closed-packed titanium. By starting with a titanium that has little oxygen, the twin network can be more easily established. The nanotwinned network improved the yield strength by 50% and ductility by 20% at room temperature. The cryogenic properties were even better, with a yield strength of two gigapascals and a tensile ductility of 100% before failure. —BG

Science, abe7252, this issue p. 1363

CRISPR

CRISPR and Caspase meet

Many prokaryotes use CRISPR RNA–bound proteins to sense viral RNA instead of DNA to set an immune response in motion that protects from virus infection. Although these ribonucleoproteins are typically composed of many protein subunits, van Beljouw *et al*. discovered that CRISPR-Cas type III-E systems are formed by a large, single-component effector protein capable of double RNA cleavage. Distinct from other systems, this effector forms a complex with a peptidase from the caspase family, raising the intriguing possibility that viral RNA activates a protease activity to prevent virus propagation by host suicide. —DJ

Science, abk2718, this issue p. 1349

PROTEIN BIOGENESIS

Barrels that build barrels

Cells produce specialized machinery to produce functional β-barrel proteins that are involved in cross-membrane transport and membrane protein biogenesis in eukaryotic organelles and some bacteria. Wang *et al*. studied one of these systems that is itself a β barrel, the mitochondrial sorting and assembly machinery (SAM), in complex with one of its client proteins, translocase of the

outer membrane (TOM). TOM subunits can be added one at a time while the protein is bound to SAM. Compared with the full TOM core complex, the final TOM core subunit clashes with SAM, suggesting that the release of TOM may be driven by its association with SAM. —MAF

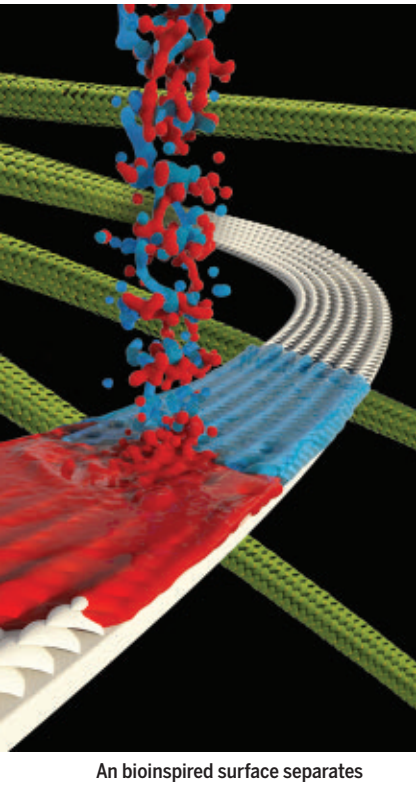
Science, abh0704, this issue p. 1377

FLUID MECHANICS

Surfaces directing fluid flows

Although surfaces can be made to attract or repel liquids using coatings, surface textures with specific curvature can also be used to achieve the same effect. However, fluid transport is usually limited by the specific pattern that only drives flow at the surface itself. Feng *et al*. created a dual-reentrant surface that has an asymmetric profile so that fluids spread out at the surface and subsurface layers. Furthermore, these surfaces can be designed so that different liquids will naturally steer in opposing directions simply because of their specific interactions with the surface. —MSL

Science, abg7552, this issue p. 1344



An bioinspired surface separates liquids with different surface tensions using 3D capillary action.

ADDITIVE MANUFACTURE

Designer beams for metal 3D printing

Metal additive manufacturing (AM) uses high-power lasers to heat and fuse powders to produce complex designs. However, the mechanical performance of the structures can be degraded by turbulence and spattering in the melt pool. Shaping the laser beam could allow for spatio-temporal control, improving the efficiency of the process and performance of the part. Tumkur *et al.* introduce designer Bessel beams that provide control over the print quality, thus reducing defects and improving the mechanical properties of the printed structures. Such beams may be implemented directly into existing hardware, providing a low-cost solution to improving AM processes. Continued development may increase the speed and throughput of metal AM and potentially expand metal AM to new materials. —MCM

Sci. Adv. 10.1126/sciadv.abg9358 (2021).

TRANSPLANTATION

Prolonging pulmonary preservation

Lungs can only be preserved on ice for about 6 to 8 hours before transplantation, which imparts geographic and logistical restrictions on organ use. Ali *et al.* used pig lungs and ex vivo lung perfusion to show that increasing the static storage temperature from 4 to 10°C could maintain organ function while prolonging storage time. Increased storage temperature preserved mitochondrial function and led to greater abundance of mitochondrial metabolites. Human lungs stored at 10°C were successfully transplanted into five patients after storage times of about 10 to 16 hours, supporting the clinical utility of this approach. —CC

Sci. Transl. Med. **13**, eabf7601 (2021).

IN OTHER JOURNALS

Edited by **Caroline Ash** *and* **Jesse Smith**



STEM WORKFORCE

Trump policies stir unintentional activism

The Trump administration was an impediment to diversity efforts in STEM. McGee begins to quantify the damage by surveying an ethnically diverse group of Black doctoral students pursuing a STEM career during the Trump presidency. Unsurprisingly, results support increased anxiety concerning opportunities to work for and/or be funded by a government whose policies reestablished structural and institutional racism and diminished the role of science. However, respondents also detailed ways that they were rethinking traditional STEM careers to center on social justice, underlying a heightened sense of urgency and intent for these students to become future change agents for racial justice in STEM. In this way, the Trump administration may have unintentionally started a much-needed revolution among our future STEM workforce. —MMc

Int. J. Qual. Stud. Educ. 10.1080/09518398.2021.1930246 (2021).

CANCER

TIM-4 abets lung cancer spread

Cancer immunotherapy has been highly successful in certain patients, but many patients do not respond. Peritoneal and plural tumor metastasis is associated with poor prognosis for non-small-cell lung cancer. In patients treated with checkpoint inhibitor immunotherapies, Chow *et al.* found that resident macrophages express TIM-4, a phosphatidylserine receptor.

IMAGE: ZUANKAI WANG AND PINGAN ZHU/CITY UNIVERSITY OF HONG KONG



PHOTO: VIDKA/ISTOCK.COM

Yellow coat color in canids is explained by repeated hybridization and backcrossing.

GENOMICS

Evolution of yellow dogs

Dog breeds are identified by their varied coat colors and patterns, yet it is unclear how genes control this observed variation. In many mammals, Agouti (ASIP) controls the production of eumelanin, which gives rise to black or brown pigment, and pheomelanin, which gives rise to yellow to white coloration. Examining dog skin RNA transcripts, Bannasch *et al.* identified distinct genetically linked regions (haplotypes) of structural variants affecting ASIP gene expression in both the ventral promoter and hair cycle promoter. Combinations of these genetic variants explain five common yellow and black dog coat patterns by affecting the regulation of ASIP. Comparing these genetic variants with ASIP in other canid species suggests that introgression from a now extinct lineage that diverged from grey wolves approximately 2 million years ago introduced the variant underlying the dominant yellow coloration patterns into populations of wolves and their dog descendants. —LMZ *Nat. Ecol. Evol.* 10.1038/s41559-021-01524-x (2021).

INTERGALACTIC MEDIUM

Late reionization from small galaxies

During the epoch of reionization, ultraviolet photons that escaped from galaxies converted the neutral intergalactic medium (IGM) into ionized plasma. The timing of this process has been difficult to determine both observationally and theoretically because the IGM is clumpy and galaxies are not distributed uniformly. Cain *et al.* simulated the reionization process using a subgrid method to account for the clumping and incorporated observational measurements of the mean free path of ultraviolet photons. The authors found that reionization was dominated by small galaxies that were too far and too faint to observe, and that the second half of ionizations were visible at redshifts of 7 to 5, later than previous estimates. —KTS

Astrophys. J. Lett. 10.3847/2041-8213/ac1ace (2021).

TRANSCRIPTION

PIC your move

Protein-coding genes make up about 1% of our DNA, and at any given time only a fraction of these DNAs is transcribed and translated into proteins. Transcription of most genes is performed by RNA polymerase II (Pol II), which is recruited by a preinitiation complex (PIC) assembled at the gene promoters. In the nucleus of a cell, where thousands of promoters are distributed along chromatin, it is not clear how different parts of PIC find promoters and assemble the enormous transcription machinery. Nguyen *et al.* explored the dynamics of PIC by single-molecule tracking in live cells of the eukaryote *Saccharomyces cerevisiae*. The authors found that in a few seconds, Pol II initiation factors instructed a hierarchical assembly of PIC in a process coordinated by nucleosome encroachment and chromatin remodeling. —DJ

Mol. Cell **81**, 3560 (2021).

TIM-4 binding to phosphatidylserine on cytotoxic effector CD8$^+$ T cells created an immunosuppressive microenvironment and limited antitumor activity. Administration of a TIM-4–blocking antibody or genetic deletion of TIM-4 improved response to cancer immunotherapy in a mouse model. —PNK

Cancer Cell **39**, 973 (2021).

POLYMERS

Solving a water problem

In between melt-processed thermoplastics and irreversible thermoset polymers are vitrimers, which contain dynamic cross-links that enable reshaping and recycling of these materials. There has been interest in vinylogous urethane vitrimers obtained by the polycondensation of acetoacetate and amine monomers, but this reaction releases water, leading to undesirable bubble formation and porosity. Spiesschaert *et al.* demonstrate a one-pot method in which alkyne esters are used in a polyaddition polymerization with amines, eliminating the water formation problem. The material properties are largely similar to the acetoacetate-based ones, and the viscoelastic properties can be tuned by adjusting the monomer ratios. The greater reactivity of alkyne esters allows for the use of less-reactive amine monomers. However, a small tendency to amide-bond–forming side reactions needs to be addressed. —MSL

Macromolecules 10.1021/acs.macromol.1c01049 (2021).

SIGNALING

Signals for allergy

Antigens stimulate signaling through tyrosine phosphorylation coupled to a membrane-bound kinase. Involvement of the plasma membrane implicates lipid-phase interactions. Bag *et al.* explored the contributions of lipid and protein interactions during receptor activation in rat mast cells. Diffusion of probe proteins by imaging fluorescence correlation spectroscopy was used to examine activation of the receptor for immunoglobulin E, which mediates inflammatory and allergic responses. Interestingly, the authors found that localized lipid changes near cross-linked receptors promoted phosphorylation of the receptor by the protein kinase Lyn and excluded the protein tyrosine phosphatase, which opposes the effects of Lyn. —LBR

Proc. Natl. Acad. Sci. U.S.A. **118**, e2026583118 (2021).

ALSO IN *SCIENCE* JOURNALS

Edited by **Michael Funk**

MEDICINE

Improving preclinical drug development

Traditional preclinical drug development involves animal models and in vitro human cell cultures that can poorly predict drug safety and efficacy in humans, contributing to failed clinical trials. In a Perspective, Roth *et al.* discuss the application of microfluidic organs-on-chips as a better preclinical model of drug efficacy. These microphysiological systems are already being used in some preclinical drug safety assessments, but the authors argue that they could also be used to test drug efficacy. For example, a key application could be to develop personalized medicine approaches by seeding chips with patient cells, thus allowing the most effective treatments to be identified. Although there are many challenges in developing organs-on-chips for preclinical drug development, there is hope that these devices might improve translation to the clinical setting. —GKA

Science, abc3734, this issue p. 1304

IMMUNOLOGY

SAAving vitamin A–mediated immunity

The vitamin A metabolite retinol is critical for B and T cell development and homing to the gut. Intestinal myeloid cells such as dendritic cells and macrophages take up retinol and process it into retinoic acid (RA), which in turn initiates RA-dependent gene expression programs in lymphocytes. Bang *et al*. identified LDL receptor-related protein 1 (LRP1) as a myeloid cell surface receptor for retinol. LRP1 binds retinol chaperoned by serum amyloid A (SAA) proteins, and SAA–retinol complexes are then endocytosed and metabolized by myeloid cells. Mice lacking either Saa or myeloid-specific Lrp1 exhibited profound impairments in vitamin A–mediated immunity. B and T cell trafficking to the intestine, immunoglobulin A production by B cells, and protection from enteric *Salmonella* Typhimurium infection were all diminished when either of these crucial players was missing. —STS

Science, abf9232, this issue p. 1323

QUANTUM OPTICS

Electrons see the quantum nature of light

We know that light is both a wave and a particle, and this duality arises from the classical and quantum nature of electromagnetic excitations. Dahan *et al*. observed that all experiments to date in which light interacts with free electrons have been described with light considered as a wave (see the Perspective by Carbone). The authors present experimental evidence revealing the quantum nature of the interaction between photons and free electrons. They combine an ultrafast transmission electron microscope with a silicon-photonic nanostructure that confines and strengthens the interaction between the light and the electrons. The "quantum" statistics of the photons are imprints onto the propagating electrons and are seen directly in their energy spectrum. —ISO

Science, abj7128, this issue p. 1324; see also abl6366, p. 1309

CORONAVIRUS

Antibodies dovetail with protection

Immune correlates of protection are clinical end points used to gauge vaccine-induced immunogenicity and protection. Corbett *et al*. studied nonhuman primate (NHP) immune responses to various doses of the mRNA-1273 (Moderna) vaccine to provide a range of immune responses and protective outcomes. They determined that circulating spike protein–specific antibodies correlated with protection against severe acute respiratory syndrome coronavirus 2 (SARS-CoV-2) replication in the airways. Passively transferred NHP antibodies were sufficient to mediate protection against SARS-CoV-2 challenge in hamsters, emphasizing that antibodies are mechanistic correlates. Protection of the lower respiratory tract required lower serum antibody concentrations, possibly explaining why most current vaccines are highly effective against severe lower airway disease. The higher antibody threshold required for reducing upper airway infection has potential implications for boosting to limit transmission. —STS

Science, abj0299, this issue p. 1325

QUANTUM GASES

Fermionic superradiance

Placing an atomic gas inside an optical cavity can have profound effects such as inducing long-range atomic interactions through coupling with the cavity's photons. Such experiments have been done with bosonic atoms but realizing them with fermions has proven trickier. Zhang *et al*. placed an ultracold gas of fermionic lithium-6 atoms in a cavity pumped by a laser beam orthogonal to the cavity axis. For sufficiently strong pumping, the researchers detected a checkerboard pattern in the atoms' momentum space corresponding to a superradiant phase transition in the cavity. The Pauli exclusion principle, which applies to fermions but not bosons, slowed down the atomic dynamics. —JS

Science, abd4385, this issue p. 1359

NEUROMORPHIC CHIPS

Memory and logic in the same device

Future artificial intelligence applications and data-intensive computations require the development of neuromorphic systems beyond traditional heterogeneous device architectures. Physical separation between a peripheral signal-processing unit and a memory-operating unit is one of the main bottlenecks of heterogeneous architectures, blocking further improvements in efficient resistance matching, energy consumption, and integration compatibility. Tong *et al*. present a transistor-memory architecture based on a homogeneous tungsten selenide-on-lithium niobate device array (see the Perspective by Rao and Tao). Analog peripheral signal preprocessing and nonvolatile memory were possible within the same device structure, promising diverse neuromorphic functionalities and offering potential improvements in neuromorphic systems on-chip. —YS

Science, abg3161, this issue p. 1353 see also abl4110, p. 1310

CORONAVIRUS

A boost for boosters

The evolution of severe acute respiratory syndrome coronavirus 2 (SARS-CoV-2) variants of concern poses a potential obstacle to achieving vaccine-induced immunity. Pegu *et al*. examined how viral variants, including the B.1.351 (Beta) and B.1.617.2 (Delta) variant, affected the immune response in a small number of individuals who received the Moderna mRNA-1273 vaccine. By analyzing sera obtained 6 months after the second shot in the primary vaccine series, the researchers found that neutralizing antibody titers persisted against all variants tested. However, neutralizing antibodies against the B1.351 variant had dropped considerably by 6 months, and some individuals had weak, and in some cases no, neutralizing activity. These data will help to guide public health policies regarding additional booster vaccinations. —PNK

Science, abj4176, this issue p. 1372

DENDRITIC CELLS

Lung dendritic cells find a home in the spleen

Adaptive immune responses to respiratory virus infections are believed to be primarily initiated by lung-derived migratory dendritic cells (DCs) that traffic to lung-draining mediastinal lymph nodes (med-LNs), where they prime naïve T cells. In mice infected with influenza A virus, Jenkins *et al.* demonstrate that DCs can also leave the med-LNs and cross-present lung-derived antigens to $CD8^+$ T cells in the spleen. Compared with med-LN–primed T cells, those primed in the spleen expressed higher levels of a crucial transcription factor, more efficiently gave rise to long-lived memory cells, and displayed superior expansion during reinfection. —CO

Sci. Immunol. **6**, eabg6895 (2021).

MICROBIAL FUEL CELLS

Silver in the linings

The bacterium *Shewanella oneidensis* is well known to use extracellular electron sinks, metal oxides, and ions in nature or electrodes when cultured in a fuel cell to power the catabolism of organic material. However, the power density of microbial fuel cells has been limited by various factors that are mostly related to connecting the microbes to the anode. Cao *et al*. found that a reduced graphene oxide–silver nanoparticle anode circumvents some of these issues, providing a substantial increase in current and power density (see the Perspective by Gaffney and Minteer). Electron microscopy revealed silver nanoparticles embedded or attached to the outer cell membrane, possibly facilitating electron transfer from internal electron carriers to the anode. —MAF

Science, abf3427, this issue p. 1336; see also abl3612, p. 1308

SOCIAL EVOLUTION

Mammal societies

Although a few types of structures prevail, social systems among mammals are relatively varied. New techniques, from monitoring to genetics, have allowed for a deeper understanding of this variation, how it is related to the environment, and how it has evolved. Clutton-Brock reviews the forms of and drivers of the different types of breeding systems and how they have been shaped by ecology and history. The author discusses how mammalian social interactions may be affected by human activities that are driving environmental change. —SNV

Science, abc9699, this issue p. 1322

MICROBIOLOGY

Lengthening pili with c-di-GMP turnover

Bacterial pili are polar appendages that mediate twitching motility and contribute to virulence. Low intracellular concentrations of the second messenger cyclic-di-guanosine monophosphate (c-di-GMP) induce pilus extension, which depends on the c-di-GMP–binding protein FimX and its association with the type 4 pilus assembly complex. Wei *et al*. found that the histidine kinase PdeK and its downstream effector, the phosphodiesterase PdeR, promoted pilus extension and virulence in the rice pathogen *Xanthomonas oryzae* pv. *oryzicola* by degrading c-di-GMP and mediating the unipolar localization of FimX. —AMV

Sci. Signal. **14**, eabi9589 (2021).

CANCER

Defining tumor cell immune evasion

Mouse models used to study cancer often lack a full immune system, allowing implantation of human tumors into the mice. By contrast, naturally evolving tumors must contend with a fully functional immune system and its destruction of some of the cells (see the Perspective by Ho and Wood). Two groups now report studies on mouse models with a fully intact immune system. Martin *et al*. started with preexisting murine tumor cell lines and examined their continued evolution in vivo, whereas Del Poggetto *et al*. examined the development of new pancreatic tumors in the context of inflammation, as is often seen in human patients. In each study, the authors found that the immune system exerted a selective pressure on cells that would give rise to tumors, promoting the survival of those that had lost expression of tumor suppressor genes or activated a specific oncogene. The findings suggest a major role for the immune system in driving tumor evolution across multiple types of cancer. —YN

Science, abg5784, this issue p. 1327, abj0486, this issue p. 1326; see also abl5376, p. 1306

REVIEW SUMMARY

SOCIAL EVOLUTION

Social evolution in mammals

Tim Clutton-Brock

BACKGROUND: Whereas early studies of animal evolution focused principally on the adaptations of different species to their physical environment, more recent studies have explored the effects of variation in social environments. Field studies of mammals have played a particularly important role in exploring the causes and consequences of variation in social organization and breeding systems, which vary widely between species, and an increasing number of long-term, individual-based studies have been able to document the structure of breeding groups and have explored the causes of variation in the breeding success of both sexes.

ADVANCES: Over the past 40 years, long-term, individual-based field studies have been able to use genetic techniques to explore the evolution of social organization and breeding systems in an increasing number of wild mammals. These range from species where members of both sexes live alone for part or all of the year to those where breeding adults live in pairs or small groups of close relatives where all members help to raise offspring born to the dominant female, as in meerkats and mole-rats, to species where multiple breeding females form stable, multigenerational groups that are often defended by one or more resident males. In most social mammals, groups consist of "natal" females that have remained in their birth group and are consequently related to each other while breeding males are immigrants from other groups, but in a minority of species (including all three African apes), females habitually disperse from their natal group or community after reaching sexual maturity, and groups typically consist of unrelated immigrant females and one or more resident males who may either be natal animals or immigrants.

Combined with genetic information, field studies of mammals have shown how differences in social organization are associated with differences in mating systems that affect the degree of reproductive skew in both sexes, the intensity of reproductive competition, and the evolution of sex differences in growth, size, weaponry, and reproductive anatomy. The intensity of reproductive competition in males and the development of traits that increase their competitive ability are often associated with reductions in the duration of the breeding life spans of males compared with those of females as well as with increased susceptibility of males to adverse environmental conditions and food shortages. Differences in social organization and mating systems also affect the kinship structure of groups and the average degree of kinship between group members, which are associated with differences in the frequency of cooperation and conflict between group members as well as with patterns of dispersal.

OUTLOOK: Many important questions about the causes and consequences of mammalian breeding systems remain unresolved. A broader range of field studies that includes more solitary, nocturnal, and marine species is needed. Future studies should also explore the demographic consequences of contrasting breeding systems and their implications for the conservation and management of populations as well as for evolutionary processes. ■

Department of Zoology, University of Cambridge, Cambridge, UK.
Email: thcb@cam.ac.uk
Cite this article as T. Clutton-Brock, *Science* 373, eabc9699 (2021). DOI: 10.1126/science.abc9699

READ THE FULL ARTICLE AT
https://doi.org/10.1126/science.abc9699



Twenty-two mammalian species that are the subject of continuing long-term, individual-based field studies covering multiple generations. Years indicate the approximate start date of each study. Gene-based estimates of variation in the breeding success of individuals of both sexes are now available for most of these species. (**A**) Rhesus macaque, (**B**) chimpanzee, (**C**) yellow-bellied marmot, (**D**) spotted hyena, (**E**) African lion, (**F**) northern elephant seal, (**G**) mountain gorilla, (**H**) red deer, (**I**) yellow baboon, (**J**) bighorn sheep, (**K**) African elephant, (**L**) black-tailed prairie dog, (**M**) African cheetah, (**N**) northern muriqui, (**O**) sifaka, (**P**) Soay sheep, (**Q**) red squirrel, (**R**) white-faced capuchin, (**S**) Kalahari meerkat, (**T**) banded mongoose, (**U**) red-fronted lemur, and (**V**) owl monkey.

PHOTOS: (A) ALEX GEORGIEV; (B) IAN C. GILBY; (C) DAN BLUMSTEIN; (D) TIM H. CLUTTON-BROCK; (E) CRAIG PACKER; (F) BURNEY LE BOEUF; (G) ALEXANDER HARCOURT/KELLY STEWART/ ANTHROPHOTO; (H) TIM H. CLUTTON-BROCK; (I) ELIZABETH ARCHIE; (J) FANIE PELLETIER; (K) HARVEY CROZE; (L) ELAINE MILLER BOND; (M) DOM CRAM; (N) THIAGO CAVALCANTE/PROJETO MURIQUI DE CARATINGA; (O) CLAUDIA FICHTEL; (P) ARPAT OZGUL; (Q) RYAN W. TAYLOR; (R) TOM HOUSLAY; (S) TIM H. CLUTTON-BROCK; (T) HARRY MARSHALL; (U) CLAUDIA FICHTEL; (V) E. WHITE/OWL MONKEY PROJECT

REVIEW

SOCIAL EVOLUTION

Social evolution in mammals

Tim Clutton-Brock

Long-term, individual-based field studies, the application of genetic techniques, and phylogenetic reconstructions have led to substantial advances in our understanding of the diversity and evolution of mammalian breeding systems and their consequences. These studies show how differences in ecology, life histories, and phylogeny affect the distributions of breeding females and breeding males; how the distributions of both sexes affect the evolution of breeding systems and the composition and kinship structure of social groups; how differences in breeding systems and the social environment that individuals encounter affect the selection pressures operating on both sexes and the evolution of their behavior, physiology, and morphology; and how these differences affect the demography and dynamics of populations and their responses to variation in density, climate, and human impact.

Early studies of animal evolution focused principally on adaptations to the physical environment that were likely to increase the survival of individuals (*1*–*3*). In contrast, research since the 1960s has explored the selection pressures operating through individual differences in reproductive success as well as survival in both sexes and has shown how differences in breeding systems and social environments affect the selection pressures operating on females and males and the evolution of their behavior, physiology, morphology, and ecology (*4*–*6*). While important contributions to our understanding of animal breeding systems and their consequences have been made by studies of a wide range of animals, research on mammals has played a particularly important role, because field studies of species with contrasting breeding systems have been able to explore the extent and causes of variation in lifetime breeding success in large samples of recognizable individuals of both sexes (*7*–*9*).

Mammals are set apart from other major groups of vertebrates by the fact that the evolution of gestation and lactation commits all females to heavy energetic investment in their offspring (*7*, *10*). This investment intensifies intrasexual competition between females for the resources necessary to raise offspring and often reduces the potential benefits of parental investment for males, increasing the competition between them to guard access to multiple breeding partners and contributing to the evolution of polygynous mating systems (*7*, *11*). As a result, the principal factor limiting breeding success in male mammals is commonly their access to breeding females, whereas the principal factor limiting reproductive success in females is often their access to resources (*7*, *12*, *13*). Where breeding females live in groups, average kinship between group members is reduced (*14*) (Fig. 1) and competition for breeding opportunities is intensified in both sexes with far-reaching consequences for the evolution of their reproductive strategies and social behavior (*7*, *15*).

Over the past 40 years, our understanding of the diversity and evolution of mammalian societies and breeding systems has improved rapidly as a result of three principal developments. First, an increasing number of long-term field studies of social mammals have monitored the movements and life histories of large numbers of recognizable individuals from birth to death in successive generations (*8*, *16*). Second, the application of genetic analysis has provided quantitative measures of individual breeding success and kinship in both sexes in an increasing number of species (*17*), making it possible to move on from categorical descriptions of mating systems to direct estimates of the relative breeding success of individuals and the degree of reproductive skew (*16*). In some cases, it has also been possible to construct multigenerational pedigrees that can be used to assess the heritability of particular traits and the extent of inbreeding (*18*). And third, the development of gene-based phylogenies has made it possible to reconstruct evolutionary sequences and to identify major transitions in behavior and life-history parameters and explore their social and ecological correlates (*19*–*21*).

Here, I review developments in our understanding of the evolution of mammalian breeding systems and their downstream consequences for the morphology, behavior, and ecology of females and males. Because the factors limiting breeding success often differ between females and males, it is useful to start by considering the evolution of reproductive strategies in each of the sexes separately before exploring how their strategies interact (*7*). To begin, I divide mammals into two groups: singular breeders, referring to species where breeding females live in separate ranges and are usually intolerant of each other during the breeding season even if they aggregate outside of it, and plural breeders, referring to species where multiple breeding females share a common range and frequently assemble in groups (*7*, *22*) (see Box 1). I then describe how differences in the size, stability, and kinship composition of female groups affect the evolution of reproductive strategies and phenotypes of both sexes, as well as their population dynamics and demography.

Singular breeders

Solitary breeders

Phylogenetic reconstructions suggest that some form of singular breeding probably represents the ancestral condition in several orders where plural breeding also occurs, including primates and carnivores (*23*–*25*). It may also have been the ancestral form of social organization in the earliest mammals (*26*), given that all three contemporary monotremes are solitary breeders (*27*). A combination of the high energetic costs of gestation and lactation, the limited mobility of nonvolant mammals, and the need for crypsis to minimize predation on neonates and adults probably explains why breeding females are solitary in most mammalian species (*7*, *10*). As might be expected, systems where breeding females live in separate ranges and avoid or are intolerant of each other during the breeding season (i.e., solitary breeders) are particularly common in insectivores and carnivores as well as in many small mammals, nocturnal species, and forest-dwelling terrestrial herbivores (*7*, *10*).

To date, few of these species have been studied in detail, and the ecological factors maintaining solitary lifestyles are not well understood (*7*, *28*). Aspects of their feeding ecology, antipredation tactics, and reproduction may all constrain the aggregation of breeding females in these species (*7*, *29*). In some of them, females produce litters of relatively altricial young that need to be concealed or protected from predators or conspecifics in nests or burrows (*30*). Others, including many of the smaller cats and nocturnal mongooses, feed on mobile prey that would be disturbed if several individuals foraged together (*31*), although many terrestrial frugivores and herbivores living in closed habitats are also singular breeders, suggesting that feeding competition or the need for crypsis to avoid predation may also limit the evolution of female sociality (*23*, *28*, *32*).

Social relationships between males and females vary widely across species. In some, such as North American red squirrels, males and females occupy separate territories and only come together to mate (*33*, *34*), but in many others—rodents, cats, bears, and nocturnal primates, for example—males occupy

Department of Zoology, University of Cambridge, Cambridge, UK.
Email: thcb@cam.ac.uk

Box 1. Definitions.

Breeding systems

Singular breeders

Solitary breeders: Species or populations in which most breeding females live in separate ranges that overlap to varying extents and breeding females avoid or are intolerant of each other during the breeding season, although they may aggregate at other times of the year. Males may occupy separate ranges or ranges overlapping those of several adult females, providing access to more than one potential breeding partner.

Pair breeders: Species in which a single adult male and a single adult female, along with her dependent offspring, share the same range and usually breed together in successive seasons or breeding attempts. Populations may also contain unattached "floaters" of either or both sexes.

Singular cooperative breeders: Species living in groups that include more than one adult of either or both sexes, wherein only one female breeds regularly and subordinates of either or both sexes help rear her young.

Plural breeders

Group-living species or populations in which two or more breeding females share the same range and associate with each other in stable or unstable groups during the breeding season, either foraging together in cohesive groups or foraging in unstable parties. Breeding groups may include one adult breeding male (single male groups) or more than one breeding male (multi-male groups). Where female groups are unstable, males may defend temporary groups of females, cruise between female groups, or defend mating territories in areas regularly used by foraging females or in clusters that are visited by receptive females (leks). In some species, groups of related females or breeding groups that include both sexes aggregate in larger herds (multilevel societies).

Mating systems

Monogamy: Mating system wherein the same mixed-sex pair usually mate together in successive breeding attempts.

Polygyny: Mating system wherein single males commonly mate with several different females in the same breeding season, and multiple breeding females may mate with the same male.

Polyandry: Mating system wherein individual females commonly mate with multiple males in the course of a single season, while males do not mate with more than one female.

Polygynandry: Mating system wherein both sexes commonly mate with multiple partners in the same or successive breeding seasons.

Benefits and costs

Direct fitness benefits or costs: Increments or reductions to the survival or breeding success of individuals

Indirect fitness benefits or costs: Increments or reductions to the survival or breeding success of nondescendant relatives.

ranges or territories that are larger than those of females and overlap the ranges of several females (*7*). The number of breeding partners that males can access consequently depends on the density of females and the relative size of the ranges of the two sexes and often varies with population density (*7*, *35*, *36*). The intensity of intrasexual competition between males probably varies with the relative size of male and female ranges (*7*) and with the adult sex ratio (*37*), but comparative data are scarce. Males can be substantially heavier than females, similar in size, or slightly smaller, and they rarely contribute much to the care of young (*38*–*41*).

The offspring of most solitary breeders typically disperse from their mother's range when they reach breeding age, but the timing of dispersal and the distance moved varies with social and ecological conditions and often differs between the sexes (*7*, *42*). Breeding females can be more tolerant of their own daughters than of immigrants, and female recruits may settle in areas adjoining their mother's range, so that populations often have a well-defined genetic structure (*43*, *44*). In North American red squirrels, females even prepare food caches for their adolescent offspring that will support them through their first winter, and they change their ranging patterns to allow their offspring to take over part of their original territory (*45*).

Pair breeders

In some singular-breeding species, individual males occupy ranges or territories whose boundaries coincide closely with those of one breeding female, and adults form mixed-sex pairs where partners share a common range and the offspring of both sexes typically disperse from their parents' ranges (*7*, *46*). Pairs commonly persist until one partner dies or is displaced, and "divorce" is often uncommon (*7*). Pair breeding is frequently associated with the defense of shared ranges by partners of both sexes and is widely distributed, although it is relatively common in rodents, primates, and carnivores (*7*). Pair breeding often appears to have evolved from solitary breeding (*24*, *26*), but reversions from plural breeding also occur (*24*, *47*). In diurnal species where single males and females share ranges—for example, titi monkeys and owl monkeys (*48*) or klipspringers and dik-diks (*49*)—partners commonly forage and sleep together, forming small family groups with their adolescent offspring. In other species, including some nocturnal lemurs, pairs share feeding territories and may sleep together but often forage alone and, in some cases, only associate with each other during the mating season (*50*, *51*). Pair breeders are often described as monogamous (see Box 1), but genetic analyses have shown that, although partners often breed with each other, both sexes may breed with other individuals too (*46*, *52*) and that differences in the frequency of extra-pair breeding are associated with variation in breeding seasonality, population density, and group composition (*53*, *54*).

In many (but not all) pair-breeding species, males contribute to the care of juveniles, assisting in births, guarding young at the burrow or nest, and feeding dependent young (*7*). The death or removal of males is often associated with reductions in the survival of their dependent young. For example, in pair-breeding California mice, the experimental removal of fathers reduces offspring survival by 60% (*55*). Although females are more commonly the principal caregivers, in some pair-breeding species, such as titi monkeys, males contribute more to care, and juveniles respond more strongly to the absence of their fathers than that of their mothers (*56*). Male care may also help to reduce the costs of breeding to females, and interspecific comparisons suggest that it is often associated with larger litter size and greater breeding frequency for females (*57*, *58*).

Because pair breeding constrains access to multiple partners for both sexes, important questions about its potential benefits arise (*52*, *59*, *60*). Three main groups of explanations for the evolution of pair breeding have been suggested, although none of them provides a satisfactory explanation of its distribution (*52*, *60*, *61*). First, pair breeding may evolve in species where biparental care is necessary for the protection and successful rearing of young or for their protection against predators or infanticidal attacks by other males, generating benefits to pair breeding in either or both sexes (*52*, *62*, *63*). However, in some pair-breeding species, males are not involved in provisioning or protecting young (*61*, *64*),

and two independent phylogenetic reconstructions have suggested that the evolution of pair breeding is likely to have preceded or evolved at the same time as the evolution of paternal care (*26*, *62*). In addition, there is no obvious reason why males cannot provide adequate defense against infanticide for the offspring of more than one female (*65*). A second group of arguments suggest that males are seldom able to defend breeding access to more than one female and her range at a time or that they cannot do so effectively and may maximize their breeding success by guarding breeding access to a single partner (*52*). There is anecdotal evidence that males that attempt to guard more than one female soon lose one of their partners (*64*) and comparative evidence that pair-breeding species may show low population densities, although females do not show a consistent tendency toward having unusually large ranges (*26*, *66*). A third group of explanations suggest that pair breeding enhances coordinated defense of feeding territories (*67*), although this is unlikely where pair members spend most of their time apart. There is currently no single satisfactory explanation for the distribution of pair breeding, and it seems likely that different social and ecological contexts favor its evolution in different taxa (*60*, *61*, *68*).

Pair breeding has important evolutionary consequences. In many pair-breeding species, females and males both compete with members of the same sex for territories and breeding partners (*7*, *60*), and sex differences in reproductive skew, selection for competitive ability, and the development of weaponry and ornamentation are typically smaller than in plural-breeding species whose females live in groups and males can monopolize access to multiple breeding partners (*7*). Sex differences in adult size, foraging behavior, and mortality are usually small too, and, in some species, females are larger than males (*7*, *41*, *69*, *70*). The incidence of sperm competition is also reduced, and males typically have relatively small testes and lack the reproductive adaptations found in species where sperm competition is common (*71*). The consequences of pair breeding for population dynamics in mammals have not yet been systematically explored, but early studies of the population dynamics of territorial birds suggested that pair breeding may be associated with greater stability in population size (*72*), and adult sex ratios in pair-breeding mammals are usually close to parity, suggesting that sex differences in survival are typically small (*7*).

Singular cooperative breeders

In a small number of mammalian species, several adult females and one or more adult males share a common range and aggregate in breeding groups, but a single dominant female in each group prevents most other females from breeding regularly and is the mother of a large proportion (usually >75%) of young born in the group (*7*, *22*, *73*). Breeding systems of this kind have been most intensively studied in rodents, canids, social mole-rats, social mongooses, and marmosets and tamarins (*74*, *75*). Subordinate females frequently show lower levels of estrogen, luteinizing hormone, and progesterone than dominants and can be temporarily infertile, although they are usually able to activate their reproductive systems within a few days or weeks of the death of breeding females (*76*–*78*). Because subordinate females are often "natal" individuals that have not left the group they were born into, they often lack regular access to unrelated males within their group, and this, too, may contribute to reproductive suppression (*7*, *76*, *79*). All group members often help protect and provision young born to the breeding female, and in some species, females are unable to breed successfully without assistance from nonbreeding helpers (Fig. 2) (*7*, *22*). Subordinates also contribute to communal activities that benefit all group members (*80*), which can include defense of the group's range against intruders (most species), maintaining foraging tunnels (mole-rats), communal hunting (several canids), and alternating as sentinels while the group is feeding (meerkats) (*80*).

Phylogenetic reconstructions suggest that singular cooperative breeders have usually evolved from pair-breeding ancestors (*81*), although this may not be true for marmosets and tamarins (*75*). Groups are usually stable but vary widely in size both within and between species, ranging from less than five individuals to more than a hundred, as in some colonies of naked mole-rats (*82*). Among meerkats and mole-rats, female immigration is rare, whereas among some canids and tamarins, both sexes may immigrate into established breeding groups (*7*, *75*, *83*). Cooperative breeders share some of the characteristics of eusocial insects, but subordinate helpers are only temporarily

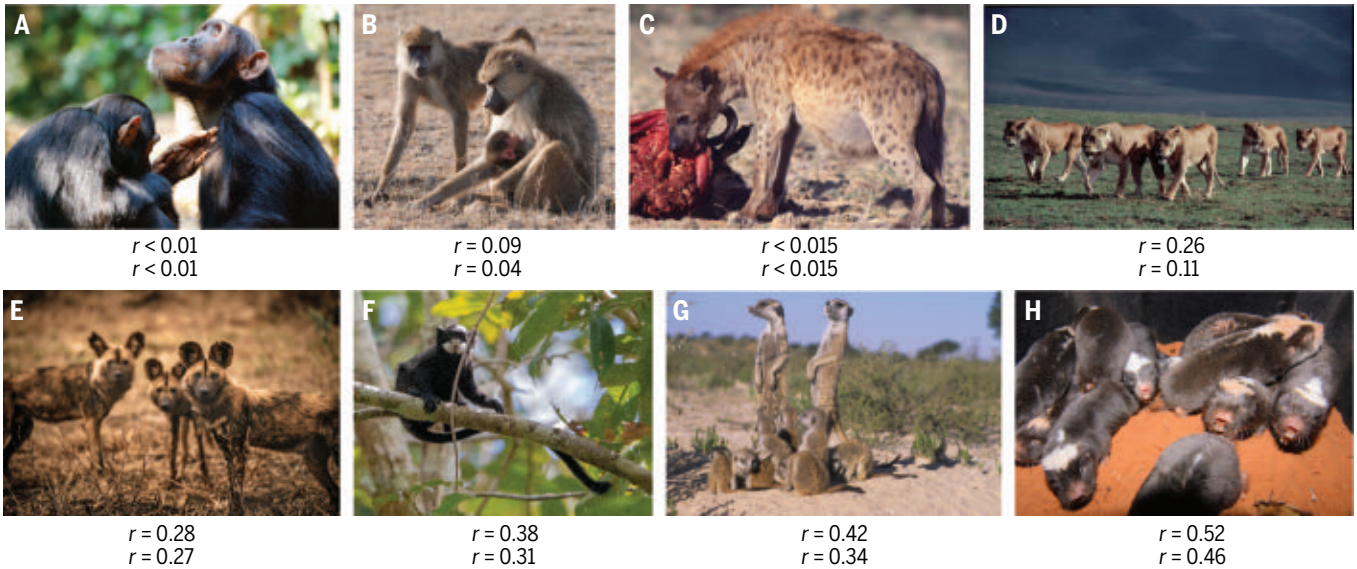


Fig. 1. Average kinship between group members in four plural-breeding and four singular-breeding species. The figure shows average coefficients of relatedness between resident females ("F"; upper values) and all group members ("All"; lower values) for four plural-breeding species (*94*, *95*) [top row: (**A**) chimpanzees (*139*, *217*), (**B**) yellow baboons, (**C**) spotted hyenas (*218*), and (**D**) African lions (*219*)] and four singular-breeding species [bottom row: (**E**) African wild dogs (*220*), (**F**) moustached tamarins (*221*), (**G**) Kalahari meerkats (*222*, *223*), and (**H**) Damaraland mole-rats (*224*)].

PHOTOS: (A) IAN C. GILBY; (B) E. ARCHIE; (C) T. CLUTTON-BROCK; (D) CRAIG PACKER; (E) LORNA HARVEY; (F) HECTOR BOTTAI UNDER CREATIVE COMMONS ATTRIBUTION - SHAREALIKE 4.0 INTERNATIONAL

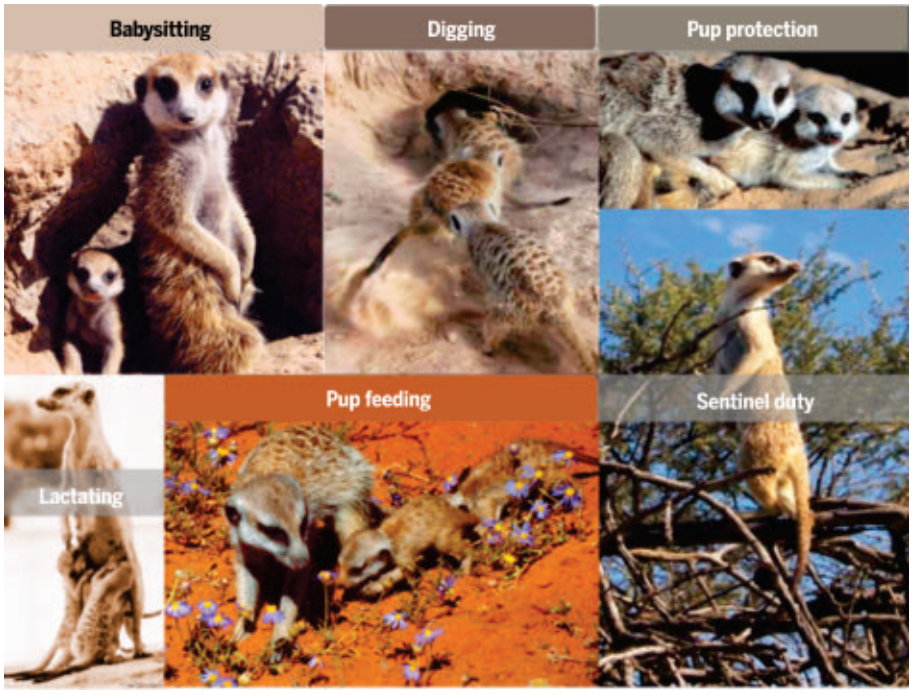


Fig. 2. Cooperative activities in Kalahari meerkats. In meerkats (*Suricata suricatta*), nonbreeding subordinates of both sexes assist dominant breeders by caring for their young, guarding and feeding pups, and acting as sentinels when their group is foraging (*90*).

infertile in all cooperative vertebrates, and there is no clear evidence of discrete castes that have divergent patterns of development in any cooperative vertebrates (*80*, *84*), so it is debatable whether any mammals should be regarded as eusocial (*85*). Moreover, qualitative differences in the form and context of cooperation often make it difficult to compare the extent to which breeders rely on helpers or to distinguish clearly between direct and indirect fitness benefits (*80*).

The evolution of singular-breeding systems and cooperative care of young raises important evolutionary questions. First, why do dominant females of some species suppress subordinates, kill their young, and evict them from their group, despite these subordinates often being their own offspring who are likely to act as helpers? Studies of meerkats have shown that subordinate breeding can impose substantial costs on dominants: Pregnant subordinates often kill pups born to dominants (*86*, *87*), and the presence of pups from other litters reduces the growth of the dominant female's offspring (*88*). In addition, suppressing the reproduction of subordinates may increase their contributions to rearing the dominant's offspring (*7*).

Second, why do subordinate females allow themselves to be suppressed and remain in their birth groups rather than resisting suppression or dispersing, as they do in many plural-breeding species? Part of the answer appears to be that resident groups are territorial, local habitats are often saturated, and mortality during dispersal is often high, so that a female's best chance of acquiring a breeding position may often be to remain in her breeding group and to maximize the chance that she will inherit the dominant position there (*7*, *89*, *90*). When vacant habitat is available, adolescents commonly disperse and attempt to breed independently, so social groups may be reduced to breeding pairs (*91*, *92*). Given that dominants often evict subordinates that attempt to breed, breeding attempts may also reduce the chances that subordinates will inherit the breeding position in their birth group (*7*).

Third, why do subordinates assist with rearing the offspring of dominants rather than conserving their resources? There is little evidence either that cooperative behavior is enforced or that it is directed selectively at an individual's closest relatives in any of these species (*7*, *93*). However, genetic analyses suggest that, in most groups, a single female and a single male are usually the parents of a large proportion of the surviving young and that average kinship between group members is unusually high (*94*, *95*) (Fig. 1). As a result, the indirect benefits of helping are often likely to be relatively large, facilitating the evolution of cooperation (*94*). Moreover, the contributions of helpers to cooperative activities are often adjusted to their foraging success and condition, so that the fitness costs of helping may be small (*96*, *97*). Finally, dominant breeders are often more likely to rear young successfully than subordinates so that investing in their mother's offspring may be more productive than attempting to breed themselves. As a result, the combined direct and indirect fitness benefits that subordinates derive from attempting to breed may often be lower than those of forgoing reproduction and helping to rear the dominant's pups.

Singular cooperative breeding systems have a number of unusual evolutionary consequences. Individual differences in female breeding success are large, and competition for breeding status between females is intense (*98*). For example, in meerkats, most females that reach sexual maturity fail to breed at any stage in their lives, while successful female breeders can rear more than 80 surviving young over the course of their lives (*90*), and even larger differences in breeding success may occur in the social mole-rats, whose litter size is larger and potential breeding life spans are longer than those of meerkats (*80*, *99*). In several of these species, breeding females have unusually high testosterone levels (*77*, *100*) and tend to be more frequently aggressive than males and dominant over them, even where sex differences in growth and adult size are small (*7*). In some species (including meerkats and social mole-rats), individuals that acquire breeding positions also show a secondary period of growth in the months following their acquisition of dominant status, associated with increases in their size and in their capacity to maintain their position against potential competitors or to bear larger litters (*77*, *101*, *102*). In meerkats, subordinates also show increased growth rates in response to potential breeding opportunities and to potential challenges by competitors (*101*, *103*).

Cooperative breeding also has demographic consequences. In some cases, it is associated with greater breeding frequency. For example, among the African mole-rats, species that breed cooperatively also breed more frequently than solitary breeders and often produce comparatively large litters (*80*). By distributing the costs of raising young among multiple adults, helpers also mitigate the effects of adverse climatic conditions and low food availability on growth, survival, and reproduction (*104*, *105*), which probably explains why cooperative breeders are often found in challenging, unpredictable environments (*106*, *107*). However, as the breeding success of dominant females is positively related to the number of helpers, which falls when population density declines, recruitment rates per group often fall when population density is low, generating an inverse density dependence and delaying the recovery of populations (*7*, *108*). Environmental events that reduce population density, such as droughts and epidemics, may consequently depress recruitment in cooperative breeders and groups, and local populations

PHOTOS: KALAHARI RESEARCH TRUST

can be slow to recover, which increases their instability and the risk of local extinctions (*108*, *109*).

Although cooperative breeding systems involving nonbreeding helpers have often evolved in association with singular breeding, they also occur among some plural breeders. For example, banded mongooses live in large groups of around 20 or more individuals in more mesic environments than meerkats (*110*). Unlike meerkats and dwarf mongooses, multiple banded mongoose females in each group breed in almost perfect synchrony, mostly giving birth on the same day, and pups born out of synchrony are usually killed (*110*). Alloparental care by females is limited, but nonbreeding males escort and feed particular pups, who are not necessarily close relatives. Why dominant females do not suppress breeding in subordinate females in banded mongooses is still unclear, but one possibility is that reductions in relatedness between group members resulting from increases in group size (average coefficient of relatedness, r = 0.11) (*111*) limit the indirect fitness that subordinate females can gain by helping to rear the dominant female's young and so make them more resistant to suppression.

Plural breeders

Female sociality in plural-breeding species

In plural-breeding species, multiple breeding females typically share a common range and aggregate in stable or unstable groups (*7*, *22*, *112*). All adult females are usually fertile and attempt to breed regularly, although individuals differ in their breeding success. Plural breeding systems of this kind are common in bats, rodents, ungulates, primates, and cetaceans and are less common in carnivores and insectivores (*7*, *22*, *73*, *113*). In several orders, including primates and ungulates, plural breeding appears to have evolved from solitary breeding or pair-breeding ancestors (*23*, *24*, *26*), often in association with the production of single, relatively precocial young (*73*). In some species, populations oscillate between singular breeding when density is low and plural breeding when it is high, while in others, females continue either to occupy separate ranges or to live in groups at all densities, although territory size often declines when density is high (*114*, *115*).

Because the movements and distributions of breeding females commonly fluctuate according to the distribution of resources, whereas those of breeding males are adjusted to the distribution of receptive females or to the distribution of resources that attract them, it is often useful to explore the factors affecting sociality in females and males separately (*7*, *12*, *22*, *112*). Groups of breeding females vary widely in size from small, stable groups that frequently defend feeding territories and usually include no more than two or three breeding females to the unstable herds of migratory deer and antelope that can include several thousand individuals (*7*, *23*, *116*) and the colonies of some bats that can have more than a million members (*116*). Group size also varies widely both within and between populations and commonly increases with population density (*114*, *115*, *117*).

The stability of female groups also varies widely. In plural-breeding species that live in relatively small ranges or territories, such as many primates and carnivores, females commonly live in "closed" groups where female immigration is rare, group membership is stable over long periods, and group members are often hostile to intruders (*7*). Members of closed groups may either forage together, as do meerkats and chacma baboons, or in unstable parties whose size varies with food abundance and distribution, as do chimpanzees and spotted hyenas (*118*, *119*). In species where females range over relatively large areas, including many deer and antelope and some bats, cetaceans, and seals, females often form "open" groups whose membership changes from hour to hour as individuals or parties join or leave each other (*7*, *120*). In some of these species—red deer and African elephants, for example—maternally related females associate with each other disproportionately often, and larger herds usually consist of females from several different kin groups (*120*, *121*), while in some migratory species, such as blue wildebeest, there may be no long-lasting social connections between individuals (*122*).

Interspecific differences in female sociality usually appear to be a consequence of variation in the relative costs and benefits of group living to females, although these can be affected by the reproductive strategies of males (*7*, *123*). Differences in female sociality are often associated with differences in life-history parameters, diet, habitat type, and activity timing or with variation in the risk of predation and antipredator tactics (*7*, *23*, *29*, *32*), and associations between group size and food distribution are common within species too (*7*, *124*). The costs of living in groups can include reductions in foraging success, breeding success, or life span as a result of increases in direct or indirect competition for resources (*7*, *23*, *125*), increased detectability of groups by predators (*126*), increased transmission of parasites (*127*), and increased breeding interference between resident females (*128*). Direct benefits of sociality are sometimes divided into benefits associated with the defense of resources or nests and those associated with foraging (*129*) and can include heat conservation (*130*); the defense of territories against neighboring groups (*131*); increases in the ability of individuals to find, catch, or subdue prey (*83*); and reduced risks of predation as a result of dilution effects or improvements in vigilance or defense (*7*). Where resident individuals are related, sociality may also generate important indirect fitness benefits arising from the benefits of aggregation to the fitness of kin (*7*, *132*).

The kinship composition of female groups also varies widely. In many plural-breeding species that live in stable groups, females are individuals that have either remained in their birth groups or have founded new groups, so that most female group members are maternal relatives. In contrast, in a minority of species (including some bats, several social equids, several Old and New World monkeys, and all three African apes), females usually disperse from their natal groups and often immigrate into established breeding groups, so that most coresident females are unrelated (*7*, *133*). There is extensive evidence of inbreeding costs in wild mammals and of female avoidance of mating with familiar males that are likely to be close relatives (*7*, *134*, *135*), and differences in female dispersal often appear to be related to variation in the breeding tenure of resident males and the risks of inbreeding to females who remain in their natal group (*7*). Where the breeding tenure of individual males is relatively short, so that breeding males have usually been replaced by the time their daughters reach sexual maturity, females do not need to disperse to obtain access to unrelated breeding partners and often remain and breed in their birth groups (*133*), avoiding mating with familiar males that are likely to be siblings (*7*). In many of these species, males usually disperse from their birth groups after reaching sexual maturity (*7*, *133*, *136*). In contrast, in species where the tenure of individual breeding males or male kin groups is typically longer than the age at which females mature, females often disperse to breed after reaching sexual maturity and either join other established groups or found new groups (*137*, *138*). In some of these species (including several of the larger New World monkeys and chimpanzees), males may remain in their birth groups, mating with females that immigrate from neighboring groups (*137*, *139*). One interesting exception to the tendency for members of one sex to disperse from their birth groups occurs in killer whales, where both sexes may remain in their birth groups throughout their lives and adults of both sexes usually mate with members of other groups (*140*, *141*).

Plural breeding and competition between females

The aggregation of breeding females often intensifies reproductive competition between females, although escalated fights are seldom as frequent as they are in males, which probably explains why weaponry is seldom as highly developed in females (*7*, *142*). Increases in group size reduce levels of maternal kinship between

group members, and average coefficients of relatedness between group members fall rapidly as the number of breeding females increases (*14*, *95*) or where female immigration is common, as in chimpanzees, intensifying conflicts of interest between group members (Fig. 1). In species that live in relatively large, stable groups, where average levels of kinship are low, aggressive interactions between females are often relatively common and related females frequently support each other, so that the status, breeding success, and longevity of individuals often depends on the number of relatives and allies that will support them (*143*, *144*). Intense competition between females can be associated with reductions in the relative survival of female juveniles. For example, among spotted hyenas, siblicide is more frequent between female littermates than between males (*145*), while in some plural-breeding species where related females form coalitions with relatives, dominant females focus aggression on the daughters of subordinates (*7*, *146*).

In a substantial number of plural-breeding species, resident females also interfere directly with each other's breeding attempts, and both socially induced abortions and female infanticide are common in subordinate females (*147*, *148*). Where female competition is particularly intense, as in spotted hyenas and some lemurs, females can have relatively high androgen levels and may show a variety of male-like anatomical and physiological traits (*149*, *150*). The evolutionary consequences of intense female competition are well illustrated by research on Alpine fighting cows, where selective breeding of females for competitive ability over multiple generations has raised testosterone levels in females and produced a complex of male-like traits, so that females closely resemble males (*151*) (Fig. 3).

Male sociality in plural-breeding species

Because the size and stability of female groups affect the number of females that individual males can guard, female sociality also increases the intensity of direct competition between males and affects the tactics they adopt, which vary widely both between and within species (*7*, *152*). Where females live in small, stable groups and mating is not highly synchronized, single males often defend access to female groups throughout the year, whereas in larger stable groups, several breeding males frequently associate with each group of females, forming multi-male groups, and both sexes often mate with more than one partner (*7*, *153*). In litter-bearing species, such as lions and meerkats, males commonly emigrate from their birth groups together and immigrate into established groups together, so that coresident males are often close relatives that have been familiar with each other since birth. In contrast, in species that produce single young, such as many group-living monkeys, males usually emigrate and immigrate independently, so that coresident males are seldom closely related to each other (*7*, *95*). In some species, such as plains zebras and gelada baboons, multiple stable breeding units aggregate together in large, unstable herds (*154*, *155*).

In species where female groups are unstable and females range widely but regularly visit resource-rich sites—for example, many antelope and some deer—breeding males often defend resource-based territories in areas regularly used by females (*156*, *157*) or small, clustered territories on traditional mating grounds, or leks, where they are joined by receptive females, as in some bats and a number of ungulates (*158*–*160*). Finally, where the density of receptive females is low and receptive females are widely dispersed, as in whales and elephants, males often cruise in search of receptive partners, defending individual females for short periods before moving on to search for other breeding opportunities (*7*, *152*).

Plural breeding and male competition

The aggregation of breeding females commonly increases the number of females that individual males can guard, leading to increases in reproductive skew among males and intensifying reproductive competition between them (*7*). Fighting is particularly frequent among plural breeders whose mating is seasonal and individual males collect and defend large harems of females, mating with females as they become receptive, as in many deer and land-breeding seals (*7*, *161*, *162*) (Fig. 4). The aggregation of multiple breeding females often generates strong selection in males for traits that increase their competitive ability and is frequently associated with the evolution of large sex differences in body size and weaponry, especially in species where single males guard access to female groups and breeding is seasonal (*7*, *163*). Where females form relatively large, stable groups, several males often associate with each female group, polygynandrous mating systems and sperm competition are common, and the reproductive anatomy of males is frequently adapted to maximize their success in fertilizing mating partners. Ejaculate volumes and testes are often unusually large, penises may be modified to displace sperm from previous mating, and the size and swimming speed of sperm is often increased (*164*–*166*).

Intense breeding competition between males also has important consequences for their treatment of females. In plural-breeding species with polygynous mating systems, males often adopt coercive mating tactics to induce females to mate with them; these can include persistent attempts to mate, forced copulation, and punishment of females that are reluctant to mate or that associate with subordinate males (*167*, *168*). Male coercion can cause



Fig. 3. Consequences of selection for competitive ability in female fighting cows. In spring in the Italian Western Alps, fights are staged between cows that have been selectively bred for their aggressiveness and fighting ability and now share many of the characteristics of bulls, including relatively high testosterone levels.

PHOTO: CRISTINA SARTORI

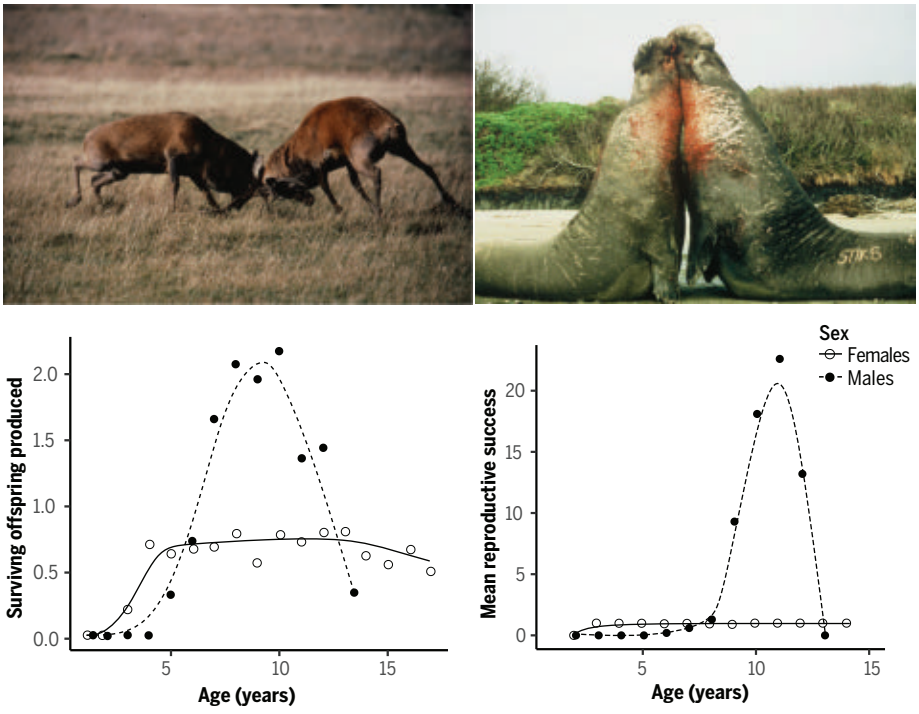


Fig. 4. Age-related changes in reproductive success in male red deer and elephant seals. In many polygynous mammal species, such as red deer and elephant seals, there is intense competition between breeding males, with the result that only "prime" males breed successfully and males have substantially shorter breeding life spans than females (*225*, *226*).

serious injuries to females, who may be wounded during the attempts of males to mate with them or in the course of punishing attacks by dominant males (Fig. 5). Although this might appear to be counterproductive for males, if coercive tactics increase their chances of mating, collateral damage to females is unlikely to constrain the evolution of coercive tactics, unless costs to females are very large (*169*). Males that have recently acquired breeding positions may also kill dependent young fathered by their predecessors if this advances the next conception of females and thus increases their mating opportunities, and in some species, male infanticide is one of the most common causes of mortality in infants and juveniles (*170*, *171*). For example, among lions and bears, male infanticide can be frequent enough to affect rates of recruitment and population size (*172*, *173*). Females frequently respond by cooperatively defending their young, by forming close social bonds with mating partners or, in some species, by prematurely aborting young that are likely to be killed (*174*, *175*).

Breeding competition between males can have profound consequences for the evolution of male life histories. Intense competition among males often delays the onset of successful breeding in males until they approach full adult weight, while their capacity to guard females successfully often ends as soon as their strength and condition begin to decline with increasing age (*7*). As a result, the breeding careers of males can be very short (*176*) and are often considerably shorter than those of females (*7*, *177*) (Fig. 4). Several processes contribute to reductions in the duration of male tenure and increased mortality in males, including fighting injuries, loss of appetite and condition during the breeding season, increased susceptibility to predators, and reductions in immune response associated with increased parasite loads (*176*, *178*, *179*).

The shortening of breeding life spans in males has important consequences for both sexes. In males, it is often associated with the evolution of tactics that help extend their breeding lives. For example, in Cape buffalo and Uganda kob, breeding males alternate between periods of reproductive activity and resting periods in bachelor groups (*7*, *157*). In other species, it has led to the evolution of age- or size-specific breeding tactics in males (*180*) and, in some, to the evolution of alternative reproductive strategies and balanced polymorphisms in anatomy and breeding tactics (*181*) (Fig. 6). The effects of male competition on the breeding tenure of males may also help explain why males tolerate the presence of potential rivals in their group, for the tenure of breeding males declines less rapidly with female group size if more than one breeding male is present and similar effects occur within as well as across species (*7*, *65*, *182*). Reductions in the breeding tenure of males also reduce the likelihood that females will reach sexual maturity when their father still monopolizes reproduction in their birth group and that they will need to disperse to locate unrelated breeding partners (*7*) and so may help to explain the prevalence of female philopatry and male dispersal in mammals.

The evolution of male characteristics associated with breeding competition has ecological and demographic consequences, too. In some dimorphic species, male infants are born heavier and grow faster than females and nurse more frequently, extracting more milk from their mothers, and females that have reared sons are less likely to survive the following winter than those that have raised daughters (*183*–*185*). The steeper costs of raising male infants can also enhance the effects of the mother's phenotype on the postnatal survival, development, and eventual breeding success of her sons compared with that of her daughters (*186*, *187*), which can lead to selection for qualitatively superior mothers to produce male-biased sex ratios and inferior ones to produce female-biased ones (*188*). Biased birth-sex ratios have been documented in several ungulates, but it is often difficult to tell whether these are a consequence of biases in the sex ratio at conception or of sex differences in prenatal mortality (*7*, *183*, *189*).

Sex differences in juvenile growth and adult size also increase the relative nutritional requirements of males (*7*, *190*) and, in strongly dimorphic species, are often associated with sex differences in feeding behavior, diet, and habitat use (*191*–*193*) and with male avoidance of areas of high female density outside the breeding season (*69*, *194*). Sex differences in growth are often also associated with higher parasite loads in males than females (*179*) and with increased risk of starvation (*7*, *195*), and mortality is often higher in males than females at most stages of development (*187*, *195*, *196*). Sex differences in survival are often most pronounced when weather conditions are unfavorable or food is scarce (*7*, *197*–*199*). Together with increases in male dispersal, they can generate strong female biases in local adult populations (*7*) that may have both evolutionary and ecological consequences that may even affect extinction rates (*200*). Depending on circumstances, these biases can either reduce (*197*–*198*) or increase (*201*–*202*) the intensity of breeding competition between males and the strength of selection on male traits that affect competitive ability (*197*, *198*, *202*, *203*). They can also be large enough to have important consequences for the management of populations maintained for sport hunting, because they reduce the maximum sustainable yield of males (*199*).

PHOTOS: (LEFT) TIM CLUTTON-BROCK; (RIGHT) BURNEY LE BOUEF

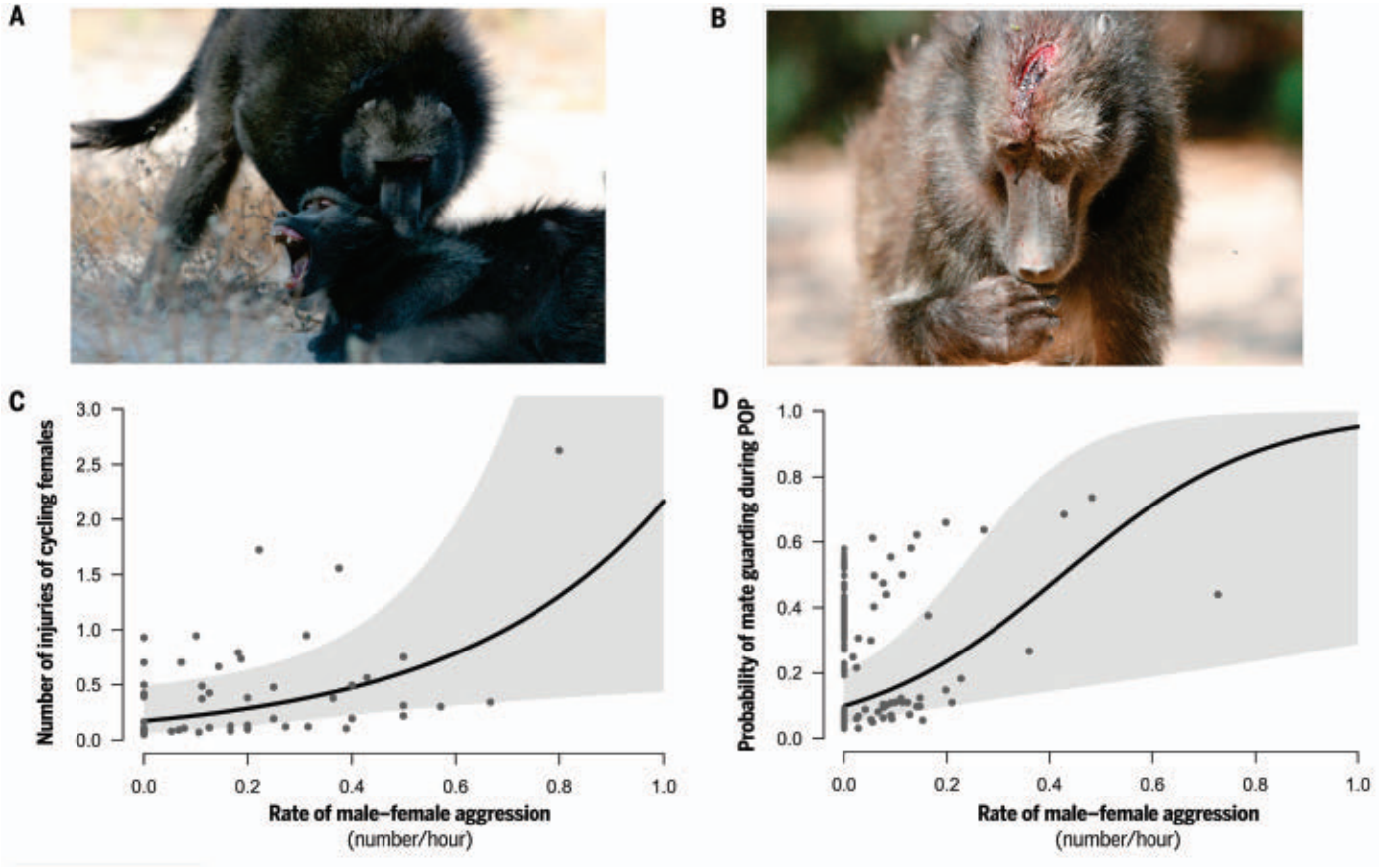


Fig. 5. Costs of male competition to female chacma baboons. Coercive mating tactics are common in males of many terrestrial mammalian species. For example, adult chacma baboon males frequently threaten or attack cycling females (**A**), sometimes inflicting serious injuries (**B**). The frequency with which cycling females show injuries increases with the rate of male–female aggression (**C**). The probability that males will be able to monopolize access to females during the periestrus (POP) period when they are likely to conceive increases with the rate at which individual males have directed aggression at them (**D**) (*168*).

Outlook

Research on mammals over the past 40 years has greatly extended our understanding of the far-reaching connections and interactions between ecology, social behavior, and evolutionary processes. It has shown how differences in ecology, life histories, and phylogeny affect the size and composition of social groups and the nature of breeding systems; how differences in breeding systems affect the selection pressures operating on both sexes and the evolution of their behavior, physiology, and morphology; and how differences in behavior, physiology, and morphology, in turn, affect the demography and dynamics of populations and their responses to changes in population density, resource availability, climatic factors, and human impact.

Technical developments in data collection and analysis have played an important role in these advances. The development of automated recording techniques has extended the range of biological parameters that can be measured in wild mammals and the species that can be studied in detail (*204*–*206*). Improvements in the storage and analysis of long-term data have made it possible to answer questions about temporal and spatial variation in a matter of minutes that would previously have taken months or years. And new developments in genetic and genomic analysis have transformed our understanding of variation in reproduction and breeding success in both sexes, of the development of social and reproductive behavior within individuals (*18*, *207*), and of evolutionary sequences and major transitions in behavior between species (*208*–*210*).

Despite these advances, many important questions are still unresolved. Much of our knowledge of the causes and consequences of mammalian breeding systems relies on detailed studies of a small number of diurnal, terrestrial plural breeders that live in open habitats, and we still know relatively little about the larger number of species whose breeding females are solitary (*7*, *211*). We still know little about the extent to which the social behavior of females and males differs between populations of the same species or about the causes and consequences of these differences. There are many specific questions that have yet to be resolved: For example, we do not yet understand the distribution of pair breeding (*60*, *61*), the factors affecting interspecific differences in male tenure (*7*), or the lack of development of weaponry in females (*142*). Additionally, we are only starting to glimpse the consequences of variation in breeding systems for the demography, dynamics, and genetic structure of populations and their responses to environmental change (*212*, *213*).

In the future, theoretical, empirical, and technical developments are all likely to play an important role in extending our understanding of the causes and consequences of breeding systems in mammals as well as in those of other species. The further development of automated recording techniques will help extend the range of biological parameters that can be measured in wild mammals and the species that can be studied in detail (*204*–*206*). Continuing improvements in genetic analysis are likely to provide new insights both into the development of behavior in individuals and the causes of individual variation (*214*). And genomic comparisons

PHOTOS: (A) ALECIA CARTER; (B) ALICE BANIEL

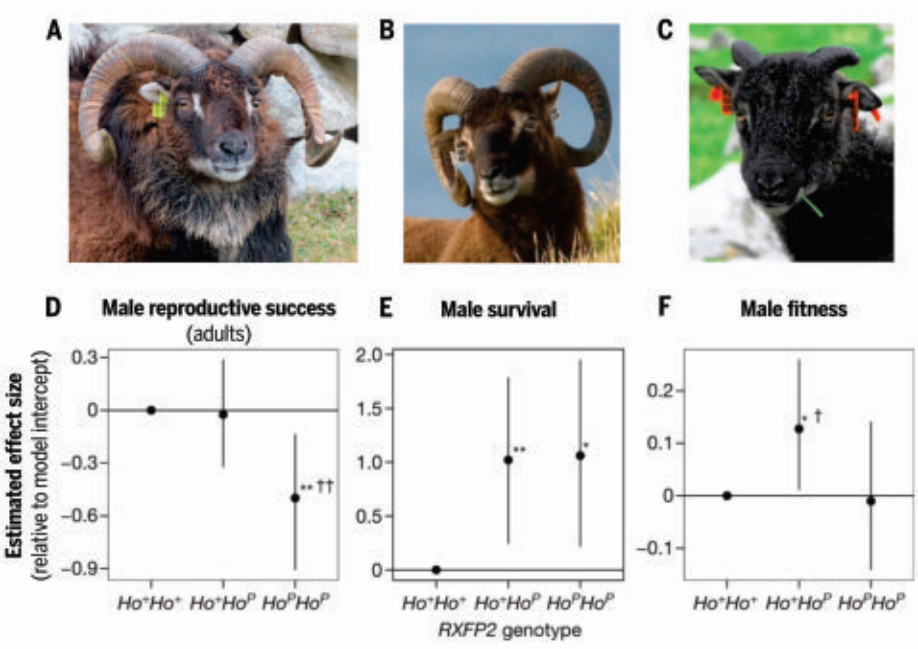


Fig. 6. The evolution of horn types in Soay sheep. Among Soay sheep on the island of St. Kilda, the high survival costs of breeding competition between males maintain a balanced polymorphism in horn size, which is associated with differences in behavior. Fully horned males (**A** and **B**) are either homozygous or heterozygous for an allele (Ho^+) at the horns locus (*RXFP2*), while males that either have very small horns or no horns at all (**C**) are homozygous for an alternative allele (Ho^P). Males that are homozygous or heterozygous for Ho^+ have higher annual breeding success than individuals that are homozygous for Ho^P (**D**), while individuals that are heterozygous for Ho^+ and those that are homozygous for Ho^P show higher survival than those that are homozygous for Ho^+ (**E**). As a result, Ho^+ heterozygotes have the highest fitness (**F**), and both alleles are maintained in the population.

should provide an improved understanding of evolutionary sequences and the causes of major transitions in behavior (*215*, *216*). However, neither automated recording techniques nor genetic analyses can replace the information that can be gained from long-term, individual-based field studies that can monitor the development and reproductive success of recognizable individuals throughout their lives. As a result, maintaining existing long-term studies and developing new ones will continue to be a priority.

REFERENCES AND NOTES

1. C. Darwin, *On the Origin of Species by Means of Natural Selection* (John Murray, 1859).
2. E. Mayr, *Animal Species and Evolution* (Harvard Univ. Press, 1963).
3. W. L. J. Brown, General adaptation and evolution. *Syst. Zool.* **7**, 157–168 (1958).
4. G. C. Williams, *Adaptation and Natural Selection: A Critique of Some Current Evolutionary Thought* (Princeton Univ. Press, 1966).
5. E. O. Wilson, *Sociobiology: The New Synthesis* (Harvard Univ. Press, 1974).
6. D. R. Rubenstein, P. Abbot, Eds., *Comparative Social Evolution* (Cambridge Univ. Press, 2017).
7. T. Clutton-Brock, *Mammal Societies* (Wiley Blackwell, 2016).
8. L. D. Hayes, C. Schradin, Long-term field studies in mammals: What the short-term study cannot tell us. *J. Mammal.* **98**, 600–602 (2017). doi: 10.1093/jmammal/gyx027
9. H. A. Hofmann *et al*., An evolutionary framework for studying mechanisms of social behavior. *Trends Ecol. Evol.* **29**, 581–589 (2014). doi: 10.1016/j.tree.2014.07.008; pmid: 25154769
10. J. F. Eisenberg, *The Mammalian Radiations: An Analysis of Trends in Evolution, Adaptation, and Behavior* (Univ. of Chicago Press, 1981).
11. J. M. Smith, Parental investment: A prospective analysis. *Anim. Behav.* **25**, 1–9 (1977). doi: 10.1016/0003-3472(77)90062-8
12. S. T. Emlen, L. W. Oring, Ecology, sexual selection, and the evolution of mating systems. *Science* **197**, 215–223 (1977). doi: 10.1126/science.327542; pmid: 327542
13. R. L. Trivers, in *Sexual Selection and the Descent of Man, 1871–1971*, B. Campbell, Ed. (Aldine-Atherton, 1972), pp. 136–179.
14. D. Lukas, V. Reynolds, C. Boesch, L. Vigilant, To what extent does living in a group mean living with kin? *Mol. Ecol.* **14**, 2181–2196 (2005). doi: 10.1111/j.1365-294X.2005.02560.x; pmid: 15910336
15. D. Lukas, T. Clutton-Brock, Social complexity and kinship in animal societies. *Ecol. Lett.* **21**, 1129–1134 (2018). doi: 10.1111/ele.13079; pmid: 29797749
16. T. Clutton-Brock, B. C. Sheldon, Individuals and populations: The role of long-term, individual-based studies of animals in ecology and evolutionary biology. *Trends Ecol. Evol.* **25**, 562–573 (2010b). doi: 10.1016/j.tree.2010.08.002; pmid: 20828863
17. T. Burke, G. Dolf, A. J. Jeffreys, R. Wolff, Eds., *DNA Fingerprinting: Approaches and Applications* (Birkhauser Verlag, 1991).
18. A. Charmantier, D. Garant, L. E. B. Kruuk, Eds., *Quantitative Genetics in the Wild* (Oxford Univ. Press, 2014).
19. M. Pagel, The maximum likelihood approach to reconstructing ancestral character states of discrete characters on phylogenies. *Syst. Biol.* **48**, 612–622 (1999). doi: 10.1080/106351599260184
20. A. Di Fiore, D. Rendall, Evolution of social organization: A reappraisal for primates by using phylogenetic methods. *Proc. Natl. Acad. Sci. U.S.A.* **91**, 9941–9945 (1994). doi: 10.1073/pnas.91.21.9941; pmid: 7937922
21. V. Hanson-Smith, B. Kolaczkowski, J. W. Thornton, Robustness of ancestral sequence reconstruction to phylogenetic uncertainty. *Mol. Biol. Evol.* **27**, 1988–1999 (2010). doi: 10.1093/molbev/msq081; pmid: 20368266
22. J. E. Smith, E. A. Lacey, L. D. Hayes, in *Comparative Social Evolution*, D. R. Rubenstein, P. Abbot, Eds. (Cambridge Univ. Press, 2017), pp. 284–319.
23. P. J. Jarman, The social organisation of antelope in relation to their ecology. *Behaviour* **48**, 215–267 (1974). doi: 10.1163/156853974X00345
24. P. M. Kappeler, L. Pozzi, Evolutionary transitions toward pair living in nonhuman primates as stepping stones toward more complex societies. *Sci. Adv.* **5**, eaay1276 (2019). doi: 10.1126/sciadv.aay1276; pmid: 32064318
25. V. Federico, D. Allainé, J.-M. Gaillard, A. Cohas, Evolutionary pathways to communal and cooperative breeding in carnivores. *Am. Nat.* **195**, 1037–1055 (2020). doi: 10.1086/708639; pmid: 32469664
26. D. Lukas, T. H. Clutton-Brock, The evolution of social monogamy in mammals. *Science* **341**, 526–530 (2013). doi: 10.1126/science.1238677; pmid: 23896459
27. S. C. Nicol, in *Neurobiology of Monotremes*, K. W. S. Ashwell, Ed. (CSIRO Publishing, 2013), pp. 1–21.
28. P. M. Kappeler, C. P. van Schaik, Evolution of primate social systems. *Int. J. Primatol.* **23**, 707–740 (2002). doi: 10.1023/A:1015520830318
29. L. A. Ebensperger, L. D. Hayes, On the dynamics of rodent social groups. *Behav. Processes* **79**, 85–92 (2008). doi: 10.1016/j.beproc.2008.05.006; pmid: 18586412
30. P. M. Kappeler, Nests, tree holes, and the evolution of primate life histories. *Am. J. Primatol.* **46**, 7–33 (1998). doi: 10.1002/(SICI)1098-2345(1998)46:1<7::AID-AJP3>3.0.CO;2-#; pmid: 9730211
31. J. P. Rood, in *Ecological Aspects of Social Evolution: Birds and Mammals*, D. I. Rubenstein, R. W. Wrangham, Eds. (Princeton Univ. Press, 1986), pp. 131–152.
32. P. J. Jarman, Social behavior and organization in the Macropodoidea. *Adv. Stud. Behav.* **20**, 1–50 (1991). doi: 10.1016/S0065-3454(08)60318-6
33. C. C. Smith, The coevolution of pine squirrels (*Tamiasciurus*) and conifers. *Ecol. Monogr.* **40**, 349–371 (1970). doi: 10.2307/1942287
34. J. E. Lane, S. Boutin, M. R. Gunn, D. W. Coltman, Sexually selected behaviour: Red squirrel males search for reproductive success. *J. Anim. Ecol.* **78**, 296–304 (2009). doi: 10.1111/j.1365-2656.2008.01502.x; pmid: 19040682
35. D. F. Lott, Sexual behavior and intersexual strategies in American bison. *Z. Tierpsychol.* **56**, 97–114 (1981). doi: 10.1111/j.1439-0310.1981.tb01289.x
36. C. Schradin *et al*., Social flexibility and social evolution in mammals: A case study of the African striped mouse (*Rhabdomys pumilio*). *Mol. Ecol.* **21**, 541–553 (2012). doi: 10.1111/j.1365-294X.2011.05256.x; pmid: 21883591
37. R. Schacht, K. L. Kramer, T. Székely, P. M. Kappeler, Adult sex ratios and reproductive strategies: A critical re-examination of sex differences in human and animal societies. *Philos. Trans. R. Soc. London Ser. B.* **372**, 20160309 (2017). doi: 10.1098/rstb.2016.0309; pmid: 28760753
38. S. M. J. G. Steyaert *et al*., in *Bears of the World: Ecology, Conservation and Management*, V. Penteriani, M. Melletti, Eds. (Cambridge Univ. Press, 2020), pp. 21–35.
39. P. Lindenfors, J. L. Gittleman, K. E. Jones, in *Sex, Size and Gender Roles: Evolutionary Studies of Sexual Size Dimorphism*, D. J. Fairbairn, W. U. Blanckenhorn, T. Székely, Eds. (Oxford Univ. Press, 2007), pp. 16–26.
40. K. Ralls, Mammals in which females are larger than males. *Q. Rev. Biol.* **51**, 245–276 (1976). doi: 10.1086/409310; pmid: 785524
41. K. Ralls, Sexual dimorphism in mammals: Avian models and unanswered questions. *Am. Nat.* **111**, 917–938 (1977). doi: 10.1086/283223
42. N. G. Solomon, A re-examination of factors influencing philopatry in rodents. *J. Mammal.* **84**, 1182–1197 (2003). doi: 10.1644/BLe-013
43. P. M. Kappeler, B. Wimmer, D. Zinner, D. Tautz, The hidden matrilineal structure of a solitary lemur: Implications for primate social evolution. *Proc. Biol. Sci.* **269**, 1755–1763 (2002). doi: 10.1098/rspb.2002.2066; pmid: 12350262
44. S. A. Poindexter, K. A. I. Nekaris, in *Evolution, Ecology and Conservation of Lorises and Pottos*, K. A. I. Nekaris, A. M. Burrows, Eds. (Cambridge Univ. Press, 2020), pp. 129–137.

PHOTO: ARPAT OZGUL

45. K. Price, S. Boutin, Territorial bequeathal by red squirrel mothers. *Behav. Ecol.* **4**, 144–150 (1993). doi: 10.1093/beheco/4.2.144
46. C. T. Lambert, A. C. Sabol, N. G. Solomon, Genetic monogamy in socially monogamous mammals is primarily predicted by multiple life history factors: A meta-analysis. *Front. Ecol. Evol.* **6**, 139 (2018). doi: 10.3389/fevo.2018.00139
47. J. F. Eisenberg, in *Biology and Management of the Cervidae*, C. M. Wemmer, Ed. (Smithsonian Institution Press, 1987), pp. 60–64.
48. S. Van Belle, A. M. Porter, E. Fernandez-Duque, A. Di Fiore, Ranging behavior and the potential for territoriality in pair-living titi monkeys (*Plecturocebus discolor*). *Am. J. Primatol.* **83**, e23225 (2021). doi: 10.1002/ajp.23225; pmid: 33368565
49. P. N. M. Brotherton, J. M. Pemberton, P. E. Komers, G. Malarky, Genetic and behavioural evidence of monogamy in a mammal, Kirk's dik-dik (*Madoqua kirkii*). *Proc. Biol. Sci.* **264**, 675–681 (1997). doi: 10.1098/rspb.1997.0096; pmid: 9178540
50. O. Schülke, P. M. Kappeler, So near and yet so far: Territorial pairs but low cohesion between pair partners in a nocturnal lemur, *Phaner furcifer*. *Anim. Behav.* **65**, 331–343 (2003). doi: 10.1006/anbe.2003.2018
51. P. M. Kappeler, Determinants of primate social organization: Comparative evidence and new insights from Malagasy lemurs. *Biol. Rev. Camb. Philos. Soc.* **72**, 111–151 (1997). doi: 10.1017/S0006323196004999; pmid: 9116164
52. M. Huck, A. Di Fiore, E. Fernandez-Duque, Of apples and oranges? The evolution of "Monogamy" in non-human primates. *Front. Ecol. Evol.* **7**, 472 (2020). doi: 10.3389/fevo.2019.00472
53. T. H. Clutton-Brock, K. Isvaran, Paternity loss in contrasting mammalian societies. *Biol. Lett.* **2**, 513–516 (2006). doi: 10.1098/rsbl.2006.0531; pmid: 17148276
54. A. Cohas, D. Allainé, Social structure influences extra-pair paternity in socially monogamous mammals. *Biol. Lett.* **5**, 313–316 (2009). doi: 10.1098/rsbl.2008.0760; pmid: 19324647
55. D. J. Gubernick, T. Teferi, Adaptive significance of male parental care in a monogamous mammal. *Proc. Biol. Sci.* **267**, 147–150 (2000). doi: 10.1098/rspb.2000.0979; pmid: 10687819
56. K. A. Hoffman, S. P. Mendoza, M. B. Hennessy, W. A. Mason, Responses of infant titi monkeys, *Callicebus moloch*, to removal of one or both parents: Evidence for paternal attachment. *Dev. Psychobiol.* **28**, 399–407 (1995). doi: 10.1002/dev.420280705; pmid: 8557176
57. P. Stockley, L. Hobson, Paternal care and litter size coevolution in mammals. *Proc. Biol. Sci.* **283**, 20160140 (2016). doi: 10.1098/rspb.2016.0140; pmid: 27097924
58. H. E. R. West, I. Capellini, Male care and life history traits in mammals. *Nat. Commun.* **7**, 11854 (2016). doi: 10.1038/ncomms11854; pmid: 27299954
59. J. F. Wittenberger, R. L. Tilson, The evolution of monogamy: Hypotheses and evidence. *Am. Rev. Ecol. Syst.* **11**, 197–232 (1980). doi: 10.1146/annurev.es.11.110180.001213
60. C. Kvarnemo, Why do some animals mate with one partner rather than many? A review of causes and consequences of monogamy. *Biol. Rev. Camb. Philos. Soc.* **93**, 1795–1812 (2018). doi: 10.1111/brv.12421; pmid: 29687607
61. H. Klug, Why monogamy? A review of potential ultimate drivers. *Front. Ecol. Evol.* **6**, 30 (2018). doi: 10.3389/fevo.2018.00030
62. C. Opie, Q. D. Atkinson, R. I. Dunbar, S. Shultz, Male infanticide leads to social monogamy in primates. *Proc. Natl. Acad. Sci. U.S.A.* **110**, 13328–13332 (2013). doi: 10.1073/pnas.1307903110; pmid: 23898180
63. Y. Iwasa, Y. Harada, Female mate preference to maximize paternal care. II. Female competition leads to monogamy. *Am. Nat.* **151**, 367–382 (1998). doi: 10.1086/286125; pmid: 18811327
64. P. N. M. Brotherton, P. E. Komers, in *Monogamy: Mating Strategies and Partnerships in Birds, Humans and Other Mammals*, U. H. Reichard, C. Boesch, Eds. (Cambridge Univ. Press, 2003), pp. 42–58.
65. D. Lukas, T. Clutton-Brock, Evolution of social monogamy in primates is not consistently associated with male infanticide. *Proc. Natl. Acad. Sci. U.S.A.* **111**, E1674 (2014a). doi: 10.1073/pnas.1401012111; pmid: 24706849
66. F. S. Dobson, B. M. Way, C. Baudoin, Spatial dynamics and the evolution of social monogamy in mammals. *Behav. Ecol.* **21**, 747–752 (2010). doi: 10.1093/beheco/arq048
67. S. R. Tecot, B. Singletary, E. Eadie, Why "monogamy" isn't good enough. *Am. J. Primatol.* **78**, 340–354 (2016). doi: 10.1002/ajp.22412; pmid: 25864507
68. A. Jungwirth, R. A. Johnstone, Multiple evolutionary routes to monogamy: Modeling the coevolution of mating decisions and parental investment. *Am. Nat.* **193**, E29–E40 (2019). doi: 10.1086/700698; pmid: 30720358
69. K. E. Ruckstuhl, P. Neuhaus, Sexual segregation in ungulates: A new approach. *Behaviour* **137**, 361–377 (2000). doi: 10.1163/156853900502123
70. S. M. Larson, F. Colchero, O. R. Jones, L. Williams, E. Fernandez-Duque, Age and sex-specific mortality of wild and captive populations of a monogamous pair-bonded primate (*Aotus azarae*). *Am. J. Primatol.* **78**, 315–325 (2016). doi: 10.1002/ajp.22408; pmid: 25866126
71. A. F. Dixson, *Sexual Selection and the Origins of Human Mating Systems* (Oxford Univ. Press, 2009).
72. J. L. Brown, Territorial behavior and population regulation in birds, a review and re-evaluation. *Wilson Bull.* **81**, 293–329 (1969).
73. D. Lukas, T. Clutton-Brock, Monotocy and the evolution of plural breeding in mammals. *Behav. Ecol.* **31**, 943–949 (2020). doi: 10.1093/beheco/araa039; pmid: 32760176
74. P. A. Garber, One for all and breeding for one: Cooperation and competition as a tamarin reproductive strategy. *Evol. Anthropol.* **5**, 187–199 (1997). doi: 10.1002/(SICI)1520-6505(1997)5:6<187::AID-EVAN1>3.0.CO;2-A
75. P. A. Garber, L. M. Porter, J. Spross, A. Di Fiore, Tamarins: Insights into monogamous and non-monogamous single female social and breeding systems. *Am. J. Primatol.* **78**, 298–314 (2016). doi: 10.1002/ajp.22370; pmid: 25573250
76. A. J. Young, in *Reproductive Skew in Vertebrates: Proximate and Ultimate Causes*, R. Hager, C. B. Jones, Eds. (Cambridge Univ. Press, 2009), pp. 397–436.
77. N. C. Bennett, C. G. Faulkes, *African Mole-Rats: Ecology and Eusociality* (Cambridge Univ. Press, 2000).
78. D. W. Macdonald *et al*., Monogamy: Cause, consequence, or corollary of success in wild canids? *Front. Ecol. Evol.* **7**, 341 (2019). doi: 10.3389/fevo.2019.00341
79. R. Cooney, N. C. Bennett, Inbreeding avoidance and reproductive skew in a cooperative mammal. *Proc. Biol. Sci.* **267**, 801–806 (2000). doi: 10.1098/rspb.2000.1074; pmid: 10819150
80. T. M. Houslay, P. Vullioud, M. Zottl, T. H. Clutton-Brock, Benefits of cooperation in captive Damaraland mole-rats. *Behav. Ecol.* **31**, 711–718 (2020). doi: 10.1093/beheco/araa015
81. D. Lukas, T. Clutton-Brock, Cooperative breeding and monogamy in mammalian societies. *Proc. Biol. Sci.* **279**, 2151–2156 (2012). doi: 10.1098/rspb.2011.2468; pmid: 22279167
82. R. A. Brett, in *The Biology of the Naked Mole-Rat*, P. W. Sherman, J. U. M. Jarvis, R. D. Alexander, Eds. (Princeton Univ. Press, 1991), pp. 97–136.
83. S. Creel, N. M. Creel, *The African Wild Dog: Behavior, Ecology, and Conservation* (Princeton Univ. Press, 2002).
84. J. Thorley *et al*., No task specialization among helpers in Damaraland mole-rats. *Anim. Behav.* **143**, 9–24 (2018). doi: 10.1016/j.anbehav.2018.07.004; pmid: 30245525
85. H. Burda, R. L. Honeycutt, S. Begall, O. Locker-Grutjen, A. Scharff, Are naked and common mole-rats eusocial and, if so, why? *Behav. Ecol. Sociobiol.* **47**, 293–303 (2000). doi: 10.1007/s002650050669
86. A. J. Young, T. Clutton-Brock, Infanticide by subordinates influences reproductive sharing in cooperatively breeding meerkats. *Biol. Lett.* **2**, 385–387 (2006). doi: 10.1098/rsbl.2006.0463; pmid: 17148410
87. D. Cram, A. Jungwirth, H. Spence-Jones, T. Clutton-Brock, Reproductive conflict resolution in cooperative breeders. *Behav. Ecol.* **30**, 1743–1750 (2019). doi: 10.1093/beheco/arz143
88. M. B. V. Bell *et al*., Suppressing subordinate reproduction provides benefits to dominants in cooperative societies of meerkats. *Nat. Commun.* **5**, 4499 (2014). doi: 10.1038/ncomms5499; pmid: 25047446
89. C. Duncan, D. Gaynor, T. Clutton-Brock, The importance of being beta: Female succession in a cooperative breeder. *Anim. Behav.* **146**, 113–122 (2018). doi: 10.1016/j.anbehav.2018.10.013
90. T. Clutton-Brock, M. Manser, in *Cooperative Breeding in Vertebrates: Studies of Ecology, Evolution, and Behavior*, W. D. Koenig, J. L. Dickinson, Eds. (Cambridge Univ. Press, 2016), pp. 294–317.
91. J. Komdeur *et al*., Transfer experiments of Seychelles warblers to new islands: Changes in dispersal and helping behaviour. *Anim. Behav.* **49**, 695–708 (1995). doi: 10.1016/0003-3472(95)80202-9
92. C. Schradin, B. König, N. Pillay, Reproductive competition favours solitary living while ecological constraints impose group-living in African striped mice. *J. Anim. Ecol.* **79**, 515–521 (2010). doi: 10.1111/j.1365-2656.2009.01651.x; pmid: 20059610
93. C. Duncan, D. Gaynor, T. Clutton-Brock, M. Dyble, The evolution of indiscriminate altruism in a cooperatively breeding mammal. *Am. Nat.* **193**, 841–851 (2019). doi: 10.1086/703113; pmid: 31094597
94. M. Briga, I. Pen, J. Wright, Care for kin: Within-group relatedness and allomaternal care are positively correlated and conserved throughout the mammalian phylogeny. *Biol. Lett.* **8**, 533–536 (2012). doi: 10.1098/rsbl.2012.0159; pmid: 22496080
95. M. Dyble, T. Clutton-Brock, Contrasts in kinship structure in mammalian societies. *Behav. Ecol.* **31**, 971–977 (2020). doi: 10.1093/beheco/araa043
96. T. H. Clutton-Brock *et al*., Contributions to cooperative rearing in meerkats. *Anim. Behav.* **61**, 705–710 (2001a). doi: 10.1006/anbe.2000.1631
97. A. F. Russell, L. L. Sharpe, P. N. M. Brotherton, T. H. Clutton-Brock, Cost minimization by helpers in cooperative vertebrates. *Proc. Natl. Acad. Sci. U.S.A.* **100**, 3333–3338 (2003a). doi: 10.1073/pnas.0636503100; pmid: 12629209
98. T. H. Clutton-Brock *et al*., Intrasexual competition and sexual selection in cooperative mammals. *Nature* **444**, 1065–1068 (2006). doi: 10.1038/nature05386; pmid: 17183322
99. J. G. Ruby, M. Smith, R. Buffenstein, Naked mole-rat mortality rates defy Gompertzian laws by not increasing with age. *eLife* **7**, e31157 (2018). doi: 10.7554/eLife.31157; pmid: 29364116
100. C. S. Davies *et al*., Exceptional endocrine profiles characterise the meerkat: Sex, status, and reproductive patterns. *Sci. Rep.* **6**, 35492 (2016). doi: 10.1038/srep35492; pmid: 27752129
101. E. Huchard, S. English, M. B. V. Bell, N. Thavarajah, T. Clutton-Brock, Competitive growth in a cooperative mammal. *Nature* **533**, 532–534 (2016). doi: 10.1038/nature17986; pmid: 27225127
102. J. Thorley, "The life history of Damaraland mole-rats *Fukomys damarensis*: Growth, ageing and behaviour," thesis, University of Cambridge, Cambridge, UK (2018).
103. C. Dubuc, T. H. Clutton-Brock, Male immigration triggers increased growth in subordinate female meerkats. *Ecol. Evol.* **9**, 1127–1134 (2018). doi: 10.1002/ece3.4801; pmid: 30805146
104. E. M. Wiley, A. R. Ridley, The effects of temperature on offspring provisioning in a cooperative breeder. *Anim. Behav.* **117**, 187–195 (2016). doi: 10.1016/j.anbehav.2016.05.009
105. F. Groenewoud, T. Clutton-Brock, Meerkat helpers buffer the detrimental effects of adverse environmental conditions on fecundity, growth and survival. *J. Anim. Ecol.* **90**, 641–652 (2021). doi: 10.1111/1365-2656.13396; pmid: 33241582
106. W. Jetz, D. R. Rubenstein, Environmental uncertainty and the global biogeography of cooperative breeding in birds. *Curr. Biol.* **21**, 72–78 (2011). doi: 10.1016/j.cub.2010.11.075; pmid: 21185192
107. D. Lukas, T. Clutton-Brock, Climate and the distribution of cooperative breeding in mammals. *R. Soc. Open Sci.* **4**, 160897 (2017). doi: 10.1098/rsos.160897; pmid: 28280589
108. F. Courchamp, B. Grenfell, T. H. Clutton-Brock, Population dynamics of obligate cooperators. *Proc. Biol. Sci.* **266**, 557–563 (1999a). doi: 10.1098/rspb.1999.0672
109. F. Courchamp, T. Clutton-Brock, B. Grenfell, Inverse density dependence and the Allee effect. *Trends Ecol. Evol.* **14**, 405–410 (1999b). doi: 10.1016/S0169-5347(99)01683-3; pmid: 10481205
110. M. A. Cant, H. J. Nichols, F. J. Thompson, E. Vitikainen, in *Cooperative Breeding in Vertebrates: Studies of Ecology, Evolution, and Behavior*, W. D. Koenig, J. L. Dickinson, Eds. (Cambridge Univ. Press, 2016), pp. 318–337.
111. H. J. Nichols, N. R. Jordan, G. A. Jamie, M. A. Cant, J. I. Hoffman, Fine-scale spatiotemporal patterns of genetic variation reflect budding dispersal coupled with strong natal philopatry in a cooperatively breeding mammal. *Mol. Ecol.* **21**, 5348–5362 (2012). doi: 10.1111/mec.12015; pmid: 22994210
112. D. R. Rubenstein, C. A. Botero, E. A. Lacey, Discrete but variable structure of animal societies leads to the false perception of a social continuum. *R. Soc. Open Sci.* **3**, 160147 (2016). doi: 10.1098/rsos.160147; pmid: 27293796
113. L. A. Ebensperger, A review of the evolutionary causes of rodent group-living. *Acta Theriol. (Warsz.)* **46**, 115–144 (2001). doi: 10.4098/AT.arch.01-16
114. C. Schradin, W. Kenkel, S. Krackow, C. S. Carter, Staying put or leaving home: Endocrine, neuroendocrine and behavioral

consequences in male African striped mice. *Horm. Behav.* **63**, 136–143 (2013). doi: 10.1016/j.yhbeh.2012.10.004; pmid: 23079108
115. C. Schradin *et al*., Geographic intra-specific variation in social organization is driven by population density. *Behav. Ecol. Sociobiol.* **74**, 113 (2020). doi: 10.1007/s00265-020-02896-z
116. J. Ortega, Ed., *Sociality in Bats* (Springer, 2016).
117. D. T. Blumstein, Yellow-bellied marmots: Insights from an emergent view of sociality. *Philos. Trans. R. Soc. London Ser. B.* **368**, 20120349 (2013). doi: 10.1098/rstb.2012.0349; pmid: 23569297
118. J. C. Mitani, D. P. Watts, J. S. Lwanga, in *Behavioural Diversity in Chimpanzees and Bonobos*, C. Boesch, G. Hohmann, L. F. Marchant, Eds. (Cambridge Univ. Press, 2002), pp. 102–111.
119. K. E. Holekamp *et al*., Patterns of association among female spotted hyenas (*Crocuta crocuta*). *J. Mammal.* **78**, 55–64 (1997). doi: 10.2307/1382638
120. T. H. Clutton-Brock, F. E. Guinness, S. D. Albon, *Red Deer: Behavior and Ecology of Two Sexes* (Univ. of Chicago Press, 1982).
121. E. A. Archie, C. J. Moss, S. C. Alberts, The ties that bind: Genetic relatedness predicts the fission and fusion of social groups in wild African elephants. *Proc. Biol. Sci.* **273**, 513–522 (2006). doi: 10.1098/rspb.2005.3361; pmid: 16537121
122. R. D. Estes, *The Gnu's World: Serengeti Wildebeest Ecology and Life History* (Univ. of California Press, 2014).
123. P. M. Kappeler, Sex roles and adult sex ratios: Insights from mammalian biology and consequences for primate behaviour. *Philos. Trans. R. Soc. London Ser. B.* **372**, 20160321 (2017). doi: 10.1098/rstb.2016.0321; pmid: 28760762
124. C. A. Chapman, L. J. Chapman, R. W. Wrangham, Ecological constraints on group size: An analysis of spider monkey and chimpanzee subgroups. *Behav. Ecol. Sociobiol.* **36**, 59–70 (1995). doi: 10.1007/BF00175729
125. D. T. Blumstein, D. M. Williams, A. N. Lim, S. Kroeger, J. G. A. Martin, Strong social relationships are associated with decreased longevity in a facultatively social mammal. *Proc. Biol. Sci.* **285**, 20171934 (2018). doi: 10.1098/rspb.2017.1934; pmid: 29343594
126. R. Woodroffe, J. R. Ginsberg, Edge effects and the extinction of populations inside protected areas. *Science* **280**, 2126–2128 (1998). doi: 10.1126/science.280.5372.2126; pmid: 9641920
127. R. Woodroffe *et al*., Social group size affects Mycobacterium bovis infection in European badgers (*Meles meles*). *J. Anim. Ecol.* **78**, 818–827 (2009). doi: 10.1111/j.1365-2656.2009.01545.x; pmid: 19486382
128. T. H. Clutton-Brock, E. Huchard, Social competition and selection in males and females. *Philos. Trans. R. Soc. London Ser. B.* **368**, 20130074 (2013b). doi: 10.1098/rstb.2013.0074; pmid: 24167304
129. S.-F. Shen, S. T. Emlen, W. D. Koenig, D. R. Rubenstein, The ecology of cooperative breeding behaviour. *Ecol. Lett.* **20**, 708–720 (2017). doi: 10.1111/ele.12774; pmid: 28480586
130. K. B. Armitage, in *Rodent Societies: An Ecological and Evolutionary Perspective*, J. O. Wolff, P. W. Sherman, Eds. (Univ. of Chicago Press, 2007), pp. 356–367.
131. R. W. Wrangham, Female choice of least costly mates: A possible factor in the evolution of leks. *Z. Tierpsychol.* **54**, 357–367 (1980). doi: 10.1111/j.1439-0310.1980.tb01252.x
132. M. Port *et al*., The evolution of social philopatry in female primates. *Am. J. Phys. Anthropol.* **173**, 397–410 (2020). doi: 10.1002/ajpa.24123; pmid: 32779763
133. D. Lukas, T. H. Clutton-Brock, Group structure, kinship, inbreeding risk and habitual female dispersal in plural-breeding mammals. *J. Evol. Biol.* **24**, 2624–2630 (2011). doi: 10.1111/j.1420-9101.2011.02385.x; pmid: 21955169
134. J. F. Nielsen *et al*., Inbreeding and inbreeding depression of early life traits in a cooperative mammal. *Mol. Ecol.* **21**, 2788–2804 (2012). doi: 10.1111/j.1365-294X.2012.05565.x; pmid: 22497583
135. J. Huisman, L. E. B. Kruuk, P. A. Ellis, T. Clutton-Brock, J. M. Pemberton, Inbreeding depression across the lifespan in a wild mammal population. *Proc. Natl. Acad. Sci. U.S.A.* **113**, 3585–3590 (2016). doi: 10.1073/pnas.1518046113; pmid: 26979959
136. O. P. Höner *et al*., Female mate-choice drives the evolution of male-biased dispersal in a social mammal. *Nature* **448**, 798–801 (2007). doi: 10.1038/nature06040; pmid: 17700698
137. L. Dib, J. Figueira, K. Strier, Social dynamics of male muriquis (*Brachyteles arachnoides hypoxanthus*). *Behaviour* **139**, 315–342 (2002). doi: 10.1163/156853902760102690
138. T. H. Clutton-Brock, D. Lukas, The evolution of social philopatry and dispersal in female mammals. *Mol. Ecol.* **21**, 472–492 (2012). doi: 10.1111/j.1365-294X.2011.05232.x; pmid: 21883582
139. K. E. Langergraber, J. C. Mitani, L. Vigilant, The limited impact of kinship on cooperation in wild chimpanzees. *Proc. Natl. Acad. Sci. U.S.A.* **104**, 7786–7790 (2007). doi: 10.1073/pnas.0611449104; pmid: 17456600
140. R. W. Baird, in *Cetacean Societies: Field Studies of Dolphins and Whales*, J. Mann, R. C. Connor, P. L. Tyack, H. Whitehead, Eds. (Univ. of Chicago Press, 2000), pp. 127–172.
141. E. H. Stredulinsky, C. T. Darimont, L. Barrett-Lennard, G. M. Ellis, J. K. B. Ford, Family feud: Permanent group splitting in a highly philopatric mammal, the killer whale (*Orcinus orca*). *Behav. Ecol. Sociobiol.* **75**, 56 (2021). doi: 10.1007/s00265-021-02992-8
142. A. Berglund, Why are sexually selected weapons almost absent in females? *Curr. Zool.* **59**, 564–568 (2013). doi: 10.1093/czoolo/59.4.564
143. K. E. Holekamp, L. Smale, M. Szykman, Rank and reproduction in the female spotted hyaena. *J. Reprod. Fertil.* **108**, 229–237 (1996). doi: 10.1530/jrf.0.1080229; pmid: 9038781
144. J. B. Silk, Social components of fitness in primate groups. *Science* **317**, 1347–1351 (2007). doi: 10.1126/science.1140734; pmid: 17823344
145. W. H. James, H. Hofer, A note on sex ratios and sex combinations in Serengeti spotted hyenas: Siblicide and sub-binomial variance. *Appl. Anim. Sci.* **65**, 153–158 (1999). doi: 10.1016/S0168-1591(99)00054-4
146. J. B. Silk, C. B. Clark-Wheatley, P. S. Rodman, A. Samuels, Differential reproductive success and facultative adjustment of sex ratios among captive female bonnet macaques (*Macaca radiata*). *Anim. Behav.* **29**, 1106–1120 (1981). doi: 10.1016/S0003-3472(81)80063-2
147. J. L. Hoogland, *The Black-Tailed Prairie Dog: Social Life of a Burrowing Mammal* (Univ. of Chicago Press, 1995).
148. D. Lukas, E. Huchard, The evolution of infanticide by females in mammals. *Philos. Trans. R. Soc. London Ser. B.* **374**, 20180075 (2019). doi: 10.1098/rstb.2018.0075; pmid: 31303157
149. C. M. Drea, Sex and seasonal differences in aggression and steroid secretion in *Lemur catta*: Are socially dominant females hormonally 'masculinized'? *Horm. Behav.* **51**, 555–567 (2007). doi: 10.1016/j.yhbeh.2007.02.006; pmid: 17382329
150. J. M. A. Petty, C. M. Drea, Female rule in lemurs is ancestral and hormonally mediated. *Sci. Rep.* **5**, 9631 (2015). doi: 10.1038/srep09631; pmid: 25950904
151. P. Plusquellec, M. Bouissou, Behavioural characteristics of two dairy breeds of cows selected (Hérens) or not (Brune des Alpes) for fighting and dominance ability. *Appl. Anim. Behav. Sci.* **72**, 1–21 (2001). doi: 10.1016/S0168-1591(00)00198-2; pmid: 11259823
152. T. H. Clutton-Brock, Review lecture: Mammalian mating systems. *Proc. R. Soc. London Ser. B* **236**, 339–372 (1989). doi: 10.1098/rspb.1989.0027
153. J. C. Mitani, J. Gros-Louis, J. H. Manson, Number of males in primate groups: Comparative tests of competing hypotheses. *Am. J. Primatol.* **38**, 315–332 (1996). doi: 10.1002/(SICI)1098-2345(1996)38:4<315::AID-AJP3>3.0.CO;2-1; pmid: 31918481
154. D. I. Rubenstein, in *Ecological Aspects of Social Evolution*, D. I. Rubenstein, R. W. Wrangham, Eds. (Princeton Univ. Press, 1986), pp. 282–302.
155. N. Snyder-Mackler, S. C. Alberts, T. J. Bergman, Concessions of an alpha male? Cooperative defence and shared reproduction in multi-male primate groups. *Proc. Biol. Sci.* **279**, 3788–3795 (2012). doi: 10.1098/rspb.2012.0842; pmid: 22764162
156. A. M. Rosser, Resource distribution, density, and determinants of mate access in puku. *Behav. Ecol.* **3**, 13–24 (1992). doi: 10.1093/beheco/3.1.13
157. R. T. Bowyer, D. R. McCullough, J. L. Rachlow, S. Ciuti, J. C. Whiting, Evolution of ungulate mating systems: Integrating social and environmental factors. *Ecol. Evol.* **10**, 5160–5178 (2020). doi: 10.1002/ece3.6246; pmid: 32551090
158. T. H. Clutton-Brock, J. C. Deutsch, R. J. C. Nefdt, The evolution of ungulate leks. *Anim. Behav.* **46**, 1121–1138 (1993). doi: 10.1006/anbe.1993.1302
159. K. Isvaran, Lek territory size and the evolution of leks: A model and a test using an ungulate with a flexible mating system. *Front. Ecol. Evol.* **8**, 444 (2020).
160. K. Isvaran, The lekking puzzle: The evolution of costly mating behaviour. *Resonance* **25**, 353–362 (2020). doi: 10.1007/s12045-020-0950-x
161. B. J. Le Boeuf, S. Mesnick, Sexual behavior of male northern elephant seals: I. Lethal injuries to adult females. *Behaviour* **116**, 143–162 (1991). doi: 10.1163/156853990X00400
162. T. H. Clutton-Brock, S. D. Albon, R. M. Gibson, F. E. Guinness, The logical stag: Adaptive aspects of fighting in red deer (*Cervus elaphus* L.). *Anim. Behav.* **27**, 211–225 (1979b). doi: 10.1016/0003-3472(79)90141-6
163. J. M. Plavcan, C. P. van Schaik, P. Kappeler, Competition, coalitions and canine size in primates. *J. Hum. Evol.* **28**, 245–276 (1995). doi: 10.1006/jhev.1995.1019
164. P. Stockley, A. Purvis, Sperm competition in mammals: A comparative study of male roles and relative investment in sperm production. *Funct. Ecol.* **7**, 560–570 (1993). doi: 10.2307/2390132
165. S. A. Ramm, G. A. Parker, P. Stockley, Sperm competition and the evolution of male reproductive anatomy in rodents. *Proc. Biol. Sci.* **272**, 949–955 (2005). doi: 10.1098/rspb.2004.3048; pmid: 16024351
166. A. H. Harcourt, P. H. Harvey, S. G. Larson, R. V. Short, Testis weight, body weight and breeding system in primates. *Nature* **293**, 55–57 (1981). doi: 10.1038/293055a0; pmid: 7266658
167. T. H. Clutton-Brock, G. A. Parker, Punishment in animal societies. *Nature* **373**, 209–216 (1995a). doi: 10.1038/373209a0; pmid: 7816134
168. A. Baniel, G. Cowlishaw, E. Huchard, Male violence and sexual intimidation in a wild primate society. *Curr. Biol.* **27**, 2163–2168.e3 (2017). doi: 10.1016/j.cub.2017.06.013; pmid: 28690113
169. T. H. Clutton-Brock, G. A. Parker, Sexual coercion in animal societies. *Anim. Behav.* **49**, 1345–1365 (1995). doi: 10.1006/anbe.1995.0166
170. S. B. Hrdy, Infanticide among animals: A review, classification, and examination of the implications for the reproductive strategies of females. *Ethol. Sociobiol.* **1**, 13–40 (1979). doi: 10.1016/0162-3095(79)90004-9
171. C. P. van Schaik, in *Infanticide by Males and Its Implications*, C. P. van Schaik, C. H. Janson, Eds. (Cambridge Univ. Press, 2000), pp. 27–60.
172. J. E. Swenson *et al*., Infanticide caused by hunting of male bears. *Nature* **386**, 450–451 (1997). doi: 10.1038/386450a0
173. K. Whitman, A. M. Starfield, H. S. Quadling, C. Packer, Sustainable trophy hunting of African lions. *Nature* **428**, 175–178 (2004). doi: 10.1038/nature02395; pmid: 14990967
174. E. K. Roberts, A. Lu, T. J. Bergman, J. C. Beehner, A Bruce effect in wild geladas. *Science* **335**, 1222–1225 (2012). doi: 10.1126/science.1213600; pmid: 22362878
175. R. A. Palombit, in *The Evolution of Primate Societies*, J. C. Mitani, J. Call, P. M. Kappeler, R. A. Palombit, J. B. Silk, Eds. (Univ. of Chicago Press, 2012), pp. 432–468.
176. N. Owen-Smith, Comparative mortality rates of male and female Kudus: The costs of sexual size dimorphism. *J. Anim. Ecol.* **62**, 428–440 (1993b). doi: 10.2307/5192
177. J.-F. Lemaître, V. Ronget, J.-M. Gaillard, Female reproductive senescence across mammals: A high diversity of patterns modulated by life history and mating traits. *Mech. Ageing Dev.* **192**, 111377 (2020). doi: 10.1016/j.mad.2020.111377; pmid: 33031803
178. C. D. Fitzgibbon, Mixed-species grouping in Thomson's and Grant's gazelles: The antipredator benefits. *Anim. Behav.* **39**, 1116–1126 (1990). doi: 10.1016/S0003-3472(05)80784-5
179. K. Wilson, B. T. Grenfell, J. G. Pilkington, H. E. G. Boyd, F. M. D. Gulland, in *Soay Sheep: Dynamics and Selection in an Island Population*, T. Clutton-Brock, J. M. Pemberton, Eds. (Cambridge Univ. Press, 2004), pp. 113–165.
180. D. J. Irschick, S. P. Lailvaux, Age-specific forced polymorphism: Implications of ontogenetic changes in morphology for male mating tactics. *Physiol. Biochem. Zool.* **79**, 73–82 (2006). doi: 10.1086/498194; pmid: 16380929
181. S. E. Johnston *et al*., Life history trade-offs at a single locus maintain sexually selected genetic variation. *Nature* **502**, 93–95 (2013). doi: 10.1038/nature12489; pmid: 23965625
182. S. Chowdhury, M. Pines, J. Saunders, L. Swedell, The adaptive value of secondary males in the polygynous multi-level society of hamadryas baboons. *Am. J. Phys. Anthropol.* **158**, 501–513 (2015). doi: 10.1002/ajpa.22804; pmid: 26174200
183. T. H. Clutton-Brock, S. D. Albon, F. E. Guinness, Parental investment in male and female offspring in polygynous mammals. *Nature* **289**, 487–489 (1981). doi: 10.1038/289487a0
184. C. H. Berube, M. Festa-Bianchet, J. T. Jorgenson, Reproductive costs of sons and daughters in Rocky Mountain bighorn sheep. *Behav. Ecol.* **7**, 60–68 (1996). doi: 10.1093/beheco/7.1.60

185. H. Froy, C. A. Walling, J. M. Pemberton, T. H. Clutton-Brock, L. E. B. Kruuk, Relative costs of offspring sex and offspring survival in a polygynous mammal. *Biol. Lett.* **12**, 20160417 (2016). doi: 10.1098/rsbl.2016.0417; pmid: 27601725
186. L. E. B. Kruuk, T. H. Clutton-Brock, K. E. Rose, F. E. Guinness, Early determinants of lifetime reproductive success differ between the sexes in red deer. *Proc. Biol. Sci.* **266**, 1655–1661 (1999b). doi: 10.1098/rspb.1999.0828; pmid: 10501037
187. T. H. Clutton-Brock, *The Evolution of Parental Care*, J. R. Krebs, T. H. Clutton-Brock, Eds. (Monographs in Behavior and Ecology, Princeton Univ. Press, 1991).
188. R. L. Trivers, D. E. Willard, Natural selection of parental ability to vary the sex ratio of offspring. *Science* **179**, 90–92 (1973). doi: 10.1126/science.179.4068.90; pmid: 4682135
189. S. A. West, B. C. Sheldon, Constraints in the evolution of sex ratio adjustment. *Science* **295**, 1685–1688 (2002). doi: 10.1126/science.1069043; pmid: 11823605
190. T. H. Clutton-Brock, in *The Development and Integration of Behaviour: Essays in Honour of Robert Hinde*, P. Bateson, Ed. (Cambridge Univ. Press, 1991), pp. 229–253.
191. T. H. Clutton-Brock, Feeding levels and feeding sites of red colobus (*Colobus badius tephrosceles*) in the Gombe National Park. *Folia Primatol. (Basel)* **19**, 368–379 (1973). doi: 10.1159/000155552; pmid: 4203424
192. P. J. Funston, M. G. L. Mills, H. C. Biggs, P. R. K. Richardson, Hunting by male lions: Ecological influences and socioecological implications. *Anim. Behav.* **56**, 1333–1345 (1998). doi: 10.1006/anbe.1998.0884; pmid: 9933529
193. B. J. Le Boeuf, D. E. Crocker, S. B. Blackwell, P. A. Morris, P. H. Thorson, Sex differences in diving and foraging behaviour of northern elephant seals. *Symp. Zool. Soc. Lond.* **66**, 149–178 (1993).
194. L. Conradt, T. H. Clutton-Brock, F. E. Guinness, Sex differences in weather sensitivity can cause habitat segregation: Red deer as an example. *Anim. Behav.* **59**, 1049–1060 (2000). doi: 10.1006/anbe.2000.1409; pmid: 10860532
195. T. H. Clutton-Brock, S. D. Albon, F. E. Guinness, Parental investment and sex differences in juvenile mortality in birds and mammals. *Nature* **313**, 131–133 (1985). doi: 10.1038/313131a0
196. J.-F. Lemaître *et al*., Sex differences in adult lifespan and aging rates of mortality across wild mammals. *Proc. Natl. Acad. Sci. U.S.A.* **117**, 8546–8553 (2020). doi: 10.1073/pnas.1911999117; pmid: 32205429
197. T. H. Clutton-Brock, K. E. Rose, F. E. Guinness, Density-related changes in sexual selection in red deer. *Proc. Biol. Sci.* **264**, 1509–1516 (1997). doi: 10.1098/rspb.1997.0209; pmid: 9364790
198. J. Pérez-González, J. Carranza, Female aggregation interacts with population structure to influence the degree of polygyny in red deer. *Anim. Behav.* **82**, 957–970 (2011). doi: 10.1016/j.anbehav.2011.07.023
199. T. H. Clutton-Brock, M. E. Lonergan, Culling regimes and sex ratio biases in Highland red deer. *J. Appl. Ecol.* **31**, 521–527 (1994). doi: 10.2307/2404447
200. M. J. F. Martins, T. M. Puckett, R. Lockwood, J. P. Swaddle, G. Hunt, High male sexual investment as a driver of extinction in fossil ostracods. *Nature* **556**, 366–369 (2018). doi: 10.1038/s41586-018-0020-7; pmid: 29643505
201. H. Kokko, M. D. Jennions, Parental investment, sexual selection and sex ratios. *J. Evol. Biol.* **21**, 919–948 (2008). doi: 10.1111/j.1420-9101.2008.01540.x; pmid: 18462318
202. A. Liker *et al*., Evolution of large males is associated with female-skewed adult sex ratios in amniotes. *Evolution* **75**, 1636–1649 (2021). doi: 10.1111/evo.14273; pmid: 34021590
203. T. Clutton-Brock, Reproductive competition and sexual selection. *Philos. Trans. R. Soc. London Ser. B.* **372**, 20160310 (2017). doi: 10.1098/rstb.2016.0310; pmid: 28760754
204. J. E. Smith, N. Pinter-Wollman, Observing the unwatchable: Integrating automated sensing, naturalistic observations and animal social network analysis in the age of big data. *J. Anim. Ecol.* **90**, 62–75 (2021). doi: 10.1111/1365-2656.13362; pmid: 33020914
205. R. J. Moll *et al*., A terrestrial animal-borne video system for large mammals. *Comput. Electron. Agric.* **66**, 133–139 (2009). doi: 10.1016/j.compag.2009.01.001
206. M. S. Norouzzadeh *et al*., Automatically identifying, counting, and describing wild animals in camera-trap images with deep learning. *Proc. Natl. Acad. Sci. U.S.A.* **115**, E5716–E5725 (2018). doi: 10.1073/pnas.1719367115; pmid: 29871948
207. M. B. Petelle, J. G. Martin, D. T. Blumstein, Heritability and genetic correlations of personality traits in a wild population of yellow-bellied marmots (*Marmota flaviventris*). *J. Evol. Biol.* **28**, 1840–1848 (2015). doi: 10.1111/jeb.12700; pmid: 26214760
208. D. E. Runcie *et al*., Social environment influences the relationship between genotype and gene expression in wild baboons. *Philos. Trans. R. Soc. London Ser. B* **368**, 20120345 (2013). doi: 10.1098/rstb.2012.0345; pmid: 23569293
209. A. J. Lea *et al*., Dominance rank-associated gene expression is widespread, sex-specific, and a precursor to high social status in wild male baboons. *Proc. Natl. Acad. Sci. U.S.A.* **115**, E12163–E12171 (2018). doi: 10.1073/pnas.1811967115; pmid: 30538194
210. R. L. Young *et al*., Conserved transcriptomic profiles underpin monogamy across vertebrates. *Proc. Natl. Acad. Sci. U.S.A.* **116**, 1331–1336 (2019). doi: 10.1073/pnas.1813775116; pmid: 30617061
211. C. Schradin, L. D. Hayes, A synopsis of long-term field studies of mammals: Achievements, future directions, and some advice. *J. Mammal.* **98**, 670–677 (2017). doi: 10.1093/jmammal/gyx031
212. R. Lande, S. Engen, B.-E. Saether, *Stochastic Population Dynamics in Ecology and Conservation* (Oxford Univ. Press, 2003).
213. P. Gienapp, J. E. Brommer, in *Quantitative Genetics in the Wild*, A. Charmantier, D. Garant, L. E. B. Kruuk, Eds. (Oxford Univ. Press, 2014), pp. 254–274.
214. N. Perrin, E. J. Petit, N. Menard, Social systems: Demographic and genetic issues. *Mol. Ecol.* **21**, 443–446 (2012). doi: 10.1111/j.1365-294X.2011.05404.x; pmid: 22239244
215. D. R. Rubenstein, H. A. Hofmann, Proximate pathways underlying social behavior. *Curr. Opin. Behav. Sci.* **6**, 154–159 (2015). doi: 10.1016/j.cobeha.2015.11.007
216. E. Treanore, N. Derstine, E. Amsalem, What can mechanisms underlying derived traits tell us about the evolution of social behavior? *Ann. Entomol. Soc. Am.* saaa033 (2020). doi: 10.1093/aesa/saaa033
217. K. Langergraber, J. Mitani, L. Vigilant, Kinship and social bonds in female chimpanzees (*Pan troglodytes*). *Am. J. Primatol.* **71**, 840–851 (2009). doi: 10.1002/ajp.20711; pmid: 19475543
218. R. C. Van Horn, A. L. Engh, K. T. Scribner, S. M. Funk, K. E. Holekamp, Behavioural structuring of relatedness in the spotted hyena (*Crocuta crocuta*) suggests direct fitness benefits of clan-level cooperation. *Mol. Ecol.* **13**, 449–458 (2004). doi: 10.1046/j.1365-294X.2003.02071.x; pmid: 14717899
219. G. Spong, J. Stone, S. Creel, M. Bjorklund, Genetric structure of lions (*Panthero leo* L.) in the Selous Game Reserve: Implications for the evolution of sociality. *J. Evol. Biol.* **15**, 945–953 (2002). doi: 10.1046/j.1420-9101.2002.00473.x
220. D. J. Girman, M. G. L. Mills, E. Geffen, R. K. Wayne, A molecular genetic analysis of social structure, dispersal, and interpack relationships of the African wild dog (*Lycaon pictus*). *Behav. Ecol. Sociobiol.* **40**, 187–198 (1997). doi: 10.1007/s002650050332
221. M. Huck, P. Löttker, U. R. Böhle, E. W. Heymann, Paternity and kinship patterns in polyandrous moustached tamarins (*Saguinus mystax*). *Am. J. Phys. Anthropol.* **127**, 449–464 (2005). doi: 10.1002/ajpa.20136; pmid: 15624210
222. A. S. Griffin, J. M. Pemberton, P. N. M. Brotherton, D. Gaynor, T. H. Clutton-Brock, A genetic analysis of breeding success in the cooperative meerkat (*Suricata suricatta*). *Behav. Ecol.* **14**, 472–480 (2003). doi: 10.1093/beheco/arg040
223. G. F. Spong, S. J. Hodge, A. J. Young, T. H. Clutton-Brock, Factors affecting the reproductive success of dominant male meerkats. *Mol. Ecol.* **17**, 2287–2299 (2008). doi: 10.1111/j.1365-294X.2008.03734.x; pmid: 18410290
224. T. M. Burland, N. C. Bennett, J. U. M. Jarvis, C. G. Faulkes, Eusociality in African mole-rats: New insights from patterns of genetic relatedness in the Damaraland mole-rat (*Cryptomys damarensis*). *Proc. Biol. Sci.* **269**, 1025–1030 (2002). doi: 10.1098/rspb.2002.1978; pmid: 12028759
225. T. H. Clutton-Brock, S. D. Albon, F. E. Guinness, in *Reproductive Success: Studies of Individual Variation in Contrasting Breeding Systems*, T. H. Clutton-Brock, Ed. (Univ. of Chicago Press, 1988), pp. 325–343.
226. B. J. Le Boeuf, J. Reiter, in *Reproductive Success: Studies of Individual Variation in Contrasting Breeding Systems*, T. H. Clutton-Brock, Ed. (University Press, Chicago, 1988), pp. 344–362.

ACKNOWLEDGMENTS

For discussion of the evolution of mammal societies extending over many years, I am grateful to D. Lukas, P. Kappeler, C. van Schaik, J. Silk, R. Dunbar, S. Shultz, D. Blumstein, and R. Wrangham and to three anonymous referees; for preparation of many drafts, I am indebted to P. Roth, and for the production of figures to T. Houslay. I am very grateful for all those who have contributed photographs of the species they have worked on. For kinship figures for yellow baboons in Fig.1, I am indebted to J. Tung and members of the Amboseli Baboon Research Project. **Funding:** This research is part of a project that has received funding from the European Research Council (ERC) under the European Union's Horizon 2020 research and innovation program (grants 294494 and 742808) and from the Human Frontier Science Program (grant RGP0051/2017). **Competing interests:** I know of no competing interests to this submission.

10.1126/science.abc9699

RESEARCH ARTICLE SUMMARY

IMMUNOLOGY

Serum amyloid A delivers retinol to intestinal myeloid cells to promote adaptive immunity

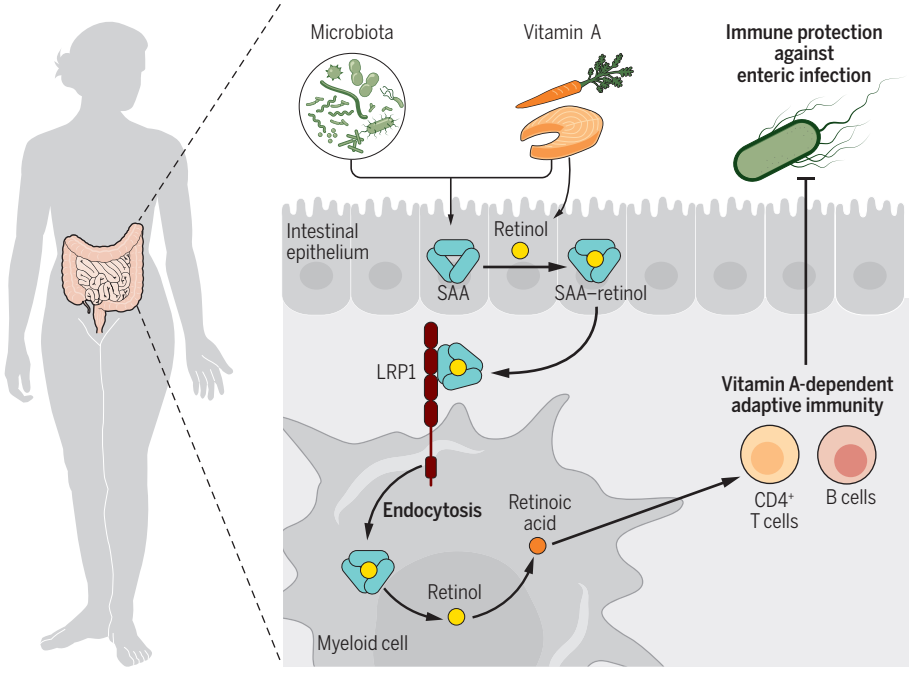
Ye-Ji Bang, Zehan Hu, Yun Li, Sureka Gattu, Kelly A. Ruhn, Prithvi Raj, Joachim Herz, Lora V. Hooper*

INTRODUCTION: Vitamin A is a lipid-soluble nutrient that is absorbed from the diet by intestinal epithelial cells and converted to retinol. This product of vitamin A metabolism is essential for intestinal adaptive immunity because it directs the development of B and T cells and promotes their recruitment to the intestine. Consequently, vitamin A deficiency confers increased susceptibility to infectious diseases of the intestine.

Intestinal myeloid cells play a central role in the development of vitamin A–dependent intestinal immunity. Certain myeloid cells convert retinol to retinoic acid (RA) and then pass the RA to developing B and T cells. This activates RA-dependent gene expression programs that direct B and T cells to home to the intestine and induces immunoglobulin A (IgA) production by B cells.

RATIONALE: A major unanswered question is how intestinal myeloid cells acquire retinol for conversion to RA. Retinol is lipophilic, necessitating transport by retinol-binding proteins that shield it from the aqueous environment. However, proteins that deliver retinol to myeloid cells remain unidentified.

Serum amyloid A (SAA) proteins are retinol-binding proteins expressed in the intestinal epithelium. Epithelial cell expression of SAAs requires both the intestinal microbiota and dietary vitamin A. SAAs are also produced by the liver and circulate in the serum with bound retinol after systemic bacterial infection. Thus, SAAs are retinol-binding proteins that transport retinol in response to microbial challenge. However, the cellular targets of SAA-retinol complexes are unclear. In this study, we identified a receptor for SAA-retinol complexes that mediates retinol uptake into intestinal myeloid cells. Moreover, we determined how this retinol uptake mechanism affects vitamin A–dependent immunity.



SAA proteins deliver retinol to intestinal myeloid cells through LRP1 to promote adaptive immunity. SAAs are retinol-binding proteins induced in intestinal epithelial cells by the microbiota and vitamin A. SAAs deliver retinol to retinoic acid–producing myeloid cells by binding to the endocytic receptor LRP1. LRP1 and SAAs promote development of vitamin A–dependent adaptive immunity in the intestine and enhance resistance to enteric infection.

RESULTS: Using biochemical approaches, including chemical cross-linking and mass spectrometry, we identified low-density lipoprotein (LDL) receptor–related protein 1 (LRP1) as a cell surface receptor for SAAs that binds SAA-retinol complexes with high affinity. We showed that LRP1 mediates cell surface binding and the endocytosis of SAA-retinol complexes in cultured cells. In the intestine, the highest levels of LRP1 expression were on CD11c$^+$ myeloid cells, which efficiently bound SAA-retinol complexes, thereby internalizing retinol. The physiological roles of SAAs and their LRP1 receptor were identified in vivo using two mouse models: *Saa*$^{-/-}$ mice with a deletion of the entire *Saa* gene locus and *Lrp1*$^{\Delta Cd11c}$ mice with a myeloid cell–specific deletion of the *Lrp1* gene. Studies of these mice revealed that SAAs and their LRP1 receptor facilitated retinol uptake by intestinal myeloid cells in vivo and promoted the expression of enzymes that convert retinol to RA. Accordingly, SAAs and myeloid cell LRP1 were required for the development of vitamin A–dependent adaptive immunity, including B and T cell homing to the intestine and IgA production. Finally, we found that SAAs and LRP1 promoted immunity to enteric infection after immunization.

CONCLUSION: We have identified SAAs as retinol-binding proteins that deliver retinol to RA-producing intestinal myeloid cells. SAA-retinol complexes bind to LRP1 on the myeloid cell surface and are endocytosed, providing retinol for the enzymatic generation of RA. Consequently, SAAs and LRP1 promote the development of vitamin A–dependent adaptive immunity in the intestine and enhance resistance to enteric infection after immunization.

Our findings identify a mechanism by which retinol is acquired by intestinal myeloid cells and show that this mechanism promotes vitamin A–dependent intestinal adaptive immunity. Because expression of SAAs by intestinal epithelial cells requires the microbiota, our findings suggest that the microbiota promotes the development of adaptive immunity in part by regulating epithelial SAA expression. These findings also suggest that SAAs could deliver retinol to myeloid cells that reside in other tissues. By illuminating how vitamin A is mobilized to the intestinal immune system, our results may offer additional approaches for enhancing resistance to infection and for increasing the efficacy of mucosal vaccines, which depend on adequate dietary vitamin A. ■

The list of author affiliations is available in the full article online.
*Corresponding author. Email: lora.hooper@utsouthwestern.edu
Cite this article as Y.-J. Bang *et al.*, *Science* **373**, eabf9232 (2021). DOI: 10.1126/science.abf9232

READ THE FULL ARTICLE AT
https://doi.org/10.1126/science.abf9232

RESEARCH ARTICLE

IMMUNOLOGY

Serum amyloid A delivers retinol to intestinal myeloid cells to promote adaptive immunity

Ye-Ji Bang[1], Zehan Hu[1], Yun Li[1], Sureka Gattu[1]†, Kelly A. Ruhn[1], Prithvi Raj[1], Joachim Herz[2,3,4,5], Lora V. Hooper[1,6]*

Vitamin A and its derivative retinol are essential for the development of intestinal adaptive immunity. Retinoic acid (RA)–producing myeloid cells are central to this process, but how myeloid cells acquire retinol for conversion to RA is unknown. Here, we show that serum amyloid A (SAA) proteins—retinol-binding proteins induced in intestinal epithelial cells by the microbiota—deliver retinol to myeloid cells. We identify low-density lipoprotein (LDL) receptor–related protein 1 (LRP1) as an SAA receptor that endocytoses SAA-retinol complexes and promotes retinol acquisition by RA-producing intestinal myeloid cells. Consequently, SAA and LRP1 are essential for vitamin A–dependent immunity, including B and T cell homing to the intestine and immunoglobulin A production. Our findings identify a key mechanism by which vitamin A promotes intestinal immunity.

Vitamin A is a lipid-soluble nutrient that is absorbed from the diet by intestinal epithelial cells and converted to retinol. Retinol is essential for intestinal adaptive immunity because it directs the development of intestinal B and T cells and promotes their recruitment to the intestine (*1*, *2*). Consequently, vitamin A deficiency confers an increased susceptibility to infectious diseases, including those of the intestine (*3*).

Myeloid cells are central to the development of vitamin A–dependent intestinal immunity. Myeloid cells include dendritic cells (DCs) and macrophages, which circulate in the intestine and present antigens to naïve B and T cells to promote their differentiation into functional immune cells (*4*, *5*). Certain intestinal DCs and macrophages can enzymatically convert retinol to retinoic acid (RA) (*6*–*10*). These myeloid cells pass their RA to T cells, where it complexes with retinoic acid receptors (RARs)—transcription factors that activate RA-dependent gene expression programs (*11*, *12*). These programs include the expression of homing receptors, such as CCR9 and integrin α4β7, which direct T cells to the intestine (*1*, *13*). Similarly, RA-producing myeloid cells imprint homing receptors on developing B cells and induce the production of immunoglobulin A (IgA) (*2*).

[1]Department of Immunology, University of Texas Southwestern Medical Center, Dallas, TX 75390, USA. [2]Department of Molecular Genetics, University of Texas Southwestern Medical Center, Dallas, TX 75390, USA. [3]Center for Translational Neurodegeneration Research, University of Texas Southwestern Medical Center, Dallas, TX 75390, USA. [4]Department of Neurology and Neurotherapeutics, University of Texas Southwestern Medical Center, Dallas, TX 75390, USA. [5]Department of Neuroscience, University of Texas Southwestern Medical Center, Dallas, TX 75390, USA. [6]Howard Hughes Medical Institute, University of Texas Southwestern Medical Center, Dallas, TX 75390, USA.
*Corresponding author. Email: lora.hooper@utsouthwestern.edu
†Present address: Reata Pharmaceuticals Inc., Irving, TX 75063, USA.

A major unanswered question is how intestinal myeloid cells acquire retinol for conversion to RA. Retinol is lipophilic, necessitating its transport by retinol-binding proteins that shield it from the aqueous environment. However, proteins that deliver retinol to myeloid cells remain unidentified.

Serum amyloid A (SAA) proteins are a family of retinol-binding proteins expressed in the intestinal epithelium and liver (*14*, *15*). SAAs form a trimeric assembly with a central hydrophobic retinol-binding pocket (*14*, *15*). Epithelial expression of SAAs is induced by the intestinal microbiota through a signaling circuit involving DCs, innate lymphoid cells, and epithelial STAT3 (signal transducers and activators of transcription 3) (*16*), and by dietary vitamin A through epithelial RARβ (*17*). SAAs are also produced in the liver after acute bacterial infection and circulate in the serum with bound retinol (*14*, *15*). Thus, SAAs are retinol-binding proteins that transport retinol in response to microbial signals, including the microbiota and acute systemic infection. However, the cellular targets of SAA-retinol complexes are unclear.

Here, we identify a molecular basis for retinol acquisition by intestinal myeloid cells. We show that SAAs deliver retinol to RA-producing myeloid cells in the intestine and that low-density lipoprotein (LDL) receptor–related protein 1 (LRP1) mediates myeloid cell uptake of SAA-retinol complexes. Together, LRP1 and SAA facilitate myeloid cell retinol acquisition and are essential for the development of vitamin A–dependent adaptive immunity in the intestine.

Identification of LRP1 as a cell surface receptor for SAA proteins

As a first step in understanding how SAAs deliver retinol to target cells, we identified a cell surface receptor for SAA. We first screened cultured cell lines for evidence of receptor-mediated cell surface binding of SAAs. We used SAA1 for these studies because *Saa1* expression is highest among the four *Saa* isotypes in the intestine (fig. S1A). Differentiated 3T3-L1 mouse adipocytes, which are a major extrahepatic retinol storage site (*18*), bound SAA1 on their cell surface (fig. S1, B and C). Furthermore, the binding was saturable (fig. S1D), which suggests a specific receptor-mediated interaction. Finally, adipocytes acquired retinol more readily from SAA1-retinol complexes than from free retinol (fig. S1E), which suggests that SAAs deliver retinol to receptor-bearing target cells.

To identify the adipocyte SAA receptor or receptors, we used the 6X histidine tag (His-tag)–nickel resin system and a bifunctional cross-linker, allowing stabilization of the SAA-receptor interaction and purification of the complex (Fig. 1A). Recombinant His-tagged SAA1 was conjugated with the cross-linker, complexed with retinol, and added to adipocytes. After ultraviolet cross-linking, membrane solubilization, and nickel resin purification, we identified a >250-kD covalent protein complex that contained SAA1 (Fig. 1B). Mass spectrometry identified the other major protein as the transmembrane receptor LRP1 (table S1).

LRP1 is a member of the LDL receptor family that binds several distinct ligands, including lipoproteins, and facilitates their cellular uptake through endocytosis (*19*). It is composed of two noncovalently associated fragments: a long N-terminal extracellular α-fragment containing ligand-binding regions and a short membrane-anchored C-terminal β-fragment (Fig. 1C). To test whether LRP1 directly binds to SAA1, we expressed and purified the full-length ectodomain of human LRP1 (LRP1-ECD). SAA1 and LRP1-ECD eluted together during size exclusion chromatography (Fig. 1D), indicating a direct interaction. We confirmed binding by microscale thermophoresis using a fluorescently labeled SAA1 and LRP1-ECD. We observed LRP1-dependent enhancement of SAA1 fluorescence and calculated a dissociation constant (K_d) of ~33 nM (Fig. 1E). This K_d is consistent with those of other known LRP1 ligands (*20*, *21*) and indicates high-affinity binding of SAA1 to LRP1.

We next determined which LRP1 domains bind to SAA1. The ectodomain of LRP1 encompasses four ligand-binding clusters containing cysteine-rich repeats, CI to CIV (Fig. 1C). Among these, CII, CIII, and CIV directly bind ligands (*19*). We therefore tested SAA1 binding to these three clusters. Pull-down assays revealed that SAA1 preferentially bound to LRP1-CIV (Fig. 1, F and G). We then confirmed that mouse SAA3 also binds to LRP1-CIV (fig. S2). Thus, LRP1 directly binds SAAs with high affinity.

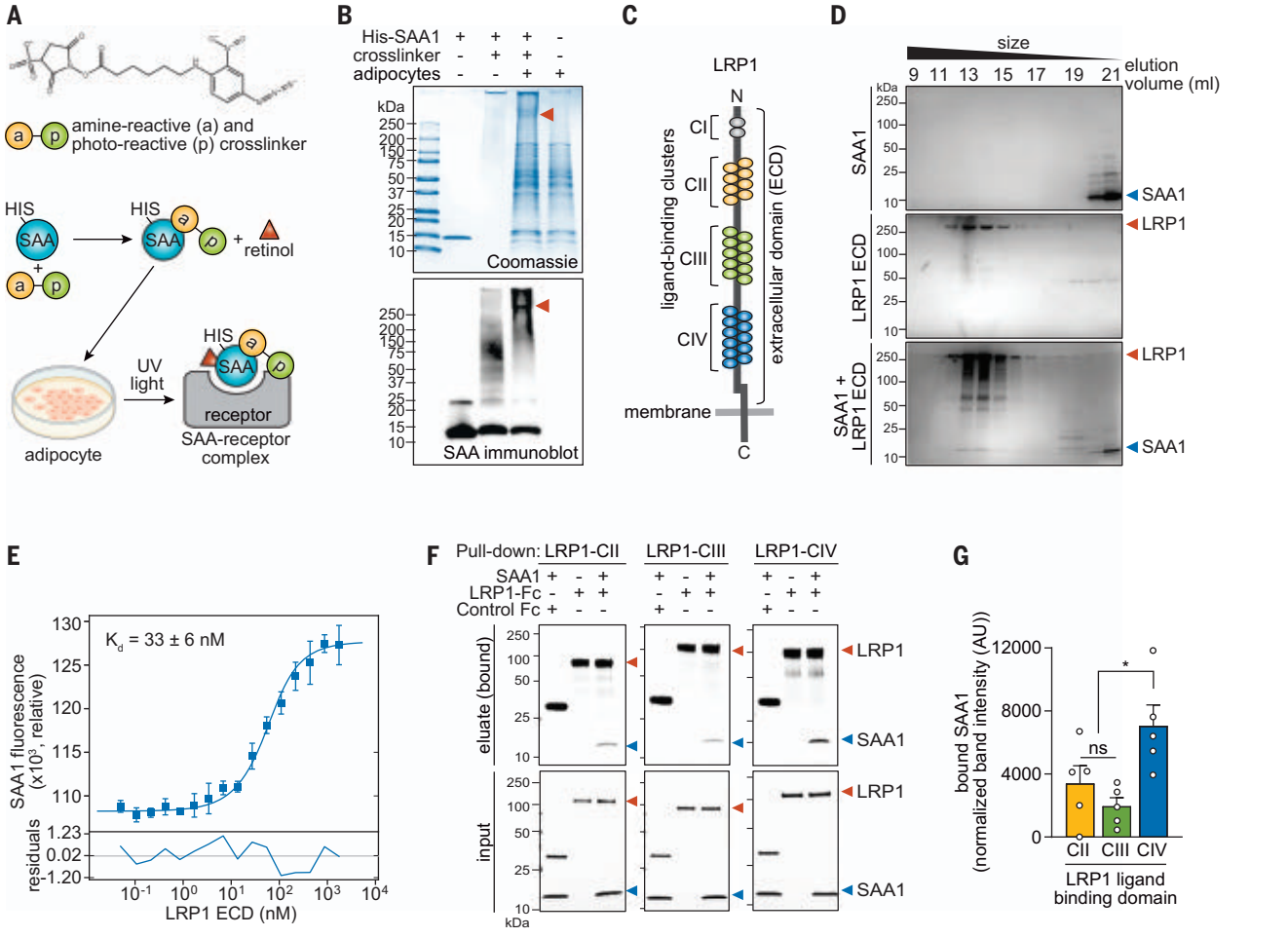


Fig. 1. LRP1 is a cell surface receptor for SAAs. (**A**) Schematic diagram of the strategy used to identify the SAA receptor. The structure of the amine-reactive and photoreactive cross-linker is shown at the top. The SAA-receptor complex was conjugated by the cross-linker as shown in the diagram and then purified and further analyzed. The cell culture image was generated in BioRender. (**B**) Protein complexes were resolved by SDS-PAGE and detected with Coomassie blue (top) or immunoblot for SAA (bottom). Red arrowheads indicate the protein complex that was subjected to mass spectrometry for receptor identification. (**C**) Schematic of the domain organization of LRP1 showing the ectodomain (ECD) and ligand-binding clusters (CI to CIV). (**D**) Formation of a complex between SAA1 and the LRP1 ectodomain (LRP1-ECD) was confirmed by size exclusion chromatography. Proteins were resolved by SDS-PAGE and detected with Coomassie blue. (**E**) Binding affinity between SAA1 and the LRP1-ECD was determined using microscale thermophoresis. Specific LRP1-dependent enhancement of fluorescence of SAA1 was used for the determination of a dissociation constant (K_d). Residuals between the fit and the data are depicted in the bottom panel. Data represent means ± SEMs from three independent assays. (**F** and **G**) Binding of SAA1 to the LRP1 ligand-binding clusters (LRP1-CII, LRP1-CIII, and LRP1-CIV) was assessed by pull-down assay. Each Fc-tagged LRP1 protein and Fc control was incubated with SAA1, and Protein G magnetic beads were used to capture the Fc-tagged proteins (top). (G) Bound SAA1 in (F) was quantified by scanning densitometry and normalized to SAA1 bound to control Fc. Results from five independent sets of pull-down assays are shown, with each data point representing one assay. In all experiments, SAA1 was preincubated with retinol (3:1, retinol:SAA1 molar ratio) at 4°C for 2 hours to allow SAA1-retinol complex formation. *P < 0.05; paired Student's t test.

LRP1 mediates cell surface binding and cellular uptake of SAA1-retinol complexes

To determine whether LRP1 functions as a SAA receptor that promotes cellular retinol uptake, we examined wild-type (*Lrp1*$^{+/+}$) and *Lrp1*-deficient (*Lrp1*$^{-/-}$) fibroblasts. We first assessed whether SAA binding to the cell surface was LRP1 dependent. His-SAA1–retinol complexes were incubated with *Lrp1*$^{+/+}$ and *Lrp1*$^{-/-}$ cell cultures at 4°C to allow the binding of SAA1 to the cell surface while preventing endocytosis (*22*). SAA1 binding was then measured by flow cytometry. More SAA1 bound to *Lrp1*$^{+/+}$ cells than to *Lrp1*$^{-/-}$ cells (Fig. 2, A and B), indicating that LRP1 mediates cell surface binding of SAA1. LRP1-dependent binding of SAA1 to the cell surface was saturable (Fig. 2C) and could be blocked by SAA1 that lacked a His tag (Fig. 2D), which provides evidence for a specific binding interaction. Finally, receptor-associated protein (RAP), a chaperone that binds to LRP1 in the endoplasmic reticulum (*23*, *24*), competed for cell surface binding by SAA1 (Fig. 2E), providing further evidence of specificity. LRP1 is therefore a specific receptor for SAA1.

Next, we tested whether LRP1 facilitates the delivery of SAA-bound retinol into cells. We added a ^{3}H-retinol tracer to fibroblasts, either as free retinol or in complex with SAA1, and measured the cell-associated retinol by scintillation counting. More retinol was acquired by *Lrp1*$^{+/+}$ cells from SAA1-retinol complexes than from free retinol. Furthermore, retinol uptake from SAA1-retinol complexes was reduced in *Lrp1*$^{-/-}$ cells (Fig. 2F). The addition of RAP as a competitive inhibitor of SAA1 binding to LRP1 reduced retinol uptake by *Lrp1*$^{+/+}$ cells (Fig. 2G). Therefore, LRP1 facilitates retinol uptake by binding to SAA1-retinol complexes.

LRP1 internalizes many of its known ligands by endocytosis (*19*, *25*), suggesting that it may

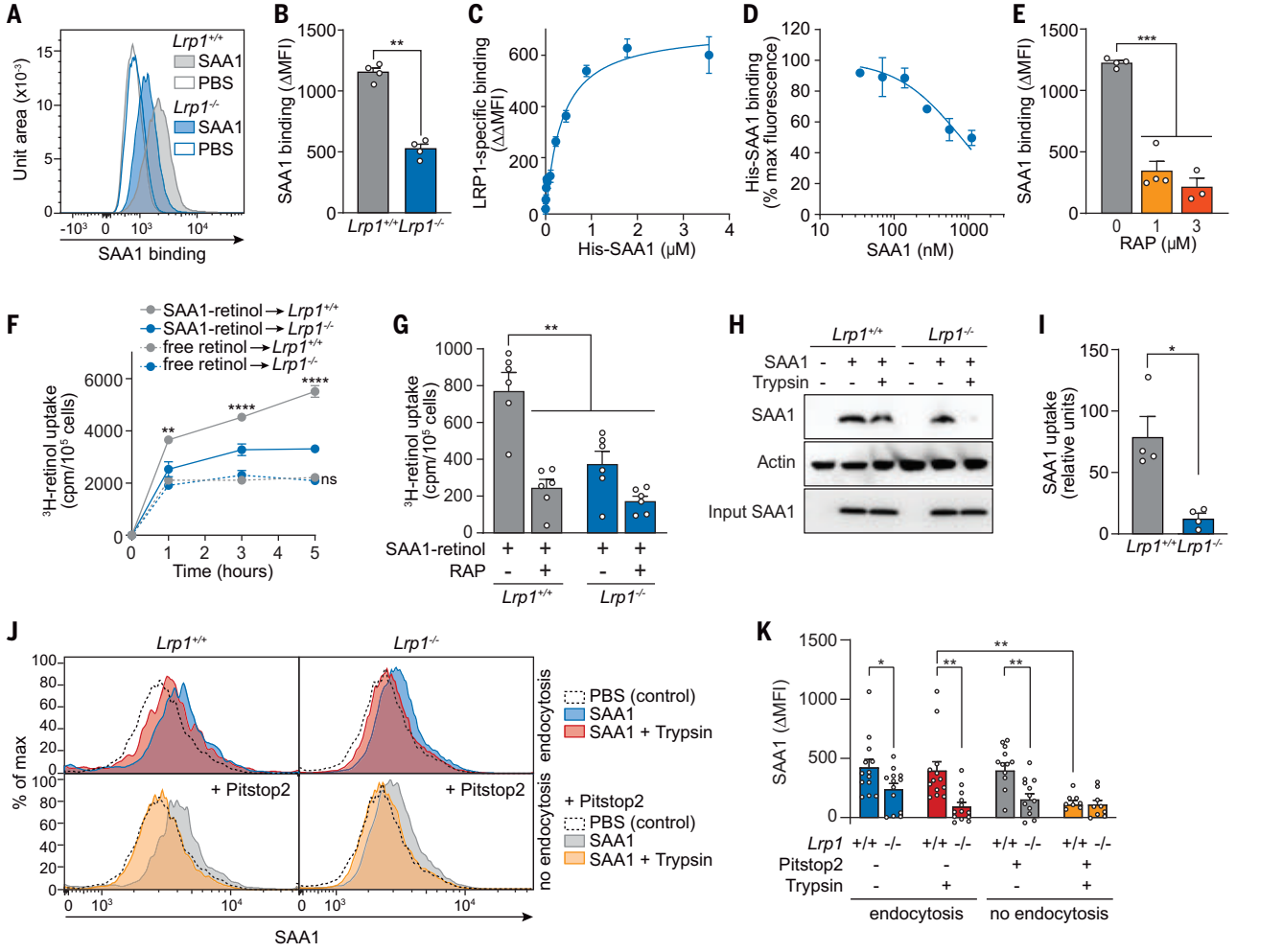


Fig. 2. LRP1 mediates cell surface binding and cellular uptake of SAA1-retinol complexes. (A to E) Wild-type (*Lrp1*$^{+/+}$) and *Lrp1*-deficient (*Lrp1*$^{-/-}$) fibroblasts were incubated with His-SAA1–retinol complexes at 4°C, and the binding of SAA to the cell surface was analyzed by flow cytometry under nonpermeabilizing staining conditions using PE-conjugated anti-His tag antibody. (**A** and **B**) His-SAA1 (1.8 μM) was added to the cells, and representative flow cytometry histograms are shown in (A). ΔMFI (MFI^{SAA}–MFI^{PBS}) representing SAA1 binding to the cell surface (B) was calculated (n = 4 replicates per condition). PBS was added instead of SAA1 in control samples. (**C**) LRP1-specific SAA1 binding to the fibroblast cell surface was calculated and indicates saturable binding. LRP1-specific binding was calculated as the difference of SAA binding (ΔMFI) to *Lrp1*$^{+/+}$ and *Lrp1*$^{-/-}$ fibroblasts ($\Delta\Delta MFI = \Delta MFI^{Lrp1+/+} - \Delta MFI^{Lrp1-/-}$) ($n$ = 4). (**D**) Competitive binding assays were conducted by adding increasing concentrations of non–His-tagged SAA1 together with His-SAA1 (1.8 μM) to the cells. LRP1-specific binding of His-SAA1 to the cell surface was calculated (ΔΔMFI) and is shown as a percentage of the maximum fluorescence (n = 3). (**E**) Receptor-associated protein (RAP) was added to wild-type fibroblasts together with His-SAA1 (1 μM). Binding of SAA1 to the cell surface was measured by flow cytometry and is shown as ΔMFI (MFI^{SAA}–MFI^{PBS}). (F and G) Cellular ^{3}H-retinol uptake was measured. (**F**) ^{3}H-retinol was added to the cells either as free retinol or in complex with SAA1. After incubation at 37°C, the counts per minute (cpm) in the cell pellets were determined and normalized to cell number ($n \geq 5$). (**G**) RAP (3 μM) was added to cells together with 0.6 μM SAA1–^{3}H-retinol complex for competition analyses. (H to K) Cellular SAA uptake was analyzed. Cells were incubated with His-SAA1–retinol complex at 37°C for 30 min and subsequently treated with trypsin for 3 min to remove surface-bound SAA1. (**H** and **I**) Cells were lysed and cellular SAA uptake was analyzed by immunoblotting using an anti-His antibody (H). SAA band intensity in the cell lysates after trypsin digestion was measured, normalized with loading controls, and is shown in relative units in (I). (**J** and **K**) LRP1 promotes SAA1 endocytosis. SAA associated with *Lrp1*$^{+/+}$ and *Lrp1*$^{-/-}$ fibroblasts was measured by flow cytometry. Representative histograms are shown in (J) and ΔMFI (MFI^{SAA}–MFI^{PBS}) representing SAA1 measurements from three independent experiments are shown (K). Cells were treated with trypsin to remove surface-bound SAA1, and Pitstop2 was added to block endocytosis. In all experiments, SAA1 was preincubated with retinol or ^{3}H-retinol (3:1, retinol:SAA1 molar ratio) at 4°C for at least 2 hours to allow SAA-retinol complex formation. Means ± SEMs are shown from one [(A) to (E)] and at least two independent experiments [(F) to (K)]. All results are representative of at least two independent experiments. *P < 0.05; **P < 0.01; ***P < 0.001; ****P < 0.0001; Student's t test.

facilitate retinol uptake through endocytosis of the SAA1-retinol complex. To test this idea, we asked whether cell-associated SAA1 is degraded by added trypsin, which can digest cell surface but not internalized proteins (*15*). We added His-tagged SAA1-retinol complexes to *Lrp1*$^{+/+}$ and *Lrp1*$^{-/-}$ fibroblasts at 4°C to allow cell surface binding, incubated at 37°C to initiate endocytosis, and then exposed the cells to trypsin. When assessed by immunoblot, SAA1 was mostly protected from trypsin proteolysis when added to *Lrp1*$^{+/+}$ fibroblasts, whereas the SAA1 added to *Lrp1*$^{-/-}$ fibroblasts was mostly digested (Fig. 2, H and I). Similarly, flow cytometry revealed that most of the SAA1 associated with *Lrp1*$^{+/+}$ fibroblasts was protected from trypsin digestion but became susceptible when the endocytosis inhibitor

Pitstop2 was added to the cells (Fig. 2, J and K). By contrast, SAA1 added to *Lrp1*$^{-/-}$ cells was susceptible to trypsin proteolysis even in the absence of Pitstop2 (Fig. 2, J and K). Thus, LRP1 promotes the endocytosis of SAA1-retinol complexes.

LRP1 is expressed on intestinal CD11c$^+$ myeloid cells

We next sought to identify intestinal cells that express LRP1 and therefore might be targets of SAA-retinol complexes. We first compared expression of *Saa1* transcripts with the expression of transcripts encoding retinol-binding protein 4 (RBP4), which delivers retinol from the liver to peripheral tissues under noninflammatory conditions (*26*). *Rpb4* transcripts were more abundant than *Saa1* transcripts in the liver, whereas *Saa1* transcripts showed greater abundance in the small intestine (Fig. 3A). Likewise, SAA protein levels were higher than RBP4 levels in the small intestine (Fig. 3, B and C). At the same time, transcripts encoding the SAA receptor LRP1 were more abundant in the small intestine than transcripts encoding two known RBP4 receptors, stimulated by retinoic acid 6 (STRA6) (*27*) and RBP receptor 2 (RBPR2) (*28*) (Fig. 3D). SAA1 and its receptor LRP1 are more highly expressed in the intestine than RBP4 and its receptors, which suggests that SAAs might play a predominant role in mobilizing retinol in the intestine.

To identify intestinal cells expressing LRP1, we measured LRP1 expression in various intestinal cell populations. *Lrp1* transcripts were less abundant in epithelial cells than in lamina propria cells, which include various immune cells (Fig. 3E). To determine whether LRP1 is expressed on immune cells, we measured LRP1 expression on various lamina propria immune cell populations using flow cytometry (figs. S3 and S4). LRP1 was highest on CD11c$^+$MHCII$^+$ myeloid cells when compared with other immune cells, including B cells, T cells, and CD11c$^-$ monocytes. CD11c$^+$MHCII$^+$ myeloid cells include F4/80$^-$ DCs and F4/80$^+$ macrophages, which both expressed LRP1 (Fig. 3, F and G). Immunofluorescence analysis of mouse small intestine confirmed LRP1 expression by intestinal lamina propria CD11c$^+$ cells (Fig. 3H and fig. S5). When His-SAA1–retinol complexes were added to lamina propria immune cells, CD11c$^+$ myeloid cells bound more SAA relative to other immune cell populations (fig. S6). Thus, CD11c$^+$ myeloid cells express LRP1 and capture SAA-retinol complexes.

LRP1 promotes myeloid cell uptake of SAA-bound retinol

Next, we examined whether LRP1 facilitates SAA binding and retinol uptake in CD11c$^+$ myeloid cells. We generated mice with a CD11c$^+$ myeloid cell–specific deletion of the *Lrp1* gene (*Lrp1*$^{\Delta Cd11c}$ mice) and investigated bone marrow–derived myeloid cells (BM-MCs). CD11c$^+$ cells were isolated by magnetic sorting from cells

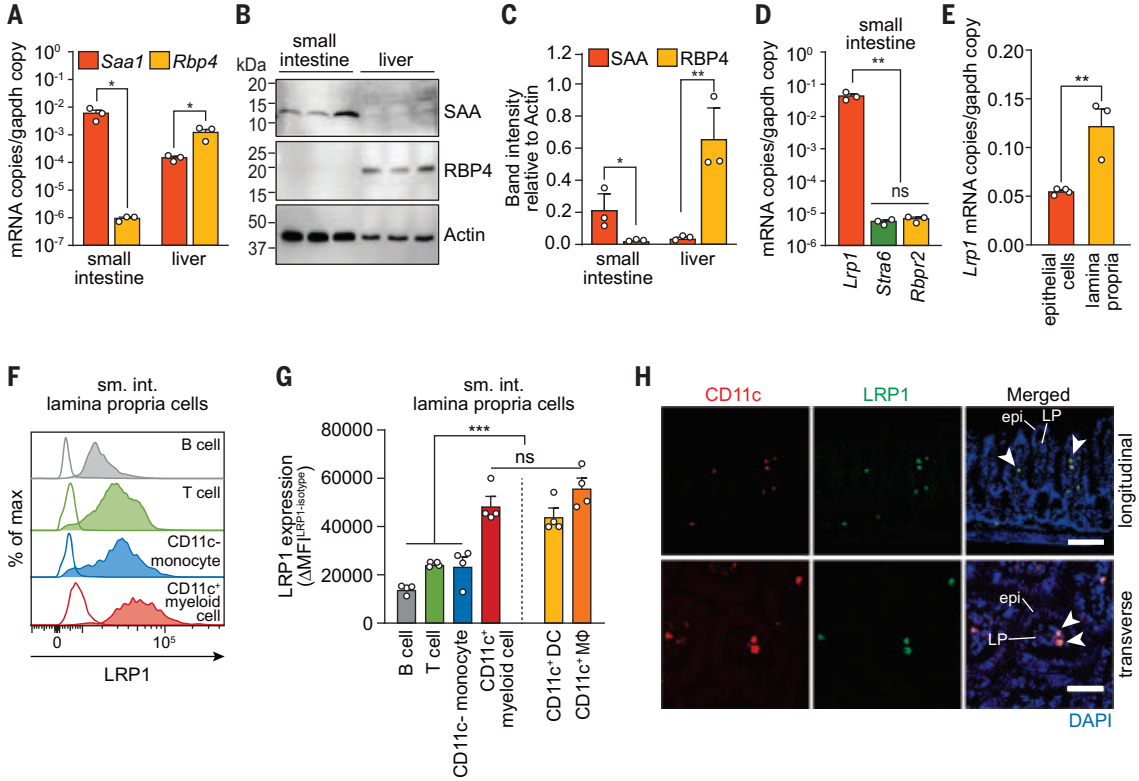


Fig. 3. LRP1 is expressed on intestinal CD11c$^+$ myeloid cells. (**A**) qPCR analysis of *Saa1* and *Rbp4* transcripts in ileum and liver. (**B** and **C**) Immunoblotting of SAA, RBP4, and actin (loading control) in mouse ileum and liver. SAA and RPB4 band intensities were measured, normalized to actin, and are shown in relative units in (C). (**D**) qPCR analysis of *Lrp1*, *Stra6*, and *Rbpr2* transcripts in mouse ileum. (**E**) qPCR analysis of *Lrp1* transcripts in small intestinal epithelial cells and immune cells isolated from the small intestinal lamina propria. (**F** and **G**) Flow cytometry analysis of LRP1 expression on B cells, T cells, monocytes, and CD11c$^+$ myeloid cells. (F) Representative histograms showing LRP1 expression. Empty histograms are from isotype controls. (G) LRP1 expression (ΔMFI) is shown as the difference in MFI between isotype-matched control and anti-LRP1 antibody staining (MFI^{LRP1}–MFI^{isotype}). (**H**) Immunofluorescence detection of CD11c (red), LRP1 (green), and nuclei (blue) in the mouse small intestine. Longitudinal (top) and transverse (bottom) sections of villi are shown. Examples of LRP1$^+$ and CD11c$^+$ cells are indicated with arrowheads. Epi, epithelium; LP, lamina propria; DAPI, 4′,6-diamidino-2-phenylindole. Scale bars in (H) indicate 100 μm (top) or 50 μm (bottom). Detection with isotype control antibody is shown in fig. S5. sm. int., small intestine; MΦ, macrophage. At least three wild-type C57BL/6 mice were analyzed in each experiment. Means ± SEMs are plotted from one [(A) to (E)] and at least two independent experiments [(F) to (H)]. For qPCR, mRNA copy numbers were calculated from the standard and normalized to *Gapdh* copy numbers. *P < 0.05; **P < 0.01; ***P < 0.001; ns, not significant; Student's t test.

grown in granulocyte-macrophage colony-stimulating factor (GM-CSF), yielding BM-MCs that included both DCs and macrophages (fig. S7, A and B) (*29*, *30*). Bone marrow–derived DCs and macrophages isolated from $Lrp1^{\Delta Cd11c}$ mice showed lowered expression of LRP1 (fig. S7C) and supported less binding of His-SAA1–retinol than BM-MCs from $Lrp1^{fl/fl}$ mice (Fig. 4, A and B, and fig. S7, D and E). Likewise, ^{3}H-retinol uptake from SAA1–^{3}H-retinol complexes was lower in BM-MCs from $Lrp1^{\Delta Cd11c}$ mice than in those from $Lrp1^{fl/fl}$ mice (Fig. 4C). Furthermore, ^{3}H-retinol uptake in $Lrp1^{fl/fl}$ BM-MCs was higher with the addition of SAA1–^{3}H-retinol than with free ^{3}H-retinol (Fig. 4C). Thus, LRP1 facilitates myeloid cell retinol uptake from SAA1-retinol complexes.

CD11c$^+$ myeloid cells convert retinol to RA through a two-step enzymatic oxidation. First, retinol is converted to retinaldehyde by alcohol dehydrogenases (ADHs) or retinol dehydrogenases (RDHs). Next, retinaldehyde is irreversibly converted to RA by members of the aldehyde dehydrogenase family [also known as retinaldehyde dehydrogenases (RALDHs)] (*31*). RALDH expression in intestinal myeloid cells is induced by vitamin A and RA (*32*). The reduced retinol uptake in $Lrp1^{\Delta Cd11c}$ myeloid cells therefore suggested that these cells might show reduced RALDH activity. We assessed RALDH activity by Aldefluor assay, which measures conversion of a fluorescent RALDH substrate by flow cytometry. The addition of SAA1-retinol increased RALDH activity in $Lrp1^{fl/fl}$ but not in $Lrp1^{\Delta Cd11c}$ myeloid cells (Fig. 4, D and E). The increase in RALDH activity was higher with SAA1-retinol than with free retinol. This activity was suppressed by the RALDH inhibitor N,N-diethylaminobenzaldehyde (DEAB) (Fig. 4, D and E). Thus, LRP1 facilitates retinol uptake from SAA1-retinol complexes, and this uptake increases RALDH activity in myeloid cells.

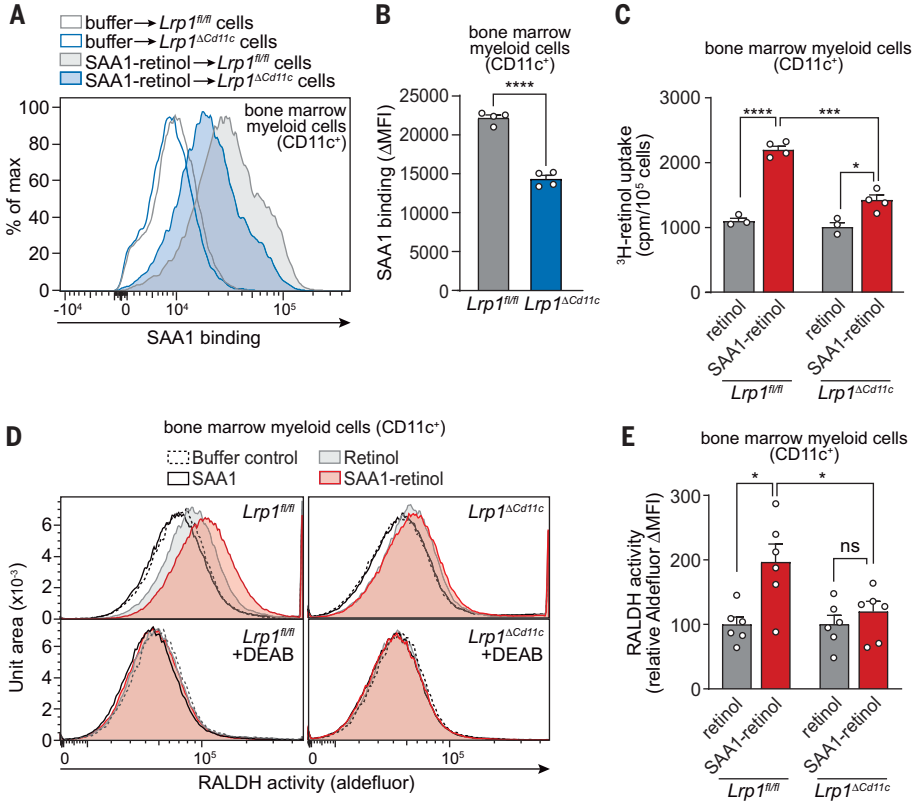


Fig. 4. LRP1 promotes myeloid cell uptake of SAA-bound retinol. CD11c$^+$ myeloid cells were isolated from bone marrow myeloid cells that were acquired from $Lrp1^{fl/fl}$ and $Lrp1^{\Delta Cd11c}$ mice and grown in GM-CSF. The CD11c$^+$ myeloid cells were used to measure SAA binding [(A) and (B)], ^{3}H-retinol uptake (C), and retinaldehyde dehydrogenase (RALDH) activity [(D) and (E)]. (**A** and **B**) Binding of SAA to CD11c$^+$ bone marrow myeloid cells was analyzed by flow cytometry under nonpermeabilizing staining conditions. A total of 1.5×10^5 cells were incubated with 1.8 μM His-SAA1–retinol complex for 1 hour at 4°C. For controls, PBS was added instead of SAA1. (A) Representative histograms are shown with empty lines representing the controls. (B) SAA binding was determined as SAA ΔMFI (MFI^{SAA}–$MFI^{control}$) and normalized to $Lrp1^{fl/fl}$ set at 100. (**C**) ^{3}H-retinol (200 nM) was added to the cells either as free retinol or in complex with SAA1. After a 2-hour incubation at 37°C, the counts per minute (cpm) in the cell pellets were determined and normalized to cell number, and $Lrp1^{fl/fl}$ were set at 100. (**D** and **E**) Measurement of cellular RALDH activity. Cells were incubated with SAA1-retinol complexes, retinol only, SAA1 only, or buffer (control) for 1 hour at 4°C. After washing and incubation for 1.5 hours at 37°C, the cells were analyzed by Aldefluor assay. The aldehyde dehydrogenase inhibitor DEAB was added to each sample as a control. (D) Representative histograms showing Aldefluor fluorescence. (E) To measure RALDH activity, the MFI of the DEAB treatment control was first subtracted from the Aldefluor MFI of each sample ($\Delta MFI = MFI^{sample} - MFI^{control}$) and then converted to relative values with the ΔMFI for the buffer control set at 0 and the retinol-only ΔMFI set at 100. Means ± SEMs are plotted from one [(A) to (C)] and two [(D) and (E)] independent experiments. All results are representative of at least two independent experiments. *$P < 0.05$; ***$P < 0.001$; ****$P < 0.0001$; ns, not significant; Student's t test.

SAAs and LRP1 promote retinol uptake by intestinal CD11c$^+$ myeloid cells in vivo

We next examined the role of SAA and LRP1 in retinol acquisition in vivo by small intestinal CD11c$^+$ myeloid cells. We previously used CRISPR-Cas9–mediated gene targeting to delete the entire mouse *Saa* locus (encompassing *Saa1* to *Saa4*) (*15*) and verified that the numbers and composition of CD11c$^+$ myeloid cells were not altered in $Saa^{-/-}$ mice (fig. S8, A and B). We measured retinol uptake by small intestinal CD11c$^+$ myeloid cells by gavaging mice with a ^{3}H-retinol tracer and tracking it to lamina propria myeloid cells. Fifteen hours after gavage, CD11c$^+$ cells from $Saa^{-/-}$ mice had acquired less ^{3}H-retinol than cells from wild-type mice (Fig. 5A and fig. S9, A and B), which indicates that SAAs promote retinol delivery to intestinal CD11c$^+$ cells. Overall ^{3}H-retinol levels were similar in the small intestines of wild-type and $Saa^{-/-}$ mice (fig. S10A), which indicates that the lowered retinol uptake by CD11c$^+$ cells from $Saa^{-/-}$ mice did not arise from a decrease in intestinal retinol absorption. ^{3}H-retinol levels were also similar in lamina propria CD11c$^-$ cells from wild-type and $Saa^{-/-}$ mice, which demonstrates that SAAs selectively promote retinol uptake in CD11c$^+$ cells.

CD11c$^+$ cells from $Saa^{-/-}$ mice had reduced expression of *Adh4*, *Rdh7*, and *Aldh1a1* (Fig. 5B). These genes encode enzymes that convert retinol to RA (*33*–*35*), and their expression is induced by retinol or RA (fig. S10B) (*32*). By contrast, expression of these genes was similar in CD11c$^-$ cells from wild-type and $Saa^{-/-}$ mice (fig. S10C), consistent with the idea that SAAs selectively deliver retinol to CD11c$^+$ cells. Likewise, RALDH activity was lower in CD11c$^+$MHCII$^+$ myeloid cells from $Saa^{-/-}$ mice than in those from wild-type mice (Fig. 5, C and D). Thus, SAAs facilitate myeloid cell retinol uptake that promotes the expression of enzymes that convert retinol to RA.

Next, we compared $Lrp1^{fl/fl}$ and $Lrp1^{\Delta Cd11c}$ mice to determine whether LRP1 also facilitates retinol uptake by intestinal CD11c$^+$ myeloid

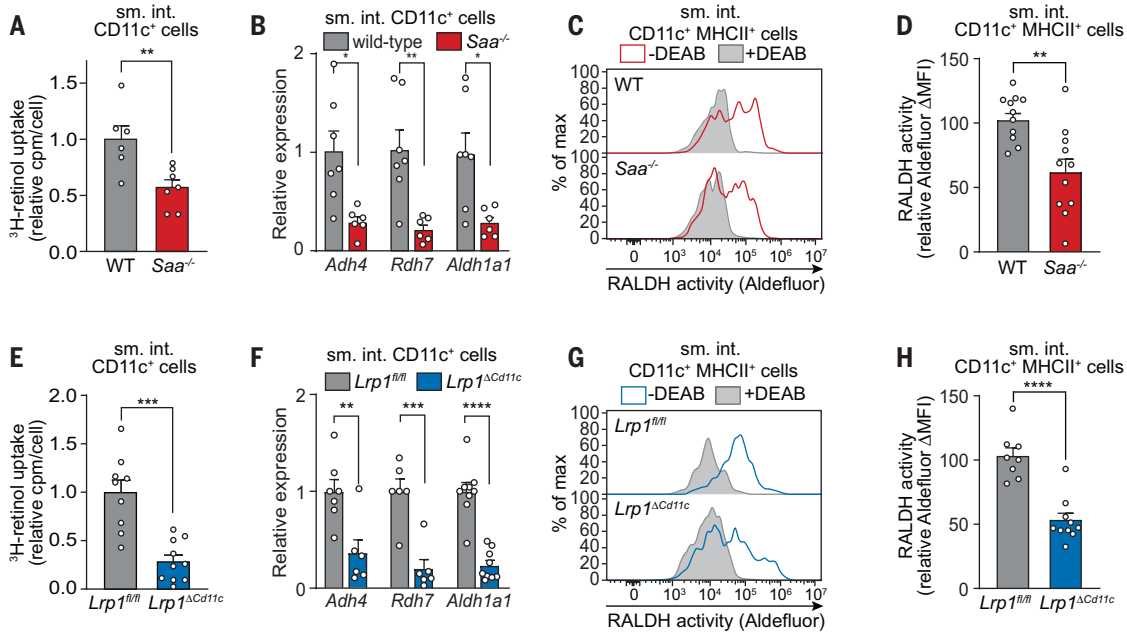


Fig. 5. SAA and LRP1 promote retinol uptake by intestinal CD11c$^+$ myeloid cells in vivo. Wild-type (WT) and *Saa*$^{-/-}$ mice [(A) to (D)] or *Lrp1*$^{fl/fl}$ and *Lrp1*$^{\Delta Cd11c}$ [(E) to (H)] mice were analyzed. (**A** and **E**) Mice were gavaged with ^{3}H-retinol and CD11c$^+$ cells were isolated from the small intestinal (sm. int.) lamina propria. Counts per minute (cpm) were determined and normalized to cell number, and wild-type (A) and *Lrp1*$^{fl/fl}$ (E) were set at 1. (**B** and **F**) qPCR analysis of transcripts encoding proteins involved in conversion of retinol to RA in small intestinal lamina propria CD11c$^+$ cells. Transcript abundances were normalized to *Gapdh* transcript abundance and expressed relative to wild-type (B) and *Lrp1*$^{fl/fl}$ mice (F). (**C** and **G**) Retinaldehyde dehydrogenase (RALDH) activity of CD11c$^+$MHCII$^+$ myeloid cells (live CD45$^+$CD11c$^+$MHCII$^+$CD3$^-$B220$^-$) was assessed by Aldefluor assay. Representative histograms showing Aldefluor fluorescence are shown. Filled gray histograms are from controls incubated with the ALDH inhibitor DEAB, and empty lines show samples without DEAB. (**D** and **H**) RALDH activity was measured as Aldefluor ΔMFI (MFI^{sample}–MFI^{control}). Means ± SEMs from at least three independent experiments with $n \geq 5$ mice per group are plotted. *$P < 0.05$; **$P < 0.01$; ***$P < 0.001$; ****$P < 0.0001$; Student's t test.

cells. We first verified that the numbers and composition of CD11c$^+$ myeloid cells did not differ between *Lrp1*$^{fl/fl}$ and *Lrp1*$^{\Delta Cd11c}$ mice (fig. S11, A and B). As expected, *Lrp1* transcripts and protein were less abundant in small intestinal CD11c$^+$ cells from *Lrp1*$^{\Delta Cd11c}$ mice than in those from *Lrp1*$^{fl/fl}$ mice while remaining similar in CD11c$^-$ cells (fig. S12, A and B). After ^{3}H-retinol gavage, CD11c$^+$ cells from *Lrp1*$^{\Delta Cd11c}$ mice acquired less ^{3}H-retinol than cells from *Lrp1*$^{fl/fl}$ mice (Fig. 5E), which indicates that LRP1 facilitates retinol uptake by intestinal CD11c$^+$ cells. Consistent with our findings in wild-type and *Saa*$^{-/-}$ mice (fig. S10A), ^{3}H-retinol levels in lamina propria CD11c$^-$ cells from *Lrp1*$^{fl/fl}$ and *Lrp1*$^{\Delta Cd11c}$ mice were similar (fig. S13A), demonstrating that LRP1 selectively promotes retinol uptake in CD11c$^+$ cells. Finally, in agreement with our findings in *Saa*$^{-/-}$ mice, CD11c$^+$ cells from *Lrp1*$^{\Delta Cd11c}$ mice showed reduced expression of *Adh4*, *Rdh7*, and *Aldh1a1* (Fig. 5F and fig. S13B) and lower RALDH activity as compared with *Lrp1*$^{fl/fl}$ mice (Fig. 5, G and H). Thus, SAAs and their LRP1 receptor promote retinol uptake by CD11c$^+$ myeloid cells and increase the expression of enzymes that convert retinol to RA.

SAA and LRP1 promote vitamin A–dependent adaptive immunity in the intestine

We next assessed whether SAA and LRP1 promote vitamin A–dependent adaptive immunity in the intestine. RA-producing myeloid cells induce expression of the gut-homing receptor CC-chemokine receptor 9 (CCR9) on B cells and CD4$^+$ T cells in mesenteric lymph nodes (mLNs) and gut-associated lymphoid tissue, which directs the lymphocytes to the intestine (*1*, *2*, *13*). Consistent with the reduced retinol uptake in their RA-producing myeloid cells, the small intestines of *Saa*$^{-/-}$ mice had reduced frequencies of CD4$^+$ T cells imprinted with CCR9 (Fig. 6, A and B), reduced numbers of CCR9$^+$CD4$^+$ T cells (Fig. 6B), and reduced overall numbers of CD4$^+$ T cells (Fig. 6C) relative to wild-type mice. CCR9$^+$ B cell frequencies (Fig. 6, D and E) and numbers (Fig. 6E) as well as overall B cell numbers (Fig. 6F) were also reduced in the small intestines of *Saa*$^{-/-}$ mice. RA also promotes the development of FOXP3$^+$ regulatory T cells (T_{regs}) (*6*, *9*, *12*). However, T_{reg} frequencies among CD4$^+$ T cells were similar when comparing the small intestines (fig. S14, A and B) and mLNs (fig. S14, C and D) of wild-type and *Saa*$^{-/-}$ mice. SAAs therefore regulate B cell and CD4$^+$ T cell homing to the intestine but do not appear to be required for the generation of intestinal T_{regs}.

Lrp1$^{\Delta Cd11c}$ mice were similar to *Saa*$^{-/-}$ mice, with reduced frequencies and numbers of CCR9$^+$CD4$^+$ T cells (Fig. 6, J and K) and reduced total numbers of CD4$^+$ T cells (Fig. 6L) in the small intestine. *Lrp1*$^{\Delta Cd11c}$ mice had decreased frequencies and numbers of CCR9$^+$ B cells (Fig. 6, M and N) and decreased total numbers of B cells (Fig. 6O) in the small intestine. T_{reg} frequencies among CD4$^+$ T cells were also similar in the small intestines (fig. S15, A and B) and mLNs (fig. S15, C and D) of *Lrp1*$^{fl/fl}$ and *Lrp1*$^{\Delta Cd11c}$ mice. Thus, LRP1 also regulates B cell and CD4$^+$ T cell homing to the intestine but is not required for the generation of intestinal T_{regs}.

T helper 17 (T_H17) cells are specialized CD4$^+$ T cells that secrete a distinct set of cytokines, including interleukin-17 (IL-17). Although SAAs are not required for T_H17 cell lineage commitment, they boost T_H17 cell effector function by stimulating IL-17A production (*16*). Accordingly, T_H17 cell frequencies among CD4$^+$ T cells were similar in the small intestines (fig. S14, A and B) and mLNs (fig. S14, C and D) of wild-type and *Saa*$^{-/-}$ mice, but IL-17A production was reduced in T_H17 cells from *Saa*$^{-/-}$ mice (fig. S14, E and F). Similarly, T_H17 cell frequencies were similar in *Lrp1*$^{fl/fl}$ and *Lrp1*$^{\Delta Cd11c}$ mice (fig. S15, A to D), but IL-17A production was reduced in T_H17 cells from *Lrp1*$^{\Delta Cd11c}$ mice (fig. S15, E and F). Thus, SAAs and myeloid cell LRP1 both regulate T_H17 cell effector function.

Finally, *Saa*$^{-/-}$ and *Lrp1*$^{\Delta Cd11c}$ mice were deficient in the production of IgA, which defends against invading intestinal pathogens and maintains homeostasis with the microbiota (*36*–*38*). *Saa*$^{-/-}$ mice had reduced frequencies and numbers of small intestinal IgA$^+$ cells (Fig. 6, G and H) and decreased fecal IgA concentrations (Fig. 6I) when compared with wild-type mice. Similarly, frequencies and numbers of IgA-producing cells (Fig. 6, P and Q)

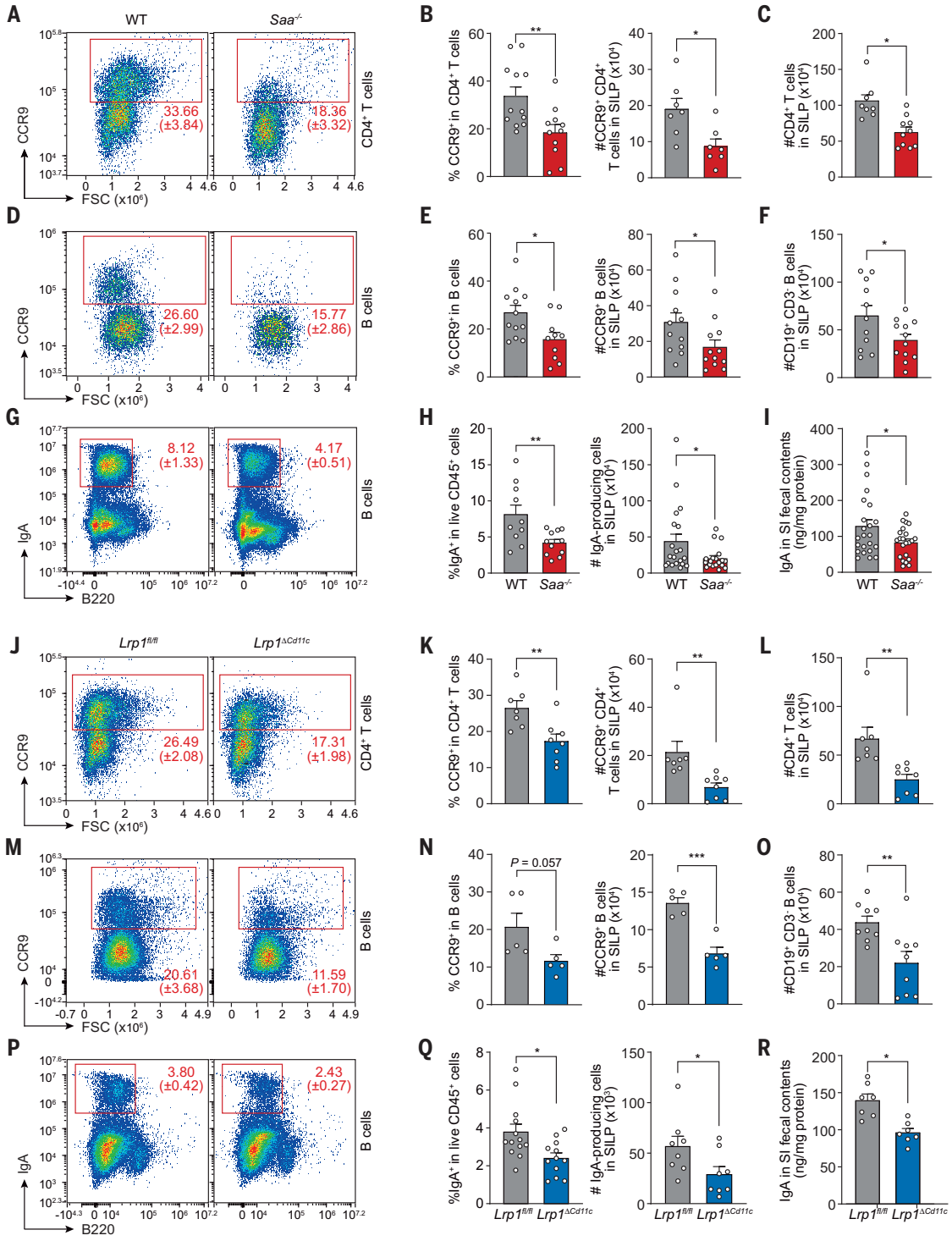


Fig. 6. SAA and LRP1 promote vitamin A–dependent immunity in the intestine. Small intestinal lamina propria (SILP) cells from wild-type (WT) and $Saa^{-/-}$ mice [(A) to (I)], and $Lrp1^{fl/fl}$ and $Lrp1^{\Delta Cd11c}$ mice [(J) to (R)] were analyzed. (**A** and **J**) Representative flow cytometry plots of $CD4^+$ T cells (live $CD45^+CD3^+CD4^+CD19^-CD8^-$). (**B** and **K**) Frequencies of $CCR9^+$ cells in $CD4^+$ T cells (left) and absolute numbers of $CCR9^+CD4^+$ T cells (right). (**C** and **L**) Total numbers of $CD4^+$ T cells ($CD45^+CD3^+CD4^+CD19^-CD8^-$). (**D** and **M**) Representative flow cytometry plots of B cells (live $CD45^+CD19^+CD3^-$). (**E** and **N**) Frequencies of $CCR9^+$ cells in B cells (left) and absolute numbers of $CCR9^+$ B cells (right). (**F** and **O**) Total numbers of B cells ($CD45^+CD19^+CD3^-$). (**G** and **P**) Representative flow cytometry plots of IgA^+ cells (live $CD45^+CD3^-$). (**H** and **Q**) Frequencies of IgA^+ cells in total live $CD45^+$ cells (left) and numbers of IgA-producing cells ($IgA^+CD45^+CD3^-$) (right). (**I** and **R**) Quantification of IgA from small intestinal fecal contents by ELISA. Data represent $n \geq 5$ mice per group from at least two independent experiments. Means ± SEMs are plotted. $^*P < 0.05$; $^{**}P < 0.01$; Student's t test.

and fecal IgA concentrations (Fig. 6R) were decreased in the small intestines of *Lrp1*$^{\Delta Cd11c}$ when compared with *Lrp1*$^{fl/fl}$ mice. These findings are consistent both with the overall reduction in intestinal B cells as a result of reduced homing and with the role of RA-producing myeloid cells in promoting the development of IgA-producing cells from B cells (*2*). The differences in immune cell frequencies did not arise from altered microbiota taxonomic composition because this was similar when comparing wild-type to *Saa*$^{-/-}$ mice and *Lrp1*$^{fl/fl}$ to *Lrp1*$^{\Delta Cd11c}$ mice (fig. S16). Thus, SAA and LRP1 promote intestinal lymphocyte homing and IgA production, thereby implicating SAA-mediated retinol delivery in the development of vitamin A–dependent intestinal immunity.

SAAs and LRP1 promote immunity to enteric bacterial infection

The importance of SAAs and LRP1 for intestinal adaptive immunity suggests that these proteins might promote immunity to enteric bacterial infection. We tested this idea using the gastrointestinal pathogen *Salmonella enterica* serovar Typhimurium (*S.* Typhimurium). Before infection, mice were immunized twice by oral gavage with heat-killed *S.* Typhimurium (Fig. 7A). This resulted in higher levels of *S.* Typhimurium–specific fecal IgA in wild-type mice compared with *Saa*$^{-/-}$ mice and in *Lrp1*$^{fl/fl}$ mice compared with *Lrp1*$^{\Delta Cd11c}$ mice (Fig. 7, B and D). Accordingly, *Saa*$^{-/-}$ and *Lrp1*$^{\Delta Cd11c}$ mice showed higher mortality when orally infected with *S.* Typhimurium after immunization (Fig. 7, C and E). Thus, SAAs and LRP1 promote specific immunity after oral immunization and resistance to enteric pathogen infection.

Discussion

We have identified SAAs as retinol-binding proteins that deliver retinol to RA-producing intestinal myeloid cells. SAA-retinol complexes bind to LRP1 on the myeloid cell surface and are endocytosed, which provides retinol for the enzymatic generation of RA. Consequently, SAAs and LRP1 promote the development of vitamin A–dependent adaptive immunity, including B and T cell homing to the intestine and IgA production, and enhance resistance to enteric infection after immunization. Our findings therefore identify a molecular basis for retinol acquisition by intestinal myeloid cells and illuminate a mechanism that is essential for vitamin A–dependent immunity (fig. S17).

Previously, we had found that vitamin A promotes epithelial cell *Saa* expression through the transcription factor RARβ, which is activated by RA and binds directly to *Saa* promoters (*17*). *Rarb*$^{\Delta IEC}$ mice, which selectively lack RARβ in intestinal epithelial cells, have defects in intestinal vitamin A–dependent immunity, including reduced gut homing of CD4$^+$ T cells and lowered IgA production (*17*). Our finding that SAAs deliver retinol to myeloid cells provides a molecular explanation for reduced vitamin A–dependent immunity in *Rarb*$^{\Delta IEC}$ mice. Furthermore, *Rarb*$^{\Delta IEC}$ mice show reduced SAA expression that is restricted to epithelial cells (*17*), suggesting that epithelial SAAs, rather than SAAs produced by the liver, deliver retinol to intestinal myeloid cells.

Our results provide molecular insight into how the intestinal microbiota shapes intestinal adaptive immunity. Expression of SAAs by intestinal epithelial cells requires the microbiota (*39*, *40*), which activates *Saa* expression through an immunological signaling circuit (*16*). Our findings suggest that gut microbes promote vitamin A–dependent adaptive immunity by regulating epithelial SAA expression. These findings help explain long-standing observations of reduced numbers of B cells and CD4$^+$ T cells and lowered IgA production in the intestines of germ-free mice (*41*).

A key question for future research is whether SAAs deliver retinol to other target cells. For example, our finding that 3T3-L1 adipocytes

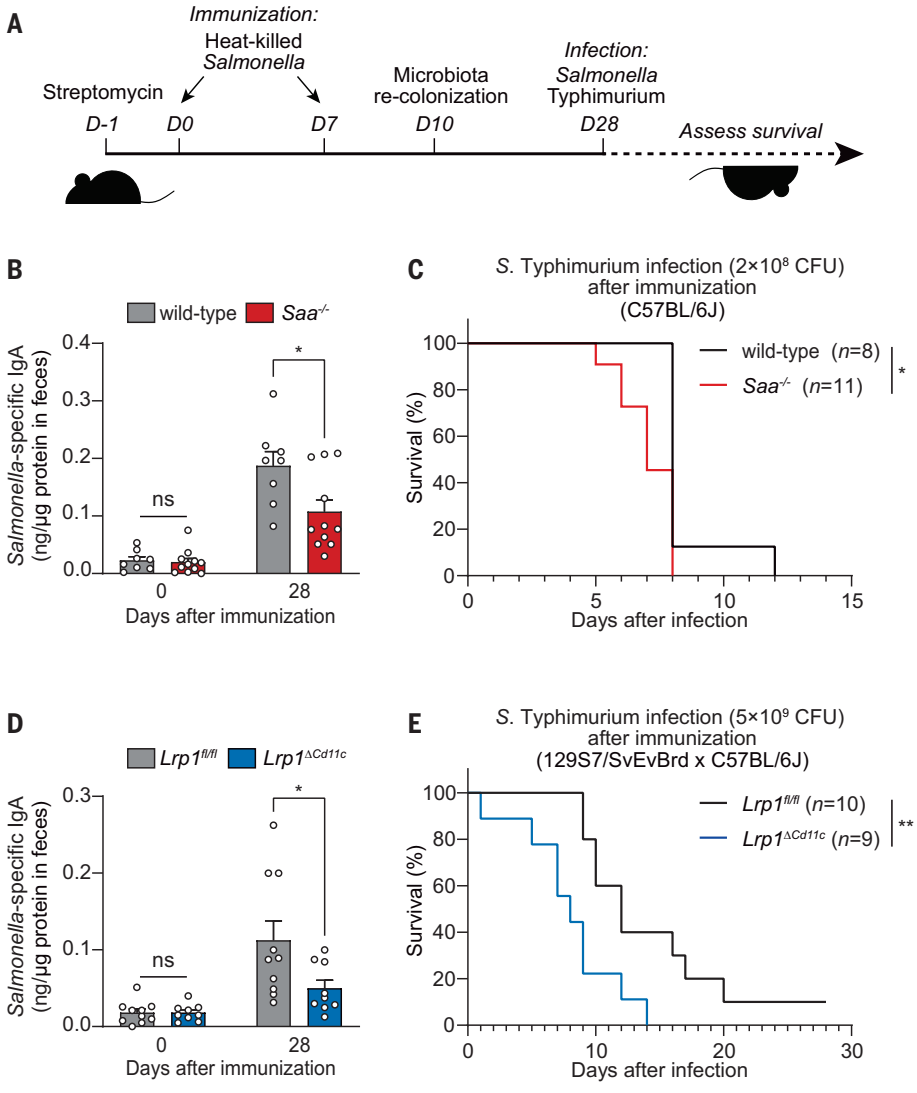


Fig. 7. SAA and LRP1 promote immunity to enteric bacterial infection. (**A**) Wild-type and *Saa*$^{-/-}$ mice [(B) and (C)] and *Lrp1*$^{fl/fl}$ and *Lrp1*$^{\Delta Cd11c}$ mice [(D) and (E)] were immunized with 10^{10} CFU of heat-killed *S.* Typhimurium twice through oral gavage. Four weeks after the first immunization, the mice were orally infected with 2×10^8 CFU (C) and 5×10^9 CFU (E) of log-phase *S.* Typhimurium (the infection dose differs because resistance to infection differs according to mouse background). (**B** and **D**) *S.* Typhimurium–specific fecal IgA was measured by ELISA. Means ± SEMs are plotted. *$P < 0.05$; Student's *t* test. (**C** and **E**) Survival rates were monitored after infection. Data represent results from five cohoused cages of wild-type and *Saa*$^{-/-}$ littermates [(B) and (D)] and five cohoused cages of *Lrp1*$^{fl/fl}$ and *Lrp1*$^{\Delta Cd11c}$ littermates [(D) and (E)]. *$P <$ 0.05; **$P < 0.01$; ns, not significant; log-rank test.

express LRP1 suggests that SAAs may deliver retinol to adipose tissue, which is a major extrahepatic retinol storage site (*18*). Additionally, SAAs may deliver retinol to T_H17 cells, thereby promoting T_H17 cell effector functions (*16*). Supporting this idea, T_H17 cell function requires vitamin A, as mice given a vitamin A–deficient diet show reduced intestinal IL-17 production (*12*), and T_H17 cells from mice lacking T cell RARα produce less IL-17 (*12*). In vitro experiments suggest that SAAs affect T_H17 cells through a direct interaction with the T cells (*16*, *42*). It is possible that the expression of LRP1 on T cells, although lower than that on myeloid cells, is sufficient to support SAA binding and retinol uptake. Alternatively, T cells may express a distinct SAA receptor. However, our finding that T_H17 cell effector functions are reduced in $Lrp1^{\Delta Cd11c}$ mice suggests the involvement of LRP1-expressing myeloid cells. This is consistent with a previously reported requirement for myeloid cells in IL-17 production by T cells in response to commensal bacteria (*43*, *44*).

SAAs also carry retinol in the circulation and protect against systemic bacterial infection (*14*). It therefore appears likely that SAAs also deliver retinol to cells that promote systemic immunity. This is a topic of ongoing and future research that should clarify whether SAAs represent a general mechanism for mobilizing retinol to the immune system during a microbiological or immunological challenge.

Finally, by illuminating how vitamin A is mobilized to the intestinal immune system, our results may offer additional approaches for enhancing resistance to infection and for increasing the efficacy of mucosal vaccines, which depend on adequate dietary vitamin A (*45*). Our findings also suggest the possibility of selectively regulating the availability of retinol to the immune system during inflammatory disease, perhaps by deploying small-molecule inhibitors of the SAA-retinol or SAA-LRP1 binding interactions.

Materials and methods

Mice

C57BL/6 wild-type, $Saa^{-/-}$, $Lrp1^{fl/fl}$, and $Lrp1^{\Delta Cd11c}$ mice were bred and maintained in the barrier facility at the University of Texas Southwestern Medical Center. $Saa^{-/-}$ mice were generated using CRISPR-Cas9 genome editing on a C57BL/6J background (*15*). $Lrp1^{fl/fl}$ mice (*46*) on a 129S7/SvEvBrd genetic background were used to generate a $CD11c^{+}$ cell-specific *Lrp1* knockout ($Lrp1^{\Delta Cd11c}$) mouse by crossing with a mouse expressing Cre recombinase under the control of the CD11c promoter [Jackson Laboratories; B6.Cg-Tg (Itgax-cre)1-1Reiz/J]. Mice 8 to 12 weeks of age were used for all experiments and cohoused littermates were used as controls. Experiments were performed using protocols approved by the Institutional Animal Care and Use Committees of the UT Southwestern Medical Center.

Cell culture

Cell lines were purchased from ATCC and cultured at 37°C under 5% CO_2. 3T3-L1 preadipocytes (ATCC CL-173) were cultured in Dulbecco's minimum essential medium (DMEM) containing 10% bovine calf serum, 100 U/ml of penicillin, and 100 μg/ml of streptomycin until confluence. Two days postconfluence, the cells were differentiated with 1.5 μg/ml of insulin, 1 μM dexamethasone, 500 μM 3-isobutyl-1-methylxanthine (IBMX), and 1 μM rosiglitazone in DMEM/F12 (1:1) containing 10% fetal bovine serum (FBS). After 48 hours of differentiation, the cells were treated with 1.5 μg/ml insulin in DMEM/F12 (1:1) with 10% (v/v) FBS, 100 U/ml of penicillin, and 100 μg/ml of streptomycin. The culture medium was changed every 2 days for 7 to 9 days. Wild-type and *Lrp1*-deficient murine embryonic fibroblasts, MEF1 (ATCC CRL-2214) and PEA13 (ATCC CRL-2216), respectively, were cultured in DMEM containing 10% FBS, 100 U/ml of penicillin, and 100 μg/ml of streptomycin. Isolated bone marrow cells from femurs and tibiae were cultured for 6 days in RPMI containing 10% FBS, 50 μM β-mercaptoethanol, 100 U/ml of penicillin, 100 μg/ml of streptomycin, and 20 ng/ml of GM-CSF (*29*). Adherent and loosely adherent cells were harvested by scraping and subjected for further experiments.

Proteins, antibodies, and reagents

Recombinant mouse SAA1 and SAA3 were expressed and purified as described previously (*14*, *15*). Recombinant Fc-tagged human LRP1-CII, -CIII, and -CIV containing ligand-binding cluster II, III, and IV of LRP1 were purchased from R&D Biosystems. 6X histidine-tagged human RAP was purchased from Molecular Innovations and was used in binding assays after histidine-tag removal as described previously (*15*). Briefly, RAP protein was digested with thrombin (Roche), incubated overnight at 4°C, and purified using size exclusion chromatography on a Superdex 75 10/300 GL column (GE Life Sciences) in phosphate-buffered saline (PBS) with 10% glycerol. Rabbit anti-SAA antiserum was produced previously (*14*). Armenian hamster monoclonal anti-CD11c (Clone N418) and rabbit monoclonal anti-LRP1 antibody (Clone EPR3724) recognizing 85-kDa light chain of LRP1 were purchased from Abcam. Mouse monoclonal anti-6X His tag (Clone HIS.H8) (Abcam) and PE-conjugated mouse monoclonal anti-6X His tag (Clone AD1.1.10) (R&D Biosystems) were used for the detection of His-tagged SAA by immunoblotting and flow cytometry respectively. Antibodies used for flow cytometry analysis are listed in table S3. All-trans retinol was purchased from Sigma-Aldrich.

Immunofluorescence assay

Mouse ileum was washed with PBS, fixed in Bouin's fixative overnight at 4°C and embedded in paraffin. Sections were washed in xylene twice and rehydrated in decreasing concentrations of ethanol (100, 95, 70, 50, and 0%). Slides were boiled in 10 mM sodium citrate (pH 6.0) for 25 min and washed twice in PBS. For immunofluorescence assay of adipocytes, cells were seeded and differentiated on cover glasses, fixed with 4% paraformaldehyde for 15 min at room temperature, and washed with PBS-T (PBS, 0.05% Tween-20). Samples were incubated with blocking buffer (10% FBS, 1% BSA, 1% Triton X-100 in PBS) for 1 hour at room temperature and incubated with primary antibodies (anti-LRP1, 1:200 dilution; anti-CD11c, 1:200 dilution) in the blocking buffer at 4°C overnight. Cy3 anti-rabbit secondary antibody (Thermo Fisher Scientific) and AlexaFluor 647-conjugated anti-Armenian hamster secondary antibody (Abcam) were diluted 1:400 and applied to slides for 1 hour at room temperature in the dark. Samples were washed and mounted with 4′,6-diamidino-2-phenylindole (DAPI) Fluoromount-G (Southern Biotechnology). For a nonpermeabilizing staining condition, buffers without Triton X-100 were used. Images were captured using a Zeiss AxioImage MI microscope with Zeiss AxioCam MRm Rev3 and Zeiss EC Plan-Neofluar 10X/0.30 M27 objective lens.

Analysis of cell surface binding of SAA by flow cytometry

Wild-type ($Lrp1^{+/+}$) and *Lrp1*-deficient ($Lrp1^{-/-}$) fibroblasts were detached from culture plates with PBS with 1.5 mM EDTA and washed twice with serum-free media. Suspensions containing 2×10^5 cells in 0.2 ml of serum-free culture media were incubated with His-SAA1. For competition studies, nontagged SAA1 proteins were added as indicated together with His-tagged SAA1 proteins. After incubation for 1 hour at 4°C, cells were washed twice with ice-cold PBS, fixed with 4% paraformaldehyde, stained with PE-conjugated anti–His-tag antibody, and subjected to flow cytometry by using LSRII (BD Bioscience) or Novocyte 3005 (ACEA Biosciences). To assess LRP1-specific SAA binding, the differences in SAA binding ($\Delta MFI = MFI^{SAA} - MFI^{PBS}$) between wild-type cells and *Lrp1*-deficient cells were analyzed, expressed as $\Delta\Delta MFI$ ($\Delta MFI^{Lrp1+/+} - \Delta MFI^{Lrp1-/-}$), and fit with GraphPad Prism 7 using the nonlinear regression, one site–binding equation. For adipocytes, His-SAA1 proteins were added to 2×10^5 differentiated adipocytes grown in 96-well plates in DMEM/F12 (1:1) and processed with the same staining procedures. To analyze SAA binding to lamina propria cells, one million small intestinal lamina propria (SILP) cells were isolated and incubated with the His-SAA1–retinol complex (7 μM)

for 20 min at 4°C in serum-free RPMI. The cells were then washed and fixed as described above and stained for His-tag to detect His-SAA1 alongside immune cell markers.

Cellular retinol uptake assay

Radioactive 11,12-^{3}H(N)-retinol was purchased from PerkinElmer. For the in vitro retinol uptake assay, SAA1 was incubated with ^{3}H-retinol at a 3:1 molar ratio at 4°C for at least 2 hours in serum-free media containing protease inhibitors (Roche). The SAA1-retinol complex was purified using PD-10 desalting column (GE Healthcare). Cells were incubated with 480 nM of SAA1–^{3}H-retinol complex or free ^{3}H-retinol in the serum-free media at 37°C and 5% CO_2 (Fig. 2F). Cells were incubated with 600 nM SAA1–^{3}H-retinol complex with and without RAP in serum-free media at 4°C for 1 hour, washed twice with cold media, and incubated at 37°C and 5% CO_2 for 3 hours (Fig. 2G) and for 2 hours (Fig. 4C). The reactions were stopped by washing the cells with ice-cold PBS and solubilizing the cells in Biosol solution (National Diagnostics). For the in vivo retinol uptake assay, ^{3}H-retinol was diluted in corn oil and fed to mice (1 μCi per mouse). Fifteen to 18 hours later, immune cells were isolated from the small intestine, and CD11c^{+} cells were isolated by magnetic sorting. Cells (2×10^{5}) were solubilized in 0.5 ml of Biosol solution. A 3.5-ml volume of Biosinct solution (National Diagnostics) was mixed with each sample and radioactivity was measured with a liquid scintillation analyzer (PerkinElmer) and normalized to cell number.

SAA-receptor purification and identification

A hetero-bifunctional cross-linker, Sulfo-SANPAH (Thermo Fisher Scientific), was used to cross-link SAA with its putative receptor on the adipocyte surface, similar to a previously described procedure (*27*). The amine-reactive group on the cross-linker was first covalently linked to the purified His-SAA1 by incubating 25 μM of purified His-SAA1 protein with 2.3 mM sulfo-SANPAH in PBS for 1 hour on ice. The reaction was stopped by adding glycine to a final concentration of 80 mM and SAA1–cross-linker conjugate was purified using a PD-10 desalting column (GE Healthcare) in PBS. The conjugate was mixed with retinol and then added to adipocytes in serum-free medium. After 20 min of incubation at 4°C, the mixture was ultraviolet (UV)–irradiated to cross-link SAA1 and its receptor using a UV transilluminator (Syngene). Cell pellets were collected and lysed by sonication in PBS containing 1% Triton X-100 and 0.1% SDS to solubilize membrane proteins. The proteins were bound to Ni-NTA resin (Qiagen) overnight at 4°C. The resin was washed twice with PBS and three times with PBS containing 25 mM imidazole. SAA1-receptor complexes were eluted in PBS containing 250 mM imidazole, mixed with SDS-loading buffer, and subjected to SDS–polyacrylamide gel electrophoresis (SDS-PAGE). The protein band identified by immunoblot as containing SAA, which was absent in the negative controls, was excised, digested with trypsin, and run on an Orbitrap Fusion Lumos mass spectrometer for liquid chromatography with tandem mass spectrometry (LC-MS/MS) analysis at the University of Texas Southwestern Medical Center Proteomics Core. Proteins were identified using Proteome Discover 2.2.

Immunoblotting assay

Tissue or cell lysates were separated using a 4 to 20% gradient SDS-PAGE gel then transferred to a polyvinylidene difluoride (PVDF) membrane. Membranes were blocked with 5% nonfat milk in TBS-T buffer (0.1% Tween-20 in Tris-buffered saline), and then were sequentially incubated with primary antibodies and horseradish peroxidase (HRP)–conjugated secondary antibodies. Membranes were visualized using a Bio-Rad ChemiDoc Touch system.

Recombinant expression and purification of full-length LRP1 ectodomain

The full-length ectodomain of human LRP1 [residues 1-4414, National Center for Biotechnology Information (NCBI) accession no.: NM_002332.3] and human RAP (NCBI accession no.: NM_002337.4) containing a C-terminal 6xHis tag were cloned into a pEZT-BM vector (*47*). The baculovirus was generated in Sf9 cells (Thermo Fisher Scientific) following the standard protocol. To boost the protein yield, the full-length ectodomain of human LRP1 was coexpressed with RAP in HEK293F cells (Life Technologies) at a ratio of 1:40 (virus:cells, v:v) and supplemented with 10 mM sodium butyrate. Cells were cultured in suspension at 37°C and the medium was harvested after 48 hours of infection. The medium containing the secreted LRP1-RAP protein complex was incubated with Ni-NTA resin (Qiagen) overnight with gentle agitation at 4°C. To purify LRP1-RAP protein complex, the resin was collected on a disposable gravity column (Bio-Rad), washed three times with buffer A (15 mM Tris-HCl pH 8.0, 150 mM NaCl, and 30 mM imidazole), and the His-tagged RAP protein together with the nontagged LRP1 protein was eluted with buffer B (15 mM Tris-HCl pH 8.0, 150 mM NaCl, and 300 mM imidazole). Size exclusion chromatography (Superose 6 Increase 10/300 GL, GE Healthcare) was used to remove the excess free RAP protein and purify the LRP1-RAP protein complex in buffer containing 10 mM Tris-HCI pH 7.2 and 100 mM NaCl. To dissociate the LRP1-RAP protein complex and purify the free LRP1 protein, fractions containing the LRP1-RAP protein complex were pooled together and subjected to size exclusion chromatography in buffer containing 10 mM MES (pH 5.5) and 100 mM NaCl. Fractions from size exclusion chromatography were analyzed by Coomassie staining after SDS-PAGE, and the fractions containing the full-length ectodomain of human LRP1 protein were pooled and concentrated for future experiments. The fractions containing RAP protein were pooled separately and used in experiments.

Pull-down assay

Fc-tagged human LRP1-CII, LRP1-CIII, LRP1-CIV, and control IgG-Fc were used (R&D Systems). LRP1 proteins (250 nM) and IgG-Fc were individually attached to 40 μl of Dynabead protein G magnetic beads (Thermo Fisher Scientific) using Fc-tags. After unbound proteins were removed by washing twice with PBS, SAA1-retinol complex (800 nM) was added to the beads and incubated for overnight at 4°C. The beads were washed five times with PBS containing 0.025% Tween-20 and the bound protein complexes were isolated by magnetic separation.

Size exclusion chromatography and purification of the SAA-retinol complex

Binding of SAA1 to the LRP1 ectodomain was confirmed by size exclusion chromatography. Purified SAA1 was incubated with retinol at a molar ratio of 1:1.5 at 4°C in the dark for 20 min to allow formation of the SAA1-retinol complex, followed by passage over a Superdex 75 10/300 GL size exclusion chromatography column (GE Healthcare) to remove the excess retinol. Next, the SAA1-retinol complex was mixed with the purified full-length ectodomain of LRP1 at a molar ratio of 10:1 in buffer containing 10 mM MES pH 5.5 and 100 mM NaCl. The mixture was incubated on ice for 1 hour and then loaded onto a Superose 6 increase 10/300 GL column (GE Healthcare). As controls, LRP1 ectodomain and SAA1-retinol were individually analyzed in the same way.

Microscale thermophoresis

The dissociation constant for the LRP1-SAA1 interaction was determined by microscale thermophoresis (*48*). Purified SAA1 was labeled with Alexa Fluor 594 using the Microscale Protein Labeling Kit (Invitrogen). Labeled SAA1 was incubated with retinol [or dimethyl sulfoxide (DMSO)] at a 3:1 molar ratio for 2 hours at 4°C in MST buffer (150 mM NaCl, 5 mM $CaCl_2$, 0.05% (v/v) Tween 20, and 20 mM HEPES, pH 6.5). Next, a 16-fold titration series of purified LRP1 ectodomain (0 to 1.75 μM) diluted 1:1 with the MST buffer was mixed with SAA1 at 50 nM. The mixtures containing diluted LRP1 and SAA1 were incubated for 30 min at room temperature in the dark to enable binding. Each titration sample was then loaded into a premium capillary (NanoTemper)

and analyzed on a Monolith NT.115 Pico (NanoTemper). LRP1-dependent fluorescence enhancement was observed, and absolute fluorescence was used to calculate the K_d. The specificity of the binding event was carefully validated by the SDS-denaturation test according to the manufacturer's protocol. Binding isotherms were deduced by using PALMIST software (*49*) and the graph was created in GUSSI (*50*).

Trypsin protection assay

Wild-type and *Lrp1*-deficient fibroblasts (2.5×10^5) were incubated with His-SAA1–retinol complex (1 μM) at 4°C in serum-free DMEM for 1 hour to allow SAA to bind to cell surface LRP1. Unbound SAAs in the media were removed and cells were washed twice with cold PBS. Prewarmed DMEM was added, and the cells were moved to 37°C to initiate endocytosis. In some cases, 25 μM Pitstop2 (Abcam) was added to the cells to block clathrin-mediated endocytosis before the 37°C incubation. After 30 min, cells were treated with 0.0125% Trypsin-EDTA (Thermo Fisher Scientific) for 3 min at 37°C. Cells were then lysed for immunoblotting analyses or fixed with 4% paraformaldehyde for flow cytometry analyses, and SAA1 was detected using the anti–His-antibody.

Quantitative real-time polymerase chain reaction (qPCR)

cDNA was synthesized from purified RNA using M-MLV Reverse Transcriptase (Thermo Fisher Scientific). qPCR was performed using TaqMan assays (Thermo Fisher Scientific) on a QuantStudio 7 Flex Real-Time PCR System (Applied Biosystems). Relative expression values were determined using the comparative Ct (ΔΔCt) method (*51*), and transcript abundances were normalized to *Gapdh* transcript abundance. Absolute RNA transcript copy numbers were determined from standards and the results are reported as copies of transcript of interest/copies of *Gapdh*. TaqMan probe assay IDs are provided in table S2.

Lamina propria immune cell isolation and flow cytometry analysis

Immune cells from small intestinal lamina propria were isolated as previously described with minor modification (*17*). Briefly, the small intestine was flushed with 20 ml of ice-cold PBS with 3% FBS, opened longitudinally, cut into 1.5-cm pieces, and washed three times with vortexing for 1 min in 10 ml of ice-cold PBS with 3% FBS. The pieces were incubated with 15 ml of PBS with 3% FBS, 1 mM EDTA, and 1 mM dithiothreitol (DTT) for 15 min at 37°C with rotation on a platform shaker (250 rpm). The epithelial cells and intraepithelial lymphocytes were collected by passing through a 100-μm cell strainer. The intestine pieces were washed in PBS with 3% FBS and placed in 20 ml of digestion solution [RPMI, 3% FBS, 0.2 mg/ml of collagenase IV (Sigma), 0.15 mg/ml of DNase I (Sigma), and 0.75 U/ml of Dispase II (Sigma)]. After incubation at 37°C for 25 min with rotation on a platform shaker (250 rpm), the solution was vortexed and passed through a 40-μm cell strainer. Cells from EDTA treatment and enzyme digestion were combined and filtered through a glass wool column (Thermo Fisher Scientific) to remove epithelial cells. The immune cells were further isolated by Percoll gradient separation collected at the 40 to 80% interphase of the Percoll gradient. After washing twice with PBS (3% FBS), the cells were either used immediately for experiments or fixed overnight in 1 ml of PBS with 3% FBS, 2 mM EDTA, and 0.2% paraformaldehyde at 4°C. For the analyses shown in Fig. 6 and fig. S4, Peyer's patches were removed before the immune cell isolation process. For intracellular staining (LRP1, IgA, FOXP3, RORγt, and IL-17A), cells were first stained with surface markers, and then fixed, permeabilized, and stained using eBioscience™ Foxp3/Transcription factor staining buffer set (Thermo Fisher Scientific). Flow cytometry was performed with a LSRII or a Novocyte 3005 and data were analyzed with FlowJo (Tree Star) and NovoExpress (ACEA Biosciences) softwares. For $CD11c^+$ cell isolation, dead cells were first removed by using dead cell removal kit following manufacturer's protocol (Miltenyi Biotec). Cells were incubated with anti-CD11c microbeads and then immunomagnetically sorted by sequential passage over two MACS separation columns (Miltenyi Biotec), resulting in ~90% purity (fig. S9, A and B). To analyze IL-17 production in figs. S14 and S15, 1×10^6 cells were treated with 50 ng/ml of phorbol myristate acetate, 1 mM ionomycin, and 1 mg/ml of brefeldin A for 4 hours at 37°C (*17*). Antibodies used for flow cytometry analysis are listed in table S3.

Measurement of RALDH activity by Aldefluor assay

RALDH activity was measured by Aldefluor assay (Stemcell Technologies) following the manufacturer's protocol with minor modifications. One million immune cells recovered from the small intestine were resuspended in 1 ml of assay buffer. Aldefluor reagent was added to each sample and incubated at 37°C for 30 min. The brightly fluorescent RALDH-expressing cells were detected by flow cytometry in the green channel (520 to 540 nm). As a control, the ALDH/RALDH inhibitor diethylaminobenzaldehyde (DEAB) was added to half of each sample.

16S ribosomal RNA (rRNA) gene sequencing and data analysis

Fecal contents from the ileum and colon were collected from wild-type and $Saa^{-/-}$ littermates and $Lrp1^{fl/fl}$ and $Lrp1^{\Delta Cd11c}$ littermates, which were cocaged. DNA was extracted and purified using the FastDNA Spin Kit (MP Biomedicals) and the FastPrep-24 Homogenizer (MP Biomedicals) following the manufacturer's protocol (*52*). 16*S* rRNA gene sequencing and data analysis were done by the UT Southwestern Microbiome Research Laboratory. Briefly, sequencing libraries were prepared following the Illumina Nextera protocol (Part no. 15044223 Rev. B) with primers flanking the hypervariable regions V3-V4. Sequencing was performed on MiSeqDX using the PE300 (paired end 300 bp) v3 kit. Taxonomic classification and Operational Taxonomic Unit (OTU) abundance were analyzed using the CLC Bio microbial genomics module. Principle component analysis was performed using the "prcomp" function in R and differential abundance analysis was performed using DESeq2 (*53*).

S. *Typhimurium infection*

Mouse survival after infection with *Salmonella enterica* serovar Typhimurium (*S.* Typhimurium) was measured after immunization with heat-killed bacteria as described elsewhere (*54*, *55*). *S.* Typhimurium strain SL1344 (streptomycin-resistant) was grown in Luria-Bertani (LB) broth containing 50 μg/ml of streptomycin at 37°C. For immunization, heat-killed *S.* Typhimurium was prepared in PBS by incubation at 65°C for 3 hours. Mice were treated with streptomycin (20 mg per mouse) by oral gavage a day before immunization, and then orally immunized with heat-killed *S.* Typhimurium [10^{10} colony-forming units (CFU) equivalents per mouse] twice at 7-day intervals. Three days after the second immunization, mice were colonized with a normal gut microbiota by inoculation with a fecal slurry prepared from the intestinal contents of conventional wild-type mice reared in the UT Southwestern mouse facility. Four weeks after the first immunization, mice were inoculated by oral gavage with 2×10^8 bacteria for wild-type and $Saa^{-/-}$ mice (on a C57BL/6J background) or with 5×10^9 bacteria for $Lrp1^{fl/fl}$ and $Lrp1^{\Delta Cd11c}$ mice (on a 129S7/SvEvBrd × C57BL/6J background). The dose varied because resistance to *S.* Typhimurium infection varies according to mouse background.

S. Typhimurium–specific IgA was measured in feces as previously described (*56*). Briefly, lipopolysaccharide (LPS) was purified from *S.* Typhimurium SL1344 cultures using the LPS extraction kit (Abcam) and used as antigen for enzyme-linked immunosorbent assay (ELISA). Then, 96-well microplates (Greiner Bio-one) were coated with LPS (1 μg per well) in carbonate coating buffer (Thermo Scientific). The plates were then blocked with 5% w/v skim milk in TBST, and the fecal extracts were added to the plates. After washing, bound IgA was detected using HRP-conjugated goat

anti-mouse IgA antibody (Invitrogen) and Super-Signal ELISA Pico Chemiluminescent Substrate (Thermo Scientific).

REFERENCES AND NOTES

1. M. Iwata *et al*., Retinoic acid imprints gut-homing specificity on T cells. *Immunity* **21**, 527–538 (2004). doi: 10.1016/j.immuni.2004.08.011; pmid: 15485630
2. J. R. Mora *et al*., Generation of gut-homing IgA-secreting B cells by intestinal dendritic cells. *Science* **314**, 1157–1160 (2006). doi: 10.1126/science.1132742; pmid: 17110582
3. P. Bhaskaram, Micronutrient malnutrition, infection, and immunity: An overview. *Nutr. Rev.* **60**, S40–S45 (2002). doi: 10.1301/00296640260130722; pmid: 12035857
4. T. Sun, A. Nguyen, J. L. Gommerman, Dendritic Cell Subsets in Intestinal Immunity and Inflammation. *J. Immunol.* **204**, 1075–1083 (2020). doi: 10.4049/jimmunol.1900710; pmid: 32071090
5. B. Koscsó *et al*., Gut-resident CX3CR1^{hi} macrophages induce tertiary lymphoid structures and IgA response in situ. *Sci. Immunol.* **5**, eaax0062 (2020). doi: 10.1126/sciimmunol.aax0062; pmid: 32276965
6. J. L. Coombes *et al*., A functionally specialized population of mucosal CD103$^+$ DCs induces Foxp3$^+$ regulatory T cells via a TGF-β– and retinoic acid–dependent mechanism. *J. Exp. Med.* **204**, 1757–1764 (2007). doi: 10.1084/jem.20070590; pmid: 17620361
7. T. L. Denning, Y. C. Wang, S. R. Patel, I. R. Williams, B. Pulendran, Lamina propria macrophages and dendritic cells differentially induce regulatory and interleukin 17–producing T cell responses. *Nat. Immunol.* **8**, 1086–1094 (2007). doi: 10.1038/ni1511; pmid: 17873879
8. D. Mucida *et al*., Reciprocal T_H17 and regulatory T cell differentiation mediated by retinoic acid. *Science* **317**, 256–260 (2007). doi: 10.1126/science.1145697; pmid: 17569825
9. C.-M. Sun *et al*., Small intestine lamina propria dendritic cells promote de novo generation of Foxp3 T reg cells via retinoic acid. *J. Exp. Med.* **204**, 1775–1785 (2007). doi: 10.1084/jem.20070602; pmid: 17620362
10. T. L. Denning *et al*., Functional specializations of intestinal dendritic cell and macrophage subsets that control Th17 and regulatory T cell responses are dependent on the T cell/APC ratio, source of mouse strain, and regional localization. *J. Immunol.* **187**, 733–747 (2011). doi: 10.4049/jimmunol.1002701; pmid: 21666057
11. J. Nolting *et al*., Retinoic acid can enhance conversion of naive into regulatory T cells independently of secreted cytokines. *J. Exp. Med.* **206**, 2131–2139 (2009). doi: 10.1084/jem.20090639; pmid: 19737861
12. J. A. Hall *et al*., Essential role for retinoic acid in the promotion of CD4$^+$ T cell effector responses via retinoic acid receptor alpha. *Immunity* **34**, 435–447 (2011). doi: 10.1016/j.immuni.2011.03.003; pmid: 21419664
13. J. R. Mora *et al*., Selective imprinting of gut-homing T cells by Peyer's patch dendritic cells. *Nature* **424**, 88–93 (2003). doi: 10.1038/nature01726; pmid: 12840763
14. M. G. Derebe *et al*., Serum amyloid A is a retinol binding protein that transports retinol during bacterial infection. *eLife* **3**, e03206 (2014). doi: 10.7554/eLife.03206; pmid: 25073702
15. Z. Hu, Y. J. Bang, K. A. Ruhn, L. V. Hooper, Molecular basis for retinol binding by serum amyloid A during infection. *Proc. Natl. Acad. Sci. U.S.A.* **116**, 19077–19082 (2019). doi: 10.1073/pnas.1910713116; pmid: 31484771
16. T. Sano *et al*., An IL-23R/IL-22 Circuit Regulates Epithelial Serum Amyloid A to Promote Local Effector Th17 Responses. *Cell* **163**, 381–393 (2015). doi: 10.1016/j.cell.2015.08.061; pmid: 26411290
17. S. Gattu *et al*., Epithelial retinoic acid receptor β regulates serum amyloid A expression and vitamin A-dependent intestinal immunity. *Proc. Natl. Acad. Sci. U.S.A.* **116**, 10911–10916 (2019). doi: 10.1073/pnas.1812069116; pmid: 31097581
18. S. K. Frey, S. Vogel, Vitamin A metabolism and adipose tissue biology. *Nutrients* **3**, 27–39 (2011). doi: 10.3390/nu3010027; pmid: 22254074
19. A. P. Lillis, L. B. Van Duyn, J. E. Murphy-Ullrich, D. K. Strickland, LDL receptor-related protein 1: Unique tissue-specific functions revealed by selective gene knockout studies. *Physiol. Rev.* **88**, 887–918 (2008). doi: 10.1152/physrev.00033.2007; pmid: 18626063
20. M. Z. Kounnas, J. Henkin, W. S. Argraves, D. K. Strickland, Low density lipoprotein receptor-related protein/α 2-macroglobulin receptor mediates cellular uptake of pro-urokinase. *J. Biol. Chem.* **268**, 21862–21867 (1993). doi: 10.1016/S0021-9258(20)80620-6; pmid: 7691818
21. P. J. Lenting *et al*., The light chain of factor VIII comprises a binding site for low density lipoprotein receptor-related protein. *J. Biol. Chem.* **274**, 23734–23739 (1999). doi: 10.1074/jbc.274.34.23734; pmid: 10446132
22. P. H. Weigel, J. A. Oka, Temperature dependence of endocytosis mediated by the asialoglycoprotein receptor in isolated rat hepatocytes: Evidence for two potentially rate-limiting steps. *J. Biol. Chem.* **256**, 2615–2617 (1981). doi: 10.1016/S0021-9258(19)69656-0; pmid: 6259136
23. J. Herz, J. L. Goldstein, D. K. Strickland, Y. K. Ho, M. S. Brown, 39-kDa protein modulates binding of ligands to low density lipoprotein receptor-related protein/α2-macroglobulin receptor. *J. Biol. Chem.* **266**, 21232–21238 (1991). doi: 10.1016/S0021-9258(18)54845-6; pmid: 1718973
24. G. Bu, H. J. Geuze, G. J. Strous, A. L. Schwartz, 39 kDa receptor-associated protein is an ER resident protein and molecular chaperone for LDL receptor-related protein. *EMBO J.* **14**, 2269–2280 (1995). doi: 10.1002/j.1460-2075.1995.tb07221.x; pmid: 7774585
25. Y. Li, M. Paz Marzolo, P. van Kerkhof, G. J. Strous, G. Bu, The *YXXL* motif, but not the two *NPXY* motifs, serves as the dominant endocytosis signal for low density lipoprotein receptor-related protein. *J. Biol. Chem.* **275**, 17187–17194 (2000). doi: 10.1074/jbc.M000490200; pmid: 10747918
26. W. S. Blaner, Retinol-binding protein: The serum transport protein for vitamin A. *Endocr. Rev.* **10**, 308–316 (1989). doi: 10.1210/edrv-10-3-308; pmid: 2550213
27. R. Kawaguchi *et al*., A membrane receptor for retinol binding protein mediates cellular uptake of vitamin A. *Science* **315**, 820–825 (2007). doi: 10.1126/science.1136244; pmid: 17255476
28. P. Alapatt *et al*., Liver retinol transporter and receptor for serum retinol-binding protein (RBP4). *J. Biol. Chem.* **288**, 1250–1265 (2013). doi: 10.1074/jbc.M112.369132; pmid: 23105095
29. J. Helft *et al*., GM-CSF Mouse Bone Marrow Cultures Comprise a Heterogeneous Population of CD11c$^+$MHCII$^+$ Macrophages and Dendritic Cells. *Immunity* **42**, 1197–1211 (2015). doi: 10.1016/j.immuni.2015.05.018; pmid: 26084029
30. Y. R. Na, D. Jung, G. J. Gu, S. H. Seok, GM-CSF Grown Bone Marrow Derived Cells Are Composed of Phenotypically Different Dendritic Cells and Macrophages. *Mol. Cells* **39**, 734–741 (2016). doi: 10.14348/molcells.2016.0160; pmid: 27788572
31. R. Blomhoff, H. K. Blomhoff, Overview of retinoid metabolism and function. *J. Neurobiol.* **66**, 606–630 (2006). doi: 10.1002/neu.20242; pmid: 16688755v
32. R. Molenaar *et al*., Expression of retinaldehyde dehydrogenase enzymes in mucosal dendritic cells and gut-draining lymph node stromal cells is controlled by dietary vitamin A. *J. Immunol.* **186**, 1934–1942 (2011). doi: 10.4049/jimmunol.1001672; pmid: 21220692
33. C. F. Chou, C. L. Lai, Y. C. Chang, G. Duester, S. J. Yin, Kinetic mechanism of human class IV alcohol dehydrogenase functioning as retinol dehydrogenase. *J. Biol. Chem.* **277**, 25209–25216 (2002). doi: 10.1074/jbc.M201947200; pmid: 11997393
34. J. Su, X. Chai, B. Kahn, J. L. Napoli, cDNA cloning, tissue distribution, and substrate characteristics of a cis-Retinol/3α-hydroxysterol short-chain dehydrogenase isozyme. *J. Biol. Chem.* **273**, 17910–17916 (1998). doi: 10.1074/jbc.273.28.17910; pmid: 9651397
35. I. Gagnon, G. Duester, P. V. Bhat, Enzymatic characterization of recombinant mouse retinal dehydrogenase type 1. *Biochem. Pharmacol.* **65**, 1685–1690 (2003). doi: 10.1016/S0006-2952(03)00150-3; pmid: 12754104
36. S. Boullier *et al*., Secretory IgA-mediated neutralization of Shigella flexneri prevents intestinal tissue destruction by down-regulating inflammatory circuits. *J. Immunol.* **183**, 5879–5885 (2009). doi: 10.4049/jimmunol.0901838; pmid: 19828639
37. S. J. Forbes, T. Bumpus, E. A. McCarthy, B. Corthésy, N. J. Mantis, Transient suppression of *Shigella flexneri* type 3 secretion by a protective O-antigen-specific monoclonal IgA. *mBio* **2**, e00042-11 (2011). doi: 10.1128/mBio.00042-11; pmid: 21610121
38. J. J. Bunker *et al*., Innate and Adaptive Humoral Responses Coat Distinct Commensal Bacteria with Immunoglobulin A. *Immunity* **43**, 541–553 (2015). doi: 10.1016/j.immuni.2015.08.007; pmid: 26320660
39. I. I. Ivanov *et al*., Induction of intestinal Th17 cells by segmented filamentous bacteria. *Cell* **139**, 485–498 (2009). doi: 10.1016/j.cell.2009.09.033; pmid: 19836068
40. C. S. Reigstad, G. Ö. Lundén, J. Felin, F. Bäckhed, Regulation of serum amyloid A3 (SAA3) in mouse colonic epithelium and adipose tissue by the intestinal microbiota. *PLOS ONE* **4**, e5842 (2009). doi: 10.1371/journal.pone.0005842; pmid: 19513118
41. J. J. Cebra, S. B. Periwal, G. Lee, F. Lee, K. E. Shroff, Development and maintenance of the gut-associated lymphoid tissue (GALT): The roles of enteric bacteria and viruses. *Dev. Immunol.* **6**, 13–18 (1998). doi: 10.1155/1998/68382; pmid: 9716901
42. J. Y. Lee *et al*., Serum Amyloid A Proteins Induce Pathogenic Th17 Cells and Promote Inflammatory Disease. *Cell* **180**, 79–91.e16 (2020). doi: 10.1016/j.cell.2019.11.026; pmid: 31866067
43. C. Panea *et al*., Intestinal Monocyte-Derived Macrophages Control Commensal-Specific Th17 Responses. *Cell Rep.* **12**, 1314–1324 (2015). doi: 10.1016/j.celrep.2015.07.040; pmid: 26279572
44. Y. Goto *et al*., Segmented filamentous bacteria antigens presented by intestinal dendritic cells drive mucosal Th17 cell differentiation. *Immunity* **40**, 594–607 (2014). doi: 10.1016/j.immuni.2014.03.005; pmid: 24684957
45. R. R. Penkert *et al*., Influences of Vitamin A on vaccine immunogenicity and efficacy. *Front. Immunol.* **10**, 1576 (2019). doi: 10.3389/fimmu.2019.01576; pmid: 31379816
46. A. Rohlmann, M. Gotthardt, T. E. Willnow, R. E. Hammer, J. Herz, Sustained somatic gene inactivation by viral transfer of Cre recombinase. *Nat. Biotechnol.* **14**, 1562–1565 (1996). doi: 10.1038/nbt1196-1562; pmid: 9634821
47. C. L. Morales-Perez, C. M. Noviello, R. E. Hibbs, Manipulation of Subunit Stoichiometry in Heteromeric Membrane Proteins. *Structure* **24**, 797–805 (2016). doi: 10.1016/j.str.2016.03.004; pmid: 27041595
48. J. M. Rainard, G. C. Pandarakalam, S. P. McElroy, Using Microscale Thermophoresis to Characterize Hits from High-Throughput Screening: A European Lead Factory Perspective. *SLAS Discov.* **23**, 225–241 (2018). doi: 10.1177/2472555217744728; pmid: 29460707
49. T. H. Scheuermann, S. B. Padrick, K. H. Gardner, C. A. Brautigam, On the acquisition and analysis of microscale thermophoresis data. *Anal. Biochem.* **496**, 79–93 (2016). doi: 10.1016/j.ab.2015.12.013; pmid: 26739938
50. C. A. Brautigam, Calculations and Publication-Quality Illustrations for Analytical Ultracentrifugation Data. *Methods Enzymol.* **562**, 109–133 (2015). doi: 10.1016/bs.mie.2015.05.001; pmid: 26412649
51. T. D. Schmittgen, K. J. Livak, Analyzing real-time PCR data by the comparative C_T method. *Nat. Protoc.* **3**, 1101–1108 (2008). doi: 10.1038/nprot.2008.73; pmid: 18546601
52. Z. Kuang *et al*., The intestinal microbiota programs diurnal rhythms in host metabolism through histone deacetylase 3. *Science* **365**, 1428–1434 (2019). doi: 10.1126/science.aaw3134; pmid: 31604271
53. M. I. Love, W. Huber, S. Anders, Moderated estimation of fold change and dispersion for RNA-seq data with DESeq2. *Genome Biol.* **15**, 550 (2014). doi: 10.1186/s13059-014-0550-8; pmid: 25516281
54. R. H. Waldman, R. Grunspan, R. Ganguly, Oral immunization of mice with killed *Salmonella typhimurium* vaccine. *Infect. Immun.* **6**, 58–61 (1972). doi: 10.1128/iai.6.1.58-61.1972; pmid: 4564152
55. A. A. Kolodziejczyk, D. Zheng, E. Elinav, Diet-microbiota interactions and personalized nutrition. *Nat. Rev. Microbiol.* **17**, 742–753 (2019). doi: 10.1038/s41579-019-0256-8; pmid: 31541197
56. C. Xu *et al*., Live attenuated *Salmonella* typhimurium vaccines delivering SaEsxA and SaEsxB via type III secretion system confer protection against *Staphylococcus aureus* infection. *BMC Infect. Dis.* **18**, 195 (2018). doi: 10.1186/s12879-018-3104-y; pmid: 29699491

ACKNOWLEDGMENTS

We thank B. Hassell for assistance with mouse experiments and the UT Southwestern Proteomics Core for assistance for proteomics analysis. **Funding:** This work was supported by NIH

grant R01 DK070855 (to L.V.H.), Welch Foundation grant I-1874 (to L.V.H.), the Walter M. and Helen D. Bader Center for Research on Arthritis and Autoimmune Diseases (L.V.H.), and the Howard Hughes Medical Institute (L.V.H.). J.H. was supported by NIH grants R37 HL63762, R01 NS108115, R01 NS093382, and RF1 AG053391 and BrightFocus Foundation A2016396S. Y.-J.B. was supported by a Crohn's and Colitis Foundation of America Research Fellowship award (509845). **Author contributions:** Y.-J.B., Z.H., Y.L., S.G., and L.V.H. designed the research. Y.-J.B., Z.H., Y.L., S.G., K.A.R., and P.R. performed research. J.H. provided mice and edited the manuscript. Y.-J.B., Z.H., Y.L., S.G., P.R., and L.V.H. analyzed data. Y.-J.B. and L.V.H. wrote the paper. **Competing interests:** The authors declare no competing interests. **Data and materials availability:** 16S rRNA gene sequencing data (fig. S16) have been submitted to the Sequence Read Archive (SRA) with BioProject IDs PRJNA727197 and PRJNA727212. *Lrp1*$^{fl/fl}$ mice are available under a material transfer agreement with UTSW. All other lines in the study are commercially available. All other data are available in the main text or the supplementary materials.

SUPPLEMENTARY MATERIALS

https://science.org/doi/10.1126/science.abf9232
Figs. S1 to S17
Tables S1 to S3
MDAR Reproducibility Checklist

29 November 2020; accepted 4 August 2021
10.1126/science.abf9232

Science
JOURNALS AAAS



Publish your research in the *Science* family of journals

The *Science* family of journals (*Science, Science Advances, Science Immunology, Science Robotics, Science Signaling*, and *Science Translational Medicine)* are among the most highly-regarded journals in the world for quality and selectivity. Our peer-reviewed journals are committed to publishing cutting-edge research, incisive scientific commentary, and insights on what's important to the scientific world at the highest standards.

Submit your research today!

Learn more at **Science.org/journals**

RESEARCH ARTICLE SUMMARY

QUANTUM OPTICS

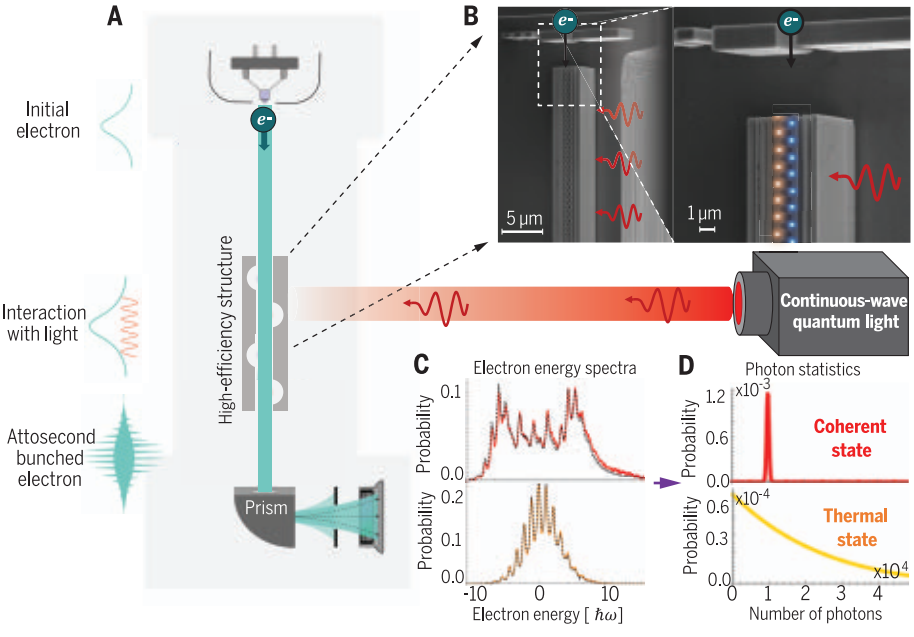
Imprinting the quantum statistics of photons on free electrons

Raphael Dahan†, Alexey Gorlach†, Urs Haeusler†, Aviv Karnieli†, Ori Eyal, Peyman Yousefi, Mordechai Segev, Ady Arie, Gadi Eisenstein, Peter Hommelhoff, Ido Kaminer*

INTRODUCTION: The science of light has undergone two major revolutions over the previous two centuries. The first—by Grimaldi, Huygens, Fresnel, Young, and Maxwell—established light as a wave phenomenon, and the second—by Planck, Einstein, and Glauber—established light as a combined particle-wave quantum phenomenon. Despite the quantum revolution, entire areas of science still find the classical wave description of light sufficient, especially so for interactions between light and charged particles such as free electrons. Light and all forms of electromagnetic fields remain pure wave phenomena at the frontiers of free-electron physics, microscopy, accelerators, and radiation sources. We present experiment and theory in which the quantum nature of light plays the key role in its interaction with free electrons.

RATIONALE: From the viewpoint of quantum optics, the wave theory of light is sufficient to model its interaction with matter, provided that light and matter do not become entangled during their interaction. This wave description was justified thus far because classical light can be described as coherent states, which stay approximately unchanged under interactions and thus do not become entangled.

Our work demonstrates the interaction of free electrons with light of nontrivial quantum photon statistics. The electron evolves into an entangled joint state with the photons, imprinting their quantum statistics on the electron energy spectrum. By measuring the electron spectrum, we extracted the quantum photon statistics of light, finding the second-order photon correlations $g^{(2)}(0)$ and higher-order correlations $g^{(n)}(0)$. We demonstrate quantitative measurement of different photon statistics using an optical amplifier operated in different amplification regimes, showing transition from Poissonian statistics in deep saturation to super-Poissonian statistics due to amplified spontaneous emission and eventually a thermal state with Bose-Einstein statistics. Electrons can perform nondestructive quantum measurements, inspiring possibilities in quantum optics such as ultrafast free-electron–based quantum tomography of light at deep suboptical wavelength resolution.



Quantum optics with free electrons. A silicon-photonics device integrated in an electron microscope provides efficient electron interactions with CW light, enabling the detection of the quantum photon statistics. (**A**) CW modulation of electron wave functions in transmission electron microscopy. (**B**) Highly efficient electron-light interaction facilitated by an inverse-designed silicon-photonic nanostructure (scanning electron microscope image), consisting of a Bragg mirror and a periodic channel that achieves quasi–phase-matching of electron and quantum light. (**C**) The electron energy spectrum after the interaction with two types of light states: coherent and thermal. (**D**) The corresponding photon statistics reconstructed from the measured spectra.

RESULTS: The interacting electron in our experiment acts as a "walker," performing a quantum/classical walk on the ladder of energy levels, each step corresponding to single-photon emission or absorption. When light interacts as a wave (coherent state, Poissonian statistics), the resulting electron dynamics is also that of a wave—quantum walk, in which a well-defined phase is maintained between the electron energy states. By contrast, when the particle-nature of light becomes dominant (super-Poissonian statistics), the resulting electron dynamics is also that of a particle—classical random walk, in which collapse washes out the relative phase between the electron energy states. This emergence of classical random walk represents a manifestation of Bohr's correspondence principle between classical and quantum physics—one of the cornerstones of quantum mechanics since its earliest days.

CONCLUSION: We overcame the challenge of the usually weak coupling between light and free electrons by exploiting an inverse design silicon-photonic nanostructure that combines two critical ingredients: photonic cavities and phase-matching between electron wave functions and light waves. Our integrated solution can equip state-of-the-art microscopes with capabilities for temporal electron wave modulation by using continuous-wave (CW) lasers, paving the way toward microscopes operating at simultaneous subangstrom-spatial and few-attosecond-temporal resolution. Coherent temporal modulation of electron wave functions opens possibilities for electron microscopy of phenomena that cannot be explored by other means: imaging nonequilibrium quantum states of matter, measuring their coherence properties and decoherence rates. ■

The list of author affiliations is available in the full article online.
*Corresponding author. Email: kaminer@technion.ac.il
†These authors contributed equally to this work.
Cite this article as R. Dahan *et al.*, *Science* 373, eabj7128 (2021). DOI: 10.1126/science.abj7128

READ THE FULL ARTICLE AT
https://doi.org/10.1126/science.abj7128

RESEARCH ARTICLE

QUANTUM OPTICS

Imprinting the quantum statistics of photons on free electrons

Raphael Dahan[1,2]†, Alexey Gorlach[1,2]†, Urs Haeusler[3]†‡, Aviv Karnieli[1,2,4]†, Ori Eyal[1,2], Peyman Yousefi[3]§, Mordechai Segev[1,2,5], Ady Arie[6], Gadi Eisenstein[1,2], Peter Hommelhoff[3], Ido Kaminer[1,2]*

The interaction between free electrons and light stands at the base of both classical and quantum physics, with applications in free-electron acceleration, radiation sources, and electron microscopy. Yet to this day, all experiments involving free-electron–light interactions are fully explained by describing the light as a classical wave. We observed quantum statistics effects of photons on free-electron–light interactions. We demonstrate interactions that pass continuously from Poissonian to super-Poissonian and up to thermal statistics, revealing a transition from quantum walk to classical random walk on the free-electron energy ladder. The electron walker serves as the probe in nondestructive quantum detection, measuring the second-order photon-correlation $g^{(2)}(0)$ and higher-orders $g^{(n)}(0)$. Unlike conventional quantum-optical detectors, the electron can perform both quantum weak measurements and projective measurements by evolving into an entangled joint state with the photons. These findings inspire hitherto inaccessible concepts in quantum optics, including free-electron–based ultrafast quantum tomography of light.

Understanding of light as a wave phenomenon was firmly established in the early days of the 19th century, forming the foundations of Maxwell's equations (*1*), the entirety of electrodynamics, and the study of light-matter interactions. Later discoveries revealed the quantum-particle nature of light: starting from the photoelectric (*2*) to the discovery of entanglement many decades later (*3*), constituting modern quantum optics (*4*, *5*). Yet, entire areas of science still find the wave description of light fully sufficient. This is true for light in the optical range and for all other forms of electromagnetic waves. For example, classical electromagnetic waves determine the dynamics of charged particles in numerous applications, from free-electron lasers and synchrotrons to radars, communication satellites, and even microwave ovens. Light remains purely a wave phenomenon also at the frontier of free-electron–light experiments, in which laser-driven electron acceleration [specifically, wakefield accelerators (*6*, *7*) and dielectric laser accelerators (*8*–*12*)] still consider the particle motion by using a wave description of the laser. Thus far, the quantum-particle nature of light in its interactions with free electrons has remained hidden, without any direct consequences. This is in sharp contrast to the quantum nature of the electron, which is now regularly observed in ultrafast transmission electron microscopy (*13*–*16*). The critical role of the electron quantum wave function in its interaction with light is already well understood (*17*–*22*): The electron exchanges integer multiples of the photon energy, as shown in the theoretical description of the technique called photon-induced near-field electron microscopy (PINEM) (*13*, *17*, *18*). However, even in this case—in which the electron must be treated quantum-mechanically—the description of light as a classical wave was sufficient in all experiments to date.

Here, we present experiments showing that quantum statistics of photons alter their interaction with free electrons; we demonstrate free-electron–light interactions that cannot be described by treating light as a wave phenomenon. Moreover, we used the electron-light interaction to measure the photon statistics of the light. This capability stems from a fundamental aspect of quantum optics: The interaction with light can create entanglement between the light and the interacting object. Consequently, the joint free-electron–light state becomes a nonseparable state from which we can extract the photon statistics by measuring the electron energy spectrum. Our experiment demonstrates this concept on amplified light, exhibiting different photon statistics for varying amplification regimes. The free-electron interaction enables us to characterize the amplifier output, showing its transition from a coherent state with Poissonian statistics in the regime of deep saturation to super-Poissonian statistics owing to amplified spontaneous emission and eventually to a thermal state with Bose-Einstein statistics. Our experiments offer a pathway for using free electrons for quantum-state tomography of light, with high resolution in both time and frequency (*23*).

Bohr's correspondence principle: From free-electron quantum walk to random walk

Our experiment shows that the measured electron acts as a "walker" performing a generalized quantum/classical walk (Fig. 1) on the ladder of energy levels (separated by the single-photon energy $\hbar\omega$), similar to an upside-down (quantum) Galton board experiment (Fig. 1A). At each infinitesimal step, the electron walker either remains in its current energy level, moves to a lower energy level by emitting a photon, or moves to a higher energy level by absorbing a photon. Each step either maintains a well-defined phase between the electron energy states, such as in interactions with a coherent state of light (Fig. 1, left), or washes out the phase and acts in a random fashion, such as in interactions with thermal light (Fig. 1, right). We observed the walk dynamics by measuring the electron energy spectrum as a function of illumination power for different photon statistics (Fig. 1, C and D). The measurement shows that when light interacts as a wave (coherent state), the resulting electron dynamics is also that of a wave—a pure quantum walk. By contrast, when the particle-nature of light becomes dominant (super-Poissonian and thermal statistics), the resulting electron dynamics is also that of a particle—a classical random walk. This emergence of the classical dynamics of random walk from the interaction of a free electron with super-Poissonian light represents a new manifestation of the correspondence principle between classical and quantum physics, which has been one of the cornerstones of quantum mechanics since its earliest days (*24*).

We begin by formulating the theory of light–free-electron interaction and its dependence on photon statistics. The theory, henceforth called the electron walker theory (explained in Fig. 1, A and B), captures the entire range of experimental parameters, including both limiting cases of coherent and thermal states of light: For the interaction with coherent-state light (Fig. 1, left), the electron undergoes pure quantum walk in energy-space [as shown in (*14*)], and for the interaction with thermal light (Fig. 1, right), the electron undergoes pure random walk. The intermediate cases of interactions

[1]Department of Electrical Engineering, Russell Berrie Nanotechnology Institute, Technion–Israel Institute of Technology, Haifa 32000, Israel. [2]Solid State Institute, Technion–Israel Institute of Technology, Haifa 32000, Israel. [3]Department of Physics, Friedrich-Alexander-Universität Erlangen-Nürnberg (FAU), Staudtstraße 1, Erlangen 91058, Germany. [4]Raymond and Beverly Sackler School of Physics and Astronomy, Tel Aviv University, Tel Aviv 69978, Israel. [5]Department of Physics, Technion–Israel Institute of Technology, Haifa 32000, Israel. [6]School of Electrical Engineering, Fleischman Faculty of Engineering, Tel Aviv University, Tel Aviv 69978, Israel.
***Corresponding author. Email: kaminer@technion.ac.il**
†These authors contributed equally to this work.
‡Present address: Cavendish Laboratory, University of Cambridge, JJ Thomson Avenue, Cambridge CB3 0HE, UK.
§Present address: Fraunhofer-Institut für Keramische Technologien und Systeme IKTS, Äussere Nürnberger Strasse 62, Forchheim 91301, Germany.

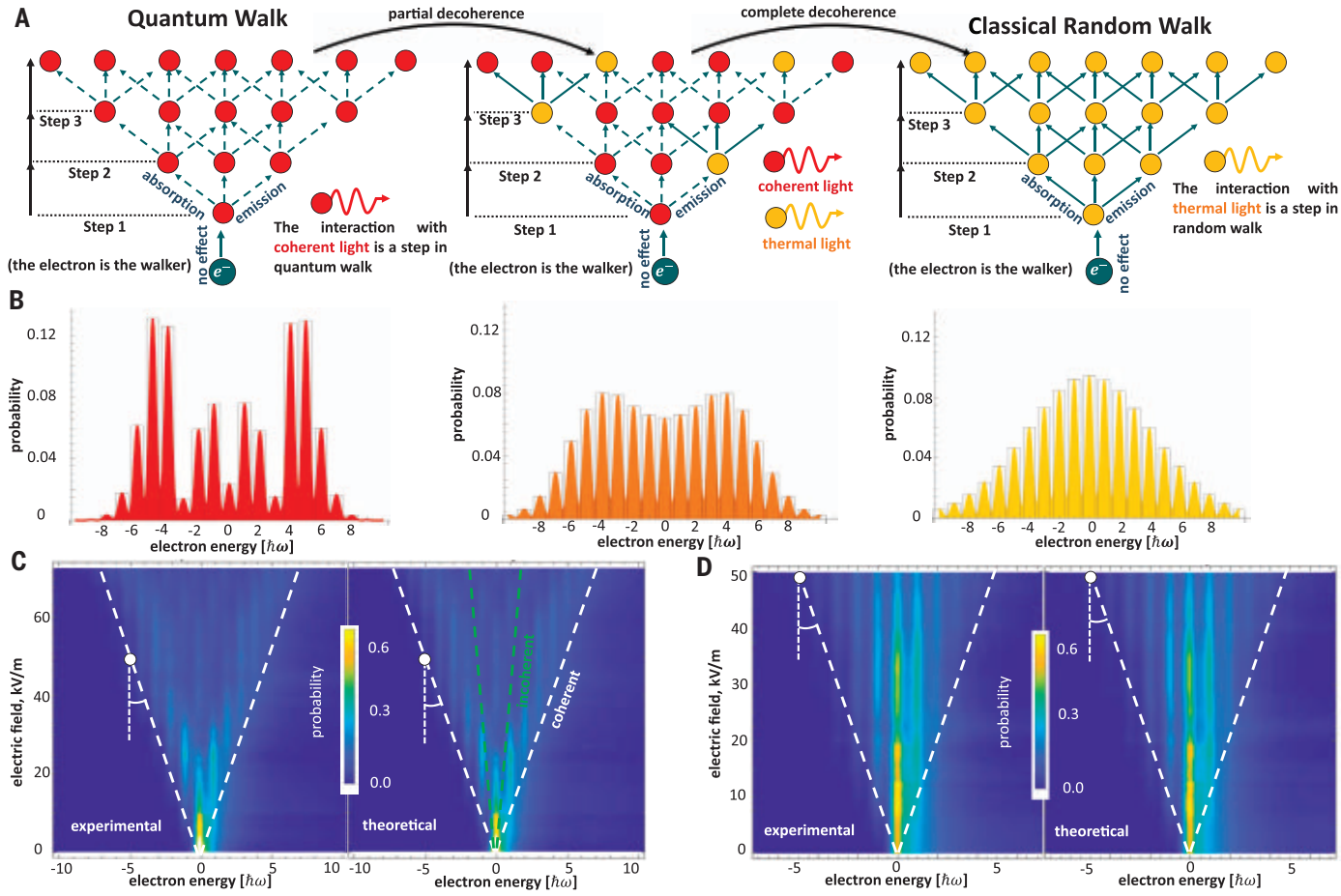


Fig. 1. Free-electron–light interactions imprint the quantum photon statistics on the electron energy spectra, demonstrating the transition from quantum walk to classical random walk of a free electron. (**A**) The electron walker performs consecutive interactions with the photons. At each infinitesimal step, there are three possibilities: (i) the electron remains in its current energy level; (ii) the electron emits a photon, moving to a lower energy level; or (iii) the electron absorbs a photon, moving to a higher energy level. Each such emission or absorption either maintains a well-defined phase between the electron energy states, as in interactions with coherent-state light (red), or "collapses" and acts in a random fashion, as in interactions with thermal light (yellow). The collapse washes out the phase between the electron energy states. The transition from quantum walk to random walk is expressed by the continuous transition in the photon statistics from Poissonian (coherent state) to super-Poissonian and all the way to a thermal light state. (**B**) The electron walker theory exactly matches with the Q-PINEM theory, in which the shape of the photon statistics determines the degree of decoherence of the electron. The resulting electron energy spectra show either quantum walk, random walk, or an intermediate case displaying partial decoherence, depending on the photon statistics (a measurement of the continuous transition is provided in Fig. 3). (**C** and **D**) Electron energy spectra for coherent and thermal states evolving with the electric field amplitude. Theory gives an excellent agreement with experimental results, measured in the setup presented in Fig. 2, with more data shown in fig. S13. The white circles indicate that the observed electron energy width is the same for the same driving light intensity, regardless of the quantum statistics. This comparison reveals that the electron interactions with thermal states are as efficient as interactions with coherent states. In (C), we indicate with green dashed lines the electron energy width for light with partial optical coherence (spatial coherence length of 1 μm; calculation with other values are shown in fig. S16), predicting a different slope than for the measured data that corresponds to light with full optical coherence, indicated with white lines in (C) and (D). Thus, we conclude that the measurements in (D) cannot be explained by a short optical coherence length (further discussion and results are in supplementary text S6 and fig. S16). This shows that the interaction of super-Poissonian light with a free electron does not cause the electron to decohere in time or space. Rather, the electron remains in a coherent superposition of energy states that become more entangled with the light for stronger super-Poissonian statistics, with maximum entanglement for thermal light. The electron energy axis here and in all figures refers to energy loss, as is conventional in electron energy loss spectroscopy.

with super-Poissonian light all correspond to mixtures of quantum walk and random walk, showing a continuous transition between the two phenomena. We show in supplementary text S1 that despite its simplicity, the walker theory provides the same results as those of the quantum-optical generalization of PINEM (Q-PINEM), proposed theoretically in (*25*, *26*) [in particular, Fig. 1D precisely matches the prediction in (*26*)]. The comparisons in Fig. 1, C and D, show that the theories successfully describe the measured electron energy spectra, the experimental details of which we describe below.

The agreement of both walker and Q-PINEM theories with the experimental data in Fig. 1, C and D, allows us to draw decisive conclusions about the role of quantum decoherence in the interaction. The photon statistics directly determine the degree of decoherence of the electron walker: Broader photon distributions (such as super-Poissonian) increase the free-electron decoherence in energy (*27*) during the electron walk. The limit of thermal light can be understood exactly as the complete decoherence of the electron quantum state at every step of the walk, showing the emergence of classical random walk from the decoherence of quantum walk. The phenomenon of quantum walk has been observed experimentally in a wide range of

physical systems (28–33). In our experiment, there is a fundamental difference: the quantum-to-classical transition of the electron walker we observed arises from the photon distribution rather than from dephasing and disorder-induced decoherence as in many other systems (30, 33–37).

Experimental setup: High-efficiency silicon-photonic electron-light coupler

Our experiment achieved an efficient electron-light interaction by use of two critical ingredients: photonic cavities (38, 39) and phase-matching between the electron wave function and the light wave (40), inspired by phase-matching of classical electron-light interactions (41). We used quasi–phase-matching in custom-made silicon-photonic nanostructures to create efficient free-electron–quantum-light interactions inside a transmission electron microscope (TEM) (Fig. 2A). Our nanostructures are inspired by miniaturized electron accelerators (8–11), which were recently used in a silicon photonics PINEM experiment (12). We used photonic inverse design methods to design and optimize a high-efficiency electron-light coupler (Fig. 2D) (11, 42), operating at a wavelength of 1064 nm and electron kinetic energy of 189 keV (Fig. 2). The quantum statistics of the output light is modified by controlling the input power to a fiber amplifier and then coupling the light into the nanostructure inside the TEM by using two cylindrical lenses (supplementary materials, materials and methods).

Our experiment realizes strong electron-light interactions; each electron exchanges multiple photons with the light field. Such strong interactions were previously only realized with intense laser pulses synchronized with photo-emitted free electrons (8–15, 38–40, 43). In contrast with such intense laser pulses that can be considered as coherent states (classical waves), all other states of light are usually not so intense. The low intensity poses a challenge for investigating their interactions with free electrons. We thus developed nanostructures for enhancing the interaction efficiency, reaching the desired strong electron-light interaction with lower-intensity light, which is especially important for quantum light. The interaction efficiency is high enough to enable the use of continuous-wave (CW) light while still maintaining the strong interaction. Recent experimental works have shown that even weak CW electron-light interactions (up to one photon absorbed or emitted by the electron) have intriguing applications (44–47). Our experiment offers an avenue for taking these ideas forward to regimes of stronger interactions with CW light and specifically enables us to probe the quantum statistics of the photons.

Free-electron–quantum-light interactions

In all free-electron experiments to date, the electron dynamics has been accurately captured by its interaction with classical electromagnetic fields. The dynamics of a single-electron wave function has been fully described by the time-dependent Schrödinger equation (or the Dirac equation in the more general relativistic

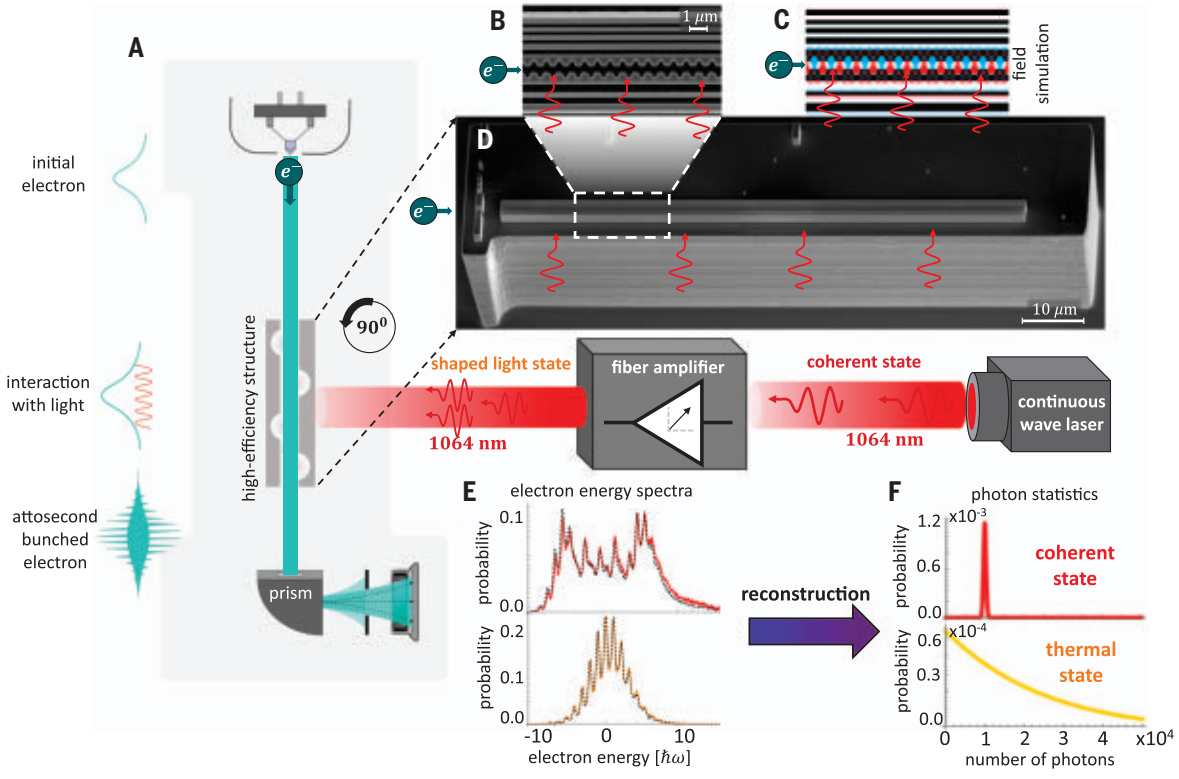


Fig. 2. Free electron interaction with light of different photon statistics in a high-efficiency silicon-photonic nanostructure. (**A**) We used a high-efficiency electron-light coupler in a transmission electron microscope (TEM) to facilitate efficient interaction of free electrons with CW light. With this, we observed the effect of photon statistics in electron-light interactions. The electron energy spectrum was measured with an energy resolution better than that of the single-photon energy, using EELS. The photon statistics is varied continuously with the fiber amplifier from Poissonian to super-Poissonian and up to thermal. (**B**) Scanning electron microscope image of the coupling structure. Light and electrons are efficiently coupled by using a resonating quasi–phase-matched structure consisting of a periodic channel and a Bragg mirror. (**C**) Simulation of the longitudinal quasi–phase-matched electric field in the nanostructure, optimized with photonic inverse design methods for efficient free-electron–light interaction. (**D**) Image of the entire nanostructure in three dimensions. More information is provided in the supplementary materials, materials and methods, and fig. S1. (**E**) Electron energy spectra for interactions with coherent and thermal states. The colored curves denote the theory (fit is explained in fig. S13 and supplementary text S4), and dashed black curves denote the experiment, showing almost perfect overlap. (**F**) The measured electron spectra are used to extract the photon statistics shown here. The slight asymmetry between gain and loss observed in (E) and in Fig. 3D is explained in supplementary text S4.3.

case) with the classical vector $\mathbf{A}$ and scalar V potentials

$$i\hbar\partial_t|\psi\rangle_{\mathrm{el}} = \left[(\mathbf{p}+e\mathbf{A}(t))^2/2m + eV(t)\right]|\psi\rangle_{\mathrm{el}} \quad (1)$$

where $\mathbf{p}=-i\hbar\nabla$ is the momentum operator, e and m are the electron charge and mass, and $|\psi\rangle_{\mathrm{el}}$ denotes the electron quantum state. This description was justified so far because in the quantum picture, classical electromagnetic fields can be described as coherent states $|\alpha\rangle_{\mathrm{ph}}$ (*48*), and intense coherent states stay approximately unchanged under interactions. Consequently, in a full quantum description, the joint electron-photon state $|\psi\rangle_{\mathrm{el-ph}} \approx |\psi\rangle_{\mathrm{el}} \otimes |\alpha\rangle_{\mathrm{ph}}$ remains separable after the interaction with an intense classical field.

By contrast, for some of the photonic states we considered in this work, the joint electron-photon state after the interaction is nonseparable—that is, entangled (*49*). This situation cannot be described by the commonly used theoretical analysis of a time-dependent Schrödinger equation with nonquantized potentials (Eq. 1) but requires a quantum-optics theory. Below, we present the formulation of the quantum interaction of light with a highly paraxial free-electron beam—the Q-PINEM theory (*23*, *25*, *26*), which has the scattering matrix

$$S = \exp\left(g_{\mathrm{q}} b a^{\dagger} - g_{\mathrm{q}}^{*} b^{\dagger} a\right) \quad (2)$$

where g_{q} is the quantum coupling constant; a and $a^{\dagger}$ are the photonic annihilation and creation operators, respectively; and b and $b^{\dagger}$ are the free-electron energy ladder operators describing the electron losing or gaining a single-photon energy quantum, respectively. The resulting joint electron-photon state is generally nonseparable, and its density matrix can be written as

$$\rho_{\mathrm{el-ph}} = \sum_{n,m=0}^{\infty} \rho_{\mathrm{ph}}(n,m)|\psi^n\rangle_{\mathrm{el-ph}}\langle\psi^m|_{\mathrm{el-ph}} \quad (3)$$

where $\rho_{\mathrm{ph}}(n,m) = \langle n|\rho_{\mathrm{ph}}|m\rangle$ is the density matrix element of the light in Fock space. Each pure-state component $|\psi^n\rangle_{\mathrm{el-ph}}$ is a superposition of electron-photon product states. The experimental conditions allow us to consider the initial electron as a single-energy state $|E_0\rangle_{\mathrm{el}}$ with energy uncertainty smaller than the energy $\hbar\omega$ of a single photon of the field with which it interacts. In this case, we can express the joint electron–photon state as

$$|\psi^n\rangle_{\mathrm{el-ph}} = \sum_{k=-\infty}^{\infty} c_k^n |E_0 - k\hbar\omega\rangle_{\mathrm{el}} \otimes |n+k\rangle_{\mathrm{ph}} \quad (4)$$

where $|n+k\rangle_{\mathrm{ph}}$ is a Fock state of light with $n+k$ photons, and $|E_0 - k\hbar\omega\rangle_{\mathrm{el}}$ is the electron state with energy $E_0 - k\hbar\omega$. Equation 4 shows that the free-electron–light interaction can create nonseparable quantum states. By solving Eq. 2 for the state evolution, we find the coefficients $c_k^n = |g_{\mathrm{q}}|^{-1}(-1)^n e^{i\varphi_g k} W_{n+\frac{1}{2}(k+1),\frac{1}{2}|k|}\left(|g_{\mathrm{q}}|^2\right)/\sqrt{(n+k)!n!}$, where W is the Whittaker function and φ_{g} is the phase of g_{q} (supplementary text S2). In the limit of weak interaction and a large number of photons, the coefficients become $c_k^n \approx e^{i\varphi_g k} J_k(2|g_{\mathrm{q}}|\sqrt{n})$ (*23*, *26*), which is reminiscent of the PINEM theory (*17*, *18*).

Extracting the photon statistics from the electron energy spectrum

The photon statistics encapsulated in the photonic density matrix ρ_{ph} can dramatically change the measured electron energy spectrum (*23*, *25*, *26*). We used this concept to experimentally demonstrate how the statistics of light interacting with free electrons is imprinted on the corresponding electron energy spectra. The probability P_k to measure an electron energy shifted by k photons depends on ρ_{ph} through $P_k = \sum_n \left|c_{-k}^{n+k}\right|^2 \rho_{\mathrm{ph}}(n+k,n+k)$. By inverting this relation, we can extract the photon statistics from the measured electron energy spectrum (Fig. 3). Specifically, five electron energy spectra (experiment and theory, respectively) are shown in Fig. 3, A and B, throughout the continuous transition between amplified spontaneous emission and amplified coherent-state of light; the extracted photon statistics for each case are shown in Fig. 3C.

To unveil the role of photon statistics, the state of light (Fig. 3A) was gradually varied from coherent to thermal, and the statistics were reconstructed at each stage (Fig. 3C). The statistics were determined by varying the power of a laser beam seeding the fiber amplifier, varying the gain saturation and output power (*50*, *51*). The optical power entering the electron microscope was kept constant by using an attenuator. This way, the photon statistics can be changed without changing the average number of photons (Fig. 3F). Therefore, the measurement in Fig. 3A directly corresponds to the quantum-to-classical transition of the free-electron quantum/classical walk shown in Fig. 1, A and B. As explained in supplementary text S4.4 and fig. S16, our observations cannot arise from the lack of spatial or temporal optical coherence nor from spatial or temporal inhomogeneity of the light driving the interaction.

To clarify, the term "coherence" is used in two different contexts: (i) The classical optical coherence is characterized by spatial coherence lengths and temporal coherence duration. All types of light in our experiment have the same optical coherence during the interaction with the electron (supplementary text S6). (ii) The quantum coherence relates to the quantum photon statistics and is defined by the correlations $g^{(n)}$. Specifically, $g^{(2)}$ is different for coherent and thermal states. Here, in the context of quantum optics, the term "coherent" also appears as the name of the "coherent state" as defined by Glauber (*52*). In this sense, the thermal light is incoherent (given by a diagonal density matrix). This notion of coherence generalizes the classical optical coherence, which is given as the special case of $g^{(1)}$. The effect of quantum coherence is what we studied in our experiment.

The limiting case of a coherent state corresponds to an approximately separable $\rho_{\mathrm{el-ph}}$, whereas the other limiting case of a thermal state corresponds to a nonseparable $\rho_{\mathrm{el-ph}}$. This can be directly seen in Eq. 3, where ρ_{ph} of thermal light is diagonal, making the joint $\rho_{\mathrm{el-ph}}$ nonseparable. Both limiting cases, and all cases in between, can be accurately captured by the Q-PINEM theory (Eqs. 2 to 4). To quantify the quantum-optical state of light, the corresponding second-order degree of coherence $g^{(2)}(0)$ was extracted from each electron spectrum (Fig. 3F), as first proposed in (*26*). Moreover, because the entire photon distribution can be extracted (Fig. 3C), it directly provides all the photon-number moments $\langle n^m\rangle$ (*23*) and thus also the higher-order $g^{(n)}(0)$ (*26*).

The ability to control and measure the photon statistics during light–free-electron interaction offers a variety of applications. As a proof-of-concept application, we characterize the amplifier output when it undergoes a transition from the limit of Poissonian statistics in the regime of deep saturation to super-Poissonian statistics created by amplified spontaneous emission (*5*). The amplifier has a coherent input seed of amplitude α and a saturable gain $\mathcal{G} = \mathcal{G}\left(|\alpha|^2\right)$, generating light with the following photon statistics (supplementary text S3):

$$\rho_{\mathrm{ph}}(n,n) = e^{-|\alpha|^2}\frac{1}{\mathcal{G}}\left(1-\frac{1}{\mathcal{G}}\right)^n L_n\left(-\frac{|\alpha|^2}{\mathcal{G}-1}\right) \quad (5)$$

where $L_n(x)$ is the nth Laguerre polynomial. By tuning α and $\mathcal{G}$, the photon statistics of the output light can be continuously tuned between amplified coherent state (for $|\alpha|\gg 1$ saturated $\mathcal{G}$, approaching a Poissonian photon distribution) to thermal amplified spontaneous emission (for $|\alpha| \approx 0$ linear $\mathcal{G} \gg 1$, approaching a thermal photon distribution).

We extracted the amplifier gain curve from the analysis of the electron energy spectrum (fig. S10) and performed two additional independent measurements of the amplifier gain that both show good agreement (fig. S10E), from the optical spectra and from direct power measurements. This comparison supports our estimation of the photon statistics from the amplifier model. Furthermore, the gain curves can be used to estimate the quantum coupling

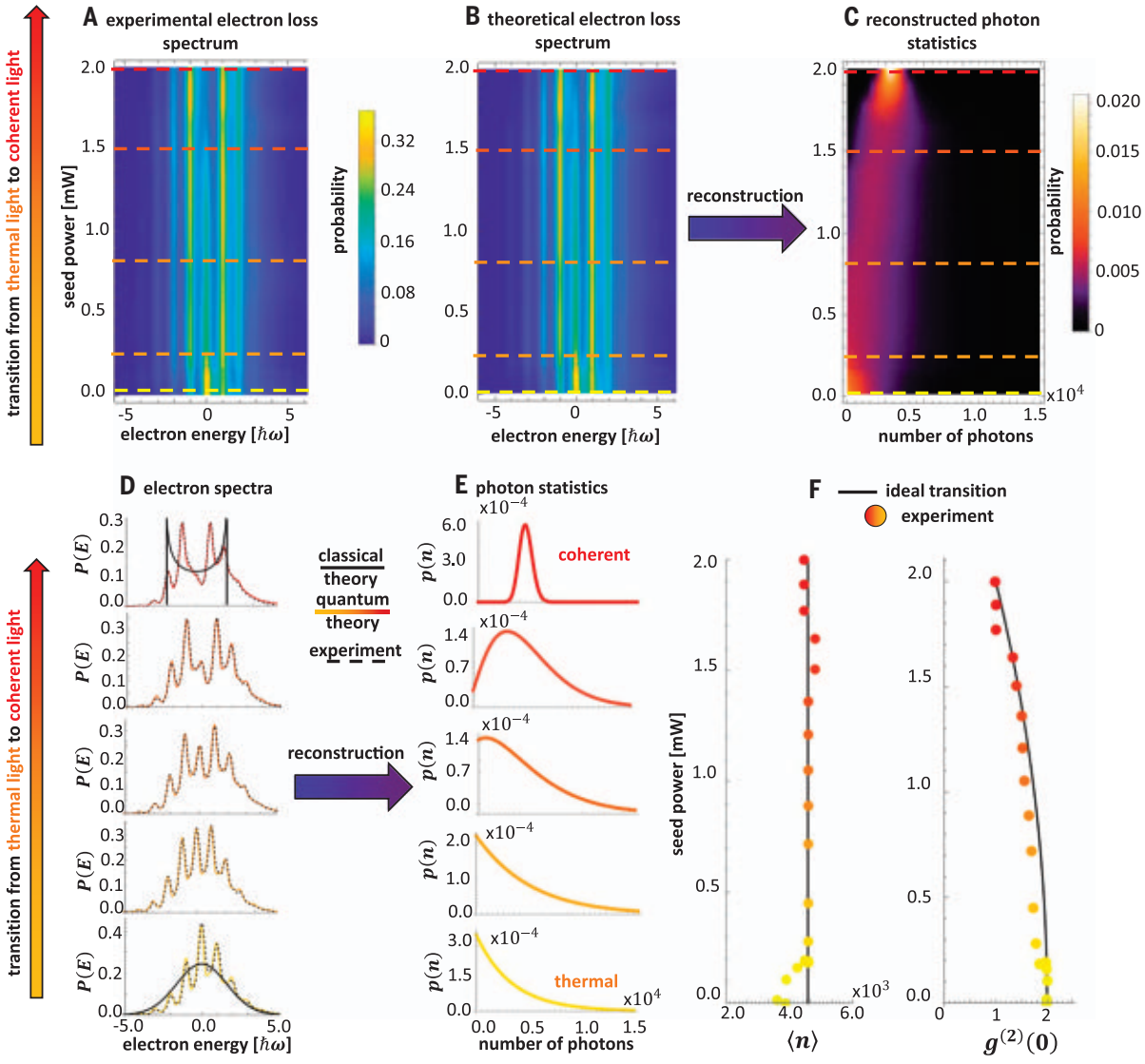


Fig. 3. Experimental reconstruction of photon statistics from electron energy spectra. (**A**) The measured electron energy spectra for a range of fiber amplifier parameters, showing a continuous transition from coherent Poissonian light in the regime of deep saturation to super-Poissonian and eventually thermal light, created through amplified spontaneous emission. The average photon number is the same in all cases. (**B**) The corresponding theoretical calculation of the electron spectra is based on the Q-PINEM theory (Eqs. 2 to 4) with the quantum-optical amplifier model (Eq. 5 and supplementary text S3). (**C**) We reconstructed the photon statistics of light from the experimentally obtained electron spectra (A) by using the fitted parameters of the theoretical model (B) and substituted them in the amplifier model (supplementary text S4). (**D**) Selected cases of measured electron energy spectra after the interaction with different states of light. The data (dashed black curve) show an excellent match to the Q-PINEM theory (colored solid curve). By contrast, simulations using a point electron (solid black curve) do not at all agree with the quantum predictions, indicating that the effects cannot be obtained from an incoherent point electron mixture or collapse in time (supplementary text S7). (**E**) Reconstructed photon statistics corresponding to the selected cases of (D). (**F**) The average number of photons $\langle n \rangle$ and second-order correlation (degree of coherence) $g^{(2)}(0)$ extracted from the measurements. The black curves correspond to the theory (supplementary text S2) with the same parameters.

constant g_q up to the coupling efficiency of the light to the structure (supplementary text S4). In this fashion, the free-electron quantum-optical detection can be applied to extract the ultrafast quantum statistics emerging from amplifiers operating on subpicosecond and even subfemtosecond time scales.

The free electron as a probe of quantum weak measurement

The free electron can serve as the probe in quantum nondestructive detection of the state of light ρ_{ph} (*53*), as suggested theoretically in the context of PINEM (*54*). The electron plays the role of the measurement device and pointer, and the light plays the role of the system to be measured. Specifically, the electron detection in the electron energy loss spectrometer (EELS) is a strong projective measurement of the electron that can be modeled by a set of projection operators $M_k = |E_0 - k\hbar\omega\rangle\langle E_0 - k\hbar\omega|$. After a projection by M_k, the state of light changes from ρ_{ph} to a new state denoted by ρ_{ph}^k (the superscript k indicates the correlation with the electron measurement). The density matrix of this light ρ_{ph}^k may or may not differ significantly from the original state ρ_{ph}, depending on the level of entanglement with the electron. The difference is quantified by the fidelity $F_k = \left[\mathrm{tr}\left\{\sqrt{\sqrt{\rho_{ph}}\rho_{ph}^k\sqrt{\rho_{ph}}}\right\}\right]^2$ (*55*) between ρ_{ph} and ρ_{ph}^k for each value of k (plotted in Fig. 4A). High fidelity ($F_k \to 1$) means that the light is mostly unchanged by the measurement, whereas low fidelity ($F_k \to 0$) means that the light is substantially changed by the measurement.

The electron can act as a probe for weak quantum measurements (*56*–*60*) with a near-unity fidelity for interactions with a coherent state of light—that is, the electron performs a measurement of the light yet does not substantially affect the quantum state of the light, which is why the process is a weak quantum measurement. By contrast, the interaction with thermal light causes a substantial reduction in the fidelity, implying that the electron probe acts more like a projective measurement that does alter the state of light. Therefore, the same electron probe manifests both extremes: weak measurement and projective measurement (Fig. 4A), depending on the state of the measured system. To test this observation, a direct measurement of the outgoing state of light after the interaction could be performed by using high-efficiency coupling into or out of the nanophotonic structure (supplementary text S5.4), which is beyond the scope of this work.

To show theoretically the role of the electron probe in the measurement process, we calculated the purity of the post-interaction electron (Fig. 4B), which shows that the electron maintains a purity of unity for coherent state of light, but the purity substantially decreases for thermal light. Such a substantial reduction in purity can be understood as the "collapse" of the electron wave function in the energy domain. The walker theory we developed (supplementary text S1) shows that this description accurately captures the measured effect and precisely matches the Q-PINEM theory. Through the walker theory, the electron-light interaction can be understood as consecutive infinitesimal steps at which the electron quantum state partially collapses in energy, with full collapse occurring for a thermal state of light, resulting in a pure random walk, or no collapse occurring for a coherent state of light, resulting in a pure quantum walk. The electron wave function never collapses in time and space but only in the energy domain. Spatially and temporally, the electron remains a

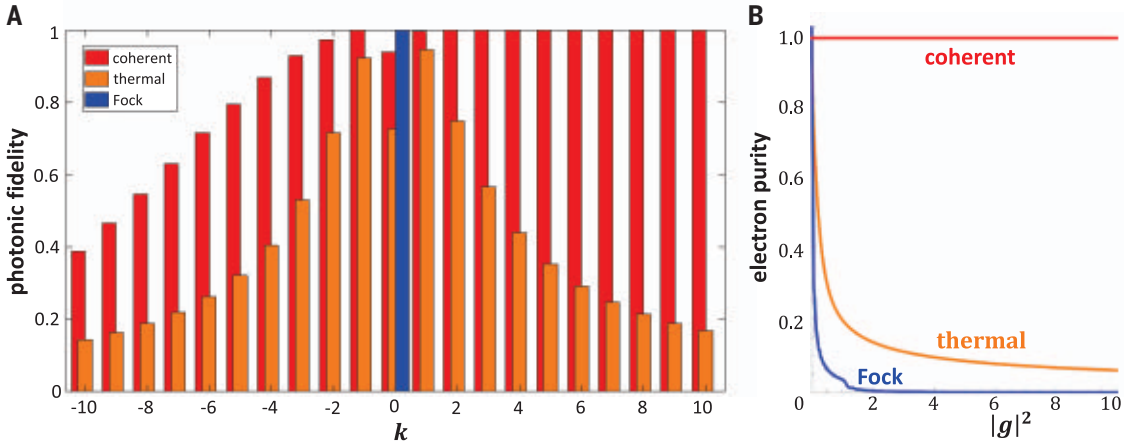


Fig. 4. Photonic fidelity and electron purity after a free-electron–quantum-light interaction. (**A**) Calculated fidelities between the photonic state before and after its interaction with a free electron, which subsequently undergoes a projective measurement. The fidelity is plotted as a function of the energy state $|E_0 - \hbar\omega k\rangle$ in which the electron is detected. We present the fidelity for different states of light, all with an average photon number $\langle n\rangle = 100$ and quantum coupling g_q = 0.1. The fidelity is high for a coherent state, indicating that for small-enough g_q, the electron can serve as a probe of quantum weak measurement. For the thermal state, the fidelity is much lower, indicating a behavior closer to strong projective measurement. As a comparison, we also present the fidelity for a Fock state, for which the measurement is projective (fidelity of zero) for any $k \neq 0$. The fidelity asymmetry for the coherent case is explained by the fundamental difference between subtracting or adding photons to a coherent state (supplementary text S2). (**B**) Electron purity after its interaction with different states of light as a function of the classical coupling strength $|g|^2 = |g_q|^2\langle n\rangle$. The electron stays pure after an interaction with a coherent state, but its purity diminishes much faster for a thermal state, as an indication of emerging entanglement between the electron and light.

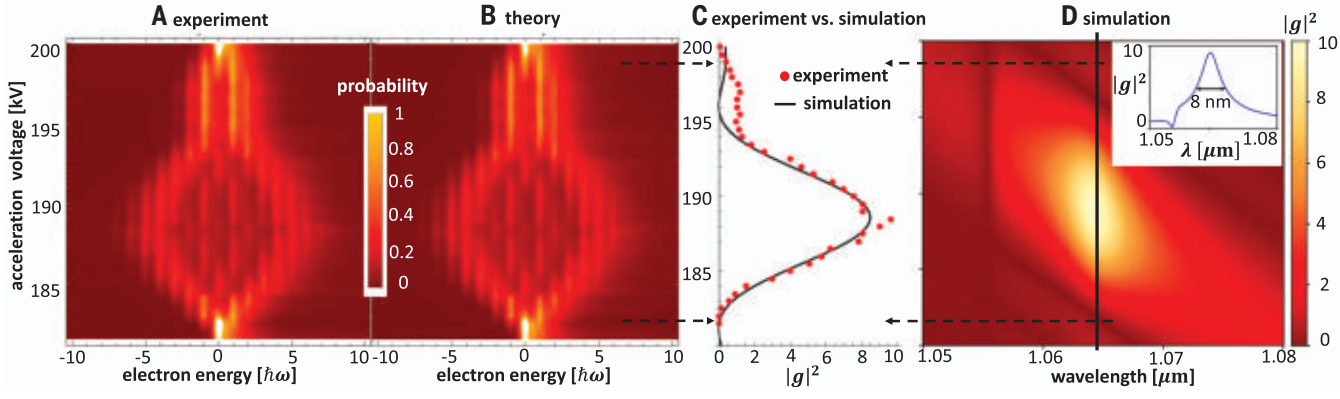


Fig. 5. Measurement of the quasi–phase-matching condition. (**A**) Electron energy spectra measured for a range of electron kinetic energies, (**B**) showing a good agreement with theory. (**C**) The classical interaction strength $|g|^2 = |g_q|^2\langle n\rangle$ and effective interaction length are extracted from the data by comparing it with the quasi–phase-matching theory (supplementary text S5). (**D**) Simulation of $|g|^2$ as a function of electron kinetic energy and laser wavelength, showing the resonant nature of the quasi–phase-matched interaction. A version of (D) for a longer structure is provided in fig. S15, allowing a better frequency resolution for isolating a single mode in the structure.

coherent wave function that extends over many cycles of the field, as evident by the emergence of discretized energy peaks (such as in Fig. 3D and in all other figures), occurring even with thermal light. A collapse in time or space, if it ever appears, would manifest as an incoherent mixture of point particles interacting with the light field, which cannot result in discrete energy peaks (Fig. 3D, solid black curves, and supplementary text S7). By contrast, the collapse in energy occurring in our experiment causes the electron to split into multiple extended wave functions, in a joint quantum state entangled with the state of light.

The role of quasi–phase-matching and connection to the Smith-Purcell effect

The key to the efficient electron-light coupling that enables our entire experiment is matching the electron velocity with the phase velocity of light trapped in the nanostructure. This phenomenon is known as quasi–phase-matching between free electrons and light (supplementary text S5), also known as the inverse Smith-Purcell effect (*9*, *61*). Our realization of this effect goes beyond conventional realizations of inverse Smith-Purcell experiments in three ways: (i) using CW light rather than laser pulses; (ii) having an electron wave function rather than a classical point electron, as proposed theoretically in (*62*–*64*); and (iii) varying the photon statistics so that the experiment deviates from the semiclassical theory treated in (*62*, *63*) and generally cannot be described by any time-dependent Schrödinger equation (Eq. 1). To highlight and quantify the quasi–phase-matching, we scanned over the electron energy (Fig. 5), searching for the optimal electron-light coupling conditions. The optimal acceleration voltage was found to be 189 keV, and we estimate the effective interaction length to be 56 μm, shorter than the structure length of 84 μm. This deviation arises from the 51-μm full width at half maximum transverse intensity profile of the light beam (supplementary materials, materials and methods).

Discussion and outlook

The underlying quantum-optical theory that describes our experiment is best understood in light of recent theoretical advances (*25*, *26*, *64*), which have caused a paradigm shift in how we think about the interaction of free electrons and light. Specifically, these and other works show how the interaction becomes sensitive to the photon statistics (*23*, *25*, *26*, *64*–*67*) and provide opportunities for shaping electron wave functions (*65*). These promising ideas provide new opportunities for research in free-electron quantum optics, suggesting new concepts such as electron-light entanglement that can induce electron-electron entanglement (*25*, *68*, *69*). This entanglement can in turn be used to create new quantum light sources (*66*), improve cathodoluminescence techniques (*68*, *70*), and develop future Cherenkov detectors for particle physics (*71*). Because all previous free-electron–light experiments worked with classical (coherent state) light, our experiment is a proof of concept for the predictions on interactions between free electrons and nonclassical light, paving the path for these exciting applications.

On the technical side, our experiment highlights new applications of silicon-photonic nanostructures in the field of quantum optics, in which free electrons provide a mechanism to extract the quantum photon statistics. This concept can be extended into full quantum-state tomography of light (*23*) by using Ramsey-type experiments (*19*). This approach to quantum-state tomography does not have to destroy or absorb the measured light. Such free-electron–based quantum-optical detectors can have extremely broad bandwidths and the ability to selectively detect individual modes by using phase-matching (supplementary materials S5). The outlook of such quantum-optical detection techniques depends on the efficient coupling of light into the nanostructure that performs the electron-light interaction; the necessary coupling capabilities are already available as on-chip technology (*11*, *72*).

Our small electron probe (30 nm in diameter) is sensitive to minute transverse changes in the field across the channel of the nanostructure, mapping the field at deep subwavelength resolution. Thus, our methods can help identify optimal operation conditions of these nanostructures for different applications, such as laser-driven electron acceleration. Future experiments would enable comparing performances of different electron accelerators: between the more traditional pillars-based nanostructures (*73*) and ones based on inverse design optimization (*11*). We can characterize the spectral response with a resolution limited only by the excitation linewidth, being extremely narrow if using a tunable CW source.

Over the past decade, coherent shaping of spatial electron wave functions (*43*, *74*–*78*) has opened new avenues in electron microscopy, such as electron magnetic circular dichroism (*75*) and aberration corrections (*79*). More recently, coherent temporal modulation of electron wave functions (*14*, *19*, *47*, *65*, *80*, *81*) has excited new ideas for ultrafast light-matter interactions and free-electron coherent control (*19*, *20*, *82*). Especially interesting are the applications of modulation by CW light, showing better phase contrast (*44*), PINEM by means of electron post-selection (*45*), plasmon excitation mapping (*46*), and advances toward attosecond-resolution metrology (*47*). However, reaching strong electron modulation in a CW operation has been a longstanding challenge that remained unanswered. Our experimental demonstration paves the way toward equipping state-of-the-art microscopes with CW silicon-photonic light couplers. The modulation capabilities may be further extended to combined spatial and temporal shaping, with a structured light-electron nanophotonic coupler and/or specially shaped light beams (*83*). Such dream microscopes could operate at simultaneous subangstrom-spatial and few-attosecond-temporal resolution (*19*–*21*, *84*) and lead to breakthrough experiments in some of the hardest fundamental problems: providing direct observation of molecular excitation dynamics, electron transport phenomena, transient subcycle phenomena in optical nonlinearities, ultrafast plasma oscillations, and many more effects that cannot be explored by other means.

A related work that also shows CW PINEM by using silicon photonic structures was placed on arXiv in parallel with our work (*85*).

REFERENCES AND NOTES

1. J. C. Maxwell, A dynamical theory of the electromagnetic field. *Philos. Trans. R. Soc. Lond.* **155**, 459–512 (1865). doi: 10.1098/rstl.1865.0008
2. A. Einstein, Über einem die Erzeugung und Verwandlung des Lichtes betreffenden heuristischen Gesichtspunkt. *Ann. Phys.* **322**, 132–148 (1905). doi: 10.1002/andp.19053220607
3. A. Aspect, P. Grangier, G. Roger, Experimental realization of Einstein-Podolsky-Rosen-Bohm Gedankenexperiment: A new violation of Bell's inequalities. *Phys. Rev. Lett.* **49**, 91–94 (1982). doi: 10.1103/PhysRevLett.49.91
4. M. O. Scully, M. S. Zubairy, *Quantum Optics* (Cambridge Univ. Press, 1999).
5. R. Loudon, *The Quantum Theory of Light* (Oxford, 2000)
6. F. Amiranoff *et al*., Observation of laser wakefield acceleration of electrons. *Phys. Rev. Lett.* **81**, 995–998 (1998). doi: 10.1103/PhysRevLett.81.995
7. T. Tajima, X. Q. Yan, T. Ebisuzaki, Wakefield acceleration. *Rev. Modern Plasma Phys.* **4**, 7 (2020). doi: 10.1007/s41614-020-0043-z
8. E. A. Peralta *et al*., Demonstration of electron acceleration in a laser-driven dielectric microstructure. *Nature* **503**, 91–94 (2013). doi: 10.1038/nature12664; pmid: 24077116
9. J. Breuer, P. Hommelhoff, Laser-based acceleration of nonrelativistic electrons at a dielectric structure. *Phys. Rev. Lett.* **111**, 134803 (2013). doi: 10.1103/PhysRevLett.111.134803; pmid: 24116785
10. R. J. England *et al*., Dielectric laser accelerators. *Rev. Mod. Phys.* **86**, 1337–1389 (2014). doi: 10.1103/RevModPhys.86.1337
11. N. V. Sapra *et al*., On-chip integrated laser-driven particle accelerator. *Science* **367**, 79–83 (2020). doi: 10.1126/science.aay5734; pmid: 31896715
12. Y. Adiv *et al*. Observation of the quantum nature of laser-driven particle acceleration. CLEO conference SW4G.4. (2020).
13. B. Barwick, D. J. Flannigan, A. H. Zewail, Photon-induced near-field electron microscopy. *Nature* **462**, 902–906 (2009). doi: 10.1038/nature08662; pmid: 20016598
14. A. Feist *et al*., Quantum coherent optical phase modulation in an ultrafast transmission electron microscope. *Nature* **521**, 200–203 (2015). doi: 10.1038/nature14463; pmid: 25971512
15. L. Piazza *et al*., Simultaneous observation of the quantization and the interference pattern of a plasmonic near-field. *Nat. Commun.* **6**, 6407 (2015). doi: 10.1038/ncomms7407; pmid: 25728197
16. A. Arbouet, G. M. Caruso, F. Houdellier, in *Advances in Imaging and Electron Physics*, P. W. Hawkes, Ed. (Academic Press, 2018), vol. 207, pp. 1–72.
17. F. J. García de Abajo, A. Asenjo-Garcia, M. Kociak, Multiphoton absorption and emission by interaction of swift electrons with evanescent light fields. *Nano Lett.* **10**, 1859–1863 (2010). doi: 10.1021/nl100613s; pmid: 20415459
18. S. T. Park, M. Lin, A. H. Zewail, Photon-induced near-field electron microscopy (PINEM): Theoretical and experimental. *New J. Phys.* **12**, 123028 (2010). doi: 10.1088/1367-2630/12/12/123028
19. K. E. Priebe *et al*., Attosecond electron pulse trains and quantum state reconstruction in ultrafast transmission electron microscopy. *Nat. Photonics* **11**, 793–797 (2017). doi: 10.1038/s41566-017-0045-8

20. G. M. Vanacore *et al*., Attosecond coherent control of free-electron wave functions using semi-infinite light fields. *Nat. Commun.* **9**, 2694 (2018). doi: 10.1038/s41467-018-05021-x; pmid: 30002367
21. Y. Morimoto, P. Baum, Diffraction and microscopy with attosecond electron pulse trains. *Nat. Phys.* **14**, 252–256 (2018). doi: 10.1038/s41567-017-0007-6
22. Y. Pan, B. Zhang, A. Gover, Anomalous photon-induced near-field electron microscopy. *Phys. Rev. Lett.* **122**, 183204 (2019). doi: 10.1103/PhysRevLett.122.183204; pmid: 31144903
23. A. Gorlach *et al*., Ultrafast non-destructive measurement of the quantum state of light using free electrons. arXiv:2012.12069 [quant-ph] (2020).
24. C. Cohen-Tannoudji, B. Diu, F. Laloe, *Quantum Mechanics* (Wiley-Interscience, 2006), vol. 1.
25. O. Kfir, Entanglements of electrons and cavity photons in the strong-coupling regime. *Phys. Rev. Lett.* **123**, 103602 (2019). doi: 10.1103/PhysRevLett.123.103602; pmid: 31573279
26. V. di Giulio, M. Kociak, F. J. G. de Abajo, Probing quantum optical excitations with fast electrons. *Optica* **6**, 1524–1534 (2019). doi: 10.1364/OPTICA.6.001524
27. Analogously, although unrelated to quantum walks, broader photon distributions also lead to increased decoherence in other quantum systems, such as Rabi oscillations (*86*).
28. C. A. Ryan, M. Laforest, J. C. Boileau, R. Laflamme, Experimental implementation of a discrete-time quantum random walk on an NMR quantum-information processor. *Phys. Rev. A* **72**, 062317 (2005). doi: 10.1103/PhysRevA.72.062317
29. H. B. Perets *et al*., Realization of quantum walks with negligible decoherence in waveguide lattices. *Phys. Rev. Lett.* **100**, 170506 (2008). doi: 10.1103/PhysRevLett.100.170506; pmid: 18518267
30. M. Karski *et al*., Quantum walk in position space with single optically trapped atoms. *Science* **325**, 174–177 (2009). doi: 10.1126/science.1174436; pmid: 19589996
31. F. Zähringer *et al*., Realization of a quantum walk with one and two trapped ions. *Phys. Rev. Lett.* **104**, 100503 (2010). doi: 10.1103/PhysRevLett.104.100503; pmid: 20366407
32. P. M. Preiss *et al*., Strongly correlated quantum walks in optical lattices. *Science* **347**, 1229–1233 (2015). doi: 10.1126/science.1260364; pmid: 25766229
33. S. Dadras, A. Gresch, C. Groiseau, S. Wimberger, G. S. Summy, Quantum walk in momentum space with a Bose-Einstein condensate. *Phys. Rev. Lett.* **121**, 070402 (2018). doi: 10.1103/PhysRevLett.121.070402; pmid: 30169047
34. V. Kendon, Decoherence in quantum walks—A review. *Math. Structures Comput. Sci.* **17**, 1169–1220 (2007). doi: 10.1017/S0960129507006354
35. M. A. Broome *et al*., Discrete single-photon quantum walks with tunable decoherence. *Phys. Rev. Lett.* **104**, 153602 (2010). doi: 10.1103/PhysRevLett.104.153602; pmid: 20481989
36. A. Schreiber *et al*., Decoherence and disorder in quantum walks: From ballistic spread to localization. *Phys. Rev. Lett.* **106**, 180403 (2011). doi: 10.1103/PhysRevLett.106.180403; pmid: 21635071
37. N. C. Harris *et al*., Quantum transport simulations in a programmable nanophotonic processor. *Nat. Photonics* **11**, 447–452 (2017). doi: 10.1038/nphoton.2017.95
38. K. Wang *et al*., Coherent interaction between free electrons and a photonic cavity. *Nature* **582**, 50–54 (2020). doi: 10.1038/s41586-020-2321-x; pmid: 32494081
39. O. Kfir *et al*., Controlling free electrons with optical whispering-gallery modes. *Nature* **582**, 46–49 (2020). doi: 10.1038/s41586-020-2320-y; pmid: 32494079
40. R. Dahan *et al*., Resonant phase-matching between a light wave and a free-electron wave function. *Nat. Phys.* **16**, 1123–1131 (2020). doi: 10.1038/s41567-020-01042-w
41. M. Kozák *et al*., Acceleration of sub-relativistic electrons with an evanescent optical wave at a planar interface. *Opt. Express* **25**, 19195–19204 (2017). doi: 10.1364/OE.25.019195; pmid: 29041113
42. T. W. Hughes, I. A. D. Williamson, M. Minkov, S. Fan, Forward-mode differentiation of Maxwell's equations. *ACS Photonics* **6**, 3010–3016 (2019). doi: 10.1021/acsphotonics.9b01238
43. G. M. Vanacore *et al*., Ultrafast generation and control of an electron vortex beam via chiral plasmonic near fields. *Nat. Mater.* **18**, 573–579 (2019). doi: 10.1038/s41563-019-0336-1; pmid: 31061485
44. O. Schwartz *et al*., Laser phase plate for transmission electron microscopy. *Nat. Methods* **16**, 1016–1020 (2019). doi: 10.1038/s41592-019-0552-2; pmid: 31562475
45. P. Das *et al*., Stimulated electron energy loss and gain in an electron microscope without a pulsed electron gun. *Ultramicroscopy* **203**, 44–51 (2019). doi: 10.1016/j.ultramic.2018.12.011; pmid: 31000482
46. C. Liu *et al*., Continuous wave resonant photon stimulated electron energy-gain and electron energy-loss spectroscopy of individual plasmonic nanoparticles. *ACS Photonics* **6**, 2499–2508 (2019). doi: 10.1021/acsphotonics.9b00830
47. A. Ryabov, J. W. Thurner, D. Nabben, M. V. Tsarev, P. Baum, Attosecond metrology in a continuous-beam transmission electron microscope. *Sci. Adv.* **6**, eabb1393 (2020). doi: 10.1126/sciadv.abb1393; pmid: 33177078
48. The coherent state $|\alpha\rangle_{ph}$, electric field phasor $E_z(z)$, and time-dependent potential $\mathbf{A}(t)$ all describe the same electromagnetic field throughout the paper (*64*).
49. The nonseparable electron-photon quantum state can also involve nonlocality, once the electron and photons propagate away from the interaction area.
50. M. Shtaif, G. Eisenstein, Experimental study of the statistical properties of nonlinearly amplified signals in semiconductor optical amplifiers. *IEEE Photonics Technol. Lett.* **9**, 904–906 (1997). doi: 10.1109/68.593341
51. M. Shtaif, B. Tromborg, G. Eisenstein, Noise spectra of semiconductor optical amplifiers: Relation between semiclassical and quantum descriptions. *IEEE J. Quantum Electron.* **34**, 869–878 (1998). doi: 10.1109/3.668775
52. R. J. Glauber, Nobel Lecture: One hundred years of light quanta. *Rev. Mod. Phys.* **78**, 1267–1278 (2006). doi: 10.1103/RevModPhys.78.1267; pmid: 16888746
53. A. Reiserer, S. Ritter, G. Rempe, Nondestructive detection of an optical photon. *Science* **342**, 1349–1351 (2013). doi: 10.1126/science.1246164; pmid: 24231809
54. Y. Pan *et al*., Weak measurement, projective measurement and quantum-to-classical transitions in electron-photon interactions. arXiv:1910.11685 [quant-ph]. (2019)
55. R. Jozsa, Fidelity for mixed quantum states. *J. Mod. Opt.* **41**, 2315–2323 (1994). doi: 10.1080/09500349414552171
56. Y. Aharonov, D. Z. Albert, L. Vaidman, How the result of a measurement of a component of the spin of a spin-1/2 particle can turn out to be 100. *Phys. Rev. Lett.* **60**, 1351–1354 (1988). doi: 10.1103/PhysRevLett.60.1351; pmid: 10038016
57. G. Mitchison, R. Jozsa, S. Popescu, Sequential weak measurement. *Phys. Rev. A* **76**, 062105 (2007). doi: 10.1103/PhysRevA.76.062105
58. A. Feizpour, X. Xing, A. M. Steinberg, Amplifying single-photon nonlinearity using weak measurements. *Phys. Rev. Lett.* **107**, 133603 (2011). doi: 10.1103/PhysRevLett.107.133603; pmid: 22026853
59. M. Berry, P. Shukla, Pointer supershifts and superoscillations in weak measurements. *J. Phys. A Math. Theor.* **45**, 15301–15315 (2012). doi: 10.1088/1751-8113/45/1/015301
60. B. Tamir, E. Cohen, Introduction to weak measurements and weak values. *Quanta* **2**, 7–17 (2013). doi: 10.12743/quanta.v2i1.14
61. S. J. Smith, E. M. Purcell, Visible light from localized surface charges moving across a grating. *Phys. Rev.* **92**, 1069 (1953). doi: 10.1103/PhysRev.92.1069
62. N. Talebi, Schrödinger electrons interacting with optical gratings: Quantum mechanical study of the inverse Smith-Purcell effect. *New J. Phys.* **18**, 123006 (2016). doi: 10.1088/1367-2630/18/12/123006
63. A. Gover, Y. Pan, Dimension-dependent stimulated radiative interaction of a single electron quantum wavepacket. *Phys. Lett. A* **382**, 1550–1555 (2018). doi: 10.1016/j.physleta.2018.03.049
64. Y. Pan, A. Gover, Spontaneous and stimulated emissions of a preformed quantum free-electron wave function. *Phys. Rev. A* **99**, 052107 (2019). doi: 10.1103/PhysRevA.99.052107
65. V. di Giulio, F. J. García de Abajo, Free-electron shaping using quantum light. *Optica* **7**, 1820–1830 (2020). doi: 10.1364/OPTICA.404598
66. A. Ben Hayun *et al*., Shaping quantum photonic states using free electrons. *Sci. Adv.* **7**, eabe4270 (2021). doi: 10.1126/sciadv.abe4270; pmid: 33692108
67. F. J. García de Abajo, V. di Giulio, Optical excitations with electron beams: Challenges and opportunities. *ACS Photonics* **8**, 945–974 (2021). doi: 10.1021/acsphotonics.0c01950
68. A. Karnieli, N. Rivera, A. Arie, I. Kaminer, Superradiance and subradiance due to quantum interference of entangled free electrons. *Phys. Rev. Lett.* **127**, 060403 (2021). doi: 10.1103/PhysRevLett.127.060403
69. C. Mechel *et al*., Quantum correlations in electron microscopy. *Optica* **8**, 70 (2021). doi: 10.1364/OPTICA.402693
70. O. Kfir, V. Di Giulio, F. J. G. de Abajo, C. Ropers, Optical coherence transfer mediated by free electrons. *Sci. Adv.* **7**, eabf6380 (2021). doi: 10.1126/sciadv.abf6380; pmid: 33931451
71. A. Karnieli, N. Rivera, A. Arie, I. Kaminer, The coherence of light is fundamentally tied to the quantum coherence of the emitting particle. *Sci. Adv.* **7**, eabf8096 (2021). doi: 10.1126/sciadv.abf8096; pmid: 33931454
72. R. Marchetti, C. Lacava, L. Carroll, K. Gradkowski, P. Minzioni, Coupling strategies for silicon photonics integrated chips. *Photon. Res.* **7**, 201 (2019). doi: 10.1364/PRJ.7.000201
73. K. J. Leedle *et al*., Dielectric laser acceleration of sub-100 keV electrons with silicon dual-pillar grating structures. *Opt. Lett.* **40**, 4344–4347 (2015). doi: 10.1364/OL.40.004344; pmid: 26371932
74. M. Uchida, A. Tonomura, Generation of electron beams carrying orbital angular momentum. *Nature* **464**, 737–739 (2010). doi: 10.1038/nature08904; pmid: 20360737
75. J. Verbeeck, H. Tian, P. Schattschneider, Production and application of electron vortex beams. *Nature* **467**, 301–304 (2010). doi: 10.1038/nature09366; pmid: 20844532
76. B. J. McMorran *et al*., Electron vortex beams with high quanta of orbital angular momentum. *Science* **331**, 192–195 (2011). doi: 10.1126/science.1198804; pmid: 21233382
77. N. Voloch-Bloch, Y. Lereah, Y. Lilach, A. Gover, A. Arie, Generation of electron Airy beams. *Nature* **494**, 331–335 (2013). doi: 10.1038/nature11840; pmid: 23426323
78. K. Y. Bliokh *et al*., Theory and applications of free-electron vortex states. *Phys. Rep.* **690**, 1–70 (2017). doi: 10.1016/j.physrep.2017.05.006
79. R. Shiloh *et al*., Spherical aberration correction in a scanning transmission electron microscope using a sculpted thin film. *Ultramicroscopy* **189**, 46–53 (2018). doi: 10.1016/j.ultramic.2018.03.016; pmid: 29614394
80. O. Reinhardt, I. Kaminer, Theory of Shaping Electron Wavepackets with Light. *ACS Photonics* **7**, 2859–2870 (2020). doi: 10.1021/acsphotonics.0c01133
81. G. M. Vanacore, I. Madan, F. Carbone, Spatio-temporal shaping of a free-electron wave function via coherent light–electron interaction. *Riv. Nuovo Cim.* **43**, 567–597 (2020). doi: 10.1007/s40766-020-00012-5
82. A. Gover, A. Yariv, Free-electron-bound-electron resonant interaction. *Phys. Rev. Lett.* **124**, 064801 (2020). doi: 10.1103/PhysRevLett.124.064801; pmid: 32109105
83. S. Tsesses *et al*., Spatial modulation of free-electron wavepackets by shaping ultrafast plasmonic excitations. CLEO *Conference* FTu3B.4 (2020).
84. M. Kozák, N. Schönenberger, P. Hommelhoff, Ponderomotive generation and detection of attosecond free-electron pulse trains. *Phys. Rev. Lett.* **120**, 103203 (2018). doi: 10.1103/PhysRevLett.120.103203; pmid: 29570333
85. J.-W. Henke, A. S. Raja, A. Feist, G. Huang, G. Arend, Y. Yang, J. Kappert, R. N. Wang, M. Möller, J. Pan, J. Liu, O. Kfir, C. Ropers, T. J. Kippenberg, Integrated photonics enables continuous-beam electron phase modulation. arXiv:2105.03729 [physics.optics] (2021).
86. B. W. Shore, P. L. Knight, The Jaynes-Cummings model. *J. Mod. Opt.* **40**, 1195–1238 (1993). doi: 10.1080/09500349314551321

ACKNOWLEDGMENTS

We thank E. Cohen for the fruitful discussions regarding the classical/quantum walk description. We also thank IDES and especially S. T. Park for support, advice, and discussions. We thank T. Gondo and H. Miyazaki (Mel-Build Corporation) for the specially designed HATA-holder. The experiments were performed on the UTEM of the AdQuanta group of I.K., which is installed inside the electron microscopy center (MIKA) of the Department of Materials Science and Engineering at the Technion. We thank the MPL cleanroom staff for continued technical support. I.K., M.S., and their students gratefully acknowledge the generous support of R. Magid and R. Magid, who have made it possible to carry out these experiment at the UTEM lab at the Technion. **Funding:** This project has received funding from the European Union's Horizon 2020 research and innovation program under grant agreement 851780-ERC-NanoEP, the Israel Science Foundation (grant 830/19), the Binational USA-Israel Science Foundation (BSF) 2018288, Gordon and Betty Moore Foundation grant 4744 (ACHIP), and ERC Advanced Grant 884217 (AccelOnChip). A.K. acknowledges support by the Adams Fellowship of the Israeli Academy of Sciences and Humanities. **Author contributions:** All authors contributed substantially to this work. **Competing interests:** None declared. **Data and materials availability:** All data needed to evaluate the conclusions in the paper are present in the paper or the supplementary materials.

SUPPLEMENTARY MATERIALS

https://science.org/doi/10.1126/science.abj7128
Materials and Methods
Supplementary Text
Figs. S1 to S17
References (*87*–*97*)

27 May 2021; accepted 9 August 2021
Published online 26 August 2021
10.1126/science.abj7128

RESEARCH ARTICLE SUMMARY

CORONAVIRUS

Immune correlates of protection by mRNA-1273 vaccine against SARS-CoV-2 in nonhuman primates

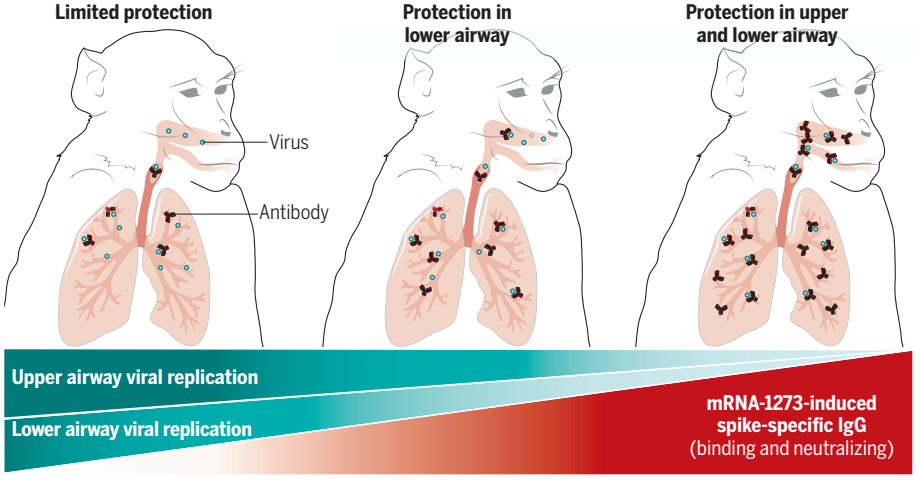
Kizzmekia S. Corbett†, Martha C. Nason†, Britta Flach, Matthew Gagne, Sarah O'Connell, Timothy S. Johnston, Shruti N. Shah, Venkata Viswanadh Edara, Katharine Floyd, Lilin Lai, Charlene McDanal, Joseph R. Francica, Barbara Flynn, Kai Wu, Angela Choi, Matthew Koch, Olubukola M. Abiona, Anne P. Werner, Juan I. Moliva, Shayne F. Andrew, Mitzi M. Donaldson, Jonathan Fintzi, Dillon R. Flebbe, Evan Lamb, Amy T. Noe, Saule T. Nurmukhambetova, Samantha J. Provost, Anthony Cook, Alan Dodson, Andrew Faudree, Jack Greenhouse, Swagata Kar, Laurent Pessaint, Maciel Porto, Katelyn Steingrebe, Daniel Valentin, Serge Zouantcha, Kevin W. Bock, Mahnaz Minai, Bianca M. Nagata, Renee van de Wetering, Seyhan Boyoglu-Barnum, Kwanyee Leung, Wei Shi, Eun Sung Yang, Yi Zhang, John-Paul M. Todd, Lingshu Wang, Gabriela S. Alvarado, Hanne Andersen, Kathryn E. Foulds, Darin K. Edwards, John R. Mascola, Ian N. Moore, Mark G. Lewis, Andrea Carfi, David Montefiori, Mehul S. Suthar, Adrian McDermott, Mario Roederer, Nancy J. Sullivan, Daniel C. Douek, Barney S. Graham*, Robert A. Seder*

INTRODUCTION: Mass vaccination against severe acute respiratory syndrome coronavirus 2 (SARS-CoV-2) offers the most efficient public health intervention to control the COVID-19 pandemic. Two mRNA-based vaccines, Moderna's mRNA-1273 and Pfizer/BioNTech's BNT162b2, both of which encode the prefusion-stabilized spike glycoprotein S-2P, showed >94% efficacy against symptomatic COVID-19 in interim phase 3 analyses and are currently being administered globally. Several other vaccines have shown 60 to 80% efficacy against symptomatic COVID-19 in phase 3 trials, and a number of candidate vaccines are in earlier stages of clinical development. An immune correlate of protection can be used to inform potential dose reduction, advance approval of other vaccine candidates in lieu of phase 3 efficacy data, extend indications for use to other age groups, and provide insights into the immune mechanisms of protection.

RATIONALE: In assessing immunogenicity and protection of vaccines against SARS-CoV-2, nonhuman primates (NHPs) have been a useful model for clinical translation. NHP innate immune responses and B and T cell repertoires show much greater similarity to humans than do those of rodents, allowing immune responses to be assessed using clinically applicable vaccine doses and regimens. After SARS-CoV-2 infection, NHPs have transient viral replication in the upper and lower airways and mild inflammation in the lung that recapitulates the features of mild infection in humans. Here, we used immunogenicity and protection assessments from a previous NHP mRNA-1273 vaccine study combined with new data from a dose de-escalation study. We evaluated how multiple measurements of humoral and cellular immunity correlate with the reduction of viral replication in the upper and lower airway after challenge. Antibodies in bronchoalveolar lavage (BAL) and nasal swabs (NS) after vaccination were analyzed to assess site-specific immune correlates. Finally, immunoglobulin G (IgG) from mRNA-immunized NHPs was passively transferred in a highly pathogenic Syrian hamster SARS-CoV-2 challenge model to determine whether these antibodies were sufficient for protection.

RESULTS: NHPs received either no vaccine or doses ranging from 0.3 to 100 μg of mRNA-1273, an mRNA vaccine encoding S-2P, at weeks 0 and 4. mRNA-1273 vaccination elicited circulating and mucosal antibody responses in a dose-dependent manner. Using the World Health Organization standard for measuring S-specific IgG, a 10-fold increase in S-binding titers was associated with ~10-fold reductions in viral replication in BAL and NS after challenge. No animal with S-specific IgG >336 IU/ml had BAL subgenomic RNA (sgRNA) >10,000 copies/ml, and no animal with S-specific IgG >645 IU/ml had NS sgRNA >100,000 copies/swab, so these were chosen as the thresholds for protection. These reductions in viral replication in BAL were associated with limited inflammation and viral antigen detection in lung tissue. Finally, passive transfer of vaccine-induced IgG from NHPs to naïve hamsters was sufficient to mediate protection.

CONCLUSION: mRNA-1273 vaccine–induced antibody responses are a mechanistic correlate of protection against SARS-CoV-2 infection in NHPs. Protection in the lower respiratory tract was achieved at lower serum antibody concentrations than in the upper respiratory tract. These data explain in part the consistent finding that vaccine efficacy against severe lower tract disease is greater than that against mild upper tract disease. These findings have potential implications for how additional boosting may sustain protection against severe disease in the lower respiratory tract and limit mild infection and transmission by enhancing the immunity required in the upper respiratory tract. ■



mRNA-1273 vaccine–induced humoral immune responses are a mechanistic correlate of protection against SARS-CoV-2. Levels of serum and mucosal spike-specific IgG in mRNA-1273–vaccinated NHPs were inversely correlated with the reduction of viral replication in the upper airway and lower airway after SARS-CoV-2 challenge.

The list of author affiliations is available in the full article online.
*Corresponding author. Email: rseder@mail.nih.gov (R.A.S.); bgraham@nih.gov (B.S.G.)
†These authors contributed equally to this work.
Cite this article as K. S. Corbett *et al.*, *Science* 373, eabj0299 (2021). DOI: 10.1126/science.abj0299

READ THE FULL ARTICLE AT
https://doi.org/10.1126/science.abj0299

RESEARCH ARTICLE

CORONAVIRUS

Immune correlates of protection by mRNA-1273 vaccine against SARS-CoV-2 in nonhuman primates

Kizzmekia S. Corbett[1]†‡, Martha C. Nason[2]†, Britta Flach[1], Matthew Gagne[1], Sarah O'Connell[1], Timothy S. Johnston[1], Shruti N. Shah[1], Venkata Viswanadh Edara[3], Katharine Floyd[3], Lilin Lai[3], Charlene McDanal[4], Joseph R. Francica[1]§, Barbara Flynn[1], Kai Wu[5], Angela Choi[5], Matthew Koch[5], Olubukola M. Abiona[1], Anne P. Werner[1], Juan I. Moliva[1], Shayne F. Andrew[1], Mitzi M. Donaldson[1], Jonathan Fintzi[1], Dillon R. Flebbe[1], Evan Lamb[1], Amy T. Noe[1], Saule T. Nurmukhambetova[1], Samantha J. Provost[1], Anthony Cook[6], Alan Dodson[6], Andrew Faudree[6], Jack Greenhouse[6], Swagata Kar[6], Laurent Pessaint[6], Maciel Porto[6], Katelyn Steingrebe[6], Daniel Valentin[6], Serge Zouantcha[6], Kevin W. Bock[7], Mahnaz Minai[7], Bianca M. Nagata[7], Renee van de Wetering[1], Seyhan Boyoglu-Barnum[1], Kwanyee Leung[1], Wei Shi[1], Eun Sung Yang[1], Yi Zhang[1], John-Paul M. Todd[1], Lingshu Wang[1], Gabriela S. Alvarado[1], Hanne Andersen[6], Kathryn E. Foulds[1], Darin K. Edwards[5], John R. Mascola[1], Ian N. Moore[7], Mark G. Lewis[6], Andrea Carfi[5], David Montefiori[4], Mehul S. Suthar[3,8], Adrian McDermott[1], Mario Roederer[1], Nancy J. Sullivan[1], Daniel C. Douek[1], Barney S. Graham[1]*, Robert A. Seder[1]*

Immune correlates of protection can be used as surrogate endpoints for vaccine efficacy. Here, nonhuman primates (NHPs) received either no vaccine or doses ranging from 0.3 to 100 μg of the mRNA-1273 severe acute respiratory syndrome coronavirus 2 (SARS-CoV-2) vaccine. mRNA-1273 vaccination elicited circulating and mucosal antibody responses in a dose-dependent manner. Viral replication was significantly reduced in bronchoalveolar lavages and nasal swabs after SARS-CoV-2 challenge in vaccinated animals and most strongly correlated with levels of anti–S antibody and neutralizing activity. Lower antibody levels were needed for reduction of viral replication in the lower airway than in the upper airway. Passive transfer of mRNA-1273–induced immunoglobulin G to naïve hamsters was sufficient to mediate protection. Thus, mRNA-1273 vaccine–induced humoral immune responses are a mechanistic correlate of protection against SARS-CoV-2 in NHPs.

Severe acute respiratory syndrome coronavirus 2 (SARS-CoV-2), the causative agent of COVID-19, has resulted in >180 million infections and 4 million deaths worldwide as of 13 July 2021 (*1*). Mass vaccination offers the most efficient public health intervention to control the pandemic. Two mRNA-based vaccines, Moderna's mRNA-1273 and Pfizer/BioNTech's BNT162b2, both produce a stabilized version of the spike glycoprotein (*2*, *3*), show >94% efficacy against symptomatic COVID-19 in interim phase 3 analyses (*4*, *5*), and are currently being administered globally. Several other vaccines have shown 60 to 80% efficacy against COVID-19 in phase 3 trials (*6*, *7*), and several candidate vaccines are in earlier stages of clinical development (*8*). A critical issue for optimizing the use of COVID-19 vaccines is defining an immune correlate of protection. This predictor of vaccine efficacy can be used to inform potential dose reduction, advance approval of other vaccine candidates in lieu of phase 3 efficacy data, extend indications for use to other age groups, and provide insights into durability of protection, necessity for booster vaccination, and immune mechanisms of protection (*9*).

The nonhuman primate (NHP) model has been used to demonstrate immunogenicity and protective efficacy against SARS-CoV-2 with several vaccine candidates (*10*–*13*). The high level of protection achieved with mRNA vaccines in NHPs using clinically relevant dose regimens parallels results from human trials. This model exhibits upper and lower airway infection and pathology similar to clinical presentations of mild COVID-19 in humans (*14*). Although immune responses associated with protection after primary infection have been assessed in NHPs (*15*), there are no studies to date that have specifically defined immune correlates of protection in upper and lower airways after vaccination with any COVID-19 vaccine approved for use in humans.

We used immunogenicity and protection assessments from our previous NHP mRNA-1273 vaccine study (*13*) to test the hypothesis that serum antibody serves as an immune correlate of protection. Here, in a dose de-escalation study, we evaluated how multiple measurements of humoral and cellular immunity correlate with the reduction of viral replication in the upper and lower airway after challenge. Antibody analyses were also performed on bronchoalveolar lavages (BALs) and nasal washes after vaccination to assess correlates relevant for clinical disease and transmission, respectively. Finally, we demonstrated the ability of passively transferred immunoglobulin G (IgG) from mRNA-immunized NHPs to protect against SARS-CoV-2 infection of animals. Thus, this work delineates spike (S)–specific antibodies as a correlate of protection, highlights the ability of localized mucosal antibodies to control upper and lower airway viral replication, and confirms that mRNA-1273–induced IgG is sufficient for protection against SARS-CoV-2 infection in nonclinical models.

Results

mRNA-1273 vaccination elicits antibody responses in a dose-dependent manner

We previously demonstrated dose dependency of serum antibody responses in NHPs after vaccination with 10 or 100 μg of mRNA-1273, with high-level protection against SARS-CoV-2 challenge in both dose groups (fig. S1A) (*13*). These and other immunogenicity outcomes from an additional NHP study in which animals were vaccinated with 30 μg of mRNA-1273 (fig. S1B) were used to design a study to evaluate immune correlates of protection after mRNA-1273 vaccination in the current study (fig. S1C). Doses of mRNA-1273 ranging from 0.3 to 30 μg were administered in the standard clinical regimen at weeks 0 and 4 to generate a range of immune responses and protective outcomes.

We first assessed temporal serum S–specific antibody binding, avidity, and neutralization responses after prime and after boost. Consistent with our previous report (*13*), S-specific binding antibody (*2*, *3*) was increased over baseline after each immunization, reaching 7900 and 64,000 median reciprocal end-point titers by 4 weeks after prime and after boost, respectively, after immunization with 30 μg of mRNA-1273 (fig. S2A). There was an 8- to 10-fold increase in S-specific binding antibodies after the boost in all dose groups except for the 0.3-μg dose, for which boosting elicited 300-fold more S-specific antibodies. The boost

[1]Vaccine Research Center, National Institute of Allergy and Infectious Diseases, National Institutes of Health, Bethesda, MD 20892, USA. [2]Biostatistics Research Branch, Division of Clinical Research, National Institute of Allergy and Infectious Diseases, National Institutes of Health, Bethesda, MD 20892, USA. [3]Center for Childhood Infections and Vaccines of Children's Healthcare of Atlanta, Department of Pediatrics, Department of Microbiology and Immunology, Emory Vaccine Center, Emory University, Atlanta, GA 30322, USA. [4]Department of Surgery, Duke University Medical Center, Durham, NC 27708, USA. [5]Moderna Inc., Cambridge, MA 02139, USA. [6]Bioqual Inc., Rockville, MD 20850, USA. [7]Infectious Disease Pathogenesis Section, National Institute of Allergy and Infectious Diseases, National Institutes of Health, Bethesda, MD 20892, USA. [8]Department of Microbiology and Immunology, Atlanta, GA 30329, USA.
*Corresponding author. Email: rseder@mail.nih.gov (R.A.S.); bgraham@nih.gov (B.S.G.)
†These authors contributed equally to this work.
‡Present Address: Department of Immunology and Infectious Diseases, Harvard T.H. Chan School of Public Health, Boston, Massachusetts 02124.
§Present Address: AstraZeneca, Gaithersburg, Maryland, 20878, USA.

improved not only antibody quantity but also binding strength, as shown by S-specific antibody avidity, which increased twofold after the boost in all vaccine groups except for the 0.3-μg dose, with no differences between the vaccine groups (fig. S2B). We detected neutralizing antibody responses against D614G, a previously dominant variant, in the 10- and 30-mg dose groups as early as 4 weeks after prime [30 mg; median reciprocal dose (ID_{50}) = 76]. These responses are also found against many current circulating variants worldwide. The boost elicited neutralizing antibodies in all but the lowest (0.3-μg) dose groups and increased by ~1 $\log_{10}$ after boost in the highest-dose group (fig. S2C).

For analyses of immune correlates, we used data from six different qualified antibody assays performed at the time of SARS-CoV-2 challenge 4 weeks after boost. Anti–S-specific (Fig. 1A) and anti–receptor binding domain (RBD) (Fig. 1B) antibodies, which are critical for mitigating SARS-CoV-2 infection, were assessed with the same techniques used to analyze sera from the phase 3 clinical SARS-CoV-2 vaccine trials and normalized to international units (IU) defined according to World Health Organization (WHO) standards. Binding antibody titers increased compared with control animals in a dose-dependent manner, ranging from a

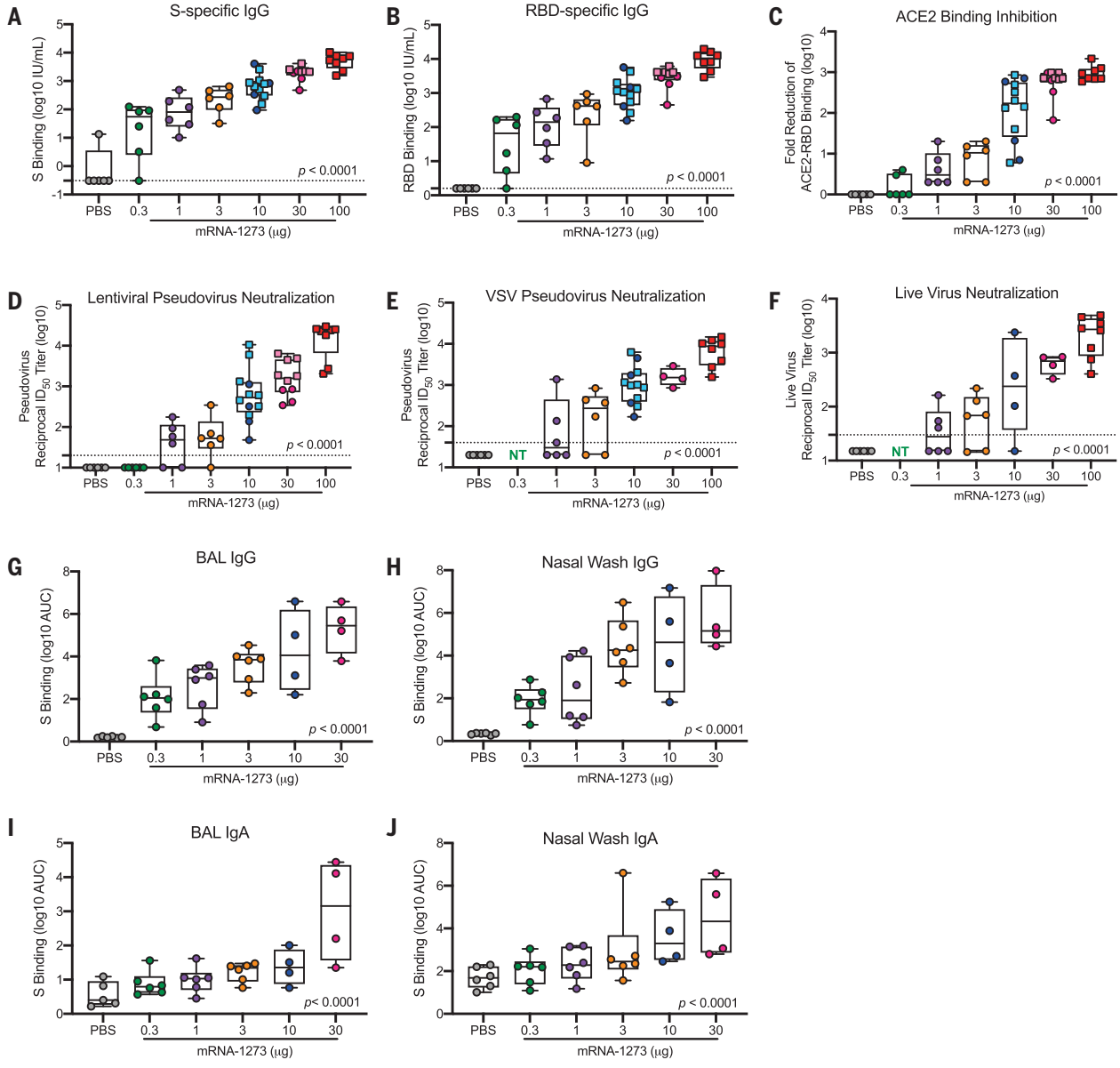


Fig. 1. Antibody responses after mRNA-1273 immunization. (**A** to **F**) Rhesus macaques were immunized according to fig. S1 with PBS (gray) or mRNA-1273 (0.3 μg, green; 1 μg, purple; 3 μg, orange; 10 μg, blue; 30 μg, pink; 100 μg, red). Sera collected 4 weeks after boost, immediately before challenge, were assessed for SARS-CoV-2 S-specific (A) and RBD-specific (B) IgG by multi-array ELISA, inhibition of ACE2 binding to RBD (C), SARS-CoV-2 lentiviral-based pseudovirus neutralization (D), SARS-CoV-2 VSV-based pseudovirus neutralization (E), and SARS-CoV-2 EHC-83E focus reduction neutralization (F). (**G** to **J**) BAL [(G) and (I)] and nasal washes [(H) and (J)] collected 2 weeks after boost were assessed for SARS-CoV-2 S-specific IgG [(G) to (H)] and IgA [(I) to (J)] by multi-array ELISA. Squares represent NHPs in previous experiments (S1A, VRC-20-857.1; S1B, VRC-20-857.2) and circles represent individual NHPs in experiment S1C, VRC-20-857.4. Boxes and horizontal bars denote the interquartile range (IQR) and medians, respectively. Whisker end points are equal to the maximum and minimum values. Dotted lines indicate assay limits of detection, where applicable. NT, not tested. All measures were significantly correlated with dose ($P < 0.0001$), as determined by Spearman's correlation test.

median of 55 to 5800 IU/ml at 0.3 and 100 μg, respectively, for S-specific IgG and 66 to 10,400 IU/ml for RBD-specific IgG (Fig. 1, A and B). There was also a dose-dependent reduction in median ACE2-binding inhibition comparing 100 μg with 1 μg of mRNA-1273 (Fig. 1C), reaching a maximum difference between these two dose groups of 270-fold. In vitro virus–neutralizing activity was determined using three different assays. First, a lentiviral-based D614G pseudovirus neutralization assay revealed a dose-dependent increase in neutralizing activity with a median reciprocal ID_{50} titer of 23,000 at the 100-μg dose and 49 after immunization with 1 μg of mRNA-1273 (Fig. 1D). Vesicular stomatitis virus (VSV)–based pseudovirus (Fig. 1E) and live-virus (Fig. 1F) neutralization followed the same significant trend of dose dependency. Assessments of antibody binding and neutralizing responses were highly correlated with one another, suggesting that mRNA-1273 immunization and elicitation of high-titer S-binding antibody responses predicts functional antibody responses (Fig. 2).

Given the increasing circulation of SAR-CoV-2 variants of concern, some of which have shown a significant reduction in neutralization sensitivity to vaccine-elicited and convalescent sera from subjects previously infected with SARS-CoV-2 (*16*–*20*), we assessed the ability of mRNA-1273 immune NHP sera to neutralize two different SAR-CoV-2 variants of concern. Live viral neutralization of the alpha (B.1.1.7) variant (*21*), which is highly transmissible and has previously been circulating worldwide (*22*), was not appreciably decreased compared with D614G (fig. S3A). The beta (B.1.351) variant, which contains multiple mutations in RBD and NTD and has been reported to show the greatest reduction of neutralization by vaccine-induced sera (*16*, *23*, *24*), exhibited a ninefold reduction compared with D614G in the 100-μg dose group. Nine of 12 animals immunized with 30 or 100 μg of mRNA-1273 had reciprocal ID_{50} titers >100, whereas only one of four animals in the 10-μg dose group had detectable neutralization activity to the beta variant (fig. S3B). The reduction in beta neutralization capacity of mRNA-1273–induced antibodies mirrors what has been previously shown in NHPs and humans using doses of only 30 or 100 μg (*16*, *20*). However, these data further suggest that the mRNA-1273 dose may have a profound effect on eliciting neutralizing antibodies against the beta variant.

mRNA-1273 vaccination elicits upper and lower airway antibodies

To provide additional immune data on correlates of protection at the site of infection, antibody responses in the lower and upper

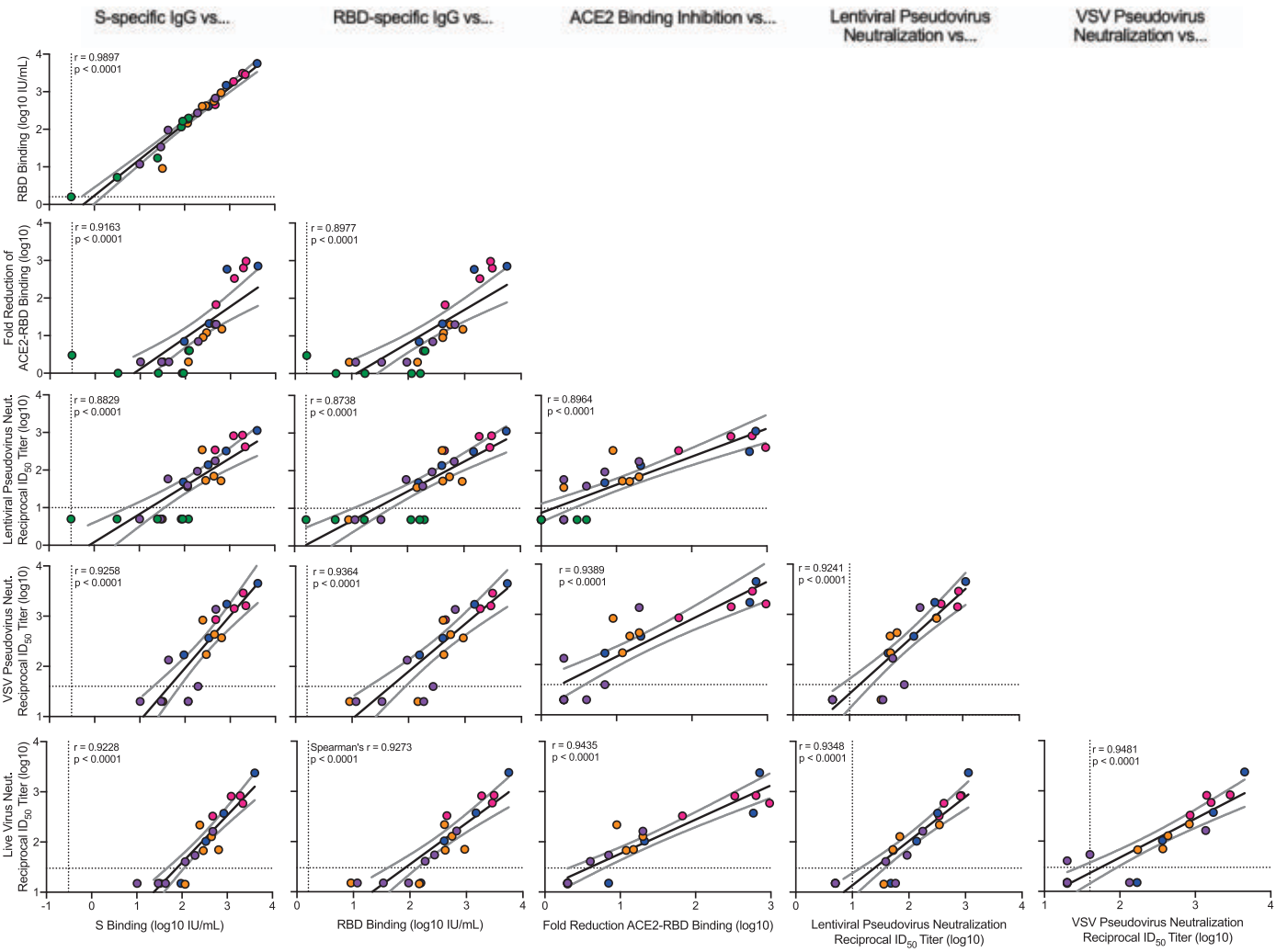


Fig. 2. Correlations of humoral antibody analyses. Rhesus macaques were immunized according to fig. S1C. Plots show correlations between SARS-CoV-2 S-specific IgG, RBD-specific IgG, ACE2-binding inhibition, lentiviral-based pseudovirus neutralization, VSV-based pseudovirus neutralization, and EHC-83E focus reduction neutralization at 4 weeks after boost. Circles represent individual NHPs, and colors indicate the mRNA-1273 dose as defined in fig. S1C. Dotted lines indicate assay limits of detection. Black and gray lines indicate linear regression and 95% confidence interval, respectively. *r* is Spearman's correlation coefficient and *P* is the corresponding *P* value.

airways were assessed from BAL and nasal wash samples, respectively, at 2 weeks after boost. There was a dose-dependent increase in BAL and nasal wash S-specific IgG and IgA after two doses of mRNA-1273 (Fig. 1, G to J). BAL S-specific IgG levels after 0.3 and 30 μg of mRNA-1273 ranged from a median of 110 to 280,000 area under the curve (AUC) (Fig. 1G). Nasal wash S-specific IgG titers ranged from 86 to 142,200 AUC (Fig. 1H). The dose-dependent trend for S-specific IgA was similar albeit at lower levels where 30 μg of mRNA-1273 elicited 1400 and 21,300 AUC IgA in BAL (Fig. 1I) and nasal washes (Fig. 1J), respectively. Additionally, upper and lower airway antibody responses correlated with one another and with S-specific IgG and serum-neutralizing activity. The one exception was that there was no correlation with BAL and nasal wash S-specific IgA (fig. S4). Thus, mRNA-1273 vaccination elicits S-specific IgG and IgA antibodies in both the upper and lower airways, which potentially provide immediate protection at the site of infection and limit transmission.

mRNA-1273 vaccination elicits S-specific CD4 T cell responses

S-specific CD4 and CD8 T cell responses were assessed 2 weeks after boost (fig. S5). There was a direct correlation between dose and the proportion of T helper type 1 (T_H1) cells [interleukin 2–positive ($IL\text{-}2^+$), tumor necrosis factor–positive (TNF^+), and/or interferon-γ–positive ($IFN\text{-}\gamma^+$)] among peripheral blood memory CD4 T cells ($P = 0.006$), because all animals in the 30-μg dose group had T_H1 responses (fig. S6A). By contrast, T_H2 responses ($IL\text{-}4^+$and/or $IL\text{-}5^+$) were low to undetectable in all vaccine dose groups (fig. S6B). By contrast, CD8 T cell responses were also low to undetectable in all vaccine dose groups (fig. S6E). T follicular helper (T_{FH}) cells found within secondary lymphoid organs play an important role in B cell responses because of their localization within germinal centers. Thus, we extended our analysis to S-specific T_{FH} cells that express the surface marker CD40L, which causes direct activation of B cells to secrete IgG, and the canonical cytokine IL-21, which is critical for developing robust long-term antibody responses. Most vaccinated animals exhibited S-specific $CD40L^+$ T_{FH} cell responses, whose magnitude directly correlated with dose ($P < 0.001$) (fig. S6C). There was also a direct correlation between dose and magnitude of S-specific IL-21 T_{FH} cell responses ($P = 0.010$) (fig. S6D). Thus, in agreement with previous results (*13*, *25*, *26*), mRNA-1273 vaccination induces T_H1- and T_{FH}-skewed CD4 T cell responses.

mRNA-1273 vaccination protects against upper and lower airway SARS-CoV-2 replication

To evaluate the impact of mRNA-1273 vaccine dose on protection, animals were challenged 4 weeks after boost with a total dose of 8×10^5 plaque-forming units (PFU) of a highly pathogenic stock of SARS-CoV-2 (USA-WA1/2020) by combined intranasal and intratracheal routes for upper and lower airway infection, respectively (fig. S1C). The challenge dose was chosen to induce viral loads similar to or higher than those detected in nasal secretions of humans after SARS-CoV-2 infection (*27*). The primary efficacy end-point analysis used subgenomic RNA (sgRNA) quantitative reverse transcription polymerase chain reaction for the nucleocapsid (N) gene (Fig. 3) because N sgRNA is the most highly expressed sgRNA species as a result of discontinuous transcription and thus provides greater sensitivity than the envelope (E) gene (fig. S7) (*28*), which is most commonly used in other NHP SARS-CoV-2 vaccine studies (*13*) to quantify replicating virus.

We observed a vaccine dose effect for protection against viral replication in the upper and lower airways. On days 2 and 4 after challenge, there were approximately two and five $\log_{10}$ reductions in sgRNA_N in BAL compared with control animals at doses of 1 and 30 μg, respectively (Fig. 3A). Moreover, by day 4 after challenge, most animals vaccinated with 1 μg or higher had low to undetectable sgRNA_E in BAL (fig. S7A). By contrast, the reduction in sgRNA in nasal swabs was primarily limited to animals receiving 30 μg of mRNA-1273 compared with control animals (Fig. 3B and fig. S7B). These data highlight differences in immune responses required for reduction in viral replication for upper and lower airway protection. The virus was more rapidly cleared from

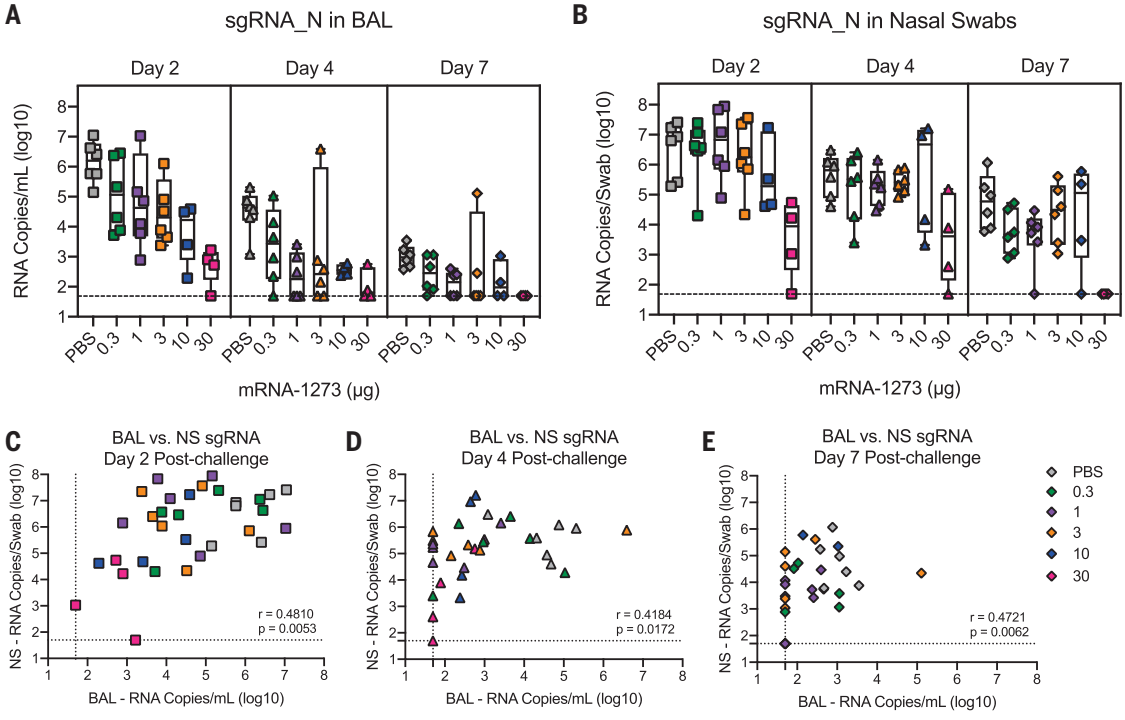


Fig. 3. Efficacy of mRNA-1273 against upper and lower respiratory viral replication. (**A** and **B**) Rhesus macaques were immunized and challenged as described in fig. S1C. BAL (A) and nasal swabs (NS) (B) were collected on days 2 (squares), 4 (triangles), and 7 (diamonds) after challenge, and viral replication was assessed by detection of SARS-CoV-2 N-specific sgRNA. In (A) and (B), Boxes and horizontal bars denote the IQR and medians, respectively. Whisker end points are equal to the maximum and minimum values. (**C** to **E**) Correlations shown between BAL and NS sgRNA at days 2 (C), 4 (D), and 7 (E) after challenge are Spearman's correlation coefficients (r) and corresponding P values. Symbols represent an individual NHP and may overlap, i.e., $n = 6$ animals plotted at assay limit (dotted line) for both BAL and NS in (E).

BAL compared with nasal swab samples. Although we observed a strong correlation between sgRNA in the upper and lower airways, there was a time-dependent loss of concordance in the correlations with upper and lower airways samples (Fig. 3, C to E), suggesting distinct mechanisms for viral clearance in the two compartments.

mRNA-1273–vaccinated NHPs have limited virus and inflammation in the lungs

Animals in each of the dose groups were assessed for the presence of virus in the lung and histopathology 7 or 8 days after SARS-CoV-2 challenge. In the control animals, SARS-CoV-2 infection caused patchy, moderate to severe inflammation that often involved the small airways and the adjacent alveolar interstitium, consistent with previous reports (*29*–*31*). Alveolar air spaces occasionally contained inflammatory cell infiltrates, and alveolar capillary septa were moderately thickened. Moreover, moderate and diffuse type II pneumocyte hyperplasia was observed. Multiple pneumocytes in the lung sections from the control group were positive for SARS-CoV-2 viral antigen by immunohistochemistry (IHC) (fig. S8 and table S1). Viral antigen was detected in both control animals but only sporadically across vaccinated animals in various dose groups (table S1). These observations show that naïve NHP develop mild inflammation in the lung >1 week after SARS-CoV-2 infection, and that vaccination limits or completely prevents inflammation or detection of viral antigen in the lung tissue.

Postchallenge anamnestic antibody responses are increased in low-dose vaccine groups

After SARS-CoV-2 challenge, we assessed antibody responses in blood, BAL, and nasal washes for up to 28 days to determine whether there were anamnestic or primary responses to S or N proteins, respectively (fig. S9). This analysis provides a functional immune assessment of whether the virus detected in the upper and lower airways by PCR after challenge is sufficient to boost vaccine-induced S-specific antibody responses or elicit primary N responses. In sera, there was no postchallenge increase in S-specific (fig. S9A), RBD-specific (fig. S9B), or neutralizing antibodies (fig. S9C) in the 3-, 10-, or 30-μg dose groups. By contrast, at doses below 1 μg, there were increased S-specific (fig. S9A), RBD-specific (fig. S9B), and neutralizing antibody responses (fig. S9C) at day 28 after challenge compared with before challenge. Similar primary S-specific antibody response trends were also apparent with BAL and nasal wash IgG and IgA responses (fig. S10). When prechallenge N-specific IgG responses were compared with postchallenge responses, we only observed seroconversion in the control animals and animals immunized with <3 μg of mRNA-1273 (fig. S9D).

The reduction of viral replication as determined by sgRNA coupled with limited pathology in the lung and no detectable anamnestic S responses or induction of primary responses to N provide three distinct measures suggesting that vaccine-elicited immune responses, particularly at high doses, were protective. To understand this further, and to establish immune correlates of protective immunity, we next explored relationships between immune parameters and viral load.

Antibody responses correlate with protection against SARS-CoV-2 replication

Before conducting the dose–response study in NHPs (fig. S1C), we prespecified that our analysis to define a potential correlate would focus initially on the relationship between S-specific binding antibodies and sgRNA levels in nasal swabs (NS). Correlations with sgRNA levels in BAL served as an important secondary analysis. The predefined primary hypothesis of the study was that S-specific IgG at 4 weeks after boost at the time of challenge would inversely correlate with viral replication in the NS at day 2 after challenge. The secondary hypotheses were analogous for the relationship between S-specific IgG at 4 weeks after boost and day 2 BAL sgRNA.

Using a univariate (log) linear model, S-specific IgG at the time of challenge correlated strongly with sgRNA in both the NS ($P = 0.003$, adjusted $R^2 = 0.29$) (Fig. 4G and table S2) and BAL ($P = 0.001$, adjusted $R^2 = 0.35$) (Fig. 4A and table S2) at day 2. A 1-$\log_{10}$ change in S-specific IgG corresponded to a 1-$\log_{10}$ change in sgRNA at day 2 in the NS and a 0.9-$\log_{10}$ change in BAL sgRNA at day 2 (table S2). Once the S-specific IgG was included in a multivariate linear model predicting sgRNA, including dose in the model did not substantially increase the adjusted R^2, nor was the coefficient significant ($P = 0.115$ for NS and $P = 0.214$ for BAL). Thus, the dose effect on day 2 sgRNA in NS and BAL appears to be fully captured by the adjustment for S-specific IgG. Moreover, in this model, S-specific IgG meets our prespecified criteria to be considered as a correlate of sgRNA levels in NS and BAL.

Because RBD-specific IgG, ACE2-binding inhibition, pseudovirus neutralization, and live virus neutralization all correlated with S-specific IgG (Fig. 2), we analyzed these endpoints as potential correlates of sgRNA. All six antibody measurements were highly correlated with one other (Fig. 2), with vaccine dose (Fig. 1), and with sgRNA in BAL (Fig. 4, A to F) and NS (Fig. 4, G to L). For all six antibody measurements, the dose was not significantly predictive of sgRNA in the BAL after adjusting for antibody levels (table S2A). For NS, the dose remained significantly predictive after adjusting for VSV-based pseudovirus neutralization and marginally significant after adjusting for live virus neutralization. In addition to S-specific IgG, RBD-specific IgG, ACE2-binding inhibition, and lentiviral-based pseudovirus neutralization appear to meet our criteria for potential correlates of protection. Furthermore, lower and upper airway S-specific antibodies in the BAL and NS negatively correlated with BAL (fig. S11, A and B) and NS sgRNA levels, respectively (fig. S11, C and D).

To assess the robustness of these findings, these analyses were repeated using logistic regression to model the probability that the sgRNA was below a threshold, defined as 10,000 sgRNA copies for BAL and 100,000 sgRNA copies for NS. These thresholds were chosen to lie below all of the sgRNA values in the control animals and within the range of the values for the mRNA-1273–vaccinated animals. The results of these analyses were similar to the primary analyses performed on the (log) linear models. No animal with S-specific IgG >*336* IU/ml or >*645* IU/ml had BAL (Fig. 4A) or NS (Fig. 4G) sgRNA, respectively, greater than the thresholds defining protection (>10,000 copies/ml BAL or >100,000 copies/swab NS). Finally, no animals with an S-binding titer of >488 IU/ml exhibited higher N-specific primary antibody responses after challenge above the background value at the time of challenge. Consistent with this, there was a strong negative correlation between prechallenge S-specific antibodies and postchallenge N-specific antibodies (Fig. 4M). Additionally, there was limited to no lung pathology or viral antigen detected in animals with <10,000 sgRNA copies/ml in BAL, providing additional evidence that mRNA-1273–vaccinated animals were protected from lower airway disease.

We also examined the correlations between T cell responses and sgRNA and found that $CD40L^+$ T_{FH} cell and T_H1 cell responses were each univariately associated with reduced sgRNA in both BAL and NS. After adjustment for S-specific IgG, neither of these remained significantly associated with sgRNA levels in the BAL, suggesting that these T cell measures do not predict sgRNA independently of the binding antibody measured in BAL. However, $IL\text{-}21^+$ T_{FH}, $CD40L^+$ T_{FH}, and T_H1 cell responses remained significantly predictive of sgRNA levels in NS (table S2B). Thus, clearance of virus from BAL and NS have distinct immunological requirements (Fig. 3, C to E).

Passively transferred mRNA-1273–induced IgG mediates protection against SARS-CoV-2

High-titer antibody responses in blood and upper and lower airways were associated with the rapid control of viral load and lower airway pathology in the lung. This suggested that antibody was the primary immunological mechanism of protection. To directly address whether vaccine-induced antibody was sufficient to mediate protection, IgG was purified

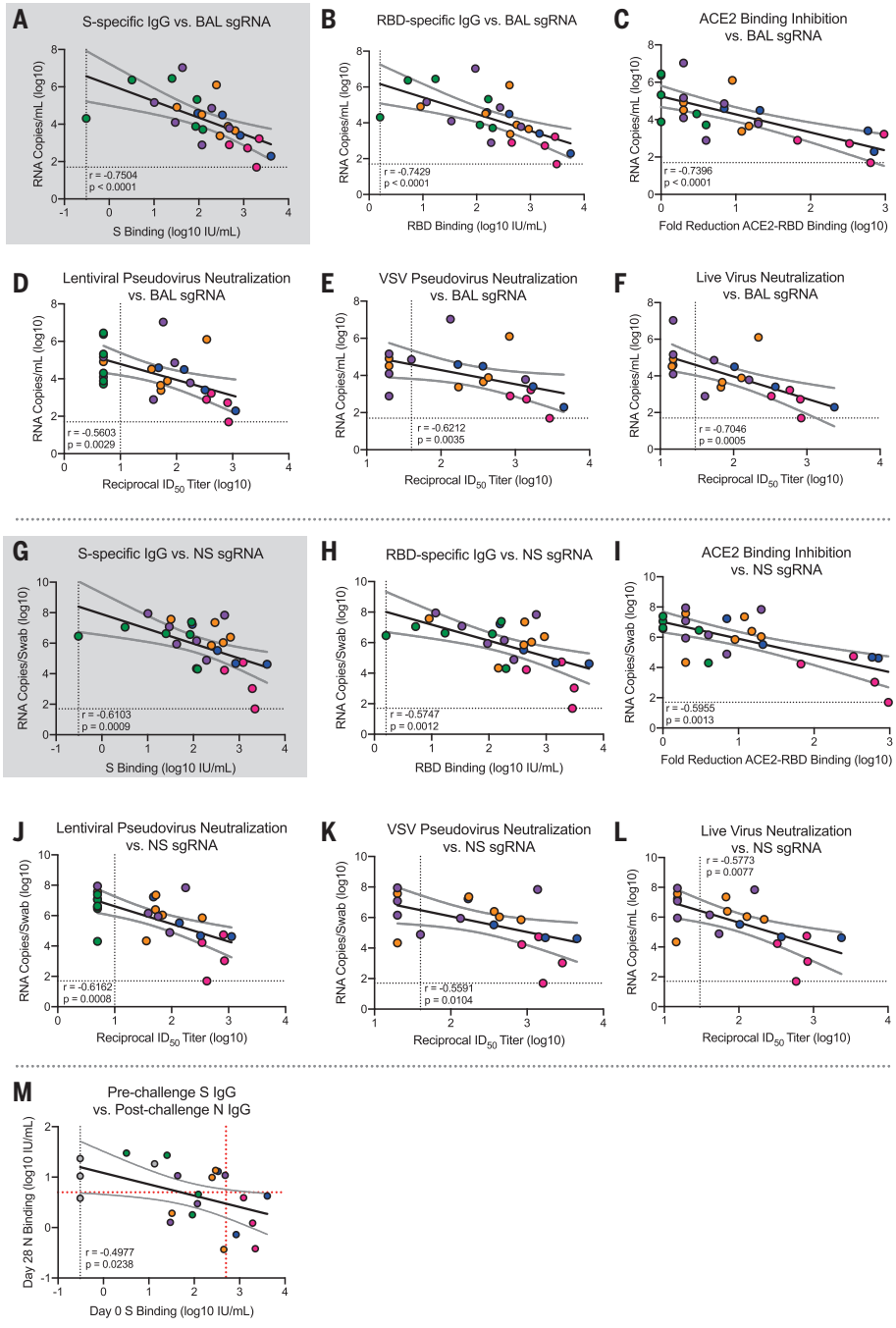


Fig. 4. Antibody correlates of protection. Rhesus macaques were immunized and challenged as described in fig. S1C. Plots show correlations between SARS-CoV-2 N-specific sgRNA in BAL [(**A**) to (**F**)] and NS [(**G**) to (**L**)] at day 2 after challenge and before challenge (week 4 after boost) SARS-CoV-2 S-specific IgG [(A) and (G)], RBD-specific IgG [(B) and (H)], ACE2-binding inhibition [(C) and (I)], SARS-CoV-2 lentiviral-based pseudovirus neutralization [(D) and (J)], SARS-CoV-2 VSV-based pseudovirus neutralization [(E) and (K)], and SARS-CoV-2 EHC-83E focus reduction neutralization [(F) and (L)]. Gray shading for S-specific IgG represents the use of this assessment as primary predictor of protection outcome as stated in primary hypothesis. (**M**) Plot showing correlation between prechallenge (week 4 after boost) SARS-CoV-2 S-specific IgG with day 28 postchallenge SARS-CoV-2 N-specific IgG. Circles represent individual NHPs, and colors indicate the mRNA-1273 dose. Dotted lines indicate assay limits of detection. Black and gray lines indicate linear regression and 95% confidence interval, respectively. In (M), a red dotted horizontal line represents N-binding titers of 6, the maximum of all prechallenge values across all groups, and a red dotted vertical line represents a reciprocal S-specific IgG titer of 500, above which none of the animals had day 28 reciprocal N-binding titers >6.

from pooled sera from mRNA-1273–immunized NHPs (*13*) (Fig. 5A) and passively transferred into hamsters (Fig. 5B). Hamsters that received preimmune IgG or 2 μg of mRNA-1273–immune IgG showed ~10% weight loss by day 6 (*32*). By contrast, hamsters that received 10 μg of mRNA-1273–immune NHP IgG showed little to no weight loss after challenge (Fig. 5E). Thus, mRNA-1273 immune IgG alone is sufficient to mediate protection from disease in vivo against SARS-CoV-2 infection.

Discussion

Defining immune correlates of protection is a critical aspect of vaccine development for extending the use of approved vaccines, facilitating the development of new candidate vaccines, and defining potential mechanisms of protection. For SARS-CoV-2, a primary goal of current vaccines is to prevent symptomatic COVID-19. This is achieved by reducing viral load in lower airways, which reduces moderate to severe disease, and reducing viral load in both lower and upper airways, preventing mild disease. An additional benefit of upper airway protection is that limiting nasal carriage of virus will also reduce the risk of transmission. Here, we established that the level of S-specific antibody elicited by mRNA-1273 vaccination correlates with control of upper and lower airway viral replication after SARS-CoV-2 challenge in NHPs and that vaccine-elicited antibodies are sufficient for protection against disease in the highly pathogenic golden Syrian hamster model of SARS-CoV-2 infection.

A key parameter to assess correlates of protection in NHPs is the amount of virus used for challenge. In this study, a challenge dose of 8×10^5 PFUs of a well-characterized, pathogenic SARS-CoV-2 USA-WA1/2020 strain was used to achieve a level of viral replication comparable to or exceeding that observed from nasal swabs of humans with symptomatic infection measured by sgRNA (*33*) or genomic viral RNA (*34*–*36*). The sgRNA levels for N or E of 10^6 to 10^7 in control animals at day 2 after challenge are among the highest reported for NHP challenge studies and likely models viral load in humans at the upper end of inoculum size. We used the same qualified antibody binding and pseudovirus neutralization assays for assessing immune responses as in human phase 3 vaccine trials. In addition, the use of WHO standards to report binding titers in international units enables the comparison of immune responses and outcomes with other NHP vaccine studies and benchmarking to human vaccine clinical trials. We have shown that a 10-fold increase in S-binding titers was associated with ~10-fold reductions in viral replication in BAL and NS after challenge. No animal with S-specific IgG >336 IU/ml or >645 IU/ml had BAL or NS sgRNA, respectively, greater than the thresholds defining

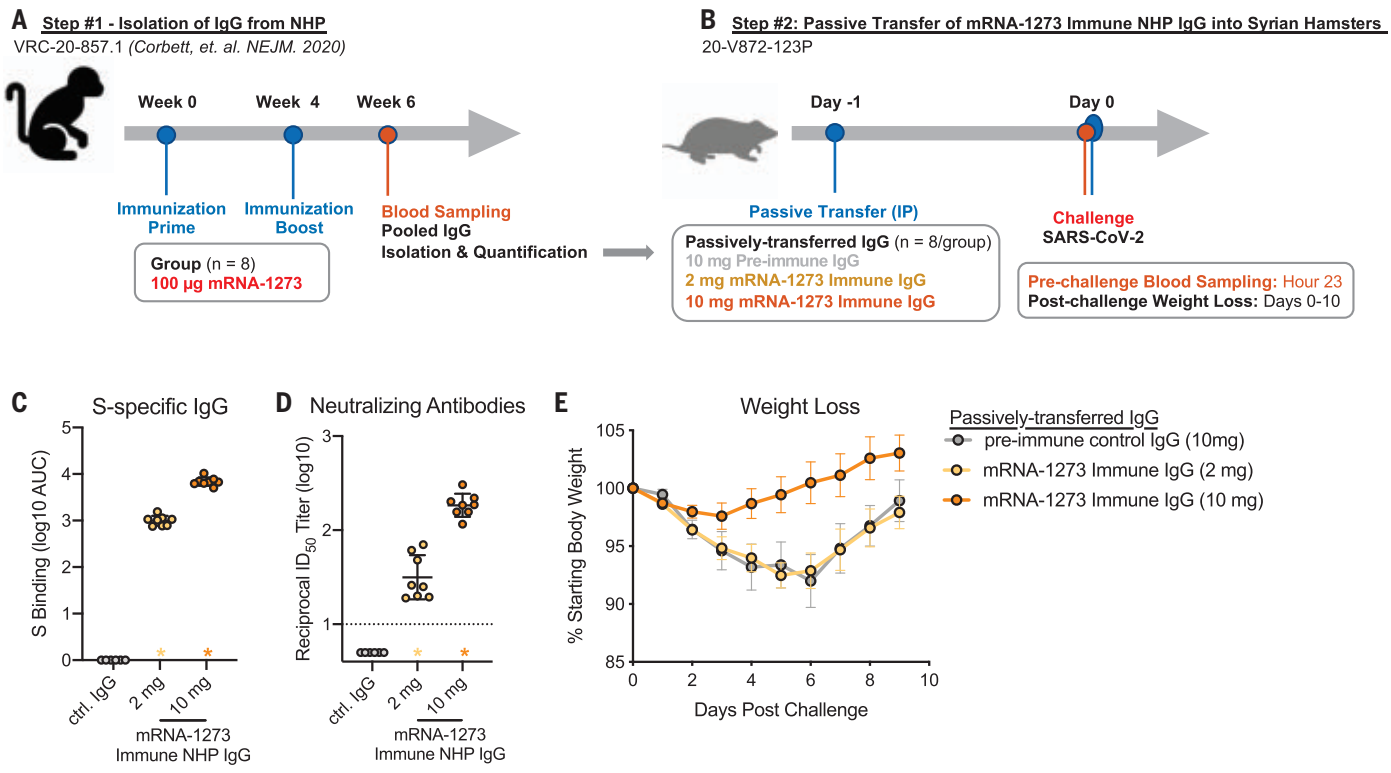


Fig. 5. Passive transfer of mRNA-1273 immune NHP IgG into Syrian hamsters. (**A**) Sera were pooled from all NHPs that received 100 µg of mRNA-1273 in a primary vaccination series. (**B**) mRNA-1273 immune NHP IgG (2 µg, yellow; 10 µg, orange) or preimmune NHP IgG (10 µg, gray) was passively transferred to Syrian hamsters (*n* = 8/group) 24 hours before SARS-CoV-2 challenge. (**C** and **D**) Twenty-three hours after immunization, hamsters were bled to quantify circulating S-specific IgG (C) and SARS-CoV-2 pseudovirus-neutralizing antibodies (D). (**E**) After challenge, hamsters were monitored for weight loss. In (C) and (D), circles represent individual NHPs. Bars and error bars represent GMT and geometric SD, respectively. Asterisks at the axis represent animals that did not receive adequate IgG through passive transfer and were thus excluded from weight loss analyses. In (D), the dotted line indicates the neutralization assay limit of detection. In (E), circles and error bars represent means and SEM, respectively.

protection (>10,000 copies/ml BAL or >100,000 copies/swab NS). These reductions in viral replication compared with controls were associated with limited inflammation and viral antigen detection in the lung tissue and appeared to be sufficient to prevent moderate or severe lower airway infection. Even animals in the 1- and 3-µg dose groups, for which the elicited S-specific antibody levels were 81 and 272 IU/ml, respectively, and reciprocal pseudovirus neutralization titers were 49 and 53, respectively, exhibited ~2- to 4-$\log_{10}$ less viral replication in BAL compared with the control animals at day 2 after challenge (*34*). Thus, a lower antibody level is needed for the reduction of viral replication in the lower airway than in the upper airway. Moreover, these data highlight how immune correlates may differ in their ability to confer protection against severe disease in the lung versus mild infection in the upper airway, which has potential implications for determining whether higher immune responses will be required to limit transmission and if this will require additional boosting.

The antibody titers required in this high-dose challenge NHP model for a reduction in viral replication may be a conservative estimate for what is required to prevent clinical disease in humans. The strong correlation and proportional changes between S-specific binding titers with serum-neutralizing activity support using easy-to-measure binding titers as the primary metric for defining a correlate of protection in humans, at least for mRNA-based vaccines delivering similar antigens and eliciting similar patterns of immunogenicity.

Mucosal antibody responses are thought to be an important mechanism of protection against a variety of upper respiratory viral infections (*37*–*41*). Both BAL and nasal wash S-specific IgG and IgA were predictive for reducing sgRNA in these compartments. Serum antibody levels were a strong predictor of IgA and IgG responses in BAL and nasal washes, as well as for protection measured by viral replication in these sites. Because mRNA-1273 is administered intramuscularly, localized upper and lower airway antibodies may be transudated from serum, which suggests that serum antibody levels may be a surrogate for BAL and NS antibody levels after mRNA-1273 vaccination.

Additionally, we considered whether the infection could boost vaccine-induced antibodies. There were no anamnestic S-specific responses or increase in N-specific responses in blood or BAL within 28 days after infection in the >3-µg dose groups compared with prechallenge, consistent with these doses inducing higher antibody responses and preventing viral replication. By contrast, there were increased anamnestic S-binding antibody responses in the <1-µg dose groups. Thus, the boosting of vaccine-induced antibodies may occur after upper airway infection in animals that have minimal viral replication in the lower airway. Therefore, the necessity and timing of subsequent vaccine boosting will depend on the goal of the vaccination program. One goal would be to prevent severe disease and lower airway infection while allowing community exposure to provide mucosal immunity from upper airway infection and boosting of the vaccine response; another would be to achieve persistent high-level immunity against mild infection through vaccination to more rapidly reduce transmission.

There are limitations of this study for predicting the real-world human immune correlate(s)

of protection against currently circulating virus variants. First, SARS-CoV2 infection of NHPs models mild disease with relatively little lung pathology. Second, this study used the benchmark WA-1 strain for challenge and the results will need to be extended to continually evolving circulating strains and variants. Third, this was a short-term study in which immune responses were assessed at the peak of the postimmunization response and challenge occurred 4 weeks after the boost. Thus, the relationship of serum antibody levels to protection against virus infection or disease using longer challenge intervals after vaccination remains to be determined.

In conclusion, this study establishes the critical role of antibodies as a correlate of protection against SARS-CoV-2 in the NHP model and shows that, for mRNA-1273, S-specific binding antibody is a surrogate marker of protection. Ongoing NHP studies will assess the durability of mRNA-1273–elicited protection and the efficacy of mRNA-1273 vaccination against global SARS-CoV-2 variants. These findings anticipate the correlates analysis comparing virus replication in NS with serum antibody being performed on samples from vaccinated subjects in phase 3 clinical trials who experienced breakthrough infection.

Materials and Methods

Preclinical mRNA-1273 mRNA and lipid nanoparticle production

A sequence-optimized mRNA encoding prefusion-stabilized SARS-CoV-2 S-2P protein (*2*, *3*) was synthesized in vitro and formulated as previously reported (*13*, *25*).

Rhesus macaque model

Animal experiments were performed in compliance with all pertinent National Institutes of Health regulations and approval from the Animal Care and Use Committees of the Vaccine Research Center and Bioqual Inc. (Rockville, MD). Studies were conducted at Bioqual Inc. The experimental details of VRC-20-857.1 (fig. S1A) were published previously (*13*). For VRC-20-857.3 (fig. S1B) or VRC-20-857.4 (fig. S1C), 3- to 8-year-old rhesus macaques of Indian origin were sorted by sex, agem and weight and then stratified into groups. Animals were immunized intramuscularly at week 0 and at week 4 with doses ranging from 0.3 to 30 μg of mRNA-1273 in 1 ml of PBS into the right hindleg. Placebo-control animals were administered an equal volume of PBS. At week 8 (4 weeks after boost), all animals were challenged with a total dose of 8×10^5 PFUs of SARS-CoV-2. The stock of 1.99×10^6 TCID50 or $3{\times}10^6$ PFU/ml SARS-CoV-2 USA-WA1/2020 strain (BEI: NR-70038893) was diluted and administered in 3-ml doses by the intratracheal route and in 1-ml doses by the intranasal route (0.5 ml per nostril). Pre- and postchallenge sample collection are detailed in fig. S1C.

Passive transfer of purified IgG into golden Syrian hamsters

Sera from NHPs immunized with 100 μg of mRNA-1273 in VRC-20-857.1 (*13*) (fig. S1A) were collected 2 weeks after boost and pooled. Total IgG was purified from pooled sera using Protein G Sepharose 4 Fast Flow resin (Cytiva), according to the manufacturer's instructions, and quantified by NanoDrop OneC Microvolume UV-Vis Spectrophotometer (ThermoFisher Scientific). The eluted protein dialyzed against PBS, pH 7.4 (Invitrogen), and concentrated to 10 mg/ml using Amicon Ultra centrifugal Filter (Millipore Sigma-Aldrich). Golden Syrian hamsters, aged 6 to 8 weeks, were randomized into groups of eight on the basis of weight, with each group containing a 1:1 ratio of males to females. Two or 10 mg of total mRNA-1273 immune IgG was passively transferred by intraperitoneal injection 1 day before challenge. Immediately before challenge, sera were collected for assessments of S-specific IgG (Fig. 5C) and neutralization titers (Fig. 5D) to confirm the relative antibody responses of the mRNA-1273 immune IgG in the hamsters. Hamsters were inoculated intranasally with 3×10^4 PFUs of USA-WA1/2020 SARS-CoV-2 (BEI, NR-53780) in a final volume of 100 μl split between each nostril. Body weight and clinical observations were made daily after challenge.

Quantification of SARS-CoV-2 sgRNA

Using previously published methods (*42*), specimens were processed, stored, and subgenomic SARS-CoV-2 E mRNA was quantified with reverse transcription-polymerase chain reaction (RT-PCR). Subgenomic SARS-CoV-2 N mRNA was quantified similarly (forward: 5′-CGATCTCTTGTAGATCTGTTCTC-3′, probe: 5′-FAM-TAACCAGAATGGAGAACGCAGTGGG-BHQ1-3′, reverse: 5′-GGTGAACCAAGACGCAGTAT-3′). The lower limit of quantification was 50 copies.

Histopathology and IHC

As previously described (*13*), NHP lung tissue sections were stained with hematoxylin and eosin for routine histopathology and a rabbit polyclonal SARS-CoV-2 (GeneTex, GTX135357) for detection of SARS-CoV-2 virus antigen. All samples were evaluated by a board-certified veterinary pathologist.

4-Plex meso-scale ELISA

MSD SECTOR plates (MSD) were precoated with SARS-CoV proteins (S-2P, RBD, and N) and a bovine serum albumin control in each well and blocked for 60 min at room temperature (RT) with MSD blocker A solution. Plates were washed with 1× MSD wash buffer, and an MSD reference standard (calibrator), QC test sample (pool of COVID-19 convalescent sera), and heat-inactivated sera were serially diluted and added in duplicate. A reference standard and MSD control sera were added undiluted in triplicates. Samples were incubated at RT for 4 hours with shaking at 1500 rpm. After washing, MSD SULFO-TAG anti-human IgG detection antibody was added for 60 min at RT with shaking. Plates were washed and MSD GOLD read buffer was added. Detection was completed on a MESO Sector S 600 system, and analyses were performed using MSD Discovery Workbench software version 4.0. Calculated ECLIA parameters to measure binding antibody activities included interpolated concentrations or assigned arbitrary units per milliliter read from the standard curve.

Defining IUs

Recently the arbitrary units were bridged to the WHO international standard and a conversion factor was calculated and confirmed. Parallelism between MSD reference standard and the WHO international standard was established for SARS-CoV proteins (S-2P, RBD, and N). Concentration assignments were performed and then confirmed by MSD and as part of a multisite confirmation study. Sample results reported here have been converted to international units per milliliter. S-specific IgG had a lower limit of detection of 0.3076 IU/ml; RBD-specific IgG had a lower limit of detection of 1.5936 IU/ml.

ELISA for temporal NHP serum antibodies and hamster serum antibodies

SARS-CoV-2 S-specific IgG in serum was quantified by ELISA, and the methods used were similar to those previously published (*25*). Here, the only amendment to previously published methodology is the resulting data are depicted as end-point titers, which were calculated as the mean serum titer that reached 10× SD using GraphPad Prism version 9.0.2 software.

Meso-scale ELISA for mucosal antibody responses

Total S-specific IgG and IgA were determined by multi-array ELISA using Meso Scale technology (Meso Scale Discovery, MSD) as previously described (*42*).

Serum antibody avidity assay

Avidity was assessed using a sodium thiocyanate (NaSCN)–based avidity ELISA against the full-length SARS-CoV-2 S-2P antigen as previously described. The avidity index was calculated using the ratio of IgG binding to S-2P in the absence or presence of NaSCN. The reported avidity index is the average of two independent experiments, each containing duplicate samples.

ACE2-binding inhibition assay

ACE2-binding inhibition was completed, as previously described (*43*), on 1:40 diluted sera samples using Mesoscale Discovery 384-well,

4-Spot Custom Serology SECTOR plates precoated with SARS-CoV-2 RBD. Binding was detected using SULFO-TAGTM–labeled ACE2. Both reagents were generously supplied by the manufacturer.

Lentiviral pseudovirus neutralization assay

Pseudotyped lentiviral reporter viruses were produced by the cotransfection of plasmids encoding S proteins from Wuhan-1 strain (GenBank no. MN908947.3) with a D614G mutation, a luciferase reporter, lentivirus backbone, and human transmembrane protease serine 2 (TMPRSS2) genes into HEK293T/17 cells (ATCC CRL-11268) as previously described (*43*). Sera, in duplicate, were tested for neutralizing activity against the D614G pseudoviruses by quantification of luciferase activity in relative light units. Percent neutralization was normalized considering uninfected cells as 100% neutralization and cells infected with pseudovirus alone as 0% neutralization. ID_{50} titers were determined using a log(agonist) versus normalized response (variable slope) nonlinear regression model in GraphPad Prism version 9.0.2 software. The lower limit of quantification was 1:40 ID_{50}.

VSV pseudovirus neutralization assay

To make SARS-CoV-2 pseudotyped recombinant VSV-ΔG-firefly luciferase virus, BHK21/WI-2 cells (Kerafast, EH1011) were transfected with the S plasmid expressing full-length S with a D614G mutation and subsequently infected with VSVΔG-firefly-luciferase as previously described (*44*). Neutralization assays were completed on A549-ACE2-TMPRSS2 cells with serially diluted serum samples as previously described (*16*). The lower limit of quantification was 1:40 ID_{50}.

Focus reduction neutralization test (FRNT)

VeroE6 cells (ATCC, #CRL-1586) were cultured, viral stocks [EHC-083E (D614G SARS-CoV-2) (*18*), B.1.1.7 (PMID 33739374), and B.1.351 (PMID 33972938)] were propagated and titered, and FRNT assays were performed as previously described (*45*). Antibody neutralization was quantified by counting the number of foci for each sample using the Viridot program (*46*). The neutralization titers were calculated as follows: 1 – [ratio of the mean number of foci in the presence of sera and foci at the highest dilution of respective sera sample]. Each specimen was tested in duplicate. The FRNT-50 titers were interpolated using a four-parameter nonlinear regression in GraphPad Prism version 9.0.2.4.3 software. Samples that do not neutralize at the limit of detection at 50% are plotted at 5 and was used for geometric mean calculations.

Intracellular cytokine staining

Analysis of spike-specific T cell immune responses from cryopreserved peripheral blood mononuclear cells after vaccination was performed as previously described (*13*). The antibody clones, conjugates, commercial source, and analysis purpose for each reagent is shown in table S5. Data were collected on FACS A5 Analyzers (BD Biosciences) and analyzed using FlowJo versions 9.9.6 and 10.7 software (BD Biosciences).

Correlations and statistical analysis

Graphs show data from individual animals, with dotted lines indicating assay limits of detection. Correlations between antibody measurements and between antibody measurements and dose of vaccine were estimated and tested against zero using Spearman's nonparametric correlation. Univariate and multivariate linear models were used to evaluate the potential role of antibodies as correlates of protection. Following the Prentice criteria (*47*), we categorized antibody measures as potential correlates of protection if they were significantly univariately predictive of log10 sgRNA as a measure of viral replication or if the addition of log10 dose to the linear model did not significantly improve prediction, as assessed by a likelihood ratio test. Univariate and multivariate linear models were also used to explore the combination of T cell responses and antibody responses in prediction of sgRNA. Comparisons before and after challenge were assessed using paired *t* tests and were based on the last measurement (day 28 after challenge when available; day 14 when not). Intracellular cytokines likely response labels were derived using the MIMOSA (*48*) package. Analyses were performed in R version 4.0.2 and GraphPad Prism version 9.0.2 software.

REFERENCES AND NOTES

1. E. Dong, H. Du, L. Gardner, An interactive web-based dashboard to track COVID-19 in real time. *Lancet Infect. Dis.* **20**, 533–534 (2020). doi: 10.1016/S1473-3099(20)30120-1; pmid: 32087114
2. J. Pallesen *et al*., Immunogenicity and structures of a rationally designed prefusion MERS-CoV spike antigen. *Proc. Natl. Acad. Sci. U.S.A.* **114**, E7348–E7357 (2017). doi: 10.1073/pnas.1707304114; pmid: 28807998
3. D. Wrapp *et al*., Cryo-EM structure of the 2019-nCoV spike in the prefusion conformation. *Science* **367**, 1260–1263 (2020). doi: 10.1126/science.abb2507; pmid: 32075877
4. F. P. Polack *et al*., Safety and efficacy of the BNT162b2 mRNA Covid-19 vaccine. *N. Engl. J. Med.* **383**, 2603–2615 (2020). doi: 10.1056/NEJMoa2034577; pmid: 33301246
5. L. R. Baden *et al*., Efficacy and safety of the mRNA-1273 SARS-CoV-2 vaccine. *N. Engl. J. Med.* **384**, 403–416 (2021). doi: 10.1056/NEJMoa2035389; pmid: 33378609
6. M. Voysey *et al*., Safety and efficacy of the ChAdOx1 nCoV-19 vaccine (AZD1222) against SARS-CoV-2: An interim analysis of four randomised controlled trials in Brazil, South Africa, and the UK. *Lancet* **397**, 99–111 (2021). doi: 10.1016/S0140-6736(20)32661-1; pmid: 33306989
7. D. Y. Logunov *et al*., Safety and efficacy of an rAd26 and rAd5 vector-based heterologous prime-boost COVID-19 vaccine: An interim analysis of a randomised controlled phase 3 trial in Russia. *Lancet* **397**, 671–681 (2021). doi: 10.1016/S0140-6736(21)00234-8; pmid: 33545094
8. G. Forni, A. Mantovani; COVID-19 Commission of Accademia Nazionale dei Lincei, Rome, COVID-19 vaccines: Where we stand and challenges ahead. *Cell Death Differ.* **28**, 626–639 (2021). doi: 10.1038/s41418-020-00720-9; pmid: 33479399
9. S. A. Plotkin, P. B. Gilbert, Nomenclature for immune correlates of protection after vaccination. *Clin. Infect. Dis.* **54**, 1615–1617 (2012). doi: 10.1093/cid/cis238; pmid: 22437237
10. P. J. Klasse, D. F. Nixon, J. P. Moore, Immunogenicity of clinically relevant SARS-CoV-2 vaccines in nonhuman primates and humans. *Sci. Adv.* **7**, eabe8065 (2021). doi: 10.1126/sciadv.abe8065; pmid: 33608249
11. J. Yu *et al*., DNA vaccine protection against SARS-CoV-2 in rhesus macaques. *Science* **369**, 806–811 (2020). doi: 10.1126/science.abc6284; pmid: 32434945
12. N. B. Mercado *et al*., Single-shot Ad26 vaccine protects against SARS-CoV-2 in rhesus macaques. *Nature* **586**, 583–588 (2020). doi: 10.1038/s41586-020-2607-z; pmid: 32731257
13. K. S. Corbett *et al*., Evaluation of the mRNA-1273 Vaccine against SARS-CoV-2 in Nonhuman Primates. *N. Engl. J. Med.* **383**, 1544–1555 (2020). doi: 10.1056/NEJMoa2024671; pmid: 32722908
14. V. J. Munster *et al*., Respiratory disease in rhesus macaques inoculated with SARS-CoV-2. *Nature* **585**, 268–272 (2020). doi: 10.1038/s41586-020-2324-7; pmid: 32396922
15. K. McMahan *et al*., Correlates of protection against SARS-CoV-2 in rhesus macaques. *Nature* **590**, 630–634 (2021). doi: 10.1038/s41586-020-03041-6; pmid: 33276369
16. K. Wu *et al*., Serum neutralizing activity elicited by mRNA-1273 vaccine. *N. Engl. J. Med.* **384**, 1468–1470 (2021). doi: 10.1056/NEJMc2102179; pmid: 33730471
17. X. Shen *et al*., Neutralization of SARS-CoV-2 variants B.1.429 and B.1.351. *N. Engl. J. Med.* **384**, 2352–2354 (2021). doi: 10.1056/NEJMc2103740; pmid: 33826819
18. V. V. Edara *et al*., Infection- and vaccine-induced antibody binding and neutralization of the B.1.351 SARS-CoV-2 variant. *Cell Host Microbe* **29**, 516–521.e3 (2021). doi: 10.1016/j.chom.2021.03.009; pmid: 33798491
19. B. Huang *et al*., Serum sample neutralisation of BBIBP-CorV and ZF2001 vaccines to SARS-CoV-2 501Y.V2. *Lancet Microbe* **2**, e285 (2021). doi: 10.1016/S2666-5247(21)00082-3; pmid: 33870240
20. Y. Liu *et al*., Neutralizing activity of BNT162b2-elicited serum. *N. Engl. J. Med.* **384**, 1466–1468 (2021). doi: 10.1056/NEJMc2102017; pmid: 33684280
21. D. Frampton *et al*., Genomic characteristics and clinical effect of the emergent SARS-CoV-2 B.1.1.7 lineage in London, UK: A whole-genome sequencing and hospital-based cohort study. *Lancet Infect. Dis.* S1473-3099(21)00170-5 (2021). doi: 10.1016/S1473-3099(21)00170-5; pmid: 33857406
22. N. G. Davies *et al*., Estimated transmissibility and impact of SARS-CoV-2 lineage B.1.1.7 in England. *Science* **372**, eabg3055 (2021). doi: 10.1126/science.abg3055; pmid: 33658326
23. H. Tegally *et al*., Emergence and rapid spread of a new severe acute respiratory syndrome-related coronavirus 2 (SARS-CoV-2) lineage with multiple spike mutations in South Africa. medRxiv 2020.2012.2021.20248640 [Preprint]. 22 December 2020. doi: 10.1101/2020.12.21.20248640
24. D. Planas *et al*., Sensitivity of infectious SARS-CoV-2 B.1.1.7 and B.1.351 variants to neutralizing antibodies. *Nat. Med.* **27**, 917–924 (2021). doi: 10.1038/s41591-021-01318-5; pmid: 33772244
25. K. S. Corbett *et al*., SARS-CoV-2 mRNA vaccine development enabled by prototype pathogen preparedness. *bioRxiv* 2020.06.11.145920 (2020). pmid: 32577634
26. N. Pardi *et al*., Nucleoside-modified mRNA vaccines induce potent T follicular helper and germinal center B cell responses. *J. Exp. Med.* **215**, 1571–1588 (2018). doi: 10.1084/jem.20171450; pmid: 29739835
27. L. Zou *et al*., SARS-CoV-2 viral load in upper respiratory specimens of infected patients. *N. Engl. J. Med.* **382**, 1177–1179 (2020). doi: 10.1056/NEJMc2001737; pmid: 32074444
28. D. Kim *et al*., The architecture of SARS-CoV-2 transcriptome. *Cell* **181**, 914–921.e10 (2020). doi: 10.1016/j.cell.2020.04.011; pmid: 32330414
29. V. J. Munster *et al*., Respiratory disease in rhesus macaques inoculated with SARS-CoV-2. *Nature* **585**, 268–272 (2020). doi: 10.1038/s41586-020-2324-7; pmid: 32396922
30. A. Chandrashekar *et al*., SARS-CoV-2 infection protects against rechallenge in rhesus macaques. *Science* **369**, 812–817 (2020). doi: 10.1126/science.abc4776; pmid: 32434946
31. B. Rockx *et al*., Comparative pathogenesis of COVID-19, MERS, and SARS in a nonhuman primate model. *Science* **368**, 1012–1015 (2020). doi: 10.1126/science.abb7314; pmid: 32303590
32. M. Imai *et al*., Syrian hamsters as a small animal model for SARS-CoV-2 infection and countermeasure development. *Proc. Natl. Acad. Sci. U.S.A.* **117**, 16587–16595 (2020). doi: 10.1073/pnas.2009799117; pmid: 32571934

33. R. Wölfel *et al*., Virological assessment of hospitalized patients with COVID-2019. *Nature* **581**, 465–469 (2020). doi: 10.1038/s41586-020-2196-x; pmid: 32235945
34. D. Shan *et al*., N-protein presents early in blood, dried blood and saliva during asymptomatic and symptomatic SARS-CoV-2 infection. *Nat. Commun.* **12**, 1931 (2021). doi: 10.1038/s41467-021-22072-9; pmid: 33771993
35. J. Fajnzylber *et al*., SARS-CoV-2 viral load is associated with increased disease severity and mortality. *Nat. Commun.* **11**, 5493 (2020). doi: 10.1038/s41467-020-19057-5; pmid: 33127906
36. D. E. Dimcheff *et al*., SARS-CoV-2 total and subgenomic RNA viral load in hospitalized patients. medRxiv 2021.02.25.21252493 [Preprint]. 1 March 2021. doi: 10.1101/2021.02.25.21252493
37. S. C. Adenyi-Jones, H. Faden, M. B. Ferdon, M. S. Kwong, P. L. Ogra, Systemic and local immune responses to enhanced-potency inactivated poliovirus vaccine in premature and term infants. *J. Pediatr.* **120**, 686–689 (1992). doi: 10.1016/S0022-3476(05)80228-8; pmid: 1315853
38. P. L. Ogra, Mucosal immune response to poliovirus vaccines in childhood. *Rev. Infect. Dis.* **6** (Suppl 2), S361–S368 (1984). doi: 10.1093/clinids/6.Supplement_2.S361; pmid: 6740074
39. P. L. Ogra, D. T. Karzon, F. Righthand, M. MacGillivray, Immunoglobulin response in serum and secretions after immunization with live and inactivated poliovaccine and natural infection. *N. Engl. J. Med.* **279**, 893–900 (1968). doi: 10.1056/NEJM196810242791701; pmid: 20617594
40. I. M. Onorato *et al*., Mucosal immunity induced by enhance-potency inactivated and oral polio vaccines. *J. Infect. Dis.* **163**, 1–6 (1991). doi: 10.1093/infdis/163.1.1; pmid: 1845806
41. G. Zhaori, M. Sun, P. L. Ogra, Characteristics of the immune response to poliovirus virion polypeptides after immunization with live or inactivated polio vaccines. *J. Infect. Dis.* **158**, 160–165 (1988). doi: 10.1093/infdis/158.1.160; pmid: 2839578
42. J. R. Francica *et al*., Vaccination with SARS-CoV-2 spike protein and AS03 adjuvant induces rapid anamnestic antibodies in the lung and protects against virus challenge in nonhuman primates. bioRxiv 433390 [Preprint]. 2 March 2021. doi: 10.1101/2021.03.02.433390
43. L. A. Jackson *et al*., An mRNA vaccine against SARS-CoV-2: Preliminary report. *N. Engl. J. Med.* **383**, 1920–1931 (2020). doi: 10.1056/NEJMoa2022483; pmid: 32663912
44. M. A. Whitt, Generation of VSV pseudotypes using recombinant ΔG-VSV for studies on virus entry, identification of entry inhibitors, and immune responses to vaccines. *J. Virol. Methods* **169**, 365–374 (2010). doi: 10.1016/j.jviromet.2010.08.006; pmid: 20709108
45. A. Vanderheiden *et al*., Development of a rapid focus reduction neutralization test assay for measuring SARS-CoV-2 neutralizing antibodies. *Curr. Protoc. Immunol.* **131**, e116 (2020). doi: 10.1002/cpim.116; pmid: 33215858
46. L. C. Katzelnick *et al*., Viridot: An automated virus plaque (immunofocus) counter for the measurement of serological neutralizing responses with application to dengue virus. *PLOS Negl. Trop. Dis.* **12**, e0006862 (2018). doi: 10.1371/journal.pntd.0006862; pmid: 30356267
47. R. L. Prentice, Surrogate endpoints in clinical trials: Definition and operational criteria. *Stat. Med.* **8**, 431–440 (1989). doi: 10.1002/sim.4780080407; pmid: 2727467
48. G. Finak *et al*., Mixture models for single-cell assays with applications to vaccine studies. *Biostatistics* **15**, 87–101 (2014). doi: 10.1093/biostatistics/kxt024; pmid: 23887981

ACKNOWLEDGMENTS

We thank M. Sriparna for key editing after review of the manuscript; T. Ruckwardt, N. Doria-Rose, and additional members of all included laboratories for critical discussions and advice pertaining to experiments included in the manuscript; J. Stein and M. Young for technology transfer and administrative support, respectively; members of the NIH NIAID VRC Translational Research Program, including C. Case, H. Bao, E. McCarthy, J. Noor, A. Taylor, and R. Woodward, for technical and administrative assistance with animal experiments; H. Mu and M Farzan for the ACE2-overexpressing 293 cells; members of the P. Kwong laboratory for providing protein for use in ELISA assays for detection of mucosal antibodies; A. Pekosz for the B.1.351 variant used in FRNT assays; E. Boritz for assistance with B.1.351 sequencing and analysis; and M. Brunner and M. Whitt for kind support on recombinant VSV-based SARS-CoV-2 pseudovirus production. **Funding:** This work was supported by the Intramural Research Program of the VRC, NIAID, NIH; Department of Health and Human Services, Office of the Assistant Secretary for Preparedness and Response, Biomedical Advanced Research and Development Authority, Contract 75A50120C00034; Undergraduate Scholarship Program, Office of Intramural Training and Education, Office of the Director, NIH (K.S.C.); NIAID Research Participation Program, administered by the Oak Ridge Institute for Science and Education through an interagency agreement between the U.S. Department of Energy and NIAID (R.W.); Emory Executive Vice President for Health Affairs Synergy Fund Award (M.S.S.); Pediatric Research Alliance Center for Childhood Infections and Vaccines and Children's Healthcare of Atlanta (M.S.S.); and Woodruff Health Sciences Center 2020 COVID-19 CURE Award (M.S.S.). **Author contributions:** K.S.C., M.C.N., B.F., M.G., S.O., T.S.J., S.N.S., V.V.E., K.F., L.L., C.M., J.F., B.F., K.W., A.C., M.K., A.P.W., J.I.M., O.M.A., S.F.A., M.M.D., J.F., D.R.F., E.L., A.T.N., S.T.N., S.J.P., A.C., A.D., A.F., J.G., S.K., L.P., M.P., K.S., D.V., S.Z., K.W.B., M.M., B.M.N., R.V., H.A., K.E.F., D.K.E., J.R.M., I.N.M., M.G.L., A.C., D.M., M.S.S., A.M., N.J.S., M.R., D.C.D., B.S.G., and R.A.S. designed, completed, and/or analyzed experiments. O.M.A., S.B-B., K.L., W.S., E.S.Y., Y.Z., and L.W. provided critical published reagents and/or analytic tools. K.S.C., M.C.N., N.J.S., M.R., B.S.G., and R.A.S. wrote the manuscript. K.S.C., M.C.N., M.G., and G.A. prepared figures and tables. All authors contributed to discussions about and editing of the manuscript. **Competing interests:** K.S.C. and B.S.G. are inventors on U.S. Patent No. 10,960,070 B2 and International Patent Application No. WO/2018/081318 entitled "Prefusion Coronavirus Spike Proteins and Their Use." K.S.C., O.M.A., and B.S.G. are inventors on U.S. Patent Application No. 62/972,886 entitled "2019-nCoV Vaccine." M.S.S. is on the advisory board of Moderna. D.V. holds equity in Johnson & Johnson and ABBVIE. **Data and materials availability:** All data are available in the main text or the supplementary materials. mRNA1273 was provided under a regional cooperative agreement with Moderna. To discuss access to this reagent, researchers should contact A.C. or D.K.E. This work is licensed under a Creative Commons Attribution 4.0 International (CC BY 4.0) license, which permits unrestricted use, distribution, and reproduction in any medium, provided the original work is properly cited. To view a copy of this license, visit https://creativecommons.org/licenses/by/4.0/. This license does not apply to figures/photos/artwork or other content included in the article that is credited to a third party; obtain authorization from the rights holder before using such material.

SUPPLEMENTARY MATERIALS

https://science.org/doi/10.1126/science.abj0299
Figs. S1 to S11
Tables S1 to S5
MDAR Reproducibility Checklist

20 April 2021; accepted 27 July 2021
Published online 29 July 2021
10.1126/science.abj0299

RESEARCH ARTICLE SUMMARY

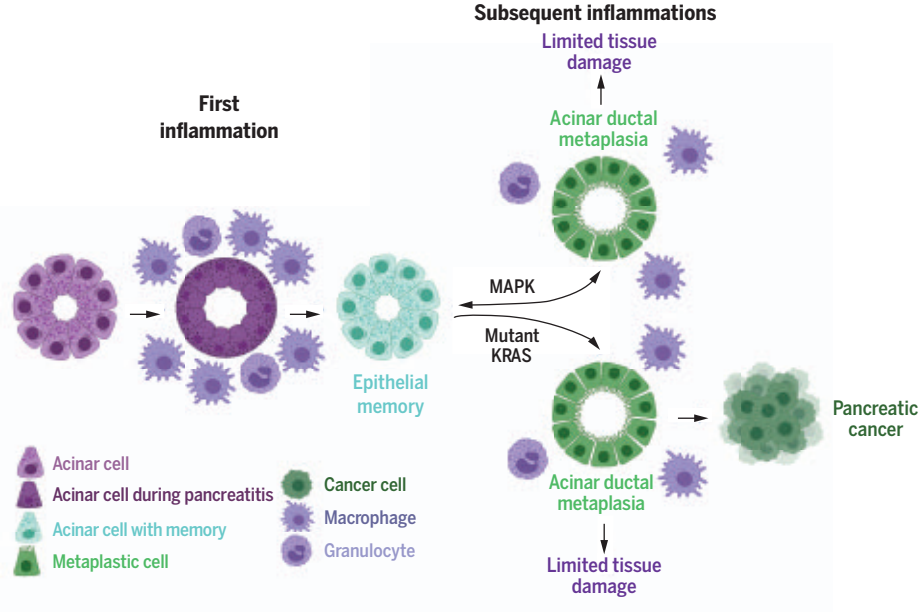
CANCER

Epithelial memory of inflammation limits tissue damage while promoting pancreatic tumorigenesis

Edoardo Del Poggetto†, I-Lin Ho†, Chiara Balestrieri, Er-Yen Yen, Shaojun Zhang, Francesca Citron, Rutvi Shah, Denise Corti, Giuseppe R. Diaferia, Chieh-Yuan Li, Sara Loponte, Federica Carbone, Yoku Hayakawa, Giovanni Valenti, Shan Jiang, Luigi Sapio, Hong Jiang, Prasenjit Dey, Sisi Gao, Angela K. Deem, Stefan Rose-John, Wantong Yao, Haoqiang Ying, Andrew D. Rhim, Giannicola Genovese, Timothy P. Heffernan, Anirban Maitra, Timothy C. Wang, Linghua Wang, Giulio F. Draetta, Alessandro Carugo, Gioacchino Natoli, Andrea Viale*

INTRODUCTION: The association between tumors and inflammation is a long-established clinical observation. Although many studies have demonstrated that the inflammatory microenvironment can promote tumor growth through the activation of survival and proliferation programs in cancer cells, the reason why inflammation, an evolutionarily conserved response to damage aimed at reestablishing tissue integrity upon injury, might be integral to tumorigenesis remains unknown.

RATIONALE: Pancreatic ductal adenocarcinoma, a tumor characterized by poor prognosis, represents a distinctive example of cooperation between inflammation and activated oncogenes. Frequently developed in a context of chronic pancreatitis, pancreatic cancer is associated with an inflammatory microenvironment. As supported by a substantial body of evidence across a multitude of experimental models, when occurring in the context of pancreatitis, mutations of *KRAS*, the universal oncogenic driver of pancreatic cancer, lead to accelerated tumor development and induce the appearance of neoplastic precursor lesions, such as acinar-to-ductal metaplasia and pancreatic intraepithelial neoplasia, which can evolve into invasive tumors. Interestingly, preneoplastic pancreatic alterations, specifically acinar-to-ductal metaplasia, have been previously identified during acute and chronic pancreatitis in the absence of oncogene activation, suggesting an alternative role other than oncogenic transformation. To better understand the relationship between inflammatory processes and pancreatic tumorigenesis, we used different mouse models to investigate the long-term effects of transient inflammatory events in response to acute pancreatic damage and how resolved inflammation cooperates with activated oncogenes to drive tumor progression in normal epithelial cells.



Epithelial adaptation in response to inflammation protects pancreas from subsequent inflammatory events and promotes tumorigenesis. Epithelial cells undergo sustained transcriptional and epigenetic reprogramming after a single inflammation (epithelial memory). This adaptation limits tissue damage during subsequent inflammatory events by activation of a transdifferentiation program in acinar cells (metaplasia). In this context, mutations of *Kras*, which stabilize metaplastic lesions, are beneficial and protective against tissue damage accumulation.

RESULTS: By investigating the effects of inflammation on normal pancreatic epithelial cells in different mouse models, we discovered that long after the complete resolution, a transient inflammatory event primes pancreatic epithelial cells to cooperate with oncogenic *Kras* to induce pancreatic tumors. Indeed, upon recovery from a single acute inflammation, epithelial pancreatic cells display an enduring adaptive response associated with sustained transcriptional and epigenetic reprogramming that leads to the activation of multiple gene expression programs, including embryonic programs activated during cancer progression. While promoting tumor development, such adaptation to tissue damage facilitates the prompt acquisition of acinar-to-ductal metaplasia upon subsequent inflammatory events. This rapid dedifferentiation program of acinar cells, that lasts for the length of the stimulus and from which the tissue promptly and apparently completely recovers, represents a physiological mechanism for limiting tissue damage through the rapid decrease of zymogen production that would otherwise fuel further damage and inflammation. As a result, pancreatic tissues exposed to initial inflammation undergo a markedly attenuated response and limited tissue damage to subsequent inflammatory episodes. Because metaplastic lesions are mediated by the activation of mitogen-activated protein kinase (MAPK) signaling, we demonstrate that activating mutations of *Kras*, maintaining an irreversible acinar-to-ductal metaplasia through MAPK constitutive signaling, are protective against tissue damage induced by pancreatic inflammation.

CONCLUSION: We have uncovered a new physiologic role of somatic mutations in preserving tissue homeostasis during repeated damages. We propose that *KRAS* mutations, independent from the eventual contribution to tumorigenesis, may be beneficial and under strong positive selection in the context of recurrent pancreatitis, perhaps representing a nearly universal event in the development of pancreatic cancer. ■

The list of author affiliations is available in the full article online.
***Corresponding author. Email: aviale@mdanderson.org**
†These authors contributed equally to this work.
Cite this article as E. Del Poggetto *et al.*, *Science* 373, eabj0486 (2021). DOI: 10.1126/science.abj0486

READ THE FULL ARTICLE AT
https://doi.org/10.1126/science.abj0486

CREDIT: CREATED WITH BIORENDER.COM

RESEARCH ARTICLE

CANCER

Epithelial memory of inflammation limits tissue damage while promoting pancreatic tumorigenesis

Edoardo Del Poggetto[1]†‡, I-Lin Ho[1,2]†, Chiara Balestrieri[3,4], Er-Yen Yen[1,2], Shaojun Zhang[1]§, Francesca Citron[1], Rutvi Shah[1,2], Denise Corti[1]¶, Giuseppe R. Diaferia[5], Chieh-Yuan Li[1,2]#, Sara Loponte[1], Federica Carbone[1]**, Yoku Hayakawa[6], Giovanni Valenti[6], Shan Jiang[1], Luigi Sapio[1]††, Hong Jiang[1], Prasenjit Dey[7]‡‡, Sisi Gao[1], Angela K. Deem[1], Stefan Rose-John[8], Wantong Yao[9], Haoqiang Ying[10], Andrew D. Rhim[11], Giannicola Genovese[12], Timothy P. Heffernan[13], Anirban Maitra[14], Timothy C. Wang[6], Linghua Wang[1], Giulio F. Draetta[1], Alessandro Carugo[13], Gioacchino Natoli[5,15], Andrea Viale[1]*

Inflammation is a major risk factor for pancreatic ductal adenocarcinoma (PDAC). When occurring in the context of pancreatitis, KRAS mutations accelerate tumor development in mouse models. We report that long after its complete resolution, a transient inflammatory event primes pancreatic epithelial cells to subsequent transformation by oncogenic KRAS. Upon recovery from acute inflammation, pancreatic epithelial cells display an enduring adaptive response associated with sustained transcriptional and epigenetic reprogramming. Such adaptation enables the reactivation of acinar-to-ductal metaplasia (ADM) upon subsequent inflammatory events, thereby limiting tissue damage through a rapid decrease of zymogen production. We propose that because activating mutations of KRAS maintain an irreversible ADM, they may be beneficial and under strong positive selection in the context of recurrent pancreatitis.

The association between tumors and inflammation is a long-established clinical observation (*1*). Many studies have demonstrated that the inflammatory microenvironment can promote tumor growth through the activation of survival and proliferation programs in cancer cells (*2*, *3*). However, the reasons why inflammation, an evolutionarily conserved response to damage aimed at reestablishing tissue integrity upon injury, might be integral to tumorigenesis remain unknown, although recent evidence suggests that inflammation-induced chromatin changes may play an important role (*4*).

Pancreatic ductal adenocarcinoma (PDAC), a tumor characterized by poor prognosis (*5*), represents a distinctive example of cooperation between inflammation and activated oncogenes. Frequently developed in the context of chronic pancreatitis, PDAC is associated with an inflammatory microenvironment (*6*). As supported by a substantial body of evidence across a multitude of experimental models, induction of inflammation in pancreatic tissue expressing oncogenic *KRAS* hastens tumor progression (*7*, *8*), inducing the appearance of neoplastic precursor lesions, such as acinar-to-ductal metaplasia (ADM) and pancreatic intraepithelial neoplasia (PanIN). These precursors can evolve into invasive tumors (*9*–*11*), although alternative models of PanIN-independent progression have been proposed (*12*, *13*), for example, if oncogenic signaling is activated in the ductal compartment (*14*).

Additionally, preneoplastic pancreatic alterations, specifically ADM, have been identified previously in acute and chronic pancreatitis in the absence of oncogene activation (*15*–*19*). Because ADM involves the rapid shutdown of pancreatic enzyme expression, it may represent an adaptive response to inflammation aimed at limiting tissue damage. In this conceptual framework, any genetic event that is able to promote or stabilize ADM, such as activating KRAS mutations, may result in the positive selection of mutant cells within an inflamed tissue. To better understand the relationship between inflammation and pancreatic tumorigenesis, we investigated in different mouse models the long-term consequences of transient inflammatory events in response to acute pancreatic damage and monitored how resolved inflammation cooperates with activated oncogenes to drive transformation of normal epithelial cells.

Results

Transient inflammation promotes the development of pancreatic cancer after resolution

To investigate the long-term effects of inflammation on the transformation of normal pancreatic epithelial cells, we used caerulein (hereafter referred to as CAE), a decapeptide analog of cholecystokinin (*20*), to trigger damage and subsequent inflammation in a well-characterized PDAC mouse model [inducible KRAS (iKRAS)] in which oncogenic $KRAS^{G12D}$ expression is induced in the pancreas by doxycycline administration (TetO-LSL-$Kras^{G12D}$_ROSA26-LSLrtTa-IRES-GFP_p48-Cre) (*21*–*23*). To avoid confounding effects linked to chronic CAE administration, such as stromal and microenvironmental remodeling, we used a 2-day CAE administration protocol to induce acute inflammation (*24*), whereas control animals received intraperitoneal injections with phosphate-buffered saline (PBS) on the same schedule (Fig. 1A). Immediately after CAE administration, we observed transient pancreatic inflammation, with edema and inter- and intralobular infiltration of inflammatory cells, followed by rapid restoration of tissue integrity by day 7 (fig. S1A). Immunostaining was consistent with the histological analysis, revealing that inflammatory cell infiltration (CD45-positive cells) and proliferation (Ki67 staining) present at day 1 after CAE treatment returned to pre–CAE treatment levels by day 28 (fig. S1B), indicative of a complete histological resolution. In addition, we observed strong nuclear staining of two pivotal transcriptional activators of inflammation, nuclear factor κB (NF-κB) (*25*) and STAT3 (*26*), in epithelial and stromal cells immediately after the induction of pancreatitis (Fig. 1B and fig. S1, C to E). The normalization of these two transcription factors (TFs), together with recovery of the normal pancreatic histology, suggested that the inflammatory response was extinguished 1 week after CAE treatment. Therefore, we explored the effects of $KRAS^{G12D}$ after resolution of this single inflammatory event by inducing its expression at 28 days after the initial CAE protocol

[1]Department of Genomic Medicine, The University of Texas MD Anderson Cancer Center, Houston, TX 77030, USA. [2]MD Anderson UTHealth Graduate School of Biomedical Sciences, Houston, TX 77030, USA. [3]Experimental Hematology Unit, San Raffaele Research Hospital, Milan 20132, Italy. [4]Center for Omics Sciences, IRCCS San Raffaele Scientific Institute, Milan 20132, Italy. [5]Department of Experimental Oncology, European Institute of Oncology IRCCS, Milan 20139, Italy. [6]Department of Digestive and Liver Diseases, Columbia University Medical Center, New York, NY 10032, USA. [7]Department of Cancer Biology, The University of Texas MD Anderson Cancer Center, Houston, TX 77030, USA. [8]Department of Biochemistry, Christian-Albrechts-Universität zu Kiel, Kiel 24098, Germany. [9]Department of Translational Molecular Pathology, The University of Texas MD Anderson Cancer Center, Houston, TX 77030, USA. [10]Department of Molecular and Cellular Oncology, The University of Texas MD Anderson Cancer Center, Houston, TX 77030, USA. [11]Department of Gastroenterology Hepatology and Nutrition, The University of Texas MD Anderson Cancer Center, Houston, TX 77030, USA. [12]Department of Genitourinary Medical Oncology, The University of Texas MD Anderson Cancer Center, Houston, TX 77030, USA. [13]TRACTION, The University of Texas MD Anderson Cancer Center, Houston, TX 77030, USA. [14]Sheikh Ahmed Center for Pancreatic Cancer Research, The University of Texas MD Anderson Cancer Center, Houston, TX 77030, USA. [15]Humanitas University, Pieve Emanuele, Milan 20089, Italy.

***Corresponding author. Email: aviale@mdanderson.org**

†These authors contributed equally to this work.

‡Present address: AXXAM, Bresso, Milan 20091, Italy.

§Present address: Medical Research Center, Guangdong Provincial People's Hospital, Guangdong Academy of Medical Sciences, Guangzhou 510080, China.

¶Present address: F. Hoffmann-La Roche Ltd., Basel 4070, Switzerland.

#Present address: Mission Bio, South San Francisco, CA 94080, USA.

**Present address: Nerviano Medical Sciences, Nerviano 20014, Italy.

††Present address: Department of Precision Medicine, University of Campania "Luigi Vanvitelli," Naples 80138, Italy.

‡‡Present address: Department of Immunology, Roswell Park Comprehensive Cancer Center, Buffalo, NY 14263, USA.

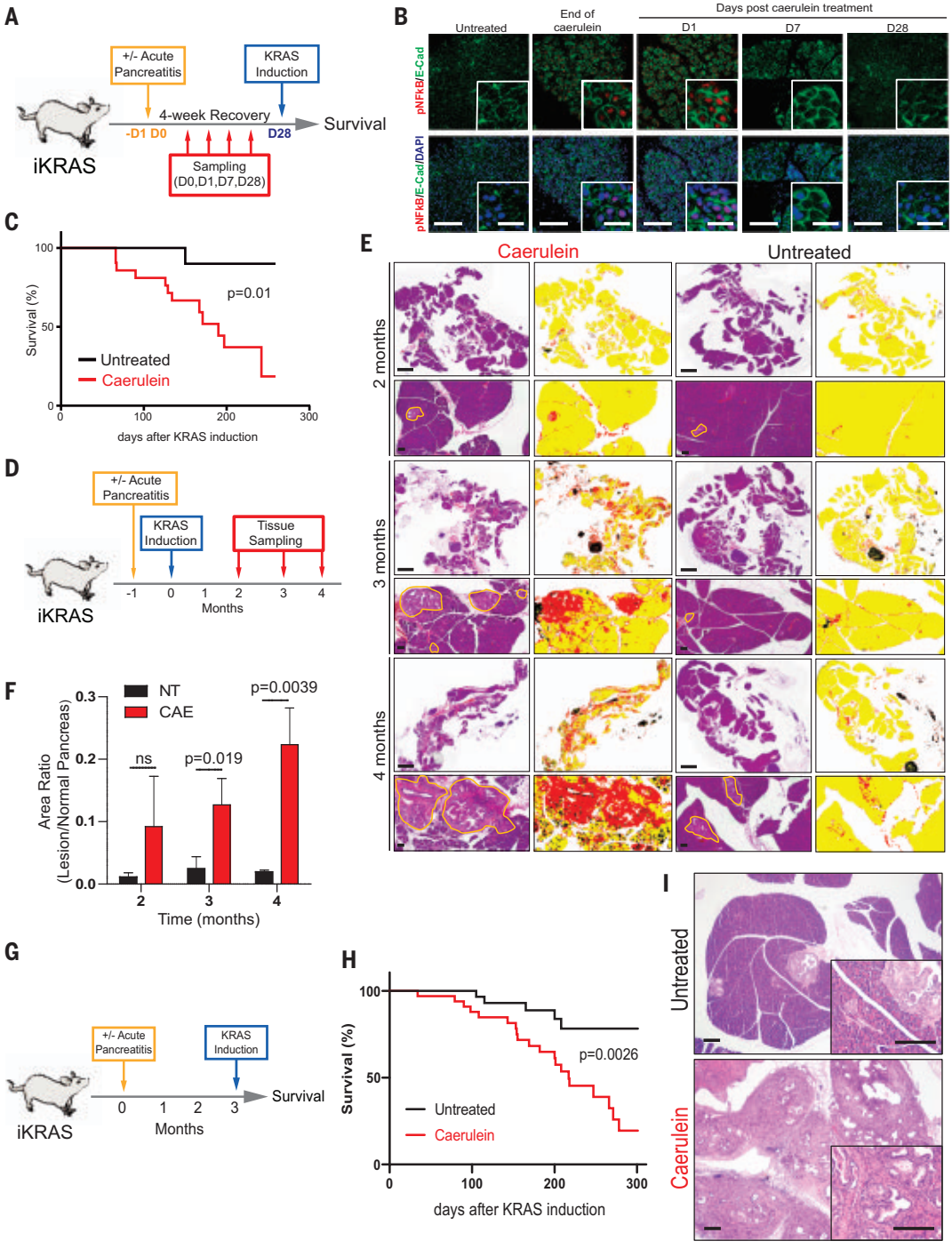


Fig. 1. Transient inflammation promotes tumor progression long after resolution. (**A**) Schematics representing the experimental design. Briefly, iKRAS mice are treated for 2 days (−D1, D0) with CAE to induce acute pancreatitis and followed for 4 weeks. When pancreatitis had fully resolved (D28), CAE-treated and control mice were administered doxycycline to induce the expression of mutated KRAS and then observed for tumor development. D, day. (**B**) Immunofluorescence staining for NF-κB (phospho-Ser^{536}, red), E-cadherin (green), and 4′,6-diamidino-2-phenylindole (DAPI, blue) in pancreatic samples at different time points before and after CAE treatment. Scale bars are 200 μm for main images and 50 μm for insets. n = 3 mice per group. (**C**) Kaplan-Meier survival plot of mice previously exposed to inflammation (caerulein, n = 21) or control mice (untreated, n = 10) after KRAS induction. (**D**) Schematic representing the experimental design for (E) and (F). In brief, KRAS was induced in iKRAS mice at 1 month after acute pancreatitis, and pancreata were sampled for histological analysis at 2, 3, and 4 months after KRAS induction. Mice that did not receive acute inflammation were used as controls. (**E**) Histopathological evaluation and quantification of KRAS-driven changes over time. For each time point, four images are shown per experimental group: top images, hematoxylin and eosin (H&E) staining at low magnification (left) and corresponding quantification mask (right); bottom images, high magnification details of the H&E (left) and corresponding quantification mask (right). Tumor lesions in high magnification H&E panels are highlighted by orange lines. The color code for quantifying the mask is as follows: red, tumor lesion; yellow, normal pancreatic tissue; and black, spleen or lymphoid tissues. Scale bars are 2000 μm in the top images and 100 μm in the bottom images. (**F**) Quantification of tumor burden (ratio of lesions to normal pancreas) over time as in (E). Data are shown as mean ± SD; n = 3 mice per time point per group. Statistical significance was assessed with unpaired Student's t test. ns, not significant. NT, nontreated. (**G**) Schematic representing the experimental design for (H) and (I). In brief, KRAS is induced in iKRAS mice at 3 months after acute pancreatitis. Mice without acute inflammation are included as controls. Animals were followed for tumor development. (**H**) Kaplan-Meier survival analysis of mice exposed to inflammation (caerulein, n = 22) or control mice (untreated, n = 12) 3 months before KRAS induction as described in (G). (**I**) H&E staining shows pancreas histology of matched samples as in (H). Scale bars are 200 μm.

and monitoring tumor development (Fig. 1A). CAE-treated mice developed tumors with high penetrance and succumbed to disease earlier than control animals (median survival of 190 days in CAE-treated versus nonreached in control because the majority of the animals were still alive at the end of the study; p = 0.01) (Fig. 1C and fig. S1F). This observation was also confirmed by magnetic resonance imaging (MRI) (fig. S1G) and histological analysis at different time points over a period of 4 months after KRAS activation, which demonstrated an earlier onset and larger neoplastic lesions in CAE-treated animals (Fig. 1, D to F). Notably, the cooperation between oncogenic KRAS and

resolved inflammation extended far beyond 28 days, because we observed accelerated tumorigenesis even when KRAS was activated 3 months after a single inflammatory event (median survival of 217 days in CAE-treated versus nonreached in untreated controls because the majority of the animals were still alive at the end of the study; $p = 0.0026$) (Fig. 1, G to I). This observation was independent of the modality used to induce inflammation (fig. S1H) and appeared to have similar penetrance as conventional protocols of accelerated pancreatic tumorigenesis in which inflammation is induced in the context of ongoing oncogenic signaling (fig. S1H). Overall, these data demonstrate that transient inflammatory events have persistent effects on normal epithelial cells and can cooperate with oncogene activation long after the resolution of inflammation.

Long-term effects of resolved inflammation are cell-autonomous

To determine whether differences in outcome between CAE-treated and untreated animals resulted from epithelial cell–autonomous effects or from the influence of long-term stroma activation, we established epithelial cultures from pancreata of mice 4 weeks after acute CAE treatment or PBS treatment in control animals. Pancreatic cells were cultured as spheroids, an effective culturing system that allows the expansion of three-dimensional (3D) epithelial structures (*27*). Spheroids derived from CAE-treated wild-type (WT) animals, although numerically and morphologically similar (fig. S2, A to C), showed an increased size with respect to spheroids derived from control animals, suggesting that epithelial cells previously exposed to inflammation can expand more efficiently in vitro (Fig. 2, A and B). This difference was further exacerbated in 2D conditions where only cells derived from CAE-treated mice were able to reach confluency after the first passage. Replicative exhaustion in primary cultures has been linked to senescence (*28*), and suppression of senescence programs during pancreatitis has been reported (*8*). We thus evaluated senescence markers, including β-galactosidase (β-Gal) activity, histone H3 lysine 9 trimethylation (H3K9me3), and p16 expression, which revealed suppression of the senescence program in CAE-treated pancreata compared with control pancreata (Fig. 2, C to E), indicating that inflammation-induced reprograming can allow epithelial cells to evade senescence.

In parallel, pancreatic epithelial spheroids derived from iKRAS animals were orthotopically transplanted into inflammation-naïve recipients (250,000 cells per animal) after 5 weeks in culture, and KRAS was induced (Fig. 2F). Mice that received cells derived from CAE-treated pancreata developed aggressive tumors with high penetrance (Fig. 2G), which were characterized by poorly differentiated histology and liver metastasis (Fig. 2H and fig. S2D, left panels). Although these tumors did not display classical features of pancreatic differentiation, the expression of green fluorescent protein (GFP) and the exclusion of CD45 immunoreactivity confirmed their pancreatic origin (Fig. 2H and fig. S2D, middle and right panels). In line with this observation, upon digestion and subcutaneous retransplantation of isolated primary tumor cells, the tumors acquired a more differentiated histology, as indicated by the organization of epithelial structures and acquisition of CK19 expression (fig. S2E). Together, these data suggest that the inflammation-induced long-lasting epithelial modifications that cooperate with oncogenic signaling are cell-autonomous and maintained by pancreatic epithelial cells irrespectively of the microenvironment.

Transient inflammatory events induce sustained gene expression and chromatin reprogramming

To identify the molecular changes in epithelial cells responsible for the long-term effect on pancreatic tumorigenesis, we performed a single-cell transcriptomic analysis on WT pancreata at different time points (1, 7, and 28 days) after treatment with CAE as well as on untreated animals as a control. To minimize interanimal variability, for each time point we pooled pancreata from three independent animals, and samples were depleted of CD45-positive cells to maximize epithelial contribution, especially at early time points after inflammation. Exocrine epithelial cell populations were identified by differentiation markers (fig. S3, A and B), and subsequent clustering analysis revealed the kinetics of transcriptomic deregulation specifically in the acinar compartment upon inflammation (Fig. 3A). Indeed, acinar cells underwent profound transcriptomic changes immediately after inflammation (day 1). Among them, an impairment of pancreatic digestive functions, including suppression of acinar zymogens (such as amylase, elastase, and pancreatic ribonuclease) and the concomitant up-regulation of ductal markers (such as cytokeratins 18 and 19 and Mucin1), was apparent at day 1 and resolved by day 28 (Fig. 3B). Notably, these changes were compatible with the molecular program of ADM (*15*). Beyond these transient changes, CAE-treated acinar cells retained a modified gene transcriptional program at day 28 after inflammation that was not observed in the ductal compartment (Fig. 3A). Ingenuity pathway analysis (IPA) of signature genes that define different acinar states uncovered the activation of programs related to cell death and survival, proliferation, and cell transformation specifically in CAE-treated animals (Fig. 3C and table S1). Moreover, a set of genes coregulated during pancreatic embryonic development and tumorigenesis (*29*) were also significantly enriched ($p < 4.37 \times 10^{-12}$) (fig. S3C). These findings support the notion that epithelial acinar cells maintain an adaptive response to tissue damage that involves the sustained activation of multiple gene expression programs, including embryonic programs reactivated during cancer progression.

To identify the regulatory networks responsible for this sustained transcriptional signature, we identified DNA sequence motifs that were statistically overrepresented in the promoters of deregulated genes at day 28, which are recognized by distinct TF families, including Sp, Kruppel-like factors (KLF), E2F, and early growth response (EGR) (Fig. 3D and table S2). To investigate whether the long-term transcriptomic response to inflammation is associated with persistent chromatin modifications, we mapped chromatin accessibility of pancreatic cells after inflammation. Assay for transposase-accessible chromatin using sequencing (ATAC-seq) analysis of pancreata at different time points during and after the inflammatory episode revealed increased chromatin accessibility at thousands of transcription start site (TSS)–proximal and TSS-distal genomic regulatory elements (corresponding to promoters and putative enhancers, respectively) in CAE-treated animals compared with controls (table S3). Both gene promoters and putative enhancers that showed increased accessibility during early inflammation (day 1) either maintained or increased their accessibility after full recovery of the pancreatic tissue (day 28), demonstrating that the long-term transcriptomic response to transient pancreatitis is accompanied by persistent chromatin modifications in acinar cells (Fig. 3, E and F). Not surprisingly, functional analysis of genes associated with the open genomic regions identified biological processes involved in abnormal inflammation, development, and cancer (Fig. 3G). Moreover, motif enrichment analysis of differentially accessible regions mapped to the same families of TFs that we identified as enriched in the promoters of transcriptionally deregulated genes (Fig. 3, H and I). Expression of some members of these TF families by acinar cells after inflammation, as indicated by single-cell RNA sequencing (RNA-seq) data, further corroborates their putative role in sustaining the enduring response to inflammation (Fig. 3J and fig. S3D). Taken together, these data demonstrate that after normal pancreatic epithelial cells recover from a transient episode of inflammation, they acquire a lasting adaptive response maintained by a persistent transcriptional and epigenetic reprogramming.

Persistent inflammation-induced reprogramming in acinar progenitor cells

Epithelial spheroids derived from post–CAE treatment animals can support KRAS-mediated

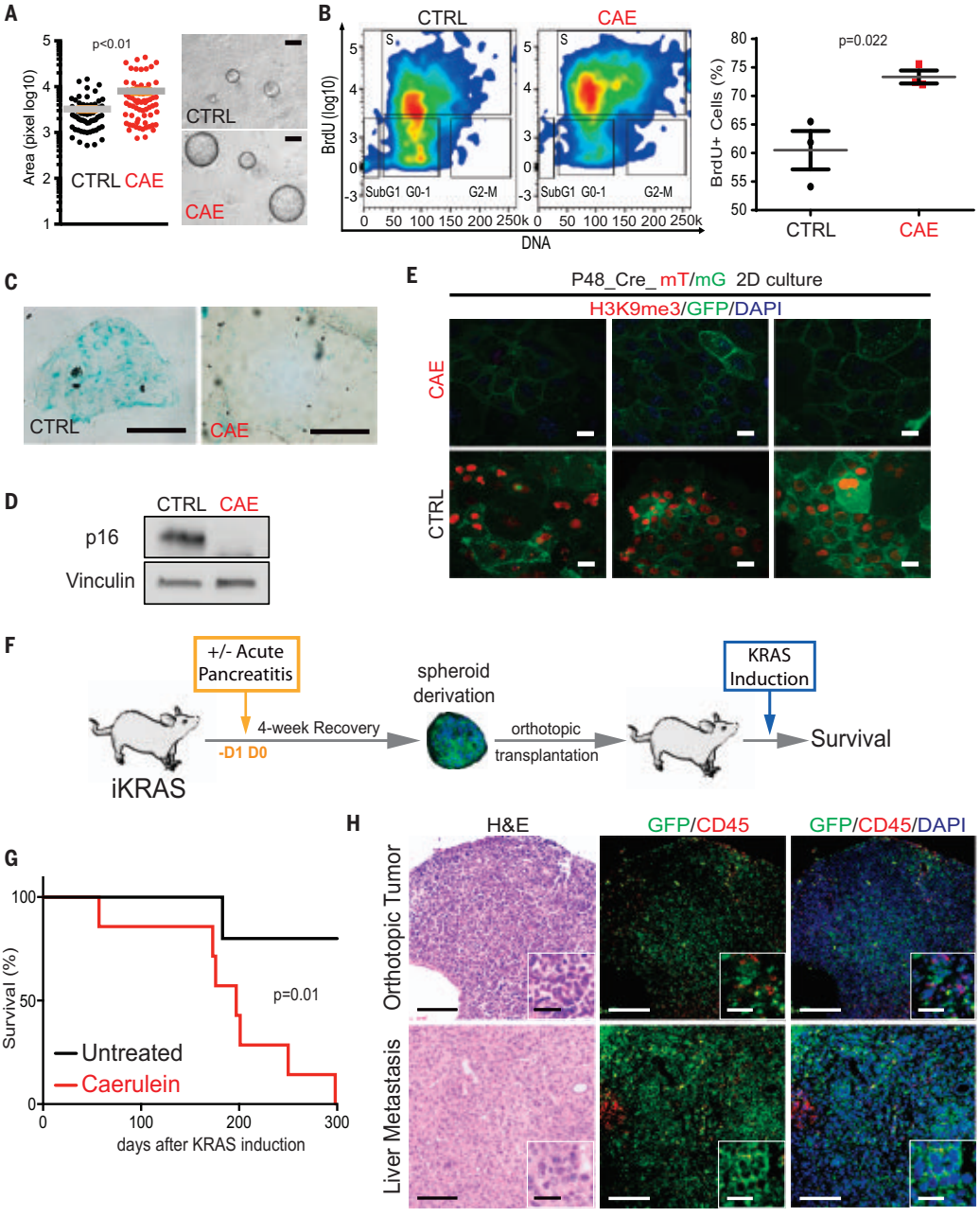


Fig. 2. Cell-autonomous effects of resolved inflammation. (**A**) Quantification of spheroid size from the pancreas of WT mice that recovered from CAE-induced inflammation (CAE) or controls (CTRL). Size was evaluated as pixel log10 scale (nine fields for each condition from three independent experiments; CAE $n = 69$, CTRL $n = 58$; $p < 0.01$). Gray lines indicate the mean of represented values. Representative microscopic images of spheroids are shown. Scale bars are 50 μm. (**B**) Flow cytometry analysis and quantification of 5-bromo-2-deoxyuridine (BrdU) incorporation by epithelial spheroids derived from WT mice either preexposed or not exposed to CAE. DAPI is used for DNA content. Data are shown as mean ± SD of three independent experiments. Statistical significance is assessed with unpaired Student's *t* test ($p = 0.022$). (**C**) β-Gal staining of 2D epithelial cultures derived from pancreata of WT mice recovered from inflammation (CAE) or control animals (CTRL). Scale bars are 100 μm. (**D**) Immunoblots for p16 and vinculin on epithelial cells derived from WT pancreata recovered from inflammation (CAE) or controls (CTRL). (**E**) Immunofluorescence staining for H3K9me3 (red) on epithelial cultures derived from pancreata of P48-Cre_mT/mG mice recovered from inflammation (CAE) or controls (CTRL). GFP (green) indicates pancreatic origin of the cells. Cell nuclei are stained with DAPI (blue). Scale bars are 20 μm. (**F**) Schematic representing the experimental design. Briefly, spheroids derived from iKRAS pancreas recovered from animals with pancreatitis (4-week recovery) or controls were orthotopically injected into recipient animals not previously exposed to inflammation. KRAS expression was induced, and mice were followed for tumor development. (**G**) Kaplan-Meier survival plot of mice transplanted with iKRAS spheroids derived from pancreata recovered from pancreatitis (caerulein, $n = 7$) and control mice (untreated, $n = 5$) after KRAS induction. (**H**) H&E staining and immunofluorescence staining for GFP (green) and CD45 (red) of orthotopic tumors and corresponding liver metastases developed from animals injected with spheroids derived from the pancreata of animals previously exposed to inflammation. Cell nuclei are stained with DAPI (blue). Scale bars are 200 μm for main images and 50 μm for insets.

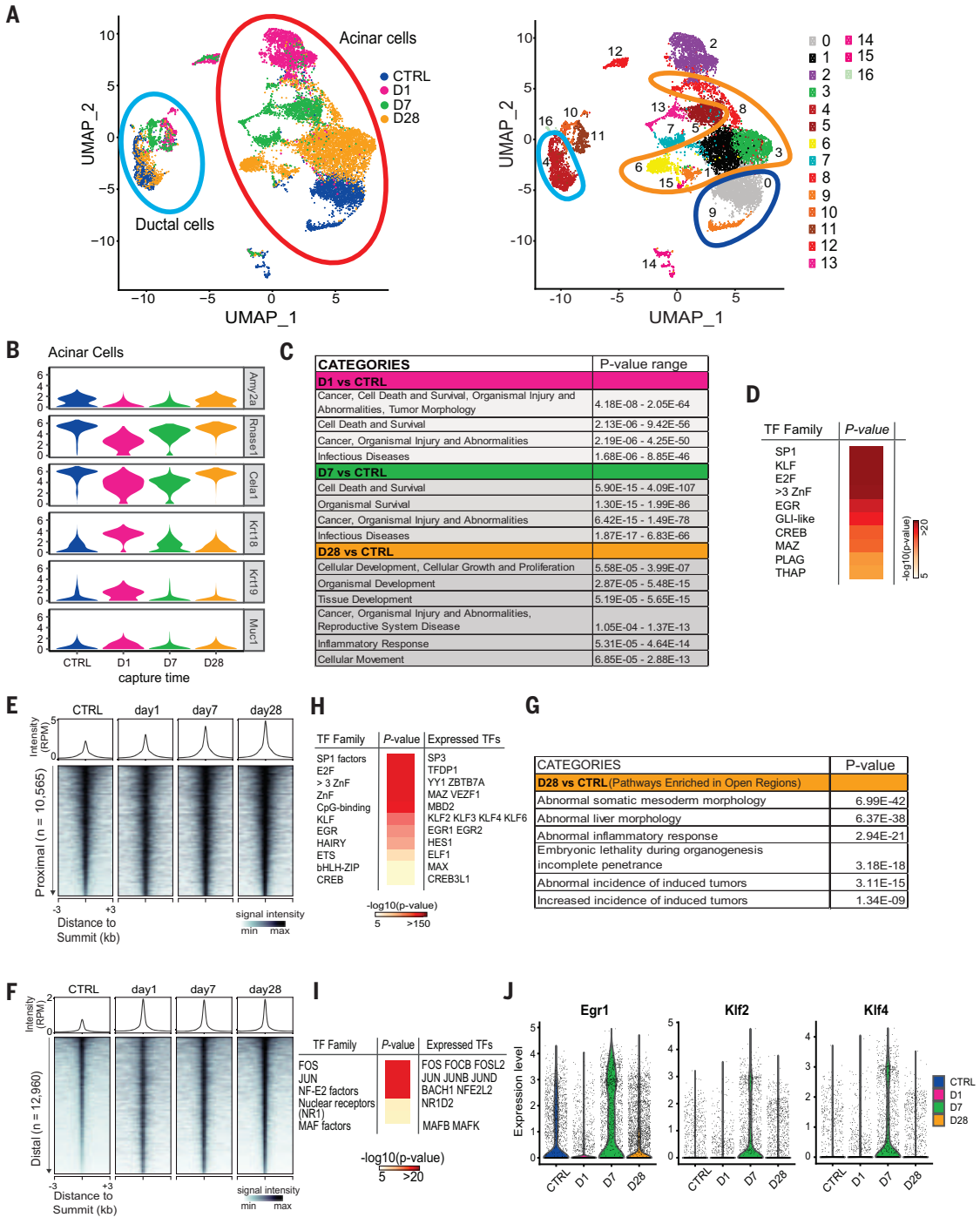


Fig. 3. Pervasive transcriptional deregulation and chromatin changes in pancreatic epithelial cells recovered from inflammation. (**A** to **D**) Single-cell RNA-seq of ex vivo pancreatic cells before (CTRL) and after acute inflammation at different time points (D1, D7, and D28). In (A), epithelial clusters (acinar and ductal compartments), as identified based on cell type–specific markers, revealed transcriptomic deregulation after inflammation mainly in acinar cells. Specifically, acinar cells at D28 remained in a different transcriptional state with respect to control cells (left). Unsupervised clustering (right) recognized acinar cells at D28 after inflammation (orange circle) belonging to separate clusters with respect to untreated control (CTRL) (blue circle), whereas ductal CTRL and D28 cells clustered together (cyan circle). In (B), gene expression dynamics of acinar and ductal markers in acinar compartment across different time points are shown. In (C), diseases and biological processes scoring in pathway analysis (IPA) associated with genes expressed in acinar cells at D1, D7, and D28 versus CTRL is shown. In (D), TF binding sequences enriched in motif analysis of promoter regions of deregulated genes at D28 versus CTRL in acinar cells are shown. (**E** to **I**) ATAC-seq of ex vivo epithelial pancreatic cells before (CTRL) and after acute inflammation (D1, D7, and D28). In (E) and (F) density plots and heat maps depicting dynamics of enriched open regions, proximal (E) or distal (F) to gene TSS, at D28 versus CTRL across different time points are shown. RPM, reads per million. In (G), pathway analysis (GREAT) of enriched chromatin open region–associated genes at D28 versus CTRL is shown. In (H) and (I), motif enrichment analysis of open chromatin regions at D28 versus CTRL identifying overrepresented sequences recognized by TF families in proximal (H) or distal (I) regions is shown. (**J**) Expression of TFs identified through motif enrichment analysis [(D), (H), and (I)] in single-cell RNA-seq across different time points before and after acute inflammation.

tumorigenesis upon orthotopic transplantation (Fig. 2, F to H), whereas acinar cells are the major target of inflammation-induced reprogramming in vivo. We therefore investigated the relationship between epithelial spheroids and acinar cells. Epithelial spheroids derive from doublecortin-like kinase 1 (DCLK1)–positive progenitor cells (*30*–*33*). To confirm that, in our experimental setting, epithelial spheroids originated from DCLK1-positive cells, we used a mouse model in which ZsGreen (a green fluorescent protein) is expressed under the control of the *Dclk1* gene promoter (Dclk1-DTR-ZsGreen) (*30*) (fig. S4A) and observed that only the ZsGreen-positive fraction of pancreatic cells was able to generate spheroids (Fig. 4A and fig. S4B). To further demonstrate the role of DCLK1-positive cells in maintaining spheroid cultures, we used the diphtheria toxin (DT) receptor coexpressed alongside ZsGreen to specifically target DCLK1-positive cells in epithelial spheroids. Exposure to DT dramatically affected the expansion of epithelial spheroids derived from Dclk1-DTR-ZsGreen mice but did not have any effect on spheroids derived from WT animals, confirming the specificity of the results and the critical importance of DCLK1-positive cells in spheroid maintenance (fig. S4C). Because the vast majority of DCLK1-positive cells display acinar differentiation (*30*, *31*, *34*) and sustain acinar regeneration upon tissue damage in vivo (*30*), we assessed the functional ability of DCLK1-positive progenitor cells from epithelial spheroids to regenerate normal pancreatic tissue upon damage. We derived GFP-positive spheroids from P48_Cre_R26-mT/mG animals and transplanted them orthotopically into syngeneic recipients in which pancreata were previously damaged by CAE treatment. Four weeks after implantation, GFP-positive acinar lobules were clearly detected in the pancreas, and their differentiation was confirmed by amylase immunostaining (Fig. 4B). Lineage-tracing experiments also demonstrated that after inflammation, spheroids derived from Mist1-Cre^{ERT2}-mT/mG animals were strongly GFP positive, suggesting that the DCLK1-positive cells at the origin of the spheroids have acinar properties (Fig. 4C). Together, these findings further corroborate previous observations that DCLK1-positive cells represent a reservoir of pancreatic progenitor cells able to sustain both epithelial spheroids in vitro and acinar regeneration in vivo upon tissue damage (*30*).

To understand the gene regulatory bases underlying reprogramming, we performed ATAC-seq on DCLK1-positive cells isolated from untreated or CAE-treated pancreas (table S4). Compared with controls, DCLK1-positive cells isolated 28 days after CAE treatment were characterized by increased chromatin accessibility at thousands of genomic regions (Fig. 4, D and E), and differentially accessible chromatin regions were enriched in motifs similar to those previously identified in acinar cells ex vivo (EGR, Sp, KLF, and E2F) (Fig. 4, F and G). We also characterized epithelial spheroids derived from WT animals and performed a transcriptomic analysis 9 weeks after CAE or control treatments (specifically after 4 weeks of in vivo recovery before 5 weekly passages ex vivo; fig. S4D and table S5). IPA of deregulated genes in epithelial spheroids derived from CAE-treated animals showed activation of gene expression programs similar to those previously identified in acinar cells ex vivo, which included genes controlling development, organismal injury and abnormalities, cell movement, survival, and cancer (Fig. 4H). Gene set enrichment analysis (GSEA) demonstrated that key PDAC tumorigenic pathways, such as KRAS and p53, as well as functional categories related to pancreatic embryonic development and tumorigenesis (*29*) were deregulated as well (Fig. 4I). Moreover, chromatin immunoprecipitation sequencing (ChIP-seq) experiments on paired spheroids from inflamed and noninflamed pancreata using antibodies for H3 lysine 27 acetylation (H3K27Ac), which detects active genomic regulatory elements, revealed a large number of persistent differences in histone acetylation, 90% of which were located distally from gene promoters and thus represented putative enhancers (fig. S4E and table S6). DNA sequences statistically overrepresented in the promoters of deregulated genes relative to all other RefSeq genes, as well as in the differentially acetylated distal regions (Fig. 4J), were characterized by the overrepresentation of motifs recognized by similar families of TFs, and the expression of some of the TFs of these families was concordantly deregulated, suggesting a possible causative role (fig. S4D). Of note, TF families like EGR, NK, FOX, and SOX overlapped with those identified in DCLK1-positive cells ex vivo (Fig. 4, F and G), thus suggesting that inflammation-induced reprogramming of DCLK1-positive cells is maintained in culture conditions. Our data support a model in which, upon damage and tissue regeneration, the long-term epigenomic modifications and gene expression programs acquired by DCLK1-positive cells can be maintained in their differentiated progeny, represented by epithelial spheroids in vitro or acinar cells in vivo.

EGR1 promotes pancreatic tumorigenesis after recovery from inflammation

DCLK1-positive cells have been reported to be the cell of origin of pancreatic cancer (*30*, *31*, *35*–*37*). Indeed, the intense DCLK1 staining of tumors derived from the transplantation of epithelial spheroids is consistent with the notion that the reprogramming of pancreatic progenitor cells may play an important role in inflammation-promoted tumorigenesis (fig. S4F). To better understand how inflammation-induced reprogramming affects oncogenic KRAS-mediated transformation in pancreatic epithelial cells, we chose to study the biological relevance of EGR1, a transcriptional regulator of the EGR gene family involved in tissue regeneration (*38*) that consistently scored across all omics analyses reported above as one of the most prominent TFs involved in cell reprogramming. We first assessed EGR1 expression in pancreatitis tissue. EGR1 was highly expressed in the nuclei of the vast majority of epithelial cells 1 day after CAE treatment, whereas it was undetectable in control tissue. EGR1 expression persisted in pancreatitis tissue through 28 days after CAE treatment, though with lower intensity (fig. S4, G and H). EGR1 expression was also up-regulated in human samples of acute and chronic pancreatitis compared with normal pancreas tissue, as analyzed by immunostaining (fig. S4I). Next, to determine whether EGR1 is involved in pancreatic tumorigenesis in the context of resolved inflammation, we generated *Egr1*-null iKRAS animals by crossing *Egr1*$^{-/-}$ mice with TetO-LSL-*Kras*^{G12D}_ROSA26-LSL-rtTA-IRES-GFP_p48-Cre animals. Although inflammatory cell recruitment was not affected in the absence of EGR1 (fig. S5A), oncogenic KRAS activation in matched *Egr1*$^{+/+}$ and *Egr1*$^{-/-}$ iKRAS animals 4 weeks after inflammation revealed that *Egr1*$^{+/+}$ iKRAS animals developed tumors with high penetrance and had dramatically shorter survival than *Egr1*$^{-/-}$ iKRAS mice (310 days median survival in *Egr1*$^{+/+}$ animals versus nonreached in *Egr1*$^{-/-}$ group because the majority of the animals were still alive at the end of the study; $p < 0.01$) (Fig. 4K). As expected, when mice were euthanized at the study endpoint, histological analysis of *Egr1*$^{-/-}$ iKRAS pancreas revealed minimal tumor burden (Fig. 4L), suggesting that EGR1 is a critical player in pancreatic tumorigenesis and epithelial cell reprogramming induced by inflammation.

Interleukin-6 mediates epithelial reprogramming during inflammatory events

To test whether epithelial reprogramming is dependent on the activity of inflammatory cells and to identify mediators responsible for this phenotype, we cultured epithelial spheroids derived from iKRAS pancreata with medium conditioned by CD45-positive cells isolated from mice with acute pancreatitis. After 1 week, spheroids were transferred to conventional medium and maintained in culture for an additional 4 weeks to minimize the acute effects of cytokine exposure (Fig. 5A). Spheroids exposed to CD45-conditioned medium or control spheroids were then orthotopically transplanted into recipient mice, and KRAS expression was induced. Only mice injected with CD45-conditioned cells developed tumors

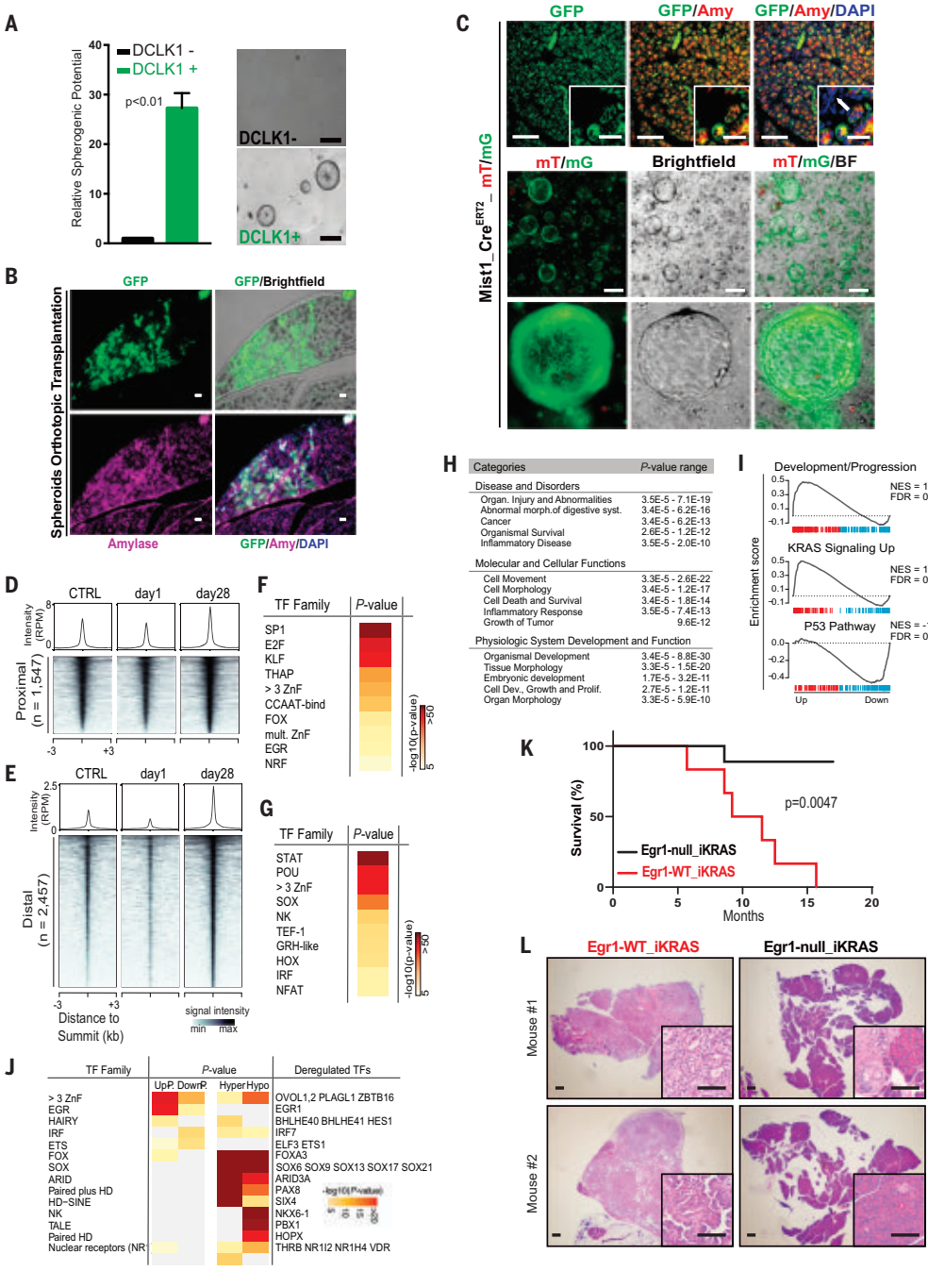


Fig. 4. Progenitor cells undergo persistent reprogramming after inflammation, and EGR1 is a critical player in promoting tumorigenesis. (**A**) Relative spherogenic potential of cells sorted from a single-cell suspension of pancreata isolated from Dclk1-DTR-ZsGreen mice based on their fluorescence: ZsGreen positive (DCLK1^{+}) and ZsGreen negative (DCLK1^{-}) (n = 3). Data are shown as mean ± SD. Statistical significance was assessed by unpaired Student's t test. Scale bars are 50 μm. (**B**) Green spheroids derived from untreated P48-Cre_mT/mG mice were orthotopically transplanted into the pancreas of WT mice 48 hours after CAE treatment. Cryosections of pancreas harvested from mice 4 weeks after implantation revealed GFP-positive lobules (green) colocalized with acinar functional marker amylase (purple). Cell nuclei were stained with DAPI (blue). Scale bars are 20 μm. (**C**) (Top) Mist1-CreERT2_mT/mG mice were treated with tamoxifen to induce nuclear transfer of Cre recombinase followed by acute inflammation induction. The pancreas was collected, and part of the tissue was stained to detect GFP (green) and amylase (red) to show efficiency of Cre recombination in the acinar compartment. DAPI was used to counterstain nuclei (blue). The white arrow indicates a nonrecombined ductal and stromal structure. Scale bars are 200 μm for main images and 50 μm for insets. (Middle and bottom) The other part of the collected tissues was used to establish epithelial spheroid cultures. The GFP-positivity of spheroids indicates the acinar origin. (**D** to **G**) ATAC-seq of isolated DCLK1-positive cells before (CTRL) and after acute inflammation (D1 and D28). In (D) and (E), density plots and heat maps depict dynamics of enriched open TSS proximal (D) or distal (E) regions at D28 versus CTRL across different time points in DCLK1-positive cells. In (F) and (G), motif analysis of enriched chromatin open regions at D28 versus CTRL identifies overrepresented sequences recognized by TF families in proximal (F) or distal (G) regions. (**H** and **I**) Bulk RNA-seq on WT mouse pancreatic spheroids derived from pancreas either preexposed or not exposed to inflammation. In (H), pathway analysis (IPA) of genes associated with diseases or biological functions enriched after inflammation versus control is shown. Highest-ranked terms are shown. In (I), GSEA enrichment plots show the hallmark signature "Kras signaling" and the "development and progression" signature, including genes coregulated during development and carcinogenesis in pancreatic cells (*29*). The "p53 pathway" signature, which is enriched in down-regulated genes, is also shown. Genes are ranked from left to right based on signed p value, with genes on the left showing significantly higher expression after inflammation treatment. FDR, false discovery rate; NES, normalized enrichments score. (**J**) Motif enrichment analysis of TF binding site overrepresentation at promoters and distal regions. The overrepresented families of TFs at the promoters of up-regulated (UpP) and down-regulated (DownP) genes in spheroid bulk RNA-seq relative to all RefSeq genes are shown on the left. The right panel shows the overrepresented TF families at the differentially acetylated TSS-distal regions in spheroid ChIP-seq (using the FANTOM5 collection of enhancers as background). The heat map shows the negative logarithm of the enrichment p value determined by a two-tailed Welch's t test. (**K**) Kaplan-Meier survival plot of Egr1-WT_iKRAS mice (n = 6) and Egr1-null_iKRAS mice (n = 9) after oncogenic KRAS induction at D28 after acute inflammation. (**I**) H&E staining of Egr1-WT_iKRAS mice and matched Egr1-null_iKRAS mice. Scale bars are 500 μm for main images and 50 μm for insets.

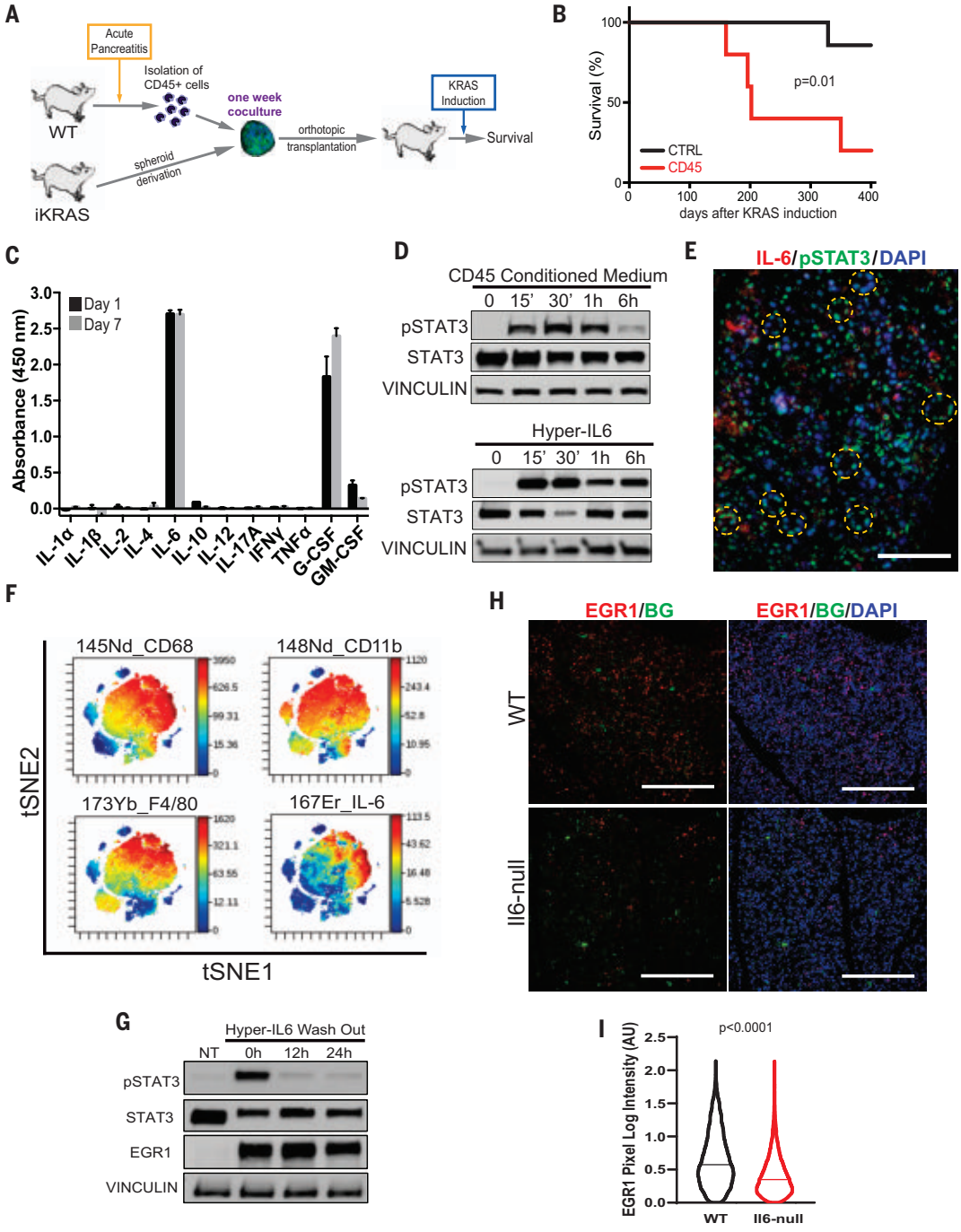


Fig. 5. IL-6 is a mediator of epithelial memory. (**A**) Schematic representing the experimental design. Briefly, spheroids derived from iKRAS mice were cocultured in the presence or absence of CD45-positive cells isolated from animals with acute pancreatitis. After 1 week, conditioned spheroids were moved to conventional medium for another 4 weeks and then transplanted orthotopically into recipient mice and KRAS induced. (**B**) Kaplan-Meier survival plot of mice transplanted with conditioned (CD45, $n = 5$) or nonconditioned spheroids (CTRL, $n = 7$) after KRAS induction. (**C**) Cytokine array of medium conditioned for 1 or 7 days with CD45. Absorbance for different antibodies is reported. Data are shown as mean ± SD. (**D**) Immunoblotting for pSTAT3 (phospho-Tyr^{705}), STAT3, and vinculin in spheroids exposed to CD45 conditioned medium (top) or hyper-IL-6 200 ng/ml (bottom) for the indicated amounts of time. (**E**) Immunofluorescence staining for IL-6 (red), pSTAT3 (green), and DAPI (blue) in pancreatic samples at day 1 after CAE treatment showing multiple pSTAT3 nuclear–positive cells, including many acinar structures (yellow dashed lines), interspersed among IL-6–positive cells. Scale bar is 120 μm. (**F**) CyTOF immunophenotyping of CD45-positive cells infiltrating the pancreas during acute pancreatitis. tSNE plots for CD68, CD11b, F4/80, and IL-6 are presented. (**G**) Immunoblotting for pSTAT3 (phospho-Tyr^{705}), STAT3, EGR1, and vinculin in spheroids exposed to hyper-IL-6 200 ng/ml for 24 hours and then sampled at the indicated time points after hyper-IL-6 wash-out. NT, nontreated. (**H**) Pancreas from WT or *Il6*-null mice at day 1 after acute inflammation were harvested and immunostained for EGR1 (red). Cell nuclei were counterstained with DAPI (blue). Green channel (BG), although unstained, has been acquired and used to highlight tissue architecture and vessels. Scale bars are 200 μm. (**I**) Quantification of nuclear signal as pixel log10 intensity for EGR1 as in (H). Data are shown as violin plots ($n = 3$ mice per group). Statistical significance was assessed by unpaired Student's t test. AU, arbitrary units.

that histologically resembled those obtained from transplantation of spheroids derived from CAE-treated pancreas (Fig. 5B and fig. S5B, top panel). The epithelial origin of these tumors was confirmed by GFP positivity and the mutual exclusivity of CD45 staining (fig. S5B, middle and bottom panels). Thus, epithelial cells undergo reprogramming in vitro in response to soluble molecules released by the inflammatory cells that mediate inflammation-induced changes in the pancreatic epithelium in vivo. Enzyme-linked immunosorbent assay (ELISA) analysis of CD45-conditioned medium revealed high concentrations of interleukin-6 (IL-6) and granulocyte colony-stimulating factor (G-CSF) (Fig. 5C). Because the G-CSF receptor is not expressed in pancreatic cells according to our dataset (table S5), we posited that IL-6, for which a role in PDAC progression is supported by a large body of evidence (*11*, *39*–*42*), was likely a critical mediator of epithelial reprogramming. Exposure of spheroids to CD45-conditioned medium, as well as to recombinant hyper-IL-6, a potent chimeric molecule able to engage gp130 trans-signaling (*42*), confirmed strong induction of STAT3 phosphorylation at Tyr^{705} (Fig. 5D). Similarly, in vivo immunostaining analysis detected expression of IL-6–positive infiltrating cells and nuclear phospho-STAT3 signal in virtually all acinar cells in pancreatic samples immediately after CAE treatment (day 1) (Fig. 5E and fig. S5C).

Mass cytometry immunophenotyping of CD45 cells recruited to the pancreas upon acute CAE exposure (day 1) revealed a massive infiltration of macrophages ($CD68^+$, $F4/80^+$, $CD11^+$) (Fig. 5F) with only a marginal contribution of lymphoid cells (CD4, CD8, B220, NK1.1) (fig. S5D). Furthermore, t-distributed stochastic neighbor embedding (tSNE) representation of immunoreactivity for IL-6 completely overlapped with CD68, F4/80, and CD11 markers, identifying macrophages as the major source of IL-6 production in vivo (Fig. 5F). Next, we measured the expression of the key TF EGR1 by immunoblot analysis, which revealed its strong and sustained up-regulation after exposure of spheroids to hyper-IL-6 for 24 hours (Fig. 5G). To determine the role of IL-6 in EGR1 expression in vivo, we analyzed the pancreas from *Il6*-null mice. As anticipated, even though inflammatory cell recruitment was not affected (fig. S5E), EGR1 expression was markedly impaired in *Il6*-null pancreatic tissue after CAE treatment compared with *Il6*-proficient controls (Fig. 5, H and I). These in vitro and in vivo findings suggest that IL-6 is a key mediator of the inflammation-induced reprogramming of epithelial cells.

ADM is facilitated by epithelial memory and limits tissue damage

As in any adaptive process, epithelial memory of previous inflammation should improve organismal fitness. Because of the transcriptional reprogramming of the acinar compartment in vivo, one possibility is that such memory provides a defense mechanism in the case of recurring inflammatory events that are common in the pancreas and that would otherwise result in the repeated release of pancreatic enzymes and cumulative tissue damage. To understand how a discrete inflammatory episode can influence subsequent inflammatory events, we rechallenged WT mice that had recovered from CAE-induced acute pancreatitis with a secondary inflammatory trigger (Fig. 6A). Early evaluation of pancreatic enzymes (Fig. 6B) as well as lactate dehydrogenase (LDH, a marker of cell lysis) (Fig. 6C) in the blood of WT mice 24 hours after pancreatitis induction revealed that concentrations of both enzymes in the rechallenged group were comparable to those in untreated control animals. This suggests that a sustained adaptive response triggered by the first inflammatory event attenuated pancreatic damage induced by a secondary episode of acute inflammation. Indeed, at the histological level, only animals receiving the first inflammatory trigger had extensive acinar damage in the pancreas (fig. S6A), as further confirmed by immunostaining for cleaved caspase 3 (CC3) (Fig. 6D). Unexpectedly, in the pancreas of rechallenged animals, the secondary inflammatory event resulted in extensive ADM, as indicated by the increased CK19/amylase staining ratio and the associated morphological changes (Fig. 6E). Such ADM was much more pervasive than that observed in animals exposed to a single inflammatory challenge and completely manifested within 48 hours after CAE administration. Despite its pervasive character, ADM was completely resolved by day 7 after CAE administration, as demonstrated by the full recovery of normal pancreatic tissue (fig. S6B). Thus, the sustained adaptive response triggered in the pancreatic epithelium by an acute inflammatory event resulted in a markedly attenuated response to subsequent inflammatory episodes. Such decreased tissue damage was accompanied by the rapid dedifferentiation of acinar cells that lasted for the length of the stimulus, and from which the tissue appeared to promptly and completely recover.

To explore the hypothesis that ADM is a physiologic, fast, and reversible adaptation mediated by epithelial memory that limits the detrimental effects of repeated pancreatitis, we evaluated the effects of pharmacological modulation of ADM in iKRAS mice subjected to repeated inflammation. Because ADM is mediated by the activation of mitogen-activated protein kinase (MAPK) signaling (*18*, *43*, *44*), we counteracted or promoted ADM formation with a highly selective clinical MAPK kinases 1 and 2 (MEK1/2) inhibitor (trametinib) (*45*) or epidermal growth factor (EGF) (a MAPK activator) (*46*), respectively (Fig. 6A). Mice that were pretreated with EGF before and during CAE rechallenge had a further increase of ADM formation with respect to control mice rechallenged with CAE alone ($p = 0.036$), with decreased tissue damage as indicated by CC3 immunostaining ($p = 0.01$) (Fig. 6, F to H, and fig. S6C) and decreased LDH concentrations in peripheral blood (Fig. 6I). Conversely, animals pretreated with trametinib developed minimal ADM (Fig. 6, F and G and fig. S6C), accompanied by a very severe pancreatitis with massive apoptosis and extensive acinar loss (Fig. 6, F to I). Taken together, these data support a model in which sustained epithelial adaptation in response to inflammation involves the facilitation of ADM. By blocking the production of acinar zymogens during sequential inflammatory events, ADM provides strong protection from tissue damage.

Because ADM has protective effects against pancreatic damage, we posited that selection of mutations that confer constitutive activation of MAPK signaling, such as mutations of *KRAS*, may be beneficial and thus be under strong positive evolutionary pressure. Toward an initial evaluation of this possibility, we studied the impact of inducing mutant KRAS before a second inflammatory event. Indeed, in animals with epithelial memory, constitutive activation of KRAS signaling before the second CAE exposure resulted in massive ADM (Fig. 6, F and G, and fig. S6D) and virtually no overt tissue damage (Fig. 6, F to I).

Discussion

The inflammatory process evolved as a nonspecific damage response that coordinates the activation of innate immunity with tissue repair to accelerate parenchymal regeneration and the restoration of tissue integrity after injury (*40*, *47*). Whereas the cellular and molecular events that lead to the activation of the immune compartment during an inflammatory response have been extensively characterized, the short- and long-term effects of inflammation on parenchymal cells are much less understood. Although quiescent stem cells resident in tissues can be activated by a variety of damage signals during injury (*30*, *48*–*50*), only recently have adaptations of the stem cell compartment in response to inflammation-inducing damage been reported. For example, it has been reported that the regenerative capability of stem cells is strongly increased after tissue damage, suggesting the existence of a cellular memory-like phenotype, namely a sustained adaptive response, in the stem cell compartment (*51*, *52*). In this context, the ability to sustain the acute adaptive response would represent an evolutionary advantage, because it enables faster recovery after injury. However, the long-term effects of inflammation on tissue properties, and specifically on

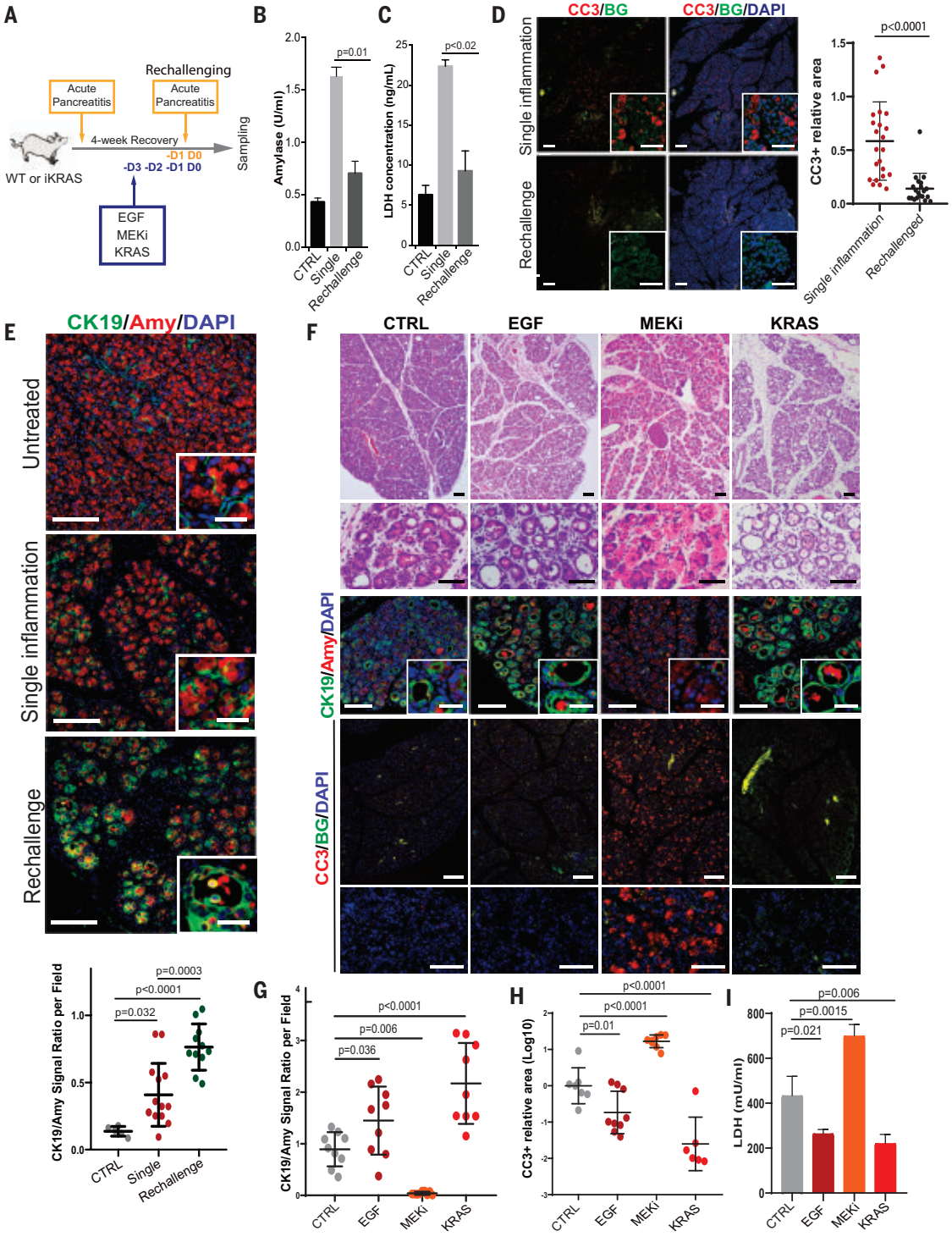


Fig. 6. ADM as a physiological and reversible adaptation to limit tissue damage. (**A**) Schematic representing the experimental design. To investigate the role of epithelial memory, WT or iKRAS mice were rechallenged with secondary acute pancreatitis after complete recovery from the previous inflammatory event. Pharmacologic modulation of ADM or KRAS induction was achieved by treating mice with EGF, MEK inhibitor, or doxycycline (KRAS induction) 2 days before and during the administration of CAE. (**B** and **C**) Concentrations of amylase (B) and LDH (C) detected in the peripheral blood at 24 hours after the induction of acute pancreatitis (D0) in WT mice: mice without memory after a single inflammatory event (single, $n = 3$), mice with memory after rechallenge (rechallenge, $n = 3$), or untreated mice (CTRL, $n = 3$). Data are shown as mean ± SD. Statistical significance was assessed with one-way analysis of variance (ANOVA). (**D**) Immunofluorescence staining for CC3 (red) and DAPI (blue) in pancreas at 24 hours after the induction of acute pancreatitis (D0) in WT mice with (rechallenged) or without memory (single inflammation). Green channel (BG), although unstained, was acquired and used to highlight tissue architecture and vessel. Scale bars are 200 μm for main images and 100 μm for insets. Quantification of CC3 in the single inflammation and rechallenged groups is shown (right). Each dot represents the CC3-positive area per field. $n = 4$ mice per group. Statistical significance was assessed by unpaired Student's t test. (**E**) Immunofluorescence staining for CK19 (green), amylase (Amy, red), and DAPI (blue) at 24 hours (day 1) after a 2-day inflammation in WT mice (untreated)

or mice with (rechallenge) or without memory (single inflammation). Scale bars are 200 μm for main images and 50 μm for insets. Quantification of CK19/Amy ratio in the same experimental groups is shown at the bottom. Each dot represents the CK19/Amy ratio per field. *n* = 3 mice per group. Data are shown as mean ± SD. Statistical significance was assessed with one-way ANOVA. (**F**) (Top) H&E staining of pancreata of iKRAS mice at day 1 after rechallenge in the presence or absence of pharmacological treatment with EGF, MEK inhibitor, or induction of KRAS. Scale bars are 100 μm. (Middle) Immunofluorescence staining for CK19 (green), amylase (red), and DAPI (blue) at 24 hours (day 1) after rechallenge in the presence or absence of pharmacological treatment with EGF, MEK inhibitor, or induction of KRAS. Scale bars are 200 μm for main images and 50 μm for insets. (Bottom) Damage evaluation in iKRAS-rechallenged mice, as shown by immunofluorescence staining for CC3 (red) and DAPI (blue) at 24 hours (day 1) after rechallenge in the presence or absence of pharmacological treatment with EGF, MEK inhibitor, or induction of KRAS. Green channel (BG), although unstained, has been acquired and used to highlight tissue architecture and vessels. Scale bars are 200 μm for main images and 50 μm for insets. (**G**) Extent of ADM in the middle panels of (F) is quantified as the CK19/Amy ratio. Each dot represents the CK19/Amy ratio per field. *n* = 3 mice per group. Data are shown as mean ± SD. Statistical significance was assessed with one-way ANOVA. (**H**) Pancreatic damage quantification evaluated as CC3-positive area (log10 scale), with the same setting as in the bottom panels of (F). Each dot represents the CC3-positive area per field. *n* = 3 mice per group. Data are shown as mean ± SD. Statistical significance was assessed with one-way ANOVA. (**I**) Concentrations of LDH detected in the peripheral blood at 24 hours (D1) after rechallenge in the presence or absence of pharmacological treatment with EGF, MEK inhibitor, or induction of KRAS (*n* = 3 for each group). Data are shown as mean ± SD. Statistical significance was assessed with one-way ANOVA.

the resilience of tissues exposed to repeated inflammation, have yet to be assessed. In the specific case of the pancreas, the production of highly active and potentially tissue-destructive enzymes by acinar cells brings about a high risk of widespread organismal damage in the context of inflammation-induced acinar damage. Using a mouse model of acute pancreatitis, we demonstrated that a short inflammatory episode has a long-lasting effect on pancreatic epithelial cells that results in marked protection of tissue integrity. Specifically, upon a second discrete inflammatory event, acinar cells promptly underwent massive ADM, a dedifferentiation process that leads to the accumulation of progenitor-like cells that have ductal features and are thus unable to secrete zymogens (*15*, *31*). This fast and reversible adaptation appears to be of critical importance given the pathogenesis of pancreatitis, wherein zymogens, normally excreted in the duodenum, are prematurely activated within the pancreatic tissue and are also released in the circulation. During repeated inflammatory events, the proclivity of adapted acinar cells to activate the ADM program may serve two critical functions: (i) to shut down zymogen production that would otherwise fuel further damage and (ii) to prompt acinar cells to acquire ductal features that render them more resistant to the detrimental effects of enzymatic activation. That ADM represents a physiologic process that limits pancreatic damage during pancreatitis is an emerging concept (*53*) further supported by the sustained adaptation described here. Indeed, by facilitating a rapid acquisition of ADM, memory promptly counteracts damage, reducing inflammation and promoting tissue regeneration. Because ADM is mediated by the activation of MAPKs (*18*, *43*, *44*), stabilization of the metaplastic phenotype through constitutive signaling plausibly exerts an important protective role to limit tissue damage, making activating mutations of *KRAS* beneficial events in the context of recurrent pancreatitis. It is thus not surprising that activating mutations of *KRAS* are found in ~25 to 37% of chronic pancreatitis cases, as well as in the vast majority of early PanIN lesions (*54*, *55*).

This study, consistent with recent observations in other organ contexts (*56*), unmasks a previously unappreciated role of oncogenic mutations in preserving tissue homeostasis during repeated damage. Such a positive effect, independent from the eventual contribution to tumorigenesis, can explain why some oncogenic mutations, such as *KRAS* in the pancreas, represent a nearly universal event in specific disease contexts. Given these observations, it is possible that pharmacological induction of ADM with MAPK agonists, such as transforming growth factor–α (TGFα) and EGF, or epigenetic drugs might ameliorate pancreatitis by protecting acinar cells from tissue damage while also reducing the positive pressure to mutate *KRAS* and hindering the progression to PDAC.

Materials and methods summary

Animal models

Mice were housed in a pathogen-free facility at the University of Texas MD Anderson Cancer Center (MDACC). All manipulations were performed under the Institutional Animal Care and Use Committee (IACUC)–approved protocol (00001843-RN00). Male and/or female animals were used for experiments.

iKRAS (TetO-LSL-Kras^{G12D}; ROSA26-LSLrtTa-IRES-GFP; p48_Cre) mice were generated as previously described (*21*) and provided by H. Ying.

Dclk1-DTR-ZsGreen mice were generated and provided by T. C. Wang's laboratory, as described here. The *DTR-2A-Zsgreen-pA-FrtNeoFrt* cassette was ligated into a pL451 plasmid. A bacterial artificial chromosome (BAC) clone RP23-283D6 containing an ~50-kb 5′ sequence of the *Dclk1* gene-coding region (CHORI) was isolated and transferred into SW105-competent cells. The correct sequence was confirmed by using restriction enzyme digestion and polymerase chain reaction (PCR) in the region of interest. The purified *DTR-2A-Zsgreen-pA-FrtNeoFrt* with a probe containing a 75–base pair sequence homologous to the BAC sequence directly upstream and downstream of the ATG in exon 2 of mouse *Dclk1* gene was electroporated into SW105 *Dclk1*-BAC–containing cells. BAC DNA (fig. S4A) was isolated, linearized, and then microinjected into the pronucleus of fertilized CBA × C57BL/6J oocytes at the Columbia University Transgenic Animal Core facility. One positive founder was identified and backcrossed to C57BL/6J mice.

B6.129(Cg)-Gt(ROSA)26Sor$^{tm4(ACTB-tdTomato,-EGFP)Luo}$*/J* (referred to as R26-mT/mG) mice were generated in L. Luo's laboratory (*57*) and purchased from The Jackson Laboratory (stock no. 007676). These animals were bred with B6.129-Bhlha15tm3(cre/ERT2)Skz/J and B6 p48-Cre for tracing experiments.

B6.129S2-Il6tm1Kopf/J (referred to as *Il6*-null) mice were generated by M. Kopf and G. Kohler (Max Planck Institut Fur Immunbiologie, Freiburg, Germany) (*58*) and purchased from The Jackson Laboratory (stock no. 002650).

B6N;129-Egr1tm1Jmi/J (referred to as *Egr1*-null) mice were generated by J. Milbrandt (Washington University School of Medicine, St. Louis, MO, USA) (*59*) and purchased from The Jackson Laboratory (stock no. 012924).

B6.129-Bhlha15tm3(cre/ERT2)Skz/J (referred to as *Mist1_Cre*^{ERT2}) mice were generated by S. Konieczny (Purdue University, West Lafayette, IN, USA) (*60*) and purchased from The Jackson Laboratory (stock no. 029228).

p48-Cre (*Ptf1a-Cre*) mice were generated as described in Kawaguchi *et al.* (*61*) and purchased from The Jackson Laboratory (stock no. 023329). The mice were then backcrossed to C57BL/6J.

NCR-NU immunodeficient mice used as recipients for transplantation experiments of iKRAS spheroids were purchased from Taconic.

All WT animals (C57BL/6J) used as controls or recipients for transplantation experiments of p48-Cre_ R26-mT/mG spheroids were purchased from The Jackson Laboratory (stock no. 000664).

Human samples

Human tissue slides containing cases of acute and chronic pancreatic inflammation were

purchased from US Biomax, Inc., and used for immunofluorescence staining following the protocol described in the supplementary materials.

REFERENCES AND NOTES

1. R. Virchow, *Cellular Pathology as Based Upon Physiological and Pathological Histology* (J. B. Lippincott, Philadelphia, 1863).
2. A. Mantovani, P. Allavena, A. Sica, F. Balkwill, Cancer-related inflammation. *Nature* **454**, 436–444 (2008). doi: 10.1038/nature07205; pmid: 18650914
3. S. I. Grivennikov, F. R. Greten, M. Karin, Immunity, inflammation, and cancer. *Cell* **140**, 883–899 (2010). doi: 10.1016/j.cell.2010.01.025; pmid: 20303878
4. D. Alonso-Curbelo *et al*., A gene-environment-induced epigenetic program initiates tumorigenesis. *Nature* **590**, 642–648 (2021). doi: 10.1038/s41586-020-03147-x; pmid: 33536616
5. H. Ying *et al*., Genetics and biology of pancreatic ductal adenocarcinoma. *Genes Dev.* **30**, 355–385 (2016). doi: 10.1101/gad.275776.115; pmid: 26883357
6. C. W. Steele *et al*., Exploiting inflammation for therapeutic gain in pancreatic cancer. *Br. J. Cancer* **108**, 997–1003 (2013). doi: 10.1038/bjc.2013.24; pmid: 23385734
7. S. Y. Gidekel Friedlander *et al*., Context-dependent transformation of adult pancreatic cells by oncogenic K-Ras. *Cancer Cell* **16**, 379–389 (2009). doi: 10.1016/j.ccr.2009.09.027; pmid: 19878870
8. C. Guerra *et al*., Pancreatitis-induced inflammation contributes to pancreatic cancer by inhibiting oncogene-induced senescence. *Cancer Cell* **19**, 728–739 (2011). doi: 10.1016/j.ccr.2011.05.011; pmid: 21665147
9. J. L. Kopp *et al*., Identification of Sox9-dependent acinar-to-ductal reprogramming as the principal mechanism for initiation of pancreatic ductal adenocarcinoma. *Cancer Cell* **22**, 737–750 (2012). doi: 10.1016/j.ccr.2012.10.025; pmid: 23201164
10. G. Y. Liou *et al*., Macrophage-secreted cytokines drive pancreatic acinar-to-ductal metaplasia through NF-κB and MMPs. *J. Cell Biol.* **202**, 563–577 (2013). doi: 10.1083/jcb.201301001; pmid: 23918941
11. Y. Zhang *et al*., Interleukin-6 is required for pancreatic cancer progression by promoting MAPK signaling activation and oxidative stress resistance. *Cancer Res.* **73**, 6359–6374 (2013). doi: 10.1158/0008-5472.CAN-13-1558-T; pmid: 24097820
12. F. Notta *et al*., A renewed model of pancreatic cancer evolution based on genomic rearrangement patterns. *Nature* **538**, 378–382 (2016). doi: 10.1038/nature19823; pmid: 27732578
13. F. X. Real, A "catastrophic hypothesis" for pancreas cancer progression. *Gastroenterology* **124**, 1958–1964 (2003). doi: 10.1016/S0016-5085(03)00389-5; pmid: 12806629
14. J. M. Bailey *et al*., p53 mutations cooperate with oncogenic Kras to promote adenocarcinoma from pancreatic ductal cells. *Oncogene* **35**, 4282–4288 (2016). doi: 10.1038/onc.2015.441; pmid: 26592447
15. P. Storz, Acinar cell plasticity and development of pancreatic ductal adenocarcinoma. *Nat. Rev. Gastroenterol. Hepatol.* **14**, 296–304 (2017). doi: 10.1038/nrgastro.2017.12; pmid: 28270694
16. T. Miyatsuka *et al*., Persistent expression of PDX-1 in the pancreas causes acinar-to-ductal metaplasia through Stat3 activation. *Genes Dev.* **20**, 1435–1440 (2006). doi: 10.1101/gad.1412806; pmid: 16751181
17. P. P. Prévot *et al*., Role of the ductal transcription factors HNF6 and Sox9 in pancreatic acinar-to-ductal metaplasia. *Gut* **61**, 1723–1732 (2012). doi: 10.1136/gutjnl-2011-300266; pmid: 22271799
18. E. P. Sandgren, N. C. Luetteke, R. D. Palmiter, R. L. Brinster, D. C. Lee, Overexpression of TGFα in transgenic mice: Induction of epithelial hyperplasia, pancreatic metaplasia, and carcinoma of the breast. *Cell* **61**, 1121–1135 (1990). doi: 10.1016/0092-8674(90)90075-P; pmid: 1693546
19. I. Houbracken *et al*., Lineage tracing evidence for transdifferentiation of acinar to duct cells and plasticity of human pancreas. *Gastroenterology* **141**, 731–741.e4 (2011). doi: 10.1053/j.gastro.2011.04.050; pmid: 21703267
20. J. H. Bowie, "Chapter 48 – Caeruleins" in *Handbook of Biologically Active Peptides*, A. J. Kastin, Ed. (Academic Press, ed. 2, 2013), pp. 338–341.
21. H. Ying *et al*., Oncogenic Kras maintains pancreatic tumors through regulation of anabolic glucose metabolism. *Cell* **149**, 656–670 (2012). doi: 10.1016/j.cell.2012.01.058; pmid: 22541435
22. A. Viale *et al*., Oncogene ablation-resistant pancreatic cancer cells depend on mitochondrial function. *Nature* **514**, 628–632 (2014). doi: 10.1038/nature13611; pmid: 25119024
23. A. Kapoor *et al*., Yap1 activation enables bypass of oncogenic Kras addiction in pancreatic cancer. *Cell* **158**, 185–197 (2014). doi: 10.1016/j.cell.2014.06.003; pmid: 24954535
24. J. Mayerle, M. Sendler, M. M. Lerch, "Secretagogue (Caerulein) induced pancreatitis in rodents." Pancreapedia: Exocrine Pancreas Knowledge Base (American Pancreatic Association, 2013); https://www.pancreapedia.org/tools/methods/secretagogue-caerulein-induced-pancreatitis-in-rodents.
25. M. S. Hayden, S. Ghosh, NF-κB, the first quarter-century: Remarkable progress and outstanding questions. *Genes Dev.* **26**, 203–234 (2012). doi: 10.1101/gad.183434.111; pmid: 22302935
26. H. Yu, D. Pardoll, R. Jove, STATs in cancer inflammation and immunity: A leading role for STAT3. *Nat. Rev. Cancer* **9**, 798–809 (2009). doi: 10.1038/nrc2734; pmid: 19851315
27. A. Grapin-Botton, Three-dimensional pancreas organogenesis models. *Diabetes Obes. Metab.* **18**, 33–40 (2016). doi: 10.1111/dom.12720; pmid: 27615129
28. C. J. Sherr, R. A. DePinho, Cellular senescence: Mitotic clock or culture shock? *Cell* **102**, 407–410 (2000). doi: 10.1016/S0092-8674(00)00046-5; pmid: 10966103
29. M. Reichert *et al*., The Prrx1 homeodomain transcription factor plays a central role in pancreatic regeneration and carcinogenesis. *Genes Dev.* **27**, 288–300 (2013). doi: 10.1101/gad.204453.112; pmid: 23355395
30. C. B. Westphalen *et al*., Dclk1 defines quiescent pancreatic progenitors that promote injury-induced regeneration and tumorigenesis. *Cell Stem Cell* **18**, 441–455 (2016). doi: 10.1016/j.stem.2016.03.016; pmid: 27058937
31. J. M. Bailey *et al*., DCLK1 marks a morphologically distinct subpopulation of cells with stem cell properties in preinvasive pancreatic cancer. *Gastroenterology* **146**, 245–256 (2014). doi: 10.1053/j.gastro.2013.09.050; pmid: 24096005
32. R. May *et al*., Identification of a novel putative pancreatic stem/progenitor cell marker DCAMKL-1 in normal mouse pancreas. *Am. J. Physiol. Gastrointest. Liver Physiol.* **299**, G303–G310 (2010). doi: 10.1152/ajpgi.00146.2010; pmid: 20522640
33. S. M. Sureban *et al*., DCAMKL-1 regulates epithelial-mesenchymal transition in human pancreatic cells through a miR-200a-dependent mechanism. *Cancer Res.* **71**, 2328–2338 (2011). doi: 10.1158/0008-5472.CAN-10-2738; pmid: 21285251
34. K. E. DelGiorno *et al*., Tuft cell formation reflects epithelial plasticity in pancreatic injury: Implications for modeling human pancreatitis. *Front. Physiol.* **11**, 88 (2020). doi: 10.3389/fphys.2020.00088; pmid: 32116793
35. F. M. Ferguson *et al*., Discovery of a selective inhibitor of doublecortin like kinase 1. *Nat. Chem. Biol.* **16**, 635–643 (2020). doi: 10.1038/s41589-020-0506-0; pmid: 32251410
36. T. Maruno *et al*., Visualization of stem cell activity in pancreatic cancer expansion by direct lineage tracing with live imaging. *eLife* **10**, e55117 (2021). doi: 10.7554/eLife.55117; pmid: 33393460
37. B. Zhou *et al*., MicroRNA-195 suppresses the progression of pancreatic cancer by targeting DCLK1. *Cell. Physiol. Biochem.* **44**, 1867–1881 (2017). doi: 10.1159/000485876; pmid: 29224010
38. G. Thiel, G. Cibelli, Regulation of life and death by the zinc finger transcription factor Egr-1. *J. Cell. Physiol.* **193**, 287–292 (2002). doi: 10.1002/jcp.10178; pmid: 12384981
39. S. Grivennikov *et al*., IL-6 and Stat3 are required for survival of intestinal epithelial cells and development of colitis-associated cancer. *Cancer Cell* **15**, 103–113 (2009). doi: 10.1016/j.ccr.2009.01.001; pmid: 19185845
40. M. Karin, H. Clevers, Reparative inflammation takes charge of tissue regeneration. *Nature* **529**, 307–315 (2016). doi: 10.1038/nature17039; pmid: 26791721
41. A. Fukuda *et al*., Stat3 and MMP7 contribute to pancreatic ductal adenocarcinoma initiation and progression. *Cancer Cell* **19**, 441–455 (2011). doi: 10.1016/j.ccr.2011.03.002; pmid: 21481787
42. M. Lesina *et al*., Stat3/Socs3 activation by IL-6 transsignaling promotes progression of pancreatic intraepithelial neoplasia and development of pancreatic cancer. *Cancer Cell* **19**, 456–469 (2011). doi: 10.1016/j.ccr.2011.03.009; pmid: 21481788
43. C. J. Halbrook *et al*., Mitogen-activated protein kinase kinase activity maintains acinar-to-ductal metaplasia and is required for organ regeneration in pancreatitis. *Cell. Mol. Gastroenterol. Hepatol.* **3**, 99–118 (2017). doi: 10.1016/j.jcmgh.2016.09.009; pmid: 28090569
44. G. Shi *et al*., Maintenance of acinar cell organization is critical to preventing Kras-induced acinar-ductal metaplasia. *Oncogene* **32**, 1950–1958 (2013). doi: 10.1038/onc.2012.210; pmid: 22665051
45. R. Zeiser, H. Andrlová, F. Meiss, Trametinib (GSK1120212). *Recent Results Cancer Res.* **211**, 91–100 (2018). doi: 10.1007/978-3-319-91442-8_7; pmid: 30069762
46. J. Schlessinger, A. Ullrich, Growth factor signaling by receptor tyrosine kinases. *Neuron* **9**, 383–391 (1992). doi: 10.1016/0896-6273(92)90177-F; pmid: 1326293
47. T. J. Koh, L. A. DiPietro, Inflammation and wound healing: The role of the macrophage. *Expert Rev. Mol. Med.* **13**, e23 (2011). doi: 10.1017/S1462399411001943; pmid: 21740602
48. M. Hill, A. Wernig, G. Goldspink, Muscle satellite (stem) cell activation during local tissue injury and repair. *J. Anat.* **203**, 89–99 (2003). doi: 10.1046/j.1469-7580.2003.00195.x; pmid: 12892408
49. S. H. Cheshier, S. S. Prohaska, I. L. Weissman, The effect of bleeding on hematopoietic stem cell cycling and self-renewal. *Stem Cells Dev.* **16**, 707–717 (2007). doi: 10.1089/scd.2007.0017; pmid: 17999593
50. M. A. Essers *et al*., IFNalpha activates dormant haematopoietic stem cells in vivo. *Nature* **458**, 904–908 (2009). doi: 10.1038/nature07815; pmid: 19212321
51. J. T. Rodgers *et al*., mTORC1 controls the adaptive transition of quiescent stem cells from G_0 to G_{Alert}. *Nature* **510**, 393–396 (2014). doi: 10.1038/nature13255; pmid: 24870234
52. S. Naik *et al*., Inflammatory memory sensitizes skin epithelial stem cells to tissue damage. *Nature* **550**, 475–480 (2017). doi: 10.1038/nature24271; pmid: 29045388
53. Y. Zhang *et al*., Epithelial-myeloid cell crosstalk regulates acinar cell plasticity and pancreatic remodeling in mice. *eLife* **6**, e27388 (2017). doi: 10.7554/eLife.27388; pmid: 28980940
54. M. Kanda *et al*., Presence of somatic mutations in most early-stage pancreatic intraepithelial neoplasia. *Gastroenterology* **142**, 730–733.e9 (2012). doi: 10.1053/j.gastro.2011.12.042; pmid: 22226782
55. J. L. van Laethem, Ki-Ras oncogene mutations in chronic pancreatitis: Which discriminating ability for malignant potential? *Ann. N. Y. Acad. Sci.* **880**, 210–218 (1999). doi: 10.1111/j.1749-6632.1999.tb09525.x; pmid: 10415866
56. M. Zhu *et al*., Somatic mutations increase hepatic clonal fitness and regeneration in chronic liver disease. *Cell* **177**, 608–621.e12 (2019). doi: 10.1016/j.cell.2019.03.026; pmid: 30955891
57. M. D. Muzumdar, B. Tasic, K. Miyamichi, L. Li, L. Luo, A global double-fluorescent Cre reporter mouse. *Genesis* **45**, 593–605 (2007). doi: 10.1002/dvg.20335; pmid: 17868096
58. M. Kopf *et al*., Impaired immune and acute-phase responses in interleukin-6-deficient mice. *Nature* **368**, 339–342 (1994). doi: 10.1038/368339a0; pmid: 8127368
59. S. L. Lee, L. C. Tourtellotte, R. L. Wesselschmidt, J. Milbrandt, Growth and differentiation proceeds normally in cells deficient in the immediate early gene NGFI-A. *J. Biol. Chem.* **270**, 9971–9977 (1995). doi: 10.1074/jbc.270.17.9971; pmid: 7730380
60. N. Habbe *et al*., Spontaneous induction of murine pancreatic intraepithelial neoplasia (mPanIN) by acinar cell targeting of oncogenic Kras in adult mice. *Proc. Natl. Acad. Sci. U.S.A.* **105**, 18913–18918 (2008). doi: 10.1073/pnas.0810097105; pmid: 19028870
61. Y. Kawaguchi *et al*., The role of the transcriptional regulator Ptf1a in converting intestinal to pancreatic progenitors. *Nat. Genet.* **32**, 128–134 (2002). doi: 10.1038/ng959; pmid: 12185368

ACKNOWLEDGMENTS

We thank J. S. Lee in the Department of Systems Biology at MDACC for sharing a dataset used for GSEA; R. Nguyen in the Department of Genomic Medicine at MDCC for lab management; E. Q. Chang and N. Feng in TRACTION at MDACC for support in tissue imaging acquisition and drug formulation; C. Kingsley in the Small Animals Imaging Facility at MDACC; W. N. Hittelman and the Center for Targeted Therapy for confocal microscopy; and BioRender.com for the summary print page schematic. **Funding:** This study was supported by Cancer Research and Prevention Institute of Texas (CPRIT) grant RP190599; the Andrew Sabin Family Foundation; the V Foundation (V2020-018); NIH/NCI SPORE in gastrointestinal cancer grant P50CA221707; NIH grant NIH/NCI R01CA258917; UT MD Anderson Cancer Center Start-Up Funds to A.V.; UT MD Anderson Cancer Center Pancreatic Cancer Moon Shot and Pancreatic Cancer Action Network (PanCAN) to G.F.D.; NIH/NCI P01 CA117969-12 to A.V. and G.F.D.; Associazione Italiana Ricerca sul Cancro (AIRC IG and 5x1000 grants) to G.N.; Sheikh Khalifa Foundation to A.M.; K99 grant 4R00CA218891-03 to P.D.; AIRC and the European Union's Horizon 2020 research and innovation program under the Marie Skłodowska-Curie grant agreement no. 800924 to F.Ci.; MD Anderson UTHealth GSBS Pauline Altman-Goldstein Foundation Discovery Fellowship to I.-L.H.;

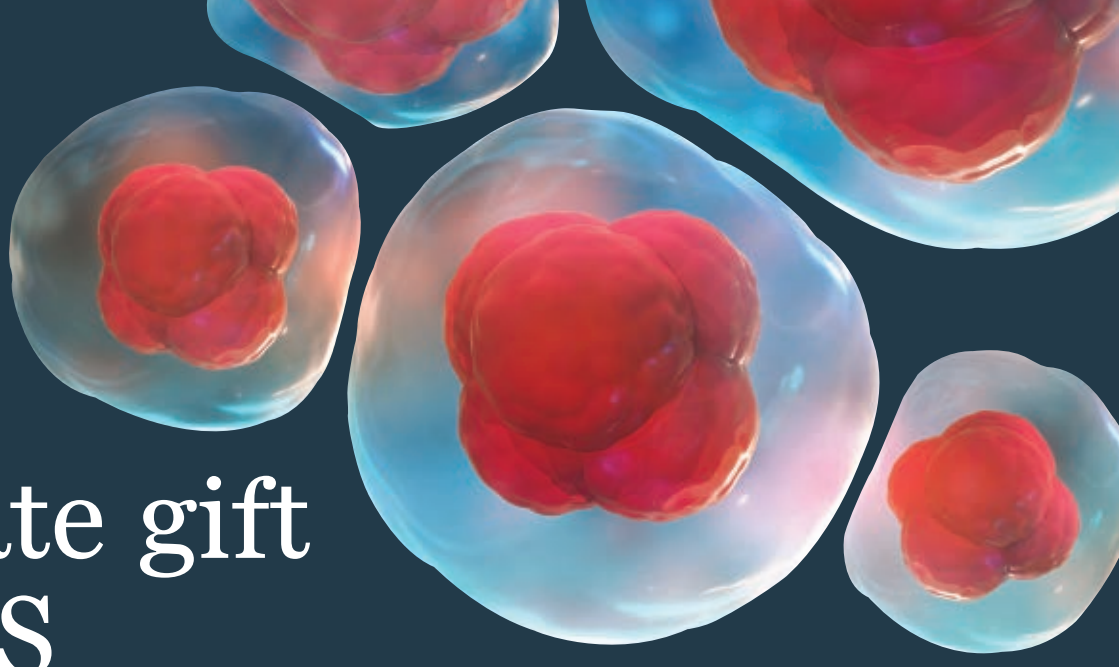
NCI grant CA016672 to the MDACC Sequencing and Microarray Facility; and NCI grant P30CA16672 to the MDACC Flow Cytometry and Cellular Imaging Core Facility. **Author contributions:** E.D.P., I.-L.H., and A.V. designed the studies, interpreted the data, and wrote the manuscript; C.B. and G.N. analyzed and interpreted computational data and assisted with data discussion and manuscript writing; E.D.P., I.-L.H., E.-Y.Y., F.Ci., R.S., D.C., G.R.D., C.-Y.L., S.L., F.Ca., and L.S. performed the experiments; S.Z. performed single-cell data analysis; P.D. assisted with mass cytometry (CyTOF) analysis; Y.H., G.V., W.Y., H.Y., S.R.-J., and T.C.W. contributed essential reagents and resources; S.J. assisted with animal colony maintenance; H.J. assisted with animal genotyping; A.D.R., G.G., T.P.H., A.M., T.C.W., L.W., G.F.D., A.C., and G.N. assisted with data discussion and interpretation; and A.K.D. and S.G. edited the manuscript and assisted with data discussion. **Competing interests:** A.V., A.C., E.D.P., and I.-L.H. are inventors on patent number PCT/US2021/033024 submitted by the University of Texas System that covers the use of ADM pharmacological inducers to treat pancreatitis and prevent pancreatic cancer. **Data and materials availability:** All sequencing data related to the manuscript are available at the Gene Expression Omnibus (https://www.ncbi.nlm.nih.gov/geo/) using access number GSE180212. Requests for further information and for resources and reagents should be directed to A.V.

SUPPLEMENTARY MATERIALS

https://science.org/doi/10.1126/science.abj0486
Materials and Methods
Figs. S1 to S6
Tables S1 to S6
References (*62*–*87*)
MDAR Reproducibility Checklist

22 April 2021; accepted 3 August 2021
10.1126/science.abj0486

1848 SOCIETY
AAAS



An estate gift to AAAS

Going all the way back to 1848, our founding year, the American Association for the Advancement of Science (AAAS) has been deeply committed to advancing science, engineering and innovation around the world for the benefit of all people.

Today, we are dedicated to advocating for science and scientific evidence to be fully and positively integrated into public policy and for the community to speak with one voice to advance science and engineering in the United States and around the world.

By making AAAS a beneficiary of your will, trust, retirement plan or life insurance policy, you will become a member of our 1848 Society and will help fuel our work on behalf of science and society – including publishing the world's most promising, innovative research in the *Science* family of journals and engaging in the issues that matter locally, nationally and around the world.

"As a teacher and instructor, I bear responsibility for the younger generations. If you have extra resources, concentrate them on organizations, like AAAS, that are doing work for all."

—Prof. Elisabeth Ervin-Blankenheim, 1848 Society member

If you intend to include AAAS in your estate plans, provide this information to your lawyer or financial adviser:

Legal Name: American Association for the Advancement of Science
Federal Tax ID Number: 53-0196568
Address: 1200 New York Avenue, NW, Washington, DC 20005

If you would like more information on making an estate gift to AAAS, cut out and return the form below or send an email to philanthropy@aaas.org. Additional details are also available online at **www.aaas.org/1848Society**.

AMERICAN ASSOCIATION FOR THE ADVANCEMENT OF SCIENCE

cut here

Yes, I would like more information about joining the AAAS 1848 Society.

1848 SOCIETY
AAAS

PLEASE CONTACT ME AT:

Name: _____

Address: _____

City: _____ State: _____ Zip code: _____ Country: _____

Email: _____ Phone: _____

RETURN THIS FORM TO:
AAAS Office of Philanthropy and Strategic Partnerships • 1200 New York Avenue, NW • Washington, DC 20005 USA

RESEARCH ARTICLES

CANCER

The adaptive immune system is a major driver of selection for tumor suppressor gene inactivation

Timothy D. Martin[1]†, Rupesh S. Patel[1]†, Danielle R. Cook[2,3], Mei Yuk Choi[1], Ajinkya Patil[1], Anthony C. Liang[1], Mamie Z. Li[1], Kevin M. Haigis[2,3], Stephen J. Elledge[1]*

During tumorigenesis, tumors must evolve to evade the immune system and do so by disrupting the genes involved in antigen processing and presentation or up-regulating inhibitory immune checkpoint genes. We performed in vivo CRISPR screens in syngeneic mouse tumor models to examine requirements for tumorigenesis both with and without adaptive immune selective pressure. In each tumor type tested, we found a marked enrichment for the loss of tumor suppressor genes (TSGs) in the presence of an adaptive immune system relative to immunocompromised mice. Nearly one-third of TSGs showed preferential enrichment, often in a cancer- and tissue-specific manner. These results suggest that clonal selection of recurrent mutations found in cancer is driven largely by the tumor's requirement to avoid the adaptive immune system.

The genesis of tumors is a complex adaptive process that involves alterations in many cellular functions, including cell differentiation status, telomere maintenance, cell proliferation control, adaptation to altered nutritional states, evolution of angiogenesis capabilities, avoidance of cell death, and adaptation to proteotoxic and genomic stressors. These alterations, which we will refer to as growth and survival adaptation (GSA), allow the tumor to escape the normal constraints of tissue homeostasis and to evolve into a relatively independent and distinctive tissue in its own right, with new rules and properties. Cancer research over the past 40 years has primarily occupied itself with understanding how genetic changes in the tumor allow these GSAs to come about.

Identification of cancer driver genes has traditionally proceeded along two main paths. The first was genetic and biochemical analyses looking either at viral oncogenes (*1*–*3*) or genes activated by viral insertions (*4*). The second involved identification of recurring mutations, first in familial cancer syndromes (*5*–*13*) and later sporadic cancers (*14*–*16*). Modern analyses have streamlined these approaches by improved genetic approaches using transposons (*17*), RNA interference (RNAi) (*18*–*20*), CRISPR (*21*–*23*), and cDNA overexpression (*24*, *25*) together with breakthroughs in high-throughput sequencing to provide exhaustive lists of potential drivers. However, elucidation of how these genes function to drive cancer has lagged behind. Historically, systematic functional analysis of the genes responsible for GSA has been the main focus of cancer driver function, and many of the genetic screens have been limited to assessing functionality in traditional monoculture systems in vitro. These two-dimensional (2D) systems revealed genes required for tumor cell proliferation and survival but cannot account for the complexity of cell types and interactions that define the tumor microenvironment. Indeed, many known cancer driver mutations do not exhibit strong phenotypes in these 2D growth assays, raising the possibility that cancer-relevant phenotypes are being missed simply because of the assay system itself (*26*). For example, genetic screens in vivo using either RNAi or CRISPR have revealed phenotypes for putative squamous cell carcinoma drivers not appreciated in vitro (*27*, *28*).

In addition to the GSAs that allow tumor emergence, there is another major barrier to overcome: the immune system. The immune system treats the tumor as an emerging pathogen and unleashes a response that aims to eliminate the tumor, thereby selecting for alterations that result in immune surveillance adaptation (ISA). Recently, in vitro CRISPR screens using co-cultures of isolated CD8 T cells and tumor cells have identified genes that regulate a tumor's response to cytotoxic T cells (*29*), but these screens are predisposed toward uncovering genes involved in antigen presentation by major histocompatibility complex (MHC) class I and cannot account for other tumor and immune cell interactions found in vivo. The growing appreciation that immune evasion facilitates tumorigenesis has focused recent attention on this aspect of tumorigenesis and has led to revolutionary therapeutic approaches that overcome this evasion (*30*). Although immunoediting is a major mechanism of immune escape, several genes central to antigen presentation have been found to be recurrently mutated in cancer—for example, β_2 microglobulin (*B2M*) and the human leukocyte antigen (*HLA*) alleles (*31*). In addition, a small number of cancer drivers such as *KRAS*, *CDK4/6*, and *MYC* have been implicated in aspects of immune evasion. However, the spectrum of genes involved in promoting immune recognition and their roles in cancer are not broadly known.

Here we exploit syngeneic tumor models to perform CRISPR-based genetic screens in vitro and as tumor transplants in vivo in both immunocompetent [wild-type (WT)] and immunocompromised [$Rag1^{null}$ or severe combined immunodeficient (SCID)] mice that lack an adaptive immune system and uncovered a pronounced overlap between adaptive immune system–specific hits and the genes that are among the most frequently mutated in human tumors.

Results

CRISPR screening in syngeneic mice using 4T1 breast tumor cells

To initiate a screen for immune regulatory genes, we generated a five single guide RNA (sgRNA) per gene mouse lentiviral CRISPR library targeting ~7500 known or putatively druggable genes (table S1). We chose to first examine the 4T1 mouse mammary tumor model and infected these cells with the library (*32*, *33*). After selection, cells were concurrently grown in vitro for 10 population doublings (PDs) or as subcutaneous tumor transplants in immunocompetent (WT) or SCID BALB/c mice (Fig. 1A). Growing the cells as tumors in WT mice allows for immune surveillance of the tumor with an intact tumor microenvironment. We reasoned that by comparing the results of the screens in WT to those in immunodeficient mice, we can functionally identify the genes required for tumor growth in the presence of an adaptive immune system. Tumors were harvested upon reaching ~2 cm^3, and sgRNA abundance was determined by next-generation sequencing. Our screening results in SCID mice identified an enrichment for known growth-regulating genes, including *Pten* (Fig. 1B). We identified *B2m* and *Jak1*, known regulators of antigen presentation and immune signaling (*34*), near the top of the WT list of genes (Fig. 1C), validating the quality of the screen. However, also among the top-scoring genes in WT mice, we noticed a number of familiar tumor suppressors. We then obtained a list of TSGs ranked on the basis of the mutational frequency of deleterious mutations per size of the coding regions in humans calculated using the TUSON Explorer algorithm and the pancancer mutations

[1]Division of Genetics, Brigham and Women's Hospital, Howard Hughes Medical Institute, Department of Genetics, Harvard Medical School, Boston, MA 02115, USA. [2]Department of Cancer Biology, Dana-Farber Cancer Institute, Boston, MA 02115, USA. [3]Department of Medicine, Brigham and Women's Hospital and Harvard Medical School, Boston, MA 02115, USA.
*Corresponding author. Email: selledge@genetics.med.harvard.edu
†These authors contributed equally to this work.

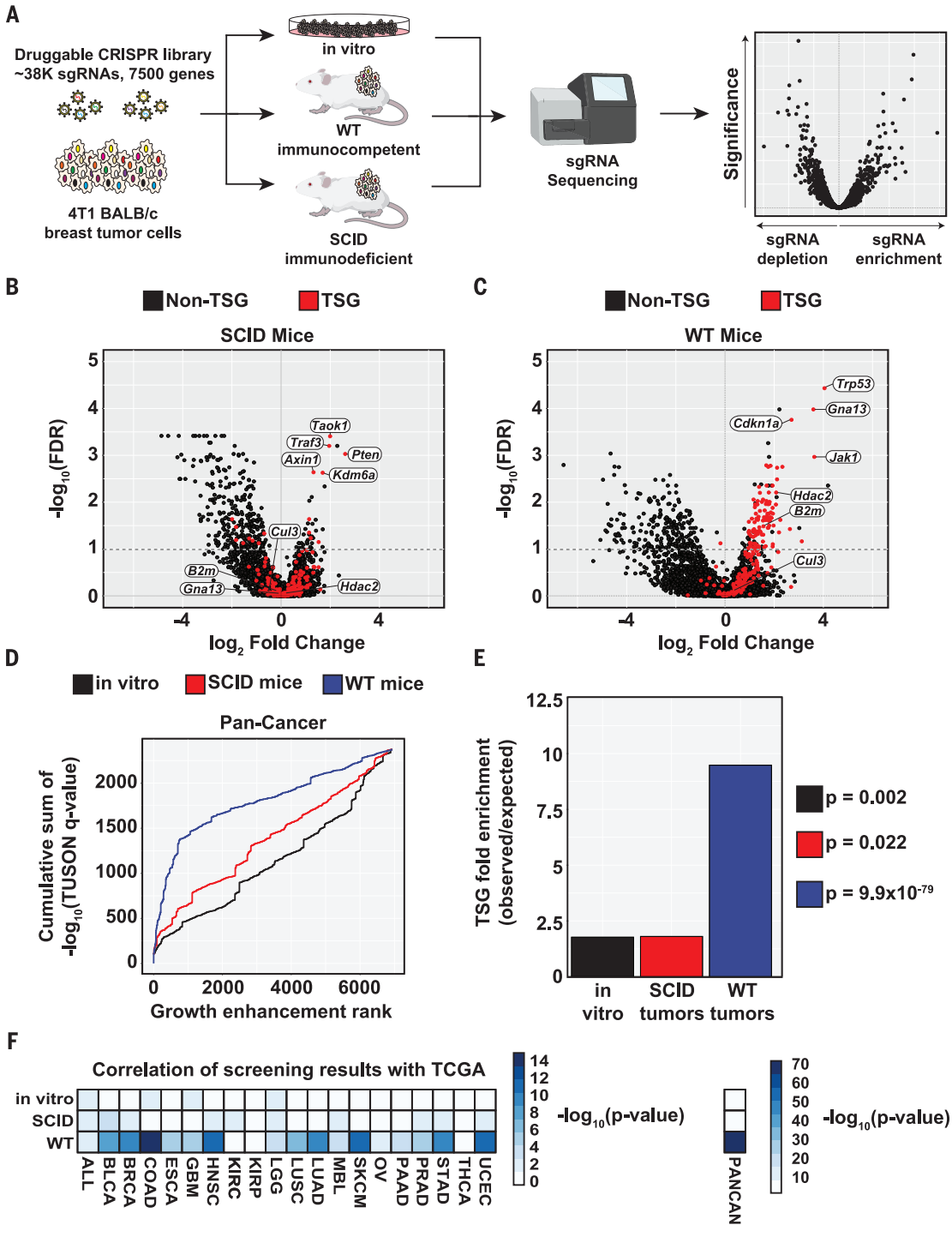


Fig. 1. CRISPR-based genetic screens in 4T1 breast tumor cells to identify genes required for tumor growth with and without an adaptive immune system. (**A**) A CRISPR library targeting druggable genes was transduced into 4T1 mouse breast tumor cells. Cells were maintained in vitro or transplanted subcutaneously on flanks of either SCID or WT BALB/c mice. Following tumor formation or 10 PDs in vitro, tumor cells were harvested and sgRNAs were sequenced. (**B**) Druggable CRISPR Screen and TSG performance in tumors from SCID mice. Volcano plots of the analyses of the screening results in SCID mice. (**C**) Presence of an adaptive immune system leads to strong selection of TSGs. Volcano plots of the analyses of the screening results in immunocompetent WT mice. In (B) and (C), black dots represent druggable genes, and TSGs are in red. Horizontal dotted line indicates a screening FDR <0.1. (**D**) Comparison of TSG selection in vitro and in SCID or WT mice. All genes in the druggable CRISPR library were ranked based on the median $\log_2$ fold change (*x* axis) and plotted against the cumulative sum of $-\log_{10}$(TUSON pan cancer q-value) (*y* axis). (**E**) Enrichment of TSGs among the top-scoring genes in WT mice. The observed number of TSGs with an FDR <0.1 were compared to the number of expected TSGs based on a hypergeometric distribution. The fold enrichment was determined for each screening condition with *p* values from a Fisher's exact test. (**F**) The top-scoring genes in WT mice are among the most mutated genes observed in human tumors. Gene lists from the in vitro, SCID, and WT conditions were compared to the ranked list of TSGs from each TCGA cancer type and pancancer (PANCAN) derived from TUSON Explorer using a Fisher's exact test. The heatmap represents the $-\log_{10}$(*p* value). Tumor type acronyms are as follows: ALL (acute lymphoid leukemia), BLCA (bladder urothelial carcinoma), BRCA (breast invasive carcinoma), COAD (colon adenocarcinoma), ESCA (esophageal carcinoma), GBM (glioblastoma multiforme), HNSC (head and neck squamous cell carcinoma), KIRC (kidney renal clear cell carcinoma), KIRP (kidney renal papillary cell carcinoma), LGG (lower grade glioma), LUSC (lung squamous cell carcinoma), LUAD (lung adenocarcinoma), MBL (medulloblastoma), SKCM (skin cutaneous melanoma), OV (ovarian serous cystadenocarcinoma), PAAD (pancreatic adenocarcinoma), PRAD (prostate adenocarcinoma), STAD (stomach adenocarcinoma), THCA (thyroid carcinoma), and UCEC (uterine corpus endometrial carcinoma).

in human cancers (*16*) using a false discovery rate (FDR) cutoff of 0.1. The TSGs contained in our druggable CRISPR library are marked in red on the volcano plots (Fig. 1, B and C, and table S2). We observed a marked positive selection for the enrichment of sgRNAs targeting known human TSGs in immunocompetent WT mice compared with either immunodeficient SCID mice or in vitro culture (Fig. 1, B and C; fig. S1A; and table S2). This is notable because other large-scale CRISPR screening efforts in human tumor cell lines using traditional in vitro 2D tissue culture do not show phenotypes for most of the known TSGs, as exemplified by the CERES scores in the cancer dependency map (DEPMAP) dataset (*35*) (fig. S2). We compared our screening results in 4T1 mouse cells to a previous CRISPR screen that we performed in immortalized but nontransformed human mammary epithelial cells (HMECs) (*24*), and this revealed that the enrichment of TSGs is most notable in the presence of an adaptive immune system and is not a result of differences between human and mouse cells themselves or between transformed and nontransformed cells (fig. S1A). When compared to the starting library, SCID mice and 2D culture screens did identify TSGs that were enriched at a lower frequency, and these were distinct from the most potent genes enriched in WT mice. The enhanced enrichment for TSGs in WT mice cannot be explained solely by increased proliferation. For example, although there is a strong positive selection for loss of TSGs that increase proliferation in vitro, including disruption of *Pten*, *Men1*, and *Pawr*, these genes all perform either comparably or better in the SCID mice compared to WT mice. If enhanced proliferation was the driving force behind the TSG enhancement in the presence of an adaptive immune system, these genes would have been expected to score even better in WT mice.

To further analyze the behavior of TSGs relative to our screen, we generated a ranked list of genes in our library on the basis of their median $\log_2$ fold change, where the gene ranked #1 is the most enriched, and compared that ranked list to the cumulative sum of the negative $\log_{10}$ of the TUSON Explorer pancancer q value for each gene (*16*). This showed a clear selection for TSGs when the screens were performed in vivo with even better performance in the presence of an adaptive immune system (Fig. 1D). In addition, though we observed a much greater recognition of TSGs in sgRNAs in WT mice, the SCID mice screen also outperformed the in vitro screen as previously shown by Bassik and colleagues (*26*).

Analysis of the genes that showed positive selection using a FDR cutoff of 0.1 revealed an almost 9.5-fold enrichment in observed TSGs compared to the expected value in WT mice, with much smaller enrichments occurring in the in vitro and SCID settings (Fig. 1E). We used gene set enrichment analysis (GSEA) with a gene set composed of all 218 TSGs predicted by enhanced mutational frequencies determined by tumor sequencing contained in our druggable CRISPR library and compared the enrichments observed in each screening condition. Only the screen performed in WT mice resulted in an enrichment of the TSG gene set (Fig. S1B). We compared our hits in each arm of the screen to the mutational patterns observed in different human cancer types, including breast (BRCA) and pancancer samples (Fig. 1F). We found a stronger correlation between genes with enhanced mutation frequencies in TCGA and genes scoring in the screens performed in WT mice compared with the other screening conditions. Lastly, we analyzed the performance of the top 40 predicted breast cancer (BRCA) TSGs (*16*). We observed increased positive selection for sgRNAs targeting these BRCA TSGs in WT mice, suggesting that screening in the presence of an adaptive immune system better uncovers relevant human tumor phenotypes in the cell type (breast) that we screened (fig. S1C). The top genes, including both TSGs and non-TSGs, that were preferentially enriched in the presence of an adaptive immune system are presented as a heatmap (fig. S1D).

CRISPR screening in syngeneic mice using CT26 colon tumor cells

To rule out cell type–specific effects, we performed similar screens with the same CRISPR library targeting druggable genes in CT26 cells, a carcinogen-induced mouse colon tumor cell line (*36*). Following these screens, we ranked the genes on the basis of their median $\log_2$ fold enrichment and plotted that against the cumulative sum of significance of pancancer mutations as was done for the 4T1 screening results. Similar to the 4T1 data, we observed that in vivo screens were better predictors of the mutational patterns found in human tumors, with the screens in WT mice outperforming those in SCID mice (Fig. 2A, fig. S3A, and table S3). Notably, the hits from the SCID mouse screen showed a stronger enrichment for TSGs than the equivalent screen conducted by using 4T1 cells. One possible explanation for this differential enrichment is that CT26 cells are less optimized for proliferation.

Analysis of the genes with a positive selection FDR cutoff of 0.1 revealed an almost 12-fold enrichment in observed TSGs in WT mice compared to the expected value, with much smaller enrichments seen in the in vitro analysis or SCID (1.8-fold) screens (Fig. 2B). Using GSEA with the TSG gene set, as was done for the 4T1 cells, we found an increased enrichment of TSGs in the screens performed in WT mice compared with either SCID or in vitro settings (fig. S3B). We compared the hits from each screen to the mutational patterns observed in different human cancer types, including colon (COAD) and pancancer samples. We again found a statistically stronger correlation with human tumor mutational data with the screens performed in WT mice compared with the other screening conditions (Fig. 2C). Examination of the performance of the top 40 predicted TSGs in human colon (COAD) tumors showed stronger phenotypes in WT mice compared with either SCID mice or in vitro (fig. S3C), again demonstrating a role for the adaptive immune system's presence in positively selecting for TSG inactivation. The top-scoring genes from the CT26 cell line, including both TSGs and non-TSGs, that were preferentially enriched in the presence of an adaptive immune system are shown in a heatmap (fig. S3D).

We classified genes in our druggable CRISPR library as either TSGs, essential genes, or all genes on the basis of previous reports and compared the performances of these gene classes in all of our in vitro and in vivo screens (*16*, *22*). As expected, essential genes uniformly dropped out across all screening conditions (fig. S4, A and B). Loss of TSGs increased growth and survival most strongly in WT mice compared with all other screening conditions (fig. S4, A and B). This strong positive selection for loss of TSGs in CT26 and 4T1 tumors grown in WT mice is in sharp contrast to results obtained when examining TSG performance in previous in vitro CRISPR screens in tumor cell lines as reported in the literature (*21*) (fig. S2). We analyzed potential neoantigens present in CT26 (*37*) and 4T1 (*38*) cells for prediction of strong drivers of immune escape in WT mice (fig. S5, A and B). Overall, we observed no correlation between putative neoantigens and gene performance in the in vivo screens. To help rule out an enrichment of TSGs due to multiple integrants from the lentiviral library infection, we examined our CT26 and 4T1 CRISPR library of infected cells for puromycin resistance gene copy number by droplet digital polymerase chain reaction (ddPCR) and verified that each cell contained a single sgRNA (fig. S5C).

Among the top-scoring genes in the CT26 screens (fig. S3D), we focused on *Gna13*, *Cul3*, and *Hdac2* because of their stronger phenotypes observed in WT mice in both the CT26 and 4T1 screens and their unknown roles in regulating tumor cell responses to the adaptive immune system. To validate these candidates, we generated a cutting control CRISPR library targeting the introns of ~4000 expressed genes and mixed in four sgRNAs targeting *Gna13* not present in our original screening library (Fig. 2D and table S4). Cells were grown in vitro or as subcutaneous tumor transplants in BALB/c WT or SCID mice as was done in the earlier screens. Each *Gna13*-targeting sgRNA showed

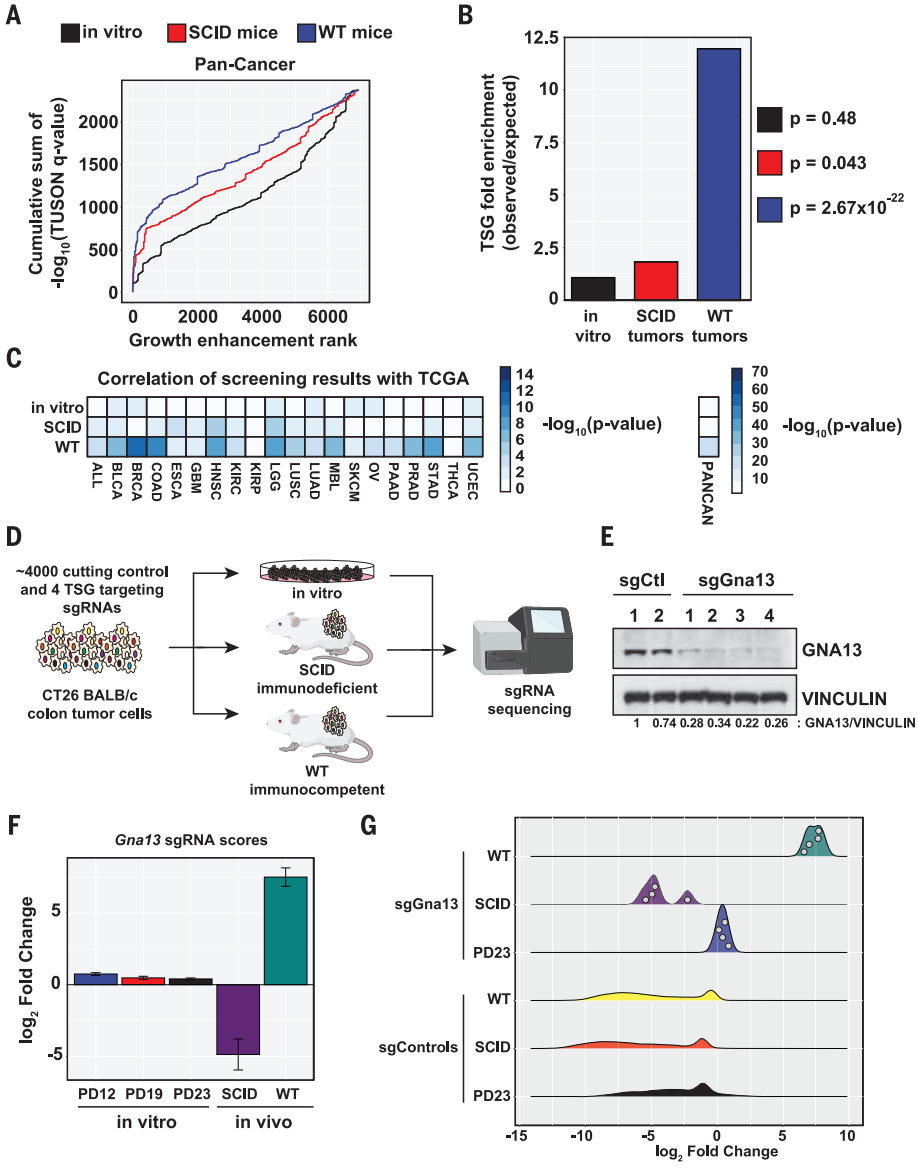


Fig. 2. CRISPR-based genetic screens in CT26 colon tumor cells to characterize tumor and immune system interactions. (**A**) Comparison of TSG selection in vitro and in SCID or WT mice. CT26 cells were transduced with the druggable CRISPR library used in the 4T1 screen and were maintained in vitro or transplanted subcutaneously on flanks of either SCID or WT BALB/c mice. After tumor formation or 10 PDs in vitro, tumor cells were harvested and sgRNAs were sequenced. Genes were ranked on the basis of the median $\log_2$ fold change plotted against the cumulative sum of significance as done for the 4T1 screen in Fig. 1D. (**B**) Stronger enrichment of TSGs in WT compared to SCID mice or in vitro. The observed number of TSGs with an FDR <0.1 were compared to the number of expected TSGs based on a hypergeometric distribution. The fold enrichment was determined for each screening condition with *p* values from a Fisher's exact test. (**C**) The top-scoring genes in WT mice are among the most mutated genes observed in human tumors. Gene lists from the in vitro, SCID, and WT conditions were compared to the ranked list of TSGs from each TCGA cancer type and pan-cancer derived from TUSON Explorer using a Fisher's exact test. The heatmap represents the $-\log_{10}$(*p*value). (**D**) Experimental design of validation experiments. CT26 cells were infected with a library of ~4000 control sgRNAs targeting the introns of expressed genes and 4 sgRNAs targeting the gene to be validated. Cells were grown in vitro or as tumors in SCID or WT mice, and sgRNA abundance was measured by sequencing. (**E**) CRISPR-mediated disruption of *Gna13*, a top-scoring TSG in both the 4T1 and CT26 screens. Four sgRNAs targeting *Gna13* and two control sgRNAs with Cas9 were stably expressed in CT26 cells. After selection, cell lysates were immunoblotted to verify loss of GNA13 expression. (**F**) Loss of GNA13 results in a growth advantage only in the presence of an adaptive immune system. The $\log_2$ fold changes in the abundance of the sgRNAs targeting *Gna13* were compared during growth in vitro at different PDs and also after tumor growth in SCID or WT mice. (**G**) Comparison of the individual *Gna13* sgRNAs and negative control distribution after growth in vitro or in vivo. A similar distribution of the $\log_2$ fold changes for control sgRNAs is observed in WT and SCID mice. The distribution of the *Gna13* targeting sgRNAs (gray circles) shows positive selection only in WT mice.

depletion of GNA13 protein (Fig. 2E), and this had no effect on growth in vitro (fig. S5D). The sgRNAs with the best depletion of GNA13 (#3 and #4) also had no effect on anchorage-independent growth (fig. S5, E and F). Analysis of sgRNA abundance after PDs 12, 19, and 23 also revealed that GNA13 depletion has no effect on in vitro proliferation (Fig. 2F and table S4). We compared the performance of sgRNAs targeting *Gna13* during in vivo tumor growth and observed an enrichment in *Gna13*-targeting sgRNAs only in WT but not SCID mice, phenocopying what we observed in the 4T1 and CT26 screens (Fig. 2F and table S4). Each of the four sgRNAs targeting *Gna13* had comparable performance, and a similar distribution for the negative controls was observed in all conditions (Fig. 2G). We observed similar results when targeting the TSGs *Hdac2* and *Cul3* (fig. S6 and table S4). Together these results support an adaptive immune system–specific tumor suppressor phenotype for loss of *Gna13*, *Hdac2*, and *Cul3*.

CRISPR screens targeting TSGs using C57BL/6-derived syngeneic models

Because our druggable CRISPR library did not contain many known TSGs like *Cdkn2a*/p16, we designed a mouse CRISPR library targeting a more comprehensive set of TSGs known to be mutated in human tumors (*16*). This library contained 10 sgRNAs for each of the top ~500 predicted TSGs. We transduced three different tumor cell lines derived from diverse C57BL/6 mouse models with this TSG library, including ~3000 cutting controls, and transplanted the cells into either WT or adaptive immune-deficient *Rag1*^{null} mice (Fig. 3A). When tumor growth reached ~2 cm^3 in mice, we analyzed sgRNA abundance and compared that to the abundance in input cells to understand which TSGs were promoting growth in an adaptive immune system–specific manner. Among the top hits that showed a more pronounced effect in WT mice were *B2m* and *Hdac2*, genes that we also observed in the CT26 and 4T1 screening results (Fig. 3B and table S5). We examined genes that scored differentially among the three cell lines that we screened to look for tumor type–specific hits (fig. S7). One example is *Spred1*, whose sgRNAs only scored in the B16 melanoma cell screen and melanomas exhibit the highest frequency of *SPRED1* mutations (fig. S7A) (*16*, *39*). Another example is

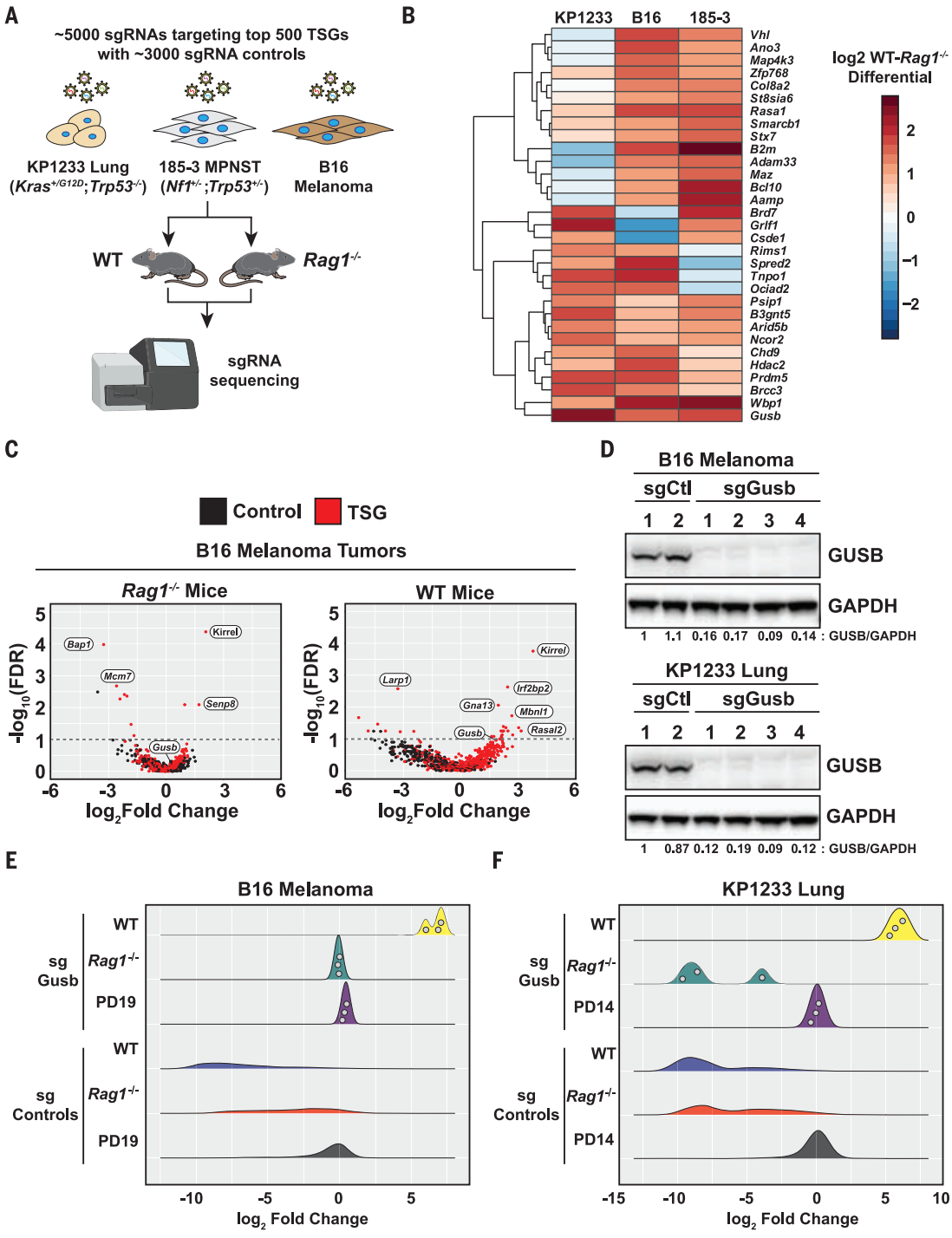


Fig. 3. Strong selection for TSG loss in tumors formed in immunocompetent mice is conserved in other mouse strains and tumor cell models. (**A**) CRISPR screening system to evaluate TSG performance in C57BL/6 mouse tumor transplants. Three tumor cell lines originally from C57BL/6 mice were infected with a library of sgRNAs targeting the top 500 tumor suppressors identified by TUSON Explorer (*16*) and 3000 sgRNA controls. After 10 PDs in vitro or tumor formation, cells were harvested and sgRNAs were sequenced. (**B**) Comparison of the top TSGs that reproducibly score more strongly in the presence of an immune system. Data from the TSG CRISPR screens were analyzed to find the top genes that score more strongly in WT tumors. Shown in the heatmap are the top 30 genes that have the largest median $\log_2$ fold change difference among the three cell lines screened (WT-*Rag1*^{null}). (**C**) Presence of an adaptive immune system leads to strong selection of TSGs in B16 melanoma tumors. Volcano plots of the analyses of the screening results in either *Rag1*^{null} or WT mice. Black dots represent controls, and TSGs are in red. (**D**) Disruption of GUSB expression in B16 melanoma and KP1233 lung tumor cell lines. Four sgRNAs targeting *Gusb* and two control sgRNAs were stably expressed in cells with Cas9. After selection, cell lysates were immunoblotted to verify loss of GUSB expression. (**E**) Comparison of the individual *Gusb* sgRNAs and negative control distribution after growth in vitro or in vivo in B16 cells. Cells expressing a negative control library of sgRNAs targeting introns or *Gusb* sgRNAs from (D) were transplanted into *Rag1*^{null} or WT mice. After tumor formation, sgRNAs were sequenced. (**F**) Comparison of the individual *Gusb* sgRNAs and negative control distribution after growth in vitro or in vivo in KP1233 cells. Cells expressing a negative control library of sgRNAs targeting introns or *Gusb* sgRNAs from (D) were transplanted into *Rag1*^{null} or WT mice. After tumor formation, sgRNAs were sequenced. A similar distribution of the $\log_2$ fold changes for control sgRNAs was observed in WT and *Rag1*^{null} mice. The distribution of the *Gusb* targeting sgRNAs (gray circles) shows positive selection only in WT mice.

Stk11, whose sgRNAs only scored in the lung tumor–derived KP1233 cells, the tumor type with the most frequent *STK11* mutations found in human cancer (fig. S7B) (*16*, *40*). Examination of the screening results in B16 melanoma cells showed a stronger selection for TSG loss in WT compared with *Rag1*^{null} mice, including *Gna13* (Fig. 3C), a TSG that was among the top scorers in WT mice in both the 4T1 (fig. S1D) and CT26 screens (fig. S3D). These results of adaptive immune-selective enrichment of TSGs obtained in C57BL/6 mouse tumors phenocopy those observed in BALB/c mice. These data support a role for TSG loss in adaptive immune evasion as a more general phenomenon and not simply due to use of particular cell lines or mouse strains.

CRISPR targeting of *Gusb*, a gene encoding a lysosomal glucouronidase involved in glycosaminoglycan degradation (*41*), showed an adaptive immune-specific positive selection phenotype in each C57BL/6 cell line tested (Fig. 3B). We chose to validate *Gusb* because it has no known role in immunosurveillance regulation in cancer and it also scored as an adaptive immune system–specific hit in the 4T1 screen (table S2). We used CRISPR to target *Gusb* in both B16 melanoma and KP1233 lung tumor cells (Fig. 3D). In vitro, loss of GUSB expression showed no effects on anchorage-dependent or -independent growth (fig. S8, A to C). We used the sequencing-based validation approach outlined in Fig. 2D, where we added four sgRNAs targeting *Gusb* into a library of ~4000 intron-targeting controls for B16 and KP1233 tumors in WT and $Rag1^{null}$ mice or in vitro. In each cell line, control sgRNAs had similar effects in both WT and $Rag1^{null}$ tumors, whereas *Gusb* sgRNAs showed positive selection only in WT mice (Fig. 3, E and F, and table S6). These results support a role for *Gusb* in regulating a tumor cell's response to an adaptive immune system.

TSGs may affect a tumor cell's ability to avoid the adaptive immune system through down-regulation of antigen presentation and/or insensitivity to CD8 T cell cytotoxicity. To determine which TSGs have roles in these processes, we designed a screening approach using C57BL/6 mouse pancreas cells expressing full-length ovalbumin, which contains the OT-I T cell receptor target motif SIINFEKL (*42*). These cells were infected with a CRISPR library targeting the top 500 TSGs plus intron-targeting controls and split into two conditions: One group was given different amounts of cytotoxic OT-I CD8 cells, and one was stained for surface expression of total HLA and SIINFEKL presentation by H-2Kb (fig. S9A). Cells that failed to express surface HLA or H-2Kb-SIINFEKL after interferon-γ (IFN-γ) treatment were sorted, and sgRNAs were sequenced. Similarly, cells that resisted OT-I CD8 killing were harvested, and sgRNA abundance was analyzed. We used two ratios of CD8:target cells that resulted in either 50% or 90% target cell killing after 6 hours. For each condition, we obtained expected hits, including *Jak1*, *Ifngr2*, and *B2m*—well-established TSGs whose perturbations are known to help cells avoid CD8 killing (fig. S9, B and C, and table S7) (*34*, *43*). Notably, sgRNAs targeting *Gna13* or *Gusb* had no effect in these screens or in validation assays, indicating that their performance in our earlier screens was not simply due to direct resistance to T cell killing (fig. S9D). TSGs that affect either total HLA or SIINFEKL presentation again included the positive controls *Jak1*, *Ifngr2*, and *B2m* (fig. 9, E and F, and table S8). We did not find that sgRNAs targeting *Gna13*, *Gusb*, *Hdac2*, or *Cul3* affected SIINFEKL antigen presentation, indicating that these TSGs may be involved in processes beyond resistance to CD8 killing or reduced antigen presentation to support immune evasion. Recently, another study examined the response to CD8 killing in CT26, 4T1, and B16 cells, three of the cell lines that we analyzed in our experiments (*29*). CRISPR targeting *Gna13*, *Gusb*, or *Hdac2* had no effect on the cellular response to cytotoxic CD8s, indicating that these genes likely affect another aspect of immune evasion beyond resistance to CD8 killing.

GNA13 loss enhances CCL2 secretion and promotion of a pro-tumor microenvironment

GNA13 has been reported to function as either an oncogene or tumor suppressor, depending on the model and assay system. Mutations in *GNA13* occur in sporadic cancers most often in lymphomas, endometrial tumors, bladder tumors, and liver carcinomas (*44*). These mutations are throughout the length of the *GNA13* gene with a high ratio of predicted damaging missense to benign mutations, a characteristic of TSGs (*16*). One tumor type, bladder cancer, contains activating hotspot mutations in codon 200 of GNA13 that have been shown to lead to oncogenic signaling and transformation (*45*). Amplification and mRNA overexpression of *GNA13* is observed in cancer, including breast and colon tumors, though forced overexpression of active GNA13 mutants has been shown to reduce the growth of breast tumor cells, including the 4T1 cell line used in this study (Fig. 1A) (*46*, *47*). Most studies of GNA13 in cancer have been limited to in vitro assays or in vivo tumor growth using human tumor cell lines in immunocompromised mice. Immunocompetent mouse models with conditional loss of GNA13 have revealed a tumor suppressor function for GNA13 in B cell lymphomas (*48*). These data, along with our results (Figs. 1C; 2, E to G; and 3C), suggest that GNA13 can act as a tumor suppressor in epithelial cells in the presence of an adaptive immune system, but the mechanism is unknown.

To understand how GNA13 regulates its adaptive immune-specific tumor suppressor activity, we generated CT26 cells deficient in GNA13 expression (fig. S5E), implanted these cells as subcutaneous tumors in WT mice or grew them in vitro, and performed transcriptome analyses using RNA sequencing (RNA-seq) (Fig. 4A and table S9). First, we compared the in vitro transcriptomes of GNA13-deficient cells to cells expressing a control sgRNA. Among the top genes that are overexpressed upon *Gna13* sgRNA expression is the chemokine *Ccl2*/MCP-1, a known tumor microenvironment modulator (Fig. 4B) (*49*). Using two *Gna13* sgRNAs, we validated that loss of GNA13 leads to elevated *Ccl2* expression, and this resulted in an increase in CCL2 secretion as measured by enzyme-linked immunosorbent assay (ELISA) (Fig. 4, C and D). Counter to targeting *Gna13* with CRISPR, expression of a doxycycline-inducible constitutively active mutant (Q226L) of GNA13 (*50*) resulted in the reverse phenotype in CT26 cells and reduced *Ccl2* expression as measured by RNA-seq (fig. S10, A and B, and table S9), further confirming the regulatory relationship.

To analyze changes in the tumor microenvironment, we performed GSEA using gene sets derived from single-cell RNA-seq data on isolated immune cell types (*51*) (table S9). We found that known immune-suppressive M2 type macrophages were the top enriched immune cell type in the GNA13-deficient tumors compared with control tumors (fig. S10, C and D). Notably, CCL2 is a known recruiter of myeloid cells, including pro-tumor macrophages and myeloid-derived suppressor cells (MDSCs) to the tumor microenvironment (*52*–*55*).

To examine whether the enhanced CCL2 secretion by GNA13-deficient tumors increases pro-tumor macrophages to affect tumor growth, we generated GNA13-deficient cells that expressed either control or *Ccl2* sgRNAs. Expression of *Ccl2* sgRNAs did not affect the in vitro proliferation of CT26 cells and abolished the enhanced CCL2 secretion conferred by loss of GNA13 (fig. S10, E and F). We observed no significant changes in tumor growth when GNA13-deficient tumors were grown in SCID mice (fig. S11A). Next, we grew subcutaneous tumors of CT26 WT and GNA13-deficient cells with control or *Ccl2* sgRNAs in WT mice and measured both tumor size and macrophage tumor infiltrate by flow cytometry. Loss of CCL2 alone showed no significant effects on tumor growth but CCL2 depletion in the background of GNA13 deficiency significantly reduced tumor growth (Fig. 4E and fig. S11B) and was epistatic to the increased macrophage infiltration observed upon GNA13 loss (fig. S11C). We also observed an increase in $CD206^+$ pro-tumor macrophages upon GNA13 loss that was reduced to approximately WT levels after CCL2 depletion (fig. S11C). We grew tumors in WT mice expressing either control or *Gna13* sgRNAs and treated the mice with liposomes containing either phosphate-buffered saline (PBS) as a control or clodronate, which will deplete macrophages. Macrophage depletion alone led to a small but nonsignificant reduction in tumor growth, similar to previous reports for CT26 cells (Fig. 4F) (*56*). By contrast, we found that the enhanced growth of GNA13-deficient tumors was dependent on the presence of macrophages (Fig. 4F). Examination of the immune infiltrate from these liposome-treated tumors showed a reduction in both total tumor macrophage and $CD206^+$ macrophage populations after clodronate treatment (Fig. 4G). We found that overexpression of exogenous CCL2 is sufficient to promote increased

tumor growth of CT26 tumor cells (fig. S11, D and E). These results support a tumor suppressor function of GNA13 through its negative regulation of CCL2 expression and secretion that can modulate pro-tumor macrophage tumor infiltration or polarization (fig. S12) and suggest a line of therapeutic intervention through antibody or small-molecule interference with CCL2 or its receptor in GNA13-deficient tumors. Future studies are necessary to examine the mechanisms behind the growth-promoting phenotypes of the other genes and pathways that we identified (fig. S13 and table S10) to help design strategies to combat immune evasion.

Discussion

In humans, tumors grow in a complex microenvironment consisting of tumor cell interactions with stromal cells, immune cells, and the vasculature. Over time, dynamically evolving tumors come under pressure from the immune system. Most genetic screens for cancer phenotypes in vitro miss this biology. In this study, we set out to capture this missing biology by simultaneously performing genetic screens in mouse tumor cells in cell culture, in syngeneic mice with an intact adaptive immune system, and in syngeneic mice lacking adaptive immunity. This design allowed us to identify gene sets whose mutation was required for ISA or GSA, respectively.

Using a druggable CRISPR library, this screen identified many known regulators of antigen presentation, including HLA components such as B2M as well as key transducers of the interferon response such as JAK1 kinases that were specifically detected in the presence of a WT immune system. In addition, dozens of other genes scored in these screens, indicating that a large network of genes functioned to promote immune recognition of tumors. Among the most strongly enriched hits were genes that in humans display the classical patterns of TSGs, showing a strong enrichment for loss-of-function mutations observed in tumors. Over a third of the tumor suppressors in the druggable library stimulated tumor growth in WT mice with an FDR cutoff of 0.1, indicating that escape from immune detection is one of the strongest selective forces on tumors. This underscores the profound conservation of regulation of the immune system between mice and humans. It is notable that these screens were performed in tumor cells that have already evolved to form tumors in the same genetic background and have therefore already escaped the immune system to a certain degree. Yet, the immune escape mechanism was clearly not optimal and could be further improved in a number of ways.

The observed increase in TSG selection in the screens performed in the presence of an adaptive immune system cannot solely be explained through increased proliferation during tumor formation. For example, in our CT26 druggable CRISPR screen, known and potent TSGs whose inactivation drive proliferation, like *Trp53* or *Pten*, show comparable phenotypes in both WT and immunocompromised animals. If there was stronger selection for pro-proliferative effects in the immunocompetent tumors, we would have expected *Trp53* and *Pten* sgRNAs to exhibit even stronger enrichment in the presence of an adaptive immune system. We found TSGs whose loss is toxic to cells in vitro and as tumors in immunocompromised mice, but whose inactivation is positively selected in immunocompetent mice. One example is the E3 ligase component protein CUL3, which we validated. *Cul3* is considered an essential gene, and loss of CUL3 expression results in a marked reduction in proliferation in vitro, but tumor cells lacking CUL3 are positively selected only in the presence of an adaptive immune system. One possible explanation for this positive selection for CUL3 loss is through regulation of PDL1 stability. Recent work has shown that a CUL3-SPOP E3 ligase complex is responsible for PDL1 degradation in response to CDK4–cyclin D activity (*57*). Consistent with this interpretation, we also found that *Spop* sgRNAs showed increased positive selection in the immunocompetent setting.

The identification of TGSs that affect immune surveillance in particular model systems is important not only for our understanding of tumor evolution, but also because it provides an opportunity to dissect the mechanism of escape, thereby providing the possibility of developing a therapeutic strategy to reverse the immune escape. A case we explored herein was GNA13, whose loss we found to recruit tumor-associated macrophages. The influx of myeloid cells, including pro-tumor macrophages (TAMs), into the tumor is known to contribute to tumor progression (*58*). For example, loss of the classical TSG *Trp53* in mouse pancreatic tumor models leads to increased TAM abundance in the tumor microenvironment that reduces CD8 cytotoxicity and promotes tumor growth (*59*). Oncogenes can also contribute to this pro-tumor remodeling of the tumor microenvironment. Mutational activation of *KRAS* in the pancreas leads to an increase in pancreas-resident macrophages (*60*), and depletion of these macrophages results in tumor regression and increased survival (*61*). Recent advances in therapeutically targeting TAMs include the use of amphipathic helical peptides that bind the TAM marker CD206 to selectively cause TAM apoptosis (*62*). Our finding that the tumor-suppressive function of *Gna13* is mediated partially through modulation of TAMs by increasing the secretion of CCL2 raises the possibility that patients with tumors deficient in GNA13 function may benefit from future TAM-targeting therapies such as interference with CCL2.

Notably, there is a tissue- or tumor type–specific difference evident between the CT26 and 4T1 screens. In the SCID screens, CT26 showed a much stronger correlation with HNSC, ESCA, and LGG compared with 4T1. In the WT screens, the 4T1 screens showed stronger TSG enrichment with GBM, SKCM, and LUAD, whereas the CT26 screens gave stronger TSG overlap with MBL, PRAD, PAAD, and LGG. *B2m*, a common partner of all MHC proteins, was not enriched in WT mice but was strongly depleted in SCID mice in the CT26 screens. One possible explanation is that *B2m* knockout in SCID mice might make the cells a target for NK cell lysis owing to reduced MHC expression on the surface. Killing by NK cells could possibly be balanced out by a relative lack of killing by the adaptive immune system in WT mice, but this needs to be tested in future experiments. Tissue specificity of cancer drivers is well known, and genetic screening has shown that for GSA phenotypes, there is a profound tissue specificity inherent in normal cells, indicating that they are wired to respond to growth stimuli differentially (*24*, *63*). The general assumption for GSA drivers was that cell proliferation is differentially programmed to respond to different signals in different tissues during development. We did not anticipate the immune response to also be differentially regulated to such a degree. Only 13% (26 genes) of the top 200 genes ranked on the differential for preventing immune evasion were common to breast and colon screens. Only 4% (2 genes) of the top 50 genes preventing immune evasion were shared between the lung, melanocyte, and nerve sheath cell line screens with the TSG libraries, and only 7% were shared between two cell lines on average. This shows that there is strong tissue specificity for immune evasion as well, with the caveat that some genes might not score in a particular tumor because of the existing spectrum of drivers present that can influence the pathways of ISA. In hindsight, tissue specificity for ISA makes sense given that nearly half of the genes identified in the druggable genome screen are TSGs and that TSGs show profound tissue specificity (*63*).

Roughly half of the ISA-driving genes identified in the breast or colon screens are known drivers in the tissue of interest. However, a perplexing observation here is that, in many cases, genes scoring for immune evasion phenotypes found in the screens are not found to be mutated in cancers derived from that tissue. For example, the TSGs *Hdac2*, *Smurf2*, *Pawr*, and *Gna13* scored in both the CT26 and 4T1 druggable CRISPR screens in immunocompetent but not immunodeficient mice, though neither is commonly mutated in colon or breast cancers. One possible explanation

is that nearly all sporadic TSGs are thought to be haploinsufficient in the tissues from which they are known to cause cancer (*16*). If loss of the first allele does not produce a phenotype, the cell number of the subsequent clone will not expand sufficiently to lose the second copy or gain additional cooperating drivers. Because CRISPR screens are potent and generate homozygous nulls in many cases, even haplosufficient genes can contribute to GSAs and ISAs to promote tumorigenesis.

We also identified a collection of non-TSGs that are enriched in either the SCID or WT mouse CRISPR screens in the CT26 and 4T1 cell lines. These non-TSGs that are enriched only in the presence of an adaptive immune system include many genes involved in interferon signaling (*Ifnar1/2*, *Irf9*, *Stat1*), whereas non-TSGs that are enriched only in the SCID screens included negative regulators of MAPK (*Lztr1*, *Dusp4*, *Dusp6*, *Ptpn12*) and mTOR

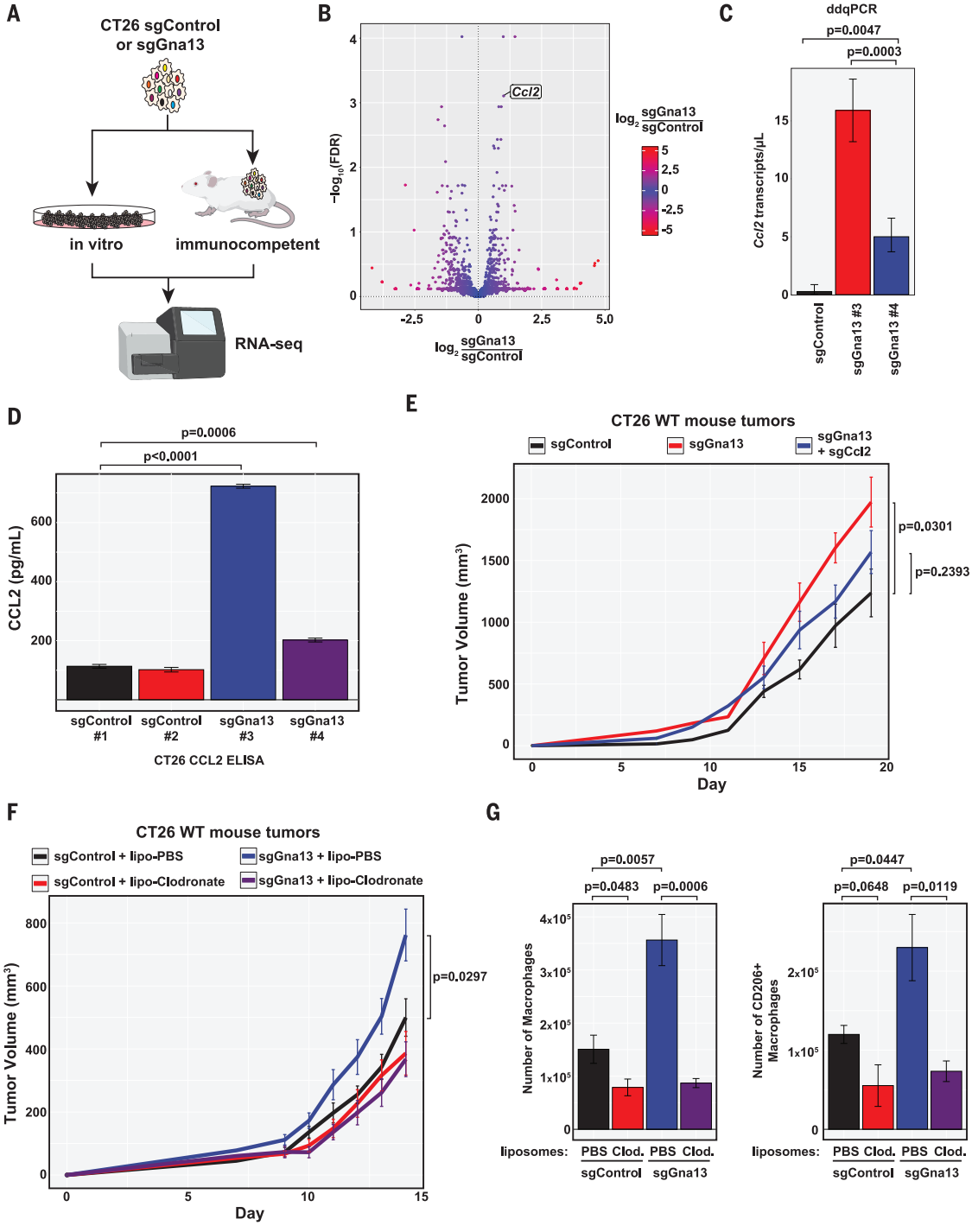


Fig. 4. The tumor-suppressive effects of GNA13 loss are due to increased CCL2 expression and secretion, leading to an increase in tumor macrophages. (**A**) Transcriptome changes after GNA13 loss. CT26 cells expressing sgControl #1 or the #3 and #4 *Gna13*-targeting sgRNAs shown in Fig. 2D were grown in vitro or as tumors in WT BALB/c mice. Subconfluent cells and tumors at 1 cm^3 were harvested, and their transcriptomes were analyzed by RNA-seq. (**B**) Expression of *Ccl2* is increased in GNA13-deficient cells in vitro. Volcano plot of RNA-seq results in GNA13-deficient versus control cells. (**C**) Validation of the increase in *Ccl2* expression after GNA13 loss in CT26 cells. Droplet digital qPCR to quantify the number of *Ccl2* transcripts was performed. (**D**) Disruption of *Gna13* leads to increased secretion of CCL2. CCL2 ELISAs were performed on cell media from cells expressing either sgControls or sgGna13 #3 and #4. (**E**) Loss of CCL2 reverses the increase in tumor growth associated with GNA13 deficiency. CT26 cells expressing the indicated sgRNAs were transplanted into WT BALB/c mice, and tumor volume was monitored by caliper measurement. (**F**) Macrophages are required for the increased tumor growth associated with GNA13 deficiency. CT26 cells expressing the indicated sgRNAs were transplanted into WT BALB/c mice. After 5 days, when tumors were ~50 mm^3, mice were treated intraperitoneally with an initial 200-μl dose of control PBS liposomes or clodronate liposomes (5 mg/ml) to deplete macrophages. Mice were then treated every other day with 100 μl of liposomes until endpoint, and tumor volume was monitored by caliper measurement. (**G**) Liposomal clodronate treatment effectively reduces both total and CD206$^+$ intratumoral macrophages. Tumors were removed and digested, and CD45$^+$ cells were isolated. CD45$^+$ cells were stained to identify immune cells, including macrophage populations.

signaling (*Nlrp2*, *Nlrp3*). These results underscore the pronounced differences observed when tumors are grown with an intact adaptive immune system compared with growth in immunodeficient mice. Activation of progrowth pathways is the main driver in SCID tumors, whereas avoidance of the immune system through modulation of pathways like interferon signaling is selected for in WT tumors.

Immune checkpoint therapies hold great therapeutic promise for several cancer types. However, other cancer types are much less responsive, perhaps because they employ immune evasion mechanisms distinct from PD-1 and CTLA4 pathways. Screens designed to find genes whose mutation may improve immune surveillance are unlikely to identify the non–cell autonomous factors that remodel the tumor microenvironment to escape as they will be masked by the bulk of the tumor. By examining resistance to the immune system, our screen allows discovery of the regulators of those remodeling mechanisms. This study has implicated dozens of human tumor suppressors and other genes that may act in this manner to promote immune evasion. Analysis of enriched pathways from genes that we found to be involved in immune evasion include antigen processing and presentation (*B2m*), protein stability regulation by E3 ubiquitin ligases (*Fbxw7, Keap1, Trip12, Smurf2, Cul3*), and transforming growth factor β (TGF-β) signaling (*Smad2*, *Tgfbr2*, *Rnf111*). The largest class of genes are chromatin interactors, including those in the PBAF and BAF complexes (*Arid1a*, *Arid1b*, *Smarca4*, *Smarcc2*), and chromatin modifiers (*Kdm5c*, *Hdac2*, *Kdm3b*, *Ep300*, *Kdm6a, Men1*). Loss-of-function mutations in the PBAF component *PBRM1* have recently been shown to predict response to immunotherapy in renal cancer and help promote response of melanoma tumors to CD8 T cells (*64*, *65*). Another top-scoring immune evasion pathway is IFN-α signaling (*Ifnar1*, *Ifnar2*, *Jak1*, *Stat1*), a pathway involved in both MHC and PDL1 expression and whose inhibition has recently been shown to increase tumor growth because of immunosuppression in colorectal and breast tumors (*66*–*68*). These genes form a vast network of activities that maintain properly functioning immune surveillance. Whether these activities are regulated under normal physiological conditions to modulate the immune system remains to be determined.

The majority of TSGs, many of which are contained in the less frequent "long tail" of identified recurrent tumor mutations (*69*), have simply not been studied in depth with respect to resistance to the host adaptive immune system. Our results demonstrate that loss of a large number of TSGs can contribute to immune evasion, increasing our understanding of tumor biology. It will be important to determine whether mutation of these TSGs can serve as biomarkers for immune modulating therapies like antibodies against CCL2 that may cooperate with immune checkpoint inhibitors. Furthermore, by establishing isogenic lines with expression or knockout of immune system adaptation TSGs, we can study how a particular TSG changes the tumor's interaction with the immune system to evade it, as we demonstrated with GNA13. That knowledge may lead to a therapeutic intervention to restore immune recognition of those cancers and synergize with immune checkpoint therapies. Future work will be required to mechanistically define how loss of these TSGs interferes with antigen presentation or alters the tumor microenvironment to generate a pro-tumor niche and whether these processes can be reversed in future cancer therapies.

REFERENCES AND NOTES

1. D. Stehelin, H. E. Varmus, J. M. Bishop, P. K. Vogt, *Nature* **260**, 170–173 (1976).
2. C. J. Der, T. G. Krontiris, G. M. Cooper, *Proc. Natl. Acad. Sci. U.S.A.* **79**, 3637–3640 (1982).
3. L. F. Parada, C. J. Tabin, C. Shih, R. A. Weinberg, *Nature* **297**, 474–478 (1982).
4. D. H. Moore *et al*., *Nature* **229**, 611–614 (1971).
5. S. H. Friend *et al*., *Nature* **323**, 643–646 (1986).
6. F. P. Li, J. F. Fraumeni Jr., *Ann. Intern. Med.* **71**, 747–752 (1969).
7. D. Liaw *et al*., *Nat. Genet.* **16**, 64–67 (1997).
8. C. Larsson, B. Skogseid, K. Oberg, Y. Nakamura, M. Nordenskjöld, *Nature* **332**, 85–87 (1988).
9. K. W. Kinzler *et al*., *Science* **253**, 661–665 (1991).
10. R. Fishel *et al*., *Cell* **75**, 1027–1038 (1993).
11. G. A. Rouleau *et al*., *Nature* **363**, 515–521 (1993).
12. F. Latif *et al*., *Science* **260**, 1317–1320 (1993).
13. M. R. Wallace *et al*., *Science* **249**, 181–186 (1990).
14. B. Vogelstein *et al*., *Science* **339**, 1546–1558 (2013).
15. J. N. Weinstein *et al*., *Nat. Genet.* **45**, 1113–1120 (2013).
16. T. Davoli *et al*., *Cell* **155**, 948–962 (2013).
17. N. G. Copeland, N. A. Jenkins, *Nat. Rev. Cancer* **10**, 696–706 (2010).
18. M. R. Schlabach *et al*., *Science* **319**, 620–624 (2008).
19. N. L. Solimini *et al*., *Science* **337**, 104–109 (2012).
20. H. W. Cheung *et al*., *Proc. Natl. Acad. Sci. U.S.A.* **108**, 12372–12377 (2011).
21. M. Ghandi *et al*., *Nature* **569**, 503–508 (2019).
22. T. Hart *et al*., *Cell* **163**, 1515–1526 (2015).
23. L. A. Gilbert *et al*., *Cell* **159**, 647–661 (2014).
24. L. M. Sack *et al*., *Cell* **173**, 499–514.e23 (2018).
25. X. Yang *et al*., *Nat. Methods* **8**, 659–661 (2011).
26. K. Han *et al*., *Nature* **580**, 136–141 (2020).
27. D. Schramek *et al*., *Science* **343**, 309–313 (2014).
28. S. K. Loganathan *et al*., *Science* **367**, 1264–1269 (2020).
29. K. A. Lawson *et al*., *Nature* **586**, 120–126 (2020).
30. M. W. LaFleur, Y. Muroyama, C. G. Drake, A. H. Sharpe, *J. Immunol.* **200**, 375–383 (2018).
31. M. Saigi, J. J. Alburquerque-Bejar, M. Sanchez-Cespedes, *Oncogene* **38**, 5921–5932 (2019).
32. D. L. Dexter *et al*., *Cancer Res.* **38**, 3174–3181 (1978).
33. C. J. Aslakson, F. R. Miller, *Cancer Res.* **52**, 1399–1405 (1992).
34. R. T. Manguso *et al*., *Nature* **547**, 413–418 (2017).
35. A. Tsherniak *et al*., *Cell* **170**, 564–576.e16 (2017).
36. D. P. Griswold, T. H. Corbett, *Cancer* **36** (Suppl), 2441–2444 (1975).
37. J. C. Castle *et al*., *BMC Genomics* **15**, 190 (2014).
38. B. Schrörs *et al*., *Front. Oncol.* **10**, 1195 (2020).
39. The Cancer Genome Atlas Network, *Cell* **161**, 1681–1696 (2015).
40. Cancer Genome Atlas Research Network, *Nature* **511**, 543–550 (2014).
41. S. Tomatsu, A. M. Montaño, V. C. Dung, J. H. Grubb, W. S. Sly, *Hum. Mutat.* **30**, 511–519 (2009).
42. K. A. Hogquist *et al*., *Cell* **76**, 17–27 (1994).
43. P. Han *et al*., *Front. Immunol.* **10**, 251 (2019).
44. ITGC/TCGA Pan-Cancer Analysis of Whole-Genomes Consortium, *Nature* **578**, 82–93 (2020).
45. M. Maziarz *et al*., *J. Biol. Chem.* **295**, 16897–16904 (2020).
46. M. O'Hayre *et al*., *Nat. Rev. Cancer* **13**, 412–424 (2013).
47. P. Kelly *et al*., *Proc. Natl. Acad. Sci. U.S.A.* **103**, 8173–8178 (2006).
48. J. R. Muppidi *et al*., *Nature* **516**, 254–258 (2014).
49. Q. Hao, J. V. Vadgama, P. Wang, *Cell Commun. Signal.* **18**, 82 (2020).
50. M. O'Hayre *et al*., *Oncogene* **35**, 3771–3780 (2016).
51. J. J. Ishizuka *et al*., *Nature* **565**, 43–48 (2019).
52. K. Matsushima, C. G. Larsen, G. C. DuBois, J. J. Oppenheim, *J. Exp. Med.* **169**, 1485–1490 (1989).
53. H. Fujimoto *et al*., *Int. J. Cancer* **125**, 1276–1284 (2009).
54. V. Maximov *et al*., *Nat. Commun.* **10**, 2410 (2019).
55. E. Chun *et al*., *Cell Rep.* **12**, 244–257 (2015).
56. G. H. Nam *et al*., *Nat. Commun.* **9**, 2165 (2018).
57. J. Zhang *et al*., *Nature* **553**, 91–95 (2018).
58. A. Mantovani, F. Marchesi, A. Malesci, L. Laghi, P. Allavena, *Nat. Rev. Clin. Oncol.* **14**, 399–416 (2017).
59. J. Blagih *et al*., *Cell Rep.* **30**, 481–496.e6 (2020).
60. M. M. Kaneda *et al*., *Cancer Discov.* **6**, 870–885 (2016).
61. J. B. Candido *et al*., *Cell Rep.* **23**, 1448–1460 (2018).
62. J. M. Jaynes *et al*., *Sci. Transl. Med.* **12**, eaax6337 (2020).
63. K. M. Haigis, K. Cichowski, S. J. Elledge, *Science* **363**, 1150–1151 (2019).
64. D. Miao *et al*., *Science* **359**, 801–806 (2018).
65. D. Pan *et al*., *Science* **359**, 770–775 (2018).
66. K. V. Katlinski *et al*., *Cancer Cell* **31**, 194–207 (2017).
67. L. Castiello *et al*., *Cancer Immunol. Res.* **6**, 658–670 (2018).
68. Q. Lan *et al*., *Oncogene* **38**, 2814–2829 (2019).
69. L. A. Garraway, E. S. Lander, *Cell* **153**, 17–37 (2013).

ACKNOWLEDGMENTS

We thank E. Wooten for bioinformatics help and all members of the Elledge lab for discussions about the screening results. B16 melanoma cells were obtained from A. Sharpe (Harvard Medical School, Boston, MA) (*71*). KP1233 lung cancer cells were immortalized from C57BL/6 $KRas^{G12D}$ mice and were a gift from T. Jacks (MIT, Koch Institute, Cambridge, MA). The 185-3 MPNST cell line was obtained from K. Cichowski (Harvard Medical School, Boston, MA) (*72*). **Funding:** This work was supported by an award from the Ludwig Institute at Harvard to S.J.E., a grant from the Cancer Research UK Grand Challenge and the Mark Foundation for Cancer Research to the SPECIFICANCER team, and by an NCI grant to S.J.E. and K.M.H. S.J.E. is an investigator with the Howard Hughes Medical Institute. **Author contributions:** T.D.M., R.S.P., D.R.C., K.M.H., and S.J.E. conceived and designed the study. M.Z.L. cloned the mouse CRISPR library used for the CRISPR screens. T.D.M., R.S.P., D.R.C., and A.C.L. performed all in vivo work. T.D.M., M.Y.C., and D.R.C. performed the in vitro CRISPR screens. T.D.M., M.Y.C., and A.P. performed the in vitro CRISPR antigen processing and presentation screens. T.D.M. and R.S.P. analyzed screening results and human tumor data. T.D.M., R.P.S, and S.J.E wrote the manuscript with input from all authors. **Competing interests:** S.J.E. is a cofounder of TSCAN Therapeutics, MAZE Therapeutics, ImmuneID, and Mirimus; serves on the Scientific Advisory Board of CRISPR Therapeutics, Homology Medicines, Inc., TSCAN Therapeutics, and X-Chem; and is an adviser for MPM. None of these affiliations represent a conflict of interest with respect to the design or execution of this study or interpretation of data presented in this manuscript. **Data and materials availability:** Sequencing data from CRISPR screens and RNA-seq experiments are available on ArrayExpress (www.ebi.ac.uk/arrayexpress) as accession numbers E-MTAB-10723, E-MTAB-10724, E-MTAB-10725, E-MTAB-10726, E-MTAB-10727, E-MTAB-10728, E-MTAB-10729, E-MTAB-10731, and E-MTAB-10737. Raw read counts are provided in the supplementary tables. CRISPR screens were analyzed using publically available MAGeCK (version 0.5.9, https://bitbucket.org/liulab/mageck-vispr/src/master/) and edgeR (version 3.30.0, https://bioconductor.org/packages/release/bioc/html/edgeR.html) packages. RNA-seq data were analyzed with edgeR.

SUPPLEMENTARY MATERIALS

https://science.org/doi/10.1126/science.abg5784
Materials and Methods
Figs. S1 to S14
Tables S1 to S10
References (*70*–*72*)
MDAR Reproducibility Checklist

14 January 2021; resubmitted 27 May 2021
Accepted 28 July 2021
10.1126/science.abg5784

MICROBIAL FUEL CELLS

Silver nanoparticles boost charge-extraction efficiency in *Shewanella* microbial fuel cells

Bocheng Cao[1,2], Zipeng Zhao[2], Lele Peng[1], Hui-Ying Shiu[2], Mengning Ding[2], Frank Song[1], Xun Guan[1], Calvin K. Lee[3], Jin Huang[2], Dan Zhu[1], Xiaoyang Fu[1], Gerard C. L. Wong[3], Chong Liu[1], Kenneth Nealson[5], Paul S. Weiss[1,2,3,4], Xiangfeng Duan[1,4]*, Yu Huang[2,4]*

Microbial fuel cells (MFCs) can directly convert the chemical energy stored in organic matter to electricity and are of considerable interest for power generation and wastewater treatment. However, the current MFCs typically exhibit unsatisfactorily low power densities that are largely limited by the sluggish transmembrane and extracellular electron-transfer processes. Here, we report a rational strategy to boost the charge-extraction efficiency in *Shewanella* MFCs substantially by introducing transmembrane and outer-membrane silver nanoparticles. The resulting *Shewanella*-silver MFCs deliver a maximum current density of 3.85 milliamperes per square centimeter, power density of 0.66 milliwatts per square centimeter, and single-cell turnover frequency of 8.6×10^5 per second, which are all considerably higher than those of the best MFCs reported to date. Additionally, the hybrid MFCs feature an excellent fuel-utilization efficiency, with a coulombic efficiency of 81%.

Microbial fuel cells (MFCs) can directly convert chemical energy stored in many sources of biodegradable organic matter to electrical energy through microorganism metabolism (*1*, *2*). A diverse range of bacterial species (*3*) and the wide range of fuels (*4*, *5*) make MFCs an attractive technology for renewable bioelectricity power generation from biomass and wastewater treatment (*6*). For this reason, MFCs have attracted increasing attention from academic and industrial communities (*7*). Among the bacteria that power these systems, *Shewanella* species are widely studied for bioremediation and environmental energy recovery because of their robust growth in both aerobic and anaerobic environments (*8*) and rich distribution in soil and seawater (*9*). However, the current density and power density obtained from typical *Shewanella* MFCs are generally too low for practical applications (*4*, *10*). The low power output is largely limited by the bacterial anodes because of low bacterial loading capacity (*6*, *11*) and/or relatively poor extracellular electron-transfer efficiency (*12*, *13*).

Considerable efforts have been devoted to improving the MFC anodic electrodes by increasing the bacteria loading capacity or enhancing the electrode conductivity (*14*). For example, three-dimensional electrodes with mesoporous structures could provide higher specific surface area and larger space for more bacteria loading (*15*, *16*). Carbon nanomaterials, such as graphene (*17*), carbon nanotubes (*18*–*20*), and their composites with noncarbon materials (*21*), have been explored for reducing the charge-transfer resistance. Additionally, metal nanoparticles have been explored to improve the cell-electrode charge transfer and the current output (*12*, *13*), whereas the exact location and the fundamental role of such nanoparticles remain elusive, and the potential of such approach to the improved MFC power output is yet to be demonstrated. Despite these strategies, the output power density of the MFCs to date has hit a plateau (*8*) and rarely exceeds 0.3 mW/cm^2, which is

[1]Department of Chemistry and Biochemistry, University of California, Los Angeles, Los Angeles, CA 90095, USA. [2]Department of Materials Science and Engineering, University of California, Los Angeles, Los Angeles, CA 90095, USA. [3]Department of Bioengineering, University of California, Los Angeles, Los Angeles, CA 90095, USA. [4]California NanoSystems Institute, University of California, Los Angeles, Los Angeles, CA 90095, USA. [5]Department of Earth Sciences, University of Southern California, Los Angeles, CA 90089, USA.
*Corresponding author. Email: xduan@chem.ucla.edu (X.D.); yhuang@seas.ucla.edu (Y.H.)

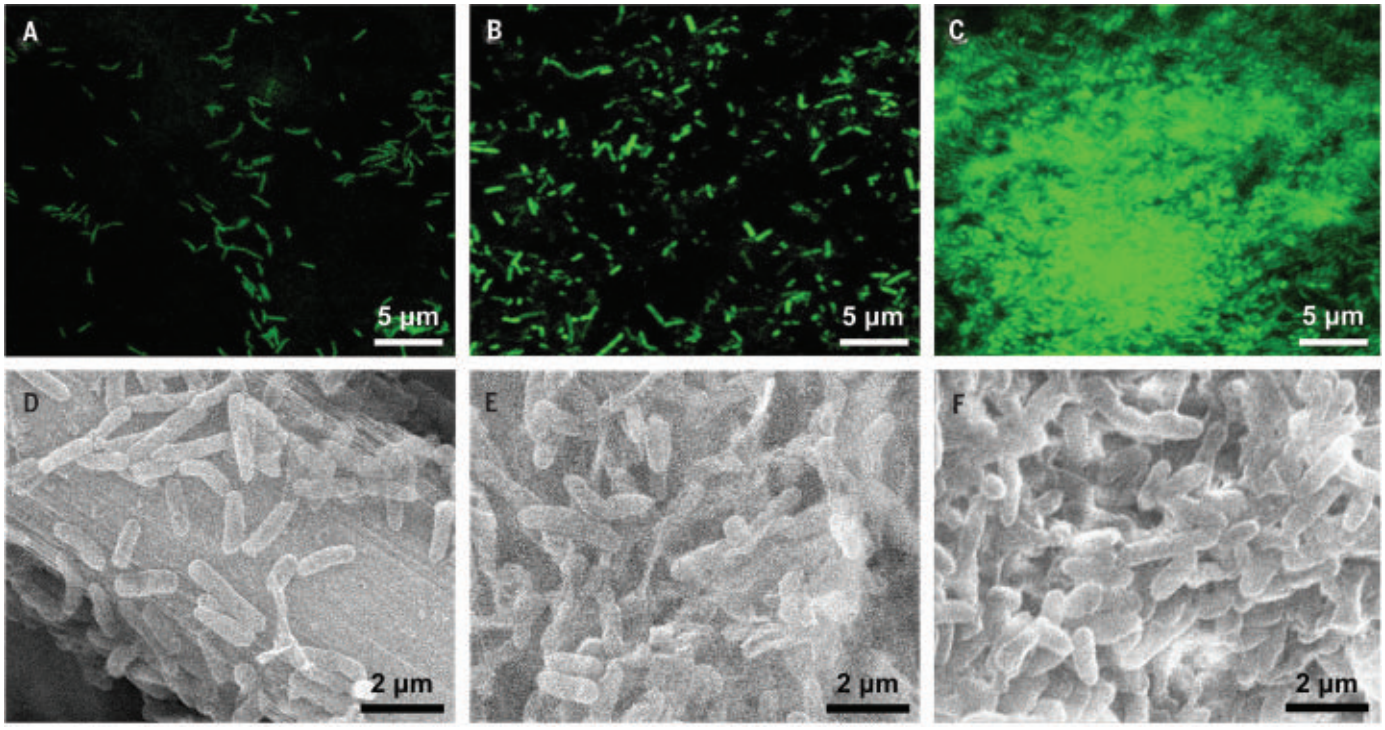


Fig. 1. Characterization of *Shewanella* biofilms. (**A** to **C**) Confocal laser scanning microscopy (CLSM) images of the *Shewanella* biofilms on (A) carbon paper, (B) rGO, and (C) rGO/Ag. (**D** to **F**) Scanning electron microscopy (SEM) images of the biofilms on the (D) carbon paper, (E) rGO, and (F) rGO/Ag.

likely due to limited efficiencies in transmembrane and extracellular electron-transfer processes (*22*).

Within the bacteria in MFCs, the electrons produced by catabolic processes in the bacterial cytoplasm are transferred to the electrode surface through a series of direct or indirect electron-transfer processes (fig. S1) (*23*–*25*). Overall, the transmembrane and extracellular electron-transfer processes generally involve sluggish electron hopping through redox centers in atypical conductors or through multiple redox cycles, which could severely limit the charge-transfer efficiency. Therefore, to break through the power limit of the current MFCs, it is essential to design anodic electrodes that can fundamentally address these charge-transfer limitations to efficiently extract the metabolic electrons to the external electrodes (*26*, *27*).

Here, we report a rational strategy to boost the transmembrane and extracellular electron-transfer processes in *Shewanella* MFCs constructed with reduced graphene oxide–silver nanoparticle (rGO/Ag) scaffolds. Our systematic studies show that the rGO/Ag can release positively charged silver ions, which facilitate *Shewanella* attachment to rGO/Ag scaffolds to form dense biofilms and produce the *Shewanella*-Ag hybrids with greatly enhanced electron-transfer efficiency to improve the bacteria turnover frequency (TOF) and boost the overall MFC performance.

Shewanella biofilm formation

To fabricate a functional MFC, the bacteria must form dense biofilms on the anode surface to ensure efficient charge transfer from the individual bacteria to the external electrode (*2*), which is the origin of the MFC current and power output (*28*). To evaluate the effectiveness of our approach, we have used three different anodic electrode materials—carbon paper, carbon paper with rGO, and carbon paper with rGO/Ag (fig. S2)—to test the compactness and thickness of the biofilms, in which the carbon paper, the most widely and commercially available MFC anodes, and rGO are used for control experiments.

Although silver is often perceived to exhibit antibacterial properties for bacteria (*29*, *30*), such as *Escherichia coli* (fig. S3), it does not appreciably affect the viability of *Shewanella*. In particular, our biocompatibility evaluation by a confocal laser scanning microscope (CLSM) alive-dead staining assay reveals distinct green fluorescence, which originates from the SYTO 9 dye in the living bacteria, indicating that the rGO/Ag electrode is biocompatible. The number of living cells on the rGO/Ag is larger than that on the carbon paper and the carbon paper rGO composite (Fig. 1, A to C). Ag thus does not undermine the *Shewanella* bacterial viability (viability of 93% for rGO/Ag versus 95% for carbon paper and 92% for rGO; see fig. S4 for more details).

Scanning electron microscopy (SEM) images can further reveal biofilm structures with greatly variable bacterial density (Fig. 1, D to F). Compact biofilms consisting of densely packed, bar-like bacteria (~0.5 μm by ~2 μm) are found on the rGO/Ag electrodes (Fig. 1F), whereas the biofilms formed on rGO or carbon fibers are much less dense. These SEM studies are largely consistent with the confocal fluorescence studies and demonstrate that the presence of the Ag is beneficial to denser biofilm formation.

Shewanella MFC tests and performance

Before constructing full MFCs, the output current density of the anode materials was first evaluated with a three-electrode system in an electrochemical half-cell (*31*). Notably, the maximum current density output from the rGO/Ag

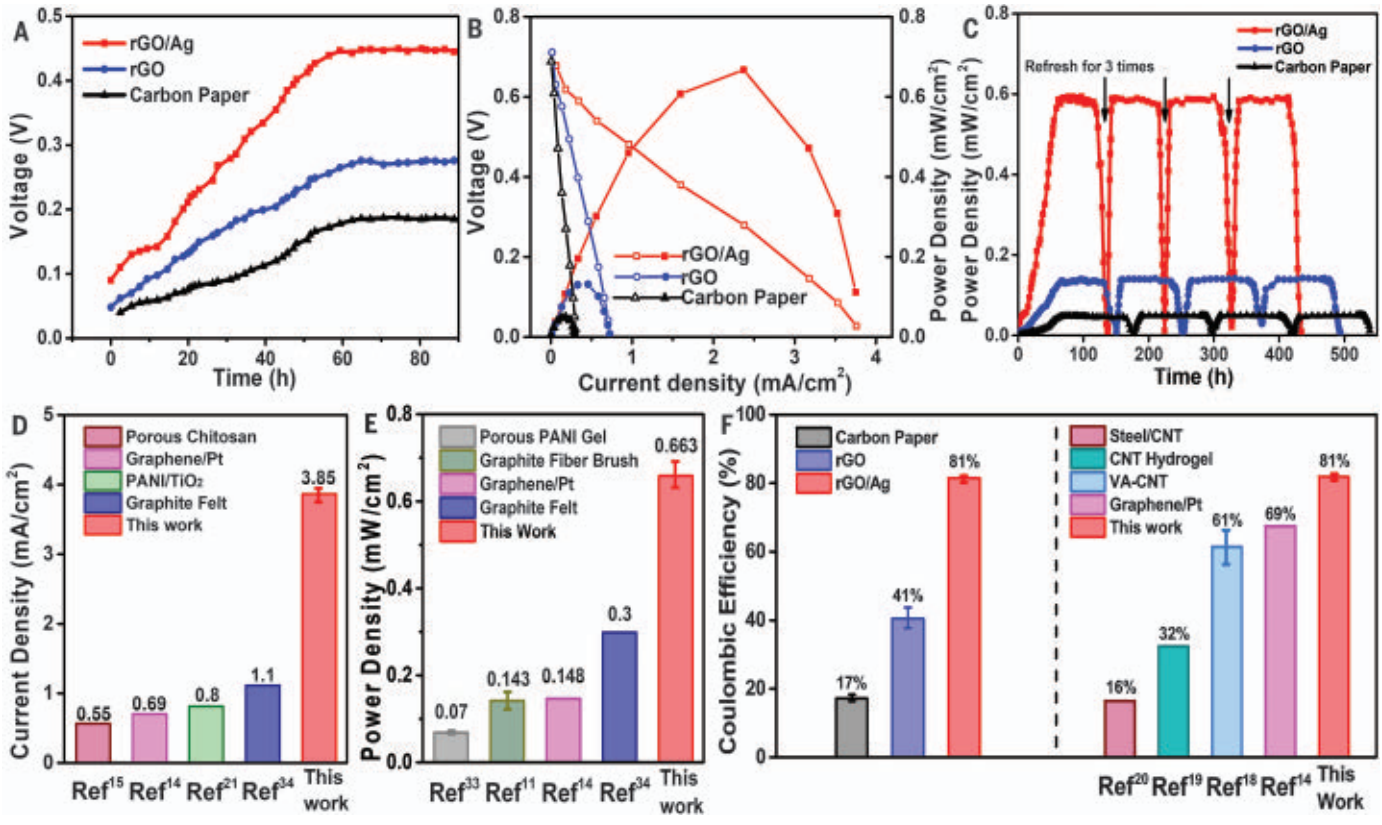


Fig. 2. Performance comparison of *Shewanella* MFCs with different anodes. (**A**) Voltage output of double-chamber MFCs with three different anodic materials. (**B**) *I-V* curves (left axis, open symbols) and power polarization (right axis, filled symbols) curves of the MFCs with three different anode materials. (**C**) MFC power density versus time curves for long-term stability and repeated cycling tests. (**D**) Comparison of the current densities with state-of-the-art MFCs. PANI, polyaniline. (**E**) Comparison of the MFC power density. (**F**) Coulombic efficiency (QE) of three different electrodes and their comparison with the state-of-art MFCs made on different electrode materials. CNT, carbon nanotube; VA, vertically aligned.

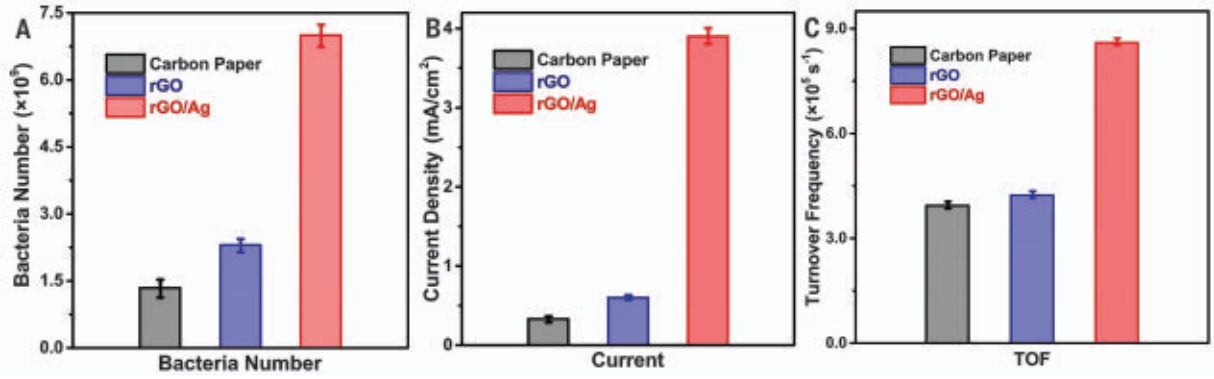


Fig. 3. Turnover frequencies (TOFs) of *Shewanella* MFCs with different anodes. (**A**) Comparison of bacterium number on three different electrodes. (**B**) Comparison of the maximum current density from three different electrodes. (**C**) Comparison of the calculated TOFs for the biofilms on the carbon paper, rGO, and rGO/Ag electrodes.

electrode can reach up to 0.92 mA/cm^2, which is considerably higher than that from either carbon paper (0.06 mA/cm^2) or rGO (0.12 mA/cm^2) electrodes (fig. S5).

To evaluate the power output, we have constructed the full-cell MFC device in a double-chamber container (fig. S6). The output voltage from the MFC increases continuously with incubation time and reaches a nearly constant value in ~2 days (Fig. 2A), indicating successful establishment of a functional MFC (*14*, *32*). When the MFC voltage output is steady, different load resistors are connected to the anode and the cathode to obtain current versus voltage (*I-V*) curves and power polarization curves (Fig. 2B). The *I-V* curves show a similar open-circuit voltage around 0.7 V for all three electrodes, which is consistent with the maximum voltage output from similar MFCs. Notably, the rGO/Ag electrode shows a maximum current output of 3.85 ± 0.05 mA/cm^2, which is much higher than that from carbon paper (0.34 mA/cm^2) or rGO (0.62 mA/cm^2) electrodes (Fig. 2D). The maximum power density from the rGO/Ag electrode reaches up to 0.66 ± 0.03 mW/cm^2, which is also much larger than that for carbon paper anodes (0.05 mW/cm^2) or rGO anodes (0.13 mW/cm^2). Such enhancements of current and power output by Ag nanoparticles are reproducible across multiple measurements (fig. S7). The output current and power observed in the *Shewanella* biofilm on rGO/Ag electrode are also higher than those reported previously with other electrode materials such as polyaniline (PANI) gel (*33*), graphite felt (*34*), and others (Fig. 2, D and E, and table S2).

We have also evaluated the output performance of the MFCs over long-term operation. Voltage output from the MFC drops sharply after ~80 hours of stable operation, which can be attributed to the exhaustion of the nutrient in the anode medium. We conducted a cyclic test by periodically refreshing the anodic medium with nutrient when the voltage output drops below 0.05 V (Fig. 2C). After adding the new medium with lactate as the nutrient, the output power density is rapidly restored to its original value, which confirms that the voltage drop is due to nutrient exhaustion. Similar behavior is observed for all three types of electrodes. On the basis of the amount of nutrient added and total charge output for each cycle, we can also derive the coulombic efficiency of the MFCs. The MFC with rGO/Ag anode shows a coulombic efficiency of ~81%, much higher than those with carbon paper (~17%) and rGO (~41%) anodes and those reported previously (Fig. 2E and table S3), which indicates more-efficient use of the nutrients for power generation.

Enhanced TOFs and charge-extraction efficiency

The increased current density from the rGO/Ag anode could be attributed to a larger number of bacteria in the anode biofilm or to more-efficient charge transport and less charge loss owing to the improved charge-transfer process. To decouple these two potential factors, we quantified and compared the number of bacteria in each type of anode by combining the hemocytometer and total nitrogen analysis kit (fig. S8). With the estimated bacteria number for each electrode (Fig. 3A) and the maximum current output (Fig. 3B), we calculated the TOF for the bacteria on each electrode (Fig. 3C). Overall, the carbon paper and rGO electrodes show a comparable TOF (~3.9 × 10^5/s for carbon paper and ~4.2 × 10^5/s for rGO), whereas the rGO/Ag electrode shows a TOF about twofold higher (~8.6 × 10^5/s), which indicates much higher electron extraction and transport efficiency in the rGO/Ag electrode.

The transmembrane structure of *Shewanella*-Ag hybrids

To elucidate the origin of the enhanced charge-extraction efficiency and the boosted TOFs in rGO/Ag electrode, we have conducted scanning transmission electron microscopy (STEM) and energy-dispersive x-ray spectroscopy (EDX) elemental mapping studies of the bacteria on the rGO/Ag anode after a complete MFC cycle. The STEM and EDX mapping studies reveal enrichment of Ag around the *Shewanella* (Fig. 4A). To evaluate the spatial distribution of Ag within an individual bacterium, we have conducted STEM image and EDX elemental mapping studies on ultrathin sections of *Shewanella*-Ag hybrids. Notably, we found abundant Ag nanoparticles near, inside, and across the membrane area of the *Shewanella* cells (Fig. 4B). The formation of Ag nanoparticles near the membrane area is not surprising considering the heavy metal tolerance of *Shewanella* and the well-known metal reduction capability of these types of bacteria (*4*, *10*). In this case, a likely scenario is that the rGO/Ag electrode slowly releases the silver ions, which diffuse toward *Shewanella* and are reduced in situ by the electrons generated by *Shewanella* metabolism to form Ag nanoparticles on and in the cytoplasmic membrane.

High-resolution STEM images and the corresponding EDX mapping images show that some Ag nanoparticles traverse the entire periplasmic space between the inner and outer membranes and break through the outer membrane (Fig. 4C). In membrane-associated cytochromes involved in transmembrane and extracellular electron-transfer processes, electrons are transferred through multistep hopping processes between Fe^{3+}/Fe^{2+} redox centers (*35*). Because the metal electronic conductivity is far higher than the redox center–mediated charge-transfer process in cytochromes (membrane or nanowires) (*36*, *37*), the transmembrane and outer-membrane Ag nanoparticles can potentially act as metallic shortcuts to bypass the sluggish electron-transfer process mediated by the redox centers, making direct contacts with external electrodes for more-efficient charge extraction.

Electrochemical impedance analysis

We conducted electrochemical impedance spectroscopy (EIS) studies to understand the roles of the Ag nanoparticles in the charge-transfer

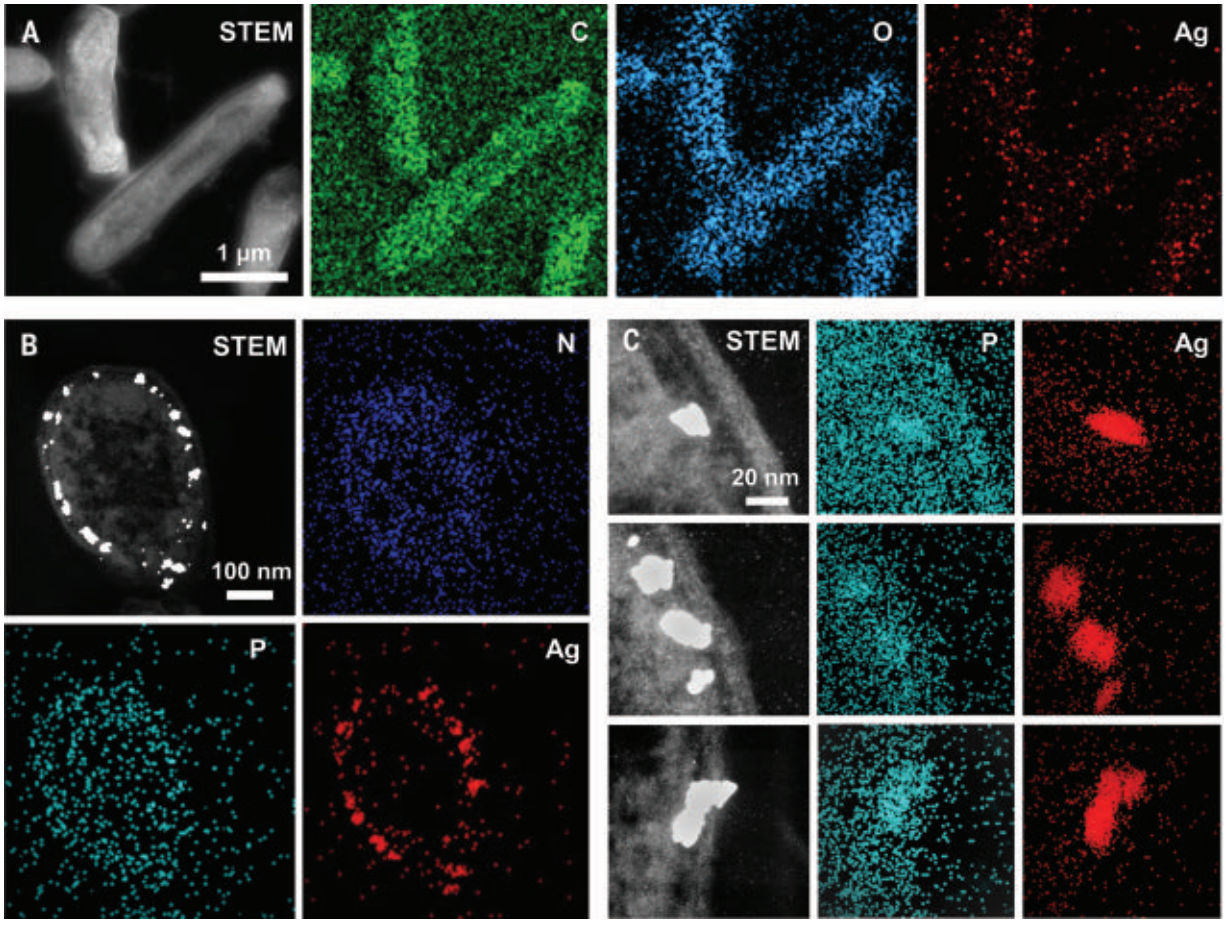


Fig. 4. Characterization of transmembrane structure of the Shewanella-silver hybrid. (**A**) Scanning transmission electron microscopy (STEM) image and energy-dispersive x-ray spectroscopy (EDX) elemental (carbon, oxygen, and silver) mapping of the bacteria on the rGO/Ag electrode. (**B**) STEM image and EDX mapping of the ultrathin sections of the bacteria on the rGO/Ag electrode. (**C**) STEM image and EDX elemental mapping of the transmembrane silver nanoparticles inside and traversing the cell membranes.

process. From the outset, both the electrochemical surface area and EIS (fig. S9) studies show rather similar values for rGO and rGO/Ag electrodes without biofilm, suggesting that the Ag nanoparticles in rGO electrode architecture do not play a notable role in the charge-transfer process and cannot explain the much higher TOFs observed in the biofilms on rGO/Ag electrode. We have further conducted EIS studies on all three types of MFCs, consisting of bacterial biofilm anodes made on carbon paper, rGO, and rGO/Ag. The Nyquist plots (Fig. 5) show two semicircles that can be attributed to the charge-transfer processes in cathode and anode (see fig. S10 for the equivalent circuit). The first semicircle for all three types of device gives a comparable charge-transfer resistance of ~7 ohms, which represents the contribution from the cathode reaction and is largely independent from the anode reaction, as also identified by the same semicircles shown in the MFC blank tests (fig. S11). The second semicircle originates from the *Shewanella* biofilm and gives distinct charge-transfer resistance values ($R_{biofilm}$) of 482, 102, and 16 ohms for the anodes with carbon paper, rGO, and rGO/Ag, respectively. It is apparent that the charge-transfer resistance of the biofilm on the rGO/Ag electrode is much lower than that of the other two electrodes, which can be attributed to increased numbers of bacteria and, especially, the improved transmembrane and extracellular electron-transfer efficiency due to the Ag nanoparticles. In particular, the improved TOFs in rGO/Ag electrode are largely attributed to the increased electron-transfer efficiency.

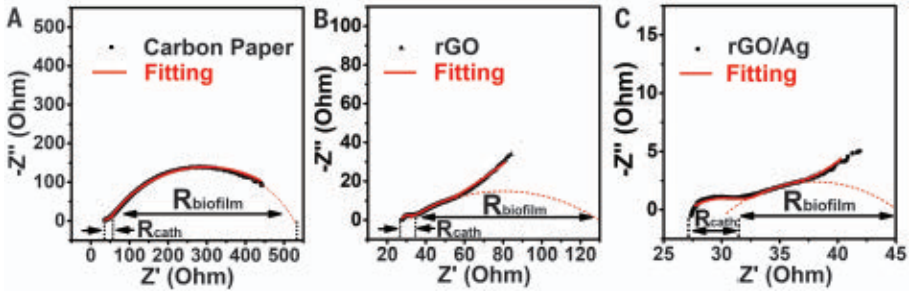


Fig. 5. EIS tests. (**A** to **C**) Electrochemical impedance spectra (EIS) of the biofilms on three different electrodes: (A) carbon paper, (B) rGO, and (C) rGO/Ag along with the fitting curves. The R_{cath} is the charge-transfer resistance of ferricyanide cathode reactions. The $R_{biofilm}$ is the charge-transfer resistance from the anode bacteria biofilm.

Under anaerobic conditions with the lactate as the sole nutrient, electrons transferred extracellularly mostly originate from lactate oxidation by lactate dehydrogenase (LDH) (*38*). It is therefore instructive to compare the TOFs achieved in our *Shewanella* biofilm

with those achieved in individual enzyme or in inorganic catalysts for similar reactions. Considering that the approximate number of copies of LDH in a bacterium is ~1000 (*39*, *40*), the TOFs estimated for single LDH are 394/s for normal *Shewanella* and 860/s for *Shewanella*-Ag hybrids, which compare favorably to those reported for isolated LDH (TOF ~ 170 to 300/s) (*41*, *42*). The higher TOFs achieved in the *Shewanella*-Ag hybrids suggest a critical role for the transmembrane Ag nanoparticles in boosting the charge-extraction and transfer efficiency. We note that the TOFs achieved in LDH in the *Shewanella* biofilms are several orders of magnitude higher than those achieved in lactate dehydrogenation inorganic catalysts (~0.03/s) (*43*), which highlights the merits of exoelectrogenic bacteria in catalyzing lactate oxidation. Together with our rGO/Ag anodic electrode, high-density *Shewanella* biofilms enable MFCs with improved power output and coulombic efficiency. *Shewanella*-metal hybrids thus provide an effective pathway to break the electron-transfer limitations of natural bacteria and push the limit of the MFCs.

REFERENCES AND NOTES

1. K. Rabaey, W. Verstraete, *Trends Biotechnol.* **23**, 291–298 (2005).
2. L. Lu *et al.*, *Nat. Sustain.* **1**, 750–758 (2018).
3. B. E. Logan, K. Rabaey, *Science* **337**, 686–690 (2012).
4. B. E. Logan, *Nat. Rev. Microbiol.* **7**, 375–381 (2009).
5. B. E. Logan, J. M. Regan, *Trends Microbiol.* **14**, 512–518 (2006).
6. B. E. Logan *et al.*, *Environ. Sci. Technol.* **40**, 5181–5192 (2006).
7. D. Simonsson, *Chem. Soc. Rev.* **26**, 181–189 (1997).
8. D. R. Lovley, *Nat. Rev. Microbiol.* **4**, 497–508 (2006).
9. H. H. Hau, J. A. Gralnick, *Annu. Rev. Microbiol.* **61**, 237–258 (2007).
10. B. E. Logan, R. Rossi, A. Ragab, P. E. Saikaly, *Nat. Rev. Microbiol.* **17**, 307–319 (2019).
11. H. Liu, R. Ramnarayanan, B. E. Logan, *Environ. Sci. Technol.* **38**, 2281–2285 (2004).
12. X. Jiang *et al.*, *Nano Lett.* **14**, 6737–6742 (2014).
13. X. Wu *et al.*, *Angew. Chem. Int. Ed.* **50**, 427–430 (2011).
14. S. Zhao *et al.*, *Sci. Adv.* **1**, e1500372 (2015).
15. Z. He, J. Liu, Y. Qiao, C. M. Li, T. T. Y. Tan, *Nano Lett.* **12**, 4738–4741 (2012).
16. Y. Yuan, S. Zhou, Y. Liu, J. Tang, *Environ. Sci. Technol.* **47**, 14525–14532 (2013).
17. C. Zhao *et al.*, *J. Mater. Chem. A Mater. Energy Sustain.* **1**, 12587–12594 (2013).
18. H. Ren *et al.*, *J. Power Sources* **273**, 823–830 (2015).
19. X. W. Liu *et al.*, *ACS Appl. Mater. Interfaces* **6**, 8158–8164 (2014).
20. Y. Zhang, J. Sun, Y. Hu, S. Li, Q. Xu, *J. Power Sources* **239**, 169–174 (2013).
21. Y. Qiao *et al.*, *ACS Nano* **2**, 113–119 (2008).
22. R. Wang *et al.*, *Adv. Mater.* **30**, e1800618 (2018).
23. T. Fu *et al.*, *Nat. Commun.* **11**, 1861 (2020).
24. M. Ding *et al.*, *ACS Nano* **10**, 9919–9926 (2016).
25. M. Y. El-Naggar *et al.*, *Proc. Natl. Acad. Sci. U.S.A.* **107**, 18127–18131 (2010).
26. S. Cestellos-Blanco, H. Zhang, J. M. Kim, Y. Shen, P. Yang, *Nat. Catal.* **3**, 245–255 (2020).
27. N. Kornienko, J. Z. Zhang, K. K. Sakimoto, P. Yang, E. Reisner, *Nat. Nanotechnol.* **13**, 890–899 (2018).
28. Y. Wang *et al.*, *ACS Nano* **10**, 6331–6337 (2016).
29. Z. M. Xiu, Q. B. Zhang, H. L. Puppala, V. L. Colvin, P. J. J. Alvarez, *Nano Lett.* **12**, 4271–4275 (2012).
30. Q. L. Feng *et al.*, *J. Biomed. Mater. Res.* **52**, 662–668 (2000).
31. U. Schröder, J. Niessen, F. Scholz, *Angew. Chem. Int. Ed.* **42**, 2880–2883 (2003).
32. X. Xie *et al.*, *Nano Lett.* **11**, 291–296 (2011).
33. R.-B. Song *et al.*, *J. Mater. Chem. A Mater. Energy Sustain.* **4**, 14555–14559 (2016).
34. B. R. Ringeisen *et al.*, *Environ. Sci. Technol.* **40**, 2629–2634 (2006).
35. L. Shi *et al.*, *Nat. Rev. Microbiol.* **14**, 651–662 (2016).
36. M. Breuer, K. M. Rosso, J. Blumberger, *Proc. Natl. Acad. Sci. U.S.A.* **111**, 611–616 (2014).
37. M. Y. El-Naggar, Y. A. Gorby, W. Xia, K. H. Nealson, *Biophys. J.* **95**, L10–L12 (2008).
38. E. D. Brutinel, J. A. Gralnick, *Appl. Environ. Microbiol.* **78**, 8474–8476 (2012).
39. J. A. H. Wodke *et al.*, *Mol. Syst. Biol.* **9**, 653 (2013).
40. G. S. Rule, E. A. Pratt, C. C. Q. Chin, F. Wold, C. Ho, *J. Bacteriol.* **161**, 1059–1068 (1985).
41. G. E. Pinchuk *et al.*, *Proc. Natl. Acad. Sci. U.S.A.* **106**, 2874–2879 (2009).
42. K. M. LeVan, E. Goldberg, *Biochem. J.* **273**, 587–592 (1991).
43. W. Zhang *et al.*, *ACS Catal.* **8**, 2365–2374 (2018).

ACKNOWLEDGMENTS

Funding: We acknowledge the support from Office of Naval Research (grant no. N00010141712608). We acknowledge the Electron Imaging Center at UCLA for STEM technical support and the Advanced Light Microscopy/Spectroscopy at UCLA for CLSM technical support. We are grateful to J. A. Gralnick in the University of Minnesota for providing *Shewanella* mutants. **Author contributions:** Y.H. and X.D. designed the research. B.C. developed the rGO/Ag approach, fabricated the microbial fuel cell devices, performed the experiments, and conducted data analysis. B.C. and Z.Z. collected the STEM and elemental mapping images. B.C., L.P., and D.Z. designed and discussed the EIS measurements and result analysis. B.C. and H.-Y.S. cultured the *Shewanella* bacteria with the assistance of C.L., B.C., and M.D. and developed the half-cell tests system. F.S., J.H., and X.G. characterized the materials. G.C.L.W., C.L., K.N., and P.S.W. contributed to discussions. X.D. and Y.H. supervised the research. B.C., Y.H., and X.D. cowrote the paper with input from all authors. **Competing interests:** An invention disclosure on MFC fabrication has been submitted to UCLA patent office [UC. Case No. 2022-005-1 (102352-0994)]. The authors declare no other competing interests. **Data and materials availability:** All data are available in the manuscript or the supplementary materials.

SUPPLEMENTARY MATERIALS

https://science.org/doi/10.1126/science.abf3427
Materials and Methods
Figs. S1 to S11
Tables S1 to S4
MDAR Reproducibility Checklist

20 October 2020; resubmitted 20 April 2021
Accepted 28 July 2021
10.1126/science.abf3427

REPORTS

QUANTUM GASES

Observation of fragmentation of a spinor Bose-Einstein condensate

Bertrand Evrard, An Qu, Jean Dalibard*, Fabrice Gerbier

Weakly interacting Bose gases usually form Bose-Einstein condensates in which most particles occupy the same single-particle state. However, when this state cannot realize a continuous symmetry of the many-body Hamiltonian, a fragmented condensate exhibiting the expected symmetry may emerge. Here, we produced a three-fragment condensate for a mesoscopic spin-1 gas of about 100 atoms, with anti-ferromagnetic interactions and vanishing collective spin. Using a spin-resolved detection approaching single-atom resolution, we show that the reconstructed state is close to the expected many-body ground state, whereas one-body observables are the same as for a completely mixed state. Our results highlight how the interplay between symmetry and interactions generates entanglement in a mesoscopic quantum system.

Bose-Einstein condensation (BEC) is a low-temperature phenomenon in which a macroscopic fraction of the particles of a fluid accumulate in the same single-particle state, ψ_0. Originally described in the context of noninteracting bosons (*1*), BEC turned out to be robust to interactions between particles. In fact, weak repulsive interactions play a decisive role in stabilizing the condensate, in particular in ensuring that only ψ_0 is macroscopically occupied even though there are many almost degenerate states nearby: a winner-takes-all situation (*2*, *3*). However, BEC is not the only low-temperature scenario for interacting bosons. For instance, in a periodic potential for repulsive interactions, a phase transition to a Mott insulator phase takes place (*4*). In this phase, no single-particle state is macroscopically occupied even at zero temperature.

A long-sought phase that is intermediate between these two limits corresponds to a fragmented condensate (*5*, *6*). In contrast to a regular condensate, a fragmented condensate is strongly entangled, which leads to a simultaneous macroscopic occupation of several single-particle states ψ_1, ψ_2,...ψ_p. More precisely, measurement outcomes for one-particle observables are the same as for a statistical mixture of the p single-particle states. Only measurements of at least few-body (sometimes even N-body) observables can reveal the quantum entanglement of the many-body ground state and the corresponding correlations. The simplest case, $p = 2$, occurs for two-component bosons with attractive intercomponent interactions forming a twin-Fock state, a two-fragment condensate (*6*). Such a state was

Laboratoire Kastler Brossel, Collège de France, CNRS, ENS-PSL University, Sorbonne Université, 75005 Paris, France.
*Corresponding author. Email: jean.dalibard@college-de-france.fr

recently realized experimentally for $N \sim 10^4$ atoms and characterized by its number squeezing (*7*). Here, we explore experimentally the situation in which fragmentation arises from the interplay between interactions and a continuous symmetry of the *N*-body Hamiltonian. BEC-like (uncorrelated) states $\psi^{\otimes N}$ form a family of degenerate, symmetry-broken states related to each other by symmetry transformations. Fragmentation and entanglement then provide a way to restore the symmetry by lowering the energy of the true fragmented ground state with respect to the symmetry-broken states.

In a generic *N*-body system with a continuous symmetry, the energy gain from fragmentation is typically subextensive and becomes immaterial in the thermodynamic limit (TL), where uncorrelated states prevail. This is a consequence of spontaneous symmetry breaking (SSB), which is revealed by adding a fictitious term $q\hat{H}_1$ to the physical Hamiltonian $\hat{H}_0$, with comparable magnitudes for $\hat{H}_0$ and $\hat{H}_1$ and with the parameter q set to zero after taking the TL. In this limit, the low part of the energy spectrum of $\hat{H}_0$, the so-called Anderson tower of states, collapses to a highly degenerate manifold. The perturbation $q\hat{H}_1$ lifts the degeneracy within this manifold and typically favors an uncorrelated, symmetry-broken state formed by a superposition of $\sim\sqrt{N}$ eigenstates of $\hat{H}_0$. As realized by Anderson (*8*), symmetry-broken states are not true energy eigenstates, but they evolve infinitely slowly in the TL and can thus be considered as stationary for all practical purposes. Explicit examples of SSB are plenty in condensed matter systems, including the center of mass of a crystal with broken translational invariance and the staggered magnetization of antiferromagnets with broken spin rotational invariance (*9*).

In this work, we observe condensate fragmentation and restoration of symmetry by quantum fluctuations for $N \sim 100$ spin-1 atoms forming an antiferromagnetic spinor condensate. Symmetry restoration corresponds to the unfolding of the SSB mechanism when sending the symmetry-breaking field to zero before the TL is taken (*10*–*14*). Experimentally, symmetry-breaking perturbations $q\hat{H}_1$ that are inevitably present in experiments must be suppressed to a very high degree, leaving a narrow energy window of width $q \propto 1/N$, inside which the symmetry of $\hat{H}_0$ is relevant. Therefore, this phenomenon is unobservable for truly macroscopic systems but becomes relevant for mesoscopic ones such as ours, which have large but finite N (*15*).

Our system is an assembly of spin-1 sodium atoms, in which the external degrees of freedom of the particles have been frozen by a tight trap (*6*, *16*–*21*). All atoms share the same spatial wave function and only the spin state of each atom labeled by the magnetic quantum number $m = 0,\pm1$ is relevant (*22*). The interaction Hamiltonian then reduces to an effective quantum rotor Hamiltonian (*16*),

$$\hat{H}_0 = \frac{U_s}{2N}\sum_{i,j=1}^{N}\hat{s}_i\cdot\hat{s}_j = \frac{U_s}{2N}\hat{S}^2 \qquad (1)$$

where $U_s > 0$, with an extensive moment of inertia $\mathcal{I} \propto N/U_s$ and a tower of states spectrum $E_S = S(S+1)/2\mathcal{I}$. Here, $\hat{s}_i$ denotes the spin operator of atom i, $\hat{S} = \sum_i \hat{s}_i$ the total spin operator, S the associated total spin quantum number, and the TL corresponds to $N \to \infty$ at constant U_s.

The mean-field version of Eq. 1 is minimized by the so-called polar states $|\Omega\rangle = |m=0\rangle_\Omega^{\otimes N}$ with all atoms in the $m = 0$ state with respect to a quantization axis along the unit vector $\mathbf{\Omega}$ (*23*, *24*). These states have zero average spin but break the rotational symmetry of $\hat{H}_0$. Conversely, the exact many-body ground state $|\Phi\rangle$ of $\hat{H}_0$ is fragmented (*16*–*19*). For even N, $|\Phi\rangle$ is an N-particle spin-singlet state with $S = 0$, a highly entangled state constructed by assembling bosons by pairs of spin zero. Spin singlets are rotationally invariant, so that the single-particle density matrix $\rho^{(1)}$ extracted from $|\Phi\rangle$ must be the same in any single-particle basis. Therefore, it must be proportional to the identity matrix with three eigenvalues equal to 1/3, thus providing a $p = 3$ fragmented condensate. When N is odd, $|\Phi\rangle$ is a state with collective spin $S = 1$, also a three-fragment condensate.

The atoms are confined in a crossed laser trap that provides a spin-independent, roughly isotropic harmonic potential with frequency $\omega/(2\pi) \sim 2$ kHz. The large difference in the spatial and spin energy scales, $\hbar\omega/U_s \sim 100$, ensures that all condensed atoms occupy the same spatial mode (*22*). The spin degrees of freedom evolve through binary collisions ($m = 0$) + ($m = 0$) ⇆ ($m = +1$) + ($m = -1$), which conserve the magnetization $\hat{S}_z = \hat{N}_{+1}^{(z)} - \hat{N}_{-1}^{(z)}$, where $\hat{N}_m^{(z)}$ counts the number of atoms in state m with z as quantization axis. The relevant Hamiltonian in the presence of a static magnetic field B parallel to z reads $\hat{H}_0 - q\hat{N}_0^{(z)}$. Here, the linear Zeeman shift $\propto S_z$ is omitted because S_z is a conserved quantity (*25*), and we keep only the next leading term, the quadratic Zeeman (QZ) shift $-q\hat{N}_0^{(z)}$, with $q \propto B^2$. The QZ term lowers the energy of $m = 0$ with respect to $m = \pm1$ and provides an explicit symmetry-breaking field. For $q \gtrsim U_s$, spin-spin interactions can be neglected and the ground state $|\Phi\rangle$ is a single, uncorrelated condensate in the polar state with $\mathbf{\Omega} = e_z$. When q is reduced to $\sim U_s/N$, the subextensive depletion of the mean-field polar state can be evaluated using a Bogoliubov approach (*26*). Finally, for very low magnetic field $q \lesssim U_s/N^2$, the depletion is extensive and $|\Phi\rangle$ is fragmented and tends to the $S = 0$ ($S = 1$) state for even (odd) N when $q \to 0$.

Because of the smallness of the energy gap (<100 pK) protecting the many-body ground state in our system, direct cooling to the fragmented state is not possible. Instead, we use an adiabatic passage induced by ramping down the magnetic field, which drives the system from the uncorrelated state at large B to the targeted state at $B \approx 0$ (Fig. 1A). The

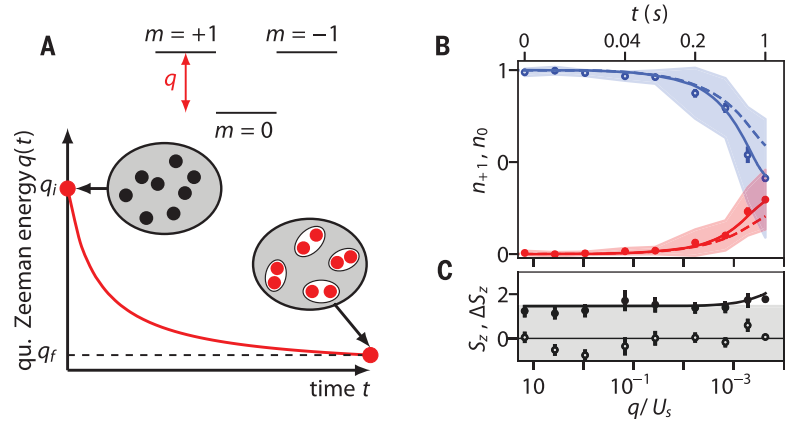


Fig. 1. Producing a fragmented condensate. (**A**) Sketch of the adiabatic ramp used to produce a fragmented condensate. Initially in a large magnetic field ($q_i \gg U_s$), the system forms a single polar condensate with all atoms in $m = 0$. When the magnetic field is decreased to a low value ($q_f \sim U_s/N^2$), the condensate fragments. For even N, the ground state is close to the singlet state $S = 0$, which can be viewed (*17*) as a condensate of $N/2$ singlet pairs of atoms. For odd N, the ground state $S = 1$ is a condensate of such pairs plus one extra atom. (**B**) Evolution of the average populations $n_m = N_m/N$ in $m = 0$ (blue circles) and $m = +1$ (red dots) toward an isotropic mixture. The shaded areas indicate the fluctuations (±1 SD around the mean), which increase substantially and become super-Poissonian for $q \sim 0$ (see Fig. 3). The solid (dashed) line shows the predictions from the stochastic (deterministic) *N*-body Schrödinger equation (*26*). (**C**) Evolution of the average magnetization (black circles) and its SD (dots). Both remain at the level of the detection noise (gray area). Error bars show the statistical error corresponding to 2 SDs.

populations in each Zeeman state are measured with a resolution of 1.2 atoms using a combination of Stern-Gerlach separation and fluorescence imaging (*27*). Figure 1B shows the evolution of the measured mean N_0 and N_1 throughout the ramp; the three Zeeman states end up with comparable populations. We also plot in Fig. 1B the results of a numerical solution of the *N*-body Schrödinger equation, taking into account the residual decoherence during the ramp through additional stochastic elements (*26*). The magnetization S_z (Fig. 1C) remains compatible with zero and its deviation ΔS_z = 1.88(10) at the end of the ramp can be attributed mostly to detection noise.

We now investigate the state of the system at the end of the ramp, focusing successively on one-, two-, and *N*-particle observables. Our main experimental tool is performing rotations in spin space around the *z* and *y* axes with adjustable angles, followed by imaging. Rotations around *z* are obtained from Larmor precession in the static magnetic field, and rotations around *y* are induced by a resonant radiofrequency field (*26*). Consider first the reduced one-body density matrix $\rho^{(1)}_{m,m'} = \langle \hat{a}^\dagger_{m'} \hat{a}_m \rangle / N$, where $\hat{a}_m$ annihilates a particle in state *m*. Using linear algebra, the average values $N^R_m(\phi)$ measured after rotation around *z* by a series of angles ϕ, followed by a rotation $\pi/4$ around *y*, allow us to reconstruct all nine real coefficients of $\rho^{(1)}$ shown in Fig. 2A. We find that $\rho^{(1)}$ has diagonal elements of values similar to one another and essentially zero off-diagonal ones. This experiment thus demonstrates that our system forms a three-fragment condensate, without any underlying assumption on the Hamiltonian or its symmetries. As a control experiment, we also reconstructed $\rho^{(1)}$ for the condensed state $\propto \left(|-1\rangle_z + \sqrt{2}|0\rangle_z - |1\rangle_z\right)^{\otimes N}$ (Fig. 2B). There, we find comparable diagonal and off-diagonal elements $\rho^{(1)}_{m,m'}$, leading to one dominant eigenvalue ≈0.94(4), as expected for a single condensate.

The fragmentation revealed by $\rho^{(1)}$ can be caused by either quantum or thermal fluctuations. Two-body observables such as $\hat{S}^2$ provide information on the existence of quantum entanglement in the system. We compute $\langle \hat{S}_z^2 \rangle$ from the measured distribution $P(S_z)$ shown in Fig. 3A. Similarly, we obtain the values of $\langle \hat{S}_i^2 \rangle$, $i = x,y$ after rotating the state. We show the distribution $P(S_x)$ in Fig. 3B. For each component *i*, we find a highly squeezed distribution around $S_i = 0$. After deconvolution of the detection noise, we get $\langle \hat{S}^2 \rangle = 9.4(1.0)$, which is ~20 times smaller than the value $\langle \hat{S}^2 \rangle = 2N$ expected for uncorrelated spin 1 particles. The counterpart of this large spin squeezing is a broad distribution of the populations of the three spin states. We show in Fig. 3, C and D, the distributions $P\left(N_0^{(i)}\right)$ of atoms in the state $m = 0$ for quantization axis $i = z,x$. These

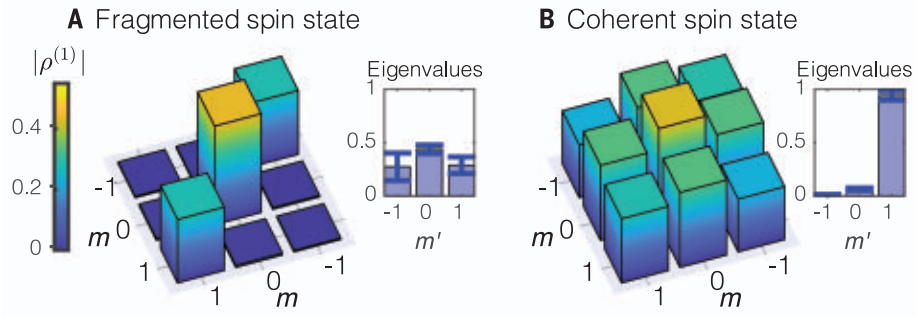


Fig. 2. One-body density matrix. Shown are the moduli of the elements of the matrix (left) and its eigenvalues (right) for a fragmented BEC (**A**) and a single BEC (**B**).

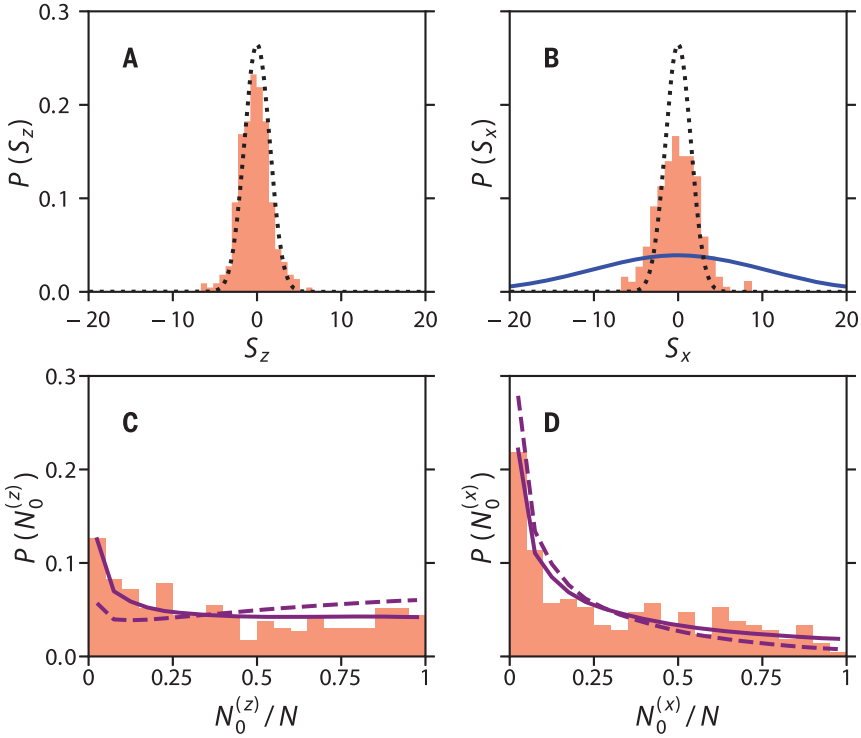


Fig. 3. Distributions of spin and number observables. (**A**) Distribution of measurements for $S_z = N_{+1}^{(z)} - N_{-1}^{(z)}$. (**B**) As in (A) but for S_x. Both distributions are very close to the detection noise (dotted line). Blue line indicates the predicted distribution $\mathcal{P}(S_x)$ for the polar state $|m = 0\rangle_z^{\otimes N}$. (**C** and **D**) Distributions of measurements for $N_0^{(z)}$ (C) and $N_0^{(x)}$ (D). As in Fig. 1B, the solid (dashed) line shows the predictions from the stochastic (respectively deterministic) *N*-body Schrödinger equation.

distributions are similar, as expected for an essentially isotropic state, and are in good agreement with the solution of the *N*-body Schrödinger equation.

We now turn to the tomography of the many-body state, which for 100 atoms can be a formidable task (*28*). Here, we restrict the analysis to the spin state only, leading to a Hilbert space dimension of ~10^4. The measurements of the spin distributions show that the state is very localized in the $|S,M\rangle$ eigenstate basis of $\hat{S}^2$ and $\hat{S}_z$. This enables a faithful reconstruction of the full quantum state using a dataset of moderate size: ~1100 measurements including all spin rotations. We used the maximum-likelihood method, which is based on Bayesian inferences (*26*, *28*–*31*). We find that the reconstructed density matrix $\rho^{(N)}$ is almost diagonal in the $|S,M\rangle$ basis and we show these diagonal elements in Fig. 4A. The lowest two spin manifolds with S = 0,1 are the most populated, and the first four manifolds contain ≈90% of the total population. We thus recover a characteristic property of strongly correlated systems: Whereas the single-particle density matrix $\rho^{(1)}$ is completely mixed, the many-body density matrix $\rho^{(N)}$ has a very low entropy.

For a complete picture, we computed the reduced spin density matrix $\rho^{(k)}$ associated

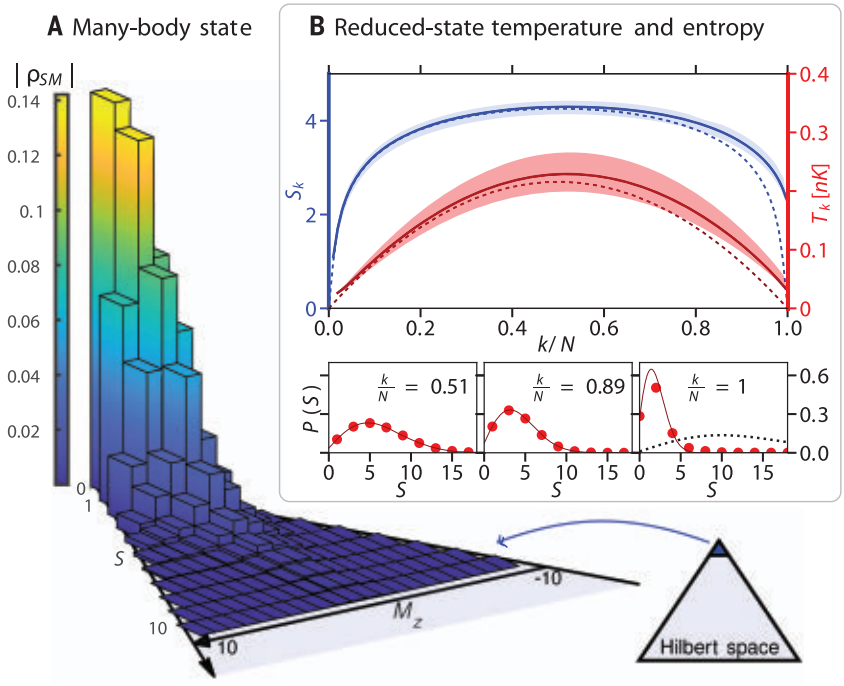


Fig. 4. Many-body state tomography. (**A**) Diagonal elements of the reconstructed state in the spin state basis. (**B**) Top: Entropy (blue line) and temperature (red line) of the reduced k-body density matrices. The shaded areas correspond to the 68% confidence interval. Bottom: Measured spin distributions (red dots) and the thermal fits (solid lines) used to extract the temperature for three values of k/N. For $k = N$, the dotted line shows the spin distribution of a statistical mixture of polar states, i.e., the mean-field ground state for $q = 0$, which extends over $\approx\sqrt{N}$ spin states.

to a subsystem of k atoms, $\rho^{(k)} = \mathrm{Tr}_{N-k}\rho^{(N)}$, where Tr_{N-k} designates the partial trace over the spin state of $N - k$ atom. For the N-body singlet state, $\rho^{(k)}_{S=0}$ is well approximated by a thermal state at an effective temperature (*26*)

$$T^{(k)}_{\mathrm{eff}} = \frac{U_s}{k_B}\frac{k}{N}\left(1-\frac{k}{N}\right) \qquad (2)$$

Using the reconstructed $\rho^{(N)}$, we calculate the von Neumann entropy $S^{(k)}$ associated to $\rho^{(k)}$, as well as its temperature $T^{(k)}_{exp}$ by fitting a thermal distribution to the spin distribution. Measured and predicted quantities show the same qualitative behavior (Fig. 4B): For small k, the entropy increases with k, as for an uncorrelated system at nonzero temperature. Then, for k slightly larger than $N/2$, we observe a back bending of both entropy and temperature. This behavior can be explained only by the existence of entanglement between atoms (*32*, *33*). For the whole system ($k = N$), the residual spin entropy $S^{(N)} \sim 3.0$ agrees with the prediction of the stochastic N-body Schrödinger equation and can be attributed to two effects: (i) the randomness of the parity of N at the beginning of the evolution and (ii) the residual decoherence during the preparation ramp (*26*). The spin temperature $T^{(N)}_{exp} \approx 30$ pK is comparable to $U_s/N \sim$ 10 pK, the typical scale for the low-lying states of the Anderson tower. We note that $T^{(N)}_{exp}$ is much smaller than the temperature of the motional degree of freedom (a few tens of nanokelvins). Such an imbalance can be maintained because of the large energy difference between excitations of the spin and spatial modes, which results in an equilibration time much longer than the experimental sequence.

Our adiabatic protocol could also be used for atoms confined in an optical lattice, in which previously unobserved phases are expected to emerge from the interplay between spatial and spin degrees of freedom (*34*–*36*). For instance, Mott insulators with an even number of atoms per site form a Bose antiferromagnet with atom pairs assembling at each site into spin-singlets (*34*). Unlike the spin-singlet fragmented BEC realized in our work, this spin-singlet insulator survives in the thermodynamic limit, making this state more robust and suitable for quantum metrology (*37*).

REFERENCES AND NOTES

1. A. Einstein, "Sitzungber" (Preuss. Akad. Wiss., 1925).
2. P. Nozières, in *Bose-Einstein Condensation*, A. Griffin, D. W. Snoke, S. Stringari, Eds. (Cambridge Univ. Press, 1995), pp. 15–30.
3. A. J. Leggett, *Rev. Mod. Phys.* **73**, 307–356 (2001).
4. M. P. A. Fisher, P. B. Weichman, G. Grinstein, D. S. Fisher, *Phys. Rev. B Condens. Matter* **40**, 546–570 (1989).
5. P. Nozières, D. Saint James, *J. Phys. (Paris)* **43**, 1133–1148 (1982).
6. E. J. Mueller, T.-L. Ho, M. Ueda, G. Baym, *Phys. Rev. A* **74**, 033612 (2006).
7. X.-Y. Luo *et al.*, *Science* **355**, 620–623 (2017).
8. P. W. Anderson, *Phys. Rev.* **86**, 694–701 (1952).
9. A. J. Beekman, L. Rademaker, J. van Wezel, *SciPost Phys. Lect. Notes* **11**, 10.21468/SciPostPhysLectNotes.11 (2019).
10. H. Neuberger, T. Ziman, *Phys. Rev. B Condens. Matter* **39**, 2608–2618 (1989).
11. T. A. Kaplan, P. Horsch, W. von der Linden, *Phys. Rev. B Condens. Matter* **42**, 4663–4669 (1990).
12. B. Bernu, C. Lhuillier, L. Pierre, *Phys. Rev. Lett.* **69**, 2590–2593 (1992).
13. P. Azaria, B. Delamotte, D. Mouhanna, *Phys. Rev. Lett.* **70**, 2483–2486 (1993).
14. F. Zhou, *Phys. Rev. Lett.* **87**, 080401 (2001).
15. J. van Wezel, J. van den Brink, J. Zaanen, *Phys. Rev. Lett.* **94**, 230401 (2005).
16. C. K. Law, H. Pu, N. P. Bigelow, *Phys. Rev. Lett.* **81**, 5257–5261 (1998).
17. T.-L. Ho, S. K. Yip, *Phys. Rev. Lett.* **84**, 4031–4034 (2000).
18. M. Koashi, M. Ueda, *Phys. Rev. Lett.* **84**, 1066–1069 (2000).
19. Y. Castin, C. Herzog, *Comptes Rendus de l'Académie des Sciences Series IV Physics* **2**, 419 (2001).
20. S. Ashhab, A. J. Leggett, *Phys. Rev. A* **65**, 023604 (2002).
21. R. Barnett, J. D. Sau, S. Das Sarma, *Phys. Rev. A* **82**, 031602 (2010).
22. S. Yi, O. E. Müstecaplıoğlu, C. P. Sun, L. You, *Phys. Rev. A* **66**, 011601 (2002).
23. T.-L. Ho, *Phys. Rev. Lett.* **81**, 742–745 (1998).
24. T. Ohmi, T. Machida, *J. Phys. Soc. Jpn.* **67**, 1822–1825 (1998).
25. D. M. Stamper-Kurn, M. Ueda, *Rev. Mod. Phys.* **85**, 1191–1244 (2013).
26. Materials and methods are available as supplementary materials.
27. A. Qu, B. Evrard, J. Dalibard, F. Gerbier, *Phys. Rev. Lett.* **125**, 033401 (2020).
28. G. M. D'Ariano, M. G. A. Paris, M. F. Sacchi, in *Advances in Imaging and Electron Physics*, P. W. Hawkes, Ed. (Elsevier, 2003), vol. 128, pp. 205–308.
29. A. I. Lvovsky, *J. Opt. B Quantum Semiclassical Opt.* **6**, S556–S559 (2004).
30. H. Strobel *et al.*, *Science* **345**, 424–427 (2014).
31. J. Peise *et al.*, *Nat. Commun.* **6**, 6811 (2015).
32. V. Vedral, *Rev. Mod. Phys.* **74**, 197–234 (2002).
33. R. Islam *et al.*, *Nature* **528**, 77–83 (2015).
34. E. Demler, F. Zhou, *Phys. Rev. Lett.* **88**, 163001 (2002).
35. A. Imambekov, M. Lukin, E. Demler, *Phys. Rev. Lett.* **93**, 120405 (2004).
36. L. Zhao, J. Jiang, T. Tang, M. Webb, Y. Liu, *Phys. Rev. Lett.* **114**, 225302 (2015).
37. I. Urizar-Lanz, P. Hyllus, I. L. Egusquiza, M. W. Mitchell, G. Tóth, *Phys. Rev. A* **88**, 013626 (2013).
38. B. Evrard, A. Qu, J. Dalibard, F. Gerbier, Experimental datasets, theory curves, and codes for numerical simulations for: Observation of fragmentation of a spinor Bose-Einstein condensate, Zenodo (2021); https://doi.org/10.5281/zenodo.5070466.

ACKNOWLEDGMENTS

We thank T.-L. Ho, Y. Castin, and the members of the BEC group at Laboratoire Kastler Brossel (LKB) for insightful discussions and K. Jiménez-Garcìa for help in the design stage of the experiment. **Funding:** This work was supported by ERC (Synergy Grant UQUAM). LKB is a member of the SIRTEQ network of Région Ile-de-France. **Author contributions:** B.E. and A.Q. conducted the experiment and acquired the data. B.E. analyzed the experimental data and performed the numerical simulations. J.D. and F.G. supervised the work. All authors contributed to the final manuscript. **Competing interests:** The authors declare no competing interests. **Data and materials availability:** Datasets, theory curves, and codes for the numerical simulations are available on Zenodo (*38*).

SUPPLEMENTARY MATERIALS

https://science.org/doi/10.1126/science.abd8206
Materials and Methods
Supplementary Text
Figs. S1 to S9
Table S1
References (*39*–*50*)

14 July 2020; accepted 13 August 2021
10.1126/science.abd8206

FLUID MECHANICS

Three-dimensional capillary ratchet-induced liquid directional steering

Shile Feng[1,2]†, Pingan Zhu[1]†, Huanxi Zheng[1], Haiyang Zhan[2], Chen Chen[2], Jiaqian Li[1], Liqiu Wang[3], Xi Yao[4], Yahua Liu[2], Zuankai Wang[1,5]*

Conventional understanding has it that a liquid deposited on a surface tends to move along directions that reduce surface energy, which is mainly dictated by surface properties rather than liquid properties, such as surface tension. Achieving well-controlled directional steering remains challenging because the liquid-solid interaction mainly occurs in the two-dimensional (2D) domain. We show that the spreading direction of liquids with different surface tensions can be tailored by designing 3D capillary ratchets that create an asymmetric and 3D spreading profile both in and out of the surface plane. Such directional steering is also accompanied by self-propulsion and high flow velocity, all of which are preferred in liquid transport.

Directional liquid transport is ubiquitous and critical to a range of practical applications, such as microfluidics (*1*), chemical reaction (*2*), water harvesting (*3*, *4*), and enhanced heat transfer (*5*). Recent efforts have demonstrated the feasibility of the spontaneous, rapid, and long-distance liquid transport on surfaces that are designed with gradients in topography (*6*–*8*), wettability (*9*, *10*), or surface charge density (*11*). In all of these studies, the liquid driving force is mainly determined by the gradients imposed by surfaces (*12*, *13*), and thus for a fixed design, the spreading direction of a liquid is not selectable by its intrinsic properties (*14*, *15*). For example, a liquid prefers to flow from the high-surface-energy area to the low-surface-energy area (*16*), as exemplified on wettability gradient surfaces that are driven by the unbalanced capillary force (*9*, *17*); from the high-curvature region to the low-curvature region on conical wires because of the difference in Laplace pressure (*18*); and from the higher liquid-pinning side to the less liquid-pinning side on asymmetric structures that result from the differentiated dynamics of liquid spreading (*12*).

We examined an unexpected liquid transport behavior on the *Araucaria* leaf, which consists of three-dimensional (3D) ratchets with transverse and longitudinal reentrant curvatures that are characterized by the low-surface-tension liquids selecting a pathway along the ratchet-tilting direction, whereas high-surface-tension liquids select an opposite

[1]Department of Mechanical Engineering, City University of Hong Kong, Hong Kong SAR 999077, P. R. China. [2]Key Laboratory for Precision and Non-traditional Machining Technology of Ministry of Education, Dalian University of Technology, Dalian 116024, P. R. China. [3]Department of Mechanical Engineering, The University of Hong Kong, Hong Kong SAR 999077, P. R. China. [4]Department of Biomedical Sciences, City University of Hong Kong, Hong Kong SAR 999077, P. R. China. [5]Center for Nature-Inspired Engineering, City University of Hong Kong, Hong Kong SAR 999077, P. R. China.
*Corresponding author. Email: zuanwang@cityu.edu.hk
†These authors contributed equally to this work.

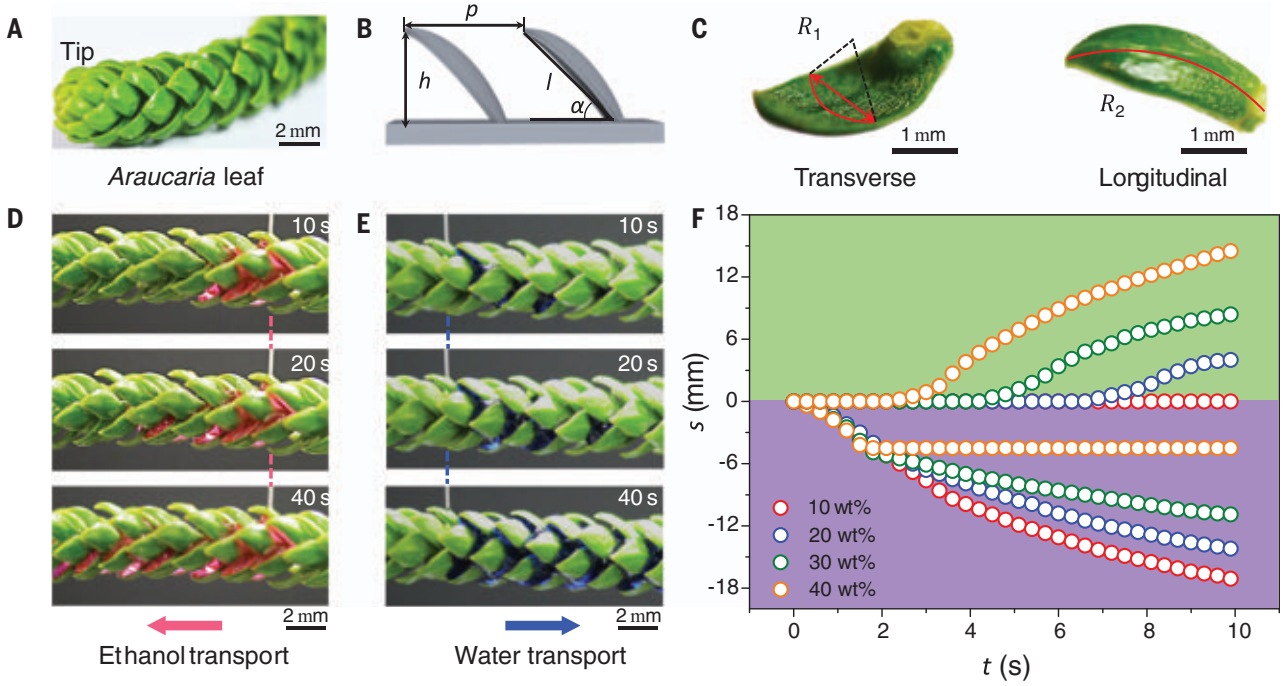


Fig. 1. Structural characteristics of *Araucaria* leaf for liquid directional steering. (**A**) Optical image of *Araucaria* leaf, which consists of periodically arranged ratchets tilting toward the leaf tip. (**B**) Structural characteristics of ratchet arrays. The height (h), tip-to-tip pitch (p), length (l), and tilt angle (α) of ratchets are ~2 mm, ~3 mm, ~2.6 mm, and ~40°, respectively. (**C**) Structural characteristics of a single ratchet. Each ratchet is endowed with the transverse curvature of radius R_1 and the longitudinal curvature of radius R_2. (**D** and **E**) Directional transport of ethanol and water on *Araucaria* leaf. Ethanol spreads along the ratchet-tilting direction (forward direction), whereas water spreads in the opposite direction (backward direction). (**F**) Transport distance (s) of water-ethanol mixtures with varied mass fraction (c) versus time (t) on *Araucaria* leaf. The transport distance s is positive for forward transport (green region) and negative for backward transport (purple region). For $c \leq 10\%$, the liquid only propagates in the backward direction with negative s; for $10 < c < 40\%$, the liquid transport is bidirectional; for $c \geq 40\%$, the liquid only propagates in the forward direction.

direction. Different from the conventional microstructures (*19*–*21*) that are widely used for directional liquid transport in the 2D domain (*22*–*26*), the *Araucaria* leaf and *Araucaria* leaf–inspired surface (ALIS) have 3D ratchets that enable liquid wicking both in and out of the surface plane. Moreover, the transverse and longitudinal reentrant curvatures impart asymmetric contact line pinning, which enables the directional steering and rapid transport of liquids with different surface tensions in a well-controlled manner.

The *Araucaria* leaf is found to consist of periodically arranged ratchets tilting toward the leaf tip (Fig. 1A). The height (h), pitch (p), length (l), and tilting angle (α) of ratchets are ~2 mm, ~3 mm, ~2.6 mm, and ~40°, respectively (Fig. 1B). Such ratchets exhibit dual-reentrant topography with a transverse curvature of radius R_1 and a longitudinal curvature of radius R_2 (Fig. 1C). The water and ethanol contact angles on the *Araucaria* leaf are ~59° and ~21°, respectively, suggesting a typical hydrophilic property (fig. S1). In contrast to our expectation, when continuously infusing water and ethanol (flow rate of 3 μl/s) on the *Araucaria* leaf, we found that ethanol spreads along the ratchet-tilting direction (Fig. 1D and movie S1A), whereas water propagates in an opposite direction (Fig. 1E and movie S1B). We define along the ratchet-tilting direction as the forward direction and against the ratchet-tilting direction as the backward direction.

We also investigated the liquid transport on the *Araucaria* leaf using water-ethanol mixtures that have different surface tensions (γ) and mass fractions of ethanol (c). Here, $c = m_e/(m_e + m_w)$, with m_e and m_w being the mass of ethanol and water, respectively. The correlation between γ and c is shown in fig. S2. When c ranges from 0 to 40%, γ decreases from 72 to 29 mN/m. The time-dependent variation of transport distance (s) is plotted in Fig. 1F for different water-ethanol mixtures. For $c \leq 10\%$, the liquid propagates only in the backward direction with negative s. For $10 < c < 40\%$, the liquid transport is bidirectional. For $c \geq 40\%$, the liquid propagates in the forward direction alone, although a slight backflow along the asymmetric ratchet was observed in the early stage of spreading (fig. S3).

Triggered by this observation, we implemented 3D printing to fabricate the ALIS. The ALIS consists of several parallel rows of ratchet arrays with pitch p = 750 μm, tilting angle α = 40°, height h = 800 μm, row-to-row width w = 1000 μm, interside-to-interside width d = 400 μm, R_1 = 400 μm, and R_2 = 650 μm (Fig. 2, A to C). We infused water-ethanol mixtures with c = 40% and c = 10% onto the ALIS at a flow rate of 3 μl/s, as shown in Fig. 2, D and E, respectively, and observed a similar transport behavior to that on the *Araucaria* leaf. The liquid mixture with c = 40% displays forward transport (Fig.

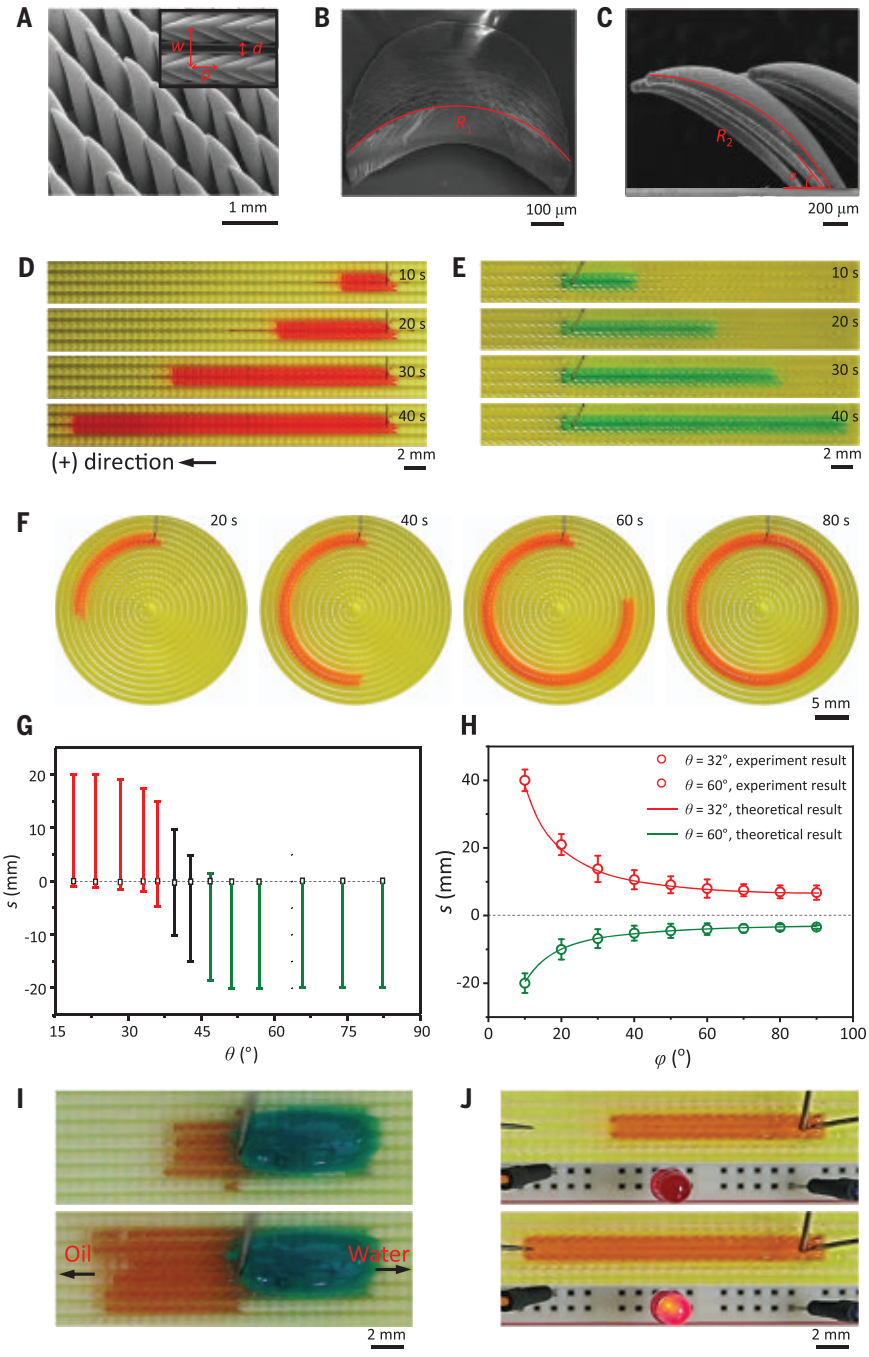


Fig. 2. Liquid directional steering on an ALIS. (**A** to **C**) Macro- and microstructures of ALIS. The row-to-row width w, interside-to-interside width d, and tip-to-tip pitch p are ~1000, 400, and 750 μm, respectively. The radii of transverse (R_1) and longitudinal (R_2) curvatures are ~400 and ~650 μm, respectively. The tilting angle of each ratchet is ~40°. (**D** and **E**) Transport of water-ethanol mixtures with c = 40% [red liquid (D)] and c = 10% [green liquid (E)] on ALIS. The liquid mixture with c = 40% displays forward transport, whereas that with c = 10% displays backward transport. (**F**) Directional spreading of liquid (θ = 32°) on circular ratchet arrays with a constant liquid width. (**G**) Variation in the transport distance s with contact angle θ, where s was measured after infusing the liquid for 60 s. As θ increases from ~20° to ~82°, the liquid transforms from forward transport to backward transport. (**H**) Plot of liquid transport on surfaces with different inclined angles φ (from 0° to 90°). The positive s stands for forward transport and negative s for backward transport. (**I**) Oil-water separation on ALIS. The liquid mixture contains water (dyed green) and oil (dyed red) with a volume ratio of 1:1. (**J**) Lighting up the light-emitting diode by directional transport of a conductive liquid on ALIS. The conductive liquid is a mixture of water, ethanol, and NaCl with a mass fraction of 40:9:1.

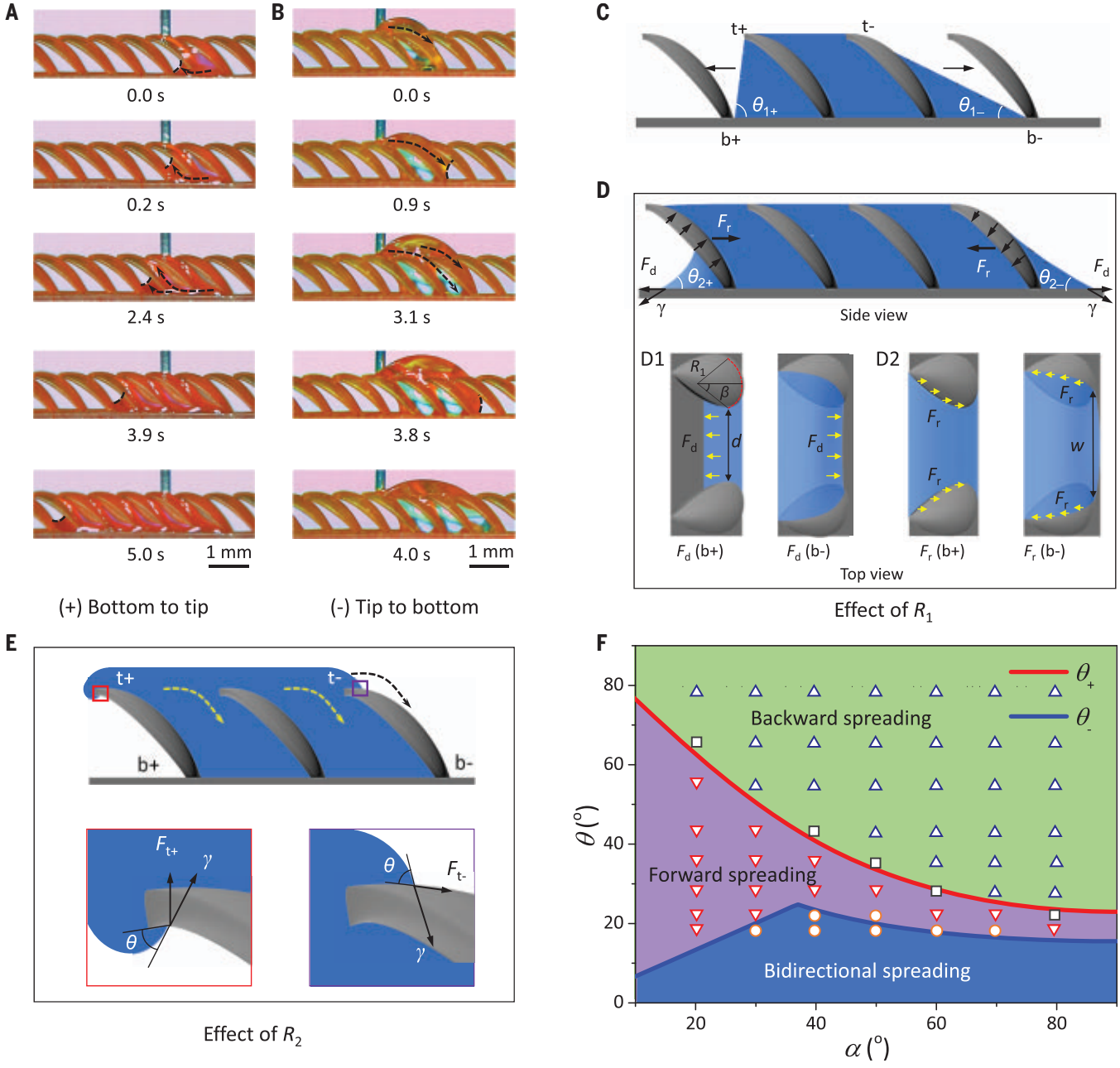


Fig. 3. Mechanism for liquid directional steering. (**A** and **B**) Two distinct spreading dynamics of liquids on ALIS. Liquid with θ = 32° wets the ratchet from bottom to top for forward spreading (A), whereas liquid with θ = 60° wets the ratchet from top to bottom for backward spreading (B). (**C**) Critical states for liquid spreading on ALIS. The symbols b+, b−, t+, and t− represent bottom-forward, bottom-backward, top-forward, and top-backward pinning sites, respectively. θ_{1+} and θ_{1-} are critical angles at which the liquid front reaches the b+ site and b− site, respectively. (**D**) Force analysis in the bottom-to-top wicking scenario with the transverse reentrant effect. The top-view schematics manifest the driving force at the bottom surface (D1) and the resistance force along the ratchets (D2) at the b+ site (left) and b− site (right), respectively. (**E**) Force analysis in the top-to-bottom wicking scenario with the longitudinal reentrant effect. In this scenario, the liquid is pinned at both the b+ and b− sites and subjected to asymmetric capillary forces at the t+ and t− sites. (**F**) Phase map for the directional steering of liquid transport. When $\theta_- < \theta < \theta_+$, liquid spreads forward (purple region marked with inverted triangle). When $\theta > \theta_+$, liquid spreads backward (green region marked with triangle). When θ is ~θ_+ (symbols marked with rectangle) or $\theta < \theta_- < \theta_+$ (blue region marked with circle), the liquid manifests a bidirectional transport.

2D and movie S2A), whereas the one with c = 10% displays backward transport (Fig. 2E and movie S2B). The width of the liquid barely changes during the spontaneous propagation on straight (Fig. 2, D and E) and circular (Fig. 2F and movie S3) ratchet arrays. These results are distinct from previous studies in which the liquid puddle gradually widens during spreading (*12*), which indicates the strong pinning of the liquid front by the curved shape of 3D ratchets (Fig. 2, B and C). Essentially, the ALIS can be treated as 3D capillary ratchets (*22*), whose characteristic lengths are comparable with the capillary length $l_c = (\gamma/\rho g)^{1/2}$. Here, γ, ρ, and g are the liquid surface tension, liquid density, and gravitational acceleration, respectively.

The transport distance s of liquids with different surface tensions γ on the ALIS is plotted

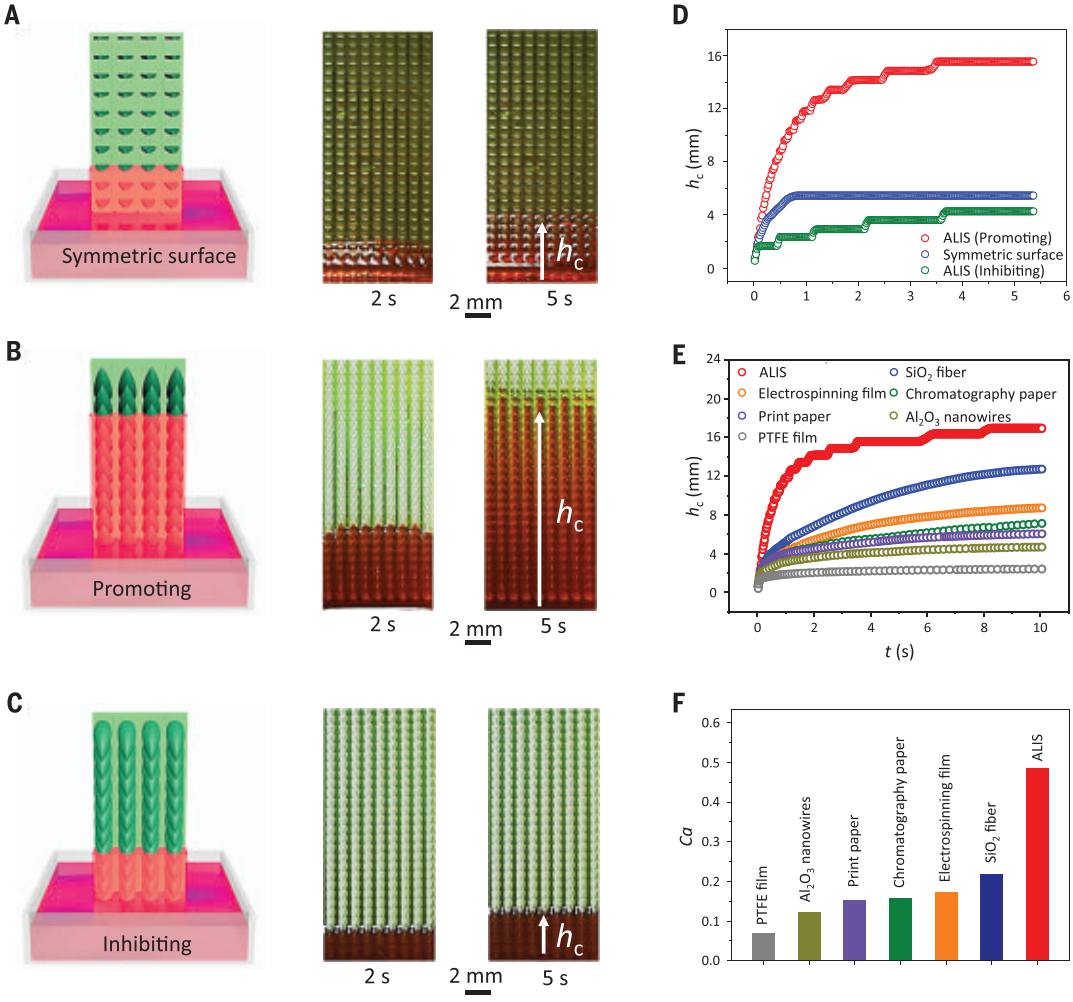


Fig. 4. Promoting or inhibiting capillary rise by the ALIS. (**A**) Capillary rise of liquid on a symmetric surface. The height of capillary rise h_c reaches ~6 mm in 5 s. (**B**) Promoting capillary rise on ALIS when the ratchet is tilting upward. h_c reaches ~16 mm in 5 s. (**C**) Inhibiting capillary rise on ALIS with ratchet tilting downward. h_c is only ~4 mm in 5 s. (**D**) Variation of capillary rise height h_c as a function of time t on ALIS and symmetric surface. (**E** and **F**) Height h_c (E) and capillary number Ca (F) on various surfaces, including polytetrafluoroethylene (PTFE) membrane, print paper, SiO_2 fibers, Al_2O_3 nanowires, electrospinning film, chromatography paper, and ALIS. $Ca = V\eta/\gamma$, representing the dimensionless velocity in which the average wicking velocity V (measured in the first 1.5 s) is normalized by the characteristic capillary velocity γ/η, denoting γ and η as the surface tension and viscosity of liquids, respectively. Both the height and velocity on the ALIS (in promoting mode) are much larger than those on other surfaces during the same transport period.

in Fig. 2G, where s was measured after infusing liquids for 60 s. The liquid contact angles increase with the surface tension of liquids on a flat surface with the same material as that of the ALIS (fig. S4). We found that as the equilibrium contact angle (θ) increases from ~20° to ~82°, the transport direction is reversed from forward to backward, during which the crossover occurs at θ = 42° ± 5°, featuring a bidirectional mode (Fig. 2G and figs. S5 and S6). These observations suggest that the spreading direction of liquids on a predetermined ALIS can be selected, with high-surface-tension liquids preferring the backward direction, whereas low-surface-tension liquids select the forward direction. Such directional steering is still maintained when the ALIS is placed under a tilt angle φ (0° < φ ≤ 90°), although the transport distance s becomes reduced with an increase in φ (Fig. 2H). The measured s shows good agreement with the theoretical data predicted by $s = [(\cos\theta - \cos\theta_c)\gamma]/(\rho g h \cos\theta_c \sin\varphi)$, for which we denote θ_c, ρ, and g as the critical contact angle for capillary wicking (*27*), liquid density, and gravitational acceleration, respectively (fig. S7). The liquid spreading is almost self-propelled at a low liquid-flow rate (~3 μl/s), above which the inertia effect starts to become non-negligible (fig. S8).

The well-controlled selection of liquid spreading direction can be harnessed for immiscible water-oil (such as dichloroethane) separation. When infusing a water-oil mixture on the ALIS with a volume ratio of 1:1, the oil and water display opposite transport directions, and a complete separation is achieved without the need of gravity (Fig. 2I), as opposed to existing separation strategies. In addition, the unidirectional transport of water on the ALIS can be used to switch on the originally isolated circuit and light up a light-emitting diode, which provides a simple route to construct a fluidic gate (Fig. 2J).

To explain the mechanisms responsible for the liquid directional steering, we first examined contact lines of two representative liquids with θ = 32° and θ = 60°. Initially, when being filled in an asperity between two adjacent ratchets (Fig. 3, A and B), liquids are confined by four critical sites (fig. S9) at the bottom forward (b+), bottom backward (b–), top forward (t+), and top backward (t–). Liquid with θ = 32° first breaks the pinning at the b+ site and then wets the ratchet from bottom to top. As it rises, a new cycle of bottom-to-top rising occurs, leading to a continuous, long-range propagation in the forward direction (Fig. 3A, fig. S10A, and movie S4A). By contrast, the liquid with θ = 60° is pinned at both the b+ and b– sites, selects the pathway toward the top (t+ and t–) sites, and propagates along the backward direction through a continuous top-to-bottom wicking (Fig. 3B, fig. S10B, and movie S4B).

We then resorted to a force analysis (*28*, *29*) to probe how a liquid selects its spreading direction (Fig. 3, C to E). For the bottom-to-top rising scenario (Fig. 3A), the spontaneous transport in a preferential direction requires two conditions. First, the liquid should be able to reach the next ratchet, which requires a smaller-equilibrium liquid contact angle compared with two critical angles defined by surface geometry, θ_{1+} and θ_{1-} (Fig. 3C), which are expressed as $\theta_{1+} = \arctan[l\sin\alpha/(p - l\cos\alpha)]$ and $\theta_{1-} = \arctan[l\sin\alpha/(p + l\cos\alpha)]$, respectively (fig. S11). Second, driving forces on the

liquid front should be large enough to overcome the pinning effect. For an ALIS, the distinct structures generate a driving force (F_d) at the contact line at the bottom surface (Fig. 3D, side and top view of D1), as well as a resistance force (F_r) at the contact line along the ratchets (Fig. 3D, side and top view of D2). Briefly, at the b+ site, F_d scales as $\sim d\gamma\cos\theta$ and $F_r \sim 2l\gamma\sin\alpha\sin(\theta + \beta)$, where β is the semiangle for the transverse ratchet arc (Fig. 3D). Balancing F_d with F_r, we have a critical angle $\theta_{2+} = \arccos[2l\sin\alpha\sin(\theta_{2+} + \beta)/d]$. Similarly, at the b− site, another critical angle, $\theta_{2-} = \arctan[w/(2l\sin\alpha)]$, is derived by balancing $F_d = w\gamma\cos\theta$ and $F_r = 2l\gamma\sin\alpha\sin\theta$ (figs. S12 and S13). The presence of a transverse reentrant curvature creates an apparent difference in θ_{2+} and θ_{2-} on one surface (Fig. 3D), opening up the room for liquids to exhibit an asymmetric spreading and to select direction along the surface.

By combining the above force analysis, the forward transport through a continuous, bottom-to-top rising demands that the equilibrium liquid contact angle falls between $\theta_- < \theta < \theta_+$ (Fig. 3F), where $\theta_+ = \min[\theta_{1+}, \theta_{2+}]$ and $\theta_- = \min[\theta_{1-}, \theta_{2-}]$ (fig. S14). Taking $\alpha = 40°$, for example, θ_+ and θ_- predicted by our model are 42° and 23°, respectively. When $23° < \theta < 42°$, we expect a forward spreading, which was indeed observed in our experiments (Fig. 3F).

Although the above force analysis can successfully explain the pinning at the bottom surface (in plane) and predict the spreading direction, it is incapable of explaining the pinning effect at the top of the 3D surface (out of the plane). For $\theta > \theta_+$, an asymmetric pinning and subsequent backward spreading through a top-to-bottom wicking were observed in Fig. 3B. To elucidate this unexpected phenomenon, we further considered the reentrant effect of longitudinal curvature. The reentrant structure at the t+ site produces an upward capillary force normal to the ratchet surface, written as $F_{t+} = \gamma\sin\theta$, that pins the liquid at the asperity of the ALIS (Fig. 3E, schematic in red rectangle). However, such a pinning effect is absent at the t− site, where a driving force along the surface ($F_{t-} = \gamma\cos\theta$) is present (Fig. 3E, schematic in purple rectangle). Under such a force asymmetry imposed by the longitudinal reentrant effect, a backward flow is favorably selected for liquid with $\theta > \theta_+ = 42°$ for the ALIS with $\alpha = 40°$.

The cooperation between the transverse and longitudinal reentrant curvature imparts an asymmetric force pinning in a 3D profile. By contrast, control surfaces without the presence of 3D capillary ratchets, including 1D stripes (fig. S15A) and 2D ratchets (fig. S15B), are only associated with contact line pinning in the plane. Thus, liquids of different surface tensions can only manifest a unidirectional transport in one way or bidirectional spreading (fig. S15 and movies S5 and S6), which eliminates the possibility for direction selection. Otherwise, a dynamic top-to-bottom wicking on the surface and subsequent spreading will not occur (*21*).

To fully build the phase map for the liquid spreading, we also considered the bidirectional transport that occurs in the transitioning region when $\theta \approx \theta_+$ (Fig. 3F, rectangles) or $\theta < \theta_- < \theta_+$ (Fig. 3F, blue region, circles). In particular, in the first case, the bidirectional transport is characterized by the manifestation of both bottom-to-top rising (forward mode) and top-to-bottom wicking (backward mode), as evidenced in our experimental visualization (fig. S6 and movie S7).

The liquid directional steering can be mutually used to promote liquid transportation such as in textile dying (*30*), inkjet printing (*31*, *32*), and seawater desalination (*33*) or to inhibit liquid wicking such as in anticorrosion and microbial spreading. To demonstrate this, we first investigated liquid transport on a surface with symmetric ratchets ($\alpha = 90°$). When the surface is inserted into a bath of ethanol, a capillary rise with a height (h_c) of ~6 mm is achieved within 5 s (Fig. 4A and movie S8). By contrast, the capillary rise on the ALIS is ~16 mm (Fig. 4B and movie S9), suggesting a notable enhancement in the spreading. However, the capillary rise can also be inhibited by designing an ALIS with the ratchet structures arranged downward (Fig. 4C and movie S10), which can be used in certain conditions in which a minimal liquid propagation is preferred. The role of the 3D capillary ratchets in promoting or inhibiting liquid wicking (Fig. 4D) is further illustrated by comparing capillary rise heights (Fig. 4E and fig. S16) on different samples, including polytetrafluoroethylene membrane, print paper, silicon dioxide (SiO_2) fibers, aluminium oxide (Al_2O_3) nanowires, electrospinning film, and chromatography paper. At the beginning of capillary rise, the measured height is consistent with that predicted by the Washburn law, which follows $h_c \sim [2\gamma h(\cos\theta - \cos\theta_c)t/3\eta\cos\theta_c]^{1/2}$ (*27*, *34*). Later, gravity becomes important, and h_c diverges on different surfaces (fig. S16). In Fig. 4F, we compare the wicking velocities on different samples, which demonstrates the intriguing prospect of the ALIS in achieving rapid liquid transport without the need for nanoscale structures. Taken together, our work demonstrates that the 3D capillary ratchets can be cleverly harnessed to impart many advantages for fluid flow, such as well-controlled directional steering, self-propulsion, high velocity, and long-distance transport.

REFERENCES AND NOTES

1. R. Seemann, M. Brinkmann, T. Pfohl, S. Herminghaus, *Rep. Prog. Phys.* **75**, 016601 (2012).
2. H. A. Stone, A. D. Stroock, A. Ajdari, *Annu. Rev. Fluid Mech.* **36**, 381–411 (2004).
3. Y. Zheng *et al.*, *Nature* **463**, 640–643 (2010).
4. K. C. Park *et al.*, *Nature* **531**, 78–82 (2016).
5. J. Li *et al.*, *Nat. Phys.* **12**, 606–612 (2016).
6. K. H. Chu, R. Xiao, E. N. Wang, *Nat. Mater.* **9**, 413–417 (2010).
7. Q. Wang, X. Yao, H. Liu, D. Quéré, L. Jiang, *Proc. Natl. Acad. Sci. U.S.A.* **112**, 9247–9252 (2015).
8. H. Chen *et al.*, *Nature* **532**, 85–89 (2016).
9. M. K. Chaudhury, G. M. Whitesides, *Science* **256**, 1539–1541 (1992).
10. N. A. Malvadkar, M. J. Hancock, K. Sekeroglu, W. J. Dressick, M. C. Demirel, *Nat. Mater.* **9**, 1023–1028 (2010).
11. Q. Sun *et al.*, *Nat. Mater.* **18**, 936–941 (2019).
12. J. Li *et al.*, *Sci. Adv.* **3**, eaao3530 (2017).
13. C. Li *et al.*, *Proc. Natl. Acad. Sci. U.S.A.* **116**, 12704–12709 (2019).
14. P. Comanns *et al.*, *J. R. Soc. Interface* **12**, 20150415 (2015).
15. Y. Liu *et al.*, *Small* **16**, e1901819 (2020).
16. J. C. Bird, S. Mandre, H. A. Stone, *Phys. Rev. Lett.* **100**, 234501 (2008).
17. S. Daniel, M. K. Chaudhury, J. C. Chen, *Science* **291**, 633–636 (2001).
18. C. Lv *et al.*, *Phys. Rev. Lett.* **113**, 026101 (2014).
19. A. Tuteja *et al.*, *Science* **318**, 1618–1622 (2007).
20. T. L. Liu, C.-J. C. Kim, *Science* **346**, 1096–1100 (2014).
21. W. Choi, A. Tuteja, J. M. Mabry, R. E. Cohen, G. H. McKinley, *J. Colloid Interface Sci.* **339**, 208–216 (2009).
22. M. Prakash, D. Quéré, J. W. Bush, *Science* **320**, 931–934 (2008).
23. C. Liu, J. Ju, Y. Zheng, L. Jiang, *ACS Nano* **8**, 1321–1329 (2014).
24. J. Li *et al.*, *Small* **16**, e1901751 (2020).
25. S. Feng *et al.*, *Sci. Adv.* **6**, eabb4540 (2020).
26. H. Linke *et al.*, *Phys. Rev. Lett.* **96**, 154502 (2006).
27. J. Bico, C. Tordeux, D. Quéré, *Europhys. Lett.* **55**, 214–220 (2001).
28. P. A. Zhu *et al.*, *Mater. Horiz.* **5**, 1156–1165 (2018).
29. X. Tian, V. Jokinen, J. Li, J. Sainio, R. H. A. Ras, *Adv. Mater.* **28**, 10652–10658 (2016).
30. M. T. Tyree, *Nature* **423**, 923–923 (2003).
31. S. Zheng *et al.*, *Adv. Funct. Mater.* **28**, 1800832 (2018).
32. J. Z. Wang, Z. H. Zheng, H. W. Li, W. T. Huck, H. Sirringhaus, *Nat. Mater.* **3**, 171–176 (2004).
33. L. Wu *et al.*, *Nat. Commun.* **11**, 521 (2020).
34. E. W. Washburn, *Phys. Rev.* **17**, 273–283 (1921).

ACKNOWLEDGMENTS

Funding: We acknowledge financial support from the Research Grants Council of Hong Kong (C1006-20WF, 11213320, and 17205421), Shenzhen Science and Technology Innovation Council (JCYJ20170413141208098), Innovation Technology Fund (GHP/021/19SZ), Tencent Foundation through the XPLORER PRIZE, National Natural Science Foundation of China (52005075), Fundamental Research Funds for the Central Universities [DUT19RC(3)055], and Star Ocean Outstanding Talents Program. **Author contributions:** S.F. and Z.W. conceived the research. Z.W. supervised the research. S.F. carried out the experiment. Hu.Z. and Ha.Z. prepared the samples, and C.C. and Y.L. designed the experimental apparatus. S.F., P.Z., and J.L. developed the theoretical model. L.W. and X.Y. examined and polished the manuscript. All authors analyzed data and wrote the paper. **Competing interests:** The authors declare no competing financial interests. **Data and materials availability:** All data are available in the main text or the supplementary materials.

SUPPLEMENTARY MATERIALS

https://science.org/doi/10.1126/science.abg7552
Materials and Methods
Figs. S1 to S16
Movies S1 to S10

26 January 2021; accepted 13 August 2021
10.1126/science.abg7552

CRISPR

The gRAMP CRISPR-Cas effector is an RNA endonuclease complexed with a caspase-like peptidase

Sam P. B. van Beljouw[1,2], Anna C. Haagsma[1,2], Alicia Rodríguez-Molina[1,2], Daan F. van den Berg[1,2], Jochem N. A. Vink[1,2], Stan J. J. Brouns[1,2]*

Type III CRISPR-Cas immunity is widespread in prokaryotes and is generally mediated by multisubunit effector complexes. These complexes recognize complementary viral transcripts and can activate ancillary immune proteins. Here, we describe a type III-E effector from *Candidatus* "Scalindua brodae" (*Sb*-gRAMP), which is natively encoded by a single gene with several type III domains fused together. This effector uses CRISPR RNA to guide target RNA recognition and cleaves single-stranded RNA at two defined positions six nucleotides apart. *Sb*-gRAMP physically combines with the caspase-like TPR-CHAT peptidase to form the CRISPR-guided caspase (Craspase) complex, suggesting a potential mechanism of target RNA–induced protease activity to gain viral immunity.

Facing constant predation by viruses and other mobile genetic elements (MGEs), prokaryotes have evolved multiple defense systems to protect themselves (*1*). Among these are the CRISPR-Cas systems, which provide adaptive immunity. Invaders are recognized and inactivated by effector ribonucleoprotein complexes, and during this process genetic memory of the invader is generated and stored as spacers in CRISPR arrays (*2*). CRISPR-Cas effector complexes consist of CRISPR-associated (Cas) proteins bound to CRISPR RNA (crRNA) derived from a long transcript of the precursor CRISPR array (pre-crRNA) (*3*). Complementary binding of the crRNA to a target nucleic acid signifies the detection of an invader, setting the immune reaction in motion. Depending on the type of effector protein, immunity is typically reached either through direct cleavage of the invader's genetic material or by the activation of ancillary nucleases. CRISPR-Cas type III proteins encompass both functionalities, making them among the most sophisticated CRISPR-Cas effector proteins known to date (*4*).

Recently, a new CRISPR-Cas subtype that resembles type III systems was bioinformatically predicted and classified as type III-E (*5*). Although type III-E effectors are related to other type III effectors (Fig. 1A), they are quite different in terms of protein architecture. Whereas type III effectors are typified by a multisubunit composition, the type III-E effector seems to have various repeat-associated mysterious protein (RAMP) domains fused together, hence the nickname g(iant)RAMP (*5*). The unusual size of ~1300 to 1900 amino acids makes gRAMP the largest single-unit effector found to date (Fig. 1B). We found that spacers embedded in type III-E CRISPR arrays have targets in MGEs (Fig. 1C and table S1) with a bias toward targeting the coding strand of open reading frames (Fig. 1D), indicating that gRAMP activity likely involves interaction with invader mRNA. Some type III-E loci carry Cas1 fused to a reverse transcriptase (fig. S1), suggesting that the type III-E acquisition machinery actively selects spacers from RNA (*6*). Curiously, the gRAMP gene clusters lack ancillary nuclease genes but often co-occur with a gene encoding a TPR-CHAT protein (fig. S1) (*5*), a caspase-like peptidase found to be involved in regulated bacterial cell death (*7*). This is suggestive of a functional relation between the CRISPR-Cas and caspase families in type III-E antiviral activity that we sought to uncover in the present study.

To investigate the molecular composition and function of the gRAMP protein, we selected gRAMP from the type III-E locus in *Candidatus* "Scalindua brodae" (*Sb*-gRAMP) (Fig. 1E) (*8*). We introduced an *Escherichia coli* codon optimized version of this protein into *E. coli*, together with a plasmid containing five copies of the first spacer from the native CRISPR array (Fig. 2A and table S2). We purified *Sb*-gRAMP to apparent homogeneity in three consecutive chromatography steps and observed distinct 260-nm absorption during size exclusion chromatography (SEC), indicative of copurifying nucleic acids (fig. S2). Multiangle light scattering (MALS) analysis indicated a homogeneous particle of 242.5 ± 2.4 kDa (Fig. 2B), consistent with the expected size for a *Sb*-gRAMP monomer bound to a single-stranded RNA (ssRNA) species in the range of 45 to 60 nucleotides (nt) (see the supplementary text and table S3). Subsequent protein analysis showed a single band at the expected size for *Sb*-gRAMP (Fig. 2C). Nucleic acid extraction revealed the presence of three well-defined RNA populations, of which the population at ~50 nt represents mature crRNA (Fig. 2D). These observations were reproducible when coexpressing *Sb*-gRAMP with a different repeat-spacer pair (fig. S3, A to D), demonstrating that *Sb*-gRAMP can be loaded with a crRNA of choice.

The *Candidatus* "Scalindua brodae" type III-E locus contains a CRISPR array comprising 11 spacers interspaced by a 36-nt repeat sequence (table S2). To investigate the characteristics of mature crRNA in more detail, we used polymerase chain reaction to amplify the native CRISPR array from *Candidatus* "Scalindua brodae" genomic DNA and coexpressed it with *Sb*-gRAMP. After RNA extraction (fig. S4) and RNA sequencing (Fig. 2E and fig. S5), we determined that this RNA contains an unusually long 5′ handle of predominantly 27 to 28 nt, including the conserved last 14 nt of the repeat (Fig. 2F and fig. S6). Although a dominant spacer portion of 20 nt was observed, by far most mature crRNAs were truncated within a window of 16 to 25 nt (Fig. 2F and figs. S3E and S6B), suggestive of less-specific processing on the 3′ end of the crRNA. In other type III systems, dedicated proteins (e.g., Cas6) are required for the generation of mature crRNA from pre-crRNA (*9*). Our discovery of spacer-sized RNA bound to *Sb*-gRAMP, combined with the absence of genes known to be involved in pre-crRNA processing (fig. S1), suggests that *Sb*-gRAMP might be capable of processing its own pre-crRNA, similar to Cas12 and Cas13 (*10*, *11*). The larger RNA molecules bound by *Sb*-gRAMP might represent pre-crRNA processing intermediates. We obtained lower *Sb*-gRAMP protein yields and more degraded forms of *Sb*-gRAMP without the provision of pre-crRNA (Fig. 2G), suggesting an essential stabilizing or chaperoning role for the crRNA in *Sb*-gRAMP-crRNA complex formation. These results demonstrate that the *Sb*-gRAMP protein and a crRNA of typically 47 nt form a single ribonucleoprotein complex.

Given the apparent structural domain homology between *Sb*-gRAMP and subunits of other type III effectors, it seems plausible that *Sb*-gRAMP has evolved through a series of domain fusions and insertions. *Sb*-gRAMP contains a small domain with remote resemblance to Cas11 (Csm2) and four domains that have structural homology to Cas7 (Csm3/Cmr4) subunits, one with a large insertion (Fig. 1E) (*5*). Because Csm3/Cmr4 have been demonstrated to be responsible for target RNA cleavage in other type III systems (*12*, *13*), we set out to investigate whether *Sb*-gRAMP also has endoribonuclease activity. We incubated purified *Sb*-gRAMP-crRNA with fluorescently labeled ssRNA substrates complementary to crRNA of spacer 1 (Fig. 3A) or spacer 3 (fig. S7A) and observed two well-defined RNA cleavage products (Fig. 3B and fig. S7B), with the smaller product accumulating over time (fig. S8). Most

[1]Department of Bionanoscience, Delft University of Technology, Delft, Netherlands. [2]Kavli Institute of Nanoscience, Delft, Netherlands.
*Corresponding author. Email: stanbrouns@gmail.com

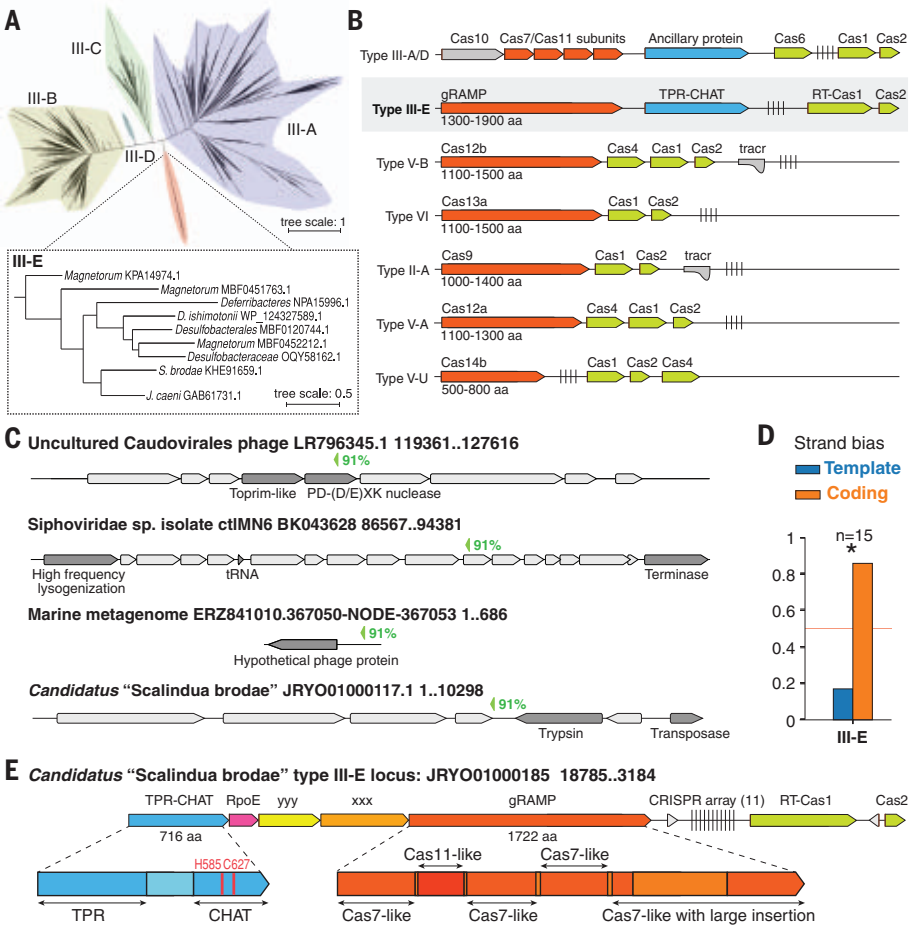


Fig. 1. CRISPR-Cas type III-E composition and characteristics. (**A**) Phylogenetic tree of type III subunit proteins (Csm3 and Cmr4) compiled with type III-E gRAMPs. The tree scale bar represents the number of substitutions per site. (**B**) Illustrations of typical organization of CRISPR-Cas types with sizes of effector proteins indicated in the number of amino acids (*25*). (**C**) Examples of contigs with matches to spacers from type III-E CRISPR arrays. (**D**) Fraction of spacers found in type III-E CRISPR arrays targeting template or coding strand (P = 0.011). (**E**) Detailed outline of the type III-E locus from *Candidatus* "Scalindua brodae."

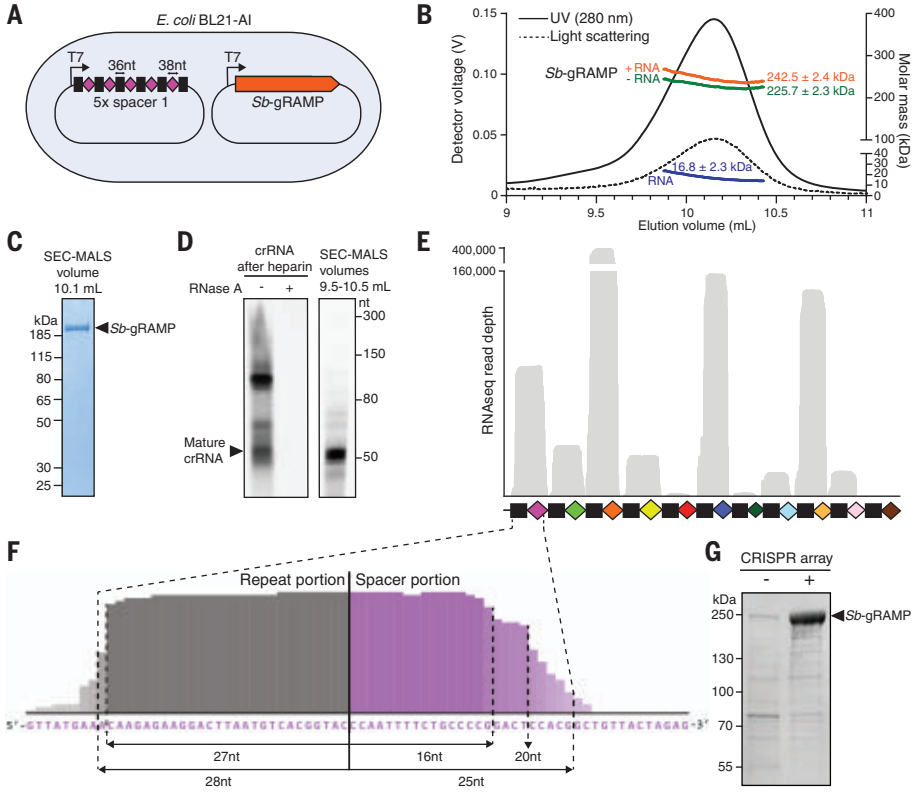


Fig. 2. *Sb*-gRAMP-crRNA is a ribonucleoprotein encoded by a single open reading frame. (**A**) Schematic of the heterologous expression system used for *Sb*-gRAMP-crRNA1 overexpression. (**B**) SEC-MALS peaks corresponding to light-scattering and ultraviolet absorbance at 280 nm (UV_{280}) profiles of purified *Sb*-gRAMP-crRNA1. The molar masses are derived from the peak half-height region (9.9 to 10.4 ml). (**C**) SDS–polyacrylamide gel electrophoresis (PAGE) analysis after SEC-MALS. (**D**) Denaturing urea PAGE analysis of the nucleic acid content in *Sb*-gRAMP-crRNA1. (**E**) RNA-sequencing reads of native crRNA with length 40 to 60 nucleotides mapped onto the native CRISPR array from *Candidatus* "Scalindua brodae." (**F**) RNA-sequencing read depth of the first repeat spacer with predominant repeat and spacer lengths indicated based on consensus processing. (**G**) SDS-PAGE analysis of *Sb*-gRAMP protein expressed in the absence and presence of a CRISPR array with five copies of spacer 1 (crRNA1).

target RNA remained uncleaved even at twofold molar excess of gRAMP (fig. S9), suggesting that endoribonuclease activity only proceeds with a limited substrate turnover. Counting from the 5′ side of the crRNA into the target, the cleavage sites were located after nucleotides 3 (site 1) and 9 (site 2) relative to the crRNA, thus 6 nt apart (Fig. 3B and figs. S7C and S10). When we tested target RNA substrates with the fluorescent label on the 3′ end instead of the 5′ end, two smaller cleavage products accumulated with a 6-nt interval (Fig. 3B and fig. S11). This nucleotide spacing between cleavage sites is reminiscent of the 6-nt periodicity found for other type III effector complexes (*14*, *15*), suggesting that the *Sb*-gRAMP retained the ancestral architectural positioning after domain fusion and insertion events. Also analogous to other type III effectors (*16*), complementarity between the protospacer flanking sequence (PFS) and the repeat portion of the crRNA retained the cleavage activity and positioning of *Sb*-gRAMP-crRNA within the complementary region of target RNA (Fig. 3C). Incubation of *Sb*-gRAMP-crRNA with an ssDNA target or noncomplementary ssRNA substrate did not yield cleavage products (Fig. 3D). We also did not observe collateral RNase activity in the presence of a target RNA (fig. S12), demonstrating that *Sb*-gRAMP is a sequence- and position-specific crRNA-guided RNA endonuclease.

The CRISPR-Cas type III Csm3 and Cmr4 domains harbor acidic residues essential for metal-ion coordination and subsequent ribonuclease catalysis (*14*, *15*, *17*). The removal of divalent cations from the cleavage buffer abolished *Sb*-gRAMP-crRNA ability to cleave target RNA (Fig. 3E), showing that RNase activity was dependent on metal ions. This raised the possibility that *Sb*-gRAMP has acidic amino acid residues essential for a functional endoribonuclease active site, akin to ancestral Csm3/Cmr4. To test this, we identified seven conserved aspartic acids and one serine residue that might be active in the ribonuclease catalytic core, based on multiple sequence alignment of various gRAMPs (fig. S13) and structural similarity to the *Streptococcus thermophilus* Csm3 (*12*) (fig. S14). Mutational analysis of these positions indeed revealed that *Sb*-gRAMP-crRNA lost its target RNA cleavage ability at site 2 upon changing a single aspartic acid residue to an alanine (D698A) (Fig. 3F). The single amino acid change renders a *Sb*-gRAMP variant able to sequence specifically cleave target RNA only at site 1, which may provide distinct benefits for biotechnological applications in which specific single RNA cleavage is desired. Despite trying the eight positions (fig. S15), the low sequence similarity of gRAMPs to Csm3/Cmr4 did not permit identifying essential active site residues responsible for the cleavage at site 1 and may require structural analysis. Currently described type III effectors cleave RNA once per Csm3/Cmr4 subunit; *Sb*-gRAMP, composed of four Csm3-like domains, only cleaved twice under our experimental conditions (Fig. 3G). This suggests that the other ribonuclease domains were either rendered dysfunctional over time or evolved into other functionalities.

In canonical type III systems, RNA target recognition with mismatching PFS leads to the activation of the cyclase domain in the Cas10 subunit, which in turn synthesizes cyclic oligo adenylates (cOAs) (*18*, *19*). The cOAs act as allosteric activators of ancillary proteins often found in or near the CRISPR-Cas loci by binding in the CRISPR-associated Rossmann fold (CARF) domain (*20*). It appears that the Cas10 subunit as well as CARF-containing proteins were lost during the evolutionary genesis of gRAMP (*5*). Because this makes cOA signaling in type III-E unlikely, we wondered what the functional relation could be with the co-occurring caspase-like protease TPR-CHAT (fig. S1) (*5*). The tetratricopeptide repeat (TPR) domain is often involved in protein-protein interaction and the formation of protein complexes (*21*), which prompted us to test physical association between TPR-CHAT and *Sb*-gRAMP-crRNA.

To assess potential interaction, we affinity purified either *Sb*-gRAMP-crRNA or TPR-CHAT from cells that coexpressed both proteins (Fig. 4A) and observed co-elution using either protein as a bait (Fig. 4B and fig. S16A). This indicated the formation of a stable complex between *Sb*-gRAMP-crRNA and TPR-CHAT (table S4), the interaction of which was retained during subsequent heparin chromatography and SEC (Fig. 4B and fig. S17). MALS revealed a single, homogeneous population with a molar mass of 315.4 ± 2.8 kDa (Fig. 4C and fig. S18), corresponding to *Sb*-gRAMP-crRNA

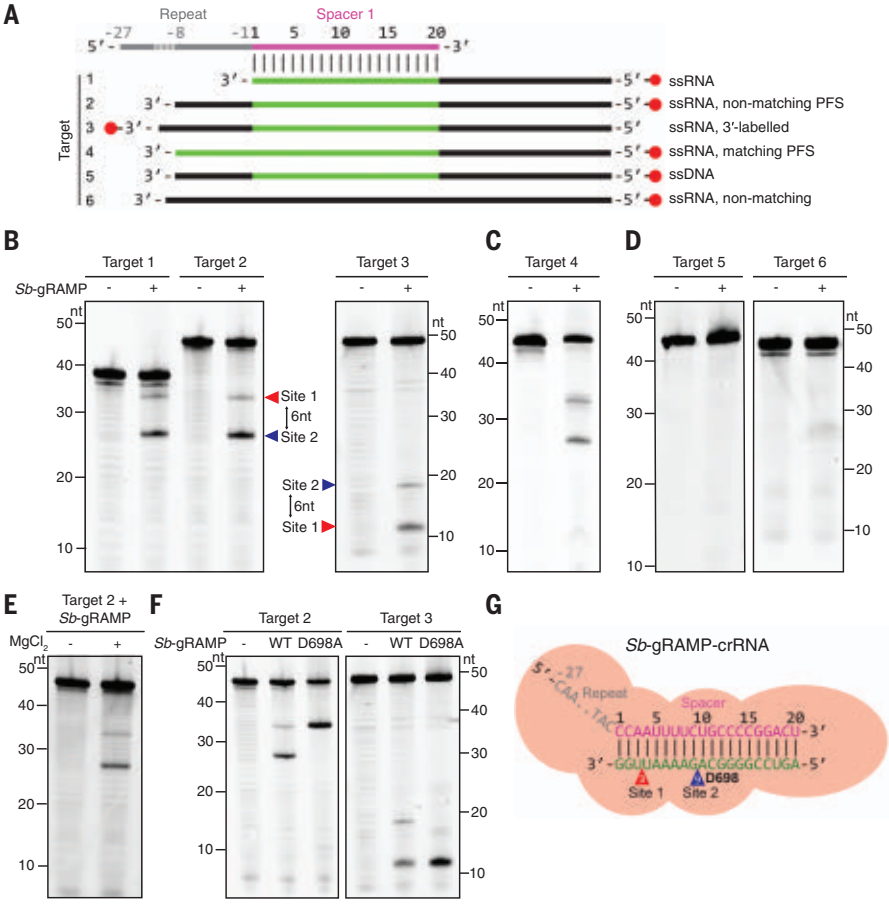


Fig. 3. *Sb*-gRAMP-crRNA drives dual ssRNA cleavage with 6-nt spacing. (**A**) Outline of the Cy5-labeled nucleic acid targets tested for *Sb*-gRAMP-crRNA1 activity. (**B** to **F**) Denaturing urea PAGE gels of *Sb*-gRAMP-crRNA1 incubated with complementary ssRNA [(B), cleavage products are indicated with arrowheads], ssRNA with a matching PFS (C), complementary ssDNA and noncomplementary ssRNA (D), and complementary ssRNA in the presence or absence of $MgCl_2$ (E) and with *Sb*-gRAMP-crRNA1 containing the D698A-inactivating mutation (F). (**G**) Schematic of *Sb*-gRAMP-crRNA1 hybridized to an ssRNA target with the exact cleavage sites indicated.

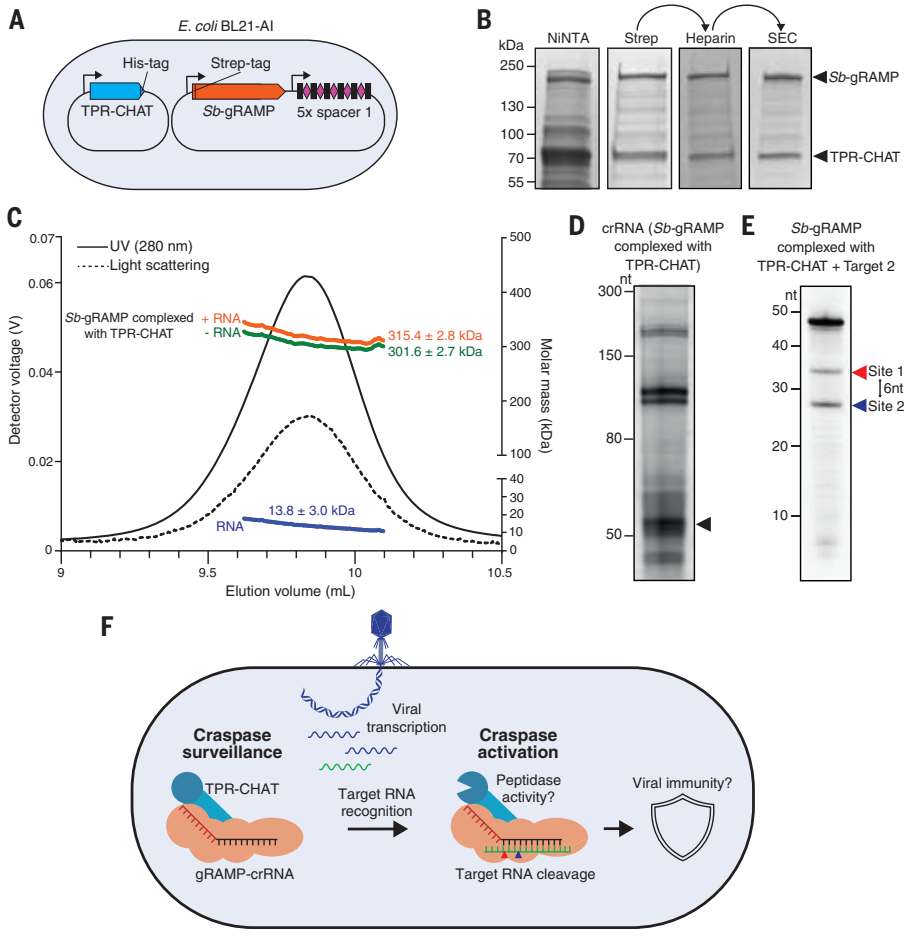


Fig. 4. *Sb*-gRAMP-crRNA and TPR-CHAT form the stable Craspase complex. (**A**) Schematic of the expression system used for overexpression of TPR-CHAT and *Sb*-gRAMP-crRNA1. (**B**) SDS-PAGE gels after the subsequent purification steps of *Sb*-gRAMP-crRNA1 complexed with TPR-CHAT. (**C**) SEC-MALS light-scattering UV_{280} absorbance profiles of *Sb*-gRAMP-crRNA1 complexed with TPR-CHAT. Molar masses are derived from the peak half-height region (9.6 to 10.1 ml). (**D**) Denaturing urea PAGE gel of RNA extracted from heparin-purified *Sb*-gRAMP-crRNA1 complexed with TPR-CHAT. Mature crRNA size is indicated with a black arrowhead and is based on the mature crRNA fraction found in *Sb*-gRAMP-crRNA1. (**E**) Denaturing urea PAGE gel of target cleavage by heparin-purified *Sb*-gRAMP-crRNA1 complexed with TPR-CHAT. Cleavage products are indicated with arrowheads. (**F**) Model of CRISPR-Cas type III-E during phage infection.

and TPR-CHAT complexed in a 1:1 stoichiometry (table S3). The retention time of the complex was shorter than that of *Sb*-gRAMP-crRNA alone, consistent with a particle of higher molecular weight (fig. S19). The heparin-purified complex contained mature crRNA (Fig. 4D) with 6-nt spaced cleavage specificity toward target RNA (Fig. 4E and figs. S20 and S16B). TPR-CHAT with inactivated predicted catalytic residues (H585A and C627A) (*7*) was also able to associate with *Sb*-gRAMP-crRNA (fig. S16), indicating that complex formation occurs independently of TPR-CHAT activity. TPR-CHAT did not dissociate from *Sb*-gRAMP-crRNA in the presence of target RNA (fig. S21), suggesting that *Sb*-gRAMP-crRNA and TPR-CHAT form a stable protein complex that remains assembled upon target RNA recognition. We here name this complex "Craspase" for "CRISPR-guided caspase."

The TPR-CHAT is a predicted protease from the caspase family, the members of which typically catalyze the hydrolysis of specific peptide bonds of target proteins (*22*), many remaining to be identified. Pathways involving caspase-like proteins are often activated during eukaryotic apoptosis but are also abundant in the bacterial kingdom, where they have been shown to function in regulated cell death (*7*). To test whether we could trigger cell death with the Craspase complex, we coexpressed it with an inducible target RNA in *E. coli* and followed the growth kinetics of the bacteria. We did not observe growth defects upon target RNA production (fig. S22), suggesting the absence of the target protein in the transplanted *E. coli* host, the requirement of additional factors for Craspase activation, or a biological role for Craspase in a context other than cell death induction.

The type III-E gRAMP effector has characteristics of both CRISPR-Cas class 1 (e.g., type III domains, 6-nt cleavage spacing, and cleavage of RNA independent of matching PFS) and class 2 (e.g., single protein composition), blurring the boundaries of the traditional CRISPR-Cas classification. Its physical association with TPR-CHAT raises the possibility of crRNA-guided caspase-like activity to reach viral immunity. Although the specific RNA cleavage capability of gRAMP-crRNA could contribute to direct antiviral defense, the primary role of target RNA recognition and cleavage may instead be the on and off switching of Craspase. This switching has been observed in other type III systems where RNA target interaction regulates second-messenger production, which in turn controls ancillary nuclease activity (*23*, *24*). Our findings that *Sb*-gRAMP-crRNA targets RNA and forms a stable complex with TPR-CHAT give rise to a model in which gRAMP-crRNA, instead of using second messengers, allosterically induces peptidase activity upon target RNA recognition to elicit a specific immune response (Fig. 4F).

REFERENCES AND NOTES

1. S. Doron *et al.*, *Science* **359**, eaar4120 (2018).
2. R. Barrangou *et al.*, *Science* **315**, 1709–1712 (2007).
3. S. J. J. Brouns *et al.*, *Science* **321**, 960–964 (2008).
4. R. Molina, N. Sofos, G. Montoya, *Curr. Opin. Struct. Biol.* **65**, 119–129 (2020).
5. K. S. Makarova *et al.*, *Nat. Rev. Microbiol.* **18**, 67–83 (2020).
6. S. Silas *et al.*, *Science* **351**, aad4234 (2016).
7. A. G. Johnson *et al.*, bioRxiv 447441 [Preprint]. 7 June 2021.
8. M. Schmid *et al.*, *Syst. Appl. Microbiol.* **26**, 529–538 (2003).
9. F. C. Walker, L. Chou-Zheng, J. A. Dunkle, A. Hatoum-Aslan, *Nucleic Acids Res.* **45**, 2112–2123 (2017).
10. I. Fonfara, H. Richter, M. Bratovič, A. Le Rhun, E. Charpentier, *Nature* **532**, 517–521 (2016).
11. A. East-Seletsky *et al.*, *Nature* **538**, 270–273 (2016).
12. L. You *et al.*, *Cell* **176**, 239–253.e16 (2019).
13. C. Benda *et al.*, *Mol. Cell* **56**, 43–54 (2014).
14. R. H. J. Staals *et al.*, *Mol. Cell* **56**, 518–530 (2014).
15. G. Tamulaitis *et al.*, *Mol. Cell* **56**, 506–517 (2014).
16. M. P. Terns, *Mol. Cell* **72**, 404–412 (2018).
17. C. R. Hale *et al.*, *Cell* **139**, 945–956 (2009).
18. M. Kazlauskiene, G. Kostiuk, Č. Venclovas, G. Tamulaitis, V. Siksnys, *Science* **357**, 605–609 (2017).
19. O. Niewoehner *et al.*, *Nature* **548**, 543–548 (2017).
20. K. S. Makarova, V. Anantharaman, N. V. Grishin, E. V. Koonin, L. Aravind, *Front. Genet.* **5**, 102 (2014).
21. L. D. D'Andrea, L. Regan, *Trends Biochem. Sci.* **28**, 655–662 (2003).
22. L. Aravind, E. V. Koonin, *Proteins* **46**, 355–367 (2002).
23. C. Rouillon, J. S. Athukoralage, S. Graham, S. Grüschow, M. F. White, *eLife* **7**, e36734 (2018).
24. J. A. Steens *et al.*, bioRxiv 429135 [Preprint]. 1 February 2021.
25. P. Pausch *et al.*, *Science* **369**, 333–337 (2020).

ACKNOWLEDGMENTS

We thank M. Jetten and G. Nuijten (Radboud University) for providing *Candidatus* "Scalindua brodae" gDNA; C. de Agrela Pinto (Delft University of Technology) for performing SEC-MALS analysis; M. Pabst and C. de Ram (Delft University of

Technology) for performing mass spectrometry analysis; R. Mans, C. Koster, C. Bastiaanssen, and J. van der Torre (Delft University of Technology) for provision of equipment and reagents; Brouns laboratory members for helpful discussions; and A. Rita Costa (Delft University of Technology) for experimental help during revisions. **Funding:** S.J.J.B. is supported by the Netherlands Organisation for Scientific Research (NWO VICI; VI.C.182.027) and has received funding from the European Research Council (ERC) CoG under the European Union's Horizon 2020 research and innovation program (grant agreement no. 101003229). **Author contributions:** Conceptualization: S.P.B.v.B., S.J.J.B.; Funding acquisition: S.J.J.B.; Investigation: S.P.B.v.B., A.C.H., A.R.-M., D.F.v.d.B., J.N.A.V.; Methodology: S.P.B.v.B., S.J.J.B., A.C.H.; Supervision: S.P.B.v.B., S.J.J.B.; Writing – original draft: S.P.B.v.B., S.J.J.B.; Writing – review and editing: S.P.B.v.B., S.J.J.B. with input from all other authors. **Competing interests:** S.P.B.v.B. and S.J.J.B. are inventors on patent application N2028346 submitted by Delft University of Technology that covers uses of gRAMP and Craspase. **Data and materials availability:** All data are available in the manuscript or the supplementary materials. Plasmids and strains are available upon request from S.J.J.B.

SUPPLEMENTARY MATERIALS
https://science.org/doi/10.1126/science.abk2718

Materials and Methods
Supplementary Text
Figs. S1 to S22
Tables S1 to S8
References (*26*–*45*)
MDAR Reproducibility Checklist

2 July 2021; accepted 16 August 2021
Published online 26 August 2021
10.1126/science.abk2718

NEUROMORPHIC CHIPS

2D materials–based homogeneous transistor-memory architecture for neuromorphic hardware

Lei Tong[1], Zhuiri Peng[1], Runfeng Lin[1], Zheng Li[1], Yilun Wang[1], Xinyu Huang[1], Kan-Hao Xue[1], Hangyu Xu[2], Feng Liu[3], Hui Xia[2], Peng Wang[2], Mingsheng Xu[4], Wei Xiong[1], Weida Hu[2]*, Jianbin Xu[5], Xinliang Zhang[1], Lei Ye[1]*, Xiangshui Miao[1]

In neuromorphic hardware, peripheral circuits and memories based on heterogeneous devices are generally physically separated. Thus, exploration of homogeneous devices for these components is key for improving module integration and resistance matching. Inspired by the ferroelectric proximity effect on two-dimensional (2D) materials, we present a tungsten diselenide–on–lithium niobate cascaded architecture as a basic device that functions as a nonlinear transistor, assisting the design of operational amplifiers for analog signal processing (ASP). This device also functions as a nonvolatile memory cell, achieving memory operating (MO) functionality. On the basis of this homogeneous architecture, we also investigated an ASP-MO integrated system for binary classification and the design of ternary content-addressable memory for potential use in neuromorphic hardware.

Recently proposed diverse neuron-inspired hardware based on various emerging nanomaterials has effectively advanced neural networks (*1*–*6*), especially for two-dimensional (2D) materials. 2D materials can provide a platform to develop transistor architectures for memory operating (MO)—including field-effect transistors (FETs), tunneling transistors, junction transistors, ferroelectric (FE) transistors, and ferromagnetic transistors—owing to their rich electrostatic control capabilities (*1*, *7*). 2D materials–based FE FETs, FE bipolar junction transistors (BJTs), and FE tunneling transistors exhibit large on-off resistance ratios, fast operation, low power consumption, nonvolatile electronic control, and weight updates under reversible polarization (*1*) because of the strong proximal coupling of FE materials with 2D materials. Therefore, these 2D materials–based FE proximal coupled devices are being intensively investigated for neuromorphic computing (*1*, *4*), in which they are used as memories by dynamically modulating the FE polarization to program the conductivity of superjacent 2D channels (*8*, *9*). Achieving computing tasks requires these memories to be integrated with peripheral circuits, because analog signal processing (ASP) is essential before and after MO (*2*). However, peripheral circuits are generally based on complementary metal-oxide semiconductor (CMOS) transistors, and thus the heterogeneous architectures between memory cells and peripheral circuits lead to their physical separation, making it necessary to consider module integration compatibility issues for chip design (*2*). In addition, an emerging challenge regards how to achieve efficient resistance matching between heterogeneous device architectures as device dimensions are scaling down, which may hinder the pursuit of higher performance and energy efficiency (*10*). Therefore, it is crucial to explore the integration between ASP and MO.

Designing an ASP-MO integrated system with a homogeneous device architecture for peripheral circuits and memory cells offers the potential to relieve the above-mentioned issues, which can also be realized by the mechanism of 2D-FE proximal coupling. On the one hand, FE polarization proximity-induced nonvolatile electronic gating in 2D materials enables the design of nonlinear transistors, including p-n diodes and BJTs (*8*, *11*–*16*). On the other hand, FE polarization can modulate the built-in potential in BJTs (*17*), enabling nonvolatile memory functionalities with an improved on-off resistance ratio. Moreover, the reconfigurable FE polarization domains can seamlessly manipulate arrayed doping domains in 2D materials, showing potential for the fabrication of massive cascaded devices with enhanced compactness. Therefore, a homogeneous, 2D material–based FE proximal coupled BJT architecture is proposed to design peripheral circuits for ASP, as well as nonvolatile memory cells for MO, enabling development of an ASP-MO integrated system.

In this work, seamlessly arrayed periodically polarized $LiNbO_3$ (LNO) domains formed a grating-like structure (fig. S1), which effectively tailored the WSe_2 channels into seamlessly arrayed junctions. ASP, MO, and their corresponding cascade were investigated to demonstrate the success of an integrated system based on the same device architecture, which included a WSe_2 channel crossing three FE domains. Our operational amplifier (OPAMP) was designed for ASP (*18*), and memory cells with encoded synapse weights were cascaded with the OPAMP to demonstrate the applicability in binary classification (*19*). Furthermore, ternary content-addressable memory (TCAM) with a two-transistor-two-resistor (2T2R) configuration was designed with the homogeneous transistor-memory architecture, yielding a ratio of 898.4 between the high-resistance state (HRS) and the low-resistance state (LRS). Such an integrated system architecture could provide a feasible approach to solve the heterogeneous issue and improve neuromorphic applications.

Few-layer WSe_2 flakes were exfoliated and transferred onto LNO to demonstrate the

[1]Wuhan National Laboratory for Optoelectronics, School of Optical and Electronic Information, Huazhong University of Science and Technology, Wuhan, Hubei 430074, China. [2]State Key Laboratory of Infrared Physics, Shanghai Institute of Technical Physics, Chinese Academy of Sciences, Shanghai 200083, China. [3]School of Power and Mechanical Engineering, Wuhan University, Wuhan, Hubei 430072, China. [4]School of Micro-Nano Electronics, State Key Laboratory of Silicon Materials, Zhejiang University, Hangzhou 310027, China. [5]Department of Electronic Engineering, Materials Science and Technology Research Center, The Chinese University of Hong Kong, Hong Kong, China.
***Corresponding author. Email: wdhu@mail.sitp.ac.cn (W.H.); leiye@hust.edu.cn (L.Y.)**

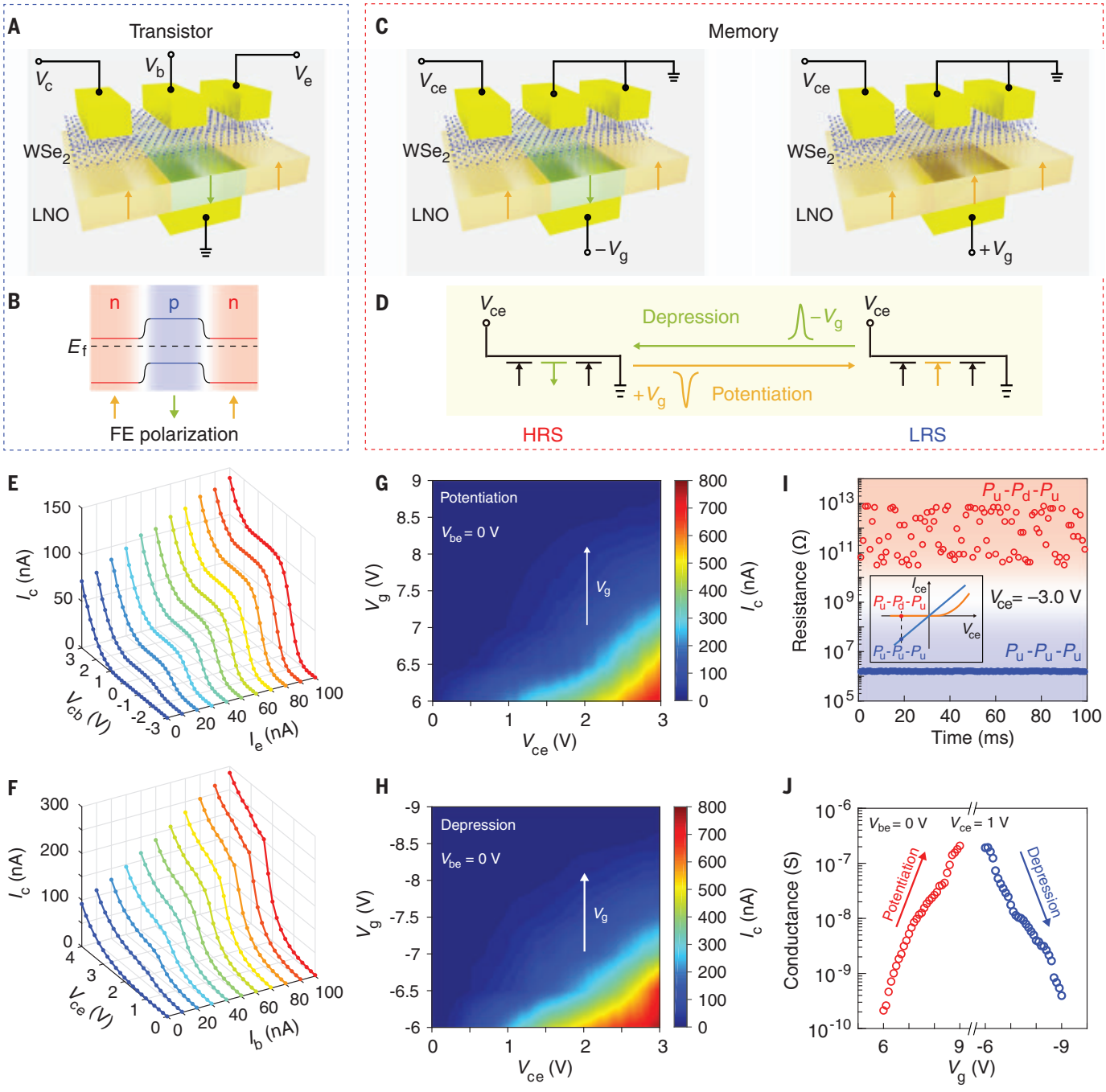


Fig. 1. Basic device and performance mechanism. (**A**) Schematic of the basic device with a homogeneous transistor-memory architecture for nonlinear transistor functionality. (**B**) Mechanism of FE proximity-induced doping in the basic device. E_f, Fermi energy. (**C**) Schematic of the basic device with a homogeneous transistor-memory architecture for the memory functionality. (**D**) Mechanism of potentiation and depression in the basic device, in which the LRS and HRS were controlled by changing the FE polarization state of the base under a positive and negative gate voltage, respectively. (**E** and **F**) Transistor functionality with common-base (E) and common-emitter (F) configuration. (**G**) Current rectification for the potentiation process, for which V_g ranged from 6 to 9 V with a step of 0.5 V. (**H**) Current rectification for the depression process, for which V_g ranged from −6 to −9 V with a step of 0.5 V. (**I**) Channel resistance for the FE polarization state of P_u-P_d-P_u and P_u-P_u-P_u under the driving voltage of V_{ce} = −3 V and V_{be} = 0 V. The inset shows a schematic of the measured current. (**J**) Conductance update for the potentiation and depression with a V_g step of 0.1 V and a width of 1 s. The drive voltages were V_{ce} = 1 V and V_{be} = 0 V.

reconfigurable electronic functionalities under FE proximal coupling (WSe_2 characterization and optical images are shown in fig. S1). The basic device functioned as a nonlinear transistor when the domain polarization state was fixed under zero gate voltage (V_g) (Fig. 1A), as the FE proximal coupling induces carrier doping in the WSe_2 (Fig. 1B). This doping mechanism was indicated by the Kelvin probe force microscopy (KPFM) mapping shown in fig. S1C, where the higher (or lower) surface potential induced by the polarization-down

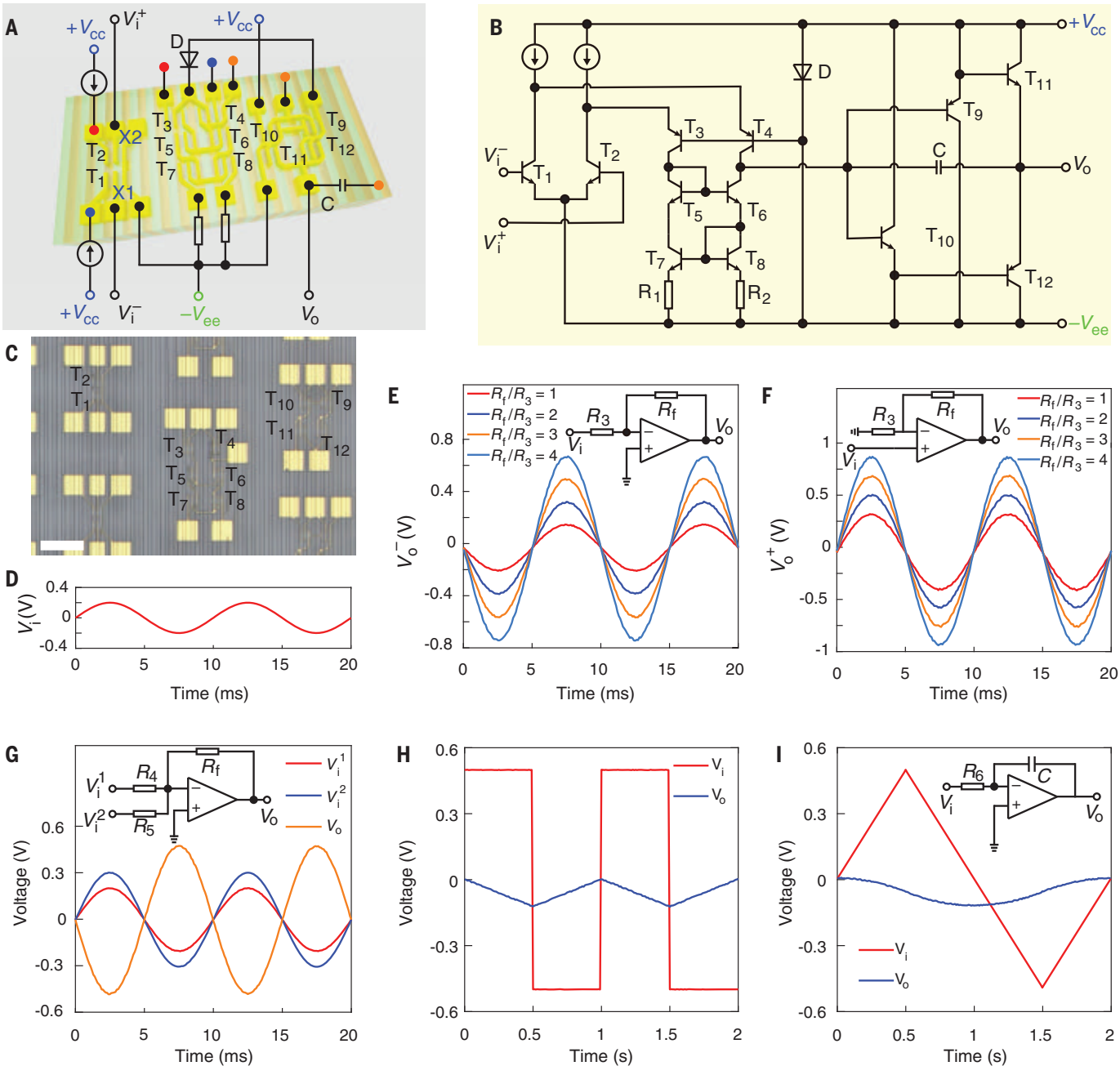


Fig. 2. OPAMP for ASP. (**A** and **B**) Experimental setup (A) and electric circuit (B) of the OPAMP. T_1 to T_{12}, BJTs; D, cascaded diode; C, cascaded capacitance. (**C**) Optical image of the OPAMP. Scale bar, 100 μm. (**D** to **F**) Analog signal inputted at one port (D). Inverted (E) and noninverted (F) output of the OPAMP, with the circuit schematics shown in the insets. (**G**) Analog input and output signals for the addition operation. The inset shows the schematic of the addition calculation. (**H**) Analog integral calculation for a square-shaped input signal and the corresponding triangle-shaped output signal. (**I**) Analog integral calculation for a triangle-shaped input signal and the approximately sinusoidal output signal. The inset shows the schematic of the integral calculation.

(P_d) [or polarization-up (P_u)] domain was in accordance with the p-doping (or n-doping) nature (*8*). Transfer curves for the intrinsic WSe_2 and FE-doped WSe_2 FETs are shown in fig. S1L. The neutral point shifts were 3.8 and −6.2 V for the P_d and P_u domains, respectively, corresponding to a hole doping density of 2.07×10^{12} cm^{-2} and an electron doping density of 3.37×10^{12} cm^{-2}. This doping character induced a built-in potential of ~0.43 eV and a depletion width (w) of 48.25 nm (fig. S1M) (*20*). For a basic n-p-n BJT on the P_u-P_d-P_u domains, current amplifications were measured under the base, collector, and emitter voltage control. The common-base configuration in Fig. 1E showed an average gain of $\alpha = \frac{I_c}{I_e} = 0.979$ (I_c, collector current; I_e, emitter current) for the active region, and the common-emitter configuration in Fig. 1F showed a maximum gain of $\beta = \frac{I_c}{I_b} = 11.2$ (I_b, base current), offering the capability to design analog circuits. More details about signal rectification, amplification, and performance uniformity are shown in figs. S2 to S5.

The basic device could also operate as a nonvolatile memory (Fig. 1C), the mechanism of which differs from those of conventional

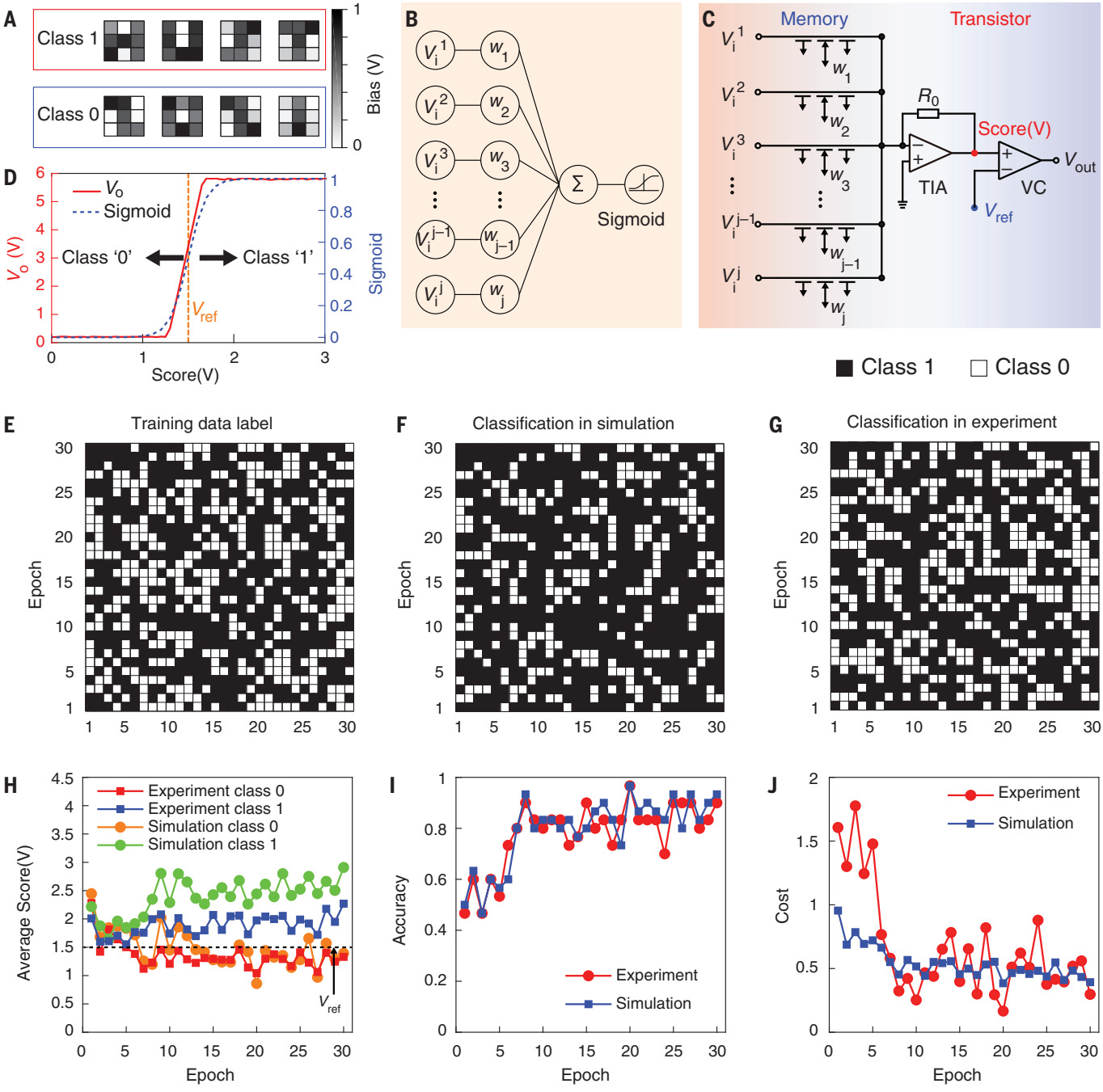


Fig. 3. ASP-MO integration for binary classification. (**A**) Class 1 with letter patterns H, U, S, and T and class 0 with number patterns 2, 0, 2, and 1. (**B**) Schematic of the classification with the sigmoid activation function. (**C**) Schematic of the circuit diagram, where the memory cells were integrated with the TIA and VC. (**D**) Output character of the VC (solid red curve), which was similar to the sigmoid function (dashed blue curve). (**E** to **G**) Training dataset label (E), predicted class in the simulation (F), and predicted class in the experiment (G). (**H** to **J**) Average Score(V) (H), accuracy (I), and cost (J) for the training process in the simulation and experiment.

FE-FET and MemFlash (*1*, *4*, *21*). The FE polarization state was fixed to be P_u for the collector and emitter, and the HRS and LRS were dominated by the built-in potential (*17*), which was controlled by V_g for the base. In the potentiation (or depression) process, a positive V_g from 6 to 9 V (or a negative V_g from −6 to −9 V) changed the FE polarization state for the base to P_u (or P_d), resulting in a low built-in potential with enhanced channel conductance (or a high built-in potential with reduced channel conductance) (Fig. 1D) (*21*, *22*). The mechanism was indicated from the modulated current rectifications under the collector-emitter voltage (V_{ce}) sweep for the potentiation (Fig. 1G) and depression (Fig. 1H) processes, respectively [base-emitter voltage (V_{be}) = 0 V; V_g step of 0.5 V]. This rectification behavior can provide a high resistance ratio between the HRS and LRS. In contrast to the conventional FE-FET structure with the WSe_2 channel

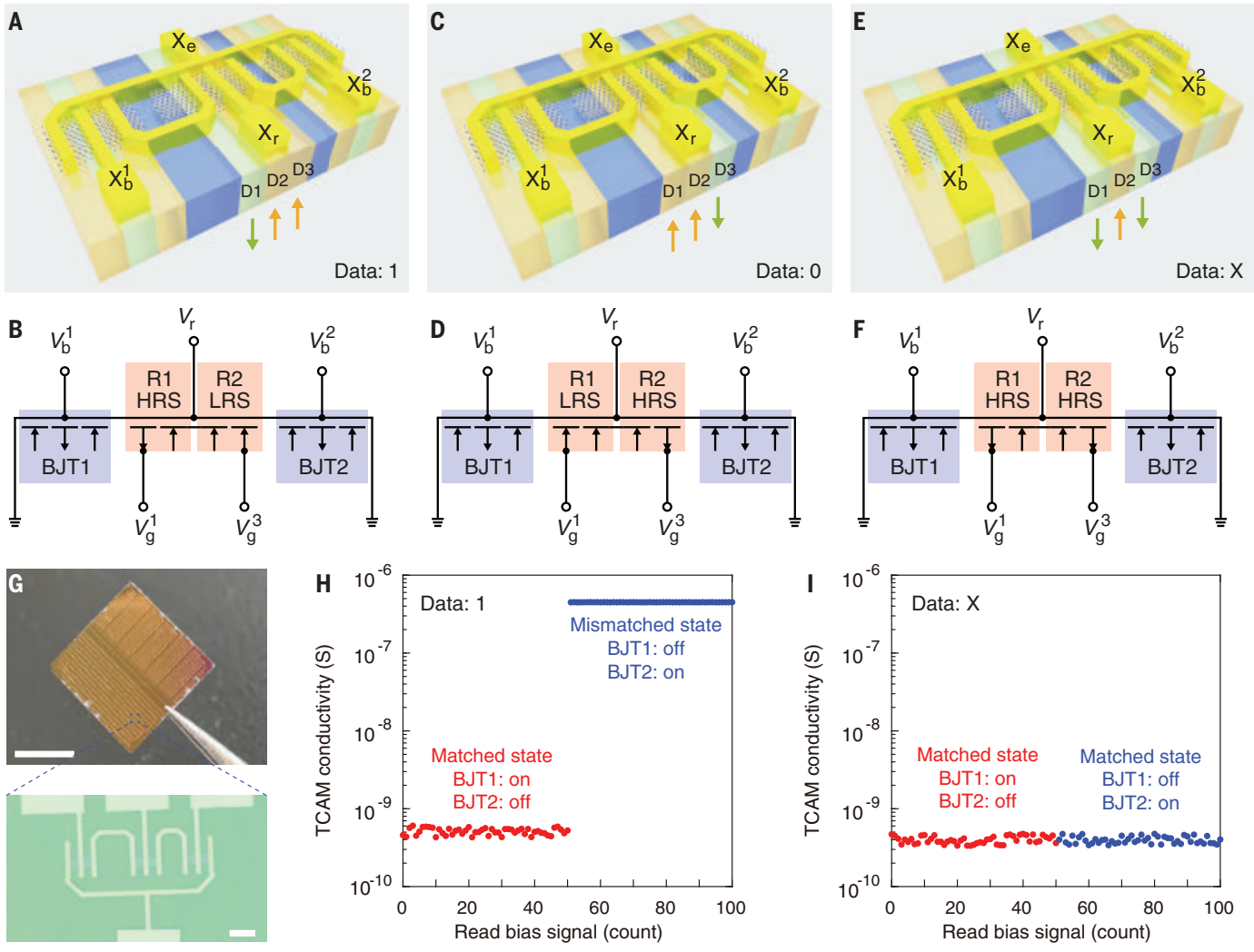


Fig. 4. TCAM cell with a 2T2R configuration based on the homogeneous transistor-memory architecture. (**A** and **B**) Schematics of the TCAM cell with bit data 1. (**C** and **D**) Schematics of the TCAM cell with bit data 0. (**E** and **F**) Schematics of the TCAM cell with bit data X. (**G**) Photograph and optical image of a TCAM cell. Photograph scale bar, 5 mm; optical image scale bar, 20 μm. (**H**) Reading of the TCAM cell with bit data 1. The TCAM cell was in the matched state (or mismatched state) with BJT1 on and BJT2 off (or BJT1 off and BJT2 on). (**I**) Reading of the TCAM cell with bit data X. The TCAM cell was always in the matched state, regardless of whether BJT1 and BJT2 were on or off.

placed on a single FE domain (fig. S6), the resistance for the FE polarization state of P_u-P_d-P_u and P_u-P_u-P_u showed an average resistance ratio of ~10^6 under driving voltages of V_{ce} = −3 V, V_{be} = 0 V, and V_g = 0 V (Fig. 1I). Moreover, as an artificial synapse, the conductance update for the potentiation or depression process with a V_g step of 0.1 V under V_{ce} = 1 V and V_{be} = 0 V (Fig. 1J) was encoded as a synapse weight (fig. S7A), and the on-off resistance ratio was ~10^3. The stable memory performance is shown in fig. S7 for measurements of multiple cycles, and the memory performances were compared with those from other studies of diverse memory architectures (table S1). The few-layer WSe_2 film grown by chemical vapor deposition was then transferred and patterned on LNO to fabricate an ASP-MO integrated system.

The OPAMP was designed by cascading multiple basic devices for ASP (Fig. 2, A to C) (*18*), with the input electrodes designated X1 and X2. The dc driving voltages were collector voltage (V_{cc}) = emitter voltage (V_{ee}) = 6 V, the resistances were $R_1 = R_2$ = 10 megohms, the capacitance (C) was 1 μF, and the input bias current was varied between 30 and 50 nA to adjust the performance. The OPAMP characteristics were discussed and compared with those of previously reported CMOS-based devices (table S2). We applied an ac input signal $V_i = 0.2\sin 200\pi \times t$ (t, time) (Fig. 2D) at only one input port, and the other port was grounded. The output signal V_o^- was inverted when the signal was input at port X1 (Fig. 2E), the output V_o^+ was noninverted when the signal was input at port X2 (Fig. 2F), and the voltage gain was related to the ratio R_f/R_3. For the addition operation, port X2 was grounded, and both input signals were cascaded to port X1, with a resistance (R_f) for negative feedback. The two ac input signals $V_i^1 = 0.2\sin 200\pi \times t$ and $V_i^2 = 0.3\sin 200\pi \times t$ and the output signal V_o are shown in Fig. 2G. Under the condition of $R_f = R_4 = R_5$ = 2 megohms, the output signal was $-V_o = V_i^1 + V_i^2$. When a capacitance was used for negative feedback, the OPAMP achieved the integral calculation with a time constant of $\tau = R_6C = 2$ s (R_6 = 2 megohms, C = 1 μF). The square input signal V_i and the corresponding integrated output signal $V_o = -\frac{V_i}{RC}t$ are shown in Fig. 2H. The triangle-shaped input signal and the approximately

sine wave–shaped integrated output signal are shown in Fig. 2I.

On the basis of the reconfigurable functionalities, the ASP-MO integrated system was used to demonstrate the proof of principle for binary classification (*23*, *24*). The input three pixel–by–three pixel patterns for the letters H, U, S, and T were labeled as class 1, and those for the numbers 2, 0, and 1 were labeled as class 0 (Fig. 3A shows eight randomly selected patterns; and the entire training dataset is shown in fig. S8). The calculation schematic and circuit diagram are shown in Fig. 3, B and C, respectively. The pixels were coded into nine input voltages (V_{ce}) to calculate the weighted average current (Eq. 1) in nine memory cells. The weighted average current was converted into a voltage Score(V) in the transimpedance amplifier (TIA) (*19*, *25*), with a resistance (R_0) of 10 megohms. The nonlinear output voltage (Eq. 2) was processed by the voltage comparator (VC) with a reference voltage (V_{ref}) of 1.5 V, which was similar to the sigmoid function (Fig. 3D)

$$\mathrm{Score(V)} = w_0 + w_1 V_i^1 + w_2 V_i^2 + w_3 V_i^3 + \ldots + w_j V_i^j \quad (1)$$

$$V_{out} = \begin{cases} V_{cc}, & \mathrm{Score(V)} > V_{ref} \\ V_{ee}, & \mathrm{Score(V)} < V_{ref} \end{cases} \quad (2)$$

The drive voltages were V_{cc} (6 V) and V_{ee} (0 V), and the conductance was updated after calculating the cross-entropy cost for each batch, as summarized in fig. S9, C and D. The system was trained for 30 epochs, after which the pattern label and predicted classes in the simulations and experiments were elucidated (Fig. 3, E to G, respectively). Score(V) is summarized in fig. S9, E and F; the average Score(V) values of classes 0 and 1, which are separated by V_{ref}, are depicted in Fig. 3H. The accuracy and cost are shown in Fig. 3, I and J. The performance was mainly limited by the output characteristics of the VC and the non-negative weight in the hardware. Analogous to conventional FE memristors, this ASP-MO integrated system could be useful for other neuromorphic algorithms, although such investigation is beyond the scope of this work.

TCAM is promising for the parallel search of massive datasets in in-memory computing (*26*, *27*), and TCAM cells with a 2T2R configuration can be constructed on the basis of homogeneous transistor-memory architecture (schematics of the mechanism are shown in Fig. 4, A to F). In our design, the TCAM cell included three WSe_2 channels on nine separated FE domains, with four terminals marked as the emitter electrode (X_e), read electrode (X_r), and base electrodes (X_b^1 and X_b^2). Three central domains, designated D1 to D3, formed two memories, with memory R1 across D1 and D2 and memory R2 across D2 and D3. The polarization state of D2 was fixed at P_u; thus, R1 (or R2) was in an HRS when the V_g of −9 V changed D1 (or D3) to P_d and was in an LRS when the V_g of 9 V changed D1 (or D3) to P_u. Moreover, R1 and R2 were connected with two BJT switches, which were switched on (or off) at a base voltage of $V_b^1 = V_b^2 = 3$ V (or $V_b^1 = V_b^2 = -3$ V) (Fig. 4, B, D, and F). X_e was grounded, and V_r (5 V) was loaded at X_r for the address search function.

The bit data 1 (or 0) in the TCAM cell was defined when R1 was in the HRS and R2 was in the LRS (or R1 in the LRS and R2 in the HRS). The matched state exhibited a low conductance for the address read at X_r and thus bit data 1 was searched by switching on BJT1 and switching off BJT2 (Fig. 4, A and B). Bit data 0 was searched by switching off BJT1 and switching on BJT2 (Fig. 4, C and D). Otherwise, the TCAM cell was in the mismatched state with a high conductance. For bit data 1, the average conductance was ~0.5 nS (where 1 S = 1 A/V) for the matched state and ~449.5 nS for the mismatched state, with an average conductance ratio $r_c = \frac{C_{high}}{C_{low}} = 899$ (Fig. 4H). The TCAM cell with an unknown bit (designated bit X) was always in the matched state, because both R1 and R2 were in the HRS (Fig. 4, E and F), with an average conductivity of ~0.4 nS (Fig. 4I). The cumulative probability was analyzed in fig. S10.

In addition to binary classification and TCAM design, the basic device should be suitable for various applications, including digital computing (fig. S11) and artificial neural systems with optical sensing abilities (fig. S12) (*28*, *29*). The basic device should also be applicable for the design of analog-to-digital converters, digital-to-analog converters, and analog filters (*2*). The device size can be reduced by scaling down the polarization domain size, which will improve the current gain and integration density. A lower coercive voltage would be helpful for achieving a lower power consumption, which can be attained by reducing the LNO thickness or using other FE materials. Finally, inspired by conventional CMOS-based chips, we have proposed a neuromorphic ASP-MO 3D stacking system derived from 2D integration (fig. S13). The main challenge lies in the growth of wafer-scale, high-quality 2D materials, and recent works have achieved promising breakthroughs to overcome this challenge (*30*). Thus, this homogeneous transistor-memory architecture will help to promote analogous neuromorphic systems on-chip.

REFERENCES AND NOTES

1. C. Liu *et al*., *Nat. Nanotechnol.* **15**, 545–557 (2020).
2. Q. Xia, J. J. Yang, *Nat. Mater.* **18**, 309–323 (2019).
3. L. Danial *et al*., *Nat. Electron.* **2**, 596–605 (2019).
4. D. Ielmini, H. P. Wong, *Nat. Electron.* **1**, 333–343 (2018).
5. W. Zhang *et al*., *Nat. Electron.* **3**, 371–382 (2020).
6. A. Sebastian, M. Le Gallo, R. Khaddam-Aljameh, E. Eleftheriou, *Nat. Nanotechnol.* **15**, 529–544 (2020).
7. M. I. B. Utama *et al*., *Nat. Electron.* **2**, 60–65 (2019).
8. G. Wu *et al*., *Nat. Electron.* **3**, 43–50 (2020).
9. X. Wang *et al*., *Nat. Commun.* **12**, 1109 (2021).
10. P. Kapur, J. P. McVittie, K. C. Saraswat, *IEEE Trans. Electron Dev.* **49**, 590–597 (2002).
11. L. Lv *et al*., *Nat. Commun.* **10**, 3331 (2019).
12. C. Baeumer *et al*., *Nat. Commun.* **6**, 6136 (2015).
13. J.-W. Chen *et al*., *Nat. Commun.* **9**, 3143 (2018).
14. H. Lu *et al*., *Nat. Commun.* **5**, 5518 (2014).
15. N. Park *et al*., *ACS Nano* **9**, 10729–10736 (2015).
16. H. Mulaosmanovic, E. T. Breyer, T. Mikolajick, S. Slesazeck, *Nat. Electron.* **3**, 391–397 (2020).
17. Z. Xiao, J. Song, D. K. Ferry, S. Ducharme, X. Hong, *Phys. Rev. Lett.* **118**, 236801 (2017).
18. D. K. Polyushkin *et al*., *Nat. Electron.* **3**, 486–491 (2020).
19. L. Mennel *et al*., *Nature* **579**, 62–66 (2020).
20. B. Wen *et al*., *ACS Nano* **13**, 5335–5343 (2019).
21. M.-K. Kim, J.-S. Lee, *Nano Lett.* **19**, 2044–2050 (2019).
22. S. Boyn *et al*., *Nat. Commun.* **8**, 14736 (2017).
23. S. Ambrogio *et al*., *Nature* **558**, 60–67 (2018).
24. S. Seo *et al*., *Nat. Commun.* **11**, 3936 (2020).
25. C. Li *et al*., *Nat. Electron.* **1**, 52–59 (2018).
26. K. Ni *et al*., *Nat. Electron.* **2**, 521–529 (2019).
27. R. Yang *et al*., *Nat. Electron.* **2**, 108–114 (2019).
28. L. Tong *et al*., *Nat. Commun.* **11**, 2308 (2020).
29. C. Y. Wang *et al*., *Sci. Adv.* **6**, eaba6173 (2020).
30. X. Xu *et al*., *Science* **372**, 195–200 (2021).
31. L. Tong *et al*., 2D materials-based homogeneous transistor-memory architecture for neuromorphic hardware, version 1.0, Zenodo (2021); https://doi.org/10.5281/zenodo.5163973.

ACKNOWLEDGMENTS

Funding: This work was supported by the National Natural Science Foundation of China (grants 61974050, 51872257, 61927817, 61725505, 11734016, 61905266, 11991063, and 61774067), the National Key Research and Development Plan of China (grants 2019YFB2205100 and 2019YFB2203102), the Priority Research Program of Chinese Academy of Sciences (grants XDPB22 and XD43010200), the Fund of Shanghai Natural Science Foundation (grants 19XD1404100 and 19YF1454600), and the Natural Science Foundation of Zhejiang Province (grant LZ20F040001). **Author contributions:** L.T., X.M., W.H., and L.Y. conceived the idea and designed the experiments. L.T., Z.P., and R.L. performed device fabrication and characterization. Z.L., X.Hua., and Y.W. conducted binary logic function measurements. K.-H.X. conducted atomic force microscopy analysis. H.Xu and P.W. conducted the optoelectronic measurements. F.L. conducted cumulative probability analysis. H.Xia conducted the KPFM measurement. M.X., W.X., J.X., and X.Z. helped with device fabrication. L.T. carried out the data analysis. L.T., W.H., and L.Y. wrote the manuscript. All authors provided critical comments and analyses. **Competing interests:** The authors declare no conflicts of interest. **Data and materials availability:** All data needed to evaluate the conclusions in the paper are present in the paper or the supplementary materials. All findings of this study are archived on Zenodo (*31*).

SUPPLEMENTARY MATERIALS

https://science.org/doi/10.1126/science.abg3161
Materials and Methods
Supplementary Text
Figs. S1 to S13
Tables S1 and S2
References (*32*–*54*)

24 December 2020; resubmitted 5 June 2021
Accepted 6 August 2021
Published online 19 August 2021
10.1126/science.abg3161

QUANTUM GASES

Observation of a superradiant quantum phase transition in an intracavity degenerate Fermi gas

Xiaotian Zhang[1], Yu Chen[2], Zemao Wu[1], Juan Wang[1], Jijie Fan[1], Shujin Deng[1], Haibin Wu[1,3,4]*

Coupling Bose-Einstein condensates to optical cavities has enabled the study of many-body states with long-range interactions. However, equivalent experiments with ultracold Fermi gases have remained largely unexplored. Here, we report an experimental realization of a superradiant quantum phase transition of a degenerate Fermi gas in a transversely pumped optical cavity. The self-ordering checkerboard density pattern of Fermi gases and superradiant transitions of the cavity field spontaneously emerge by increasing the pumping intensity above a threshold value. The effects of Fermi statistics are manifested by an inverse square root scaling of the threshold with atom number and the slow dynamics of low–atomic momentum states. Our work provides an ideal platform for studying nonequilibrium dynamics of many-body states for long-range interacting Fermi gases.

The coupling of ultracold quantum gases to an optical cavity provides an ideal system to study phase transitions in many-body physics (*1*, *2*). Such coupling is exploited in cavity quantum electrodynamics (QED) with ultracold bosonic atoms, leading to notable developments in recent years (*3*). A hallmark example of a collective interaction between the emitters and the quantum field of a photonic mode is the Dicke model (*4*), which predicts a second-order quantum phase transition (QPT) between a normal and a steady-state superradiant phase at a strong coupling strength (*5*, *6*). By using atomic momentum states of a Bose-Einstein condensate (BEC), the Dicke phase transition has been realized (*1*). The self-organized supersolid phase and a charge density wave are observed by tuning short- and long-range interactions in such systems (*7*, *8*). Owing to the inherent leakage of the cavity field and quantum backaction between matter and light, cavity QED with quantum gases can contribute to the study of nonequilibrium dynamics (*2*), symmetry breaking (*9*), fluctuations at driven-dissipative phase transition (*10*), Mott insulator transitions in self-organized lattices (*7*, *11*), and Floquet dynamics and discrete time-crystals (*12*).

In contrast to the rapid development of BECs in the frame of cavity QED, the experimental study of quantum statistics of ultracold Fermi gases with strong coupling to the cavity has remained challenging, despite considerable theoretical interest. Whether matter wave amplification can work for fermions was discussed very early on (*13*, *14*). The umklapp superradiance was recently predicted with degenerate Fermi gases in a transversely pumped cavity (*15*–*17*) where atom statistics plays an important role. Such systems have been proposed to investigate nontrivial topological states (*18*–*21*), chiral states (*22*, *23*), dynamical gauge fields (*24*), antiferromagnetic self-ordering (*25*), and charge density waves (*26*). Very recently, the coupling of fermions to cavity light has been realized, and the dressed states have been investigated (*27*); however, no quantum statistics has been observed.

Here, we realize the superradiant QPT by coupling an ultracold Fermi gas to an optical cavity. The experimental schematic is shown in Fig. 1A. We used a balanced mixture of ^{6}Li fermions in the two lowest hyperfine states

[1]State Key Laboratory of Precision Spectroscopy, School of Physics and Electronics Science, East China Normal University, Shanghai 200062, P. R. China. [2]Graduate School of China Academy of Engineering Physics, Beijing 100193, P. R. China. [3]NYU-ECNU Institute of Physics at NYU Shanghai, Shanghai 200062, P. R. China. [4]Collaborative Innovation Center of Extreme Optics, Shanxi University, Taiyuan 030006, P. R. China.
*Corresponding author. Email: hbwu@phy.ecnu.edu.cn

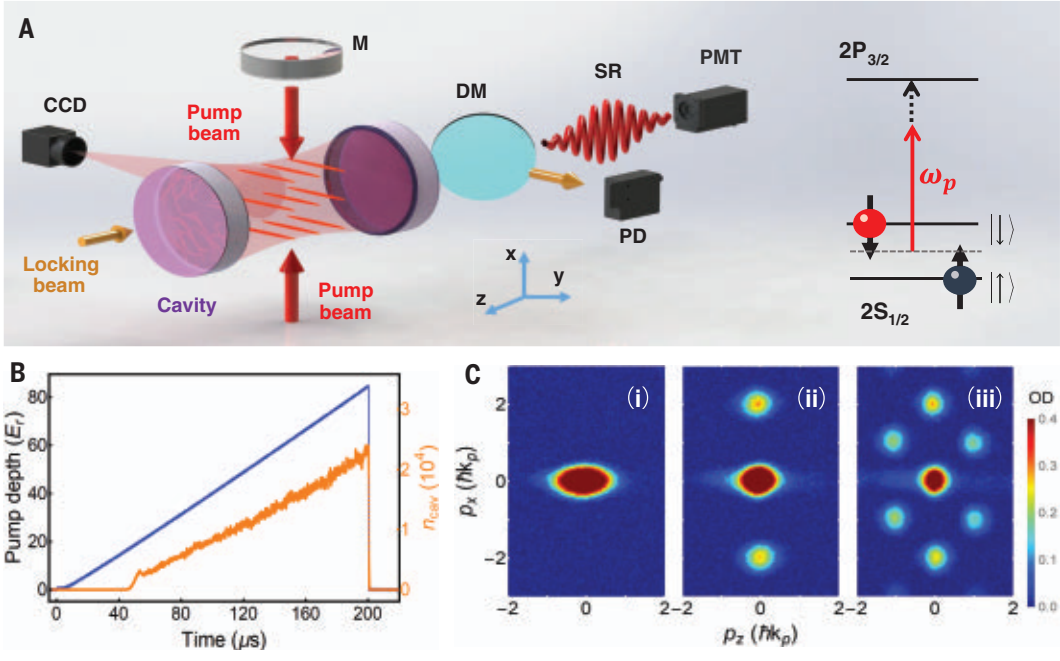


Fig. 1. Fermionic superradiance. (**A**) A schematic of the experimental setup. The frequency of the cavity is locked by laser light at 1064 nm. A laser light with frequency ω_p is red-detuned by $2\pi \times 60$ GHz from the D_2 line of ^{6}Li to transversely pump the atoms along the *x* axis. DM, dichromatic mirror; CCD, electron-enhanced charge-coupled device; FP, Fabry-Perot cavity; M, highly reflective mirror; PD, photon detector; PMT, photomultiplier; SR, superradiant light. (**B**) The time-dependent cavity transmission (yellow curve) and the pumping power (blue curve), where n_{cav} is the mean intracavity photon number. When the pumping power is ramped over a critical value (threshold), the intracavity field is abruptly built up and the gas shows a QPT. (**C**) The typical absorption images of the atoms show the optical density (OD) integrated along the *y* axis (i) without the pump lattice, (ii) with pump lattice depth 6.15 E_r (just before the QPT), and (iii) with pump lattice depth 22.7 E_r (just after the QPT) where the atoms undergo self-organization and a checkerboard pattern emerges. Here, $\Delta = -2\pi \times 1$ MHz and $T/T_{F0} = 0.27$ (0.02) ($T_{F0} \equiv E_F/k_B$ is the Fermi temperature of a harmonically trapped noninteracting Fermi gas without the pump light, where k_B is the Boltzmann constant).

$|\uparrow\rangle$ and $|\downarrow\rangle$. The cooling of atoms is similar to previous work (*28*, *29*). The atoms are loaded into a crossed dipole trap to evaporatively cool to quantum degeneracy in a magnetic field B = 340 G. Then, the magnetically induced Feshbach resonance is used to tune the interaction of the atoms to a noninteracting regime of B = 528 G. The typical trapping frequencies of the optical potential are $(\omega_x, \omega_y, \omega_z) = 2\pi \times (178, 232, 48)$Hz, where x denotes the pump axis, y represents the imaging axis and z represents the cavity axis. The atom number per spin state is about $N = 1.1(0.1) \times 10^5$, and the cloud sizes are $(R_x, R_y, R_z) = (19.6, 14.9, 72.5)\mu$m. After the gas is in the deep degeneracy regime, the dipole trap is aligned to maximize the spatial overlap between the atomic cloud and the center of an optical cavity. The cavity length is 7.57(0.01) cm and has a finesse of F = 2323(87). The decay rate of the cavity field is $\kappa = 2\pi \times 426(16)$ kHz. The system operates in the regime of weak dispersive coupling where the maximum dispersive shift of the resonance induced by atoms is far less than the cavity decay rate. A weak light at 1064 nm is used to stabilize the cavity resonant frequency ω_c, which results in a shallow lattice potential with a depth of less than 0.1 E_r (E_r is the recoil energy). A pump laser with frequency ω_p is red-detuned $\Delta_a = \omega_p - \omega_a = -2\pi \times 60$GHz from the resonant frequency ω_a of the D_2 line of ^{6}Li atoms. A mirror reflects the pump laser to form a pumping lattice along the x axis. The cavity transmission is monitored by a high-gain photomultiplier. The spatial distribution of atom clouds is probed with an electron-enhanced charge-coupled device using the standard resonant absorption imaging technique after a time-of-flight expansion time t_{tof}.

The broadening momentum distribution of Fermi gases places a constraint on realizing the superradiant phase transition. It requires that the Fermi momentum $k_F < k_p$ to clearly observe the self-organized pattern of the atomic gas, which means that $k_p\bar{x} > (48N)^{1/6}$, where $k_F \equiv (2mE_F)^{1/2}/\hbar$ is the Fermi wave vector of a gas of noninteracting ^{6}Li atoms of mass m in the harmonic trap ($\hbar$ is Planck's constant divided by 2π), $E_F \equiv \hbar\bar{\omega}(6N)^{1/3}$ is the Fermi energy, and $\bar{x} = (\hbar/m\bar{\omega})^{1/2}$ is the effective harmonic oscillator length [$\bar{\omega} \equiv (\omega_x\omega_y\omega_z)^{1/3}$]. This condition can be achieved by controlling the trap potential and atom number. In the experiment, we lower the trap frequencies and gradually increase the pump power to 86 E_r for a duration of 200 μs (ramping rate 0.43 E_r/μs) to enable the adiabaticity of the ramp of the pump intensity (*30*). Typical cavity transmission and the absorption images of the atoms are shown in Fig. 1, B and C. When the pump power is below a critical value (threshold), there is no detected light transmission of the cavity. The atoms show the expected momentum distributions for a Fermi gas loaded in a shallow optical lattice [Fig. 1C, (i) and (ii)]. Once the pump power is increased over the threshold, the intracavity field is abruptly built and the atomic density fluctuations induce the superradiant QPT. The atomic density at momenta $(p_x, p_z) = (\pm\hbar k_p, \pm\hbar k_p)$ suddenly increases, forming a self-organized checkerboard pattern [Fig. 1C, (iii)].

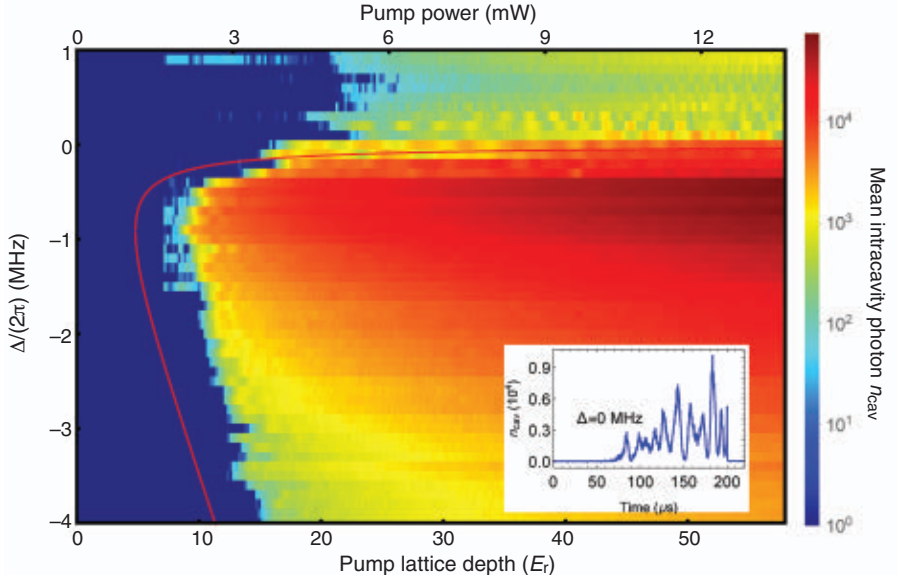


Fig. 2. The steady-state phase diagram. The boundaries of the normal, unstable, and superradiant phases are mapped by measuring the threshold as the pump-cavity detuning Δ is varied. The coupling of the cavity mode, atom profiles, and pump light is taken into account when determining the threshold. The inset shows a time trace of the cavity transmission for Δ = 0, which shows an oscillatory behavior of the cavity light between the self-organized and nonorganized phases owing to positive feedback. Here, $T/T_{F0} = 0.27$ (0.02); the red curve represents the phase boundary and is calculated using mean-field theory (*30*).

The steady-state phase diagram of the fermionic superradiance is mapped by measuring the threshold while varying the pump-cavity detuning $\Delta = \omega_p - \omega_c$. The boundaries of the normal, unstable, and superradiant phases are clearly observed in Fig. 2. The dependence of the threshold on the detuning Δ shows a tongue-like shape. The minimum critical pump power is observed at $\Delta = -2\pi \times$ 800 kHz, owing to the negligible dispersively induced frequency shift. The phase boundary becomes almost linear for the large detunings, which agrees with the dependence predicted from the Dicke model and observed for the bosonic case (*1*). Near the cavity resonance, in a range of $\Delta/2\pi$ from −300 to 800 kHz, the cavity transmission becomes unstable. The positive feedback leads to an oscillatory behavior of the cavity light between the organized and nonorganized phases, as shown in the inset of Fig. 2. For large blue pump-cavity detunings $\Delta > 0$ and red detuning Δ_a, the mean-field theory with a single cavity mode predicts no phase transitions (see eq. S8). In the experiment, we observe superradiance for such blue pump-cavity detunings, owing to a higher-order mode detuned by about 5 MHz and caused by the nearly confocal cavity used in our work. It is worth noting that fermionic superradiance of a single cavity mode is possible in the blue-detuning region only when the fermion distribution is initially far from its equilibrium distribution, which is challenging and requires further study.

We investigate the scaling of the self-organization threshold with atom number, which shows a notably different behavior compared with bosonic gases, as shown in Fig. 3. It is widely accepted that the threshold scaling is always N^{-1} for the superradiance of BECs and thermal bosonic gases in the cavity (*31*). However, for Fermi gases, owing to the Pauli exclusion principle, fermions do not have equal probability to scatter pump photons, and only fermions coupled to an unoccupied final state can experience self-organization. As a result, the scaling depends on the Fermi energy, and a sub-N^{-1} scaling of the threshold is expected (*31*–*33*). At high densities, the threshold has a universal scaling $N^{-1/2}$ [see (*30*) and inset of Fig. 3B]. In the experiment, we vary the number of atoms and keep T/T_{F0} constant by precisely controlling the evaporative cooling

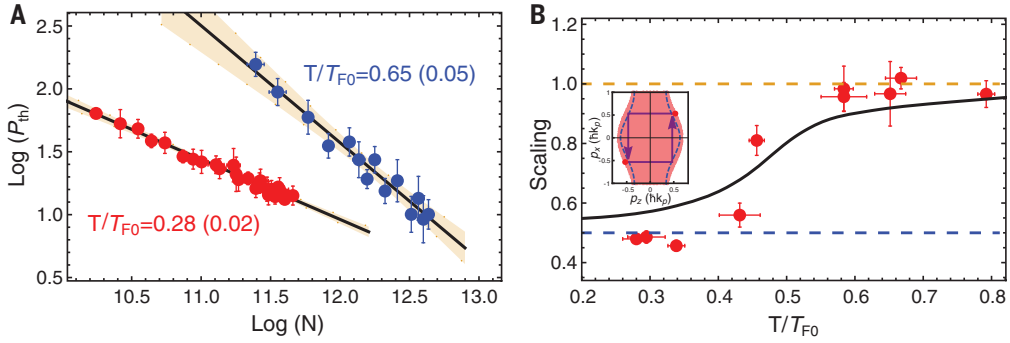


Fig. 3. The threshold scaling. (**A**) The threshold as a function of atom number at a low and high temperature. Red and blue dots are the measured data for $T/T_{F0} = 0.28\ (0.02)$ and $T/T_{F0} = 0.65\ (0.05)$ with $\Delta = -2\pi \times 1$ MHz, respectively. Error bars represent the standard deviation. The solid black lines are the fits with the simple function $P_{th} = C\ N^{-s}$. The orange regimes denote 0.99 of parameter confidence intervals of the fits. (**B**) The dependence of the threshold scaling exponent on temperature. The orange dashed line is $s = 1$ for the bosonic case, and the blue dashed line is $s = 0.5$, which is the theoretical prediction for a zero-temperature Fermi gas. The solid black line is the theoretical calculation, in which we assume that the dispersion in the pumping direction is flat and neglect k_x dependence (*30*). The inset is an illustration of the Fermi blocking effect. The pink area represents the Fermi surface, and the arrows depict transitions between momentum states. Transitions to final states that have a momentum smaller than the Fermi momentum are forbidden because of the Pauli exclusion principle.

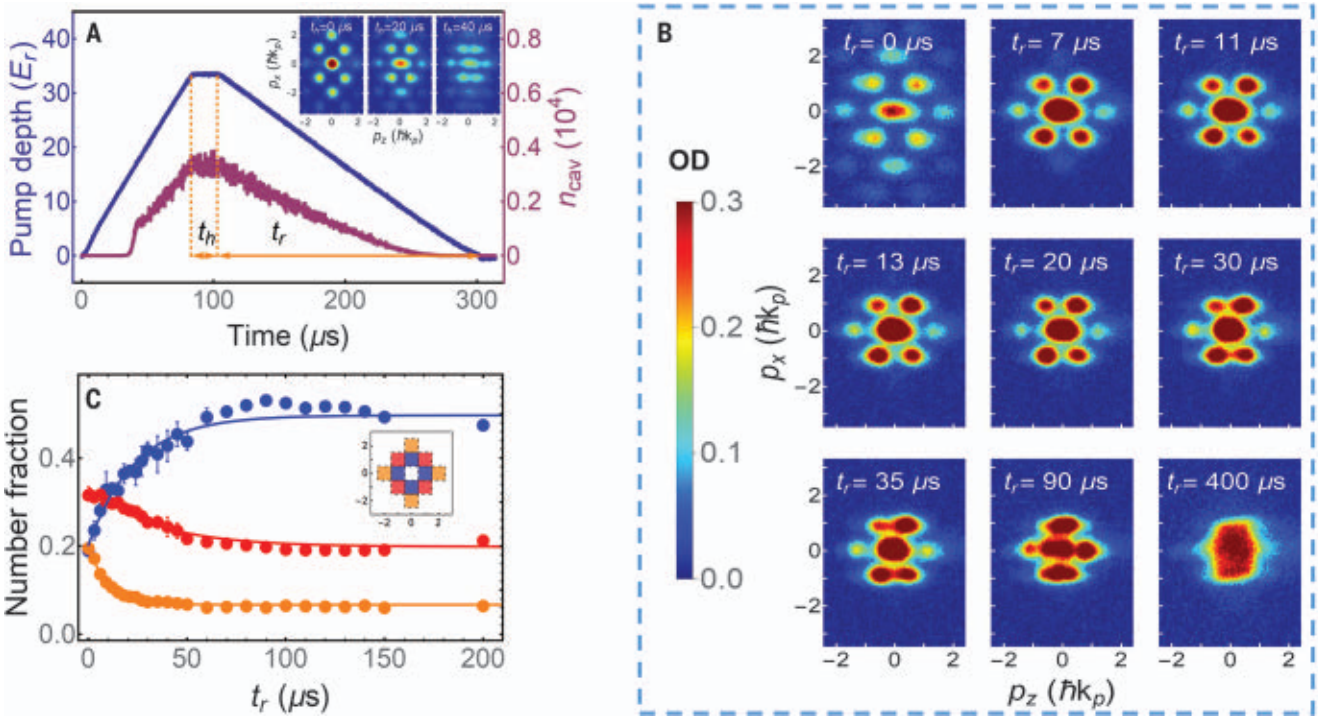


Fig. 4. Dynamic response of the fermionic superradiance by ramping the pumping power. (**A**) Control sequence (blue) of the pump power and the detected cavity transmission (brown). The inset shows absorption images of atoms with different hold times t_h. (**B**) The evolution of the atom patterns with increasing ramping time t_r. (**C**) Atom number fraction (normalized to the total atom number) for the different momentums as a function of t_r. Red, orange, and blue dots are the sums of the fractions of atom numbers with a momentum range enclosed by four red-, orange-, and blue-colored squares in the inset, corresponding to the momentum ranges $(p_x, p_z) = [\pm(0.5\ \text{to}\ 1.5), \pm(0.5\ \text{to}\ 1.5)]\hbar k_p$, $[\pm(1.5\ \text{to}\ 2.5), (-0.5\ \text{to}\ 0.5)]\hbar k_p$ and $[(-0.5\ \text{to}\ 0.5), \pm(1.5\ \text{to}\ 2.5)]\hbar k_p$, and $[(-0.5\ \text{to}\ 0.5), \pm(0.5\ \text{to}\ 1.5)]\hbar k_p$ and $[\pm(0.5\ \text{to}\ 1.5), (-0.5\ \text{to}\ 0.5)]\hbar k_p$, respectively. Solid lines are fits with the exponential function $[\exp(-t/\tau)]$ to extract the characteristic time scale τ. The error bars represent the statistical error of the repeated measurements. Here, $\Delta = -2\pi \times 1.0$ MHz, $t_{tof} = 900$ μs, and $T/T_{F0} = 0.33\ (0.03)$.

process. The relation between the superradiant threshold P_{th} and the atom number N is presented in Fig. 3A for two different temperatures. The fit with a simple function $P_{th} = C\ N^{-s}$, where C is a fit coefficient, gives a scaling $s = 0.48(0.02)$ at the lower temperature $T/T_{F0} = 0.28\ (0.02)$ (red dots in Fig. 3A), which agrees very well with the theoretical predictions $s = 1/2$. For the higher temperature $T/T_{F0} = 0.65\ (0.05)$, the measured scaling is $s = 0.97(0.04)$, which is very close to N^{-1} scaling. The scaling exponent as a function of temperature is shown in Fig. 3B. As the temperature is increased, the threshold scaling shows a

crossover and smoothly changes from $N^{-1/2}$ to N^{-1}. The dependence of the threshold scaling on temperature clearly reveals that the quantum statistics matters in fermionic superradiance.

We next studied the dynamic response of the self-organization of fermionic superradiance by measuring the atom fraction at different momentum states after ramping the pumping lattice power to zero within a time constant t_r. The strength of the pumping lattice is first ramped up to $34\ E_r$, which is larger than the calibrated threshold [$11.2(0.7)\ E_r$] of the QPT, in 80 μs. The atoms are then confined to an array of tubes in a two-dimensional optical lattice formed by a combination of the pump and the emergent intracavity field for the pump power above the threshold. The contrast of the observed interference pattern is reduced with a long holding time t_d owing to the suppressed tunnel rate of atoms between the adjacent tubes in a deep lattice (see the inset of Fig. 4A). This phase coherence can be restored by ramping the pump power to zero in the case of BEC superradiance. However, fermionic superradiance shows a different dynamical response. We change the pump power by varying the strength of the lattice laser beams. After holding the gas for 20 μs at an initial pump strength of $34\ E_r$, we linearly reduce the pump power to zero over a time interval t_r. The absorption images with $t_{tof} = 900$ μs are then analyzed to measure the atom number at different momentum states (see Fig. 4A). The evolution of the atom pattern for different t_r is presented in Fig. 4B. The atoms around the momenta $p_{x2} = (p_x, p_z) = (\pm 2\hbar k_p, 0)$ and $p_{z2} = (0, \pm 2\hbar k_p)$ are quickly restored to the atomic states with low momenta. The atoms around the p_{z2} persist a little longer, which may be because the emergent intracavity field cannot be turned off simultaneously with the pumping lattice, owing to the finite threshold and lifetime of the cavity field. However, the dynamic response of atoms around the momenta $p_1 = (\pm\hbar k_p, \pm\hbar k_p)$ is relatively slow, which is in contrast with the bosonic case where the normal state is restored very quickly (*1*, *2*). As t_r increases, an increasing number of atoms is accumulated at the atomic momentum states around $p_x = \pm\hbar k_p$ and $p_z = \pm\hbar k_p$. For long t_r, ramping the pump strength to zero can be viewed as the band mapping (i.e., $t_r = 400$μs in Fig. 4B). The number fraction at different momentum states as a function of t_r is shown in Fig. 4C. Red, orange, and blue dots are the sums of the fractions of atom numbers with a momentum range enclosed by four red-, orange-, and blue-colored squares in the inset, respectively. The time scales are obtained by using a fit of an exponential function, which gives $\tau_1 = 33.9\ (3.9)$ μs (red curve) for atoms around the momenta p_1 and $\tau_2 = 10.2\ (0.6)$ μs (orange curve) for atoms around the momenta p_{x2} and p_{z2}. τ_2 is comparable to the tunneling time τ_{tunnel} between two neighboring lattice sites, which is about 11 μs for a lattice with a potential depth of $5.0\ (0.8)\ E_r$ corresponding to the threshold measured by ramping down the pump intensity. However, τ_1 is about 3.3 times slower than τ_2 of the high-momentum states and the tunneling time τ_{tunnel}. The comparatively slow dynamics of the fermions on the interference pattern of pump light and emergent field when approaching the normal state is most likely caused by Pauli blocking, which prevents atoms from occupying the low-momentum states that are already populated at low temperatures.

We have revealed the role of the quantum statistics to the superradiant quantum phase transition and found that the Pauli exclusion changes the scaling of the critical pump strength with atom number. The realization of the coupling of the Fermi gas to the cavity field will enable the study of many-body phases and nonequilibrium dynamics with photon-mediated long-range interactions, including the antibunching density correlations associated with antiferromagnetic self-ordering, topological superradiance, cavity optomechanics with synthetic Landau levels, and many-body localization (*25*, *34*, *35*).

During the review of this report, manuscripts reporting the observation of Pauli blocking in light scattering from fermionic quantum gases in free space were posted (*36*–*38*).

REFERENCES AND NOTES

1. K. Baumann, C. Guerlin, F. Brennecke, T. Esslinger, *Nature* **464**, 1301–1306 (2010).
2. J. Klinder, H. Keßler, M. Wolke, L. Mathey, A. Hemmerich, *Proc. Natl. Acad. Sci. U.S.A.* **112**, 3290–3295 (2015).
3. H. Ritsch, P. Domokos, F. Brennecke, T. Esslinger, *Rev. Mod. Phys.* **85**, 553–601 (2013).
4. R. H. Dicke, *Phys. Rev.* **93**, 99–110 (1954).
5. K. Hepp, E. H. Lieb, *Ann. Phys.* **76**, 360–404 (1973).
6. Y. K. Wang, S. T. Hioe, *Phys. Rev. A* **7**, 831–836 (1973).
7. R. Landig *et al*., *Nature* **532**, 476–479 (2016).
8. J. Léonard, A. Morales, P. Zupancic, T. Esslinger, T. Donner, *Nature* **543**, 87–90 (2017).
9. K. Baumann, R. Mottl, F. Brennecke, T. Esslinger, *Phys. Rev. Lett.* **107**, 140402 (2011).
10. F. Brennecke *et al*., *Proc. Natl. Acad. Sci. U.S.A.* **110**, 11763–11767 (2013).
11. J. Klinder, H. Keßler, M. R. Bakhtiari, M. Thorwart, A. Hemmerich, *Phys. Rev. Lett.* **115**, 230403 (2015).
12. Z. Gong, R. Hamazaki, M. Ueda, *Phys. Rev. Lett.* **120**, 040404 (2018).
13. W. Ketterle, S. Inouye, *Phys. Rev. Lett.* **86**, 4203–4206 (2001).
14. M. G. Moore, P. Meystre, *Phys. Rev. Lett.* **86**, 4199–4202 (2001).
15. J. Keeling, M. J. Bhaseen, B. D. Simons, *Phys. Rev. Lett.* **112**, 143002 (2014).
16. F. Piazza, P. Strack, *Phys. Rev. Lett.* **112**, 143003 (2014).
17. Y. Chen, Z. Yu, H. Zhai, *Phys. Rev. Lett.* **112**, 143004 (2014).
18. F. Schlawin, D. Jaksch, *Phys. Rev. Lett.* **123**, 133601 (2019).
19. J. S. Pan, X. J. Liu, W. Zhang, W. Yi, G. C. Guo, *Phys. Rev. Lett.* **115**, 045303 (2015).
20. F. Mivehvar, H. Ritsch, F. Piazza, *Phys. Rev. Lett.* **118**, 073602 (2017).
21. A. Sheikhan, F. Brennecke, C. Kollath, *Phys. Rev. A* **94**, 061603 (2016).
22. C. Kollath, A. Sheikhan, S. Wolff, F. Brennecke, *Phys. Rev. Lett.* **116**, 060401 (2016).
23. A. Sheikhan, F. Brennecke, C. Kollath, *Phys. Rev. A* **93**, 043609 (2016).
24. W. Zheng, N. R. Cooper, *Phys. Rev. Lett.* **117**, 175302 (2016).
25. E. Colella, S. Ostermann, W. Niedenzu, F. Mivehvar, H. Ritsch, *New J. Phys.* **21**, 043019 (2019).
26. A. Sheikhan, C. Kollath, *Phys. Rev. A* **99**, 053611 (2019).
27. K. Roux, H. Konishi, V. Helson, J.-P. Brantut, *Nat. Commun.* **11**, 2974 (2020).
28. S. Deng *et al*., *Science* **353**, 371–374 (2016).
29. S. Deng *et al*., *Sci. Adv.* **4**, eaar5909 (2018).
30. See supplementary materials.
31. K. J. Arnold, M. P. Baden, M. D. Barrett, *Phys. Rev. Lett.* **109**, 153002 (2012).
32. J. K. Asbóth, P. Domokos, H. Ritsch, A. Vukics, *Phys. Rev. A* **72**, 053417 (2005).
33. R. M. Sandner, W. Niedenzu, F. Piazza, H. Ritsch, *Europhys. Lett.* **111**, 53001 (2015).
34. B. Padhi, S. Ghosh, *Phys. Rev. Lett.* **111**, 043603 (2013).
35. P. Sierant, K. Biedroń, G. Morigi, J. Zakrzewski, *SciPost Phys.* **7**, 008 (2019).
36. Y. Margalit, Y.-K. Lu, F. C. Top, W. Ketterle, arXiv:2103.06921 [quant-ph] (2021).
37. C. Sanner *et al*., arXiv:2103.02216 [quant-ph] (2021).
38. A. B. Deb, N. Kjærgaard, arXiv:2103.02319 [cond-mat.quant-gas] (2021).
39. X. Zhang, Y. Chen, Z. Wu, J. Wang, J. Fan, S. Deng, H. Wu, Data for "Observation of a superradiant quantum phase transition in an intracavity degenerate Fermi gas." Zenodo (2021); https://doi.org/10.5281/zenodo.5163775.

ACKNOWLEDGMENTS

We thank H. Zhai and Z. Yu for helpful discussions. **Funding:** This research is supported by the National Key Research and Development Program of China (grant no. 2017YFA0304201), the National Natural Science Foundation of China (NSFC) (grant nos. 11925401 and 11734008), the Shanghai Committee of Science and Technology (17JC1400500), and the Shanghai Municipal Science and Technology Major Project (grant no. 2019SHZDZX01). **Author contributions:** H.W. developed the concept, designed the experiments, and supervised the projects. Y.C. carried out the theoretical calculations. X.Z., Z.W., J.W., J.F., and S.D. performed the measurements, analyzed the data, and prepared the figures. All authors discussed the results and reviewed the manuscript. H.W., X.Z., and Y.C. wrote the manuscript. **Competing interests:** The authors declare no competing interests. **Data and materials availability:** The data are archived on Zenodo (*39*).

SUPPLEMENTARY MATERIALS

https://science.org/doi/10.1126/science.abd4385
Materials and Methods
Supplementary Text
Figs. S1 to S6
References (*40*–*42*)

21 June 2020; accepted 12 August 2021
Published online 26 August 2021
10.1126/science.abd4385

METALLURGY

Cryoforged nanotwinned titanium with ultrahigh strength and ductility

Shiteng Zhao[1,2,3]*†, Ruopeng Zhang[1,2]†, Qin Yu[4], Jon Ell[1,4], Robert O. Ritchie[1,4], Andrew M. Minor[1,2]*

Nanostructured metals are usually strong because the ultrahigh density of internal boundaries restricts the mean free path of dislocations. Usually, they are also more brittle because of their diminished work-hardening ability. Nanotwinned materials, with coherent interfaces of mirror symmetry, can overcome this inherent trade-off. We show a bulk nanostructuring method that produces a multiscale, hierarchical twin architecture in a hexagonal closed-packed, solute-free, and coarse-grained titanium (Ti), with a substantial enhancement of tensile strength and ductility. Pure Ti achieved an ultimate tensile strength of almost 2 gigapascals and a true failure strain close to 100% at 77 kelvin. The multiscale twin structures are thermally stable up to 873 kelvin, which is above the critical temperature for many applications in extreme environments. Our results demonstrate a practical route to achieve attractive mechanical properties in Ti without involving exotic and often expensive alloying elements.

Titanium (Ti) has the highest strength-to-weight ratio among all the metallic elements, which, in addition to its outstanding corrosion resistance, renders it ideal for a variety of weight- and environment-sensitive load-bearing applications (*1*). The strength of pure Ti, however, is moderate. One way to harden Ti is to alloy it with other elements such as oxygen (O), aluminum (Al), and vanadium (V), forming either a solid solution or secondary phases (*1*). The strength of these alloys is improved, but almost always at the expense of the ductility.

An alternative route to strengthening structural metals is by tailoring the grain size through thermal-mechanical processing (*2*, *3*). Specifically, reducing grain size to a submicrometer and nanometer regime leads to a substantial increase in the yield strength (*4*–*6*), whereas ductility can be preserved when certain types of interfaces are introduced (*7*, *8*). In this respect, the past two decades has witnessed the successful development of nanotwinned metals. Numerous studies in face-centered cubic (fcc) metals suggest that twinning can lead to a much-improved strength without sacrificing resistance to fracture (*9*, *10*). This observation is attributed to the coherent nature of the twin boundary, which can both block and transmit incoming dislocations, depending on their characteristics, and thus provide strength and ductility, respectively (*11*). By tailoring the spacing and orientation of twin lamellae, the mechanical properties can be optimized even further (*8*, *12*, *13*). Nanotwinned copper with a gradient microstructure exhibits enhanced strength because of an extra work-hardening capacity (*14*), whereas highly oriented nanotwinned copper displayed an enhanced fatigue resistance because of the distinct dislocation pathways (*15*). Twin boundaries also represent low-energy boundaries with a much-reduced mobility at elevated temperatures. This property renders them thermally more stable than random high-angle grain boundaries (*16*). In this regard, nanoscale twins represent an optimal feature for structural metals (*9*). However, engineering these features into materials in a cost-efficient way is nontrivial. Traditionally, this can be achieved through either "bottom-up" methods, such as electrodeposition (*12*) and sputtering (*17*), or "top-down" methods, such as severe plastic deformation (*18*, *19*). However, almost all of these methods have been successfully accomplished in fcc metals (*20*, *21*), mostly in copper and steel (*19*, *22*), whereas generalization to hexagonal close packed (hcp) metals has been challenging. This challenge extends to a general method for creating a nanotwinned structure in a bulk sample without generating unfavorable residual stresses.

We demonstrate that hierarchical nanotwinned structures can be engineered in pure Ti (nominal composition in weight percentage: 99.95% Ti and 0.05% O) through massive mechanical twinning induced by means of a cryo-mechanical process. The ultralow O content (lower than commercial purity–grade Ti) is chosen to promote the twin propensity because O suppresses twinning in Ti (*23*). The cuboid-shaped specimens were repetitively forged along the three principal axes in liquid nitrogen (Fig. 1A) (*24*). The gentle uniaxial compression at each step controls the density of twins while preserving the initial grain structure of the material, which is in sharp contrast to other anisotropic processing methods such as extrusion and rolling, in which grains are elongated in one direction (*25*, *26*). The cryo-mechanically deformed materials were then heat treated (tempered) at an intermediate temperature (673 K) for 1 hour, which relieved the undesirable residual stress without triggering additional grain coarsening.

The electron backscattered diffraction (EBSD) map (Fig. 1B) reveals a complex multiscale twin structure in the multiaxis-forged Ti. The initial equiaxed grain structure is still visible, but after cryo-mechanical treatment, each grain contains profuse lenticular-shaped twins. These deformation features, introduced through a cryo-mechanical process, are retained during the subsequent heat treatment. Grain-boundary misorientation analysis suggests that these twins are mostly $\{10\bar{1}2\}$ tensile twins and $\{11\bar{2}2\}$ compression twins (fig. S1). A group of characteristic $\{10\bar{1}2\}$ nanotwins is captured in the transmission electron microscopy (TEM) micrograph (Fig. 1C), in which a twin boundary is highlighted in the high-resolution atomic lattice image (Fig. 1D). The nanotwins can often intersect with each other, leading to a complicated twin-twin network (fig. S2). Our TEM images show the same nanotwinned structure before and after 673 K tempering step (Fig. 1, E and F). After holding the sample at 673 K for 1 hour in the TEM, the nanotwinned structure is retained, but the strain contrast within the twins is diminished owing to residual stress-strain relaxation. We illustrate this strain relaxation using a quantitative representation from a nanobeam diffraction strain map computed before and after TEM in situ annealing (fig. S3). The statistical size distributions of these multiscale structures (Fig. 1G) show a macroscale matrix of randomly distributed, equiaxed grains in tens to hundreds of micrometers, a microscale twin skeleton with twin thickness in micrometers, and nanoscale twin networks with a twin thickness in tens to a couple of hundred nanometers.

The distinct multiscale twin structures result in substantially improved mechanical properties, which we characterized with uniaxial tensile tests at both room temperature (RT) and cryogenic (77 K) temperatures. We illustrate the true stress versus true strain response of the nanotwinned titanium and compare it with conventional coarse-grained Ti (with a grain size of ~100 μm) (Fig. 2A). At RT, the nanotwinned Ti exhibits a tensile strength of 500 MPa, with a tensile ductility (strain to failure) of ~70%. These values are improved by ~50 and ~17%, respectively, compared with the coarse-grained Ti. The yield strength of the as-processed material is controlled both by the reduced mean free path of dislocations in the local nanotwinned area, as well as the relatively coarser-grained matrix, rendering less of a Hall-Petch strengthening effect than nanocrystalline Ti (*27*) but a much higher work-hardening ability.

[1]Department of Materials Science and Engineering, University of California, Berkeley, CA 94720, USA. [2]National Center for Electron Microscopy, Molecular Foundry, Lawrence Berkeley National Laboratory, Berkeley, CA 94720, USA. [3]School of Materials Science and Engineering, Beihang University, Beijing 100191, China. [4]Materials Sciences Division, Lawrence Berkeley National Laboratory, Berkeley, CA 94720, USA.
*Corresponding author. Email: szhao@buaa.edu.cn (S.Z.); aminor@berkeley.edu (A.M.M.)
†These authors contributed equally to this work.

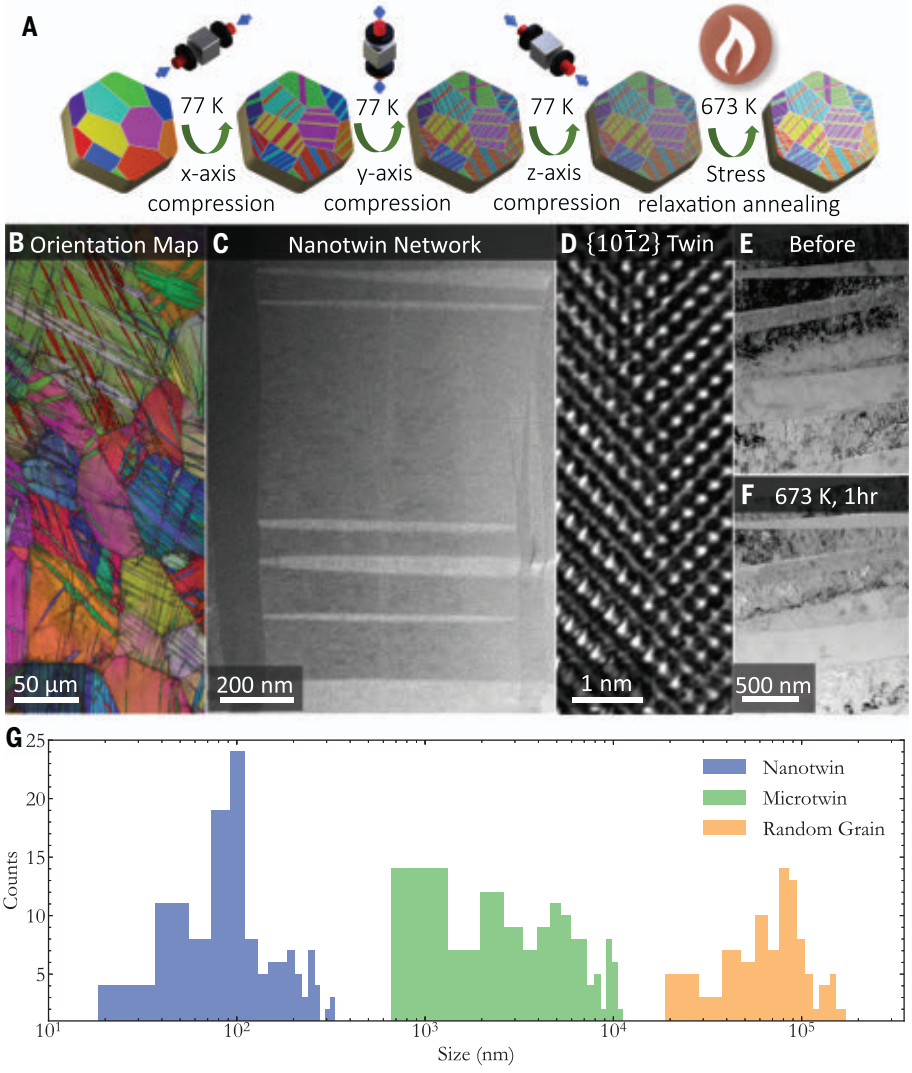


Fig. 1. Hierarchical microstructure of cryo-mechanically prepared nanotwinned Ti. (**A**) Schematic drawing of the cryo-mechanical process that results in the bulk nanotwinned Ti. (**B**) Orientation map showing the nanotwinned structure. (**C**) TEM micrograph of the nanotwin network. (**D**) Atomic-resolution image of a $\{10\bar{1}2\}$ twin boundary. (**E** and **F**) Images of (E) nanotwins at RT after cryo-mechanical process and (F) the same region after in situ TEM annealing at 673 K for 1 hour, showing the stability of the twinned structure and also the relaxation of strain fields from other internal defects. (**G**) Statistical size distribution of the hierarchical microstructure as determined with TEM (blue) and EBSD (green and yellow).

The mechanical properties of the nanotwinned Ti are further enhanced at 77 K, displaying a tensile strength of ~2 GPa and a tensile ductility of almost 100%. The combination of exceptional strength and ductility of nanotwinned Ti makes it superior to many Ti alloys and even certain cryogenic steels (fig. S4) (*28*–*30*). Different stages of plastic deformation can be qualitatively visualized from the plot of strain-hardening rate—the derivative of the flow stress with respect to strain, as a function of strain (Fig. 2B). The plot shows that the nanotwinned Ti displays better mechanical properties than those of its coarse-grained counterpart. This is manifested by a prolonged strain-hardening plateau at RT, which is followed by sizable resurgence in strain hardening at 77 K. Clearly, a sequential activation of deformation mechanisms is in evidence at different stages of plastic deformation. This evolution provides a steady, sustained source of hardening, which increases strength yet also effectively delays the necking, leading to an enhancement in ductility.

Focusing on the deformation mechanisms of the nanotwinned Ti at cryogenic temperatures, we characterized the deformation microstructures at different stages of plastic deformation by plotting the strain-hardening rate ($\theta = d\sigma/d\varepsilon$) normalized by the shear modulus (G), θ/G (Fig. 2C), as a function of the flow stress normalized by the yield stress [the Kocks-Mecking plot (*31*)] at 77 K and integrating it with the corresponding TEM observations. At the onset of plastic deformation, when the stress level is low (<~750 MPa), dislocation-mediated plasticity dominates, and a monotonic decrease in θ/G is expected. The corresponding microstructure (Fig. 2D) has dislocations confined within those prescribed twin boundaries. As the flow stress increases, twinning-induced plasticity takes over. At this stage, the nucleation and growth of primary and secondary twinning of different types evolve the twin-twin network into a more complicated multiscale hierarchy architecture, in which the twin spacing is reduced substantially into the nanoscale, leading to an enhanced dynamic Hall-Petch effect. A typical nanotwin network is shown in Fig. 2E. The increased dislocation density and the refined interspacing of the nanotwin network engender a higher activation stress for subsequent twinning, which in turn increases the flow stress (*32*). Macroscopically, this is manifested by an extended plateau followed by a rising strain-hardening rate. The strain-hardening rate drops rapidly toward the last stage of the plastic deformation, which is microstructurally associated with severe grain refinement, especially at the localization of deformation. The TEM micrograph (Fig. 2F) taken in the vicinity of the necking region shows a high density of equiaxial grains with a grain size of ~300 nm. Despite yielding a high flow stress, these ultrafine grains make both dislocation activity and twinning (*33*) difficult to operate and consequently jeopardize the strain-hardening ability. We also analyzed the microstructure in the as-fractured sample (fig. S5) and observed that the necking region displays a much finer microstructure with a sharper $\{0001\}\langle 10\bar{1}0\rangle$ texture component than in regions further away, which is consistent with the TEM observations (Fig. 2F).

Dimensional refinement has long been known to enhance strength and ductility at low temperatures (*29*). The difference here is that the structure evolves during deformation into an optimal hierarchical structure defined by the coarse grains, twin-twin skeleton, nanotwins, and ultrafine grain refinement. In addition to these strengthening mechanisms, the distinct nanotwin architecture plays an effective toughening role in retarding crack extension (*34*). We show that an advancing crack is deflected on a route across the nanotwin barrier (Fig. 2G). Further evidence that nanotwins can either deflect or block crack propagation is shown in fig. S6; the growth of microcracks was observed during in situ TEM tensile testing at RT. This implies that our nanotwinned Ti may display enhanced damage tolerance.

Among all the mechanisms described above, twinning-induced plasticity plays the pivotal role. Using quasi in situ EBSD characterizations, we were able to capture this evolution

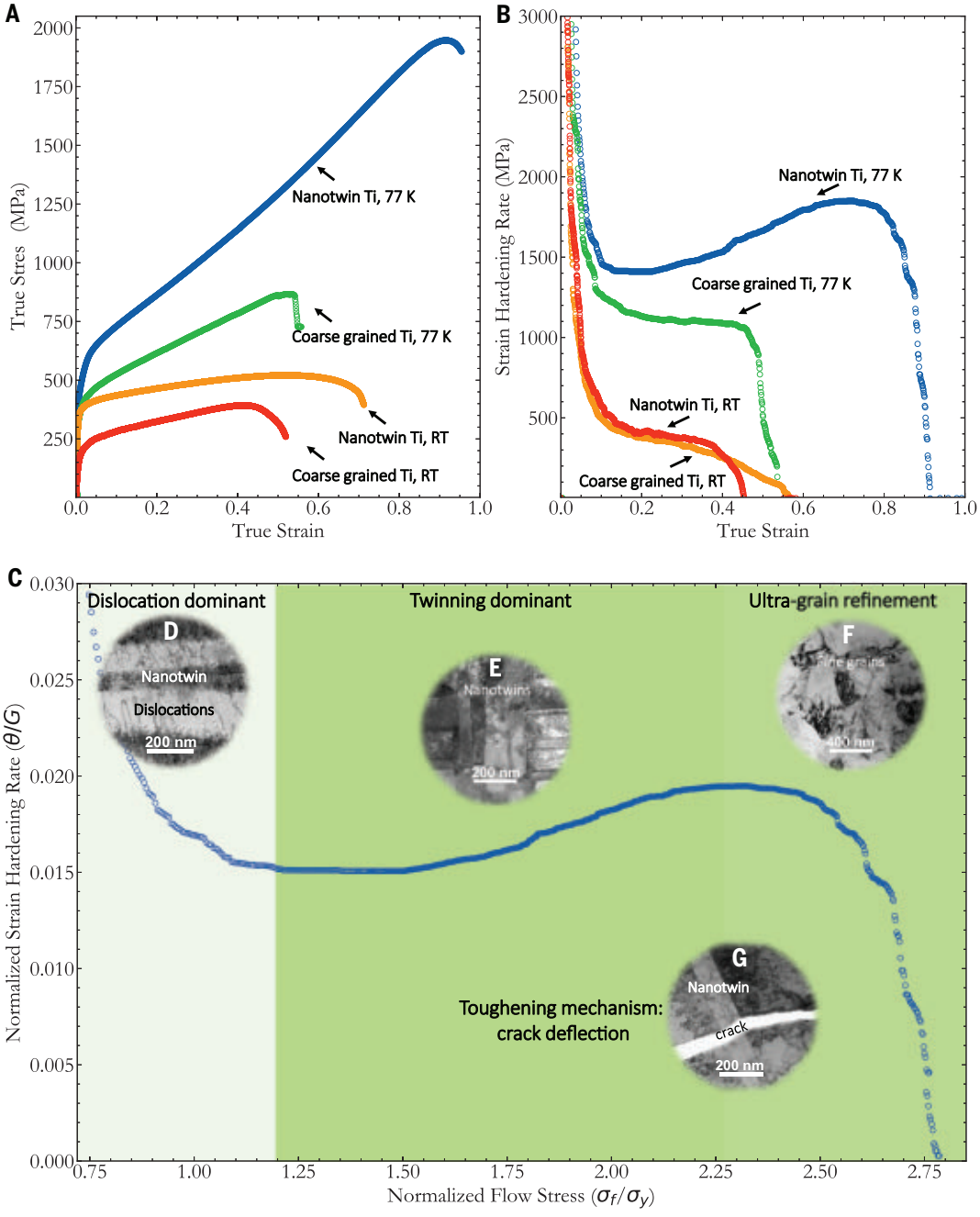


Fig. 2. Mechanical characterization of the hierarchical nanostructured Ti. (**A**) True stress versus true strain curves with a nominal strain rate of 10^{-3} s^{-1} and the comparison with its coarse-grained counterpart. (**B**) Corresponding plots of strain-hardening rate versus true strain. (**C**) The stages of plastic deformation at 77 K are shown schematically along with a plot of the strain-hardening rate normalized by the shear modulus, $\theta/G = (d\sigma/d\varepsilon)/G$, as a function of the flow stress normalized by the yield stress. The normalized strain-hardening rate versus normalized flow stress curve clearly shows that there are multiple stages of plastic deformation. (Insets) The characteristic deformation features at the different stages.

of twinning, detwinning, and retwinning. We collected a series of EBSD analyses of the same region with incremental degrees of plastic strain at 77 K (Fig. 3). We also collected orientation maps (Fig. 3, A to F) and the corresponding boundary misorientation maps (Fig. 3, G to L). We show the initial twin structure in Fig. 3A. Correspondingly, we can identify two types of twins with distinctive misorientations by the boundary misorientation map (Fig. 3G): $\{10\bar{1}2\}$ tensile twins with a misorientation angle of 85° (orange) and $\{11\bar{1}2\}$ compression twins with a misorientation angle of 65° (green). After 5% plastic strain, multiple $\{11\bar{2}2\}$ twins are nucleated at grain boundaries (Fig. 3, B and H) and grow with further deformation [engineering strain (ε) = 10%] (Fig. 3, C and I) until secondary $\{10\bar{1}2\}$ twins start to nucleate at the primary $\{11\bar{2}2\}$ twin boundaries (ε = 15%) (Fig. 3, D and G). Subsequently, these secondary $\{10\bar{1}2\}$ twins interact with the previously developed primary $\{11\bar{2}2\}$ twins, propagate (ε = 25%) (Fig. 3, E and K), and eventually consume the original grain structure (ε = 35%) (Fig. 3, F and L). Above 25% plastic deformation, the twin-twin interactions produce profuse "junctions" of fine grains within the original coarse grains. We summarized the length fractions of each type of twin and the total twin boundaries in Fig. 3M. After a rapid growth rate of the total twin fraction, the combination and competition of continuous twinning and detwinning caused a much-reduced growth rate of the twin fraction at the microscale. However, even when the microscale twin fraction saturates (~70%), the nanotwin density seems to keep increasing until severe twin-twin intersections and twin-boundary rotations come into play toward the end of plastic deformation, which is evident in the TEM observations (Fig. 2C). Despite the complex twin-structure evolution, the flow stress increases

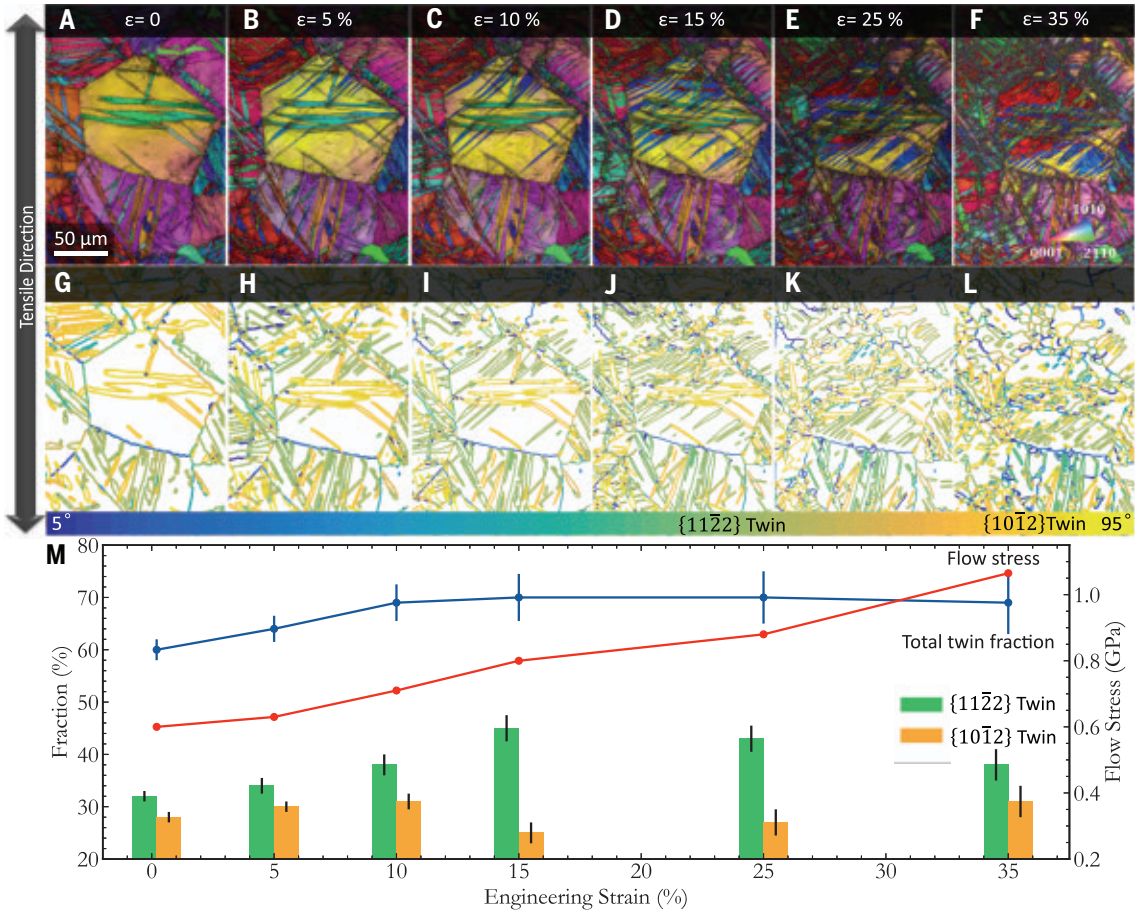


Fig. 3. Microstructure evolution of nanotwinned Ti. (**A** to **F**) Orientation maps (overlaid with image quality) captured in an area of interest at progressive strain levels of up to 35% engineering strain. (**G** to **L**) The corresponding grain boundary misorientation maps show the evolution of the two characteristic twin boundaries: $\{11\bar{2}2\}$ compression twins with a misorientation of ~65° (green), and $\{10\bar{1}2\}$ tensile twins with a misorientation of 85° (orange-yellow). Twins, which nucleate at either random grain boundaries or preexisting twin boundaries, will propagate, grow, and intersect with each other. Toward higher strains, twin-twin intersections form junctions of fine grains within the original coarse grains. (**M**) Evolution of the length fraction of the $\{11\bar{2}2\}$ and $\{10\bar{1}2\}$ twin boundaries as well as the fraction of the total twin boundaries, which increases initially and saturates at about 15% engineering strain. The full EBSD scans contain a much larger area with many more grains. For display purpose, only a fraction of the data was shown in (A) to (L). The statistics of twins in (M), however, are measured from the full datasets.

monotonically as a function of strain. We can attribute this to (i) the fraction of nanotwins still increasing beyond what can be resolved with the quasi–in situ EBSD analysis and (ii) the twin-twin junctions within the grains refining the grain size even further to produce more interfaces that impede dislocation motion (*19*). Nevertheless, both mechanisms lead to a dynamic Hall-Petch effect (*27*, *35*, *36*): mobile dislocations confined by relative rigid interfaces, which renders a higher resistance to plastic deformation. We show evidence for this (fig. S7), in which a group of mobile $\langle a \rangle$ type screw dislocations are "arrested" by two nanotwins. Moreover, the activation of twinning mode depends mostly on the maximum Schmid factor criterion (fig. S8). Such a marked microstructural evolution is also accompanied by the development of $\{0001\}\langle 10\bar{1}0\rangle$ texture (fig. S9). Such texture is not only caused by the twinning but also by $\langle a \rangle$ type dislocation slip on the $\{10\bar{1}0\}$ prismatic planes (*37*, *38*).

Nanocrystalline metals become progressively unstable at elevated temperatures because the profuse interfaces can be consumed by grain growth, through Ostwald ripening (*16*). Therefore, the temperature that marks the onset of grain coarsening, which is usually proportional to the melting point of the material, eventually limits the useful service temperature of such nanocrystalline metals. Ti has a reasonably high melting temperature (1941 K) among structural metals, and the usefulness of the nanotwinned structure is dependent on its thermal stability. In situ TEM heating experiments revealed that the nanotwin structure is thermally stable up to 873 K (Fig. 4, A and B). Further heating, however, led to aggressive oxidation (Fig. 4, C and D) because the sample was a thin electron-transparent foil, and the microscope was only under a nominal vacuum of roughly 1.3×10^{-3} Pa (~10^{-5} torr). At around 1123 K (Fig. 4E), severe oxidation started to develop (white dotted islands), yet the nanotwin network remained relatively preserved. These in situ TEM heating experiments were further corroborated by means of ex situ annealing and post mortem EBSD analysis; we show that heating of the nanotwinned Ti at 673 K for 48 hours does not result in either noticeable grain growth or an obvious reduction in the number of twin boundaries (Fig. 4, F and G). The local kernel averaged misorientation maps (Fig. 4, H and I) suggest that the annealed sample (Fig. 4I) has relatively lower misorientation within grains, inferring that the density of geometrically necessary dislocations is reduced. The good thermal stability of the nanotwinned Ti enables the preservation of the hierarchical microstructure at elevated temperatures, indicating that the material has the capacity to operate over a wide temperature range, covering the majority of traditional applications of Ti-based alloys.

Tensile tests were also conducted at elevated temperatures of up to 873 K (600°C). The yield strength decreases monotonically as a function of temperature (Fig. 4E), in both coarse-grained and nanotwinned Ti. At these low stress levels, deformation twinning is progressively difficult and eventually ceases to occur, rendering dislocations as the primary carrier of plasticity. Even so, the strength of the nanotwinned Ti is still much higher than its coarse-grained counterpart at all the temperatures studied.

By creating a synergy of deformation mechanisms—most notably, deformation

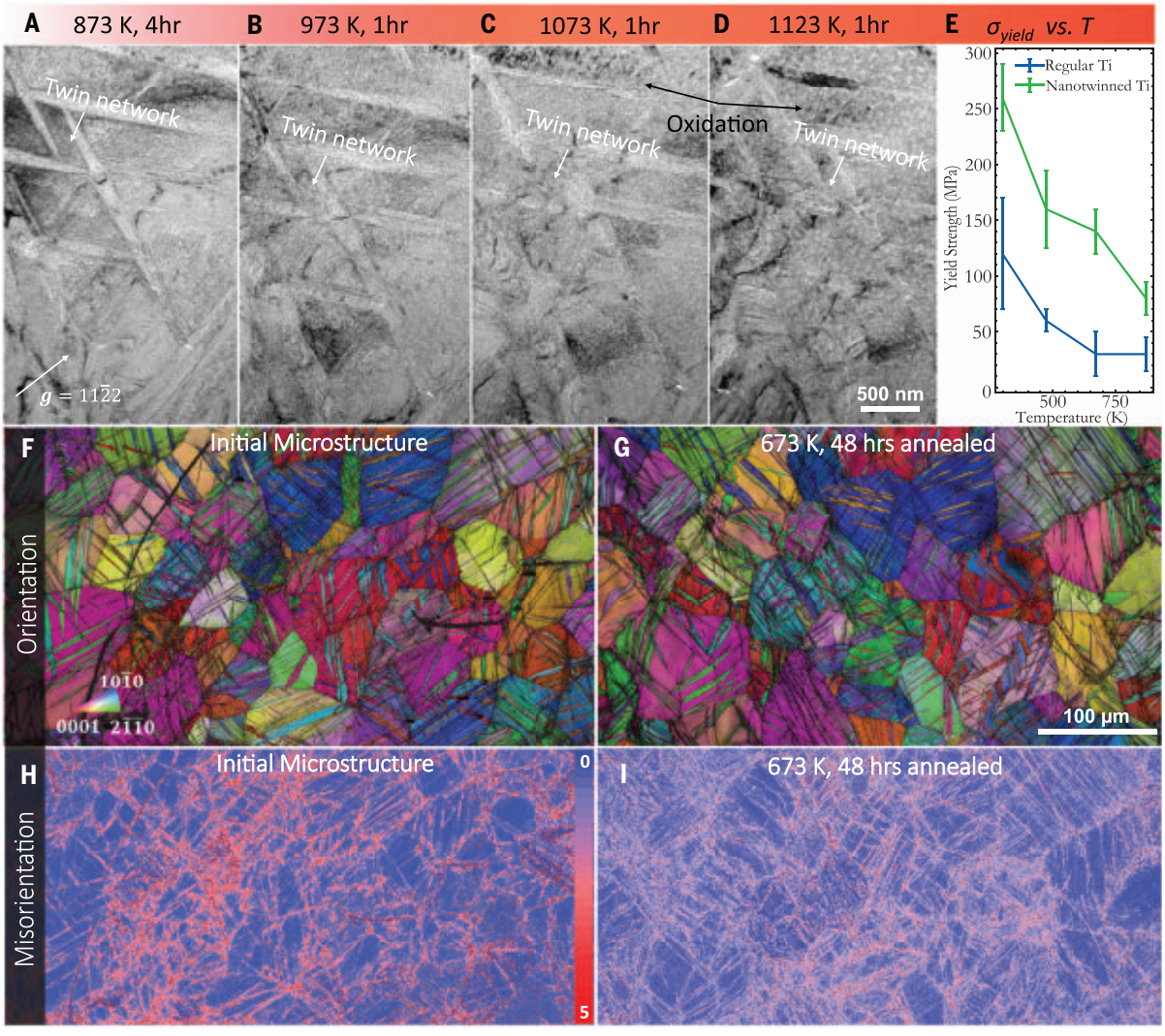


Fig. 4. Thermal stability of the nanotwinned Ti. (**A**) In situ TEM heating experiments show that the nanotwin network (white arrows) is thermally stable up to 600°C (873 K). (**B** and **C**) Above 700°C (973 K), the contrast of the twin interface is getting progressively weaker. (**D**) At around 850°C, oxide flakes start to show up in the matrix. (**E**) Yield strength of the nanotwinned Ti as a function of temperature and the comparison with the coarse-grained materials. (**F**) EBSD IPF mapping and (**H**) the corresponding kernel averaged misorientation (KAM) mapping of the as fabricated nanotwinned titanium. (**G**) IPF and (**I**) KAM maps of the same sample (in similar regions of interest) annealed at 400°C for 48 hours.

twinning—fcc materials, especially CrCoNi-based high-entropy alloys, can be developed with remarkable combinations of strength and ductility that are further enhanced at cryogenic temperature (*39*, *40*). In this work, by using cryo-mechanical processing, we have achieved this in a hcp material, Ti, without the need for any alloying elements.

We have introduced a straightforward and efficient method to produce thermally stable, bulk nanotwinned Ti. The mechanical properties of this material, specifically its strength and tensile ductility, are enhanced to a large extent from ambient to cryogenic temperatures. The introduction of a multiscale twin architecture effectively subdivides the original grains and substantially refines the mean free path of dislocations. Subsequently, the tensile and compressive twins induced during multi-axis–forging can continue to twin, detwin, and retwin, which leads to an enhanced work-hardening ability. Accordingly, nonuniform plastic flow is postponed. This combination of properties suggests that such nanotwinned Ti could be applied to a wide range of applications, especially those involving extreme temperatures.

What sets the nanotwin Ti apart from many other Ti alloys is its cryogenic performance, with attractive strength as well as ductility that is better than even the high-strength Ti-6Al-4V alloy (*41*). This suggests that nanotwin Ti is a strong candidate for cryogenic applications. Some examples include the retaining rings of superconducting magnets, structural parts of the liquefied natural gas storage tanks, and materials exposed to deep ocean and deep space environments. Historically, these are applications for cryogenic steels such as austenitic 18Mn-5Cr (*30*) and 32Mn-7Cr-0.6Mo-0.3N alloys (*42*) and ferritic Fe-9Ni alloy (*29*). Nanotwin Ti outperforms these materials in both strength and ductility (fig. S4), at half the density.

The enhanced work-hardening ability due to massive twinning at liquid-nitrogen temperature indicates that nanotwinned Ti may display a high impact resistance at higher strain rates (*43*) because twinning in hcp metals is also promoted by reducing the time scale of deformation (*44*). Nanotwinned Ti may also possess sound radiation-damage tolerance because the profuse nanotwin boundaries provide a high density of interfaces to channel

point defects and therefore prevent the formation of voids (*45*, *46*). In addition, the thermal stability of nanotwinned Ti renders it applicable at temperatures as high as 873 K, which is comparable with many industrial power plant applications, and at the lower-temperature regions in gas-turbine engines. Moreover, compared with the heavily alloyed, highly expensive high-entropy alloys (*39*, *40*, *47*) with similar mechanical properties, no alloying elements are involved in the nanotwin Ti. This makes it a "simpler" alloy that is economically attractive and easily recyclable (*2*). All of these beneficial factors make nanotwinned Ti not only scientifically interesting but also a potential industrial product.

REFERENCES AND NOTES

1. G. Lütjering, J. C. Williams, *Titanium: Engineering Materials and Processes* (Springer, ed. 2, 2007).
2. X. Li, K. Lu, *Science* **364**, 733–734 (2019).
3. X. Wu *et al*., *Proc. Natl. Acad. Sci. U.S.A.* **112**, 14501–14505 (2015).
4. S. Yip, *Nature* **391**, 532–533 (1998).
5. M. A. Meyers, A. Mishra, D. J. Benson, *Prog. Mater. Sci.* **51**, 427–556 (2006).
6. K. S. Kumar, H. Van Swygenhoven, S. Suresh, *Acta Materialia* **51**, 5743–5774 (2003).
7. R. Z. Valiev, I. V. Alexandrov, Y. T. Zhu, T. C. Lowe, *J. Mater. Res.* **17**, 5–8 (2002).
8. K. Lu, L. Lu, S. Suresh, *Science* **324**, 349–352 (2009).
9. L. Lu, X. Chen, X. Huang, K. Lu, *Science* **323**, 607–610 (2009).
10. Q. Huang *et al*., *Nature* **510**, 250–253 (2014).
11. Z. Zhang *et al*., *Nat. Commun.* **8**, 14390 (2017).
12. L. Lu, M. L. Sui, K. Lu, *Science* **287**, 1463–1466 (2000).
13. E. Ma *et al*., *Appl. Phys. Lett.* **85**, 4932–4934 (2004).
14. Z. Cheng, H. Zhou, Q. Lu, H. Gao, L. Lu, *Science* **362**, eaau1925 (2018).
15. Q. Pan, H. Zhou, Q. Lu, H. Gao, L. Lu, *Nature* **551**, 214–217 (2017).
16. G. Gottstein, L. S. Shvindlerman, *Grain Boundary Migration in Metals: Thermodynamics, Kinetics, Applications* (CRC Press, 1999).
17. A. M. Hodge, Y. M. Wang, T. W. Barbee Jr., *Scr. Mater.* **59**, 163–166 (2008).
18. R. Valiev, *Nat. Mater.* **3**, 511–516 (2004).
19. Y. Wei *et al*., *Nat. Commun.* **5**, 3580 (2014).
20. L. Sun, X. He, J. Lu, *npj Computational Materials* **4**, 6 (2018).
21. X. Li, L. Lu, J. Li, X. Zhang, H. Gao, *Nat. Rev. Mater.* **5**, 706–723 (2020).
22. F. K. Yan, G. Z. Liu, N. R. Tao, K. Lu, *Acta Mater.* **60**, 1059–1071 (2012).
23. H. Conrad, *Prog. Mater. Sci.* **26**, 123–403 (1981).
24. Materials and methods are available as supplementary materials.
25. S. W. Choi, J. W. Won, S. Lee, J. K. Hong, Y. S. Choi, *Mater. Sci. Eng. A* **738**, 75–80 (2018).
26. J. W. Won *et al*., *Scr. Mater.* **178**, 94–98 (2020).
27. Z. C. Cordero, B. E. Knight, C. A. Schuh, *Int. Mater. Rev.* **61**, 495–512 (2016).
28. K. A. Yushchenko, in *Advances in Cryogenic Engineering Materials*, A. F. Clark, Ed. (Springer, 1984), pp. 271–282.
29. C. K. Syn, S. Jin, J. W. Morris, *Metall. Trans., A, Phys. Metall. Mater. Sci.* **7**, 1827–1832 (1976).
30. R. Miura, K. Ohnishi, H. Nakajima, Y. Takahashi, K. Yoshida, in *Austenitic Steels at Low Temperatures* (Plenum Press, 1983), pp. 287–293.
31. H. Mecking, U. F. Kocks, *Acta Metall.* **29**, 1865–1875 (1981).
32. Y. T. Zhu, X. Z. Liao, X. L. Wu, *Prog. Mater. Sci.* **57**, 1–62 (2012).
33. J. L. Sun *et al*., *Scr. Mater.* **69**, 428–431 (2013).
34. Z. Zeng, X. Li, L. Lu, T. Zhu, *Acta Mater.* **98**, 313–317 (2015).
35. N. Hansen, *Scr. Mater.* **51**, 801–806 (2004).
36. F. Otto *et al*., *Acta Mater.* **61**, 5743–5755 (2013).
37. C. N. Tomé, R. A. Lebensohn, U. F. Kocks, *Acta Metall. Mater.* **39**, 2667–2680 (1991).
38. D. N. Williams, D. S. Eppelsheimer, *Nature* **170**, 146–147 (1952).
39. B. Gludovatz *et al*., *Science* **345**, 1153–1158 (2014).
40. B. Gludovatz *et al*., *Nat. Commun.* **7**, 10602 (2016).
41. K. Nagai *et al*., *ISIJ Int.* **31**, 882–889 (1991).
42. F. Ruidong, Z. Yangzeng, R. Yibin, *J. Mater. Eng. Perform.* **10**, 456–459 (2001).
43. D. R. Chichili, K. T. Ramesh, K. J. Hemker, *Acta Mater.* **46**, 1025–1043 (1998).
44. S. G. Song, G. T. Gray, *Metall. Mater. Trans., A Phys. Metall. Mater. Sci.* **26**, 2665–2675 (1995).
45. Y. Chen *et al*., *Nat. Commun.* **6**, 7036 (2015).
46. R. W. Grimes, R. J. M. Konings, L. Edwards, *Nat. Mater.* **7**, 683–685 (2008).
47. Z. Li, K. G. Pradeep, Y. Deng, D. Raabe, C. C. Tasan, *Nature* **534**, 227–230 (2016).

ACKNOWLEDGMENTS

Funding: The authors gratefully acknowledge funding from the US Office of Naval Research under grants N00014-17-1-2283 and N00014-19-1-2376. Q.Y. and R.O.R. also acknowledge the support from the US Department of Energy, Office of Science, Basic Energy Sciences, Materials Sciences and Engineering Division under contract DE-AC02-05-CH11231 to the Damage-Tolerance in Structural Materials Program (KC13) at the Lawrence Berkeley National Laboratory (LBNL). Work at the Molecular Foundry was supported by the Office of Science, Office of Basic Energy Sciences, of the US Department of Energy under contract DE-AC02-05CH11231. The authors thank Timet for providing the high purity titanium and also acknowledge helpful discussions with D. Chrzan, M. Asta, and J. W. Morris Jr.. **Author contributions:** S.Z. formulated the original ideas, which were approved by A.M.M; S.Z., R.Z, and Q.Y. conducted the tensile tests, and R.Z. performed the digital image correlation analysis to calibrate the strain. S.Z. and Q.Y. performed EBSD experiments and analyzed the data. Q.Y. and J.E. conducted mechanical testing at elevated temperatures. S.Z. performed conventional scanning TEM (STEM), TEM, and high-resolution TEM characterization as well as 4D-STEM experiments. R.Z. and S.Z. conducted the in situ TEM heating experiments. S.Z., R.O.R., and A.M.M. drafted the manuscript, and all the authors contributed to the discussions. R.O.R. and A.M.M. supervised the project. **Competing interests:** The authors declare no competing interests, financial or otherwise. Readers are welcome to comment on the online version of the paper. **Data and materials availability:** The data that support the findings of this study are available at an online data repository: https://figshare.com/projects/Cryoforged_nanotwinned_titanium_with_ultrahigh_strength_and_ductility/119352. Correspondence and requests for materials should be addressed szhao@buaa.edu.cn (S.Z.) and aminor@berkeley.edu (A.M.M.).

SUPPLEMENTARY MATERIALS

https://science.org/doi/10.1126/science.abe7252
Materials and Methods
Supplementary Text
Figs. S1 to S16
References (*48*–*58*)
Movies S1 to S3

10 September 2020; resubmitted 25 March 2021
Accepted 4 August 2021
10.1126/science.abe7252

PALEOBOTANY

Reproductive innovations and pulsed rise in plant complexity

Andrew B. Leslie[1]*, Carl Simpson[2], Luke Mander[3]

Morphological complexity is a notable feature of multicellular life, although whether it evolves gradually or in early bursts is unclear. Vascular plant reproductive structures, such as flowers, are familiar examples of complex morphology. In this study, we use a simple approach based on the number of part types to analyze changes in complexity over time. We find that reproductive complexity increased in two pulses separated by ~250 million years of stasis, including an initial rise in the Devonian with the radiation of vascular plants and a pronounced increase in the Late Cretaceous that reflects flowering plant diversification. These pulses are associated with innovations that increased functional diversity, suggesting that shifts in complexity are linked to changes in function regardless of whether they occur early or late in the history of vascular plants.

Whether measured as complexity (*1*) or disparity (*2*, *3*), morphological diversity is often thought to have been established early in evolutionary history through pulses such as the Cambrian explosion (*4*, *5*), which are characterized by developmental or ecological innovations (*4*, *5*). The generality of this pattern is unclear, however, as lineages may also show continued diversification (*6*). Green plants represent an independent radiation of multicellular life in which to explore large-scale patterns in morphological evolution, especially given that the tempo and mode of plant evolution differ from those of evolution in animals (*7*). The reproductive structures of land plants in particular are familiar examples of morphological diversity and biological complexity; flowers can be intricate structures with many specialized parts in precise arrangements (*8*–*10*). At the same time, diverse groups such as ferns produce simple reproductive structures consisting of little more than sporangia. This wide variation underlies many attempts to understand the evolution of land plants and terrestrial ecosystems given that reproductive characters are a core component of phylogenetic analyses (*11*, *12*); reproductive traits have been linked

[1]Geological Sciences Department, Stanford University, 450 Jane Stanford Way, Building 320, Room 118, Stanford, CA 94305, USA. [2]Geological Sciences, University of Colorado Museum of Natural History, University of Colorado Boulder, Campus Box 265, Boulder, CO 80304, USA. [3]School of Environment, Earth and Ecosystem Sciences, The Open University, Walton Hall, Milton Keynes MK7 6AA, UK.
***Corresponding author. Email: aleslieb@stanford.edu**

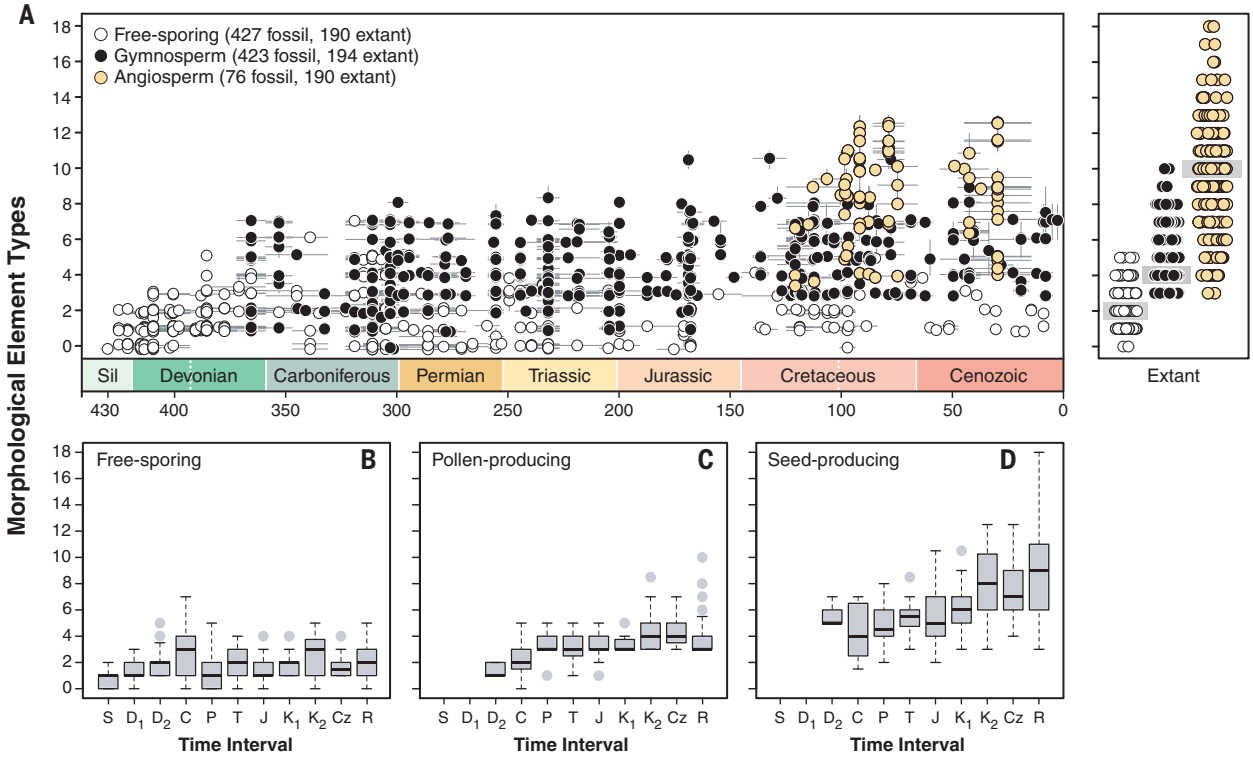


Fig. 1. Complexity patterns in vascular plant reproductive structures through time. (**A**) Number of METs through time. Free-sporing plants reproduce through spores, whereas both gymnosperms and angiosperms produce seeds; "gymnosperm" refers to any nonflowering seed plant. A small amount of random noise was added to integer MET values to better visualize patterns. Error bars represent uncertainty in age and MET count; for taxa with potential MET variation, data points represent the average between minimum and maximum. Reproductive structures from extant taxa are shown as stripcharts (right), with median values indicated by gray boxes. (**B** to **D**) Boxplots of free-sporing (B), pollen-producing (C), and seed-producing (D) structures over binned geologic time intervals. The boxes indicate interquartile ranges of aggregate MET counts with outlier taxa shown as points. The Devonian and Cretaceous periods were divided into subintervals corresponding to Early and Middle-Late Devonian and Early and Late Cretaceous; these subintervals are shown on the geologic time scale in (A) by dotted lines. S, Silurian; D_1, Early Devonian; D_2, Middle-Late Devonian; C, Carboniferous; P, Permian; T, Triassic; J, Jurassic; K_1, Early Cretaceous; K_2, Late Cretaceous; Cz, Cenozoic; R, Recent.

to diversification (*13*); and propagules such as pollen, seeds, and fruits play fundamental roles in ecology (*14*).

The plant fossil record suggests that reproductive complexity has generally increased over evolutionary history; the earliest groups produced simple structures (*15*, *16*) whereas those of some derived clades are highly differentiated (*8*–*10*). But understanding exactly when and how reproductive complexity increased is challenging because it requires consistent measurement of complexity across disparate groups (*17*). In this study, we developed a simple approach for analyzing morphological complexity on the basis of the diversity and arrangement of the basic parts that compose plant reproductive structures, which can be applied to any plant group. We focused on vascular plants—the most diverse and ecologically dominant land plant group from the late Silurian (~420 million years ago) onward.

We divided vascular plant reproductive structures into their basic morphological components and tallied the number of distinctive types of parts in any given taxon (similar to analyses of cell types) (*18*). These types consist of various kinds of sporangia (including the pollen sacs and nucellus of seed plants) and what we term morphological element types (METs), defined as geometrically distinct regions that occur between sporangia and vegetative leaves or shoots. METs encompass much of what botanists would recognize as reproductive diversity, including organ-level features such as bracts, petals, and carpels, as well as differentiated subregions of these organs (e.g., petal spurs or stigmas; see supplementary materials and methods for discussion of character scoring). After identifying basic part types, we scored how many hierarchical orders of clustering each exhibited. For example, if multiple sporangia were borne on a sporophyll and the sporophylls were reiterated around a fertile axis, the sporangia would show two orders of clustering (once on the sporophyll and once around the axis), whereas the sporophyll would show only one order of clustering (fig. S2 and supplementary methods). We use METs as our primary measure of morphological complexity and use the degree to which both sporangia and METs were reiterated as an additional measure of organizational complexity.

Using this approach, we scored a dataset of 1504 extant and fossil reproductive structures from 1338 taxa, including 866 fossil and 472 extant samples (see supplementary materials and methods for sampling details). Morphological complexity as measured by METs increased in two pulses associated with important periods of structural and ecological innovation (Fig. 1A). The first pulse corresponds to the initial radiation of vascular plants during the Devonian (*16*), culminating in the appearance of nonflowering seed plants (referred to as "gymnosperms"), and the second reflects diversification of derived lineages within one seed plant group (angiosperms, or flowering plants) during the Late Cretaceous (Fig. 1A) (*19*). Lineages with lower complexity persist throughout, but pulses increase variance (fig. S3 and table S1). Complexity

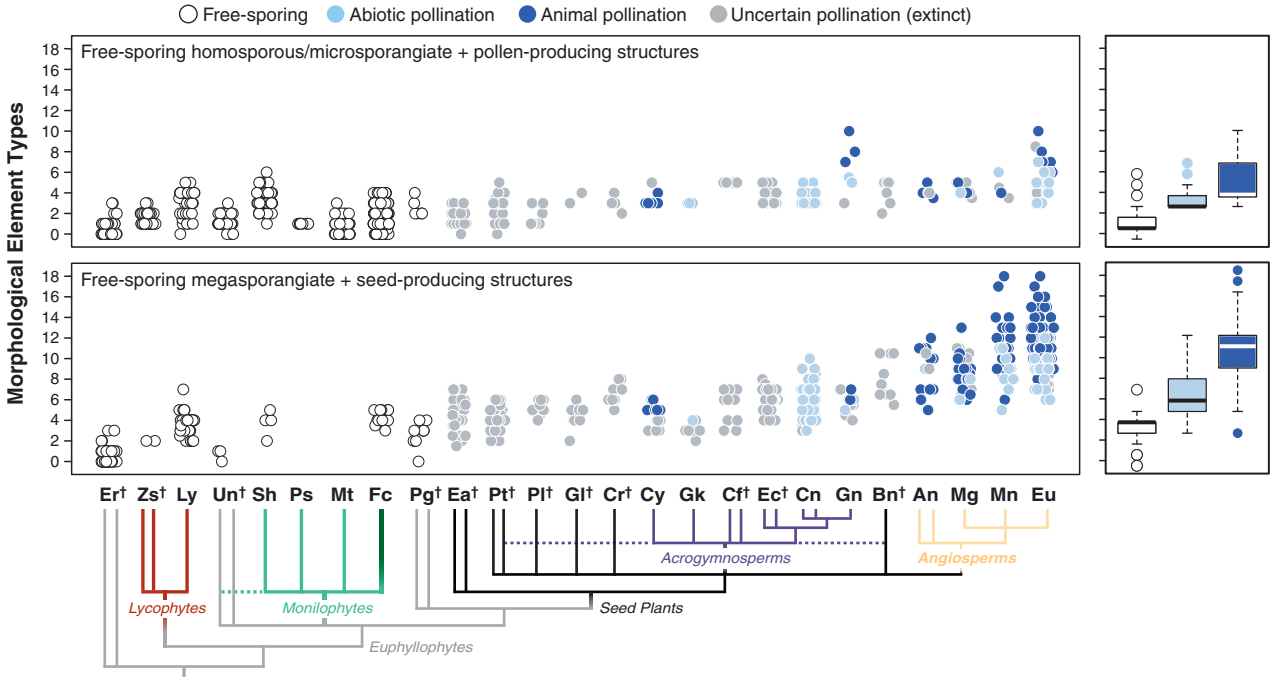


Fig. 2. Complexity patterns in vascular plant reproductive structures across groups. (Top) Stripcharts of MET number for free-sporing homosporous and microsporangiate structures, and seed plant pollen-producing structures. (Middle) Free-sporing megasporangiate and seed-producing structures; the latter may also produce pollen if bisexual. For taxa with uncertain MET number, average value is shown. Abiotic pollination includes wind and water vectors. (Bottom) Provisional phylogeny based on previous studies is shown (*11*, *12*, *32*–*34*) with major crown clades labeled. Acrogymnosperms and monilophytes are based on extant taxa and may include unresolved fossil groups (shown by dotted lines). Multiple branches leading to a group indicate potential paraphyly or polyphyly; extinct groups are indicated by a dagger. Er, early plants; Zs, zosterophylls; Ly, lycopsids; Un, unplaced early euphyllophytes; Sh, sphenophylls; Ps, Psilotales and Ophioglossales; Mt, Marattiales; Fc, Filicales; Pg, progymnosperms; Ea, early "pteridosperms"; Pt, later "pteridosperms"; Pl, Peltaspermales; Gl, Glossopteridales; Cr, Corystospermales; Cy, Cycadales; Gk, Ginkgoales; Cf, early coniferophytes; Ec, early conifers (walchians, voltziales, unplaced stem); Cn, crown conifers; Gn, Gnetales; Bn, Bennettitales; An, ANA grade angiosperms; Mg, magnoliids; Mn, monocots; Eu, eudicots.

patterns among extant taxa mirror those of fossils (Fig. 1A), although better sampling of angiosperms results in a higher maximum (see supplementary text). Differences in reproductive biology among groups help structure this basic pattern; average complexity in free-sporing vascular plants, which exhibit the ancestral reproductive biology of land plants (*20*), rises through the initial pulse but plateaus at a relatively low level thereafter (Fig. 1B and table S2). Within seed plants, dedicated pollen-producing structures (e.g., pollen cones and staminate flowers) are more similar in complexity to free-sporing reproductive structures (Fig. 1C and table S3), whereas seed-producing structures define the upper bounds and are responsible for major shifts and peaks (Fig. 1D and table S4).

These patterns are consistent across lineages; free-sporing plants have independently evolved varying levels of complexity (see discussion of homology in supplementary text) but have consistently few METs, comparable to many pollen-producing structures (Fig. 2). By contrast, seed-producing structures show notably high MET numbers in various gymnosperms (e.g., certain conifers, Gnetales, Bennettitales) and extremely high numbers in some derived angiosperms (Fig. 2) within magnoliids, monocots, and eudicots. Our data also show an expected relationship between complexity and pollination syndrome; animal pollination is associated with the highest complexity among both pollen and seed-producing structures, whereas abiotic pollination is associated with lower complexity (Fig. 2). These temporal and lineage-specific patterns of complexity remain similar when a different scoring approach is used—one based on the number of organ-level part types rather than METs (supplementary materials and methods and figs. S4 and S5)—which suggests that they are robust.

Diversity in the organization and arrangement of parts shows patterns similar to those of MET counts (Fig. 3). We used a rarefaction approach to account for differences in sampling intensity among groups (see supplementary materials and methods), where the steeper rarefaction curves of seed-producing structures indicate that they have a greater number of unique part arrangements than either free-sporing reproductive structures or dedicated pollen-producing structures in gymnosperms regardless of sampling (Fig. 3). The relative paucity of distinct arrangements in these latter two types of structures is not because their parent lineages have completely explored character space but rather because the observed number of specialized arrangements is well below expectations based on sampling theoretical space at a comparable intensity (fig. S6). Even among seed-producing structures, only those of angiosperms are consistent with a random sampling of theoretical space (fig. S6), suggesting that all other vascular plant groups have evolved a restricted set of part arrangements. The extremely steep slope of angiosperm rarefaction curves (both in pollen- and seed-producing structures) relative to those other seed plants is not surprising, as they are undersampled relative to their extreme diversity, but it is noteworthy that even our current dataset includes more part arrangements than in all other seed plant groups combined over their entire history.

Our results suggest a straightforward explanation for the evolution of plant reproductive complexity, where higher levels are associated with greater functional diversity or increased specificity in functional performance, particularly with regard to pollination. Free-sporing and wind-pollinated pollen-producing structures have few parts and change little

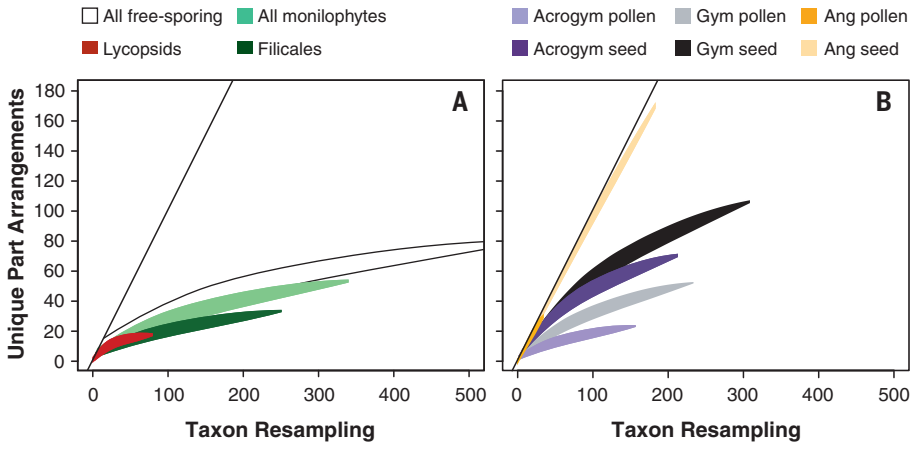


Fig. 3. Rarefaction curves comparing the number of part arrangements in vascular plant groups at different subsampling intensities. (**A**) Free-sporing plants and major subclades. (**B**) Seed plants and major subclades. Each cloud represents 95% confidence intervals based on 1000 subsampling replicates. "Gym Pollen," "Gym Seed," and "all free-sporing" do not represent clades, but we include them for comparative purposes. Seed-producing structures have steeper slopes than free-sporing and pollen-producing structures in most groups of plants, indicating more part arrangements regardless of sampling. Acrogym, Acrogymnospermae; Gym, all gymnosperms; Ang, angiosperms. "Pollen" and "seed" in the key refers to pollen-producing and seed-producing structures, respectively.

through time because they perform a limited suite of functions with optimal biomechanical solutions (*21*). METs in these structures primarily package and protect developing sporangia or pollen sacs (see discussion in supplemental text). Seed-producing structures, by contrast, perform more diverse functional roles, from pollination to protecting and dispersing seeds. Simultaneously optimizing diverse functions can generate disparity (*4*), and seed-producing structures have evolved specialized parts for specific functions (e.g., micropylar arms for capturing pollen, interlocking scales to protect seeds, and seed wings for dispersal). This process has reached notably high levels in angiosperms, where a basic innovation (a carpel that encloses seeds) allowed for the development of more specific pollination mechanisms—namely, a single reception surface (the stigma) whose precise morphology and placement relative to other organs underlies specialized animal pollination syndromes (*8*–*10*). Such syndromes often involve different floral parts functioning in concert to accommodate specific pollinators, resulting in the evolution of the complicated perianth and androecium morphologies that are largely responsible for the extremely high MET numbers (>11) in derived angiosperms (see Data S1). The carpel also increased the hierarchical organization of angiosperm flowers, and the high number of part arrangements in angiosperms reflects this increased clustering (fig. S7).

That vascular plant reproductive complexity increased over time in some clades as they evolved specialized functions is not surprising, although it is important to emphasize that complexity does not always increase. For example, *Ginkgo* reproductive structures are less complex than those of the earliest seed plants, and wind-pollinated angiosperms often evolve reduced, simple flowers (Fig. 2). What is notable in our data, however, is how the total range in reproductive complexity expanded in pulses separated by nearly 250 million years of relative stasis (Fig. 1A and fig. S3). This period, which lasted from the Carboniferous through the Early Cretaceous, is surprising given the obvious potential for higher complexity in seed-producing structures. Surviving members of seed plant lineages that were abundant during this period are known for large genomes and slow rates of evolution that might lead to morphological conservatism (*22*), but Paleozoic and Mesozoic gymnosperms nonetheless evolved disparate reproductive structures, including those with specialized insect pollination syndromes [e.g., (*23*)]. Gymnosperms are evidently capable of producing morphologically and functionally diverse structures, but the long plateau in their complexity suggests that levels seen in angiosperms were simply not accessible to seed plants before the novel geometric and functional possibilities created by the carpel. Carpel evolution does not appear to have immediately led to enhanced complexity, however; the earliest angiosperms in our dataset were no more complex than contemporary gymnosperms (Fig. 1A), and early-diverging extant lineages (with the exception of some derived Nymphaeales) have MET numbers similar to those of gymnosperm groups such as Bennettitales (Fig. 2) (Kolmogorov-Smirnov test $P = 0.52$). This offset would only be more pronounced if crown angiosperms substantially predate their first fossil appearance (*24*), as we see no evidence of shifts toward higher complexity until the well-documented radiation of more derived lineages from the mid-Cretaceous onward (*19*). Although we have emphasized the role of function, genomic and developmental innovations may also be important; for example, the origins of seed plants and angiosperms are associated with whole-genome duplication events (*25*), and angiosperms have characteristically small genome sizes and high modularity (*26*, *27*) that may have enabled lineages within angiosperms to exploit new functional possibilities created by the evolution of the carpel.

Plant evolution and animal evolution are often described as "dancing to a different beat" (*7*), and our study provides a window into the macroevolutionary history of plants that complements other large-scale analyses, such as those based on compilations of taxic richness (*28*). Both highlight the importance of the initial Devonian radiation of vascular plants and the Cretaceous diversification of flowering plants in transforming the ecological and morphological space occupied by land plants. Number of part types is only one aspect of complexity; other important aspects of reproductive diversity include fusion among parts, internal anatomy, nutritive reserves (e.g., endosperm), and specific reproductive growth patterns [e.g., phenology, pollen tube growth (*29*)]. However, our approach allows us to simplify the huge range of vascular plant reproductive morphology, identify key temporal patterns in the evolution of that diversity, and address long-standing ideas relating to its evolution [e.g., (*30*)]. As in many studies of animal morphological disparity or complexity (*2*–*4*), vascular plants show an early rise, achieving levels comparable to those of modern gymnosperms by the latest Devonian (~365 million years ago) as lineages evolve the basic suite of reproductive functions that persist to the present day. In contrast to macroevolutionary patterns among many animal groups, however, the most pronounced and substantial shift in plant reproductive complexity occurred much later, after the emergence of a distinctive clade whose innovations allowed them to explore a much more expansive functional and phenotypic space, one

characterized by the intricate interactions with pollinating animals that have long made flowers objects of fascination (*8*, *31*).

REFERENCES AND NOTES

1. D. W. McShea, *Evol. Biol.* **43**, 531–542 (2016).
2. M. Hughes, S. Gerber, M. A. Wills, *Proc. Natl. Acad. Sci. U.S.A.* **110**, 13875–13879 (2013).
3. B. Deline *et al.*, *Proc. Natl. Acad. Sci. U.S.A.* **115**, E8909–E8918 (2018).
4. C. R. Marshall, *Annu. Rev. Earth Planet. Sci.* **34**, 355–384 (2006).
5. D. H. Erwin *et al.*, *Science* **334**, 1091–1097 (2011).
6. M. J. Hopkins, A. B. Smith, *Proc. Natl. Acad. Sci. U.S.A.* **112**, 3758–3763 (2015).
7. A. Traverse, *Hist. Biol.* **1**, 277–301 (1988).
8. L. D. Harder, S. D. Johnson, *New Phytol.* **183**, 530–545 (2009).
9. P. K. Endress, *Am. J. Bot.* **98**, 370–396 (2011).
10. P. K. Endress, *Ann. Bot.* **117**, 749–767 (2016).
11. J. A. Doyle, *Int. J. Plant Sci.* **169**, 816–843 (2008).
12. J. Hilton, R. M. Bateman, *J. Torrey Bot. Soc.* **133**, 119–168 (2006).
13. T. van der Niet, S. D. Johnson, *Trends Ecol. Evol.* **27**, 353–361 (2012).
14. A. T. Moles *et al.*, *Science* **307**, 576–580 (2005).
15. D. Edwards, K. L. Davies, L. Axe, *Nature* **357**, 683–685 (1992).
16. W. L. Crepet, K. J. Niklas, *Int. J. Plant Sci.* **180**, 800–810 (2019).
17. D. W. McShea, R. N. Brandon, *Biology's First Law: The Tendency for Diversity and Complexity to Increase in Evolutionary Systems* (Univ. of Chicago Press, 2010).
18. J. W. Valentine, A. G. Collins, C. P. Meyer, *Paleobiology* **20**, 131–142 (1994).
19. E. M. Friis, P. R. Crane, K. R. Pedersen, *Early Flowers and Angiosperm Evolution* (Cambridge Univ. Press, 2011).
20. C. H. Wellman, P. L. Osterloff, U. Mohiuddin, *Nature* **425**, 282–285 (2003).
21. K. J. Niklas, *Bot. Rev.* **51**, 328–386 (1985).
22. A. R. De La Torre, Z. Li, Y. Van de Peer, P. K. Ingvarsson, *Mol. Biol. Evol.* **34**, 1363–1377 (2017).
23. I. Terry, G. H. Walter, C. Moore, R. Roemer, C. Hull, *Science* **318**, 70 (2007).
24. H. T. Li *et al.*, *Nat. Plants* **5**, 461–470 (2019).
25. J. W. Clark, P. C. J. Donoghue, *Trends Plant Sci.* **23**, 933–945 (2018).
26. K. A. Simonin, A. B. Roddy, *PLOS Biol.* **16**, e2003706 (2018).
27. A. S. Dellinger *et al.*, *Commun. Biol.* **2**, 453 (2019).
28. A. H. Knoll, K. J. Niklas, B. H. Tiffney, *Science* **206**, 1400–1402 (1979).
29. J. H. Williams, *Proc. Natl. Acad. Sci. U.S.A.* **105**, 11259–11263 (2008).
30. S. Mathews, E. M. Kramer, *New Phytol.* **194**, 910–923 (2012).
31. C. R. Darwin, *On the Various Contrivances by Which British and Foreign Orchids are Fertilised by Insects* (John Murray, 1862).
32. P. Kenrick, P. R. Crane, *Origin and Early Diversification of Land Plants* (Smithsonian Institution Press, 1997).
33. K. M. Pryer *et al.*, *Am. J. Bot.* **91**, 1582–1598 (2004).
34. J. H. Leebens-Mack *et al.*, *Nature* **574**, 679–685 (2019).
35. A. B. Leslie, C. Simpson, L. Mander, Complexity character scores for fossil and extant vascular plant reproductive structures, Dryad (2021); https://doi.org/10.5061/dryad.w0vt4b8qx.

ACKNOWLEDGMENTS

We thank K. Whang for assistance in collecting fern data and two anonymous reviewers for their helpful comments and suggestions. **Funding:** The authors declare no funding sources. **Author contributions:** A.B.L., C.S., and L.M. designed and conducted the analyses. A.B.L. collected the data and scored taxa for complexity characters. All authors contributed to writing the manuscript. **Competing interests:** The authors declare no competing interests. **Data and materials availability:** Complexity scorings for all taxa and reproductive structures are described in shorthand notation in supplementary materials. Full scoring data for all reproductive structures with citations and references for literature sources are available at Dryad (*35*).

SUPPLEMENTARY MATERIALS

https://science.org/doi/10.1126/science.abi6984
Materials and Methods
Supplementary Text
Figs. S1 to S7
Tables S1 to S4
References (*36*–*49*)
Data S1

24 March 2021; accepted 19 August 2021
10.1126/science.abi6984

CORONAVIRUS

Durability of mRNA-1273 vaccine–induced antibodies against SARS-CoV-2 variants

Amarendra Pegu[1]†, Sarah E. O'Connell[1]†, Stephen D. Schmidt[1]†, Sijy O'Dell[1]†, Chloe A. Talana[1], Lilin Lai[2], Jim Albert[3], Evan Anderson[2], Hamilton Bennett[4], Kizzmekia S. Corbett[1]‡, Britta Flach[1], Lisa Jackson[5], Brett Leav[4], Julie E. Ledgerwood[1], Catherine J. Luke[6], Mat Makowski[3], Martha C. Nason[1], Paul C. Roberts[6], Mario Roederer[1], Paulina A. Rebolledo[7], Christina A. Rostad[2], Nadine G. Rouphael[7], Wei Shi[1], Lingshu Wang[1], Alicia T. Widge[1], Eun Sung Yang[1], The mRNA-1273 Study Group§, John H. Beigel[6], Barney S. Graham[1], John R. Mascola[1], Mehul S. Suthar[2], Adrian B. McDermott[1], Nicole A. Doria-Rose[1]*

Severe acute respiratory syndrome coronavirus 2 (SARS-CoV-2) mutations may diminish vaccine-induced protective immune responses, particularly as antibody titers wane over time. Here, we assess the effect of SARS-CoV-2 variants B.1.1.7 (Alpha), B.1.351 (Beta), P.1 (Gamma), B.1.429 (Epsilon), B.1.526 (Iota), and B.1.617.2 (Delta) on binding, neutralizing, and angiotensin-converting enzyme 2 (ACE2)–competing antibodies elicited by the messenger RNA (mRNA) vaccine mRNA-1273 over 7 months. Cross-reactive neutralizing responses were rare after a single dose. At the peak of response to the second vaccine dose, all individuals had responses to all variants. Binding and functional antibodies against variants persisted in most subjects, albeit at low levels, for 6 months after the primary series of the mRNA-1273 vaccine. Across all assays, B.1.351 had the lowest antibody recognition. These data complement ongoing studies to inform the potential need for additional boost vaccinations.

Severe acute respiratory syndrome coronavirus 2 (SARS-CoV-2), the virus that causes COVID-19, has infected millions of people worldwide, fueling the ongoing global pandemic (*1*). The combination of RNA virus mutation rates, replication, and recombination in a very large number of individuals is conducive to the emergence of viral variants with improved replication capacities and transmissibilities as well as increased immunological escape. Of particular interest are the variants of concern B.1.1.7 (20I/501Y.V1 or Alpha), B.1.351 (20H/501Y.V2 or Beta), P.1 (Gamma), and B.1.617.2 (Delta) and the variants of interest B.1.526 (Iota) and B.1.429 (formerly called Epsilon). In multiple studies, B.1.351 was the most resistant to neutralization by convalescent or vaccinee sera, with 6- to 15-fold less neutralization activity for sera from individuals immunized with vaccines based on the virus strain first described in January 2020 (Wuhan-Hu-1, spike also called WA1) (*2*–*9*). Most of these prior studies have evaluated sera from vaccinated individuals at time points soon after the first or second dose and have had limited data on the durability of such responses. Likewise, clinical studies have reported somewhat reduced efficacy and effectiveness against the B.1.1.7, B.1.351, and B.1.617.2 variants (*10*–*12*). Although such data provide critical insights into the performance of the vaccines against viral variants, they have not fully addressed the durability of cross-reactive binding and functional antibodies.

Here, we investigate the effect of SARS-CoV-2 variants on recognition by sera from individuals who received two 100-μg doses of the SARS-CoV-2 vaccine mRNA-1273. mRNA-1273 encodes the full-length stabilized spike protein of the WA1 strain and was administered as a two-dose series, 28 days apart. We previously

[1]Vaccine Research Center, National Institute of Allergy and Infectious Diseases, National Institutes of Health, Bethesda, MD 20892, USA. [2]Department of Pediatrics, Division of Infectious Disease, Emory Vaccine Center, Yerkes National Primate Research Center, Emory University School of Medicine, Atlanta, GA 30322, USA. [3]Emmes Company, Rockville, MD 20850, USA. [4]Moderna, Inc., Cambridge, MA 02139, USA. [5]Kaiser Permanente Washington Health Research Institute, Seattle, WA 98101, USA. [6]Division of Microbiology and Infectious Diseases, National Institute of Allergy and Infectious Diseases, National Institutes of Health, Bethesda, MD 20892, USA. [7]Hope Clinic, Department of Medicine, Emory University School of Medicine, Decatur, GA 30030, USA.
***Corresponding author. Email: nicole.doriarose@nih.gov**
†These authors contributed equally to this work.
‡Present address: Department of Immunology and Infectious Diseases, Harvard T.H. Chan School of Public Health, Boston, MA 02115, USA.
§The mRNA-1273 Study Group members and affiliations are listed in the supplementary materials.

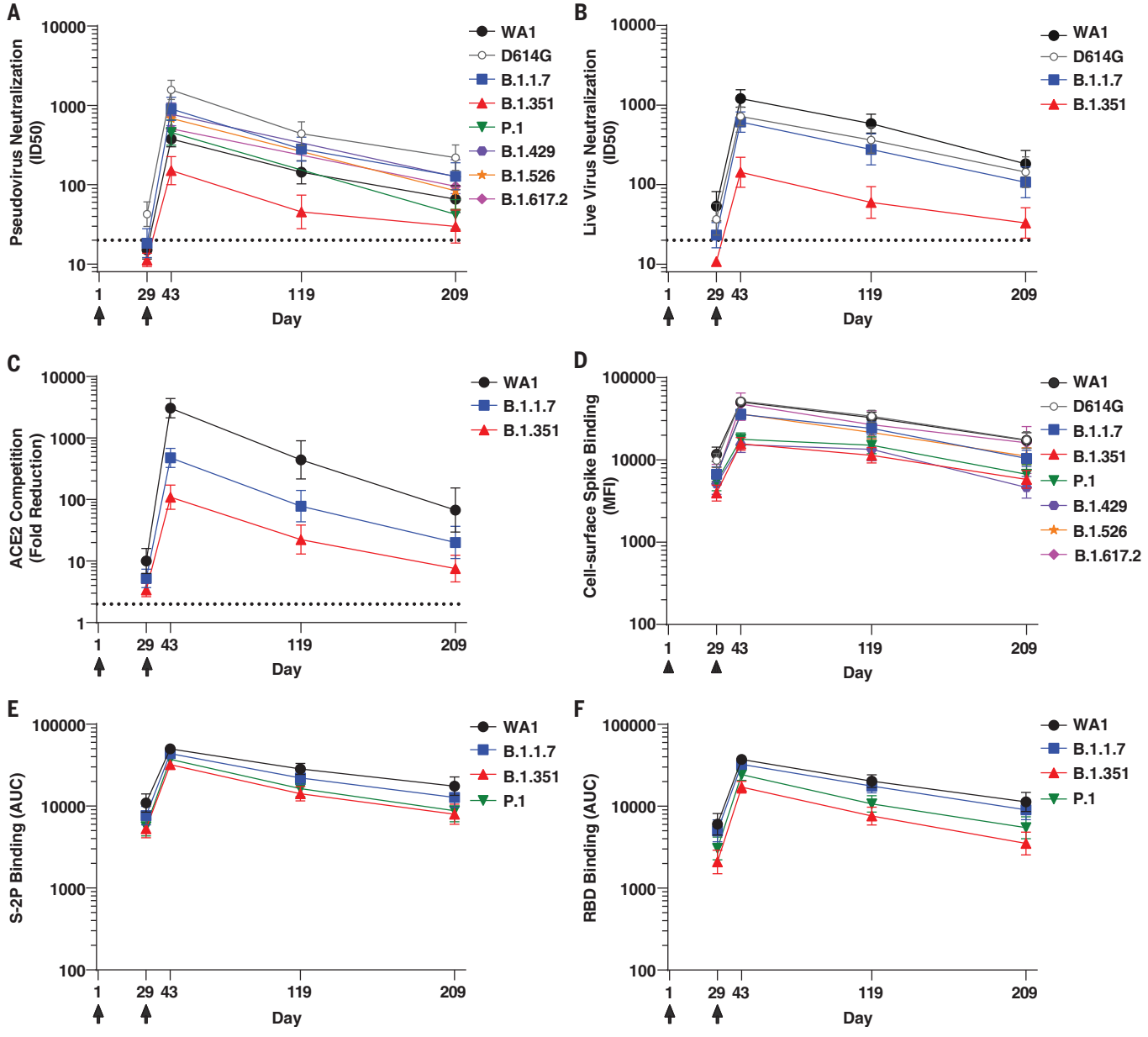


Fig. 1. Binding and functional antibodies persist for 6 months after the second dose of the mRNA-1273 vaccine. (**A**) Pseudovirus neutralization, expressed as 50% inhibitory dilution (ID_{50}). Dotted line indicates the limit of detection (>20). Pseudoviruses included WA1, D614G, B.1.1.7, B.1.351, P.1, B.1.429, B.1.526, and B.1.617.2. (**B**) Live-virus FRNT neutralization, expressed as ID_{50}. Dotted line indicates the limit of detection (>20). Viruses included WA1, 83E (spike is D614G), B.1.1.7, and B.1.351. (**C**) Competition of ACE2 binding to RBD, measured by MSD-ECLIA and expressed as fold reduction of ACE2 binding in the presence of serum compared with no-serum control. Dotted line indicates the limit of detection (>2). RBD proteins included WA1, B.1.1.7, and B.1.351. (**D**) Binding to cell surface–expressed full-length spike, measured by flow cytometry and expressed as median fluorescence intensity (MFI). Spikes included WA1, D614G, B.1.1.7, B.1.351, P.1, B.1.429, B.1.526, and B.1.617.2. (**E**) Binding to soluble spike protein S-2P, measured by MSD-ECLIA and expressed as area under the curve (AUC). S-2P proteins included WA1, B.1.1.7, B.1.351, and P.1. (**F**) Binding to RBD protein, measured by MSD-ECLIA and expressed as AUC. RBD proteins included WA1, B.1.1.7, B.1.351, and P.1. For all assays, sera from n = 24 individuals were sampled at four time points. Individuals were vaccinated with 100 μg mRNA-1273 at days 1 and 29 (arrows). Symbols show the geometric mean value, and error bars show 95% confidence intervals.

described the binding and neutralization activity against the WA1 SARS-CoV-2 spike longitudinally over the course of 7 months from the first vaccination in volunteers from the phase 1 trial of the mRNA-1273 vaccine (*13*–*16*). In the current study, we demonstrate the utility of using multiple methodologies to assess SARS-CoV-2 vaccine–elicited humoral immunity to variant viruses over time. We tested sera from a random sample of eight volunteers in each of three age groups—18 to 55, 55 to 70, and 71+ years of age—all of whom had samples available from four time points: 4 weeks after the first dose and 2 weeks, 3 months, and 6 months after the second dose (days 29, 43, 119, and 209 after the first dose, respectively).

Three functional assays and two binding assays were used to assess the humoral immune response to the SARS-CoV-2 spike protein. SARS-CoV-2 neutralization was measured using both a lentivirus-based pseudovirus assay and

a live-virus focus reduction neutralization test (FRNT) (*17*). The third functional assay was a meso scale discovery–electrochemiluminescence immunoassay (MSD-ECLIA)–based angiotensin-converting enzyme 2 (ACE2) competition assay. This method measured the ability of mRNA-1273 vaccine–elicited antibodies to compete with labeled soluble ACE2 for binding to the specific receptor-binding domain (RBD) (WA1 or variant) spotted onto the MSD plate. Antibody binding to cell surface–expressed full-length spike was analyzed by flow cytometry.

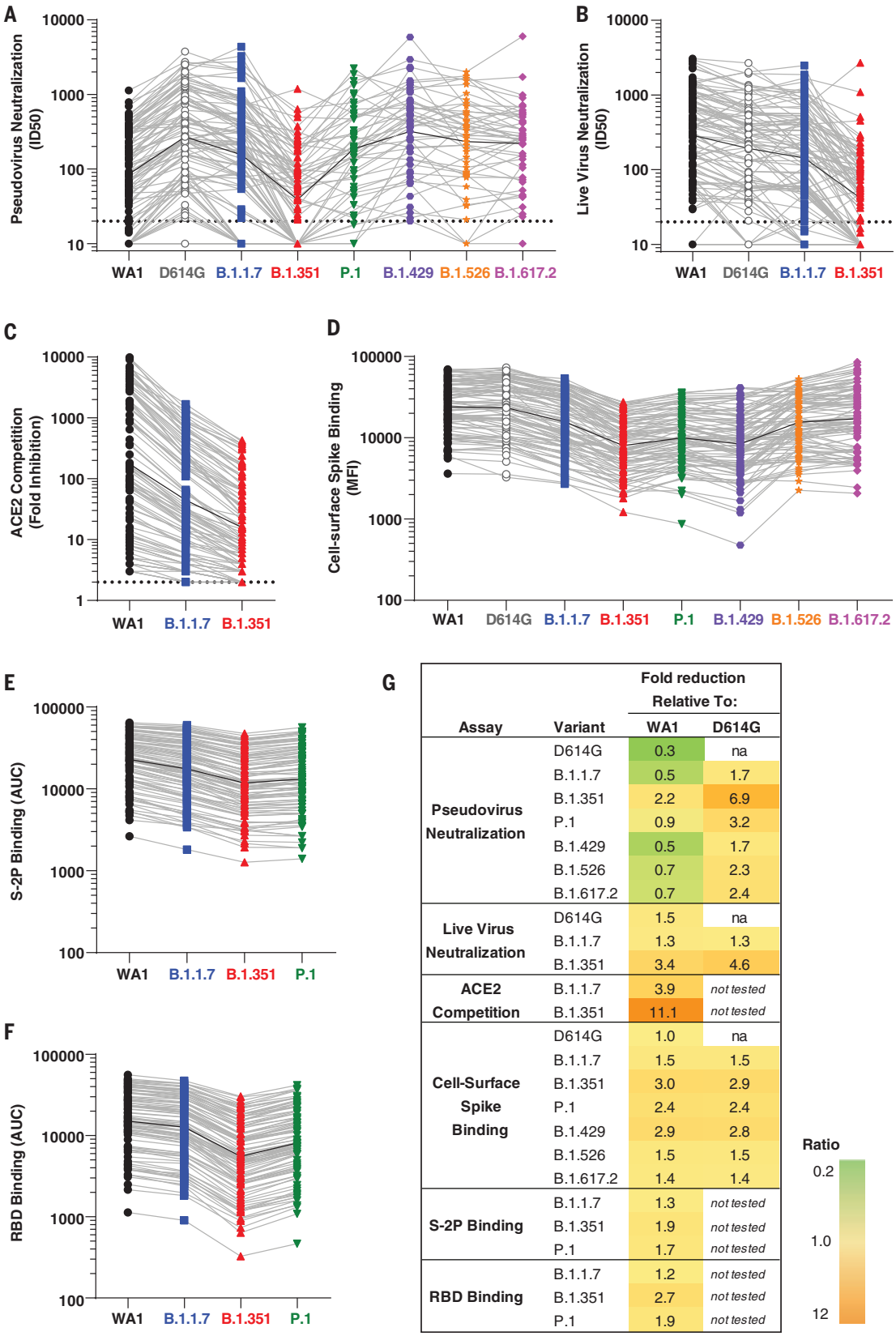


Fig. 2. The relative effect of each SARS-CoV-2 viral variant is similar across assays. (**A**) ID_{50} in pseudovirus neutralization assays. Dotted line indicates the limit of detection (>20). (**B**) ID_{50} in live virus FRNT neutralization. Dotted line indicates the limit of detection (>20). (**C**) Competition of ACE2 binding to RBD of WA1, B.1.1.7, and B.1.351, expressed as fold reduction of signal in the presence of serum compared with no-serum control. Dotted line indicates the limit of detection (>2). (**D**) Binding to cell surface–expressed full-length spike, expressed as MFI. (**E**) Binding to S-2P, expressed as AUC. (**F**) Binding to RBD protein, expressed as AUC. (**G**) Geometric mean of ratios of values. na, not applicable. In (A) to (F), symbols show data for all samples at all time points, light gray lines connect data from each sample for the variants, and black lines show geometric mean of all samples. All viruses are color coded as in Fig. 1.

G

Assay	Variant	Fold reduction Relative To: WA1	D614G
Pseudovirus Neutralization	D614G	0.3	na
	B.1.1.7	0.5	1.7
	B.1.351	2.2	6.9
	P.1	0.9	3.2
	B.1.429	0.5	1.7
	B.1.526	0.7	2.3
	B.1.617.2	0.7	2.4
Live Virus Neutralization	D614G	1.5	na
	B.1.1.7	1.3	1.3
	B.1.351	3.4	4.6
ACE2 Competition	B.1.1.7	3.9	*not tested*
	B.1.351	11.1	*not tested*
Cell-Surface Spike Binding	D614G	1.0	na
	B.1.1.7	1.5	1.5
	B.1.351	3.0	2.9
	P.1	2.4	2.4
	B.1.429	2.9	2.8
	B.1.526	1.5	1.5
	B.1.617.2	1.4	1.4
S-2P Binding	B.1.1.7	1.3	*not tested*
	B.1.351	1.9	*not tested*
	P.1	1.7	*not tested*
RBD Binding	B.1.1.7	1.2	*not tested*
	B.1.351	2.7	*not tested*
	P.1	1.9	*not tested*

Binding to soluble protein was measured by interferometry in the MSD-ECLIA platform. All samples were assessed against WA1 and the B.1.1.7 and B.1.351 variants in each of these orthogonal serology assays. Additionally, all samples were tested against WA1 containing the D614G mutation in both neutralization assays as well as binding in the cell surface assay. Further variants were tested in binding assays as follows: S-2P and RBD binding, P.1 against all samples, and cell surface spike binding, P.1, B.1.429, B.1.526, and B.1.617.2 against all samples. A subset of samples—from day 43 to capture the peak response and day 209 to look at durability—were evaluated by pseudovirus neutralization against P.1, B.1.429, B.1.526, and B.1.617.2. The specific sequences used in each assay are defined in table S1.

We first assessed the patterns of antibody activity over time. Consistently across assays, low-level recognition of all variants was observed after a single dose (day 29) (Fig. 1). Activity against all variants peaked 2 weeks after the second dose (day 43), with moderate declines over time through day 209 (Fig. 1). Notably, the values obtained for each assay on a per-sample basis correlated with each other (fig. S1). We next evaluated the relative effect of each variant, considering all time points together. Using the pseudovirus assay, the neutralizing activity was highest against D614G and lowest against B.1.351, with values for all other variants tested falling between those two variants (Fig. 1A and Fig. 2A). Similar to previous studies from our group (*15*) and others (*18*), pseudovirus neutralization titers to D614G were threefold higher than to WA1 (Fig. 2G). By contrast, using the live-virus FRNT neutralization assay (Fig. 1B and Fig. 2B), titers to WA1 were higher than those to D614G, consistent with previous studies of that assay (*19*). For all other variants, the effect in the live-virus and pseudovirus neutralization assays were concordant: titers against B.1.1.7 were similar to D614G and lower against B.1.351. ACE2 competition was highest for WA1 RBD, intermediate for B.1.1.7, and lowest for B.1.351 (Fig. 1C and Fig. 2C). Spike-binding antibodies were measured using two different methodologies. In the cell surface spike binding assay, serum antibodies were bound to full-length, membrane-embedded spike on the surface of transfected cells and measured by flow cytometry (*20*). In this assay (Fig. 1D and Fig. 2D), WA1 and D614G were nearly indistinguishable, with ~1.5-fold reduced binding to B.1.1.7, B.1.526, and B.1.617.2 and 2.4- to 3.0-fold reduced binding to P.1, B.1.429, and B.1.351. We also used the MSD-ECLIA multiplex binding assay to simultaneously measure immunoglobulin G (IgG) binding against both the stabilized soluble spike protein S-2P (*21*) and RBD proteins derived from WA1 and the B.1.1.7, B.1.351, and P.1 variants. The ECLIA assay showed slightly reduced binding to the variant S-2P (Fig. 1E and Fig. 2E) and RBD (Fig. 1F and Fig. 2F) proteins, with the rank order of highest to lowest binding as follows: WA1, B.1.1.7, P.1, and B.1.351. The overall effect of each variant in each assay is tabulated in Fig. 2G, which shows the geometric mean of the ratios between values for WA1 and variant or D614G and variant. In all assays, B.1.351 was the variant that caused the greatest reduction in titers compared with WA1 or D614G.

To quantify the breadth of responses, we calculated the number of sera that maintained detectable antibody titers in each assay and time point (Fig. 3). Antibodies that bound to S-2P and RBD of the WA1, B.1.1.7, B.1.351, and P.1 sequences were detected in all subjects at all time points. Likewise, binding to full-length cell surface–expressed spike was detected against WA1, D614G, and all six variants at all time points. By contrast, the functional assays revealed deficits in antibody recognition of the variants. In the pseudovirus neutralization assay, consistent with our previous study (*13*), 25% of sera neutralized WA1 after one dose (day 29). In contrast, 83% of day 29 sera neutralized D614G, which is more sensitive than WA1 in this assay as noted above,

Assay	Variant	% of sera with detectable antibodies			
		Day 29	Day 43	Day 119	Day 209
Pseudovirus Neutralization	WA1	25%	100%	100%	88%
	D614G	83%	100%	100%	100%
	B.1.1.7	33%	100%	100%	96%
	B.1.351	8%	100%	71%	54%
	P.1	*not tested*	100%	*not tested*	85%
	B.1.429	*not tested*	100%	*not tested*	100%
	B.1.526	*not tested*	100%	*not tested*	88%
	B.1.617.2	*not tested*	100%	*not tested*	96%
Live Virus Neutralization	WA1	79%	100%	100%	100%
	D614G	67%	100%	100%	100%
	B.1.1.7	54%	100%	100%	88%
	B.1.351	8%	100%	79%	58%
ACE2 Competition	WA1	100%	100%	100%	100%
	B.1.1.7	83%	100%	100%	100%
	B.1.351	63%	100%	100%	79%
S-2P Binding	WA1	100%	100%	100%	100%
	B.1.1.7	100%	100%	100%	100%
	B.1.351	100%	100%	100%	100%
	P.1	100%	100%	100%	100%
RBD Binding	WA1	100%	100%	100%	100%
	B.1.1.7	100%	100%	100%	100%
	B.1.351	100%	100%	100%	100%
	P.1	100%	100%	100%	100%
Cell-Surface Spike Binding	WA1	100%	100%	100%	100%
	D614G	100%	100%	100%	100%
	B.1.1.7	100%	100%	100%	100%
	B.1.351	100%	100%	100%	100%
	P.1	100%	100%	100%	100%
	B.1.429	100%	100%	100%	100%
	B.1.526	100%	100%	100%	100%
	B.1.617.2	100%	100%	100%	100%



Fig. 3. All individuals had binding antibodies to SARS-CoV-2 variants, and the majority of individuals maintained functional activity against viral variants at 6 months after the second vaccination. Values are the percentage of sera (n = 24 at each time point) for which antibodies were detected for each variant. For pseudovirus and live-virus neutralization, samples were called detectable at ID_{50} > 20; for ACE2 blocking, at a twofold decrease in signal compared with no-serum control; for S-2P and RBD binding, at AUC > 100; and for cell surface spike binding, at MFI > 100.

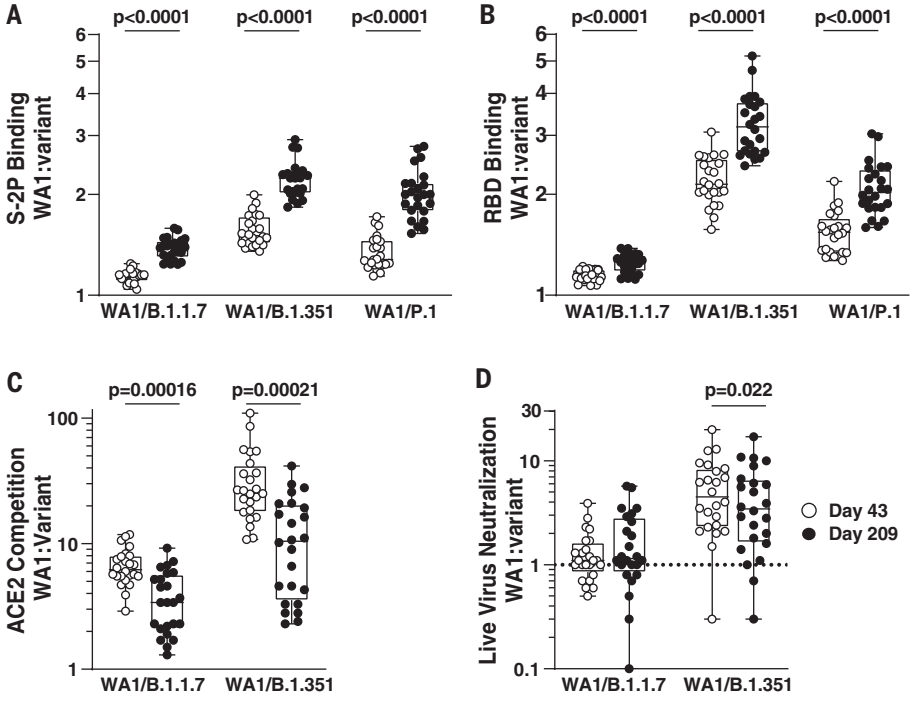


Fig. 4. Binding antibodies to viral variants decayed faster than antibodies to WA1, but the functional antibodies to variants diminished more slowly. (**A**) S-2P binding. (**B**) RBD binding. (**C**) ACE2 competition. (**D**) Live-virus neutralization. Symbols show the value for WA1 divided by the value for the indicated variant for each sample. *P* values are from paired *t* tests.

but 33% neutralized B.1.1.7 and only 8% could neutralize B.1.351. Similarly, in the live-virus assay, most day 29 sera neutralized WA1, D614G, and B.1.1.7, but only 8% neutralized B.1.351, and ACE2 competition of binding to B.1.351 RBD was detected in 63% of sera. Although a single dose of mRNA-1273 vaccine provides partial protection against COVID-19 disease in the interval before the second vaccination (*22*)—and similar data were reported for the mRNA vaccine BNT162b2 (*10*, *11*)—this observation of limited neutralizing magnitude and breadth after one dose underscores the importance of the full two-dose regimen of an mRNA vaccine for protection against SARS-CoV-2 variants.

Two weeks after the second dose (day 43), all sera neutralized all of the pseudoviruses. Responses waned over time: All sera from 6 months after the second dose (day 209) neutralized D614G and B.1.429 in this assay, but fewer sera neutralized the other variants, with 88, 96, 96, 88, 85, and 54% of sera neutralizing WA1, B.1.1.7, B.1.617.2, B.1.526, P.1, and B.1.351, respectively. Similarly, using the live-virus assay, all sera were active against WA1, D614G, B.1.1.7, and B.1.351 at day 43, and at day 209, all sera neutralized WA1 and D614G, 88% of sera neutralized B.1.1.7, and 58% neutralized B.1.351. Moreover, the ACE2 competition assay showed reduced activity against B.1.351 at the later time points (Fig. 3). Collectively, the functional assays revealed a decreased frequency of sera with detectable activity against B.1.351 and other variants after a single dose or 6 months after the second dose. Notably, all subjects had broadly cross-reactive functional activity against all variants at the peak of the response. Thus, individuals who demonstrate waning immune responses over time are likely to have memory B cells capable of delivering an anamnestic response to those variants in the event of exposure to virus, or potentially with an additional dose of vaccine.

To understand the contributions of individual mutations to the immune escape noted in the variants of concern, we assayed day 43 sera against pseudoviruses bearing D614G plus N501Y, present in B.1.1.7, P.1, and B.1.351 variants; Y453F, found in mink cluster five variants (*23*, *24*); and N439K, which is resistant to some therapeutic monoclonal antibodies (*25*). None of these mutations showed a significant impact on neutralization by day 43 sera (fig. S2). By contrast, E484K, present in B.1.351, P.1, and B.1.526, significantly affected neutralization sensitivity, with a geometric mean 2.4-fold lower 50% inhibitory dilution (ID_{50}) (fig. S2).

Immune responses to vaccination are often weaker in older adults (*26*). We previously showed that vaccination with mRNA-1273 elicited antibodies to SARS-CoV-2 WA1 in subjects aged 56 to 70 and 71 and older that are as potent (*15*) and durable (*13*) as those elicited in adults aged 18 to 55, with a slight decrease in potency for the oldest subjects in live-virus neutralization (*13*). Here, we observed a trend to lower titers against SARS-CoV-2 spike variants in the oldest individuals at day 209, with marginally statistically significant differences in some assays for some variants. Differences were small, and there was overlap between groups (figs. S3 to S5). Notably, many subjects in the oldest group retained neutralizing activity against the variants 6 months after the second vaccine dose (fig. S5).

Convalescent individuals develop B cell lineages that mature over time, increasing their activity against SARS-CoV-2 variants (*27*). To test the hypothesis that a similar phenomenon would occur in mRNA-1273–vaccinated individuals, for each time point, we calculated the ratios of activity against each variant to WA1. We then compared the ratios at day 43 with those at day 209. The ratio of WA1 to B.1.351 binding was greater at day 209 than at day 43 for both S2P and RBD, implying a more rapid decay of B.1.351-recognizing antibodies (Fig. 4). However, the opposite effect was observed for ACE2-competing antibodies and live-virus neutralization against B.1.351. This can also be seen in Fig. 1, wherein the points for variants are closer to each other at day 43 than at day 209 for S-2P and RBD binding, but closer to each other at day 209 in live-virus neutralization. The same patterns were observed for B.1.1.7. No statistically significant differences over time were noted for pseudovirus neutralization or cell surface spike binding. These data suggest that although binding antibodies to variants decayed faster than antibodies to WA1, the functional antibodies to variants may have diminished more slowly.

mRNA-1273–elicited antibody activity against SARS-CoV-2 variants persisted 6 months after the second dose, albeit at reduced levels compared with peak activity, with more than half of subjects maintaining neutralizing activity against B.1.351 at the latest time point tested. High levels of binding antibodies recognizing all tested variants, including B.1.351 and B.1.617.2, were maintained in all subjects over this time period. The results from these diverse methodologies also showed similar dynamics over 7 months after the first vaccination. The effects on antibody potency and breadth of a third dose of mRNA vaccine, encoding the WA1 spike (mRNA-1273), the B.1.351 spike (mRNA-1273.351), or coadministration of both, is currently under investigation; early results show strong boosting of responses to both D614G and variants by vaccination with either sequence (*28*). Although additional studies will be needed to address the effect of new variants that will surely arise in areas of intense viral infection, our data are encouraging for the use of this vaccine in the face of viral variation.

REFERENCES AND NOTES

1. COVID-19 Dashboard by the Center for Systems Science and Engineering (CSSE) at Johns Hopkins University (JHU) (2021); https://coronavirus.jhu.edu/map.html.
2. V. V. Edara *et al*., *Cell Host Microbe* **29**, 516–521.E3 (2021).
3. M. Hoffmann *et al*., *Cell* **184**, 2384–2393.E12 (2021).
4. X. Shen *et al*., *N. Engl. J. Med.* **384**, 2352–2354 (2021).
5. P. Wang *et al*., *Nature* **593**, 130–135 (2021).
6. C. K. Wibmer *et al*., *Nat. Med.* **27**, 622–625 (2021).
7. K. Wu *et al*., *N. Engl. J. Med.* **384**, 1468–1470 (2021).
8. D. H. Barouch *et al*., *N. Engl. J. Med.* 10.1056/NEJMc2108829 (2021).
9. N. Zhu *et al*., *N. Engl. J. Med.* **382**, 727–733 (2020).
10. L. J. Abu-Raddad, H. Chemaitelly, A. A. Butt, National Study Group for COVID-19 Vaccination, *N. Engl. J. Med.* **385**, 187–189 (2021).
11. N. Dagan *et al*., *N. Engl. J. Med.* **384**, 1412–1423 (2021).
12. A. Sheikh, J. McMenamin, B. Taylor, C. Robertson, Public Health Scotland and the EAVE II Collaborators, *Lancet* **397**, 2461–2462 (2021).
13. N. Doria-Rose *et al*., *N. Engl. J. Med.* **384**, 2259–2261 (2021).
14. A. T. Widge *et al*., *N. Engl. J. Med.* **384**, 80–82 (2021).
15. E. J. Anderson *et al*., *N. Engl. J. Med.* **383**, 2427–2438 (2020).
16. L. A. Jackson *et al*., *N. Engl. J. Med.* **383**, 1920–1931 (2020).
17. A. Vanderheiden *et al*., *Curr. Protoc. Immunol.* **131**, e116 (2020).
18. D. Weissman *et al*., *Cell Host Microbe* **29**, 23–31.E4 (2021).
19. V. V. Edara, W. H. Hudson, X. Xie, R. Ahmed, M. S. Suthar, *JAMA* **325**, 1896–1898 (2021).
20. L. Wang *et al*., *Science* **373**, eabh1766 (2021).
21. D. Wrapp *et al*., *Science* **367**, 1260–1263 (2020).
22. L. R. Baden *et al*., *N. Engl. J. Med.* **384**, 403–416 (2021).
23. R. Bayarri-Olmos *et al*., *J. Biol. Chem.* **296**, 100536 (2021).
24. M. Hoffmann *et al*., *Cell Rep.* **35**, 109017 (2021).
25. T. Tada *et al*., bioRxiv 2021.02.18.431897 [Preprint] (2021). https://doi.org/10.1101/2021.02.18.431897.
26. A. Ciabattini *et al*., *Semin. Immunol.* **40**, 83–94 (2018).
27. Z. Wang *et al*., *Nature* **595**, 426–431 (2021).
28. K. Wu *et al*., medRxiv 2021.2005.2005.21256716 [Preprint] (2021). https://doi.org/10.1101/2021.05.05.21256716.

ACKNOWLEDGMENTS

We thank D. Montefiori, R. Mason, M. Muhkamedova, K. Neuzil, C. Liu, and members of the VRC Virology Laboratory for helpful discussions and B. Hartman for assistance with graphics. We thank A. Pekosz, E. Boritz, and D. Douek for providing and sequencing the B.1.351 virus stock; H. Mu and M. Farzan for ACE2-overexpressing 293T cells; and A. Creanga for Vero-TMPRSS2 cells. **Funding:** This study received support from the Emory Executive Vice President for Health Affairs Synergy Fund Award (to M.S.S.); the Pediatric Research Alliance Center for Childhood Infections and Vaccines and Children's Healthcare of Atlanta (to M.S.S.); the Woodruff Health Sciences Center 2020 COVID-19 CURE Award (to M.S.S.); National Institutes of Health grant UM1AI148373 (to L.J.); National Institutes of Health grants UM1AI148576, UM1AI148684, and NIH P51OD011132 (to E.A. and N.G.R.); National Institutes of Health grant HHSN272201500002C (to J.A.); the Intramural Research Program of the Vaccine Research Center, NIAID, NIH (to J.R.M., A.B.M., and B.S.G.); and the Coalition for Epidemic Preparedness Innovation (to H.B. and B.L.). **Author contributions:** Conceptualization: N.A.D.-R., A.B.M., S.E.O., A.P., and M.S.S. Laboratory investigation: S.E.O., L.L., C.A.T., S.D.S., S.O., W.S., L.W., B.F., and E.S.Y. Laboratory supervision: K.S.C., B.S.G., J.R.M., N.A.D.-R., A.B.M., A.P., M.R., and M.S.S. Clinical investigation: L.J., E.A., N.G.R., A.T.W., J.E.L., J.A., B.L., H.B., C.J.L., P.C.R., P.A.R., M.M., J.H.B., and C.A.R. Writing, review, and editing: N.A.D.-R., S.E.O., A.P., A.B.M., L.J., E.A., J.E.L., P.C.R., B.L., L.W., J.R.M., M.S.S., C.J.L., and C.A.R. Statistical analysis: M.C.N. **Competing interests:** H.B. and B.L. are employees of Moderna, Inc. M.S.S. is on the Advisory Board of Moderna, Inc. B.S.G. and K.S.C. are inventors on international patent application no. WO/2018/081318 entitled "Prefusion Coronavirus Spike Proteins and Their Use" and pending US patent application no. 62/972,886 entitled "2019-nCoV Vaccine." P.C.R. and J.H.B. report a pending US patent application no. 63/025,918 entitled "Coronavirus RNA vaccines and methods of use." E.A. reports grants from Merck, PaxVax, Micron, MedImmune, GSK, Pfizer, Janssen, and Sanofi-Pasteur. E.A. reports personal fees from Pfizer, Janssen, Sanofi-Pasteur, Medscape, and Kentucky Bioprocessing, Inc., outside the submitted work. N.G.R. reports grants from Pfizer Merck, Sanofi-Pasteur, Eli Lilly, and Quidel, outside the submitted work. **Data and materials availability:** All data are available in the main text or the supplementary materials. This work is licensed under a Creative Commons Attribution 4.0 International (CC BY 4.0) license, which permits unrestricted use, distribution, and reproduction in any medium, provided the original work is properly cited. To view a copy of this license, visit https://creativecommons.org/licenses/by/4.0/. This license does not apply to figures/photos/artwork or other content included in the article that is credited to a third party; obtain authorization from the rights holder before using such material.

SUPPLEMENTARY MATERIALS

https://science.org/doi/10.1126/science.abj4176
Materials and Methods
Figs. S1 to S6
Table S1
mRNA-1273 Study Group Member List
References (*29*–*32*)
MDAR Reproducibility Checklist

12 May 2021; accepted 9 August 2021
Published online 12 August 2021
10.1126/science.abj4176

PROTEIN BIOGENESIS

Structural insight into the SAM-mediated assembly of the mitochondrial TOM core complex

Qiang Wang[1]†, Zeyuan Guan[1]†, Liangbo Qi[1]†, Jinjin Zhuang[1], Chen Wang[1], Sixing Hong[1], Ling Yan[1], Yan Wu[1], Xiaoqian Cao[1], Jianbo Cao[2], Junjie Yan[1], Tingting Zou[3], Zhu Liu[1], Delin Zhang[1], Chuangye Yan[4], Ping Yin[1]*

β barrel outer membrane proteins (β-OMPs) play vital roles in mitochondria, chloroplasts, and Gram-negative bacteria. Evolutionarily conserved complexes such as the mitochondrial sorting and assembly machinery (SAM) mediate the assembly of β-OMPs. We investigated the SAM-mediated assembly of the translocase of the outer membrane (TOM) core complex. Cryo–electron microscopy structures of SAM–fully folded Tom40 and the SAM-Tom40/Tom5/Tom6 complexes at ~3-angstrom resolution reveal that Sam37 stabilizes the mature Tom40 mainly through electrostatic interactions, thus facilitating subsequent TOM assembly. These results support the β barrel switching model and provide structural insights into the assembly and release of β barrel complexes.

In both prokaryotes and eukaryotes, β barrel outer membrane proteins (β-OMPs) fulfill various functions including membrane biogenesis, nutrient uptake, and protein transport (*1*, *2*). The biogenesis of β-OMPs requires assistance from the evolutionarily conserved machineries including the β barrel assembly machinery (BAM) in Gram-negative bacteria, the sorting and assembly machinery (SAM) in mitochondria, and outer envelope protein 80 (OEP80) in chloroplasts (*1*, *3*–*6*). How these machineries function is a long-standing question because capturing the assembly intermediates of these substrate-machine complexes is challenging owing to their transient nature (*7*, *8*). Recent work on the BAM complex has revealed potential folding intermediates (*9*–*12*), but there is limited information on fully folded substrates before release.

In yeast, the SAM complex comprises β-OMP Sam50 and peripheral subunits Sam35 and Sam37 and mediates the assembly of the main mitochondrial protein import machinery (also called the translocase of the outer membrane, or TOM) (*4*, *5*, *13*). The TOM core complex contains two copies of the β-OMP Tom40, each of which binds to four α helical transmembrane proteins, Tom5, Tom6, Tom7, and Tom22 (*14*, *15*). The TOM core complex assembly process can be divided into three main stages: assembly I, assembly II, and the TOM core complex (Fig. 1A) (*4*, *16*). During the formation of assembly I, the imported Tom40 precursor is folded and inserted into the outer membrane by SAM (*4*). Small Tom subunits are subsequently assembled onto Tom40 in a stepwise manner (*16*–*18*), beginning with Tom5 and Tom6 (*19*, *20*) and followed by Tom7, which leads to assembly II (*21*, *22*). The incorporation of Tom22 generates the TOM core complex (*14*, *15*, *23*).

Recently, structures of SAM from *Myceliophthora thermophila* (*Mt*SAM) and *Saccharomyces cerevisiae* (*Sc*SAM) have been reported (*24*, *25*), and a dynamic β barrel switching mechanism was proposed (*25*). However, how TOM is assembled by SAM remains unclear. To isolate relevant assembly intermediates, we first coexpressed the yeast Tom subunits $Tom40^{3\times Flag}$, $Tom22^{8\times His}$, Tom5, Tom6, and Tom7 in the human embryonic kidney (HEK) 293 F cell system (fig. S1A; see methods in the supplementary materials for details). Intriguingly, we failed to obtain the TOM core complex; only Tom40, which has an approximate molecular mass of 66 kDa, was detected by blue native polyacrylamide gel electrophoresis

[1]National Key Laboratory of Crop Genetic Improvement, Hubei Hongshan Laboratory, Huazhong Agricultural University, Wuhan 430070, China. [2]Public Laboratory of Electron Microscopy, Huazhong Agricultural University, Wuhan 430070, China. [3]College of Life Science and Technology, Huazhong Agricultural University, Wuhan 430070, China. [4]Beijing Advanced Innovation Center for Structural Biology, Tsinghua-Peking Joint Center for Life Sciences, School of Life Sciences, Tsinghua University, Beijing 100084, China.
***Corresponding author. Email: yinping@mail.hzau.edu.cn**
†These authors contributed equally to this work.

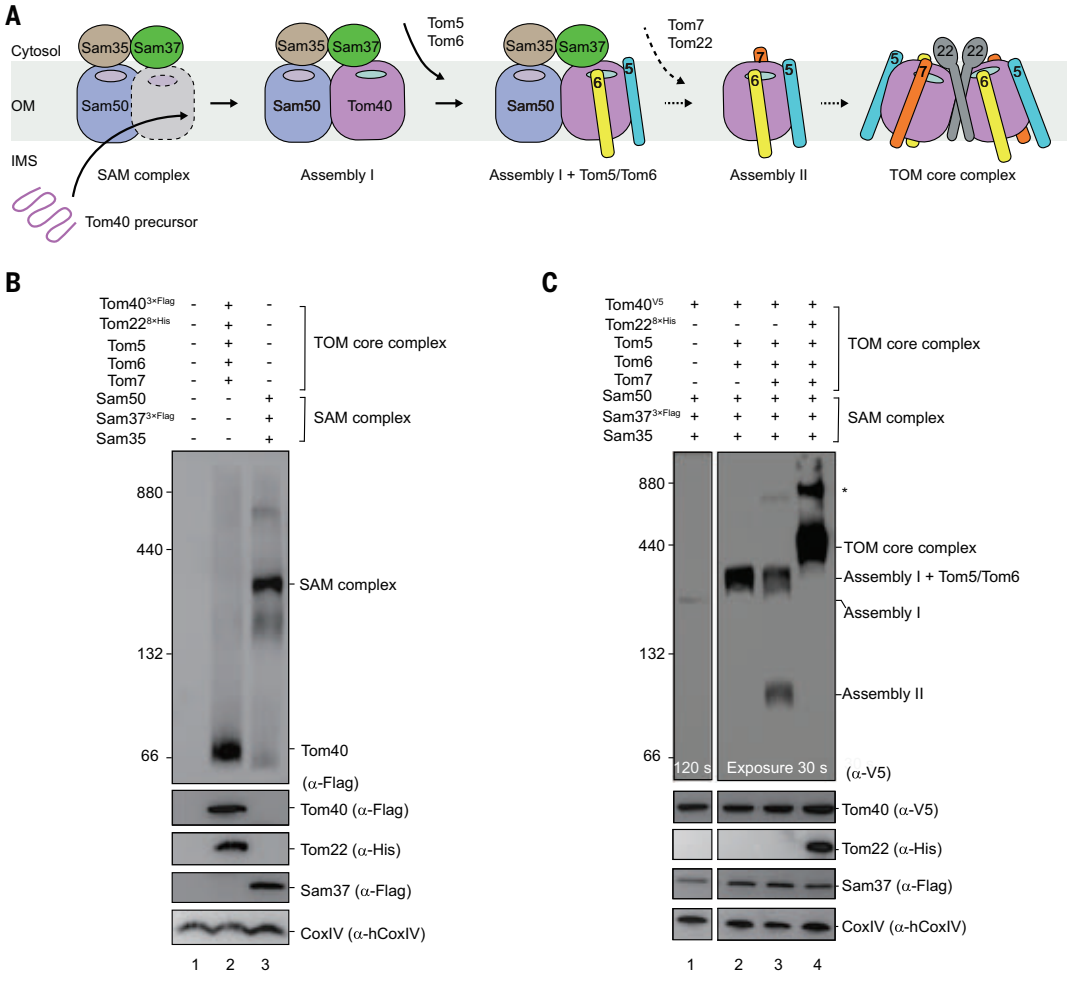


Fig. 1. Assembly of yeast TOM core complex in the mammalian cell system. (**A**) A schematic model showing the assembly process of yeast TOM core complex. The compositions and the precise protein stoichiometry of the assembly intermediates are not known. OM, outer membrane; IMS, intermembrane space. (**B**) Expression of the TOM core complex and the SAM complex in the mammalian cell system. The proteins and complexes were separated using BN-PAGE. The tagged proteins were detected by immunoblotting with antibodies against the corresponding tags. The expression of tagged proteins was also detected by SDS-PAGE and Western blotting. The cells transfected with empty plasmids were included as a control. hCoxIV was provided as the loading control. (**C**) Stepwise assembly of yeast TOM core complex in the mammalian cell system. Lane 1 was subjected to long-time exposure (120 s). An undefined band around 700 kDa is indicated with an asterisk. Components in these bands were identified via mass spectrometry.

(BN-PAGE) and immunoblotting (Fig. 1B). The detected Tom40 was likely the Tom40 precursor because it was unstable and easily degraded after cycles of freezing and thawing (fig. S1B). The lack of complete TOM complex in this assay implies that yeast Tom40 cannot fold using endogenous human SAM; in other words, the yeast and human mitochondrial import systems are not complementary. We also examined the formation of yeast SAM by co-expressing Sam50, Sam35, and Sam37$^{3\times Flag}$. A band located at ~350 kDa containing Sam37$^{3\times Flag}$ was detected (Fig. 1B); this band is consistent with a recent report on the SAM-Sam50 complex (*25*). Moreover, the putative SAM-Tom40 band was detected in mitochondria expressing the yeast SAM in import assays using [^{35}S]-labeled Tom40, whereas only Tom40 precursor was detected in control mitochondria (*26*) (fig. S1C). These results show that the functional yeast SAM complex can be obtained using this mammalian cell system.

We attempted to reproduce the assembly process of the TOM core complex in this system. First, we coexpressed SAM and C-terminal V5-tagged Tom40 (Tom40^{V5}) and obtained SAM-Tom40 (assembly I; Fig. 1C). Mass spectrometry analysis indicated that assembly I comprised Sam50, Sam35, Sam37, and Tom40; no endogenous human TOM subunits were associated (table S1). Tom40 was thus likely stalled on SAM in this mammalian cell system. To obtain a SAM-TOM intermediate between assembly I and assembly II, Tom5 and Tom6 were introduced to the assay. Although the biogenesis of single transmembrane subunits in this system remains elusive, the addition of Tom5 and Tom6 yielded a band with an increased amount of Tom40 as well as Tom5 and Tom6 (Fig. 1C and table S1), consistent with previous reports that Tom5 and Tom6 facilitate the stability of Tom40 at SAM (*20*, *27*). Addition of Tom7 yielded two major bands, representing a possible SAM-Tom40/Tom5/Tom6 complex and assembly II (Fig. 1C). However, when the N terminus (residues 2 to 64 or 2 to 80) of Tom40 was truncated, no assembly II was formed in the presence of Tom7 (fig. S1D). N-terminally truncated Tom40 (residues 65 to 387 or 81 to 387, β1 to β19) was thus arrested at SAM, consistent with previous reports (*25*, *28*). When all five full-length subunits (Tom40, Tom5, Tom6, Tom7, and Tom22) were included in the coexpression, an ~440-kDa band representing a putative TOM core complex was observed (Fig. 1C). Other small Tom subunit combinations were also tested (fig. S1E). Additionally, the expression of yeast SAM and TOM had little effect on the final protein level of endogenous human TOM subunits (fig. S1F).

The retention of TOM components at SAM in this system enabled us to capture stable substrate-bound SAM for structural studies. We purified the homogeneous SAM-Tom40 and SAM-Tom40/Tom5/Tom6 complexes and determined their cryo–electron microscopy (cryo-EM) structures (~3.0-Å resolution; Fig. 2A, figs. S2 and S3, and table S2; details in methods). The SAM-Tom40 complex comprises one copy each of Sam50, Sam35, Sam37, and Tom40 (Fig. 2A and figs. S4, A to E, and S5). The cytosolic half of the SAM-Tom40 structure consists of two peripheral membrane proteins, Sam35 and Sam37, from the SAM complex. Sam35 caps the Sam50 lumen and directly interacts with Sam37 and Sam50. Sam50 spans the mitochondrial outer membrane and forms a 16-stranded transmembrane β barrel with an N-terminal polypeptide-transport-associated (POTRA) domain. The POTRA domain (residues 25 to 121) displays a conformation similar to those of *Mt*Sam50 and

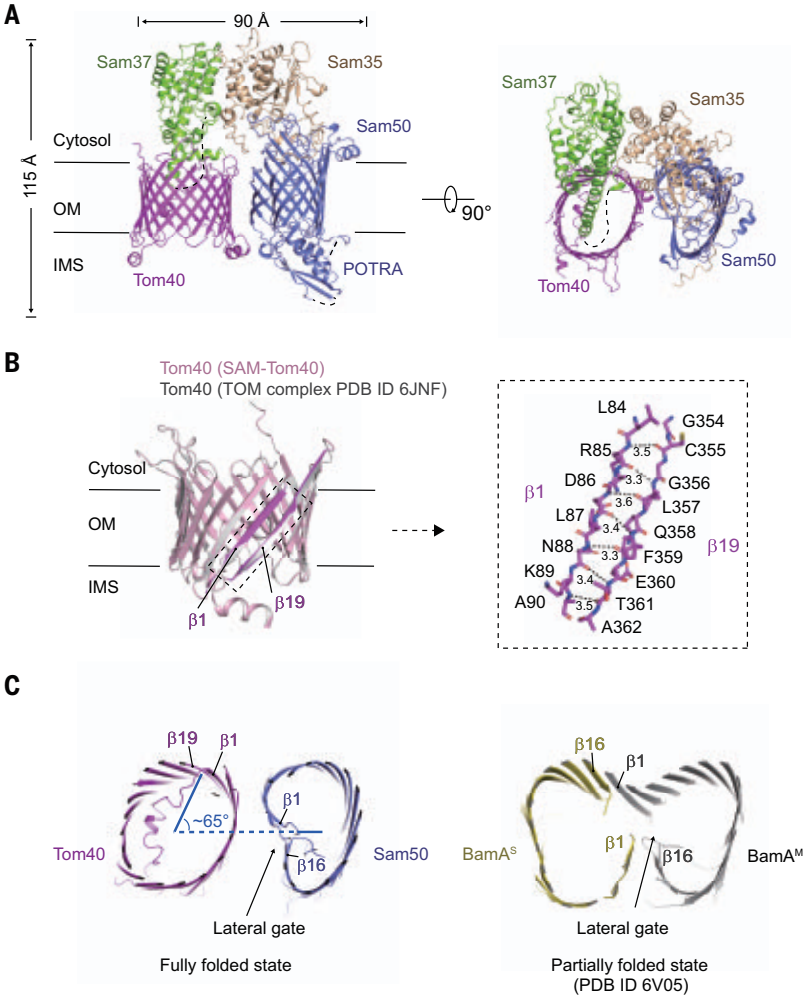


Fig. 2. Structure of the SAM-Tom40 complex. (**A**) Overall structure of the SAM-Tom40 (assembly I) complex. Missing regions (residues I175 to S199 of Sam37; G92 to P107 and H226 to S230 of Sam50) are indicated by the black dashed line. (**B**) Superposition of Tom40 (light pink) from the SAM-Tom40 complex with Tom40 (gray) from the TOM core complex (PDB ID 6JNF) (*15*). The β1 and β19 are indicated by the black dashed box. Inset shows seven hydrogen bonds (bond length is given in angstroms) between the β1 and β19 of the closed Tom40 β barrel. Single-letter abbreviations for the amino acid residues are as follows: A, Ala; C, Cys; D, Asp; E, Glu; F, Phe; G, Gly; H, His; I, Ile; K, Lys; L, Leu; M, Met; N, Asn; P, Pro; Q, Gln; R, Arg; S, Ser; T, Thr; V, Val; W, Trp; and Y, Tyr. (**C**) Top-down slice through the structures of the SAM-Tom40 complex (left) and the substrate-engaged Bam complex [right; PDB ID 6V05 (*12*); BamA^{M}, BamA within the BAM machine; BamA^{S}, BamA as the substrate].

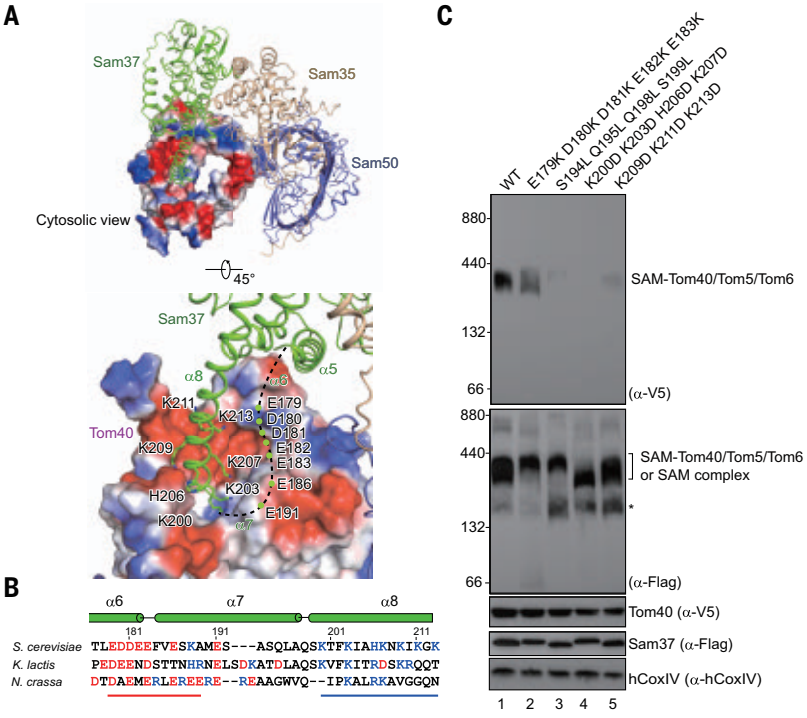


Fig. 3. The intersubunit interactions between Sam37 and Tom40. (**A**) The electrostatic potential surface of Tom40 and cartoon of SAM in the SAM-Tom40 complex. The α helices 6 and 7 of Sam37 are indicated by the black dashed line. Blue, positively charged region; red, negatively charged region. (**B**) Sequence alignment of the residues in the Sam37 hook region (α6 to α8) from *S. cerevisiae*, *Kluyveromyces lactis*, and *Neurospora crassa*. Red, negatively charged residue; blue, positively charged residue. (**C**) Structure-guided mutagenesis in the Sam37 hook region. The SAM-Tom40/Tom5/Tom6 complex and the SAM complex were detected through BN-PAGE (top two panels) or SDS-PAGE (bottom three panels) followed by immunoblotting with the antibodies against the corresponding tags. The potential SAM monomer is indicated with an asterisk.

BamA (POTRA1-5), with a classic β-α-β-β fold that is present in all these POTRA domains (fig. S6) (*12*, *24*). The β barrel domain of Sam50 in the SAM-Tom40 complex is similar to that of all other previously reported Sam50 structures with a partially open lateral gate, which is further supported by the observation that hydrogen bonds are hardly found between β1 and β16 in Sam50 (fig. S7) (*12*, *25*).

The substrate Tom40 in the SAM-Tom40 complex exhibits 19 β strands and has a completely closed β barrel; β1 and β19 are in contact through seven hydrogen bonds (Fig. 2B, right panel). Our substrate Tom40 and Tom40 in the TOM core complex have nearly identical conformations (Fig. 2B, left panel). These results jointly indicate that SAM-Tom40 is in a fully folded state prior to substrate release. Compared with the β barrel of the nascent $BamA^{S}$ (late-stage folding) in the $BamA^{M}$-$BamA^{S}$ complex (*12*), the closed β barrel of Tom40 (after folding) shows a distinct conformation, with the first and last β strands of Tom40 forming an ~65° angle relative to the lateral gate of Sam50 (Fig. 2C).

Sam37 is reported to play a role in the release of the folded β barrel substrate from SAM and the assembly of Tom40 into the TOM complex (*29*), yet the molecular basis of this function remains elusive. In the SAM-Tom40 complex, the hydrophilic α helices 6 to 8 of the Sam37 subunit form a hooklike conformation and enter the β barrel lumen of Tom40 from the cytosolic side (Fig. 3A and fig. S8). The α helices 6 and 7 are rich in negatively charged residues, whereas α helix 8 is positively charged (Fig. 3B). The interior wall of the Tom40 β barrel exhibits negatively and positively charged patches near the hook (α6 to α8) of Sam37 (Fig. 3A) and may electrostatically interact with the β strands of Tom40 from inside the lumen to stabilize Tom40 (fig. S8). Lys^{142} in the Sam37 α4 contacts the main chains of Lys^{348} and Asn^{349} from the last β strand of Tom40 (fig. S5D). Mutation of positively or negatively charged residues in the hook region or leucine substitutions of amino acids in the hydrophilic region between α helices 7 and 8 both abolished the assembly of this complex (Fig. 3C). Sam37 may thus stabilize Tom40 at the SAM complex, facilitating the formation of the SAM-Tom40/Tom5/Tom6 complex.

In the SAM-Tom40/Tom5/Tom6 complex, SAM and Tom40 display a virtually identical conformation to the SAM-Tom40 complex described above (Fig. 4, A and B, and fig. S4, F to H). The transmembrane α helices of small subunits Tom5 and Tom6 are in close proximity to β8 to β11 and β12 to β15 of Tom40 β barrel, respectively (fig. S5, E and F), which is in line with the reported location of Tom5 and Tom6 at the corresponding interaction interfaces in the TOM core complex (*15*). Superposition of the TOM subunits in our structure

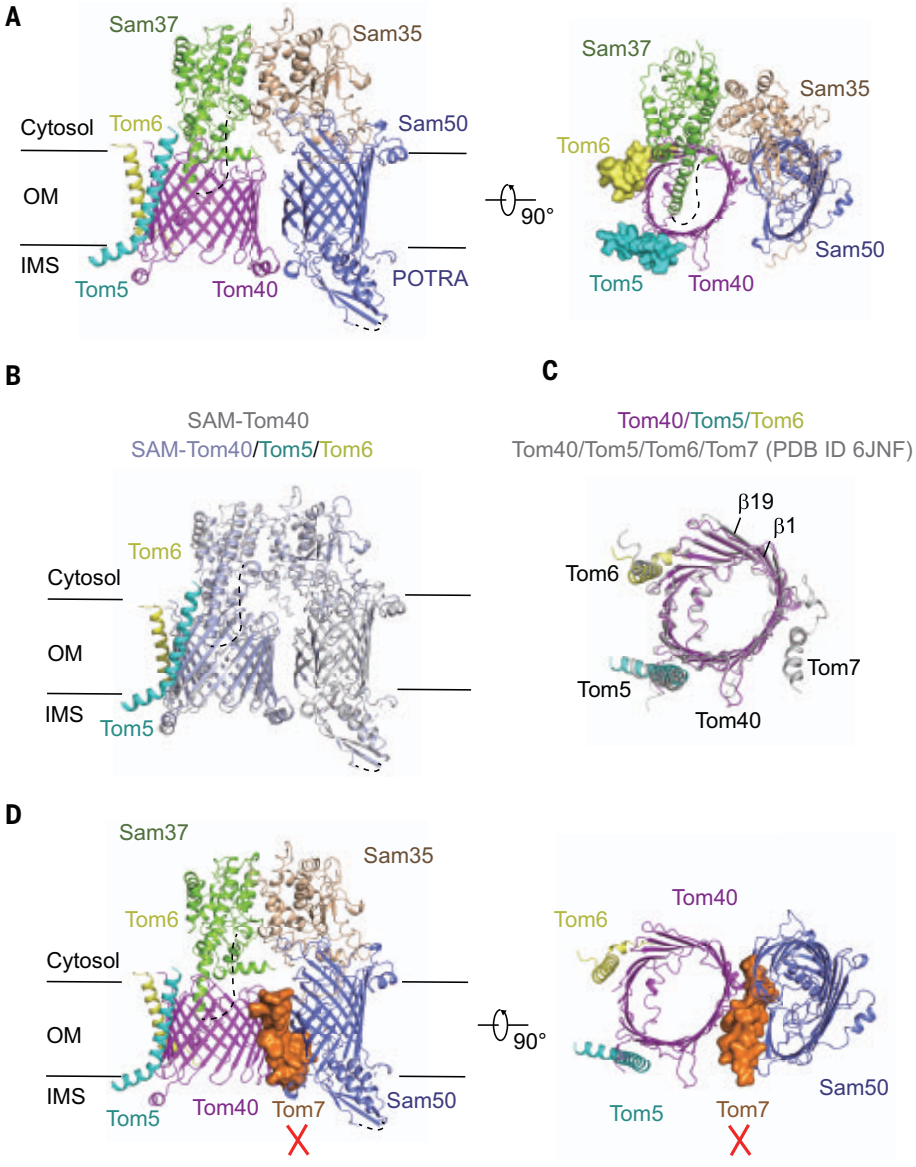


Fig. 4. Structure of the SAM-Tom40/Tom5/Tom6 complex. (**A**) Overall structure of the SAM-Tom40/Tom5/Tom6 complex. (**B**) Superposition of SAM-Tom40 (gray) with SAM-Tom40/Tom5/Tom6 (SAM-Tom40, slate; Tom5, cyan; Tom6, yellow). (**C**) Superposition of the Tom40/Tom5/Tom6 module from the SAM-Tom40/Tom5/Tom6 complex with the Tom40/Tom5/Tom6/Tom7 module from the previously reported TOM core complex [gray; PDB ID 6JNF (*15*)]. (**D**) Structural model of Tom7 at the Tom40 binding site in the SAM-Tom40/Tom5/Tom6 complex.

with the Tom40/Tom5/Tom6/Tom7 subunits in the TOM core complex [Protein Data Bank (PDB) ID 6JNF] (*15*) showed a root mean square deviation (RMSD) of 0.980 Å over 297 Cα atoms (Fig. 4C). Thus, Tom subunits retain the same conformation before and after release from the SAM complex, suggesting a stable Tom40/Tom5/Tom6 conformation. This result is consistent with our coexpression experiments and previous reports that Tom5 and Tom6 promote the formation of Tom40 (as well as TOM intermediates) at SAM (*20*, *27*, *30*). Tom7 mediates the dissociation of the β barrel protein Mdm10 (mitochondrial distribution and morphology protein 10) from the SAM complex, but the role of Tom7 in the assembly of TOM remains largely unclear (*21*, *22*, *31*). Our biochemical analysis suggests that Tom7 might induce the dissociation of TOM components from SAM (Fig. 1C and fig. S1E). A modeled Tom7 based on the TOM core complex (*15*) would clash with Sam50 (Fig. 4D) and may thus induce release of TOM components from SAM.

Our structure of Tom40-bound SAM exhibits a similar architecture to the recently reported SAM-Mdm10 complex (*25*) with a RMSD of 1.1 Å over 864 Cα atoms (fig. S9A). Sam37 interacts with Tom40 via a largely

shared "charged hook" region, which is similar to the interaction between Sam37 and Mdm10 (fig. S9B). This finding provides further evidence for the β barrel switching model in which a placeholder subunit (Sam50 or Mdm10) occupies the SAM complex upon release of folded client proteins (fig. S9C) (*25*). Mutations in the Sam37 charged hook region can strongly affect Tom40 assembly at SAM. Deletion of Sam37 results in a reduction in the amount of Tom40 and TOM complex in yeast mitochondria at elevated temperatures (30°C or higher), but the reduction was minimal at 23°C (*4*). We thus propose that Sam37 mutations might affect the stability rather than the folding of Tom40 at SAM. This model might be applicable for the other β barrel substrate precursors at SAM. Other structure-guided mutational analyses on TOM and SAM subunits are now feasible using this mammalian cell system, and we anticipate future investigation of the assembly of SAM itself and structural elucidation of the TOM-SAM supercomplex (*32*).

REFERENCES AND NOTES

1. R. Wu, R. Stephenson, A. Gichaba, N. Noinaj, *Biochim. Biophys. Acta Biomembr.* **1862**, 183062 (2020).
2. N. Noinaj, J. C. Gumbart, S. K. Buchanan, *Nat. Rev. Microbiol.* **15**, 197–204 (2017).
3. C. L. Hagan, T. J. Silhavy, D. Kahne, *Annu. Rev. Biochem.* **80**, 189–210 (2011).
4. N. Wiedemann *et al.*, *Nature* **424**, 565–571 (2003).
5. S. A. Paschen *et al.*, *Nature* **426**, 862–866 (2003).
6. L. E. Gross *et al.*, *Plant Cell* **33**, 1657–1681 (2021).
7. D. Tomasek, D. Kahne, *Curr. Opin. Microbiol.* **60**, 16–23 (2021).
8. J. Lee *et al.*, *Proc. Natl. Acad. Sci. U.S.A.* **113**, 8717–8722 (2016).
9. N. Noinaj *et al.*, *Nature* **501**, 385–390 (2013).
10. Y. Gu *et al.*, *Nature* **531**, 64–69 (2016).
11. J. Bakelar, S. K. Buchanan, N. Noinaj, *Science* **351**, 180–186 (2016).
12. D. Tomasek *et al.*, *Nature* **583**, 473–478 (2020).
13. N. Wiedemann, N. Pfanner, *Annu. Rev. Biochem.* **86**, 685–714 (2017).
14. K. Tucker, E. Park, *Nat. Struct. Mol. Biol.* **26**, 1158–1166 (2019).
15. Y. Araiso *et al.*, *Nature* **575**, 395–401 (2019).
16. A. Gupta, T. Becker, *Biochim. Biophys. Acta Bioenerg.* **1862**, 148323 (2021).
17. L. Ellenrieder, C. U. Mårtensson, T. Becker, *Biol. Chem.* **396**, 1199–1213 (2015).
18. A. Grevel, N. Pfanner, T. Becker, *Biol. Chem.* **401**, 117–129 (2019).
19. N. Thornton *et al.*, *J. Mol. Biol.* **396**, 540–549 (2010).
20. T. Becker *et al.*, *Mol. Biol. Cell* **21**, 3106–3113 (2010).
21. K. Yamano, S. Tanaka-Yamano, T. Endo, *J. Biol. Chem.* **285**, 41222–41231 (2010).
22. T. Becker *et al.*, *J. Mol. Biol.* **405**, 113–124 (2011).
23. T. Shiota *et al.*, *Science* **349**, 1544–1548 (2015).
24. K. A. Diederichs *et al.*, *Nat. Commun.* **11**, 3290 (2020).
25. H. Takeda *et al.*, *Nature* **590**, 163–169 (2021).
26. A. D. Humphries *et al.*, *J. Biol. Chem.* **280**, 11535–11543 (2005).
27. S. Schmitt *et al.*, *J. Biol. Chem.* **280**, 14499–14506 (2005).
28. S. Kutik *et al.*, *Cell* **132**, 1011–1024 (2008).
29. N. C. Chan, T. Lithgow, *Mol. Biol. Cell* **19**, 126–136 (2008).
30. J. Dukanovic, K. S. Dimmer, N. Bonnefoy, K. Krumpe, D. Rapaport, *Mol. Cell. Biol.* **29**, 5975–5988 (2009).
31. C. Meisinger *et al.*, *J. Biol. Chem.* **281**, 22819–22826 (2006).
32. J. Qiu *et al.*, *Cell* **154**, 596–608 (2013).

ACKNOWLEDGMENTS

We thank the cryo-EM Facility of Westlake University for providing cryo-EM and computation support and the Center for Protein Research and Public Laboratory of Electron Microscopy, Huazhong Agricultural University, for technical support. We thank L. Huang, X. Wang, and Z. Jiang for technical support during cryo-EM image acquisition; J. Yan for technical assistance with the mass spectrometry experiments; Y. Wang for model figure design; and three anonymous reviewers whose comments have significantly improved this manuscript. **Funding:** This work was supported by funds from the Ministry of Science and Technology of China (2018YFA0507700), the National Natural Science Foundation of China (31722017, 31870753, and 32071211), and the Fundamental Research Funds for the Central Universities (2662017PY031). Q.W. and Z.G. acknowledge the support of China National Postdoctoral Program for Innovative Talents (BX2021107 and BX2021108), China Postdoctoral Science Foundation (2021M691168), and the Baichuan Project at the College of Life Science and Technology, Huazhong Agricultural University. **Author contributions:** P.Y. conceived of the project. Q.W., L.Q., and P.Y. designed all experiments. Q.W., L.Q., J.Z., S.H., L.Y., Y.W., and X.C. performed the experiments. Q.W. and Z.G. collected the EM data. Z.G. determined the structures. All authors analyzed the data and contributed to manuscript preparation. Q.W., C.W., and P.Y. wrote the manuscript. **Competing interests:** The authors declare no competing financial interests. **Data and materials availability:** Atomic coordinates and EM densities have been deposited in the Protein Data Bank (PDB) and the Electron Microscopy Data Bank (EMDB) for the reported structures of the SAM-Tom40 complex (PDB ID 7E4H; EMDB ID EMD-30985) and the SAM-Tom40/Tom5/Tom6 complex (PDB ID 7E4I; EMDB ID EMD-30986). All other data needed to evaluate the conclusions in the paper are present in the paper and/or the supplementary materials.

SUPPLEMENTARY MATERIALS

https://science.org/doi/10.1126/science.abh0704
Materials and Methods
Figs. S1 to S9
Tables S1 and S2
References (*33*–*46*)
MDAR Reproducibility Checklist

14 February 2021; accepted 12 August 2021
Published online 26 August 2021
10.1126/science.abh0704



Discussion leaders are noted in bold italics.

Advanced Materials for Sustainable Infrastructure Development

Cement Based Materials: Reaching Net Zero

FEBRUARY 13-18, 2022
RENAISSANCE TUSCANY IL CIOCCO, LUCCA (BARGA), ITALY

CHAIRS: Karen Scrivener and Carmen Andrade
VICE CHAIRS: William Weiss and Ravindra Gettu

- **Advances in Cement Processing** *Robert McQuillan,* Alexander Pisch, Matteo Romano, Leah Ellis
- **Cement Hydration** *Thomas Matschei,* Paul Bowen, Alejandro Fernandez-Martinez, Hegoi Manzano, Pan Feng
- **Decreasing Clinker Factor and Supplementary Cementitious Materials** *Edgardo Irassar,* Elsa A. Olivetti, Ruben Snellings, Franco Zunino
- **Cement Based Materials as CO2 Sink** *Anne Dekeukelaere,* Paula Carey, Zhichao Liu, Jan Skocek, Rupert Myers
- **New Technologies** *Frank Winnefeld,* Allan Scott, David Dreisinger, Ellina Bernard
- **Concrete Design for Sustainability** *David Fernandez-Ordoñez,* Cyrille Dunant, Liberato Ferrara
- **Use of Non-Metallic Reinforcement** *Yamei Zhang,* Akio Kasuga, Alva Peled
- **Durability** *Christoph Müller,* Burkan Isgor, Fabien Georget, Klaartje De Weerdt, Alexandra Bertron
- **Corrosion** *Joost Gulikers,* Veronique Bouteiller, Fatima Montemor, Radhakrishna Pillai
- **The GRC Power Hour™**

Advanced Materials for Sustainable Infrastructure Development

GRS

Cutting Edge Solutions for Sustainable Development of Cement and Concrete

FEBRUARY 12-13, 2022

CHAIRS: Daniela Martinez and Yuvaraj Dhandapani

Alcohol and the Nervous System

Neurobiology of Alcohol Use Disorder and CNS Comorbidities

FEBRUARY 27 - MARCH 4, 2022
RESIDENCE INN AT OXNARD RIVER RIDGE, OXNARD, CA

CHAIRS: Nicholas Gilpin and Patricia Janak
VICE CHAIRS: Rajita Sinha and Joyce Besheer

- **Keynote Session: Successes and Challenges in Translational Alcohol Research** *Rajita Sinha,* George Koob, Harriet de Wit
- **Alcohol Interactions with Stress and Brain Stress Systems** *Zoe McElligott,* Kerry Ressler, Anushree Karkhanis, Marcus Weera, Danny Winder, Laverne Melon, Marvin Diaz
- **Mechanisms and Pathways Underlying Excessive Alcohol Drinking** *Karla Kaun,* Markus Heilig, Adrian Rothenfluh, Reginald Cannady, Angela Ozburn
- **Executive Control and Flexibility in Alcohol Actions** *Cody Siciliano,* Charlotte Boettiger, Christina Gremel, Michael Salling, Christina Perry, Rafiq Huda, David Moorman
- **New Tools for Biomedical Alcohol Research** *Kevin Bender,* Keri Martinowich, Jacqueline Barker, Daniel Castro, Lex Kravitz
- **Alcohol Interactions with Pain** *Imad Damaj,* Katie Witkiewitz, Scott Edwards, Yarimar Carrasquillo, Thomas Kash
- **Co-Morbid Use of Alcohol and Other Drugs** *Leandro Vendruscolo,* Lara Ray, Jibran Khokhar, Lori Knackstedt
- **Motivational and Learned Determinants of Alcohol Self-Administration** *Dorit Ron,* Ravi Das, Jocelyn Richard, David Lovinger, Segev Barak
- **Keynote Session: Alcohol Use Disorder Research: Co-Morbidities and Inequities** *Heather Richardson,* Jaideep Bains, Michael Taffe
- **The GRC Power Hour™** *Jocelyn Richard, James Jentsch*

Alcohol and the Nervous System

GRS

Multilevel Neuronal Targets for Alcohol Interventions

FEBRUARY 26-27, 2022

CHAIRS: Anel Jaramillo and Konstantin Kaganovsky

Angiotensin

The RAAS: Molecular Networking to Multi-System Pathophysiology

FEBRUARY 27 - MARCH 4, 2022
VENTURA BEACH MARRIOTT, VENTURA, CA

CHAIR: Minolfa Prieto
VICE CHAIR: Rhian Touyz

- **Keynote Session: Understanding Complexity to Maintain Cardiovascular Health** *Carlos Ferrario,* Rhian Touyz, Robson Santos, Victor Dzau
- **ACE2 as a Multifunctional Protein of the RAAS** *Kenneth Bernstein, Dulce Casarini, Eric Lazartigues,* Michael Bader, Anthony Turner, Louise Burrell, Kathryn Sandberg
- **ACE2 as a Coronavirus Receptor** *Jan Danser, Kathryn Sandberg,* Chad Roy, Daniel Batlle, Matthew Sparks, Josef Penninger
- **Signaling and Molecular Networking Through Ang Peptides and Receptors** *Catherine Llorens-Cortes, Tianxin Yang, Jia Zhuo,* Carlos Ferrario, Chrishan Samuel, Gavin Oudit, Maureen Horton, Frederique Yiannikouris
- **Advances in Pharmacogenomics, Proteomics and Metabolomics of the RAAS** *Akira Nishiyama,* Edward Sturrock, Jerald Sadoff
- **The RAAS, the Immune System and the Microbial Ecosystems in Health and Disease** *Ulrich Wenzel,* Meenakshi Madhur, Luciana Veiras, Bina Joe, Modar Kassan, Lydia Bazzano, Giacomo Rossitto
- **Sex-Differences in the Regulation of the RAAS and Changes During the Life Spam** *Analia Loria Kinsey, Jane Reckelhoff,* Barbara Alexander, Anne-Monique Nuyt, Jose Romero, Sarah Lindsey, Licy Yanes Cardozo
- **Cellular and Tissue Plasticity, Organ Remodeling and Imaging** *Maria Luisa Sequeira-Lopez, Alexander Staruschenko,* Alexander Pinto, Lisa Cassis, Ryosuke Satou, Satoru Eguchi, Oleh Pochynyuk
- **Keynote Session: The RAAS: Impact of Novel Methodologies** *Thomas Coffman, Romer Gonzalez-Villalobos,* Christine Maric-Bilkan, Joseph Wu
- **The GRC Power Hour™** *Jane Reckelhoff, Mariane Bertagnolli*

Angiotensin

GRS

RAAS System: New Concepts for an Old Challenge

FEBRUARY 26-27, 2022

CHAIRS: Rheure Lopes and Omar Guessoum

Antibody Biology and Engineering

Connecting B Cell Biology with Antibody Structure, Function and Applications

MARCH 13-18, 2022
VENTURA BEACH MARRIOTT, VENTURA, CA

CHAIRS: Jeanette Leusen and Laura Walker
VICE CHAIRS: Pierre Bruhns and Lynn Macdonald

- **Keynote Session: From B Cell Activation to Engineered Antibodies** *Janine Schuurman,* Facundo Batista, Andreas Plueckthun
- **Antibodies Against Infectious Disease Agents** *Stephen Harrison,* Eva Harris, Patrick Wilson, Penelope Moore, Kathryn Westendorf, Davide Corte
- **Antibody Interactions with Fc Receptors** *Richard Blumberg,* Diane Lidke, Sally Ward
- **Antibody Structure in Relation to Function** *Sally Ward,* Pamela Bjorkman, Erica Saphire, Thomas Sharp, Stephen Harrison
- **Antibody Engineering** *Mark Hogarth,* Dane Wittrup, Jan Terje Andersen, Paul Carter, Omid Vafa

- **Cancer Immunotherapy Employing Innate Immune Cells** *James Ernst,* Kai Wucherpfennig, Nicolas Fischer, Sophia Karagiannis, Thomas Valerius
- **Dissecting B Cell Responses** *Davide Corte,* Greg Ippolito, Justin Taylor, Julie Zikherman
- **Agonistic and Antagonistic Antibodies for Cancer Immunotherapy** *Paul Parren,* Gregory Lazar, Stephen Beers, Daniel Emerling
- **Pre-Clinical Antibody Evaluation** *Stephen Beers,* John Desjarlais, Mark Hogarth, Paul Parren
- **The GRC Power Hour™** *Diane Lidke, Penelope Moore*

Antibody Biology and Engineering
Design and Applications of Next-Generation Antibody Technologies and Therapies
MARCH 12-13, 2022
CHAIRS: Alicia Chenoweth and Stuart Ainsworth

Atomically Precise Nanochemistry

Towards the Control of Non-Scalable Properties and Functions

FEBRUARY 13-18, 2022
RESIDENCE INN AT OXNARD RIVER RIDGE, OXNARD, CA
CHAIRS: Tatsuya Tsukuda and Cathleen Crudden
VICE CHAIRS: Thalappil Pradeep and Stefanie Dehnen

- **Free Clusters in the Gas Phase** *Vlasta Bonacic-Koutecký,* Puru Jena, Lai-Sheng Wang, Nicola Gaston
- **Protected Metal Clusters and Nanoparticles** *Jianping Xie,* Rongchao Jin, Flavio Maran, De-en Jiang
- **Colloidal Nanocrystals and Nanoparticles** *Stefanie Dehnen,* Brandi Cossairt, Ray Schaak, Raffaella Buonsanti
- **Nanocarbon Materials** *Yan Li,* Hiroyuki Isobe, Colin Nuckolls
- **Advanced Structural Characterization** *Richard Palmer,* Yu Han, Peng Zhang, Sara Bals
- **Optical Nanomaterials** *Thalappil Pradeep,* Osman Bakr, Thomas Buergi, Sandrine Ithurria
- **Cluster-Based Model Catalysis** *Manfred Kappes,* Stefan Vajda, Anastassia Alexandrova, Barbara Lechner
- **Structurally Precise Heterogeneous Nanocatalysis** *Michelle Personick,* Nanfeng Zheng, Hyunjoo Lee, Nuria Lopez
- **Self-Assembly and Bioapplication** *Hannu Häkkinen,* Nonappa Nonappa, Giulia Rossi
- **The GRC Power Hour™** *Brandi Cossairt*

Atomically Precise Nanochemistry
Extending the Structural Precision of Clusters to Nanoscale Materials
FEBRUARY 12-13, 2022
CHAIR: Alexandra Brumberg

Autophagy in Stress, Development and Disease

Functions of Autophagy Proteins in Lysosome-Dependent and -Independent Mechanisms

MARCH 20-25, 2022
VENTURA BEACH MARRIOTT, VENTURA, CA
CHAIRS: Malene Hansen and Li Yu
VICE CHAIRS: Jayanta Debnath and Anne Simonsen

- **Keynote Session: Autophagy in Immunity and Neurodegenerative Diseases** *Anne Simonsen, Jayanta Debnath,* Herbert Virgin, Katja Simon, David Rubinsztein
- **Basic Autophagy Mechanisms** *Claudine Kraft,* Sharon Tooze, Zvulun Elazar, Noboru Mizushima, Hitoshi Nakatogawa, Qing Zhong
- **Molecular and Structural Mechanisms of Autophagy** *Xiaochen Wang,* Claudine Kraft, James Hurley, Nobuo Noda
- **Selective Autophagy Mechanisms** *Rushika Perera,* Ivan Dikic, Eric Baehrecke, Christian Behrends, Richard Youle
- **Autophagy in Disease: Aging and Neurodegenerative Disorders** *Mondira Kundu,* Susmita Kaushik, Ralph Nixon, Jonathan Goodwin
- **Non-Degradative Functions of Autophagy Proteins** *Christian Behrends,* Mondira Kundu, Fulvio Reggiori, Oliver Florey, Vojo Deretic
- **Autophagy in Cellular Homeostasis** *Oliver Florey,* Patricia Boya, Pura Munoz-Canoves, Hong Zhang
- **Lysosome Biology in Autophagy** *Ralph Nixon,* Andrea Ballabio, Xiaochen Wang, Marja Jaattela, Maho Hamasaki
- **Autophagy in Disease: Cancer and Immunity** *Patricia Boya,* Kevin Ryan, Rushika Perera, Eun-Kyeong Jo
- **The GRC Power Hour™** *Patricia Boya, Katja Simon*

Autophagy in Stress, Development and Disease
Molecular Regulation of Canonical and Non-Canonical Autophagy
MARCH 19-20, 2022
CHAIRS: Mathieu Bourdenx and Veronik Lachance

Basal Ganglia

Functions of the Basal Ganglia from Thought to Action

MARCH 20-25, 2022
FOUR POINTS SHERATON, HOLIDAY INN EXPRESS, VENTURA, CA
CHAIRS: Rui Costa and Margaret Rice
VICE CHAIRS: Zayd Khaliq and Ilana Witten

- **Models of Basal Ganglia and Learning** *Ann Graybiel,* Michale Fee, Michael Frank, Patricia Janak
- **Functional Heterogeneity of Basal Ganglia Projection Circuits and Dopaminergic Inputs** *Okihide Hikosaka,* Anatol Kreitzer, Rajeshwar Awatramani, Adam Carter, Ana Rodrigues, Talia Lerner, Vanessa Ruta
- **Modulating the Modulators** *Nicolas Tritsch,* Stephanie Cragg, Christopher Ford, Pascal Kaeser, Stephen Rayport
- **Basal Ganglia in Health and Disease** *Raffaella Tonini, Mary Kay Lobo,* Mark Bevan, Camilla Bellone, Meaghan Creed, Robert Edwards, Alexandra Nelson, X. William Yang
- **Motivating Movement** *Alexandra Nelson,* Helen Bronte-Stewart, David Leventhal, Paola Ortelli
- **Organization of Basal Ganglia and Extended Circuits in Spontaneous and Motivated Behavior** *Talia Lerner,* Sandeep Robert Datta, Carrie Ferrario, Alexxai Kravitz, Dayu Lin, Lauren McElvain, Mark Schnitzer
- **Dialogue Between Models of Basal Ganglia Function and Experimental Data** *Carmen Canavier,* Alison Duffy, Vikram Gadagkar, Naoshige Uchida
- **Insights into Molecular and Cellular Mechanisms from New Tools and Novel Approaches** *Veronica Alvarez,* Markita Landry, Yulong Li, David Sulzer, D. James Surmeier, Lin Tian, Laurent Venance
- **Basal Ganglia and Extended Circuits in Cognition and Decision Making** *Zayd Khaliq, Ilana Witten,* Michele Basso, Mitsuo Kawato, Richard Krauzlis, Daphna Shohamy
- **The GRC Power Hour™** *Zayd Khaliq, Ilana Witten*

Basal Ganglia
Diversity of Basal Ganglia Cells, Circuits and Systems in Health and Disease
MARCH 19-20, 2022
CHAIRS: Allison Girasole and Asha Lahiri

Batteries

How to Solve the "AND" Problem

FEBRUARY 20-25, 2022
FOUR POINTS SHERATON, HOLIDAY INN EXPRESS, VENTURA, CA
CHAIR: Venkat Viswanathan
VICE CHAIRS: Neil Dasgupta and Kelsey Hatzell

- **Circular Batteries: Manufacturing and Recycling** *Linda Gaines,* Shirley Meng
- **Solid Future for Metal Anodes** *Kelsey Hatzell,* Yet-Ming Chiang
- **Metal Anodes: Return of the Liquid** *Venkat Srinivasan,* Yi Cui
- **Machine Learning for Electrode and Electrolytes** *Austin Sendek,* Alpha Lee

"GRC cultivates an environment conducive to interdisciplinary learning and scientific discovery by fostering interactions among senior and junior academics, scientists at government laboratories and industrial associates from all over the globe."

DR. MONICA OLVERA DE LA CRUZ, Northwestern University

- **A Positive Boost: Cathodes and Interfaces** *Jeff Dahn,* Stan Whittingham
- **Technoeconomics and Control** *Rebecca Ciez,* Venkat Subramanian
- **Batt800: Conversion Electrodes** *Clare Grey,* Judy Jeevarajan
- **Squeezing the Packaging** *Judy Jeevarajan,* Chao-Yang Wang
- **Questioning the State Of Charge** *David Howey,* Shyue Ping-Ong

Batteries
Limiting Mechanisms: Why Building Better Batteries is Difficult
FEBRUARY 19-20, 2022
CHAIRS: Aashutosh Mistry and Philipp Dechent

Biology of Acute Respiratory Infection

Basic Mechanisms and Translational Science Contributing to the Global Impact of Pneumonia

FEBRUARY 27 - MARCH 4, 2022
FOUR POINTS SHERATON, HOLIDAY INN EXPRESS, VENTURA, CA
CHAIRS: Lee Quinton and Stephania Cormier
VICE CHAIRS: Bethany Moore and Charles Dela Cruz

- **Pneumonia in the Experienced Lung** *Alice Prince,* David Masopust, Joseph Mizgerd, Andreas Wack
- **Vulnerabilities Influencing Pneumonia Susceptibility** *Bethany Moore,* Dawn Bowdish, Kymberly Gowdy, Antoine Roquilly, Peter Sly
- **Immunometabolism for Infection Control** *Kymberly Gowdy,* Catharine Bosio, Michael Fessler, Mariana Kaplan
- **Molecular Networks in the Challenged Lung** *Chad Steele,* DeBroski Herbert, Hongbo Luo, Asrar Malik, Kara Mould
- **Recent Advances in Innate Immunity** *Kong Chen,* Susan Schwab, Stefanie Vogel
- **Tissue Resilience and Resolution of Inflammation** *Charles Dela Cruz,* Bruce Levy, Benjamin Singer, Anne Sperling
- **Long-Term Sequelae** *DeBroski Herbert,* Carlos Orihuela, Benjamin Singer, Jie Sun
- **Novel Advances in Pulmonary Defense** *Anne Sperling,* Avery August, Nicholas Heaton, Stacey Schultz-Cherry
- **Non-Traditional Influences on Pulmonary Immunity** *Katrina Traber,* Gordon Brown, Amanda Jamieson, Janet Lee
- **The GRC Power Hour™** *Janet Lee*

Biology of Acute Respiratory Infection
Host-Pathogen Interactions During Pulmonary Health and Disease
FEBRUARY 26-27, 2022
CHAIRS: Anukul Shenoy and Kristin Noell

Biology of Spirochetes

The Science of Spirochetology and Spirochete Disease Pathogenesis

FEBRUARY 20-25, 2022
RENAISSANCE TUSCANY IL CIOCCO, LUCCA (BARGA), ITALY

CHAIR: Scott Samuels
VICE CHAIR: Mathieu Picardeau

- **Unusual Bacteria in Disease and the Environment** *Patricia Rosa,* Melissa Caimano, Steven Norris
- **Host-Spirochete Interactions** *David Haake,* Claudia Toma, Linden Hu
- **Defense Against Spirochetes** *Linda Bockenstedt,* Michelle Visser, Jarlath Nally
- **Ecology of Spirochetes and Epidemiology of Spirochetoses** *Sven Bergström,* Dustin Brisson, Michael Marks
- **Evolution of Spirochetes and Their Genomes** *Ben Adler,* Verena Schünemann, Frédéric Veyrier, David Smajs
- **Persistence and Immune Evasion of Spirochetes** *Janis Weis,* George Chaconas, Peter Kraiczy, Nicole Baumgarth, Jon Skare
- **Structural Spirochetal Biology** *Nyles Charon,* Jun Liu, Brian Crane
- **Spirochete Physiology and Regulation** *Brian Stevenson,* Richard Marconi, Daniel Dulebohn, Chris Li
- **Spirochetes in Their Vectors and Reservoirs** *Albert Ko,* Seemay Chou, Leticia Zarantonelli
- **The GRC Power Hour™** *Linda Bockenstedt, Catherine Brissette*

Biology of Spirochetes

Spirochete Lifestyles and Their Unique Parasitic and Environmental Strategies

FEBRUARY 19-20, 2022

CHAIRS: Fabiana Ferreira and Linda Grillova

Bones and Teeth

Metabolism and Local Environments in Development, Disease and Regeneration of the Skeleton

JANUARY 16-21, 2022
RESIDENCE INN AT OXNARD RIVER RIDGE, OXNARD, CA

CHAIR: Ernestina Schipani
VICE CHAIR: Charles O'Brien

- **Metabolism and Bone Cells** *Fanxin Long,* Brendan Lee, Geert Carmeliet, Gerard Karsenty
- **Development of Skeleton and Teeth** *Karen Lyons,* Andrei Chagin, Joel Boerckel, Véronique Lefebvre, Wanida Ono
- **Origin and Fate of Bone Cells** *Deneen Wellik,* Vicki Rosen, Maria Almeida, Sarah Dallas
- **Cross Talks Among Hematopoietic, Endothelial, and Bone Cells** *Henry Kronenberg,* Laura Calvi, Anjali Kusumbe, Matthew Greenblatt, Michelle McDonald



- **Contribution of Bone Marrow Adipocytes and Stroma to Bone Homeostasis** *Clifford Rosen,* Steven Teitelbaum, Ling Qin, Michaela Reagan
- **Tumor Microenvironment in Bone** *Amato Giaccia,* Rachelle Johnson, Theresa Guise, Peter Croucher, Stavroula Kousteni
- **Development and Biomechanics of the Bone-Tendon Unit** *Elazar Zelzer,* Matthew Silva, Stavros Thomopoulos
- **Rare Bone Diseases** *Maurizio Pacifici,* Thomas Gardella, Laurence Legeai-Mallet, Anna Teti, Benjamin Levi
- **Regeneration of Bone** *Yingzi Yang,* Jerome Guicheux, Kurt Hankenson, Regina Brunauer
- **The GRC Power Hour™**

Bones and Teeth

From Bench-to-Bedside: Understanding the Skeleton for Developing Therapies

JANUARY 15-16, 2022

CHAIRS: Shauni Loopmans and Claire Arata

Chemical Separations

Fundamentals of Separation Science and Engineering

FEBRUARY 6-11, 2022
RESIDENCE INN AT OXNARD RIVER RIDGE, OXNARD, CA

CHAIR: Joan Brennecke
VICE CHAIRS: Vassiliki-Alexandra Glezakou and Mark Shiflett

- **Electrochemically Driven Separations: Dilute Solutions** *Xiao Su,* T. Alan Hatton, William Tarpeh
- **Membrane Separations: Application-Inspired Innovations** *Orson Sydora,* Matthew Hill, Surendar Venna
- **Spectroscopic Tools** *Burcu Gurkan,* Emily Smith, Heather Allen
- **Actinides, Lanthanides and Rare Earths** *Eric Schelter,* Gregory Girolami, George Goff, Vyacheslav Bryantsev
- **Electrochemically Driven Separations: Ion Exchange** *Ruilan Guo,* Merlin Bruening
- **Transport and Interfaces** *Susan Olesik,* Robbyn Anand, Aurora Clark, Christy Landes
- **Triggers and Fields** *Manish Kumar,* Philip Jessop, Kim Williams
- **Adsorption** *Krista Walton,* Jeffrey Long, Roger Rousseau, David Sholl
- **Membrane Separations: Data-Driven Discovery** *Zachary Smith,* De-en Jiang, Ryan Lively
- **The GRC Power Hour™**

Chemical Separations

Fundamentals of Separation Science and Engineering

FEBRUARY 5-6, 2022

CHAIRS: Yayuan Liu and Paola Baldaguez Medina

Chemistry and Biology of Peptides

Exploring the Natural and Unnatural of Peptide Science

FEBRUARY 6-11, 2022
VENTURA BEACH MARRIOTT, VENTURA, CA

CHAIRS: Christina Schroeder and Wendy Hartsock
VICE CHAIRS: Yftah Tal-Gan and Elizabeth Denton

- **Keynote Session: Pushing the Boundaries of Peptide Science** *Anne Conibear, Lila Gierasch,* Alanna Schepartz, Helma Wennemers
- **Chemical Biology of Peptides** *Jutta Eichler, Monika Raj,* Paramjit Arora, Ashraf Brik, Olalla Vásquez, Kathrin Lang, Stephan Pless
- **Peptide Materials** *Julie Champion, Joel Schneider,* Michael Yu, Scott Medina, Sarah Perry, Andrea Merg
- **Peptide Chemistry, Synthesis and Biosynthesis** *Jennifer Stockdill, Stephen Kent,* Fernando Albericio, Richard DiMarchi, Juan Del Valle, Alison Narayan, Rebecca Scheck, Caroline Proulx
- **Peptide Therapeutics: From Clinical Trials to Market** *Emel Adaligil, Robert Garbaccio,* Lauren Monovich, Ashok Bhandari, Christian Cunningham, Abbas Walji
- **Peptide Tools, Technologies and Techniques** *Amy Keating, Gaurav Bhardwaj,* Adriaan Bax, Carrie Haskell-Luevano, Lucy Colwell, Cameron Pye, César de la Fuente
- **Peptides in Oncology** *Kamaljit Kaur, Antoine Henninot,* Daniel DeOlivera, Hiroko Masamune, Pravin Kaumaya, Eileen Kennedy
- **Peptide Chemistry and Biology** *Florence Brunel, Philip Dawson,* Meritxell Teixido, Anna Mapp, Jan Pawlas, Nina Hartrampf, Jillian Smith-Carpenter
- **Keynote Session: The Complexity of Natural Products and Protein Function Exploration** *Elizabeth Denton, Yftah Tal-Gan,* Ved Srivastava, Margaret Brimble, Tom Muir
- **The GRC Power Hour™** *Elizabeth Denton, Yftah Tal-Gan*

Chemistry and Biology of Peptides

Rising Tide of Peptides as Research Tools, Therapeutics and Biomaterials

FEBRUARY 5-6, 2022

CHAIRS: Sorina Chiorean and Mary Miller

Colloidal, Macromolecular and Polyelectrolyte Solutions

Exploiting Force Fields to Control Assembly and Dynamics Over Multiple Length Scales

FEBRUARY 13-18, 2022
FOUR POINTS SHERATON, HOLIDAY INN EXPRESS, VENTURA, CA

CHAIRS: Sibani Lisa Biswal and Ronald Larson
VICE CHAIRS: Kelly Schultz and Daeyeon Lee

- **Polymer Electrolytes and Ionic liquids** *Jeffrey Richards,* Rachel Segalman, Nitash Balsara
- **Colloidal Assemblies: Synthesis and Applications** *Nicolas Alvarez,* Arjun Yodh, Stefano Sacanna, Serpil Williams
- **Field-Driven Colloidal Assemblies** *Kyle Bishop,* Michael Bevan, Carlos Silvera Batista
- **Propelled Colloids** *Bhuvnesh Bharti,* Ramin Golestanian, Petia Vlahovska, Orlin Velev
- **Heterogeneous and Interfacially Dominated Systems** *Vivek Sharma,* Sepideh Razavi, Jon DeGroot
- **Bioinspired Colloidal and Polyelectrolytes and Colloids in Biology** *Maria Santore,* Christopher Alabi, Nikta Fakhri, Roseanna Zia
- **Driven Elastomers** *Lilian Hsiao,* Monica Olvera de la Cruz, Joanna Aizenberg
- **Polyelectrolyte Coacervates** *Michael Rubinstein,* Charles Sing, Ilja Voets, Amanda Marciel
- **Liquid-Solid Transitions with Polymers** *Joseph Schlenoff,* Rodney Priestley, Matthew Lynch
- **The GRC Power Hour™** *Kelly Schultz*

Colloidal, Macromolecular and Polyelectrolyte Solutions

Dynamics, Nonequilibrium Phenomena and Design

FEBRUARY 12-13, 2022

CHAIRS: Chelsea Edwards and Soham Jariwala

Cornea and Ocular Surface Biology, Pathology and Regeneration

Reversing the Ravages of Time, Disease and Trauma to the Cornea and Ocular Surface

FEBRUARY 13-18, 2022
VENTURA BEACH MARRIOTT, VENTURA, CA

CHAIRS: Peter Lwigale and Sophie Deng
VICE CHAIRS: Sarah Hamm-Alvarez and Cintia de Paiva

- **Keynote Session: Novel Approaches to Data Acquisition and Analysis** *Kapil Bharti,* Michael Chiang, Aydogan Ozcan
- **Cellular Interactions, the Extracellular Matrix and Morphogenesis** *Brenda Bohnsack,* Jakub Famulski, Joseph Ciolino, Mary Ann Stepp, Joyce Tombran-Tink
- **Genomics and Gene Regulation** *Shivalingappa Swamynathan,* Majlinda Lako, Tara Moore
- **Advances in Cornea and Ocular Surface Wound Repair** *Shukti Chakravarti,* May Griffith, Julie Daniels, Melissa Krebs
- **Mechanisms of Ocular Surface Disease and Disorders** *Fiona Stapleton,* Mihaela Gadjeva, Vivien Coulson-Thomas, K. P. Connie Tam
- **Stem Cells of the Ocular Surface** *Nick Di Girolamo,* James Jester, Natasha Frank, Albert Wu



THE GRC POWER HOUR™

GRC has had a longstanding commitment to inclusion and addressing the challenges women and all underrepresented groups face in achieving equity in science. To fully address these challenges, GRC initiated The Power Hour, a new forum for conversations about the barriers to inclusivity within its 400+ communities.

- **Inflammation and Regeneration of the Ocular Surface** *Reza Dana,* Matilda Chan, Ali Djalilian
- **Sickness and Health of the Cornea and Ocular Surface** *Natalie Afshari,* Rajiv Mohan, Pablo Argueso, Edgar Espana, Krystel Huxlin
- **Translation of Ocular Surface Research into Novel Therapies** *Jod Mehta,* Sayan Basu
- **The GRC Power Hour™** *Kathryn Colby*

Cornea and Ocular Surface Biology, Pathology and Regeneration

Corneal Preservation, Repair and Regeneration: From Understanding Molecular and Cellular Mechanisms to Patient Care

FEBRUARY 12-13, 2022
VENTURA BEACH MARRIOTT, VENTURA, CA

CHAIRS: Anil Tiwari and Aurelie Dos Santos

Craniofacial Morphogenesis and Tissue Regeneration

Synergistic Interactions of Developmental Biology, and Tissue Engineering and Regenerative Medicine and Dentistry

FEBRUARY 20-25, 2022
RESIDENCE INN AT OXNARD RIVER RIDGE, OXNARD, CA

CHAIR: Pamela Yelick
VICE CHAIR: Gage Crump

- **Keynote Session: Innovations in Tissue Engineering Strategies for the Craniomaxillofacial Complex** *Justine Lee,* Tara Aghaloo, Kristi Anseth
- **Gene Networks and Epigenetics in Craniofacial Development** *Gage Crump,* Brad Amendt, Axel Visel, James Nichols
- **Clinical Genetics of Craniofacial Development and Disease** *Andrew Wilkie,* Janice Lee, Azeez Butali, Joan Richtsmeier
- **Craniofacial Stem Cells** *Michael Longaker,* Songtao Shi, Nancy Manley
- **Craniofacial Tissue Interactions and Morphogenesis** *Yang Chai,* D'Juan Farmer, Juhee Jeong
- **Strategies for Craniofacial Tissue Regeneration** *Mildred Embree,* David Dean, Sang Jin Lee, Maria Troulis
- **Mechanical and Bioelectrical Forces in CMF Tissue Development and Regeneration** *Mehran Moazen,* Michael Cunningham, Susan Herring
- **Evolution and Comparative Biology of the Craniofacial Complex** *Craig Albertson,* Liran Carmel, Chris Martin, Daniel Medeiros, Kory Evans
- **Sense Organs and Cranial Neural Crest** *Samantha Brugmann,* Marcos Simeos-Costa, Joanna Wysocka
- **The GRC Power Hour™**

Craniofacial Morphogenesis and Tissue Regeneration

From Physiology to Pathology: Mechanisms of Craniofacial Morphogenesis

FEBRUARY 19-20, 2022

CHAIRS: Daniela Roth and Pranidhi Baddam

DNA Damage, Mutation and Cancer

From DNA Damage, Repair and Replication to Immune Activation and Cancer Therapy

MARCH 6-11, 2022
VENTURA BEACH MARRIOTT, VENTURA, CA

CHAIR: Sharon Cantor
VICE CHAIR: Jeremy Stark

- **Keynote Session: Replication Gaps in Signaling, Repair and Disease** *Jeremy Stark,* Helle Ulrich, Keith Caldecott
- **DNA Damage and Checkpoint Responses** *Joann Sweasy,* Angelos Constantinou, Vanesa Gottifredi, Luis Toledo, Marcel van Vugt, Michela DiVirgilio
- **DNA Damage and Structures Engaging Repair vs. Bypass Mechanisms** *Helle Ulrich,* Orlando Schärer, Hannah Klein, Karen Vasquez, Richard Wood
- **DNA Repair, Replication and Cancer therapy** *Karlene Cimprich,* George-Lucian Moldovan, Alessandro Vindigni, Shan Zha
- **Chromosomal Dynamics, DNA Damage Signaling and Immune Responses** *Marcel van Vugt,* Helen Walden, Sandra Demaria, Agnel Sfeir
- **Replication, Collisions and Recovery** *Alessandro Vindigni,* Tovah Day, Karlene Cimprich, Martijn Luijsterburg
- **CRSIPR Screens to Gene Editing in Disease** *Shan Zha,* Daniel Durocher, Laura Sepp-Lorenzino, Joanna Loizou, Brittany Adamson
- **Cancer, Aging and Neurodegeneration** *Keith Caldecott,* Laura Niedernhofer, Bjoern Schmacher, Paul Mischel, Peter Adams
- **Genomic Instability and Emerging Targets for Therapy** *Daniel Durocher,* John Petrini, Jill Bargonetti, Ricky Sharma
- **The GRC Power Hour™** *Karen Vasquez*

DNA Damage, Mutation and Cancer

Insights into DNA Damage Responses and DNA Repair in Cancer

MARCH 5-6, 2022

CHAIRS: Emily Schleicher and Jacob Thrasher

Electrochemistry

Fundamental to Applied Electrochemistry: New Frontiers in Charge Transfer Theory, Electrocatalysis, Materials for Energy Conversion and Storage, Sensing and Separations

JANUARY 9-14, 2022
FOUR POINTS SHERATON, HOLIDAY INN EXPRESS, VENTURA, CA

CHAIR: Stephen Maldonado
VICE CHAIR: Francis Zamborini

- **In Operando Measurements of Electrode Processes** *Julie Macpherson,* Karena Chapman, William Chueh
- **Electrode Material Design for Energy Conversion and Storage** *Debra Rolison,* Linda Nazar, Kimberly See, Sara Thoi
- **Electrochemistry at the Nanoscale** *Shannon Boettcher,* Bruce Parkinson, Justin Sambur
- **Electrocatalytic Molecular Transformations** *Viola Birss,* Kyoung-Shin Choi, Hannah Shafaat, Aleksandra Vojvodic
- **Electroanalytical Modalities** *Janine Mauzeroll,* Reginald Penner, Ashley Ross
- **Complex Electrochemical Interfaces** *Charles McCrory,* Simone Ciampi, Daniel Josell, Ryan White
- **Electrochemical Separations for Sustainable Energy and Water Remediation** *Daniel Buttry,* Shane Ardo, William Tarpeh
- **Charge-Transfer Theory** *Stephen Creager,* Martin Bazant, Johna Leddy, Gerald Meyer
- **Late-Breaking Topics** *Francis Zamborini*
- **The GRC Power Hour™** *Francis Zamborini, Julie Macpherson*

Electrochemistry

Fundamental and Applied Electrochemistry in Analytical, Nanoscale and Energy

JANUARY 8-9, 2022

CHAIRS: Elizabeth Corson and Jeremy Dawkins

Food Allergy

Regulation of Food Tolerance

JANUARY 9-14, 2022
VENTURA BEACH MARRIOTT, VENTURA, CA

CHAIRS: Cecilia Berin and Hans Oettgen
VICE CHAIRS: Stephanie Eisenbarth and Simon Hogan

- **Environmental Exposures and Food Allergy** *Corinne Keet,* Kari Nadeau, Richard Locksley
- **Basic to Translational Advances in IgE Biology** *Wendy Davidson,* Duane Wesemann, Robert Anthony, Maria Curotto de Lafaille, Jamie Orengo, Stephen Quake, Scott Boyd

- **Novel Technologies and Applications in Food Allergy** *Stephen Galli,* Sindy Tang, Christopher Love
- **Early Life Immune Development, Microbiome and Immune Regulation** *Stephanie Eisenbarth,* Kirsi Jarvinen-Seppo, Michiko Oyoshi, Harald Renz, Talal Chatila, Vijay Kuchroo, Gislaine Martins
- **Antigen Receptors** *Maria Curotto de Lafaille,* Wayne Shreffler, Bjoern Peters, Derek Croote
- **Neuroimmunology of Allergic Disease** *Sarita Patil,* Esther Florsheim, Isaac Chiu, Caroline Sokol, Milena Bogunovic, Sebastien Talbot
- **IgG Antibodies and Protection from Food Allergy** *Lisa Wheatley,* Sarita Patil, Alexandra Santos, Hugh Sampson
- **Sensing at Mucosal Sites** *Patricia Fulkerson,* Raif Geha, DeBroski Herbert, William Khoury-Hanold, Noah Palm, Marc Rothenberg, Andrew Wang
- **Future Directions in Basic and Clinical Food Allergy Research** *Wayne Shreffler,* Alkis Togias, Erika von Mutius, Bruce Bochner
- **The GRC Power Hour™**

Food Allergy

Food Allergy Pathogenesis, Immunotherapy and Tolerance in the COVID-19 Pandemic

JANUARY 8-9, 2022

CHAIRS: Nicole Ramsey and Wenming Zhang

Geobiology

The Processes of Geobiological Evolution on a Living Planet

JANUARY 30 - FEBRUARY 4, 2022
RESIDENCE INN AT OXNARD RIVER RIDGE, OXNARD, CA

CHAIR: Boswell Wing
VICE CHAIRS: Karen Lloyd and Clara Chan

- **Ecology, Evolution and Existence in Extreme Environments** *John Spear,* Jackie Goordial, Trinity Hamilton, Juan Liu
- **Microbial Persistence in the Real World** *Steven Finkel,* Jessica Labonté, Nagissa Mahmoudi, Ember Morrissey
- **The Evolution of Stable Isotope Geobiology From Product to Process** *Kate Freeman,* Xiaobin Cao, Maya Gomes, Elise Wilkes
- **The Evolution of Photoautotrophy in Space and Time** *Patricia Sanchez-Baracaldo,* Jeffrey Cameron, Naomi Levine, Jodi Young
- **Comparing Theories and Evidence for the Co-evolution of Life and Earth** *Lee Kump,* Christopher Kempes, Stephanie Olson
- **The Biogeochemical Record of Early Life: Constraints From Rocks to Proteins** *Lindsay Hays,* Eli Moore, Eva Stueeken
- **From Eukaryogenesis to Multicellularity: Contrasting Geological, Genetic and Organismal Evidence** *Phoebe Cohen,* David Gold, Jana Milucka
- **Geobiology of Critical Intervals: The Causes and Consequences of Mass Extinctions** *Jeremy Jackson,* Seth Finnegan, Pincelli Hull
- **Experimental Macroevolution: Directly Testing Geobiological Hypotheses** *Michael Travisano,* Nkrumah Grant, Maria Rebolleda Gomez
- **The GRC Power Hour™** *Clara Chan, Karen Lloyd*

Geobiology

New Insights on Ancient and Modern Interactions Between Organisms and Their Environments

JANUARY 29-30, 2022

CHAIRS: Hayley Gadol and Dylan Wilmeth

Glycolipid and Sphingolipid Biology

A Holistic Approach to Understanding Simple and Complex Sphingolipids

MARCH 27 - APRIL 1, 2022
RENAISSANCE TUSCANY IL CIOCCO, LUCCA (BARGA), ITALY

CHAIR: Frances Platt
VICE CHAIR: Maurizio Del Poeta

- **Keynote Session: Sphingolipids and Glycosphingolipids in Cell Biology and Disease** *Maurizio Del Poeta, Yusuf Hannun,* Sarah Spiegel, Hugh Willison
- **Measuring and Manipulating Sphingolipids and Glycosphingolipids: Challenges and Solutions** *Yusuf Hannun, Maria Fuller,* Alfred Merrill, Liana Silva, Joost Holthuis, Giovanni D'Angelo
- **Ceramide Biology and Pathophysiology** *Tony Futerman, Gerhild Van Echten-Deckert,* Alicia Alonso, Aurora Pujol, Anthony Don, Christina Voelkel-Johnson
- **Sphingosine and Sphingosine-1-Phosphate Biology and Pathophysiology** *Sarah Spiegel, Richard Proia,* Long Nguyen, Wiebke Herzog, Johannes Morstein, Yuefeng Huang, Daniela Salvemini
- **Glycosphingolipids: Biosynthesis, Function and Disease** *Yoshio Hirabayashi, Doris Höglinger,* Maria Antonietta De Matteis, Yong Zhang, Cynthia Tifft
- **Sphingolipids and Glycosphingolipids as Modulators of Membrane Function** *Ronald Schnaar, Jin-ichi Inokuchi,* Mark Kester, Mary Kraft, Michela Deleidi, Alessandro Prinetti
- **Sphingolipids and Glycosphingolipids in Cell Growth and Differentiation** *James Shayman, Julie Saba,* Alessandra D'Azzo, Erhard Bieberich, Leah Siskind, Sandro Sonnino
- **Late-Breaking Topics** *Walter Holleran, Mylene Huebecker*
- **Sphingolipids and Glycosphingolipids in Non-Mammalian Systems** *Howard Riezman, Teresa Dunn,* Yohann Boutte, Jenny Mortimer, Eric Brown
- **The GRC Power Hour™** *Cynthia Tifft, Doris Höglinger*

Glycolipid and Sphingolipid Biology

The Complex Biology and Pathobiology of Sphingolipids and Glycosphingolipids

MARCH 26-27, 2022

CHAIR: Mylene Huebecker

Ligand Recognition and Molecular Gating

Linking Structure, Mechanism and Physiology of Ion Channels, GPCRs and Transporters

MARCH 20-25, 2022
RENAISSANCE TUSCANY IL CIOCCO, LUCCA (BARGA), ITALY

CHAIR: Alessio Accardi
VICE CHAIR: Kaspar Locher

- **Integrating Structures in Physiology** *Randy Stockbridge,* Andrew Marks, Joseph Mindell, Ardem Patapoutian
- **Mechanisms of Gating** *Crina Nimigean,* Inga Hänelt, Eduardo Perozo, Kenton Swartz, Christopher Tate
- **Novel Approaches to Investigate Membrane Protein Structure and Function** *Simon Scheuring,* Scott Blanchard, Jose Faraldo-Gomez, Andreas Plueckthun
- **Structural Insights in Membrane Protein Function** *Dirk Jan Slotboom,* Yifan Cheng, Xiaochun Li, Nicolas Reyes, Show-Ling Shyng
- **Pathophysiology of Membrane Transport and Signaling** *Henry Colecraft,* Nancy Carrasco, Edmund Kunji, Gaia Novarino, Gail Robertson



- **Protein-Membrane Interactions** *Simon Newstead,* Karen Fleming, Poul Nissen, Camilo Perez, Roderick Mackinnon
- **Structural Pharmacology** *Olga Boudker,* Jue Chen, Marta Filizola, Vera Moiseenkova-Bell, Bryan Roth
- **Structural Dynamics** *Jian Payandeh,* Joshua Levitz, Olga Boudker, Lucie Delemotte, Ina Urbatsch
- **Late-Breaking Topics** *Kaspar Locher,* Nami Tajima, Filippo Mancia
- **The GRC Power Hour™** *Karen Fleming*

Ligand Recognition and Molecular Gating

Linking Structure, Mechanism and Physiology of Ion Channels, GPCRs and Transporters

MARCH 19-20, 2022

CHAIRS: Eva Cunha and Jonathan Coleman

Liquid Phase Electron Microscopy

Conquering the Experimental Barriers to Quantitative Liquid Phase Imaging

JANUARY 30 - FEBRUARY 4, 2022
FOUR POINTS SHERATON, HOLIDAY INN EXPRESS, VENTURA, CA

CHAIRS: Nigel Browning and Deb Kelly
VICE CHAIRS: Frances Ross and Nathan Gianneschi

- **Analytical Electron Microscopy** *Ute Kaiser,* Robert Klie, M. Grace Burke
- **Applications in Biomedicine** *Utkur Mirsaidov,* Susan Lea, Niels de Jonge, Hans Elmlund
- **Controlling Reactions** *Diana Peckys,* Hong-Gang Liao, Leyla Soleymani
- **Applications in Energy Systems** *B. Layla Mehdi,* See Wee Chee, Katherine Jungjohann, Raymond Unocic
- **Correlative Methods** *Qian Chen,* Rengasayee Veeraraghavan
- **Nucleation, Growth and Corrosion in Biomedicine** *Joseph Patterson,* Jennifer Cookman, Nico Sommerdijk, Jim De Yoreo
- **Interactions in Space and Time** *Haimei Zheng,* Dwayne Miller, Patricia Abellan
- **Nucleation, Growth and Corrosion in Materials Science** *Damien Alloyeau,* Matthew Jones, Steve Granick
- **Image Analytics and Tracking** *Taylor Woehl,* Chiwoo Park, Eli Sutter
- **The GRC Power Hour™**

Liquid Phase Electron Microscopy

Observing New Pathways of Material Formation

JANUARY 29-30, 2022

CHAIRS: Aoon Rizvi and Weiqun Li

Lymphatics

Lymphatic Vessels as Multifaceted Regulators of Health and Disease

FEBRUARY 27 - MARCH 4, 2022
RENAISSANCE TUSCANY IL CIOCCO, LUCCA (BARGA), ITALY

CHAIRS: Timothy Padera and Taija Makinen
VICE CHAIRS: Hong Chen and Benjamin Hogan

- **Emerging Functions of Lymphatic Vessels** *Joseph Rutkowski,* Tatiana Petrova, Gou Young Koh, Melody Swartz
- **Organ-Specific Functions and Therapeutic Targeting of Lymphatic Vessels** *Pia Ostergaard,* Kari Alitalo, Miikka Vikkula, Friedemann Kiefer, Jonathan Kipnis, Brant Weinstein, Carrie Shawber
- **Lymphatic Vessel Morphogenesis: From Progenitors to Functional Vessels** *Benjamin Hogan,* Karina Yaniv, Oliver Stone, Yoshiaki Kubota, Kaska Koltowska
- **Lymphatic Drainage: Mechanism, Mechanics, Imaging and Emerging Therapeutic Approaches** *David Zawieja,* Brandon Dixon, Michael Davis, Max Itkin, Scott Zawieja
- **Lymphatic System in Lipid and Energy Metabolism** *Hong Chen,* Anne Eichmann, Michael Potente, Gwendalyn Randolph, Joseph Rutkowski
- **Insights from Lymphatic Development in Disease Processes** *Stefan Schulte-Merker,* Natasha Harvey, Michael Dellinger, Sathish Srinivasan, Mark Kahn, Young Hong

- **Lymphatic System in Driving Cancer Progression: Therapeutic Opportunities** *Agnes Noel,* Amanda Lund, Dennis Jones, Maria Ulvmar
- **Immunomodulatory Functions of Lymphatic Vessels** *David Jackson,* Laura Santambrogio, Cornelia Halin Winter, Beth Tamburini, Stephanie Hugues, Shan Liao
- **Lymphatic Vessel Heterogeneity in Health and Disease** *Barbara Garmy-Susini,* Michael Detmar, Kathleen Caron, Guillermo Oliver
- **The GRC Power Hour™** *Karina Yaniv, Dennis Jones*

Lymphatics
Innovations in Lymphatic Vessel Research: The Organotypic Lymphatic Vasculature
FEBRUARY 26-27, 2022
CHAIRS: Kerstin Wilhelm-Jüngling and Nils Hansmeier

Marine Natural Products

Environmental Roles, Biological Targets and Applications

MARCH 6-11, 2022
FOUR POINTS SHERATON, HOLIDAY INN EXPRESS, VENTURA, CA
CHAIR: Kerry McPhail
VICE CHAIR: Hendrik Luesch

- **Developing Marine Natural Product Therapies** *Amy Wright,* Andreas Maderna, Kris White
- **Climate Change, Marine Toxins and Environmental Solutions** *Mande Holford,* Yuko Cho, Taifo Mahmud, Assaf Vardi, Neha Garg
- **Super Resolution Imaging for Natural Product Mechanisms** *Laura Sanchez,* Edward Boyden, Manuel Liebeke
- **Imaging, Molecular Targets and Phenotypic Screening** *Daniela Trivella,* Erin Carlson, Ville Paavilainen, Lu Wei, Ashootosh Tripathi
- **Synthetic Strategies for Natural Product Lead Development** *Alison Narayan,* Leslie Aldrich, Sarah Reisman
- **Computational Workflows for Natural Products Discovery** *Roberto Berlinck,* Ruili Huang, Roger Linington, Justin van der Hooft, Donovon Adpressa, Mehdi Beniddir
- **Synthetic Biology for Natural Product Production and Engineering** *Jaclyn Winter,* Alessandra Eustaquio, Changsheng Zhang
- **Natural Products in the Context of Microbiomes and Symbioses** *Shigeki Matsunaga,* Marcy Balunas, Mohamed Donia, Margo Haygood, Lucia Pita Galan
- **Keynote Session: Integrated Strategies for Marine Natural Products Discovery** *Hendrik Luesch,* Deniz Tasdemir
- **The GRC Power Hour™** *Marcy Balunas, Alanna Condren*

Marine Natural Products
Advances in Natural Product Discovery, New Technologies and Translational Outcomes
MARCH 5-6, 2022
CHAIRS: Alanna Condren and A. Singh

Metals in Biology

Harnessing and Mimicking the Reactivity of Biological Metals for a Healthy and Sustainable Future

JANUARY 23-28, 2022
FOUR POINTS SHERATON, HOLIDAY INN EXPRESS, VENTURA, CA
CHAIR: Kara Bren
VICE CHAIR: Stephen Ragsdale

- **Keynote Session: Metal Ions in Biological Sensing and Signaling** *Caryn Outten,* Christopher Chang, Emily Weinert
- **Structural Biology of Metallobiomolecules** *Sarah Bowman,* Nozomi Ando, Thomas Barends, Amie Boal, Jennifer Bridwell-Rabb, Flora Meilleur
- **Biological Catalyst Design and Evolution** *Ambika Bhagi-Damodaran,* Rudi Fasan, Giovanna Ghirlanda, Anabella Ivancich
- **Metallocofactor Dynamics, Modification and Regulation** *R. David Britt,* Lucia Banci, Joseph Cotruvo, Jr., Nick Le Brun, Daniel Suess, Alejandro Vlla
- **Controlling and Measuring Biological Electron Flow Over Multiple Length and Time Scales** *Ekaterina Pletneva,* David Beratan, Sean Elliott, Carolyn Lubner
- **Metals, Microbes, the Environment and Sustainability** *John Magyar,* Kelly Chacon, Reza Ghiladi, Ricardo Louro, Nikhil Malvankar, Gemma Reguera
- **Metallobiochemistry of the Global Elemental Cycles** *Kyle Lancaster,* Sharon Burgmayer, Eric Hegg, Yvain Nicolet
- **Understanding and Mimicking Biomolecular Strong Bond Activation** *Jenny Yang,* Louise Berben, David Goldberg, Yunho Lee, Connie Lu, Smaranda Marinescu
- **Keynote Session: Intersections of Materials and Bioinorganic Chemistry** *Alison Butler,* Akif Tezcan, Gordana Dukovic, Woon Ju Song
- **The GRC Power Hour™**

Bioinorganic Chemistry
Inorganic Insights into Fundamental Life Processes
JANUARY 21-24, 2022
CHAIRS: Katherine Rush and Samuel Mann

Molecular and Ionic Clusters

Frontiers in Size-Selected Cluster Research: Structure, Reactivity and Dynamics

JANUARY 23-28, 2022
RENAISSANCE TUSCANY IL CIOCCO, LUCCA (BARGA), ITALY
CHAIRS: Knut Asmis and Francesco Paesani
VICE CHAIRS: Martin Beyer and Caroline Jarrold

- **Machine Learning Meets Cluster Science** *Alexandre Tkachenko,* Daniela Rupp, Olexandr Isayev
- **Biomolecules, Biomolecular Assemblies and Force Fields** *Anouk Rijs,* Kevin Pagel, Markus Meuwly, Etienne Garand
- **New Developments in Theory and Experiment of Isolated Clusters** *Jer-Lai Kuo,* Lai-Sheng Wang, Mariana Rossi
- **Catalysis and Reactivity** *Gereon Niedner-Schatteburg,* Sheng-Gui He, Anastassia Alexandrova, Héloïse Dossmann
- **Ultrafast Spectroscopy and Novel Light Sources** *Frank Stienkemeier,* Yoshiaki Kumagai, Linda Young
- **High Resolution Studies in He Droplets** *Andrey Vilesov,* Paul Scheier, Maria de Lara-Castells, Gert von Helden
- **Nucleation and Atmospheric Chemistry** *Albert Viggiano,* Valeria Molinero, Chia Wang
- **Solvation of Ionic and Neutral Aggregates** *Mark Johnson,* Martin Head-Gordon, Martina Havenith, Anne McCoy
- **Chemistry in and Physics of Water Clusters** *Daniel Neumark,* Ruth Signorell, David Wales
- **The GRC Power Hour™**

Molecular and Ionic Clusters
Probing the Microscopic Structures and Dynamics of Molecular and Ionic Clusters
JANUARY 22-23, 2022
CHAIRS: Ethan Cunningham and Summer Sherman

Multifunctional Materials and Structures

Imparting Intelligence in and Through Self-Learning Materials and Structures

JANUARY 23-28, 2022
VENTURA BEACH MARRIOTT, VENTURA, CA
CHAIRS: Jeffery Baur and Martin Dunn
VICE CHAIRS: Chiara Daraio and Ioannis Chasiotis

- **Self-Learning Soft Robotics** *Cecilia Laschi,* Jamie Paik, Pablo Valdivia y Alvarado
- **Intelligent Biological and Bio-Inspired Concepts** *Nancy Sottos,* Mason Dean, Ken Gall, Lakshminarayanan Mahadevan
- **Intelligent Chemistry Through Self-Discovery** *Vishnu Sundaresan,* Lee Cronin, Jurgen Ruhe
- **Self-Learning in Intelligent Manufacturing** *William Carter,* Qi Ge, Jennifer Lewis, Christopher Spadaccini
- **Engineered Living Systems** *Justin Gallivan,* Ryan Harne, Neel Joshi

"GRCs are an excellent mechanism for building communities that support career advancement for junior and senior scientists alike. GRCs in recent years have helped promote diversity and inclusion among their participants."

DR. CYNTHIA BURROWS, University of Utah

- **Intelligent Materials for Upcycling** *Ioannis Chasiotis,* Sankaran Thayumanavan, Magda Titirici, Christopher Bowman
- **Embedded Sensing for Intelligent Response** *Fu-Kuo Chang,* Pulickel Ajayan, Erik Thostenson
- **Intelligent Aerospace Structures** *Benjamin Dickinson,* Paolo Ermanni, Darren Hartl, Sung Kang
- **Smart Textiles** *Chiara Daraio,* Yoel Fink, Thomas Gries
- **The GRC Power Hour™** *Nancy Sottos, Chiara Daraio*

Natural Gas Hydrate Systems

Interpreting Complex Phase Behavior for Gas Hydrate Stewardship and Utilization

MARCH 13-18, 2022
RESIDENCE INN AT OXNARD RIVER RIDGE, OXNARD, CA
CHAIR: Zachary Aman
VICE CHAIR: Judith Schicks

- **Keynote Session: Hydrates as a Planetary Capacitor for Important Gases**
- **Sources and Mechanisms Driving Hydrate Occurrences**
- **Hydrate Dissociation Mechanics and Soil Interactions**
- **Slope Stability Impacts of Methane and Carbon Dioxide Hydrate**
- **Technologies for Separation and Carbon Capture**
- **The Role of Hydrates in the Low-Emissions Landscape**
- **The Role of Hydrates for Hydrogen**
- **Hydrates Throughout the Solar System**
- **Machine Learning that Changes the Future of Hydrate Research**

Natural Gas Hydrate Systems
Data-Driven Insights and Coupled Process Controls on Gas Hydrate Expression
MARCH 12-13, 2022
CHAIR: Michael Nole

Neuroelectronic Interfaces

Bridging Neural Engineering and Neurobiology Edge Effects to Divergent Innovation

MARCH 13-18, 2022
FOUR POINTS SHERATON, HOLIDAY INN EXPRESS, VENTURA, CA
CHAIRS: Thomas Stieglitz and Takashi Kozai
VICE CHAIRS: Jack Judy and Stephanie Lacour

- **Sensory Neuronal Feedback** *Stanisa Raspopovic,* Sliman Bensmaia, Robert Gaunt, Ranu Jung, Dustin Tyler
- **Stimulation of the Spinal Cord** *Scott Lempka,* Silvestro Micera, Douglas Weber, Vivian Mushahwar, Enrico Rejc
- **Robustness of Neural Implants in Translational Research** *Kari Ashmont,* Kip Ludwig, Gregg Suaning



- **New Technologies Contributing to Neural Implants** *Jack Judy,* Anne Andrews, Sangbeom Jun, Dion Khodagholy
- **Beyond Scarring: Glia and BBB as Neuromodulators** *Erin Purcell,* Katerina Akassoglou, Franca Cambi, Alberto Vazquez, Xinzhu Yu
- **Structural Biocompatibility as Key Engineering Design Features** *Chong Xie,* Maria Asplund, John Rogers, Jens Schouenborg, John Seymour
- **Promises and Challenges of Carbon as Electrode Material for Sensing and Stimulation** *Swati Sharma,* Sam Kassegne, Jinwoo Park, Justin Williams, Jose Garrido
- **Signal Processing to Decipher Neural Information** *Stephanie Lacour,* Gopala Anumanchipalli, Tonio Ball, Bradley Voytek, Maria V. Sanchez-Vives
- **Keynote Session: Ways to Understand the Brain** *Samantha Santacruz,* Robert Wykes, Michael Hasselmo, Evelyn Lake
- **The GRC Power Hour™** *Elisa Castagnola, Dawn Taylor*

Neuroelectronic Interfaces

Creating a Roadmap to Translating Neural Technologies

MARCH 12-13, 2022

CHAIRS: Maria Vomero and Nicole Pelot

New Antibacterial Discovery and Development

Disruptive Antibiotics and Non-Antibiotic Therapies to Combat Drug-Resistant Bacterial Infections

MARCH 6-11, 2022
RENAISSANCE TUSCANY IL CIOCCO, LUCCA (BARGA), ITALY

CHAIRS: Ruben Tommasi and Matthew Cooper
VICE CHAIR: Peter Smith

- **Keynote Session: Clinical and Pre-Clinical Successes and Failure Modes in Antibiotic Development** *Heike Broetz-Oesterhelt,* Steven Projan, Ryan Cirz
- **Alternatives to Antibiotics** *Robert Hancock,* Heike Broetz-Oesterhelt, Guilherme Castro, Benjamin Chan, Heather Fairhead, Victor Nizet
- **Unraveling the Requirements for Drug Permeation and Target Engagement** *Olga Lomovskaya,* Helen Zgurskaya, Muriel Masi, David Six, Paul Hergenrother
- **New Approaches to Antibacterial Hits and Leads** *Peter Smith,* Sharookh Kapadia, Nawaz Khan, David Roper, Mark Blaskovich
- **Advances in Enabling Diagnostics and PK/PD** *Alita Miller,* Eric Stern, George Drusano, William Hope
- **Learning from Successes and Failures in Antibacterial Lead Optimization** *Richard Lee,* Thomas Durand-Reville, Claudia Zampaloni, Daniel Obrecht, Scott Hecker, Alastair Parkes
- **Antibiotic Adjuvants** *Gerry Wright,* Ana Rita Brochado, Eric Brown, Olga Lomovskaya, Christian Melander
- **New Results from Clinical Studies** *Troy Lister,* Angela Talley
- **Models for Advancing Antibiotics** *Ursula Theuretzbacher,* Matthew Todd, Richard Alm
- **The GRC Power Hour™** *Heike Broetz-Oesterhelt, Alita Miller*

New Antibacterial Discovery and Development

Challenges and Innovative Approaches to Discover and Develop New Antibacterial Agents

MARCH 5-6, 2022

CHAIRS: Ashleigh Paparella and Haroon Mohammad

Origins of Life

Environments for the Origins of Life and Habitability

JANUARY 23-28, 2022
RESIDENCE INN AT OXNARD RIVER RIDGE, OXNARD, CA

CHAIR: Nita Sahai
VICE CHAIR: Laurie Barge

- **Keynote Session: Early Earth Atmosphere** *Sukrit Ranjan,* Kevin Zahnle, Paolo Sossi
- **Mineral-Biomolecule Coevolution** *Maheen Gull,* Saidul Islam, Sheref Mansy, Elisa Biondi
- **Chemical Complexity and Emergence of Biomolecule Function and Self-Assembly** *Milena Popovic,* Stuart Bartlett, Moran Frenkel-Pinter, Sara Szymkuc
- **Hydrothermal Vents: Differences Between Modern and Hadean Earth** *Mario Rivas,* Norio Kitadai, Benjamin Tutolo, Jun Korenaga
- **Deep Carbon and Endoliths** *Henry Sun,* Cara Magnabosco, Oliver Trapp, Barbara Sherwood Lollar
- **Exogenous Prebiotic Chemistry and Bolide Impact Organosynthesis** *Punam Dalai,* Yoko Kebukawa, Yoshihiro Furukawa, Wendy Brown, Jose Aponte
- **Mars: Habitability and Life Detection** *Saul Villafane-Barajas,* Armando Azua Bustos, Felipe Gomez, Meenakshi Wadhwa
- **Alternative Energetics: The Thioester World** *Eugene Wu,* Hieronim Jakubowski, Sergio Sanudo-Wilhelmy, Joshua Goldford, Kamila Muchowska
- **Selected Poster Presentations** *Laurie Barge,* John Huss
- **The GRC Power Hour™** *Laurie Barge*

Origins of Life

Challenging Paradigms in Prebiotic Chemistry

JANUARY 22-23, 2022

CHAIRS: Tyler Roche and Laura Rodriguez

Oxygen Radicals

Connecting the Chemistry of Oxygen Radicals to Medicine

JANUARY 30 - FEBRUARY 4, 2022
VENTURA BEACH MARRIOTT, VENTURA, CA

CHAIRS: Christian Schoneich and Anna-Liisa Levonen
VICE CHAIR: Clare Hawkins

- **Keynote Session: Integrative Cellular Stress Responses: Redox Control of Gene Regulation** *Albena Dinkova-Kostova, Hozumi Motohashi,* Michael Karin, Masayuki Yamamoto
- **Chemistry and Analysis of Redox Stress** *Corinne Spickett, Jacek Zielonka,* Miriam Cortese-Krott, Ned Porter, Derek Pratt, Jeffrey Spraggins
- **Redox Biochemistry of Proteins** *Kelvin Davies, Rodney Levine,* Maria Fedorova, Michael Davies, Marisa Joubert, Koji Uchida
- **Redox Signaling in Cancer Biology and Therapy** *Elias Arner, Donna Zhang,* Martin Bergo, Christine Chio, Gina DeNicola, Douglas Spitz
- **Redox Pathways in Aging and Age-Related Diseases** *Julie Andersen, Holly Van Remmen,* Tobias Dansen, James Kirkland, Malcolm Jackson, Christopher Hine
- **Redox Mechanisms in Neurological Diseases** *Manuela Lopez, Pamela Shaw,* Katerina Akassoglou, Antonio Cuadrado, Simone Di Giovanni, Manisha Patel
- **Novel Methods to Study Redox Signaling** *Tobias Dick, Dean Jones,* Yimon Aye, Liron Bar-Peled, Yvonne Janssen-Heininger, Dana Reichmann
- **Oxidative Stress in Infection, Immunity and Pulmonary Diseases** *Lin Mantell, Francisco Schopfer,* Nathalie Grandvaux, Christian Holm, Andreas Pichlmair, Victor Thannickal
- **Redox Signaling in Cardiometabolic Diseases** *Rakesh Patel, Clare Hawkins,* Christoph Binder, Hua Linda Cai, Chris Kevil
- **The GRC Power Hour™** *Holly Van Remmen, Clara Troccoli*

Oxygen Radicals

Redox Biology in Health and Disease

JANUARY 29-30, 2022

CHAIRS: Alex Gauthier and Clara Troccoli

"At the core of any GRC is exceptional technical programming and a vibrant scientific community."

DR. KRISTI ANSETH, University of Colorado Boulder

Photosensory Receptors and Signal Transduction

Mechanisms, Applications and Effects of Natural and Engineered Photoreceptors

MARCH 27 - APRIL 1, 2022
VENTURA BEACH MARRIOTT, VENTURA, CA

CHAIR: John Kennis
VICE CHAIR: Brian Crane

- **Keynote Session: Light Perception and Behavioral Responses** *Stuart Peirson,* Nina Milosavljevic, Keita Sato
- **Functions and Dynamics of Flavin-Binding Photoreceptors** *Tilman Kottke,* John Christie, Sharon Hammes-Schiffer, Maria Mittag, Kevin Gardner, Brian Zoltowski
- **Microbial Light Perception and Responses** *Annegret Wilde,* Reinhard Fischer, Laura Gomez-Consarnau, Conrad Mullineaux
- **Retinal Proteins: Sensors, Pumps and Channels** *Hideki Kandori,* Richard Cerione, Karsten Heyne, Mitsumasa Koyanagi, Valerie Panneels, Igor Schapiro
- **Advanced Techniques and Multichromatic Photoreception** *Xiaojing Yang,* Marius Schmidt
- **Signal Integration in Plant Photobiology** *Eirini Kaiserli,* Meng Chen, Hongtao Liu, Ullas Pedmale
- **Optogenetics and Synthetic Biology** *Matias Zurbriggen,* Jared Toettcher
- **Function and Structural Dynamics of Bilin-Based Photoreceptors** *Emina Stojkovic,* Janne Ihalainen, Delmar Larsen, Richard Vierstra, Beronda Montgomery
- **Light-Regulated Clocks and Magnetoreception** *Deborah Bell-Pedersen,* Luis Larrondo, Christine Merlin, Amita Sehgal
- **The GRC Power Hour™** *Emina Stojkovic*

Photosensory Receptors and Signal Transduction

Molecular Basis, Engineering and Application of Photoreceptor Proteins

MARCH 26-27, 2022

CHAIRS: Yusaku Hontani and Maria Agustina Dominguez Martin

Plasminogen Activation and Extracellular Proteolysis

Mechanisms and Therapeutic Targets of Extracellular Proteolysis in Human Disease

FEBRUARY 6-11, 2022
FOUR POINTS SHERATON, HOLIDAY INN EXPRESS, VENTURA, CA

CHAIRS: Matthew Flick and Tetsumei Urano
VICE CHAIRS: Li Zhang and Ruby Law

- **Keynote Session: Bridging Mechanisms of Extracellular Proteolysis with Novel Therapeutic Strategies for Disease** *Thomas Bugge,* Edward Plow, Nicola Mutch
- **Proteases in Cardiovascular Disease and Thrombotic Disorders** *Patricia Liaw, James Luyendyk,* Zsuzsa Bagoly, Katherine Hajjar, Luisa Iruela-Arispe, Paul Kim, Yuko Suzuki
- **Proteases in Infection and Immunity** *Shaun Lee, Lindsey Miles,* Silvio Antoniak, Rod Dunbar, Ana Flores-Mireles, Grant Blouse
- **Proteases in Metabolic Disease and Aging** *Lakmali Silva, Dudley Strickland,* Lauren Hardy, Delphine Meynard, Erica Sparkenbaugh, Douglas Vaughan
- **Proteases in Cancer and Cell Signaling** *Michael Ploug, Irit Sagi,* Toni Antalis, Benjamin Buckley, Karin List, Virginia Metrangolo
- **New Technologies and Therapeutic Advances in Extracellular Proteolysis** *Steven Gonias, Ze Zheng,* Albert Heck, Christian Kastrup, James Whisstock
- **Proteases in Tissue Remodeling and Regeneration** *Francis Castellino, Marie Ranson,* Ulrich auf dem Keller, Wendy Campana, Andrey Komissarov, Phillip Owens
- **Proteases in Neurological and Cerebrovascular Disease** *Jonathan Schoenecker, Stella Tsirka,* Eric Mullins, Ekaterina Semina, Manuel Yepes, Erin Norris
- **Proteases in Trauma** *Daniel Lawrence, Sidney Strickland,* Matthew DuVernay, Yoshifumi Itoh, Robert Medcalf, Hunter Moore
- **The GRC Power Hour™** *Ruby Law, Li Zhang*



Plasminogen Activation and Extracellular Proteolysis

Plasminogen Activation System: Emerging Techniques and Potentials for the Development of New Therapeutics

FEBRUARY 5-6, 2022

CHAIRS: Nowah Afangbedji and Yi Yang

Predator-Prey Interactions

Evolution of Form and Function

JANUARY 30 - FEBRUARY 4, 2022
RENAISSANCE TUSCANY IL CIOCCO, LUCCA (BARGA), ITALY

CHAIRS: Ken Lukowiak and Maria Thaker
VICE CHAIRS: Bridie Allan and Michael Sheriff

- **Keynote Session: Evasion Strategies at Multiple Scales** *Andy Sih,* Johanna Mappes, Robert Magrath
- **Ecology of Predator-Prey Interactions** *Brandon Barton,* Emily Lester, Aaron Wirsing, Johan Eklof
- **Sensory Ecology of Predator-Prey Interactions** *Sara Hermann,* William Feeney, Dinesh Rao
- **Anthropogenic Challenges to Predator-Prey Interactions** *Francesca Cagnacci,* Adam Ford, Daniel Fortin, Sophie Gilbert
- **Diseases and Viruses: From Fear to Ecosystems** *Abi Vanak,* Julia Buck, Burt Kotler, Menna Jones
- **Cascades and Community Ecology** *Thomas Hossie,* David Kimbro, Teresa Alcoverro, Dror Hawlena, Alex Moore
- **Functional Ecology of Predators and Prey** *Michael Sheriff,* Swanne Gordon, Paolo Domenici, Emily Rayfield
- **Reaction Norms and the Evolution of Traits** *Linda Weiss,* Kate Laskowski, Ullasa Kodandaramaiah, Natasha Tigreros
- **Surviving Risk as Groups and Collectives** *Scott Creel,* Vishwesha Guttal, Christos Ioannou
- **The GRC Power Hour™** *Bridie Allan, Maria Thaker*

Predator-Prey Interactions

Predator-Prey Interactions in Dynamic and Novel Environments

JANUARY 29-30, 2022

CHAIRS: Kaitlyn Gaynor and Justin Suraci

Protein Folding Dynamics

Folding and Misfolding: Effects of Evolution and Environment

JANUARY 9-14, 2022
RESIDENCE INN AT OXNARD RIVER RIDGE, OXNARD, CA

CHAIRS: Pernilla Wittung-Stafshede and Shachi Gosavi
VICE CHAIRS: Robert Best and Martin Gruebele

- **Keynote Session: Protein Interactions and Design** *Martin Gruebele, Caitlin Davis,* Angela Gronenborn, Stephen Mayo
- **SARS-COV-2 Proteins** *Alex Guseman, Naomi Latorraca,* Pamela Bjorkman, Alex Holehouse, Anum Glasgow
- **In Vivo Folding** *Benjamin Schuler, Andrea Soranno,* Patricia Clark, Gunnar von Heijne, Judith Frydman, Paula Booth, Stephen Fried
- **Protein Misfolding and Amyloid Formation** *Elizabeth Meiering, Michael Kovermann,* Joan-Emma Shea, Jeremy Schmit, Elin Esbjörner, Liliana Quintanar
- **Protein Folding** *Susan Marqusee, Lauren Porter,* Lila Gierasch, Sheena Radford, Dave Thirumalai, Jayant Udgaonkar
- **Functional Aggregation** *Jose Onuchic, Ellinor Haglund,* Tanja Mittag, Margaret Sunde, Peter Wolynes, Carlos Castaneda
- **AI in Protein Science** *Cecilia Clementi, Mohammed AlQuraishi,* Payel Das, Frank Noe, Pratyush Tiwary
- **Evolution in Folding and Misfolding** *Alexander Schug,* Brian Volkman, Charles Brooks
- **Keynote Session: Folding and Misfolding in Cells** *Robert Best, Alexander Buell,* Margaret Cheung, Jeffery Kelly
- **The GRC Power Hour™**

Protein Folding Dynamics

Folding and Misfolding: Effects of Evolution and Environment

JANUARY 8-9, 2022

CHAIRS: Alex Guseman and Naomi Latorraca

Protein Transport Across Cell Membranes

Biochemical, Genetic and Structural Advances Towards Mechanism and Manipulation of Protein Transport

MARCH 6-11, 2022
RESIDENCE INN AT OXNARD RIVER RIDGE, OXNARD, CA

CHAIRS: Randolph Hampton and Toshiya Endo
VICE CHAIRS: Nathan Alder and Carole Dabney-Smith

- **Nascent Chain Transport** *Roland Beckmann,* Jeffrey Gerst, Eitan Bibi, Shu-Ou Shan
- **Whole Protein Transport** *Doron Rapaport,* Johannes Herrmann, Thomas Langer, William Clemons, Agnieszka Chacinska, Peter Rehling
- **Structural Aspects of Transport Complexes** *Thomas Langer,* Roland Beckmann, Nicholas Noinaj, Eunyong Park
- **Protein Translocation Machineries** *Carla Koehler,* Ross Dalbey, Harris Bernstein, Ralf Erdmann, Yukio Fujiki, Doron Rapaport, Ping Yin
- **Trans-Organellar Mechanisms** *Johannes Herrmann,* Bianca Schrul, Tobias Walther, Robert Farese
- **Inside Proto-Symbiotic Organellar Systems** *Jürgen Soll,* Hsou-Min Li, Masato Nakai, Danja Schuenemann, Kostas Tokatlidis, Nils Wiedemann
- **New Methods and Approaches in Protein Transport** *Nathan Alder,* Arnold Driessen, Ben Berks, Tassos Economou
- **Retro-Translocation and Quality Control** *Ralf Erdmann,* Sonya Neal, Feroz Papa, Paul Jarvis, Chi-Min Ho



- **Pathogens and Diseases of Protein Transport** *Arnold Driessen,* Billy Tsai, Andre Schneider
- **The GRC Power Hour™** *Carla Koehler, Carole Dabney-Smith*

Protein Transport Across Cell Membranes

Mechanisms, Regulation and Structure of Protein Translocation Machinery

MARCH 5-6, 2022

CHAIR: Christopher Stubenrauch

Robotics

From Basic Science to Robot Systems

JANUARY 16-21, 2022
FOUR POINTS SHERATON, HOLIDAY INN EXPRESS, VENTURA, CA

CHAIRS: Paolo Dario and Henrik Christensen
VICE CHAIRS: Cecilia Laschi and Metin Sitti

- **Fundamentals of Movement in Living Creatures** *Terrence Sejnowski,* Nakamura Yoshihiko, Auke Ijspeert
- **Bioinspired Sensing, Actuation and Energy** *Barbara Webb, Polina Anikeeva,* Mark Cutkosky, Barbara Mazzolai
- **Sensory-Motor Control** *Tamar Flash,* Yasuo Kuniyoshi, Roland Johansson
- **Design and Technology of Sensing and Moving Artifacts** *Shigeo Hirose,* Kyu-Jin Cho, Rebecca Kramer-Bottiglio, Tania Morimoto
- **Applications of Sensing and Moving Artifacts** *Kaneko Harada,* Ellen Roche, Conor Walsh
- **Bioinspired Terrestrial Motion** *Barry Trimmer,* Robert Full, Sangbae Kim, Benjamin Swilling
- **Taking Inspiration from Birds: The Flights** *Dario Floreano,* Vijay Kumar, Robert Wood
- **How Robots Swim** *Cecilia Laschi,* Francesco Giorgio-Serchi, Maarja Kruusmaa, Daniela Rus
- **Swarm Intelligence and Collective Coordination** *Metin Sitti,* Marco Dorigo, Radhika Nagpal
- **The GRC Power Hour™**

Robotics

The Future of Robotics: Possibilities for Transforming Healthcare

JANUARY 15-16, 2022

CHAIRS: Debora Zrinscak and Christopher Dambrosia

Sensory Transduction in Microorganisms

Molecular Basis and Applications of Microbial Signal Detection, Transduction and Response

JANUARY 16-21, 2022
VENTURA BEACH MARRIOTT, VENTURA, CA

CHAIR: Karen Ottemann
VICE CHAIR: Birgit Scharf

- **Sensing the Environment** *Tino Krell,* Michael Johnson, Victoria Korolik, Rebecca Parales, Alexandre Persat, Peijun Zhang
- **Mechanisms of Signal Transduction: Amplification and Cooperativity** *Gerald Hazelbauer,* Simon Ringgaard, Gabriela Schlau-Cohen, Thomas Shimizu
- **Signaling and Control of Transcriptional Responses** *Linda Kenney,* Robert Bourret, Sean Crosson, Dimitris Georgellis, Victoria Stone, Ann West
- **Signaling and Control of Motility Responses** *Susan Lea,* Yann Dufour, Marc Erhardt, Keiichi Namba, Joshua Shrout, Christine Szymanski
- **Signaling in Polymicrobial Communities** *Karine Gibbs,* Lori Burrows, Steven Townsend, Karen Visick
- **Applications of Signaling Knowledge** *Ming Hammond,* Lydia Contreras, Rasika Harshey
- **Atypical Signaling Processes** *Matthew Parsek,* David Hendrixson, Daniel Pfeiffer, Steven Rutherford
- **Signaling During Host Interactions** *Gladys Alexandre,* Anne-Marie Krachler, Md Motaleb, Wei Qian, Rita Tamayo, Fitnat Yildiz
- **Mechanisms of Signal Transduction: Modulating Outputs** *Birgit Scharf,* Monica Gerth, Pushkar Lele, Lynmarie Thompson
- **The GRC Power Hour™** *Heidi Kaplan*

Sensory Transduction in Microorganisms

Signalling and Adaptation: Microbes and Scientists Adapting to a Changing Environment

JANUARY 15-16, 2022

CHAIRS: Yashasvika Duggal and Lindsey O'Neal

Sleep Regulation and Function

Systems Neuroscience and Genetic Approaches to Study Sleep Regulation and Function

MARCH 13-18, 2022
RENAISSANCE TUSCANY IL CIOCCO, LUCCA (BARGA), ITALY

CHAIR: Paul Shaw
VICE CHAIR: Derk-Jan Dijk

- **Keynote Session: Diversity of Brain Cell Types and How They Regulate Behavior** *Derk-Jan Dijk,* Nancy Ip
- **Activity-Dependent Neuronal Tagging to Reveal Sleep's Circuitry and Function** *Sara Aton,* Patrick Fuller, William Wisden, Laura DeNardo, Michael Hastings
- **Functional Analysis of Sleep Circuitry and its Impact on Global Brain Dynamics** *Julie Seibt,* Luis De Lecea, Keith Hengen, Bruno van Swinderen
- **Metabolic Drivers of the Sleep-Wake Cycle** *Stephane Dissel,* Radhika Basheer, Gero Miesenboeck, Mimi Shirasu-Hiza
- **Impact of Sleep During Development on Mental Health** *Francesca Siclari,* Yu Hayashi, Matthew Kayser, Lucia Peixoto
- **Sleep and the Regulation of Positive and Negative Emotions** *Chiara Baglioni,* Isabelle Arnulf, Eti Ben Simon, Shinjae Chung, Raphaelle Winsky-Sommerer
- **Heterogeneous Roles for Gap Junctions in Sleep Regulation** *Marcos Frank,* Sofia Axelrod, Anne Hart, Philip Haydon, Laurent Seugnet
- **Systems Approaches for Studying Sleep in Neurodegeneration** *Janet Mullington,* Helene Benveniste, Andrew Lim, Christina Schmidt
- **Sleep and Brain Function: Genetic Insights** *Paul Franken,* Ying-Hui Fu, Hiromasa Funato, Leila Tarokh
- **The GRC Power Hour™** *Mimi Shirasu-Hiza, Anne Hart*

Sleep Regulation and Function

Molecules, Cell Types and Circuits Regulating Sleep

MARCH 12-13, 2022

CHAIRS: Jaclyn Durkin and Kevin Swift

Thalamocortical Interactions

Thalamic Architecture, Dynamics and Function in Health and Disease

FEBRUARY 6-11, 2022
RENAISSANCE TUSCANY IL CIOCCO, LUCCA (BARGA), ITALY

CHAIRS: Judith Hirsch and Sonja Hofer
VICE CHAIRS: Jeanne Paz and Adam Hantman

- **Keynote Session: Thalamus: From Molecular to Whole-Brain Approaches** *W. Martin Usrey, Laszlo Acsady,* Emery Brown, Hongkui Zeng
- **Thalamocortical Circuits for Sensory Processing** *Chinfei Chen,* Na Ji, Marcel Oberlaender, Carl Petersen, Farran Briggs, Yang Dan
- **Higher-Order Sensory Pathways** *Massimo Scanziani,* Ehud Ahissar, Alison Barth, Lucy Palmer
- **Motor Functions of Thalamus** *Robert Turner,* Michael Long, Ian Duguid, Melanie Wilke, Anatol Kreitzer, Yifat Prut
- **Roles for Thalamus in Regulating Instinctive Behavior** *Michael Halassa,* Mario Penzo, Alexander Heimel, Susanne Ahmari
- **Cellular and Circuits Organization of Thalamus** *Solange Brown,* Hajnalka Bokor, Priya Rajasethupathy, Tianyi Mao, Martha Bickford, John Huguenard
- **Development of Thalamocortical Circuits** *Guillermina Lopez-Bendito,* Gordon Fishell, Denis Jabaudon, Anna Molofsky
- **Thalamocortical Alterations in Disease States** *Judith Ford,* Allan Basbaum, Guoping Feng, Wael Asaad, Audrey Brumback, Roy Sillitoe
- **Thalamus and Consciousness** *Dara Manoach,* Hal Blumenfeld, Laura Lewis, Anita Luthi
- **The GRC Power Hour™** *Sabine Kastner*

Thalamocortical Interactions

Thalamic Mechanisms of Sensorimotor Processing, Behavior and Disease

FEBRUARY 5-6, 2022

CHAIRS: Frances Cho and Hayley Fisher

Ultrafast Phenomena in Cooperative Systems

Advances in the Dynamics and Control of Quantum Materials

FEBRUARY 20-25, 2022
VENTURA BEACH MARRIOTT, VENTURA, CA

CHAIR: Richard Averitt
VICE CHAIR: Daniele Fausti

- **Metastable Light Induced Control** *Antoinette Taylor,* Michele Buzzi, Anshul Kogar
- **Phononic Property Control** *Matteo Mitrano,* Nicole Benedek, Flavio Giorgianni, Prineha Narang
- **Floquet and Parametric Dynamics** *Gil Refael,* Eugene Demler, Takashi Oka
- **Coherent and Collective Phenomena** *Thomas Devereaux,* Fahad Mahmood, Ryo Shimano, Haidan Wen
- **Two-Dimensional and Layered Materials** *David Hsieh,* Andrea Young, Liuyan Zhao
- **Topological Dynamics and Control** *James McIver,* Alessandra Lanzara, Aaron Lindenberg, Michael Sentef
- **Spin Dynamics and Control** *Flavio Giorgianni,* Andrea Caviglia, David Hsieh
- **Theory: Light-Induced Control** *Prineha Narang,* Martin Claassen, Thomas Devereaux, Dante Kennes
- **Early-Career Investigator Presentations** *Daniele Fausti*
- **The GRC Power Hour™**

Ultrafast Phenomena in Cooperative Systems

Collective Dynamics in Complex Phases of Bulk and 2D Materials

FEBRUARY 19-20, 2022

CHAIRS: Carina Belvin and Dominik Juraschek



BII | Prize for Science | Innovation

Apply for the new BII & Science Prize for Innovation today

Behind every life-changing solution is an entrepreneurial scientist–a creative mind who proved an idea in the lab and dared to carry it out in the world.

To encourage more scientists to translate their research, BioInnovation Institute (BII) & Science present a new annual award.

Our three winners will have their essays published in Science magazine and will be invited into BII's entrepreneurial ecosystem. In addition, the Grand Prize winner will receive a prize of USD 25,000 and each runner-up will receive USD 10,000 at a grand award show celebration in Copenhagen, Denmark.

The call for applications has just opened.
Apply before November 1, 2021.
www.bii.dk/scienceprize

Presented by BII & Science

BII BioInnovation Institute Science

Apply before November 1, 2021
www.bii.dk/scienceprize



Hope for the best, plan for the worst: COVID-19 brought to the forefront the necessity to create contingency plans.

Post-pandemic: The power of crisis management planning

No matter our profession, organization, sector, or ecosystem, we will always have to navigate unforeseen circumstances in our careers. The pandemic has taught faculty the power and promise of incorporating crisis management plans into our career strategies. **By Alaina G. Levine**

"A critical imperative"

It was a seminar at a war college that convinced **Chuck Zwemer**, a professor of biology at Dickinson College in Carlisle, Pennsylvania, of the importance of battling career-related emergencies head-on by establishing a personal crisis management plan. The speaker addressed how to prepare for uncertain times and stated some basics for building an effective crisis management plan: "Think strategically," he recalls learning. "Know your goals. Know your assets. Know your liabilities. Develop tactics in service of the strategy, in service of the goal." And keep lines of communications open.

These concepts seem simple enough. And Zwemer, whose expertise lies in physiology, found them to be especially relevant to his career as a faculty member. Although "you can never predict what's going to happen," he says, "understand that crises will occur and have checkpoints in place: What are your goals and how are you meeting them? What are your backups?"

New professors, brimming with enthusiasm for their upcoming career in service of discovery, contemplate their research agenda, grants to pursue, grad students and postdocs to hire, and lab equipment to procure. Very rarely do they consider crafting a crisis management plan that they could activate in the face of a calamity. And yet, in 2021, it is clear that this type of planning is essential.

"Leaders in higher education aren't always adequately prepared for the scale and scope of these roles. Crisis leadership is often viewed as an add-on to an already extensive list of competencies," says **Ralph A. Gigliotti**, assistant vice president, Office of University Strategy, and director of the Rutgers Center for Organizational Leadership at Rutgers University in New Brunswick, New Jersey. "But it is a critical imperative for anyone engaging in leading in our institutions to plan, adequately respond to, and learn from crisis."

A crisis management plan contains a list of actions that will be taken "before, during, and after a catastrophic event that preserve lives, safeguard property, and reduce the loss of resources essential to the organization's recovery," according to the International Risk Management Institute, Inc., a Dallas-based organization in that helps insurance and risk management professionals. "A crisis management plan is part of a broader business continuity management plan."

Indeed, continuity of research, teaching, training, and service programs is critical, as we have discovered. A crisis management plan can preserve and advance faculty goals as well, even in the middle of a pandemic; extreme economic uncertainty; and ambiguity about careers, education, business, and almost all social structures.

Despite that fact that faculty have not been taught to construct a crisis management plan, it is within the framework of their knowledge domain, especially for those in science, technology, engineering, and mathematics (STEM) fields. "STEM faculty can pursue it in the same way they are pursuing their own scientific inquiry," says Gigliotti. "Set up a hypothesis and decide how you would approach the crisis and what response would be the most impactful. But like any scientific project, be open to the data and learn from it. Acknowledge the limit of any study and the opportunity to do future research."

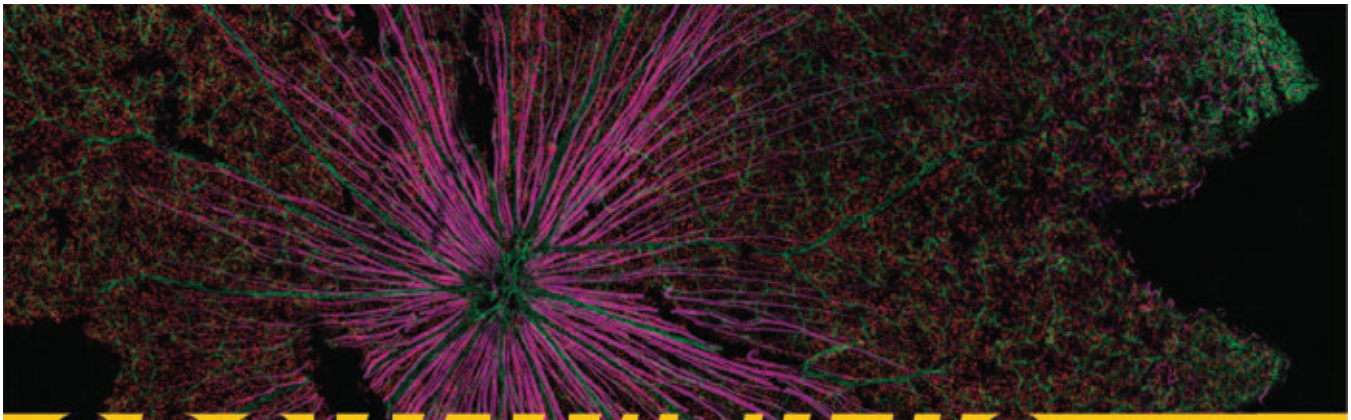
Why plan?

The pandemic has made us hyperaware of the need for a mechanism to forge our way through and beyond immediate barriers. A proper plan can enable success even in the direst of circumstances and is centered on communications. "It's important to have a crisis communications plan, because crises unfold rapidly— they lead to moments where cont.>

IMAGE: SHUTTERSTOCK.COM/SANTIMA.STUDIO

Upcoming features

- Top Employers—October 29



GROW WITH US

FACULTY POSITIONS AT THE JACKSON LABORATORY

Assistant, Associate and Full Professor / Bar Harbor, ME and Farmington, CT

The Jackson Laboratory (JAX), one of the world's leading nonprofit biomedical research organizations, is at the forefront of genetic and genomic research. As JAX continues to grow as a global organization, we are seeking accomplished Professors and Postdoctoral Associates to join our existing faculty. Be part of a research community with a unique blend of dynamic and established scientists from around the world, all supporting a common goal — to discover precise genomic solutions for disease and empower the global biomedical community in the shared quest to improve human health.

JAX is specifically interested in candidates in these research areas:

- Computational Systems Biology
- Cellular Bioengineering
- Computational Modeling
- 3D Nucleome/Genomic Structure
- Immunology/Infection
- Aging/Regeneration

Bar Harbor Faculty apply genetic and systems approaches to innovative mouse models for addressing fundamental biological problems and mechanisms of disease.

Farmington Faculty research the complex genetic causes of disease and develop precise genomic solutions tailored to an individual's unique genetic makeup.

The Jackson Laboratory values diversity in its research and team members, and is committed to building an equitable and inclusive work environment for our faculty and JAX community at large. JAX seeks Faculty and Postdoctoral Associates whose research, teaching and engagement will contribute to these efforts and provide unique approaches to solving problems impacting human health.

Learn more at https://www.jax.org

JAX faculty members enjoy distinct advantages including:

- A diverse and collaborative environment that fosters interdisciplinary "team science"
- Superior and extensive scientific support services
- Excellent research facilities in Bar Harbor, ME and Farmington, CT
- Partnerships with leading universities, medical centers, and biotechnology industry
- Predoctoral and postdoctoral training programs
- World-class courses and conferences focused on genetics, genomics and biomedicine
- Working at a top 15 "Best Places to work in Academia" as rated by The Scientist
- Competitive compensation, outstanding benefits, relocation assistance, and start-up research packages

Learn more about The Jackson Laboratory here:
https://www.jax.org

The Jackson Laboratory
Leading the search for tomorrow's cures

ScienceCareers online @sciencecareers.org
FACULTY POSITIONS

Questions to ask yourself when preparing a crisis management plan for your career:
What values do I stand for as a leader/teacher/scholar?
What are the criteria I use to identify, define, and assess the severity and impact of a crisis?
What are the crisis warning signs I need to monitor in my current role?
What are the types of crises that could potentially impact me individually as a leader/teacher/scholar, and what are the types of crises that could potentially impact my team/department/school?
In what ways would I like to respond to a crisis? What resources would I need to marshal, on whom may I need to lean, and how might I address the crisis in a coordinated, systematic, and values-driven manner?
How will I evaluate my response to the crisis? What metrics would I use to determine a successful response?
Following the crisis, what did I learn from the situation? What might I do differently if faced with a similar crisis in the future?

Source: Ralph A. Gigliotti, Ph.D.

we have to make quick decisions, and we can experience a freeze," says **Rebecca M. Rice**, assistant professor of communication studies at the University of Nevada, Las Vegas, who researches how organizations work together to respond to emergencies, including natural disasters such as fires and floods, and security threats such as terrorist attacks and mass shootings. "Those moments can be paralyzing if you don't know whom to contact and what to contact them about."

Planning for crises restores our power, which is critical when faced with seemingly insurmountable odds. "Crises have the potential to strip of us of agency, control, and influence. We feel powerless," says Gigliotti. "We know crises are inevitable at an individual level and organizational level. So it is imperative for all of us to scan the horizon, get a sense of the kind of crises that can impact us and our institutions, and develop a purposeful plan as to how we as individuals or teams may respond to the crises of tomorrow."

The planning process sharpens professors' focus by offering a situational awareness and a renewed ability to keep an eye out for changes of all types, including new trends in the job market, notes Zwemer. But there's an added value: "It creates a longer-term strategy that you follow irrespective of what's happening around you. One great aspect of the crisis management plan is that it lets you recenter when something unexpected happens," says **Alana M. Hill**, a former petroleum engineer and founder of 2Hill Consulting Services in Sugar Land, Texas, who speaks about change leadership and resiliency. "In a crisis, we want to be mindful because we can be misled to use our emotions to make decisions." Adds Zwemer, "If there is a place of refuge you can go in your head, you can help yourself."

Approaches and features

Crisis management plans are precious snowflakes: Each one is unique, and yet they all share a common set of elements. For Gigliotti, a plan starts with identifying and honoring your values. "The changing circumstances around us create deep uncertainty. So much seems out of our control," he says. "The crisis management plan is so important because it reorients us around who we want to be as leaders, scholars, and teachers, and the components of a response that we can control. Underlying all of that is a commitment to a set of values that uphold and guide our actions and behavior, and allow us to shift from being reactive to proactive in ways that are congruent with those values."

A sense of proactiveness begins with brainstorming what kinds of crises you may face. "Have some conceptualization of what we mean by crisis—define and operationalize what kinds of crises have the potential to disrupt your career," says Gigliotti, who recently authored the book *Crisis Leadership in Higher Education: Theory and Practice* (Rutgers University Press, 2019). These can include natural disasters, cyberattacks, research misconduct, financial crises, public health emergencies, and many others. "There are myriad crisis types that have the potential to trickle down to deeply impact us as individual researchers," he notes.

Rice, whose new book, *Communicating Authority in Interorganizational Collaboration*, is being published this year, has been teaching and consulting with municipalities for years about crisis planning. "I'm a prepper at heart, and in my career, I watch counties adapt to prepare for crisis every day. This can be translated to the individual level," she says. Rice suggests the following process to blue-sky and solidify your plan. Start by establishing communication expectations ahead of time. If there is an emergency, will you email or call your team? What level of information will you share in an email? "The problem in communications research is hesitancy of communicating things when you don't have all the information," she explains. Don't be afraid to clarify that you will provide updates as the situation unfolds. And yet, determine how pressing or frequent communications will be depending on the nature of the crisis. For example, if a pipe breaks and the lab samples are in peril, when, to whom, and how do we report it? Who is expected to act and who is expected to stay away? Those first thought exercises and conversations may be difficult, involving both self-reflection and chats with your team, but "there is no reason not to have those conversations about what our plan is and what will it look like if something disrupts our plan," she says.

As you discuss these issues, you should consult your institutional leadership. Get to know your colleagues in your department as well as people in biosafety, radiation control, facilities management, risk mitigation, emergency management, and the police department; after all, this is their expertise and their job is to protect the university's assets, which include the faculty and your research. Identify who is in charge in an emergency. "Risk assessment is vital for operational continuity," says **J. Levi O'Loughlin**, associate director of the Office of Research Assurances and university biosafety officer at Washington State University (WSU) in Pullman, Washington. O'Loughlin, whose doctorate is in microbiology, chaired the WSU committee tasked with helping faculty ramp up their on-campus research programs following quarantine, and assisted in COVID-19 operations for the university community. The institutional experts have resources designed to keep you going, he says.

Rules and regulations about research management can equip you with a powerful starting point for your plan, and many of these institutional offices do preparedness exercises and have their own contingency plans. "The more you start having these conversations, the more you cont.>

Crisis Type	Example
Academic crisis	Debate over tenure, widespread plagiarism or academic fraud, and significant violations of academic integrity
Athletics crisis	Child abuse scandal
Clinical crisis	Physician malpractice in academic health center
Financial or business crisis	Significant decreases in state appropriations
Human resources crisis	Employee crimes and issues surrounding hiring and firing of employees
Leadership or governance crisis	Conflict between state legislature and university leadership
Natural disaster	Flood, tornado, or hurricane
Public safety crisis	Active shooter, sexual assault, suicide, or death
Racial or identity conflict	Campus unrest due to racial or identity tensions within the community and acts of intolerance by any campus stakeholder
Student affairs crisis	Mental health crisis
Technological and facilities crisis	Water main break, chemical spill, widespread power outage, or damages to university infrastructure

Source: Gigliotti, *Crisis Leadership in Higher Education: Theory and Practice*, 2019.

Featured participants

2Hill Consulting Services, LLC
www.themsengineerway.com/consulting

Department of Communication Studies, University of Nevada, Las Vegas
www.unlv.edu/communicationstudies

Dickinson College
www.dickinson.edu

Office of Research Assurances, Washington State University
ora.wsu.edu

Rutgers Center for Organizational Leadership
ol.rutgers.edu

will find people who are doing this work," says Rice. "As individual faculty develop crisis management plans, they should ensure careful alignment with the crisis management plans of your department and institution. Rather than duplicating plans that already exist, your plan can complement the plans in place."

Of course, there are other people to consider in your planning. Institutional emergencies have command centers and task forces, and individuals can use the same lens to develop their career crisis plans. "At an organizational level, who is your response team? At the individual level, who do you call on? Your network, family, and friends," notes Gigliotti. Plan it out right and you'll know who you can turn to in any kind of trouble.

Zwemer installs "checkpoints" in his plan, which drive an "if this, then that" type of scenario. By keeping an open mind during the planning process, being flexible, and considering multiple potential emergencies, we can evaluate various contingency opportunities. For example, if we don't get this grant, is there something else we can do? Can we cobble this data together for another program? If the students can't come into the classroom, can we find another way to educate them? "Look for these points of stability. And move toward stability," he advises.

The contingency strategy is an interesting aspect of the planning, because it has to be customized to your concerns and issues and yet must be agile enough to shift as a crisis emerges or escalates. "Our plan starts with a vision, a long-term goal of where we want our career to go—the 'to be' statement," says Hill. "The change management plan is going to align the long-term goal with short-term goals to [help you] get there. It's also going to include the intentional use of agile practices, where there will be frequent adjustments but not a total change of direction." For example, she notes, given a new stressor, we may make minor adaptations to account for the current situation, but we don't want to do this at the detriment of our overarching vision. By focusing on your values, you can maintain strength while practicing flexibility.

Don't be afraid to make modifications to your plan as you speak with more people in the field and share notes and best practices. In fact, suggests Gigliotti, engage in open conversations with your colleagues about their plans. Compare notes on perceived obstacles and workarounds. Let's say there is the possibility of flood damage in your laboratory space. Ask your institutional representatives about their plan for this scenario, but also "address it with your research team and ask others in the field how they have approached or managed this, and whom they seek to archive and access backup materials," he says. Asking these questions now will endow your plan with teeth. "These types of crises have the chance to snowball from a minor incident into a major crisis and impact your work as a researcher," he says. By addressing these issues early in your career with your collaborators, you stand a better chance of weathering a very tough storm.

The power of planning

As a result of the pandemic, we have experienced a heightened sense of risk in our careers. But there is a positive outcome. "It can feel difficult or unpleasant, but we understand risks by communicating with others about them," says Rice. She sees more and more professionals openly discussing risk mitigation efforts and encourages faculty to do the same—for their research programs, teams, and ultimately, themselves.

Despite what we presently feel, our vulnerability in the global crisis is a strength—as long as we aim to comprehend the lesson. "With the department chairs I work with, I ask, 'What do you have control over?' and [advise them] to focus on that instead of getting lost in the myriad of responsibilities they can't control," says Gigliotti.

It's also important that we don't forget to review our plan after activating it, so we can improve it for next time "In the postcrisis phase, there is a postmortem that is conducted," he adds. "Precrisis, during the crisis, and postcrisis, [we should ask] how are we learning, healing, and what ways can we grow from the crisis? Being thoughtful in how we learn from individual crises makes us even more prepared for whatever crisis may come next."

Alaina G. Levine is a science writer, science careers consultant and coach, professional speaker, and author of Networking for Nerds *(Wiley, 2015).*

UMBC

TENURE TRACK FACULTY POSITION

Toxicological Chemist

THE DEPARTMENT OF CHEMISTRY AND BIOCHEMISTRY AT THE UNIVERSITY OF MARYLAND, BALTIMORE COUNTY (UMBC) invites applications for a full-time tenure-track faculty position at the **Assistant Professor** level. Applicants are expected to establish a vigorous and externally funded research program in any sub-discipline of toxicological chemistry (e.g., cancer toxicology, forensic toxicology, pharmacology, metabolite identification and degradation toxicologically-relevant organic synthesis/mechanisms, etc.). Candidates must have an outstanding record of scientific achievement, demonstrated by publications in peer-reviewed journals. Applicants should have a PhD and postdoctoral experience in any of the sub-disciplines in or related to toxicological chemistry. The selected candidate will be expected to teach at both the undergraduate and graduate (PhD and MS) levels with particular interests in toxicological chemistry, organic chemistry, biochemistry, nursing chemistry and/or analytical chemistry. Importantly, the applicant should demonstrate an understanding of and commitment to diversity and inclusive excellence in both teaching and research programs.

Candidates should submit their applications electronically to **http://apply.interfolio.com/91773.** Application materials include: curriculum vitae, a description of research plans, a statement of teaching philosophy, and a statement describing their commitment to diversity and inclusive excellence in higher education and the discipline. Candidates should also arrange for three letters of recommendation to be submitted to **http://apply.interfolio.com/91773**. For inquiries only, please email **chemsearch@umbc.edu** Review of applications will begin **October 18, 2021**, and continue until the position is filled. The appointment will commence in **August 2022**.

UMBC is an Equal Opportunity/Affirmative Action Employer. Applications from women, minorities, individuals with disabilities and other traditionally under-represented groups in the sciences are especially encouraged. As an institution that receives federal financial assistance, UMBC adheres to Title IX and does not discriminate on the basis of sex. Information about Title IX and contact information for the Title IX Coordinator is available at: ***https://oei.umbc.edu/***

RUTGERS
Ernest Mario School of Pharmacy

FACULTY POSITION

Susan L. Cullman Laboratory for Cancer Research, Department of Chemical Biology, Ernest Mario School of Pharmacy, Rutgers, The State University of New Jersey, Piscataway, NJ is seeking an outstanding investigator for a tenure-track faculty position at the **assistant or associate professor level** with preference given to those whose work complements and enhances our current research programs in cancer metabolism, cancer biology, cancer prevention, and neurodegenerative biology.

The successful candidate should hold the equivalent of a Ph.D. or M.D. degree and is expected to develop and maintain a strong extramurally funded research program and participate in departmental teaching at the undergraduate, graduate and professional levels. The position provides a strong start-up package of funding, laboratory space, and highly competitive salary and benefits.

Applicants should apply at **https://jobs.rutgers.edu/postings/136917** and include a cover letter, curriculum vitae, brief research plan, and names and addresses of three references.

HARVARD UNIVERSITY

Tenured Professor in Chemistry

Department of Chemistry and Chemical Biology
Faculty of Arts and Sciences
Harvard University

Candidates are invited to apply for a tenured professorship in the field of theory. The appointment is expected to begin on **July 1, 2022**. The tenured professor will be responsible for teaching at the undergraduate and graduate levels. We are seeking candidates who have an outstanding research record and a strong commitment to undergraduate and graduate teaching. Doctorate required by expected start date.

Please submit the following materials through the ARIeS Portal **(https://academicpositions.harvard.edu/postings/10545): 1)** Cover letter; **2)** Curriculum Vitae; **3)** Teaching/Advising statement (describing teaching philosophy and practices); **4)** Research statement; **5)** Statement describing efforts to encourage diversity, inclusion, and belonging, including past, current, and anticipated future contributions in these areas; and, **6)** Names and contact information of 3-5 referees, who will be asked by a system-generated email to upload a letter of recommendation once the candidate's application has been submitted. Three letters of recommendation are required, and the application is considered complete only when at least three letters have been received. At least one letter must come from someone who has not served as the candidate's undergraduate, graduate, or postdoctoral advisor. **Deadline:** Applications will be accepted until the position is filled.

Harvard is an equal opportunity employer and all qualified applicants will receive consideration for employment without regard to race, color, religion, sex, national origin, disability status, protected veteran status, or any other characteristic protected by law.

HARVARD UNIVERSITY

Tenure-Track Assistant Professor in Chemistry

Department of Chemistry and Chemical Biology
Faculty of Arts and Sciences
Harvard University

Candidates are invited to apply for a tenure-track **assistant professorship** in the open field of chemistry and chemical biology. The appointment is expected to begin on **July 1, 2022**. The tenure-track professor will be responsible for teaching at the undergraduate and graduate levels. We are seeking candidates who have an outstanding research record and a strong commitment to undergraduate and graduate teaching. Doctorate required by expected start date.

Please submit the following materials through the ARIeS portal **(https://academicpositions.harvard.edu/postings/10543)**: **1)** Cover letter; **2)** Curriculum Vitae; **3)** Teaching/advising statement (describing teaching philosophy and practices); **4)** Research statement; **5)** Statement describing efforts to encourage diversity, inclusion, and belonging, including past, current, and anticipated future contributions in these areas; and, **6)** Names and contact information of 3-5 referees, who will be asked by a system-generated email to upload a letter of recommendation once the candidate's application has been submitted. Three letters of recommendation are required, and the application is considered complete only when at least three letters have been received. At least one letter must come from someone who has not served as the candidate's undergraduate, graduate, or postdoctoral advisor. Applications must be submitted no later than **October 15, 2021**.

Harvard is an equal opportunity employer and all qualified applicants will receive consideration for employment without regard to race, color, religion, sex, national origin, disability status, protected veteran status, or any other characteristic protected by law.

Dartmouth
GEISEL SCHOOL OF MEDICINE

TENURE-TRACK FACULTY POSITION IN MOLECULAR AND SYSTEMS BIOLOGY

The Department of Molecular and Systems Biology at Geisel School of Medicine at Dartmouth invites applications for a tenure-track **Assistant Professor** position. We seek applicants to direct an independent and innovative research program to understand complex problems in cell or developmental biology, regeneration, neuroscience, or mechanisms of disease using approaches in genetics, genomics, epigenetics, metabolomics, bioinformatics, or computational systems biology.

Dartmouth is highly committed to fostering a diverse and inclusive population of students, faculty, and staff and we seek applicants who are able to work effectively with individuals from all backgrounds, including but not limited to: racial and ethnic minorities, women, those who identify with LGBTQ+ communities, persons with disabilities, are from lower income backgrounds, veterans, and first-generation college graduates. Applicants should state in their cover letter how their teaching, research, service, and/or life experiences prepare them to advance Dartmouth's commitments to diversity, equity, and inclusion.

Our department offers a dynamic and interactive environment where faculty members benefit from collaborative and collegial interactions across campus, with foundational and clinical departments at Geisel, the School of Arts & Sciences, the Thayer School of Engineering, and the Guarini School of Graduate and Advanced Studies.

A generous start-up package and access to state-of-the-art research facilities will be provided. Individuals will be given opportunities for mentoring and teaching graduate students in relevant PhD programs (e.g., Molecular and Cellular Biology (MCB), Quantitative Biomedical Sciences (QBS), and Integrative Neuroscience at Dartmouth (IND). The successful candidate may, as appropriate, also benefit from association with one of four NIH-sponsored Centers for Biomedical Research Excellence (COBRE) in Quantitative Biomedical Sciences, Biomolecular Targeting, Molecular Epidemiology and Cystic Fibrosis and/or the NCI-designated Norris Cotton Cancer Center.

Candidates must have a Ph.D. and/or M.D. degree and relevant postdoctoral research experience. Applicants should upload a cover letter, a separate summary (1 page or less) of their three most significant contributions to science to date (without reference to individuals, institutions, publications, metrics, or awards), a curriculum vitae (that does not include impact factors), a description of proposed research (3 pages or less) and a teaching statement to: **https://apply.interfolio.com/91485**. Letters of recommendation should be provided from three referees.

The Geisel School of Medicine at Dartmouth is located in the neighboring towns of Hanover and Lebanon on the New Hampshire and Vermont border. Dartmouth is surrounded by a vibrant, academic and professional community offering excellent schools, lively arts, and an unmatched quality of life. Boston MA, Burlington VT, and Montreal, QC are all within a few hours' drive.

Dartmouth College is an equal opportunity/affirmative action employer with a strong commitment to diversity and inclusion. We prohibit discrimination on the basis of race, color, religion, sex, age, national origin, sexual orientation, gender identity or expression, disability, veteran status, marital status, or any other legally protected status. Applications by members of all underrepresented groups are encouraged.

Consideration of applications will begin on **September 15, 2021** and continue until the position is filled.

UT Southwestern Medical Center

FACULTY POSITION – VIROLOGY

The Department of Microbiology at UT Southwestern Medical Center is seeking new faculty members in virology at the **Assistant Professor** (tenure track) level via a multi-year rolling search. The appointee will be expected to develop a front-rank, competitive, independent research program on a medically relevant viral pathogen(s). Some preference may be given to candidates working on emerging/re-emerging viruses or those that represent global threats.

An attractive start-up package, competitive salary, and generous laboratory space are available to conduct research in a highly collaborative, supportive, and dynamic environment.

Candidates also will be considered for UT Southwestern's $2.15M Endowed Scholars (start-up) Program Candidates should have a Ph.D. and/or M.D. degree with 3+ years of postdoctoral experience and an exceptional publication record.

Please send a cover letter, C.V., contact information for three letters of recommendation, and a brief summary of future research to:

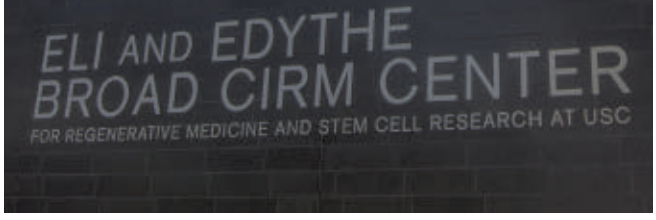
VirologySearchCommittee@utsouthwestern.edu.

UT Southwestern Medical Center is committed to an educational and working environment that provides equal opportunity to all members of the University community. As an equal opportunity employer, UT Southwestern prohibits unlawful discrimination, including discrimination on the basis of race, color, religion, national origin, sex, sexual orientation, gender identity, gender expression, age, disability, genetic information, citizenship status, or veteran status. To learn more, please visit: ***https://jobs.utsouthwestern.edu/why-work-here/diversity-inclusion/.***

Faculty Positions, Department of Stem Cell Biology and Regenerative Medicine, Keck School of Medicine of the University of Southern California (Los Angeles)

The Department of Stem Cell Biology and Regenerative Medicine (*https://stemcell.keck.usc.edu*) is recruiting outstanding faculty *at all levels* in the area of regenerative medicine. We are particularly interested in candidates developing translational efforts around strong disease indications. The department is housed in the Eli and Edythe Broad Center for Regenerative Medicine and Stem Cell Research within the Keck School of Medicine of USC. Excellent resources and collaborative opportunities exist with clinical departments at the Keck School, Children's Hospital Los Angeles, and USC campuses. Successful candidates will contribute to our educational mission encompassing undergraduate, master's, PhD, and medical students.

USC values diversity and is committed to equal opportunity in employment. Women and men, and members of all racial and ethnic groups are encouraged to apply. Online applications will be accepted; please apply to *https://usccareers.usc.edu/job/los-angeles/open-rank-tenure-track-or-tenure-assistant-associate-or-professor-of-stem-cell-biology-and-regenera/1209/13635043568.* Applications should include a letter of interest, CV, brief two- to three-page outline of research past, present and future, and four letters of reference. The applicant is responsible for ensuring that the completed application is received before October 31, 2021.



FACULTY POSITIONS
THE ROCKEFELLER UNIVERSITY

The Rockefeller University seeks exceptional, creative scientists to join its faculty. We invite applications from outstanding candidates for tenure-track positions, and also welcome applications from tenured scientists at an early stage of their career. The University is a very diverse community and we strongly encourage applications from individuals from racial and ethnic groups that are underrepresented in biomedical science.

The University has a laboratory centered rather than department based organizational structure that fosters interdisciplinary research. We encourage applications in the following areas:

- **Biochemistry, Biophysics, Chemical Biology, and Structural Biology**
- **Cancer Biology**
- **Cell Biology**
- **Genetics and Genomics**
- **Immunology, Virology, and Microbiology**
- **Mechanisms of Human Disease**
- **Neurosciences and Behavior**
- **Organismal Biology and Evolution**
- **Physical, Mathematical, and Computational Biology**
- **Stem Cells, Development, Regeneration, and Aging**

The Rockefeller University provides strong support for the work of its faculty including 100% faculty salary support, benefits that include subsidized housing and an on-site child care center from 3 months of age through preschool, generous start-up funds, new or renovated laboratory space and state-of-the-art core facilities, and support for all graduate students as well as continuing lab support. There are extensive opportunities for collaboration within the University and with neighboring institutions.

Visit **http://www.rockefeller.edu/facultysearch** to submit your application online and view further information about the positions.

Application deadline is October 1, 2021.

Address questions to **facultysearch@rockefeller.edu.**

The Rockefeller University is an equal opportunity employer and will consider all qualified applicants for employment without regard to race, color, religion, sex, sexual orientation, gender identity, national origin, disability or protected veteran status.

Caltech

Positions in Biology and Biological Engineering:
Caltech, Pasadena, CA, United States

The Division of Biology and Biological Engineering (BBE) at Caltech is seeking **new faculty in all areas of biological science and biological engineering**, with particular interest in individuals who are interested in pursuing research in areas that benefit from the interdisciplinary environment of Caltech's BBE division and its linkages to other disciplines at Caltech. Areas of interest include, but are not limited to (alphabetically): biological engineering; cellular, developmental and regulatory biology; ecological and biosphere science and engineering; neural and behavioral biology; organismal and integrative biology; and virology, immunology and infectious disease.

Successful applicants are expected to develop innovative research programs and to be committed to high quality teaching. Preference will be given to candidates at the Assistant Professor level; however, well-qualified applicants at the associate or full professor level may also be considered. The term of an initial untenured appointment is for four years and is contingent upon completion of the Ph.D. degree.

Please submit on-line applications at: **https://www.bbe.caltech.edu/jobs**, and include a brief cover letter; curriculum vitae; relevant publications, a description of proposed research; and a statement of teaching interests. Applicants should submit a diversity and inclusion statement that discusses past and/or anticipated contributions to improving diversity, equity, and inclusion in the areas of research, teaching, and/or outreach. Instructions will be provided for having 3-4 reference letters uploaded.

Applications will be reviewed starting on **1 November** and must be submitted no later than **1 December, 2021**.

EOE of Minorities/Females/Protected Vets/Disability

UMass Memorial Health | UMMS
Diabetes Center of Excellence

FACULTY POSITION

The Diabetes Center of Excellence at the University of Massachusetts Medical School invites applications for a **SENIOR TENURED** or **JUNIOR TENURE-TRACK** basic science or clinical investigator faculty position. The Diabetes Center of Excellence currently consists of basic and physician scientists representing a broad range of disciplines in the biomedical and clinical sciences, with members from several Medical School Departments and Programs working together as central New England's leading center for diabetes clinical care, innovation, and discovery. The Center occupies state-of-the-art research space on an expanding Medical School campus. Basic investigators benefit from core facilities for deep sequencing, proteomics, genotyping, fluorescence-activated cell sorting, digital imaging/confocal microscopy, genomics/bioinformatics, transgenic/knockout mice, and mouse metabolic phenotyping. Clinical and community investigators benefit from infrastructure for recruitment and retention of research participants, measurement, behavioral and nutritional intervention resources and facilities, and academic-community research partnerships. Adult and pediatric clinical efforts of the Diabetes Center are housed in a wonderful Ambulatory Clinical Care building designed so that patients can receive appropriate foot care, diabetes education, behavioral counseling, and other routine medical care at one location. The position will be highly competitive with regard to start-up funds, laboratory space (if needed) and salary. The Center seeks an individual of outstanding research potential relating to diabetes pathophysiology or treatment.

Applicants should send curriculum vitae, statement of research interests, and names and addresses of three references to:

David M. Harlan, M.D and Dale L. Greiner, Ph.D.
Co-Directors, Diabetes Center of Excellence
Search Committee Co-Chairs
c/o Patricia Cannon
55 Lake Avenue North
Albert Sherman Center, Room AS7.2049
Worcester, MA 01605
Patricia.cannon@umassmed.edu
508.856.3800

https://academicjobsonline.org/ajo/jobs/19314
As an equal opportunity and affirmative action employer, UMMS recognizes the power of a diverse community and encourages applications from individuals with varied experiences, perspectives, and backgrounds.

Perelman School of Medicine
University of Pennsylvania

Department of Physiology Faculty Positions

The Department of Physiology at the Perelman School of Medicine at the University of Pennsylvania seeks highly qualified candidates for faculty positions in the tenure track at the **Assistant** and **Associate Professor** ranks. Applicants must have a Ph.D. and/or M.D. or equivalent degree. Teaching responsibilities may include graduate and medical student instruction and training graduate students and postdoctoral fellows. Research responsibilities include developing a successful extramurally-supported research program. We seek investigators with demonstrated excellence in research grounded in fundamental mechanistic investigation that leverages molecular, biophysical, structural and cell-biological insights to inform physiological functions, particularly those emphasizing emerging areas, novel technologies, and interdisciplinary research.

Assistant Professor: Applicants in the early stage of career development are encouraged to apply. Apply online: **http://apply.interfolio.com/79065**

Associate Professor: Applicants are expected to have funding and an internationally recognized reputation of innovative research excellence and productivity, including high impact publications. Apply online: **http://apply.interfolio.com/79068**

The Perelman School of Medicine, one of the top ranked medical schools in the country for NIH funding, is a highly collaborative environment with state-of-the-art core facilities (https://www.med.upenn.edu/cores/), There are opportunities for appointments in numerous thematic institutes and centers (https://www.med.upenn.edu/psom/centers.html/), including the Cardiovascular Institute, Mahoney Institute for Neurosciences, Pennsylvania Muscle Institute, and Abramson Cancer Center. The School of Medicine is integrated within the campus of the University of Pennsylvania, a world-class institution with an easily walkable campus located near central Philadelphia. We seek candidates who embrace and reflect diversity in the broadest sense. The University of Pennsylvania is an EOE. Minorities/Women/Individuals with disabilities/Protected Veterans are encouraged to apply.

UT Southwestern Medical Center

TENURE-TRACK POSITION

The Department of Physiology invites outstanding scientists with Ph.D., M.D., or equivalent degrees to apply for tenure-track faculty positions at the level of **Assistant Professor**.

Candidates who bring innovative approaches to the study of any under-explored/unexplored questions broadly related to physiology are encouraged to apply. The scientific excellence of the candidates is more important than the specific area of research. These positions are part of the continuing growth of the Department at one of the country's leading academic medical centers. They will be supported by significant laboratory space, competitive salaries, state-of-the-art core facilities and exceptional start-up packages. The University of Texas Southwestern Medical Center is the scientific home to six Nobel Prize laureates and many members of the National Academy of Sciences and Institute of Medicine. UT Southwestern conducts more than 5,800 research projects annually totaling more than $524 million. Additional information about the Department of Physiology can be found at **http://www.utsouthwestern.edu/education/medical-school/departments/physiology/index.html**.

Information regarding careers can be found at:
https://jobs.utsouthwestern.edu/.

Applicants should submit a CV, a brief statement of current and proposed research, and a summary of your two most significant publications describing the importance of the work (100-150 words each). Please arrange to have three letters of recommendation sent on his/her behalf. All items should be submitted to: **http://academicjobsonline.org/ajo/jobs/19221**. Completed applications will be reviewed starting **November 1, 2021**. You may email questions to **ron.doris@utsouthwestern.edu**.

UT Southwestern Medical Center is an Equal Opportunity/Affirmative Action Employer. Women, minorities, veterans and individuals with disabilities are encouraged to apply.

MICHIGAN MEDICINE

FACULTY POSITIONS – BIOCHEMISTRY
DEPARTMENT OF BIOLOGICAL CHEMISTRY

The Department of Biological Chemistry at the University of Michigan Medical School invites applications for tenure-track or tenured faculty positions at the **Assistant/Associate/Full Professor** levels. We seek outstanding colleagues whose research addresses cutting-edge questions in any area of biochemistry to join an inclusive and supportive community that prioritizes transformative science along with training the next generation of scientific leaders.

Successful candidates will be part of an interactive and interdisciplinary environment with interests that span a wide range of molecular, cellular, and organismal systems. Qualifications include a Ph.D. and/or M.D., an excellent record of research accomplishments, and a strong commitment to diversity and inclusion in the biomedical sciences. Applicants for Associate and Full Professor should have a history of exceptional independent research, funding, and contributions to the scientific community. Further information about the Department is available at **http://www.biochem.med.umich.edu/**

Applications should include a cover letter, a curriculum vitae, a description of past and current research activities (up to 2 pages), a summary of future research plans (up to 2 pages), a summary of commitment to and plans for creating a diverse and inclusive scientific environment (1 page), and contact information including email address of three references. Materials should be addressed to Dr. Phyllis Hanson, Chair of Biological Chemistry and submitted via Interfolio at **http://apply.interfolio.com/91967**

Applications will be reviewed on a rolling basis with a deadline of **November 1, 2021** for full consideration. Please address any questions to Amanda Howard (**amanhowa@umich.edu**).

Michigan Medicine seeks to recruit and retain a diverse workforce as a reflection of our commitment to serve the diverse people of Michigan and to maintain the excellence of the University. We welcome applications from anyone who would bring additional dimensions to the University's research and teaching mission, including women, members of minority groups, protected veterans, and individuals with disabilities. The Department and the University are committed to a policy of nondiscrimination and equal opportunity for all persons and will not discriminate against any individual because of race, color, national origin, age, marital status, sex, sexual orientation, gender identity, gender expression, disability, religion, height, weight, or veteran status. The University of Michigan is an Equal Employment Opportunity/Affirmative Action Employer.

TEXAS A&M UNIVERSITY

Tenure-Track or Tenure Review Upon Hire (either)

Texas A&M University
College of Agriculture and Life Sciences
Department of Biochemistry and Biophysics
College Station, TX 77843

An **Assistant/Associate/Full Professor** with an emphasis in cryo-electron microscopy (cryoEM) or cryo-electron tomography (cryoET). This is a full-time nine-month, tenure-track or tenured position with research (65%), teaching (25%), and service (10%) responsibilities. The estimated start date is **August 1, 2022**.

GENERAL DUTIES AND RESPONSIBILITIES: The Department of Biochemistry and Biophysics, College of Agriculture and Life Sciences, at Texas A&M University, seeks applications for a full-time tenure-track/tenured position with a nine-month academic appointment beginning **August 1, 2022**. Applicants will be considered for the faculty titles of Assistant Professor, Associate Professor, or Professor depending on qualifications. The successful candidate will be required to develop and lead an independent, extramurally-funded, internationally recognized research program in biochemistry that extensively employs cryo-electron microscopy (cryoEM) or cryo-electron tomography (cryoET). A research emphasis in any area of biochemistry and biophysics is invited though preference will be given to topics in the areas of nucleic acid biochemistry, epigenetics or signaling. Responsibilities for this position also include teaching at both graduate and undergraduate levels, and service to the department, university, and the field, including outreach to industry.

RESOURCES: Texas A&M University is a public, land-grant institution with many high-quality academic units conducting research in the fields of biochemistry, biophysics and genetics across the life sciences. Recently, the university invested >$10M to purchase a Titan Krios G4i with a phase plate, equipped with a Gatan K3 direct detection camera with a BioContinuum imaging filter. This instrument will be housed in newly-renovated space within the Department of Biochemistry and Biophysics. The successful candidate will be offered a competitive salary, startup package and laboratory space with shared common-use equipment, within the Department of Biochemistry and Biophysics, Texas A&M AgriLife Research, the College of Agriculture and Life Sciences.

QUALIFICATIONS: A Ph.D. or equivalent degree in biochemistry, biophysics, or related field with a postdoctoral emphasis on cryo-EM or cryo-ET is required. Evidence of potential for developing an outstanding research program and indications of strong mentorship and teaching skills are required for consideration for an appointment at the Assistant Professor rank. Prior faculty-level experience, evidence of successful grantsmanship and graduate training, and outstanding research accomplishments are required for appointment at the Associate or Full Professor rank.

APPLICATION INSTRUCTIONS: Applicants must submit: **1)** a cover letter with a statement of the applicant's suitability for the position, **2)** a comprehensive curriculum vitae, **3)** a three-page statement of research plans, and **4)** a description of teaching philosophy, experience and planned strategies, **5)** a listing of contact information for three expert individuals who can provide a critical evaluation of the applicant's qualifications for the position at **apply.interfolio.com/93168**. Review of applications will begin **October 1, 2021**, and will continue until the position is filled.

For questions, email inquiries to Dr. Dorothy Shippen, Search Committee Chair, Department of Biochemistry and Biophysics, Texas A&M University, College Station, TX 77843-2128, **bcbpsearch@ag.tamu.edu**.

Equal Employment Opportunity Statement

Texas A&M University is committed to enriching the learning and working environment for all visitors, students, faculty, and staff by promoting a culture that embraces inclusion, diversity, equity, and accountability. Diverse perspectives, talents, and identities are vital to accomplishing our mission and living our core values.

Equal Opportunity/Affirmative Action/Veterans/Disability Employer committed to diversity.

ICGEB International Centre for Genetic Engineering and Biotechnology | Developing Knowledge

VACANCY NOTICE ND/GL/01-21

Applications are invited for positions of **Group Leaders/Scientists** at International Centre for Genetic Engineering and Biotechnology (ICGEB), New Delhi Component.

ICGEB is an international intergovernmental organization with components at Trieste (Italy), New Delhi (India) and Cape Town (South Africa). ICGEB is a Centre of Excellence for research and training in biotechnology addressing issues of the developing world and works under United Nations Common System. It has a high scientific reputation worldwide reflected in its many contributions to fundamental research and its translational impact. ICGEB, New Delhi has about two dozen independent groups working in three broad domains; Molecular Medicine, Plant Biology and Integrative Biology (Further information: **http://www.icgeb.org**).

Applicants can be of any nationality and must have an excellent record of research/ publications in any area of modern biology and biotechnology. While highly competent candidates under any of the research mandates of ICGEB, New Delhi will be considered, expertise in virology concerning new and emerging diseases is being currently preferred. Ability and commitment to build a dynamic program of international stature is essential. Incumbent must have significant accomplishments commensurate with their career stage and should have proven ability to compete for extramural national/international funding and head a successful research laboratory. Evidence of independent research achievements, ability to guide Ph.D. students and teach Ph.D. level courses as well as post-Ph.D. level training programmes will be an asset. ICGEB New Delhi provides competitive and supportive research environment and state-of-the-art facilities, as well as attractive employment packages linked to experience and achievements. Applicants should submit their curriculum vitae, a statement of research interests and names and addresses of three referees to The Director, ICGEB, Aruna Asaf Ali Marg, New Delhi-110 067, INDIA. Additionally, applicants should submit their full CV by completing the ICGEB's Personal History Form available online at: **https://www.icgeb.org/about-us/work-with-us/** and address it to email id: **icgeb.director@gmail.com**.

LSA Molecular, Cellular and Developmental Biology University of Michigan

UNIVERSITY OF MICHIGAN FACULTY POSITION IN PLANT BIOLOGY or NEUROSCIENCE

The Department of Molecular, Cellular, and Developmental Biology (MCDB) in the College of Literature, Science and the Arts at the University of Michigan solicits applications for a faculty position at the **assistant professor** level, but appointment at a more senior level is possible for applicants with suitable experience. The faculty position will be tenured or tenure track with a university year appointment starting **August 29, 2022** or **January 1, 2023**. Successful candidates will be expected to establish a vigorous, extramurally-funded research program and to be involved in instruction of both undergraduate and graduate students.

We welcome applications from outstanding biologists in the broad areas of plant biology and neuroscience. Experimental approaches may include (but are not limited to) genetics, genomics, structural biology, enzymology, physiology, in vivo imaging, and single cell technologies. For further information about MCDB research areas and the goals of this faculty search, please visit **www.lsa.umich.edu/mcdb**.

All applications must be submitted on-line at **https://webapps.lsa.umich.edu/Apply/MCDB21**.

You will be asked to upload the following materials: A cover letter, a curriculum vitae, a brief summary of recent research accomplishments and statement of future research plans, a statement of teaching interests and philosophy. Also include a personal statement that describes your demonstrated commitment to diversity, equity, and inclusion through scholarship/research, and/or teaching/mentoring, and/or service/engagement (this statement may overlap with your teaching statement). Candidates for appointment as an assistant professor should provide names and contact information for at least three references, as instructed in the on-line application form. To ensure full consideration, all materials should be received by **November 1, 2021**.

Highly qualified applicants are also encouraged to apply to the College of Literature, Science, and the Arts' Collegiate Fellowship Program (**https://lsa.umich.edu/ncid/fellowshipsawards/lsa-collegiate-postdoctoral-fellowship.html**), and the university's Presidential Postdoctoral Fellowship Program (**https://presidentspostdoc.umich.edu/**), both of which provide for an optional fellowship period before transitioning onto the tenure track.

Women and underrepresented minorities are encouraged to apply. The University of Michigan is supportive of the needs of dual career couples and is an equal opportunity/affirmative action employer.

USDA ARS Agricultural Research Service www.ars.usda.gov

Supervisory Research Molecular Biologist/ Geneticist

Research Leader (Center Director)
Plant Gene Expression Center
Albany, CA

The U.S. Department of Agriculture, Agricultural Research Service, Plant Gene Expression Center (PGEC) in Albany, California invites applications for a permanent, full time **Supervisory Research Molecular Biologist/ Geneticist** who will serve as the Research Leader (Center Director) for the program. The successful candidate will have expertise in plant molecular biology and/or plant genetics, and will be responsible for developing a research program in predictive agriculture that combines aspects of genomics and genetics, molecular biology, physiology, biochemistry, and/or metagenomics with computational biology to generate new tools for breeding that improve performance of agricultural crops. Areas of research interest include enhancing plant productivity, adaptation to climate change, biotic and/or abiotic stress tolerance, signal transduction, plant metabolism, and plant-microbiome interactions. The PGEC is a world-renowned institute that conducts foundational and translational plant biology research to improve agriculture. The candidate will direct PGEC research as a whole, hire and mentor new scientists, and manage resources. PGEC research is conducted through a close collaborative partnership with the University of California, Berkeley, where PGEC scientists have the opportunity for Adjunct Faculty status in the Department of Plant and Microbial Biology. The salary range is **$132,822.00 to $172,500.00** per year. A comprehensive Federal benefits package is available.

For more details and to apply, please visit **USAJOBS.gov, Announcement Number ARS-D21Y-11193664-AF.** Open period is from **Friday, September 3, 2021 to Friday, October 1, 2021**. If you have questions, please contact Dr. Jennifer Lewis at **jennifer.lewis@usda.gov**. For information about the PGEC visit **https://www.ars.usda.gov/pacific-west-area/albany-ca/pgec/**.

U.S. Citizenship is required.
The USDA/ARS is an Equal Opportunity Employer and Provider.

Who's the top employer for 2020?

Science Careers' annual survey reveals the top companies in biotech & pharma voted on by *Science* readers.

Read the article and employer profiles at sciencecareers.org/topemployers

Science 2020 TOP EMPLOYER



BOSTON UNIVERSITY

FACULTY POSITIONS IN
VIROLOGY & IMMUNOLOGY
Department of Microbiology
Boston University School of Medicine

The Department of Microbiology (**www.bumc.bu.edu/microbiology**) invites applications for multiple positions at **Assistant** or **Associate Professor** level. We invite applicants with broad research interests in virology and in immunology, with an emphasis on virus-host interactions. The successful applicant will join a collaborative, vibrant, and growing community of researchers in an environment that values creativity, collaboration and social and cultural diversity of our faculty, staff and students. The successful applicant will expand and complement existing departmental strengths in virology, host–pathogen interactions, innate immunity and inflammation. Applicants should have a demonstrated and ongoing record of research excellence with a focus that includes basic or translational studies on investigating virology and/or immune responses to human pathogens. The Boston University Medical Campus includes a number of centers of excellence which offer rich collaborative opportunities, including the Center for Regenerative Medicine, the Center for Network Systems Biology, the National Emerging Infectious Diseases Laboratories, a T32 training grant in Immunology and supports state-of-the-art core facilities. The successful candidate is expected to oversee a vigorous, innovative, and extramurally funded research program, to participate in the training of graduate students and post-doctoral fellows and the teaching activities of the department, and support our institutional commitment to ensure BU is inclusive, equitable, diverse and a place where all constituents can thrive.

To be considered, please submit a curriculum vitae, a summary of research accomplishments and future research goals, brief teaching and diversity statements, and contact information to solicit at least 3 letters of recommendation to Ms. Kathleen Marinelli (**kfurness@bu.edu**). Applications will be considered as they are received, with the positions to be filled during this academic year, beginning after **January 1, 2022**.

Boston University School of Medicine is an equal opportunity/affirmative action employer, committed to building and maintaining robust diversity within all components of its community, and strongly welcomes applications from women, persons with disabilities, protected veterans, and under-represented minorities.

UNIVERSITY of ROCHESTER

The Department of Chemistry invites applications for a tenure track **Assistant Professor** in the areas of experimental Organic and Physical Chemistry, broadly defined. Interdisciplinary areas such as (but not limited to) chemical biology, bioorganic and biophysical chemistry, and chemistry applied to quantum information are especially encouraged. Applications are at the Assistant Professor level for a position starting **July 1, 2022** or later. Candidates are expected to have a PhD, establish an outstanding program of original research and be an effective teacher at the graduate and undergraduate levels. Application materials to include curriculum vitae, statement of research interests and plans, statement of teaching, and a statement including commitment to advancing equity and fostering an inclusive and diverse community in academia should be submitted online at **http://www.rochester.edu/faculty-recruiting/positions**.

Questions may be sent to **facrec@chem.rochester.edu**. Review of completed applications will begin on **October 1, 2021**.

The University of Rochester has a strong commitment to diversity and actively encourages applications from candidates from groups underrepresented in higher education.

The University is an Equal Opportunity Employer: EOE Minorities/Females/Protected Veterans/Disabled.

McGOVERN INSTITUTE

CALL FOR NOMINATIONS:

SCOLNICK PRIZE IN NEUROSCIENCE

The McGovern Institute for Brain Research is accepting nominations for the **18th annual Edward M. Scolnick Prize in Neuroscience**. The Prize recognizes an outstanding discovery or significant advance in the field of neuroscience. The prize is **$150,000**. The recipient presents a public lecture at MIT, hosted by the McGovern Institute and followed by a dinner in Spring 2022.

Nomination Deadline: **December 15, 2021**

Nomination procedures:
Candidates for the award must be nominated by individuals affiliated with universities, hospitals, medicals schools, or research institutes, with a background in neuroscience. Self-nomination is not permitted. Each nomination should include:

- A biosketch or CV of the nominee.
- A letter of nomination with a summary and analysis of the major contributions of the nominee to the field of neuroscience.
- Up to two representative reprints will be accepted.

Selection Procedure:

- Members of the selection committee and faculty affiliated with MIT are not eligible.
- Announcement of the award recipient will be made in January 2022.
- Recipient must attend all events to be awarded the prize.

Past Scolnick Prize Recipients:
2020: Joshua Sanes, Harvard University; **2019:** Richard Huganir, Johns Hopkins University; **2018:** David J. Anderson, HHMI, Caltech; **2017:** Catherine Dulac, HHMI, Harvard University; **2016:** Cornelia Bargmann, HHMI, The Rockefeller University; **2015:** Charles Gilbert, The Rockefeller University; **2014:** Huda Zoghbi, HHMI, Baylor University; **2013:** Thomas Jessell, HHMI, Columbia University; **2012:** Roger Nicoll, UCSF; **2011:** Bruce McEwen, The Rockefeller University; **2010:** Lily and Yuh-Nung Jan, UCSF; **2009:** Jeremy Nathans, Johns Hopkins University; **2008:** Michael Davis, Emory University; **2007:** David Julius, UCSF; **2006:** Michael Greenberg, Children's Hospital/HMS; **2005:** Judith Rapoport, NIH; **2004:** Masakazu Konishi, CalTech

Send nomination packet to:
gwolf@mit.edu or
Attn: **Scolnick Prize Nomination**
McGovern Institute for Brain Research
Massachusetts Institute of Technology
77 Massachusetts Avenue 46-3160
Cambridge, MA 02139

UCONN
UNIVERSITY OF CONNECTICUT

FACULTY POSITION IN STRUCTURAL BIOLOGY, BIOCHEMISTRY & BIOPHYSICS

The Department of Molecular and Cell Biology at the University of Connecticut's main campus in Storrs invites applications for a tenure-track position at the rank of **Assistant Professor** in the area of Structural Biology, Biochemistry & Biophysics with an anticipated start date in **August 2022**.

We are particularly interested in candidates who address important questions related to the molecular mechanisms of viral infection and pathogenicity using structural biology, biophysical or biochemical approaches.

For details on the position, qualifications, and application instructions please visit **https://academicjobsonline.org/ajo/jobs/19395**.

Questions about the position can be addressed to Dr. Eric May, Chair of the Search Committee (**eric.may@uconn.edu**).

The University of Connecticut is an EEO/AA Employer.

UCONN
UNIVERSITY OF CONNECTICUT

FACULTY POSITION IN MICROBIOLOGY

The Department of Molecular and Cell Biology at the University of Connecticut's main campus in Storrs invites applications for a tenure-track position at the rank of **Assistant Professor** in the area of microbiology with an anticipated start date in **August 2022**.

We are particularly interested in candidates who address important questions in the fundamental aspects of metabolomics, physiology, or systems microbiology.

For details on the position, qualifications, and application instructions please visit **https://academicjobsonline.org/ajo/jobs/19394**.

Questions about the position can be addressed to Dr. Jonathan Klassen, Chair of the Search Committee (**jonathan.klassen@uconn.edu**).

The University of Connecticut is an EEO/AA Employer.

ScienceCareers online @sciencecareers.org

ScienceCareers
FROM THE JOURNAL SCIENCE AAAS

Confused about your next career move?

Download Free Career Advice Booklets!

ScienceCareers.org/booklets





Clinician Scientist Group Leader

RESEARCH
This is primarily a research position aiming to deliver the Crick's mission of 'Discovery without Boundaries.' As such there is no limit on the field of interest beyond its broad alignment with biomedical discovery. It is anticipated that the post holder will:

- Plan, develop and direct an independent research programme of the highest quality
- Recruit and supervise research staff and facilitate their career development
- Manage laboratory resources efficiently and effectively
- Compete successfully for external research funding (though the Crick will provide substantial support from its core resources, it is anticipated the Crick Clinician Scientists will build on this through applications to external funding bodies)
- Build collaborative research programmes with investigators at the Crick, the partner University and beyond

CLINICAL MEDICINE
One aim of this initiative is to develop the medical perspective of discovery science at the Crick. In line with this it is anticipated that the post holder will:

- Actively contribute to general scientific discourse at the Crick, particularly as it relates to clinical medicine
- Maintain a license to practice in accordance with GMC regulations

(Note that there is no specific stipulation as to the extent of clinical activity and it is understood that this may vary with specialty and research field. However within the basic funding structure this should not exceed 8 hours per week. Beyond this, additional clinical work will require agreement and bespoke co-funding with the partner University and associated NHS Trust).

EDUCATION, LEADERSHIP, CITIZENSHIP
- Participate fully in mentoring and career development particularly in relation to clinicians undergoing research training
- Participate in development of operational structures that enhance medicine at the Crick
- Promote and advance the reputation of the Crick and the partner University with clinicians, scientists and the public
- Participate and contribute to Public Engagement activities of the Crick and the university as required
- Comply with the Health and Safety policies and fulfil the safety responsibilities required of a research supervisor

PERSON SPECIFICATION
- A higher degree (PhD or equivalent) in a relevant field
- A medical degree and GMC license to practice medicine
- Certificate of completion of general and specialist medicine training (GMC or equivalent)
- Successful experience in planning and directing an established research programme
- Ability to communicate well, convey ideas and concepts clearly and effectively
- Growing reputation in the field of research demonstrated through publications and conference presentations
- To have developed a strong and distinctive research vision
- To have the potential to provide academic leadership

RECRUITMENT PACKAGE
The Crick offers a competitive package including:

- Full personal salary costs for a 6-year period. This can be renewed up to a maximum of 12 years following successful review. A competitive salary allows the Group leaders protected time to fully concentrate on their research, training and development. GLs may undertake a maximum of two clinical sessions a week.
- Salaries and consumables for up to five people, including graduate students. Research groups will have the opportunity to expand based on external grants.
- Fully equipped laboratory space for a team of up to 5 researchers. Further space for up to 6 researchers may be allocated on award of external funding.
- Expenses, travel costs and capital equipment appropriate for the research project.
- Access to its core-funded state-of-the-art science technology platforms (**https://www.crick.ac.uk/research/science-technology-platforms**).

Florida State University
Department of Chemistry and Biochemistry

ASSISTANT PROFESSOR ANALYTICAL or EXPERIMENTAL PHYSICAL CHEMSITRY
The Department of Chemistry and Biochemistry at Florida State University seeks to fill a tenure-track faculty position at the rank of **Assistant Professor** in Analytical or Experimental Physical Chemistry. Applicants developing or using advanced measurement technologies are especially encouraged to apply. The successful candidate will be expected to develop an internationally recognized and externally supported research program in addition to teaching both undergraduate and graduate courses. Applicants should upload application materials, including a cover letter, CV, a research prospectus, and a combined diversity and teaching statement at **http://jobs.fsu.edu (job ID 49869)**. In addition, applicants should arrange for three letters of recommendation to be sent by email to **facultysearch@chem.fsu.edu** to complete the application.

ASSISTANT PROFESSOR DATA DRIVEN CHEMISTRY AND BIOCHEMISTRY
The Department of Chemistry and Biochemistry at Florida State University seeks to fill a tenure-track faculty position at the rank of **Assistant Professor** in the broad area of data driven molecular science. Applicants who are interested in developing, customizing, and applying state-of-the-art data science technologies to solve cutting-edge chemical or biochemical problems are strongly encouraged to apply. Candidates would be expected to develop an internationally recognized and externally supported research program, as well as teach chemistry or biochemistry courses at both undergraduate and graduate levels. Candidates should upload application materials, including a cover letter, CV, a short research prospectus, a combined diversity and teaching statement at **http://jobs.fsu.edu (job ID 49861)**, and should arrange for three letters of recommendation to be sent by email to **facultysearch_datascience@chem.fsu.edu**.

ASSISTANT PROFESSOR BIOCHEMISTRY
The Department of Chemistry and Biochemistry at Florida State University seeks to fill a tenure-track faculty position at the rank of **Assistant Professor** in the broad area of biochemistry. Applicants seeking experimental approaches towards impactful problems at the interface of chemistry, biology and medicine are especially encouraged to apply. The successful candidate will be expected to develop an internationally recognized and externally supported research program in addition to teaching courses at undergraduate and graduate levels. Candidates should upload application materials, including a cover letter, CV, a short research prospectus, a combined diversity and teaching statement at **http://jobs.fsu.edu (job ID 49858)**, and should arrange for three letters of recommendation to be sent by email to **facultysearch_biochemistry@chem.fsu.edu**

Review of applications will begin on **October 15, 2021** and close on **January 15, 2022**.

Florida State University is an Equal Opportunity/Access/ Affirmative Action/Pro Disabled & Veteran Employer. Florida State University's equal opportunity statement can be viewed at: ***http://www.hr.fsu.edu/PDF/Publications/diversity/EEO_Statement.pdf***

SOMETIMES THE GRASS REALLY IS GREENER SOMEPLACE NEW.



Find your next job at ScienceCareers.org

There's scientific proof that when you're happy with what you do, you're better at what you do. Access career opportunities, see who's hiring and take advantage of our proprietary career-search tools. Get tailored job alerts, post your resume and manage your applications all in one place: sciencecareers.org

ScienceCareers

FROM THE JOURNAL SCIENCE AAAS

HOWARD HUGHES MEDICAL INSTITUTE

2022 Hanna H. Gray Fellows Program

hhmi

The Howard Hughes Medical Institute (HHMI) is pleased to announce the 2022 Hanna H. Gray Fellows Program competition. This program seeks to increase diversity in biomedical science by recruiting and retaining individuals from groups underrepresented in the life sciences. Through their successful careers, HHMI Hanna Gray Fellows will inspire future generations of scientists from America's diverse talent pool.

Fellows will receive funding for their postdoctoral training and may continue to receive funding during their early career years as independent faculty. The program includes opportunities for career development, including mentoring and active involvement in the HHMI scientific community. The Institute will select and support up to 15 fellows in this competition.

This grant competition is open to all eligible applicants and no nomination is required. The competition opens August 4, 2021.

Eligibility:
The program is open to individuals who:

- are from gender, racial, ethnic, and other groups underrepresented in the life sciences, including those individuals from disadvantaged backgrounds.
- hold a PhD and/or MD (or equivalent), which must be conferred by the start of the grant term.
  - U.S. citizens must have a degree from a research institution in the U.S. (including Puerto Rico) or an international research institution.
  - Non-U.S. citizens and applicants with other nationalities must have a degree from a research institution in the U.S. (including Puerto Rico).
- have no more than 27 months of postdoctoral research experience at the time of the application due date.

Applications are due on December 1, 2021. Mentor and reference letters must be received by December 8, 2021.
Further details: https://www.hhmi.org/hgf or contact fellows@hhmi.org.

UCLA

RISING TO THE CHALLENGE

TWO FACULTY POSITIONS IN NEUROSCIENCE

UCLA is recruiting two tenure-track faculty at the **Assistant Professor** level in the field of Neuroscience. One position is in the David Geffen School of Medicine with an appointment in the Department of Neurobiology and the other position is in the College of Letters and Science, Division of Life Sciences with a split appointment in the Department of Integrative Biology & Physiology and the Institute for Society and Genetics. Successful candidates will be evaluated by the respective units/departments in which they are appointed. These positions were created in partnership with the Ralph J. Bunche Center as part of the campus-wide effort to rise to the challenge expanding scholarship in the areas of racial and social justice at UCLA, sponsored by the Office of the Chancellor and the Executive Vice Chancellor & Provost. Both appointments have the opportunity to be affiliated with the UCLA Brain Research Institute.

We seek candidates whose research addresses fundamental biological, environmental, or social mechanisms influencing the nervous system that affect health, well-being, resilience, and/or physiology in Black individuals and communities living in a racialized society. Successful candidates will exhibit interdisciplinary skills and aspire to work at the intersection of neuroscience, biology, and society. Preference will be given to applicants who have strong academic scholarship, potential for joining or leading initiatives that address the health of Black communities and a strong record/potential for mentoring trainees from diverse backgrounds.

Applicants must have a Ph.D., M.D., or equivalent degree in any relevant discipline and are encouraged to apply one or both positions. For the latter, the same documents may be uploaded to both links. To apply, candidates are directed to the website **https://recruit.apo.ucla.edu** where they will be able to search for the position under **JPF06811** and **JPF06815**. The following materials are required: **1)** full curriculum vitae; **2)** a description of research plans (≤ 3 pages); **3)** a statement on teaching, mentoring, and community engagement (1-2 pages); **4)** a statement on contributions to equity, diversity, and inclusion (1-2 pages); **5)** 3-5 letters of reference. Review of applications will begin on **October 8, 2021** and continue until the position is filled. We highly encourage applications from women, underrepresented minorities, and individuals with a commitment to mentoring underrepresented groups in the sciences.

Selected applicants will be invited to present their research at a 2-day symposium at UCLA on **December 13 and 14, 2021**.

Cultural North Star: The shared values of the David Geffen School of Medicine (DGSOM) are expressed in the Cultural North Star, which was developed by members of our community and affirms our commitment to doing what's right, making things better, and being kind. These are the standards to which we hold ourselves, and one another. Please read more about this important DGSOM program at **https://medschool.ucla.edu/cultural-north-star**.

Anti-racism Roadmap: The David Geffen School of Medicine Anti-racism roadmap is our co-created path to ensuring racial justice, equity, diversity and inclusion. We are committed to actively dismantling structural racism in our organization as described in more detail at **https://medschool.ucla.edu/diversity-anti-racism-roadmap**.

The University of California is an Equal Opportunity/Affirmative Action Employer. All qualified applicants will receive consideration for employment without regard to race, color, religion, sex, national origin, disability, age, sexual orientation, gender identity, or protected veteran status. For the complete University of California nondiscrimination and affirmative action policy see: UC Nondiscrimination & Affirmative Action Policy. ***(http://policy.ucop.edu/doc/4000376/NondiscrimAffirmAct)***.

By **Nasreen Choudhury**

On my own but not alone

When I stumbled on the advertisement for the symposium, I couldn't wait to tell my colleagues. It looked like a great day of presentations highly relevant to our research, and I expected they would be eager to attend with me. To my disappointment, no one was interested. A year earlier, when I had just left my home country for a postdoc, I would not have considered going alone. Whom would I talk to and sit with? I would have spent the entire meeting feeling awkward and self-conscious, unable to focus on the science or networking opportunities. But I had grown. I had gained the confidence to strike out on my own.

I have never been a very self-assured person. Leaving India for the United Kingdom to pursue my research career, I felt more out of place than ever before. At work, I shied away from engaging in discussions or putting forward my opinions. I was afraid my colleagues would see through my sham strength and realize how weak I really felt. Some mornings, just stepping out of my room and going into the lab seemed a herculean task.

Socializing didn't help, as I constantly feared committing social blunders. I craved new experiences, but my insecurities stymied me. I started to keep more and more to myself.

That began to change after a quiet breakdown in the lab prompted me to contact the university's mental health services. The counselor suggested I attend a nearby concert by a famous singer from my home country. I couldn't miss it. So, there I was in the packed concert hall, surrounded by strangers—all of us clapping and singing along to the familiar songs. It was an exhilarating triumph, and it proved to be a turning point.

I began to do more things alone, including going out for ice cream and to the movies. Eventually, I planned a day trip to a picturesque city a few hours away. On the train, I worried I looked out of place. But once I arrived, as I listened to a church choir, took pictures of the beautiful surroundings, and enjoyed a lemonade, I realized nobody was really paying any attention to me. I didn't need to be self-conscious. I could do whatever I wanted, and nobody would care.

My confidence and self-sufficiency grew as I enjoyed more local day trips, and soon I wanted to venture farther away. I decided on a multiday solo hiking and sightseeing trip to the Alps. At first, I hesitated to join the chance conversations with strangers that sprang up on the train, at common tables in restaurants, and on guided city tours. But eventually, I started to enjoy listening to others' stories and telling mine.



"Solo traveling ... taught me that I have the competence to grow and succeed."

My growing self-confidence carried over to work, where I started to speak up and put forward my opinions. I offered to help colleagues design and troubleshoot experiments. I began to ask questions during departmental meetings (though I still framed and reframed each question in my mind beforehand). It felt reassuring that those questions often initiated healthy scientific discussions. I finally felt like a significant, active member of the group.

So, when that symposium came around, I felt comfortable registering to attend on my own—and I'm so glad I did. Not only did I meet the speakers, but I also made a point of introducing myself to other attendees and industry representatives, visiting their booths, chatting about their products, and asking them about their roles and career trajectories. The encounters inspired me to critically evaluate my own professional interests.

That was 3 years ago. Since then, I have had the confidence to move countries again, enthusiastic about new opportunities in the United States. I have also reached out to and built ties with several nonacademic connections who have mentored me in my search for a new professional role. Solo traveling did not give me any magical powers. But it taught me that I have the competence to grow and succeed, just like everyone around me, and it helped me shed the weight of self-doubt that used to hold me back. ■

Nasreen Choudhury is a postdoctoral fellow at the Rush University Medical Center. Send your career story to SciCareerEditor@aaas.org.

ILLUSTRATION: ROBERT NEUBECKER



Pushing the Boundaries of Knowledge

As AAAS's first multidisciplinary, open access journal, *Science Advances* publishes research that reflects the selectivity of high impact, innovative research you expect from the *Science* family of journals, published in an open access format to serve a vast and growing global audience. Check out the latest findings or learn how to submit your research: **ScienceAdvances.org**

Science Advances
AAAS

GOLD OPEN ACCESS, DIGITAL, AND FREE TO ALL READERS

SAMSUNG



The Samsung Ho-Am Prize was established in 1990 to honor both the philosophy of putting people first and the spirit of public service originally championed by "Ho-Am" Byung-chull Lee (1910-1987), the founder of Samsung. The Prize is awarded annually to outstanding researchers of Korean heritage around the world who have made imprtant contributions to the advancement of science.

The Samsung Ho-Am Prize ignites the passion and innovative spirit for scientific discovery

We welcome your recommendations for the 2022 Samsung Ho-Am Prize candidates.

- Award Categories : **Physics & Mathematics, Chemistry & Life Sciences, Engineering, Medicine**
- Candidate Qualifications : Researchers of Korean heritage
- Nomination Deadline : Oct. 31, 2021

  *Learn more about the prize and nomination : **www.hoamfoundation.org**

HOAM
THE HO-AM FOUNDATION